Teleportation from quantum networks to traversable wormholes: the physics and technology of entanglement

Thesis by
Samantha Isabel Davis

In Partial Fulfillment of the Requirements for the
Degree of
Doctor of Philosophy

CALIFORNIA INSTITUTE OF TECHNOLOGY
Pasadena, California

2026
Defended June 9, 2025

Samantha Isabel Davis
ORCID: 0000-00001-9994-8165

ACKNOWLEDGEMENTS

This thesis is dedicated to my parents, Rick and Maribel,
and those I've lost along the way: Sony, Thorin, and Deborah.

My time at Caltech has been one of the most challenging and rewarding chapters of my life. First and foremost, I must thank my advisor, Prof. Maria Spiropulu: my gratitude is ineffable. Thank you for your mentorship, leadership, and for providing an amazing environment for me to pursue my ambitious research goals, take risks, and learn from experts across diverse disciplines and institutions through the INQNET collaboration. INQNET has been a crucible for me to forge my path at the intersection of fundamental and applied physics, and I'm excited for the future ahead. Thank you to Dr. Raju Valivarthi, Dr. Neil Sinclair, and Dr. Nikolai Lauk for your training, guidance, friendship, and support. A special thank you to Dr. Raju Valivarthi and Lautaro Narváez who taught me nearly everything I know in the lab, and Dr. Neil Sinclair who opened my eyes to the breadth of literature and provided support and encouragement throughout challenging times of my research. Thank you to my mentors and collaborators at NASA-JPL, Fermilab, Harvard, and MIT, including Dr. Matt Shaw, Prof. Boris Korzh, Dr. Ioana Craiciu, Dr. Cristián Peña, Dr. Si Xie, Dr. Joe Lykken, Dr. Panagiotis Spentzouris, and Prof. Daniel Jafferis. Thank you to my lab mates, Dr. Andrew Mueller, Prathwiraj Umesh, Dr. Jamie Luskin, Dr. Christina Wang, Dr. Olmo Cerri, Michael Breggar, Ray Wynne, Ludovico Morri, Tommy Sievert, Elise Sledge, and Alex Albert who have been a source of great company, encouragement, and support, especially towards the end of my Ph.D. Thank you to Volkan Gurses for your partnership on quantum phased arrays. Together we overcame challenges beyond what I imagined was possible. Thank you Prof. Ali Hajimiri for allowing me to conduct this research in your laboratory and for your support and mentorship. One of the pleasures of my Ph.D. has been to travel around the world for conferences and collaborations. Thank you to Tracy Sheffer, lab administrator extraordinaire, for managing all my complicated conference and travel expenses!

Beyond Caltech, I've had the privilege of having multiple mentors throughout my academic career. Thank you to Prof. Kathryn Moler, my first physics professor at

Stanford, for allowing me to conduct research in your lab starting my first year of undergrad. My time in your group launched my physics career and your ongoing mentorship and guidance has been indispensable in my academic journey. Thank you to Dr. John Kirtley for putting up with me as a pesky undergraduate research assistant and showing me how to conduct the highest standard of experimental physics research. Thank you to Dr. Babette Dobrich and Prof. Tien-Tien Yu for your mentorship at CERN and introducing me to the world of fundamental physics research. Thank you also to Prof. Mehul Malik at Herriot-Watt University and Prof. Tim Bartley for the interesting discussions and your support of my work on photon number resolving superconducting nanowire detectors.

Although my Ph.D. took place over five and a half years at Caltech, it was truly an effort 28 years in the making. I'm extremely grateful to everyone in my life who has encouraged and supported my life-long dream of becoming a physicist. Thank you to my parents, Rick and Maribel, for instilling a love of nature, scientific curiosity and a passion for learning from a young age. Dad: your infectious love of learning, encouragement to ask deep questions, advice, and enthusiasm over broad range of topics, shaped me into the person and scientist I am today. Mom: your resilience, tenacity and unwavering support have been a source of inspiration and strength. Thank you for always being a call away.

Thank you to my extended family in Puerto Rico, Oklahoma, and the West Coast. A special thank you to the Smith family for hosting me during the last couple of months leading up to my defense. Thank you Tracy and Charlie for welcoming me to your home, and thank you Scottie for letting me use your room during dissertation writing!

Thank you to my surrogate family from around the world. Gracias a Ana Arauco, mi segunda madre, por su amor, su apoyo y sus bendiciones desde Perú. Gracias a la familia Jiménez en Costa Rica. Thank you to the Rubin-So family (Conrad, Cathy, Jeremy, and Benjamin) and the Arnoff-Fenn's (George and Paige) for the stimulating discussions at our yearly New Year's gatherings, your investment in my physics journey, and encouragement of my academic pursuits. A special thank you to Paige for your career mentorship, advice and support.

My Ph.D. journey has been a rollercoaster of immense personal and intellectual growth, sometimes at dizzying speeds, featuring some of the lowest lows and highest highs I've yet experienced. Setbacks, obstacles, and unexpected losses were at times sobering and hard lessons to take. Aunt Deborah, Titi Sony, and primo Thorin:

thank you for your indomitable spirit and teaching me how to face insurmountable challenges with integrity and grace. Thank you for supporting and encouraging to pursue my dreams for as long as I could remember. I miss you all dearly.

My fondest memories of graduate school include the new and rekindled friendships I made along the way. Thank you to Riku Fukumori, Steven Bulfer, Dr. James Williams, and Dr. Robby Gray for the fun times rallying for quantum electronics problem sets, hanging out, and going on camping and beach trips. Thank you to my bouldering buddy, Kyle Gulshen, and the Strassle family (Laura, Phil, Camila, Carmen, and Nico) for supporting me and welcoming me to your home for dinners, Thanksgiving, and social gatherings.

One of the unexpected joys of my graduate experience was digging into my roots, getting back into old hobbies and discovering new ones. Thank you to Fiona Yonkman for being my outdoor bestie and helping me get back into hiking, backpacking, and mountaineering. Thank you to Ray, Ludo, and Juliette Whiteside for helping me get back into skiing and mountaineering and teaching me how to surf. Thank you to Vassilios Kaxiras for matching my adventurous energy and for keeping me accountable training for trail running and skiing!

Last but not least, thank you to my friends from another species: Potatoes the cat, who supported me during challenging times; Indigo Smith, the adorable golden doodle, my second cousin and best friend during thesis writing; and Qubit Khal Van Drogo the Jack Russell terrier, my fairy godson and an endless source of joy, shock, and amusement.

ABSTRACT

This thesis presents developments in quantum information technologies and their applications to both quantum networks and fundamental physics. It is organized into three parts. Part I focuses on the design and implementation of state-of-the-art sources and detectors for quantum networks. Key contributions include the development of photon-number-resolving superconducting nanowire detectors and their application to heralded single-photon generation and photon-number discrimination; a high-rate multiplexed entangled photon-pair source for quantum key distribution; and on-chip balanced homodyne detectors for the detection of squeezed light. I describe how phased arrays can facilitate wireless quantum communications by introducing the concept of "quantum phased arrays" and present the first large-scale optoelectronic phased array receiver on a chip capable of interfacing with nonclassical light, with first demonstrations of coherent imaging and beamforming of squeezed states of light. Part II details the construction of quantum network testbeds at Caltech and Fermilab, designed to realize scalable architectures for the quantum internet. These systems demonstrate high-fidelity quantum teleportation over 45 km of optical fiber and entanglement swapping with time-bin qubits. The experiments are supported by the development of theoretical models that guide system optimization. I also present demonstrations of entanglement distribution at Caltech and remote sites at Fermi and Argonne National Labs with picosecond-level clock synchronization, representing milestones toward the deployment of quantum networking infrastructure across national laboratories. Part III investigates how quantum networks can be used to probe fundamental questions in physics. I report the first experimental generation of GHZ states with time-bin qubits, towards the deployment of multipartite entanglement distribution in real-word networks for tests of quantum mechanics and distributed sensing. Finally, I present the first experimental realization of a traversable wormhole teleportation protocol implemented on a quantum processor, a step in the program of quantum gravity in the lab. I conclude with an outlook and discuss future directions of this work.

PUBLISHED CONTENT AND CONTRIBUTIONS

[1] Samantha I. Davis, Joseph Lykken, Damian Musk, Neil Sinclair, and Maria Spiropulu. "Wormhole regenesis and Bell violations." In: Manuscript in preparation. (2025).
S.I.D. conceived the project and developed all theory.

[2] Samantha I. Davis, Prathwiraj Umesh, Ioana Craiciu, Raju Valivarthi, Boris Korzh, Matthew Shaw, and Maria Spiropulu. "Photon number resolution with superconducting nanowire arrays." In: Manuscript in preparation. (2025).
S.I.D. conceived the project and models, collected data, performed all theoretical work, and wrote the manuscript.

[3] Samantha I. Davis, Raju Valivarthi, Andrew Cameron, Cristian Pena, Si Xie, Lautaro Narváez, Nikolai Lauk, Chang Li, Kelsie Taylor, Rahaf Youssef, et al. "Entanglement swapping systems toward a quantum internet." In: arXiv preprint arXiv:2503.18906. Submitted. (2025).
S.I.D. performed all experimental work, led and conducted theoretical modeling, performed all data analysis, and wrote the manuscript.

[4] Volkan Gurses, Samantha I. Davis, Raju Valivarthi, Neil Sinclair, Maria Spiropulu, and Ali Hajimiri. "An on-chip phased array for non-classical light." In: Nature Communications 16.1 (2025), p. 6849.
S.I.D. conceived of all ideas, designed and built the experiment, developed the theory, performed all measurements, developed the analytical methods, performed the data analysis, and wrote the manuscript.

[5] Neil Sinclair, Samantha I. Davis, Nikolai Lauk, Chang Li, Damian R. Musk, Kelsie Taylor, Raju Valivarthi, and Maria Spiropulu. "Analytical Modeling of Real-World Photonic Quantum Teleportation." In: arXiv preprint arXiv:2503.18306. Submitted. (2025).
S.I.D. led the theoretical modeling and contributed to writing the manuscript.

[6] Prathwiraj Umesh, Samantha I. Davis, Jordan Smith, Sophie Hermans, Joaquin Chung, Prem Kumar, Boris Korzh, and Raju Valivarthi. "Regional quantum networks: recent progress and outlook." In: Manuscript in preparation for Optica Quantum. (2025).
Invited review article. S.I.D wrote the sources and quantum network testbeds sections.

[7] Volkan Gurses, Debjit Sarkar, Samantha Davis, and Ali Hajimiri. "An integrated photonic-electronic quantum coherent receiver for sub-shot-noise-limited optical links." In: Optical Fiber Communication Conference. Optica Publishing Group. 2024, Tu2C–1.
S.I.D. conceived the project, collected data, and contributed to writing the paper.

[8] Andrew Mueller, Samantha I. Davis, Boris Korzh, Raju Valivarthi, Andrew D. Beyer, Rahaf Youssef, Neil Sinclair, Cristián Peña, Matthew D Shaw, and Maria Spiropulu. "High-rate multiplexed entanglement source based on time-bin qubits

for advanced quantum networks." In: Optica Quantum 2.2 (2024), pp. 64–71.
S.I.D. performed theoretical modeling and participated in writing the manuscript.

[9] Samantha I. Davis, Chang Li, Rahaf Youssef, Neil Sinclair, Raju Valivarthi, and Maria Spiropulu. "Generation of Time-bin GHZ States." In: Optica Quantum 2.0 Conference and Exhibition. Optica Publishing Group, 2023, QTh4A.7. DOI: 10.1364/QUANTUM.2023.QTh4A.7. URL: https://opg.optica.org/abstract.cfm?URI=QUANTUM-2023-QTh4A.7.
S.I.D. performed all experimental work, led the theoretical modeling, performed the data analysis, and wrote the paper.

[10] Volkan Gurses, Samantha I. Davis, Ali Hajimiri, and Maria Spiropulu. "Quantum Phased Arrays." Patent Application Filed: 2023-06-2023. 2023.

[11] Volkan Gurses, Samantha I. Davis, Esme Knabe, Raju Valivarthi, Maria Spiropulu, and Ali Hajimiri. "A compact silicon photonic quantum coherent receiver with deterministic phase control." In: CLEO: Applications and Technology. Optica Publishing Group. 2023, AM4N–4.
S.I.D. conceived the project, collected data, and contributed to writing the paper.

[12] Keshav Kapoor, Si Xie, Joaquin Chung, Raju Valivarthi, Cristián Peña, Lautaro Narváez, Neil Sinclair, Jason P. Allmaras, Andrew D. Beyer, Samantha I. Davis, et al. "Picosecond synchronization system for the distribution of photon pairs through a fiber link between Fermilab and Argonne National Laboratories." In: IEEE Journal of Quantum Electronics 59.4 (2023), pp. 1–7.
S.I.D. conducted foundational work for the experiment, developed the data acquisition and monitoring systems, and wrote code used for data analysis.

[13] Samantha I. Davis, Andrew Mueller, Raju Valivarthi, Nikolai Lauk, Lautaro Narváez, Boris Korzh, Andrew D. Beyer, Olmo Cerri, Marco Colangelo, Karl K. Berggren, et al. "Improved heralded single-photon source with a photon-number-resolving superconducting nanowire detector." In: Physical Review Applied 18.6 (2022), p. 064007.
S.I.D. performed all experimental work, conceived and conducted all theoretical modeling, and wrote the manuscript.

[14] Daniel Jafferis, Alexander Zlokapa, Joseph D. Lykken, David K. Kolchmeyer, Samantha I. Davis, Nikolai Lauk, Hartmut Neven, and Maria Spiropulu. "Traversable wormhole dynamics on a quantum processor." In: Nature 612.7938 (2022), pp. 51–55.
S.I.D. helped develop and conduct the classical simulation and the decomposition of the protocol into quantum gates.

[15] Raju Valivarthi, Lautaro Narváez, Samantha I. Davis, Nikolai Lauk, Cristián Peña, Si Xie, Jason P. Allmaras, Andrew D. Beyer, Boris Korzh, Andrew Mueller, et al. "Picosecond synchronization system for quantum networks." In: Journal of Lightwave Technology 40.23 (2022), pp. 7668–7675.
S.I.D. conducted foundational work for the experiment, developed the data acquisition and monitoring systems, and contributed to the data analysis.

[16] Raju Valivarthi, Samantha I. Davis, Cristián Peña, Si Xie, Nikolai Lauk, Lautaro Narváez, Jason P. Allmaras, Andrew D. Beyer, Yewon Gim, Meraj Hussein, et al. "Teleportation systems toward a quantum internet." In: PRX Quantum 1.2 (2020), p. 020317.
S.I.D. built the experiment, collected the data, performed the data analysis, and participated in the writing of the manuscript.

CONTENTS

LIST OF FIGURES

LIST OF TABLES

Chapter 1

INTRODUCTION

Over the past several decades, advances in information processing have driven unprecedented developments in science and technology. Information technologies, such as personal computers, mobile phones, and precision sensors, continue to transform the modern world. The recent rise of large-data processing and artificial intelligence is further accelerating global demand for computational power, communication bandwidth, and sensing capabilities. In response, new technological paradigms are being explored to overcome current limitations in information processing capabilities. One of the most exciting directions emerging from this challenge is the development of quantum information technologies, which leverage the consequences of quantum physics to unlock new ways of sensing, processing, and transmitting information.

Quantum technologies are often grouped into three pillars: quantum sensing, quantum computing, and quantum communication. Of the three pillars, quantum sensing is the most mature and widely adopted. Quantum sensors exploit features of quantum mechanical systems such as coherence, entanglement, and quantum interference to surpass precision limits of conventional sensors. Established examples include atomic clocks, which define the international time standard, and superconducting quantum interference devices, used for ultra-sensitive magnetic field detection in both research and medical imaging. More recent developments include squeezed-light interferometry, matter-wave interferometry, quantum gas microscopes, and molecular spin qubits, offering paths toward Heisenberg-limited sensitivity in applications ranging from biological imaging to gravitational wave detection.

Quantum computing represents a new paradigm for computation based on manipulating quantum bits of information. Unlike classical computers, which operate on bits that are either 0 or 1, quantum computers operate on qubits, or states of a two-level quantum system, which can exist in a superposition of both states. This allows quantum algorithms to explore exponentially large solution spaces in ways that are inaccessible to classical computers, promising exponential speedups for specific classes of problems. A notable example is Shor's algorithm, which can factor large numbers exponentially faster than classical algorithms, posing a threat to modern

encryption systems. The discovery of Shor's algorithm catalyzed widespread interest in quantum computing and launched a global effort to build quantum processors capable of efficiently performing tasks that could are intractable in classical supercomputers. Recent milestones in quantum hardware have sparked a global race to build large-scale, fault-tolerant quantum computers that have transformative potential for simulating complex quantum systems, solving hard optimization problems, and advancing fields from biochemistry to artifical intelligence.

The threat posed by quantum computers to current cryptographic systems has also driven progress in quantum cryptography. Unlike classical cryptographic schemes, whose security depends on computational hardness assumptions, quantum cryptographic protocols such as quantum key distribution (QKD) offer information-theoretic security guaranteed by the no-cloning theorem and the irreversible nature of quantum measurement. Quantum communication systems enable these protocols by transmitting and interfering quantum states between distant locations, allowing for secure key exchange, teleportation of quantum states, and coordination of spatially separated quantum systems. By interconnecting quantum devices, such as quantum sensors and computers, at remote locations, quantum communication channels form the basis of distributed quantum networks. These quantum networks enable functionalities beyond the reach of any isolated system, including secure multiparty communication, distributed quantum sensing, and teleportation-based quantum state transfer. The long-term vision is the development of a quantum internet: a world-wide network of quantum technologies that are interconnected by quantum communication channels across the globe. Just as the classical internet revolutionized the sharing of digital information, the quantum internet will allow for the distribution of entanglement and quantum states over vast distances and unlock the full potential of quantum technologies.

Alongside the accelerating development of quantum networks, distribution of entanglement has emerged as a key thread connecting information science to the deepest questions in fundamental physics. Quantum networks capable of high-fidelity entanglement distribution have served as a platform for experimental tests of the foundations of quantum mechanics, including Bell tests that probe the validity of locality and realism. These experiments, which culminated in the 2022 Nobel Prize in Physics, confirmed that quantum correlations cannot be explained by any local hidden variable theory. More recently, connections between quantum information and gravity have sparked a new line of inquiry. Quantum teleportation protocols, for

instance, have been shown to admit a dual interpretation in gravitational theories as the transmission of information through traversable wormholes. This insight is part of a broader effort to understand the emergence of spacetime from entanglement, exemplified by the ER=EPR conjecture, which posits a deep equivalence between entangled quantum states and gravitational wormholes. Such developments suggest that quantum communication may not only be a technological tool, but also a powerful probe of the causal and geometric structure of spacetime itself.

In this thesis, I present some of the latest advances in quantum communication devices, channels, and networks, both at a technological and fundamental level. The thesis is divided into three parts. Part I focuses on quantum sources and detectors, which form the foundational building blocks of quantum networks. I begin by introducing the principles behind photon-pair sources and single-photon detectors (Chapter 2) and highlight key challenges in the current state-of-the-art. I then present progress in cutting-edge sources and detectors: photon-number-resolving superconducting nanowire detectors and their first application to improving heralded single-photon sources (Chapter 3) and high-rate photon-number discrimination (Chapter 4); a high-rate entangled photon-pair source for quantum key distribution (Chapter 5); and high-bandwidth on-chip balanced homodyne detectors (BHDs), enabling continuous-variable quantum key distribution and squeezed-light detection (Chapters 2 and 6). I also introduce the concept of a novel quantum sensor, which we call the "quantum phased array" (QPA), and present a proof-of-concept demonstration of a QPA receiver implemented in a large-scale silicon photonic-electronic platform (Chapter 6). This system integrates a directional free-space-to-chip interface for quantum light and features the first on-chip detection of squeezed light using a quantum-limited BHD array. Using this architecture, we demonstrate coherent multipixel imaging and beamforming of squeezed light, illustrating key functionalities envisioned for future wireless quantum sensors and communication systems.

Part II of this thesis describes the development of quantum network testbeds at Caltech and Fermi National Accelerator Laboratory, with a focus on designing scalable architectures for quantum networks toward the quantum internet (Chapter 7). A defining feature of quantum networks is the ability to distribute entanglement between remote nodes, which is essential for numerous quantum communication protocols including teleportation, entanglement swapping, and quantum repeaters.

We construct systems capable of high-fidelity quantum teleportation (Chapter 8) and entanglement swapping (Chapter 10) over long distances. We achieve state-of-the-art teleportation fidelities over 45 km of optical fiber and entanglement swapping visibilities with time-bin qubits. To support the development of these systems, I describe theoretical models for the experiments (Chapter 9) that guide system design and optimization. Finally, I detail our efforts to extend these capabilities to real-world metropolitan environments, and present experimental demonstrations of entanglement distribution to remote nodes at FNAL and Argonne National Laboratory with picosecond-level clock synchronization (Chapter 11). These systems are envisioned to form the backbone of a prototype quantum internet connecting the seventeen national labs of the United States.

Part III of this thesis explores the intersection of quantum communication and fundamental physics (Chapter 12). I begin by describing the experimental generation of multipartite entanglement, specifically GHZ states, in our quantum network testbeds (Chapter 13). GHZ states serve as valuable resources for foundational tests of quantum mechanics, including more stringent Bell inequalities and nonlocality tests, as well as for distributed quantum sensing protocols. Our demonstration is a first step towards establishing a field-deployed quantum sensing network at Fermilab designed to perform precision measurements for high energy physics. I then present the first experimental realization of a traversable wormhole teleportation protocol implemented on quantum computer (Chapter 14). We observe characteristic features of traversable wormhole dynamics, such as time-ordered signal propagation, the preservation of input information, and sensitivity to coupling strength, consistent with expectations from semiclassical gravity.

Finally, I conclude with an outlook on future directions and opportunities for the devices, networks, and experiments presented in this thesis (Chapter 15). I propose a new line of inquiry at the intersection of all these research domains: Bell inequalities for quantum gravity. Specifically, I formulate a concrete Bell inequality tailored for holographic systems with a wormhole dual.

Part I

Building blocks of quantum communication networks

Chapter 2

SOURCES AND DETECTORS

This chapter includes the work published as:

[1] Volkan Gurses, Samantha I. Davis, Esme Knabe, Raju Valivarthi, Maria Spiropulu, and Ali Hajimiri. "A compact silicon photonic quantum coherent receiver with deterministic phase control." In: CLEO: Applications and Technology. Optica Publishing Group. 2023, AM4N–4.

[1] Volkan Gurses, Debjit Sarkar, Samantha Davis, and Ali Hajimiri. "An integrated photonic-electronic quantum coherent receiver for sub-shot-noise-limited optical links." In: Optical Fiber Communication Conference. Optica Publishing Group. 2024, Tu2C–1.

2.1 Sources

A defining feature of quantum networks is their ability to distribute quantum information between distant nodes while preserving quantum coherence. Photons are the primary carriers of quantum information between nodes in a quantum network due to their ability to propagate over long distances in optical fiber or free space with relatively low decoherence. Quantum networks require reliable sources of indistinguishable photons for key network operations such as quantum interference. A standard approach to generating photons suitable for quantum networking is to use the strong light-matter coupling offered by solid-state bulk nonlinearities. In a bulk nonlinearity, the optical response of the nonlinear medium to a pump field is described by the polarization vector $\vec{P} = \vec{P}^{\mathrm{L}} + \vec{P}^{\mathrm{NL}}$, where $P_i^{\mathrm{L}} = \varepsilon_0 \sum \chi_{ij}^{(1)} E_j$ is the linear term containing the first order susceptibility, $\chi^{(1)}$, and $\vec{P}^{\mathrm{NL}}$ is the nonlinear term containing contributions from higher-order susceptibilities, $\chi^{(n)}$ [1]. Pairs of single photons can be probabilistically emitted from nonlinear materials via laser-driven second-order ($\chi^{(2)}$) and third-order ($\chi^{(3)}$) processes such as spontaneous parametric down-conversion and spontaneous four-wave mixing, respectively. Photon pair generation provides versatile sources of entanglement and heralded single photons with high purity, bandwidth, and tunability.

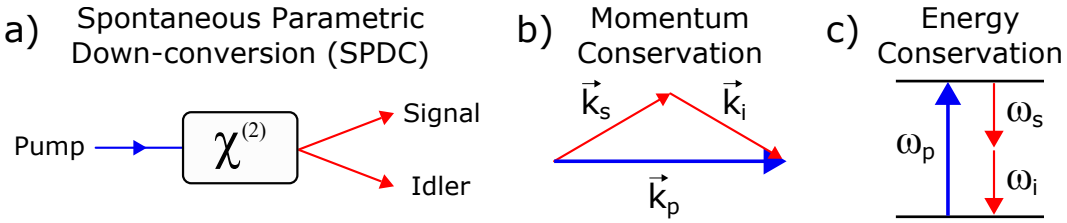

Figure 2.1: Spontaneous parametric down-conversion (SPDC). a) A pump photon is spontaneously downconverted into a pair of signal and idler photons by a $\chi^{(2)}$ bulk optical nonlinearity. The pump, signal and idler photons satisfy phase matching conditions, namely b) momentum conservation ($\vec{k}_p = \vec{k}_s + \vec{k}_i$) and c) energy conservation ($\hbar\omega_p = \hbar\omega_s + \hbar\omega_i$).

Spontaneous Parametric Down Conversion

Spontaneous parametric down-conversion (SPDC) is a three-wave mixing process involving the interaction of a pump, signal, and idler photon in a medium with a leading order $\chi^{(2)}$ bulk nonlinearity. A single pump photon with frequency ω_1 is spontaneously converted into a pair of lower-energy signal and idler photons with frequency ω_2 and ω_3, respectively (see Fig. 2.1). The SPDC process obeys energy and momentum conservation rules, also referred to as the phase-matching conditions,

$$\hbar\omega_3 = \hbar\omega_1 + \hbar\omega_2, \tag{2.1}$$

$$\Delta\vec{k} = \vec{k}_3 - \vec{k}_1 - \vec{k}_2 = 0, \tag{2.2}$$

where $\vec{k}_i$ represents the wave vector with magnitude $k_i = n(\omega_i)\omega_i/c$ and $n_i(\omega_i)$ is the index of refraction. The process is described by the interaction Hamiltonian,

$$\hat{H}_{\text{int}} = i\hbar\kappa\left(\hat{a}_1^\dagger\hat{a}_2^\dagger\hat{a}_3 + \hat{a}_1\hat{a}_2\hat{a}_3^\dagger\right) \tag{2.3}$$

where $\kappa \propto \chi^{(2)}L$ is a constant that depends on strength of the nonlinearity ($\chi^{(2)}$) and interaction length (L), and $\hat{a}$, $\hat{a}^\dagger$ are the bosonic ladder operators [2]. In Eq. 2.3, the first term corresponds to the creation of signal ($\hat{a}_1^\dagger$) and idler ($\hat{a}_2^\dagger$) photons by the annihilation of a pump photon ($\hat{a}_3$). The second term accounts for time reverse of the process, sum frequency generation (SFG) or second harmonic generation (SHG) for $\omega_1 = \omega_2$, where two photons ($\hat{a}_1$, $\hat{a}_2$) are converted into a photon ($\hat{a}_3^\dagger$) of higher energy. The quantum state at the output of the SPDC process is,

$$|\psi(t)\rangle = \exp\left(\frac{1}{i\hbar}\int_0^t \hat{H}_{\text{int}}(t')dt'\right)|0\rangle \approx \left(1 + \frac{1}{i\hbar}\int_0^t \hat{H}_{\text{int}}(t')dt' + \cdots\right)|0\rangle\,, \tag{2.4}$$

where $|0\rangle$ is the initial vacuum state. In Eq. 2.4, $|\psi(t)\rangle$ corresponds to a single mode squeezed vacuum state (SMSV) in the degenerate case ($\omega_1 = \omega_2$) and a two-mode squeezed vacuum (TMSV) state in the nondegenerate case ($\omega_1 \neq \omega_2$) of signal and idler photons. The right hand side of Eq. 2.4 is the perturbative expansion of the time evolution operator to leading order in κ in the non-depleted pump approximation, where κ is typically very small with most of the pump photons unconverted. The leading order (two-photon) component of $|\psi(t)\rangle$ is,

$$|\psi\rangle \propto \kappa \int_0^\infty \int_0^\infty f(\omega_1, \omega_2)\hat{a}_1^\dagger(\omega_1)\hat{a}_2^\dagger(\omega_2)d\omega_1 d\omega_2 \, |0\rangle_1 \, |0\rangle_2 \tag{2.5}$$

where L is the interaction length and $f(\omega_1, \omega_2)$ is the joint spectral amplitude (JSA). The JSA accounts for the spectral profile of the pump and phase matching condition,

$$f(\omega_1, \omega_2) = \psi_{\mathrm{p}}(\omega_1, \omega_2) \cdot \psi_{\mathrm{ph}}(\omega_1, \omega_2), \tag{2.6}$$

where $\psi_{\mathrm{p}}(\omega_1, \omega_2)$ is the pump envelope and $\psi_{\mathrm{ph}}(\omega_1, \omega_2)$ is the phase matching envelope. The joint spectral intensity (JSI), $|f(\omega_1, \omega_2)|^2$, is the probability distribution of signal and idler frequencies.

Phase matching Efficient generation of photon pairs requires careful design of SPDC sources to achieve the phase matching conditions as much as possible [1, 3]. For instance, the phase matching condition $\Delta k = 0$ demands appropriate refractive indices $n(\omega_3) > n(\omega_1)$ and $n(\omega_2)$, which cannot be fulfilled with centrosymmetric materials. The phase-matching condition can be satisfied naturally in birefringent materials, such as barium borate (BBO), potassium titanyl phosphate (KTP), and lithium niobate (LN), with different indices of refraction depending on the polarization and direction of propagation of the electric field for a given frequency. Phase matching can be achieved by tuning the angle of the pump field relative to the optic axis, resulting in different phase-matching configurations depending on the geometry [4]. Photon pairs can be emitted collinearly or non-collinearly depending on the type of phase-matching configuration (see Fig 2.1). In type-I SPDC, the signal and idler photons have the same polarization, which is orthogonal to the pump polarization, whereas in type-II SPDC, the signal and idler photons have orthogonal polarizations.

In type-0 SPDC, the pump, signal, and idler photons share the same polarization state; however, inherent material dispersion often prevents natural phase matching due to mismatched phase velocities of the interacting waves. Quasi-phase matching

can be achieved by periodic poling, where the sign of the nonlinear susceptibility tensor of the nonlinear crystal is spatially modulated at regular intervals, known as the poling period [5, 6]. A common technique is electric field poling, where a strong electric field is applied in a controlled pattern to induce periodic ferroelectric domain reversals. The periodic inversion compensates for the phase mismatch by effectively resetting the relative phase between the pump and generated photons at each poling period, thereby sustaining constructive interference over extended interaction lengths. The poling period is precisely engineered based on the wavelengths of the pump, signal, and idler photons, as well as the material's refractive indices, to satisfy the quasi-phase matching condition,

$$\Delta k = k_3 - k_1 - k_2 - 2\pi m/\Lambda, \tag{2.7}$$

where m is an integer and Λ is the poling period. Materials commonly subjected to periodic poling include LN and KTP due to their robust nonlinear properties and amenability to domain inversion.

Early demonstrations of photon-pair generation via type-I SPDC were crucial for fundamental tests of nonlocality [7] and two-photon interference [8]. Subsequent refinements in crystal growth, pump laser design, and alignment precision led to the development of sources with higher brightness and narrow bandwidths for practical implementations, with extensive investigation into type-II SPDC sources due to their intrinsically high-contrast polarization entanglement and convenient post-selection methods for measuring polarization correlations [4]. These advances, along with improvements in crystal purity, pump stability, and collection optics, fueled applications in entanglement-based quantum communication, culminating in demonstrations of entanglement distribution over fiber networks exceeding 10 km [9, 10] and paved the way for more complex multi-photon entanglement experiments [11]. In parallel, the advent of quasi-phase matching in periodically poled lithium niobate (PPLN) and potassium titanyl phosphate (PPKTP) led to a wide adoption of type-0 SPDC sources [10, 12], enabling higher nonlinear conversion efficiencies, flexible wavelength control, and compact waveguide implementations critical for integrated quantum networking architectures [5, 6].

Spectral Purity A typical joint spectral intensity for a type-II SPDC process is shown in Fig. 2.2, illustrating the broadband spectral correlations of photon pairs emitted by SPDC. Type-II SPDC exhibits narrower bandwidths than type-0 or type-I SPDC because orthogonal polarizations impose stricter phase matching constraints

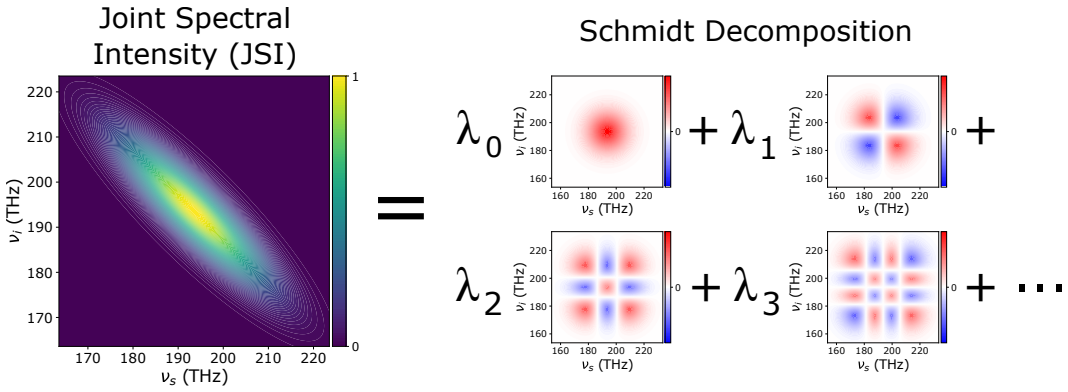

Figure 2.2: A typical joint spectral intensity for type-II SPDC for a pump photon at 775 nm, corresponding to signal and idler photons at telecom wavelengths centered at 1550 nm. By taking the singular value decomposition, the JSI can be decomposed into Schmidt modes (plotted) and associated eigenvalues $\{\lambda_n\}$, where λ_n^2 is the probability of occupying the nth mode.

[4, 13]. The degree of spectral entanglement can be characterized by the Schmidt decomposition of the two-photon state,

$$|\psi\rangle = \sum_j \sqrt{\lambda_j}\, |j\rangle_1 \, |j\rangle_2 \tag{2.8}$$

where $|\lambda\rangle_j$ are the Schmidt coefficients with $\sum_j \lambda_j = 1$ and $|j\rangle_1, |j\rangle_2$ are orthonormal states of the signal and idler modes, respectively. The Schmidt decomposition can be obtained by performing a singular value decomposition of the JSI (see Fig. 2.1e). The spectral purity of the photon pairs is quantified by the Schmidt number, $K = 1/\sum_j \lambda_j^2$, which is the effective number of occupied eignemodes. The Schmidt number is related to the purity $P = 1/K$ of the source, where $K = 1$ corresponds to signal and idler photons in a single spectral mode [14].

In practical networking implementations, bright and spectrally pure sources of photon pairs are needed for high-fidelity generation of single photons and entangled states such as Bell states. Spectral filtering is commonly employed to effectively isolate a single spectral mode and reduce multimode contributions. However, for high degrees of spectral correlations, filtering will block the majority of generated photon pairs, resulting in substantial photon loss and restricted pair production rates [15]. Instead of filtering, spectral engineering techniques [16, 17, 18, 19, 20, 21] can be employed to engineer the joint spectrum of the source. For example, in cavity-enhanced sources, optical cavities are used to enforce specific resonant frequencies, thereby selectively enhancing the generation of photon pairs within a

narrow spectral range and promoting single-mode operation [22]. Alternatively, multimode sources can be used for spectrally multiplexing to achieve high-rate photon pair production and entanglement distribution. Fiber-coupled, broadband type-0 SPDC sources at telecom wavelengths can be interfaced with commercial division wave demultiplexers to distribute photon pairs over many channels in a network [23]. Combining spectral engineering and multiplexing techniques can enable high-rate sources of indistinguishable photons required for entanglement-based protocols over long distances in advanced quantum networks.

2.2 Encoding quantum information

Photons can be used as carriers of quantum information in a number of degrees of freedom (DOFs), in both discrete variable and continuous variable encodings of quantum information.

Discrete variables

For discrete variable encodings of qubits, commonly used DOFs include polarization, time-energy, and orbital angular momentum, and time-of-arrival. Polarization encoding is among the most widely used, where horizontal and vertical polarization states define the computational basis. Polarization correlations of photon pairs, e.g., from type-II SPDC, are exploited to generate entangled states by taking advantage of the orthogonally polarized photon pairs emitted into distinguishable spatial modes. Energy-time encodings exploit the strong frequency correlations and time-energy uncertainty intrinsic to SPDC, where the emission time of an idler photon is uncertain but strongly correlated with the signal photon [24]. Orbital angular momentum (OAM) encodings use spatial modes carrying quantized angular momentum, allowing access to high-dimensional Hilbert spaces and offering greater information capacity per photon [25].

An essential feature of quantum networks is the ability to distribute entanglement across many distributed nodes over nominally long distances. An attractive approach is to leverage the commercial optical fiber infrastructure already developed at telecom wavelengths for the deployment of large-scale quantum networks. For this approach, qubits encoded in the time-of-arrival states (early $|e\rangle$ or late $|\ell\rangle$) of individual photons, or "time-bin qubits," at telecom-band wavelengths are preferred due to their ease of generation, low-loss propagation, and robustness to phase noise and polarization drift in over long-distances in optical fibers [26].

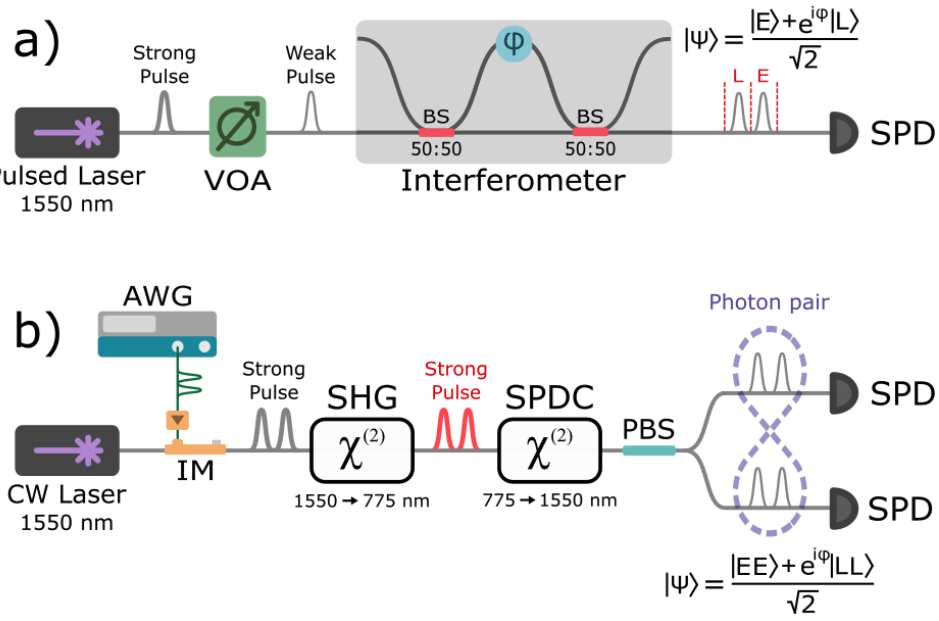

Figure 2.3: Generation of time-bin qubits at telecom wavelengths with commercially available fiber-optic components. a) Strong pulses of coherent light from a mode-locked laser are attenuated down to the single photon level by a variable optical attenuator (VOA). The weak pulses are inserted into an path-length-imbalanced interferometer, which defines early (E) and late (L) time-bins corresponding a photon passing through the short and long path, respectively. A photon at the output of the interferometer is in a coherent superposition of early and late time-of-arrival states. b) Early and late pulses are carved out from a continuous wave (CW) laser by an intensity modulator (IM), which is programmed by an arbitrary waveform generator (AWG) to define the early and late time-bins. The strong pulses are frequency-doubled by a second harmonic generator (SHG) to serve as pump light for spontaneous parametric down-conversion (SPDC), which produces pairs of single photons at telecom wavelength in an approximate Bell state. Quantum states are post-selected by a single-photon detector (SPD) that measures its time-of-arrival state.

Time-bin qubits Time-bin qubits are generated by preparing single photons in a coherent superposition of pulses separated by a fixed time delay, defining "early" and "late" temporal modes. By setting the temporal separation of the pulses much shorter than the coherence time of the channel, the relative phase between the two time-bins remains stable over long-distance fiber transmission, preserving quantum coherence. The computational (Z) basis ($|e\rangle$, $|l\rangle$) is defined by preparing a single photon in an early ("e") or late ("l") time bin. A qubit in the X basis, $|\pm\rangle = \frac{1}{\sqrt{2}}(|e\rangle \pm |l\rangle)$, or Y basis, $|\pm\rangle = \frac{1}{\sqrt{2}}(|e\rangle \pm i\,|l\rangle)$, can be prepared by sending a single photon to a path-imbalanced interferometer, where the time delay between the short and long paths inside the interferometer sets the temporal separation of the time bins (see Fig. 2.3a). The state of a photon at one of the outputs of the interferometers is described by $(|e\rangle + e^{i\phi}\,|l\rangle)/\sqrt{2}$, where ϕ is controlled by the interferometric phase shifter.

Deterministic and on-demand generation of pure single photons is a ongoing experimental challenge [27]. Due to ease of generation, a common approach is to approximate a single photons as a weak coherent state,

$$|\alpha\rangle = e^{-|\alpha|^2/2}\sum_{n=0}^{\infty}\frac{\alpha^n}{\sqrt{n!}}\,|n\rangle = e^{-|\alpha|^2/2}(|0\rangle + \alpha\,|1\rangle + O(|\alpha|^2)), \qquad |\alpha|^2 \ll 1, \tag{2.9}$$

where the subscript e (l) denotes the early (late) temporal mode, $|n\rangle$ is the photon number state of n photons, and $|\alpha|^2$ is the mean photon number. Single photons in confined temporal modes can be prepared by attenuating a series of laser pulses down the single-photon level. Each pulse defines a time bin within its clock cycle, which is set by the repetition rate of the laser. The preparation of a photon in the early or late time-bin is performed by changing the timing of the pulse within its clock cycle, for instance using a variable optical delay line. Since $|\alpha|^2 \ll 1$ in order to suppress multiphoton events ($n \geq 2$), the weak coherent pulses are primarily in the vacuum state. Quantum information protocols based on time-bin qubits are typically performed using prepare-and-measure schemes conditioned on single-photon detection, where quantum states are post-selected by single-photon detectors that measure the time-of-arrival states of the qubits.

Single photons can also be heralded from a pair source, where a signal photon is "heralded" by the detection of an idler photon (see Sec. 2.4). The output state of a photon pair produced by SPDC in a single temporal mode is described by the

two-mode squeezed vacuum state (TMSV),

$$|\text{TMSV}\rangle = \sum_{n=0}^{\infty}(-1)^n\sqrt{\frac{\mu^n}{(1+\mu)^{n+1}}}\,|n\rangle_s\,|n\rangle_i \tag{2.10}$$

$$\approx |0\rangle_i\,|0\rangle_s + \sqrt{\mu}\,|1\rangle_i\,|1\rangle_s + O(\mu) \quad \mu \ll 1. \tag{2.11}$$

Time-bin entangled states can be generated by pumping a photon pair source with a pair of strong pulses in early and late time bins (see Fig. 2.3b). The output state is described by the product state of a two-mode squeezed vacuum state (TMSV) in the early and late temporal modes,

$$|\text{TMSV}\rangle_e \otimes |\text{TMSV}\rangle_l \approx \sqrt{1-2\mu}\,|0\rangle + \sqrt{2\mu}\,\left|\Phi^+\right\rangle + O(\mu), \quad \mu \ll 1, \tag{2.12}$$

where $|0\rangle$ is the vacuum state, μ is the mean photon number, and

$$\left|\Phi^+\right\rangle = \frac{1}{\sqrt{2}}(|e\rangle_s\,|e\rangle_i + |l\rangle_s\,|l\rangle_i)$$

is a Bell state of signal (s) and idler (i) photons in the time-bin qubit basis. In Eq. 2.12, higher order terms of $O(\mu)$ correspond to multiphoton states, where $\mu \ll 1$ suppresses the probability of multiphoton events (see Sec. 2.4). A Bell state can be post-selected by conditioning on the coincident detection of signal and idler photons in either the early or late time-bin at spatially separated single-photon detectors. With photon pairs generated by type-II SPDC, for instance, Bell states can be conveniently distributed to different nodes in a network using a polarizing beamsplitter to separate signal and idler photons in orthogonal polarization states.

Continuous variables

For continuous variable protocols, quantum information is encoded in continuous DOFs, such as the amplitude and phase of the electromagnetic field quadratures, $\hat{Q}$ and $\hat{P}$. The Hamiltonian density ($\mathcal{H}$) of an electromagnetic field can be expressed in terms of the $\hat{Q}$ and $\hat{P}$ quadratures as,

$$\mathcal{H} = \frac{1}{2}(\hat{P}^2 + \omega^2\hat{Q}), \qquad \hat{P} = \frac{i(\hat{a} - \hat{a}^\dagger)}{\sqrt{2}}, \quad \hat{Q} = \frac{(\hat{a} + \hat{a}^\dagger)}{\sqrt{2}} \tag{2.13}$$

where $\hat{a}$ and $\hat{a}^\dagger$ are the pair of bosonic annhiliation and creation operators satisfying $[\hat{a}^\dagger, \hat{a}] = 1$, such that $[\hat{Q}, \hat{P}] = i$. Quantum states can be described as a function of the quadrature observables Q and P in phase space by the Wigner quasiprobability distribution, $W(Q, P)$. Gaussian states of light, characterized by Gaussian Wigner distributions, are commonly used as carriers of CV information due to their ease of

generation. The Wigner distributions of Gaussian states such as vacuum, coherent, and squeezed states are illustrated in Fig. 2.4, where the widths of the distributions are constrained by the Heisenberg uncertainty principle, $\Delta Q \Delta P \geq 1/4$. Vacuum and coherent states are represented by symmetric Gaussian distributions in phase space that saturate the uncertainty principle with $\Delta Q^2 = \Delta P^2 = 1/2$. Squeezed states are represented by ellipical Gaussian distributions in phase space characterized by a "squeezed" quadrature (Q) and "antisqueezed" quadrature (P), where the squeezed quadrature exhibits an uncertainty below ($\Delta Q^2 < 1/2$) and the antisqueezed quadrature exhibits an uncertainty above ($\Delta P^2 > 1/2$) the vacuum quadrature uncertainty.

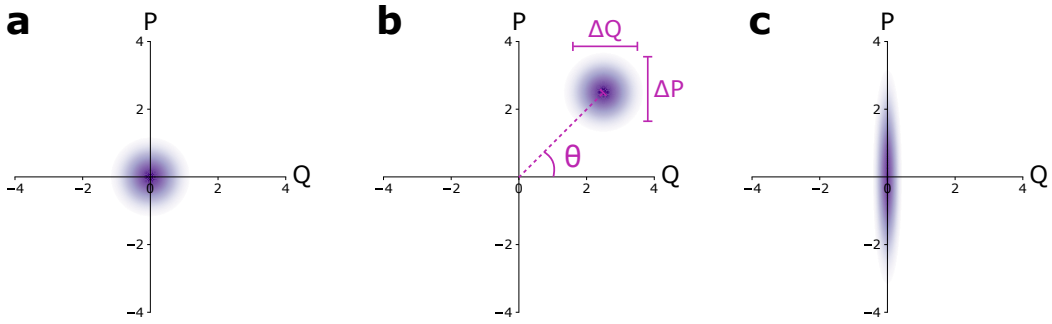

Figure 2.4: Wigner quasiprobability distribution $W(Q, P)$ for a) the vacuum state, b) a coherent state with $\alpha = 2.5$ and $\theta = \pi/4$, c) a squeezed vacuum state with $r = 1$, where Q is the squeezed quadrature and P is the antisqueezed quadrature.

Squeezing Squeezed states form an essential resource for many CV quantum protocols, including sub-shot noise sensing, CV quantum teleportation, and measurement-based quantum computing. Mathematically, squeezed states can be described by the action of the squeezing operator, $\hat{S}_1(r)$, on the vacuum state, [28],

$$\hat{S}_1(r)\,|0\rangle = \exp\left(\frac{r\hat{a}^2 - r^*\hat{a}^{\dagger 2}}{2}\right)|0\rangle\,, \tag{2.14}$$

where the squeezing parameter r determines the amount of squeezing and $\hat{a}$ and $\hat{a}^\dagger$ are the bosonic ladder operators satisfying $[\hat{a}^\dagger, \hat{a}] = 1$. The action of the squeezing operator can be modeled as the evolution of the vacuum state under the Hamiltonian,

$$\hat{H}_1 = i\hbar\alpha(r\hat{a}^2 - r^*\hat{a}^{\dagger 2})/2, \tag{2.15}$$

with time $t = r/\alpha$ such that $\hat{S}_1(r) = \exp\left(-i\hat{H}_1 t/\hbar\right)$. In the Heisenberg picture, the ladder operators evolve as,

$$\frac{d\hat{a}}{dt} = \frac{i}{\hbar}[\hat{H}_1, \hat{a}] = -\alpha\hat{a}^\dagger \tag{2.16}$$

$$\frac{d\hat{a}^\dagger}{dt} = \frac{i}{\hbar}[\hat{H}_1, \hat{a}^\dagger] = -\alpha\hat{a}. \tag{2.17}$$

After evolution over a time $t = r/\alpha$, the ladder operators are transformed as,

$$\hat{a}(r) = \hat{a}(0)\cosh r - \hat{a}^\dagger(0)\sinh r, \tag{2.18}$$

$$\hat{a}^\dagger(r) = \hat{a}^\dagger(0)\cosh r - \hat{a}(0)\sinh r, \tag{2.19}$$

referred to as a Bogoliubov transformation. The quadrature operators are transformed as,

$$\hat{Q}(r) = \frac{1}{\sqrt{2}}(\hat{a}(r) + \hat{a}^\dagger(r)) = \hat{Q}(0)e^{-r}, \tag{2.20}$$

$$\hat{P}(r) = \frac{1}{i\sqrt{2}}(\hat{a}(r) - \hat{a}^\dagger(r)) = \hat{P}(0)e^{r}, \tag{2.21}$$

which corresponds to squeezing of $\hat{Q}$ by a factor of e^{-r} and antisqueezing of $\hat{P}$ by a factor of e^r.

The state generated by $\hat{S}_1$ in Eq. 2.14 is a single mode squeezed vacuum (SMSV) state,

$$|\text{SMSV}\rangle = \hat{S}_1(r)\,|0\rangle = \sum_{n=0}^{\infty}(-1)^n\sqrt{\frac{\mu^n}{(1+\mu)^{n+1}}}\,|2n\rangle \tag{2.22}$$

$$\approx |0\rangle - \sqrt{\mu}\,|2\rangle + O(\mu), \qquad \mu \ll 1 \tag{2.23}$$

where $\mu = \langle\hat{a}^\dagger(r)\hat{a}(r)\rangle = \sinh^2(r)$ is the mean photon number. The two-mode squeezed vacuum state (TMSV) is generated by the action of the squeezing operator $\hat{S}_2(r)$ on the vacuum state,

$$|\text{TMSV}\rangle = \hat{S}_2(r)\,|0\rangle = \exp\left(\frac{r\hat{a}_1\hat{a}_2 - r^*\hat{a}_1^\dagger\hat{a}_2^\dagger}{2}\right)|0\rangle\,, \tag{2.24}$$

$$= \sum_{n=0}^{\infty}(-1)^n\sqrt{\frac{\mu^n}{(1+\mu)^{n+1}}}\,|n\rangle\,|n\rangle\,, \tag{2.25}$$

$$\approx |0\rangle\,|0\rangle - \sqrt{\mu}\,|1\rangle\,|1\rangle + O(\mu), \qquad \mu \ll 1, \tag{2.26}$$

which is expanded in the Fock basis in Eq. 2.25. The squeezing operator $\hat{S}_2(r)$ has the associated Hamiltonian $\hat{H}_2 = i\hbar\alpha(r\hat{a}_1\hat{a}_2 - r^*\hat{a}_1^\dagger\hat{a}_2^\dagger)/2$, which corresponds to the SPDC interaction Hamiltonian in Eq. 2.3.

Squeezed states of light can be prepared experimentally by nonlinear optical processes such as SPDC and SFWM. SMSV states can be produced by degenerate SPDC with collinear phase matching, for instance using a type-0 SPDC source, and TMSV states can be produced by non-degenerate SPDC, for instance using a type-I or type-II SPDC source. The experimental generation of single-mode squeezed light at telecom wavelength using commerically-available, fiber-coupled components is illustrated in Fig. 2.5a. To extract information encoded in the quadratures, quadrature measurements are typically performed using balanced homodyne detection (BHD) [29, 30]. In homodyne detection, a weak signal field ($\hat{a}$) is interfered with a strong local oscillator ($\hat{b}$) at a 50:50 beamsplitter, and the light from each output,

$$\hat{c} = \frac{1}{\sqrt{2}}(\hat{a} + \hat{b}), \tag{2.27}$$

$$\hat{d} = \frac{1}{\sqrt{2}}(\hat{a} - \hat{b}), \tag{2.28}$$

is detected by a photodiode (PD). The current from each photodiode is proportional to the mean photon number of the incident light,

$$\langle \hat{i}_c \rangle \propto \langle \hat{c}^\dagger \hat{c} \rangle = \frac{\langle \hat{a}^\dagger \hat{a} \rangle + \langle \hat{a}^\dagger \hat{b} \rangle + \langle \hat{b}^\dagger \hat{a} \rangle + \langle \hat{b}^\dagger \hat{b} \rangle}{2}, \tag{2.29}$$

$$\langle \hat{i}_d \rangle \propto \langle \hat{d}^\dagger \hat{d} \rangle = \frac{\langle \hat{a}^\dagger \hat{a} \rangle - \langle \hat{a}^\dagger \hat{b} \rangle - \langle \hat{b}^\dagger \hat{a} \rangle + \langle \hat{b}^\dagger \hat{b} \rangle}{2}. \tag{2.30}$$

The photodiodes are in a balanced configuration where the photocurrents are subtracted, resulting in an output current proportional to the quadrature of the signal field,

$$\langle \hat{i}_c - \hat{i}_d \rangle \propto \frac{\langle \hat{b}^\dagger \hat{a} \rangle + \langle \hat{a}^\dagger \hat{b} \rangle}{\sqrt{2}} \approx |\beta| \langle \hat{Q}(\theta) \rangle, \tag{2.31}$$

where $\hat{Q}(\theta) = (\hat{a}e^{-i\theta} + \hat{a}^\dagger e^{i\theta})/\sqrt{2}$. The approximation is taken in the limit of a strong local oscillator in a coherent state $|\beta\rangle$, using the substitution $\hat{b} \rightarrow |\beta| e^{i\theta}$ where θ is the relative phase of the signal and local oscillator. States of the signal field can be probed in phase space by sweeping the phase of the local oscillator, where setting $\theta = 0$ and $\theta = \pi/2$ corresponds to projections onto $\hat{Q}$ and $\hat{P}$, respectively. The state of the signal field can reconstructed by measuring the BHD output with a signal analyzer and acquiring quadrature statistics over various phases from $\theta = [0, 2\pi]$ to form a tomographically complete set of measurements. An simulation of quadrature statistics for a squeezed vacuum state measured using an oscilloscope over various

phases is shown in Fig. 2.5b. The amount of squeezing can be characterized by comparing the measured quadrature variance of the squeezed state to that of the vacuum state. For a squeezed vacuum state, the quadrature mean is $\langle \hat{Q}_\theta \rangle = 0$, and the quadrature variance is,

$$\langle \Delta \hat{Q}_\theta^2 \rangle = \frac{1}{2}(e^{-2r}\cos^2\theta + e^{2r}\sin^2\theta). \tag{2.32}$$

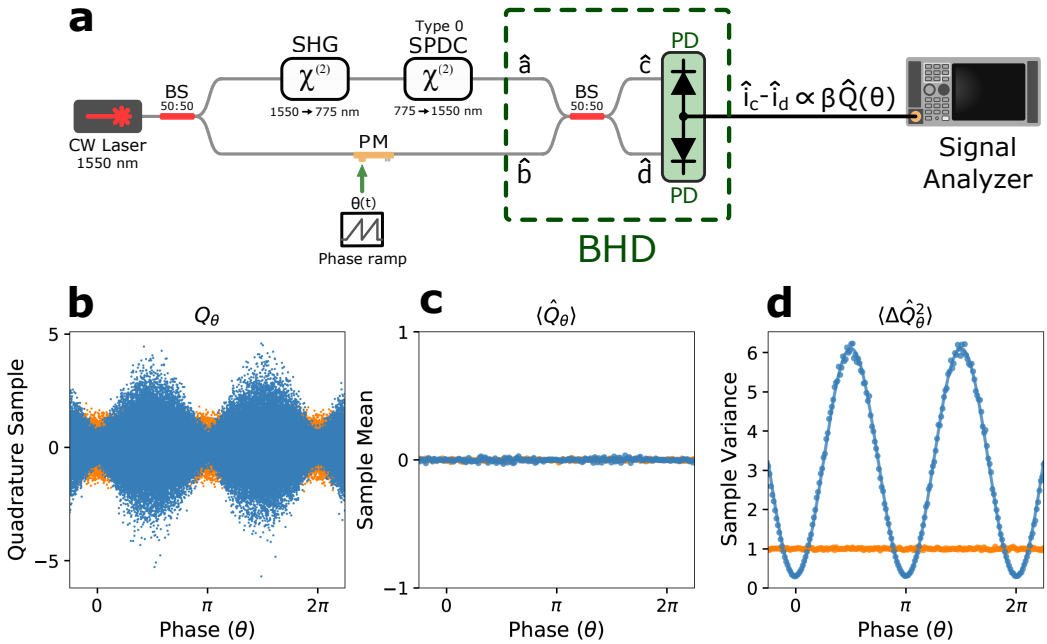

Figure 2.5: Generation of single-mode squeezed vacuum light at telecom wavelength with fiber-coupled components. a) Experimental setup. b)-d) Numerical simulation of quadrature statistics obtained from time-domain analyzer for a linear phase ramp applied to the LO. b) Quadrature samples as a function of time (phase) for a vacuum state (orange) and a squeezed vacuum state with a squeezing parameter of $r = 1$ and measurement efficiency of $\eta = 0.8$ (blue). c) Sample means and d) normalized sample variances as a function of time. The sample variances are normalized to the mean of the vacuum sample variances. The solid lines in c) and d) are the corresponding analytic predictions for the quadrature means and variances.

2.3 Detectors

Single-photon detectors

Quantum networks rely on high-fidelity single-photon detectors for state preparation and measurement. An optimal single-photon detector for quantum networking

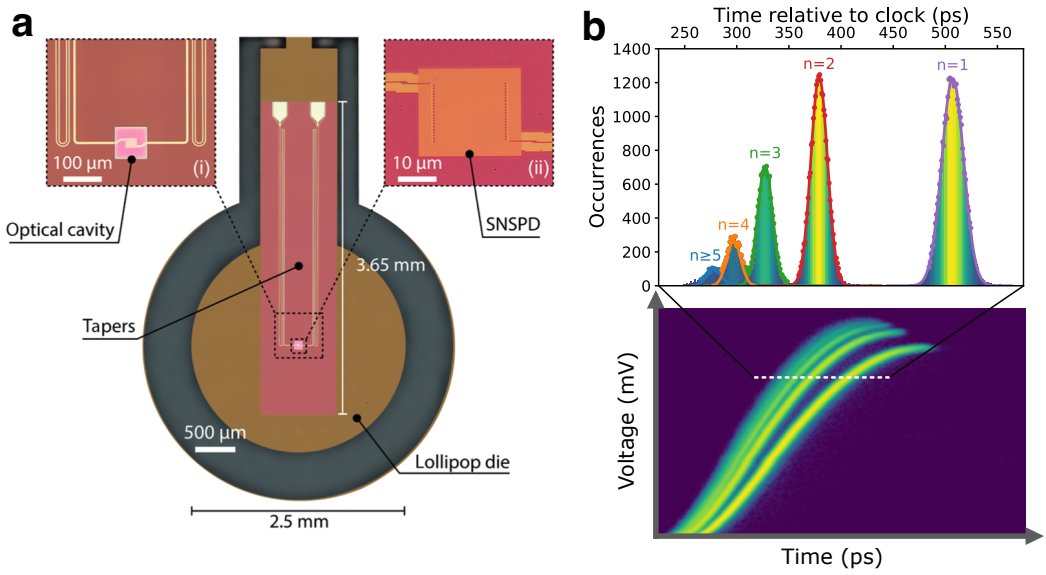

Figure 2.6: Photon-number-resolving superconducting nanowire detector. a) Optical micrograph of differential single-pixel superconducting nanowire single-photon detector.[a] b) Bottom: Measurement of RF readout pulses from impedance-matched tapered nanowire with oscilloscope in persistent mode. Photon number is encoded in the amplitude and slew rate of RF pulses. RF pulses are readout to a time-tagger with a constant voltage discriminator, where the variation in slew rate results in a variation of the registered time-tag. Top: Distribution of time-tags relative to a clock signal. Higher photon numbers correspond to higher slew rates and lower time-delays relative to the clock. Distinct Gaussian distributions of time-tags corresponding to photon number events are resolved up to 5 photons.

[a]Reprinted figure with permission from M. Colangelo, B. Korzh, J.P. Allmaras, A.D. Beyer, A.S. Mueller, R.M. Briggs, B. Bumble, M. Runyan, M.J. Stevens, A.N. McCaughan, and D. Zhu, "Impedance-matched differential superconducting nanowire detectors." Physical Review Applied, 19(4), p.044093. 2023. DOI: `https://doi.org/10.1103/PhysRevApplied.19.044093`. Copyright 2025 by the American Physical Society.

would couple unity efficiency with gigahertz-rate operation, picosecond timing jitter, negligible dark counts, and the ability to discriminate large photon numbers with high fidelity at telecom wavelengths [31, 32]. Transition-edge sensors [33, 34, 35, 36, 37] and MKIDs [38, 39] offer inherent photon-number-resolving (PNR) capability with high efficiency and low dark count rates, but their kilohertz-scale speeds and sub-Kelvin cooling conflict with the multi-gigahertz clock rates and field-deployable cryocoolers envisioned for regional links. Superconducting nanowire single-photon detectors (SNSPDs) are the leading detectors at telecom wavelengths, with up to 98% system efficiency [40], ultra low dark counts in the milli- to micro-hertz range [41], count rates $>$ 100 MHz per nanowire [42], sub-3ps timing jitter [43], and nanosecond reset times [44] demonstrated in the literature (see Fig. 2.6). In an SNSPD, a photon absorbed by a superconducting nanowire generates a time-dependent resistive hotspot, which results in a readout pulse at RF. SNSPDs are routinely used for quantum communication and already meet the speed, jitter, and operating-temperature targets for quantum networking; substantial efforts are underway to add PNR functionality to SNSPDs to complete the optimal detector performance set.

Recent progress in PNR SNSPDs follows two complementary paths. Microwave-engineered single pixel detectors use on-chip impedance-matching tapers to enhance the detector's signal-to-noise ratio so that the RF output pulse varies with photon number [45], allowing for the discrimination of up to five photons with an individual nanowire [46] while preserving picosecond-level timing and high count rates (see Fig. 15). Photon number can be extracted from the output pulse amplitude [47, 45, 48] or slew-rate [49] variation. The latter approach requires only a constant threshold voltage discriminator [27], which suitable for real-time readout with commercial time-taggers for scalable networking. A differential readout architecture optimizes the design of impedance-matched devices by canceling geometric delay-line contributions to the jitter, enabling low-jitter and large active area single pixel detectors with PNR capabilities [47]. Alternatively, quasi- photon number resolution can be achieved by spatial [50, 51, 52] or temporal [53, 54] multiplexing of detectors without requiring intrinsic PNR per pixel. To resolve photon number with high fidelity, the number of spatial or temporal bins needs to be significantly larger than the number of input photons, typically at the expense of increased complexity and low detection rate. Scalable waveguide-integrated arrays of nanowires connected in parallel [55, 56, 57] or series [58] extend the photon-count ceiling without sacrificing speed, enabling photon counting with high dynamic range. Re-

cent demonstrations include 1.5 GHz aggregate rates for a 14-pixel distributed array at 90% system efficiency [42] and a monolithic 100-pixel detector array that resolves 0–100 photons per pulse with sub-nanosecond reset time [59].

Balanced homodyne detectors

In addition to single-photon detectors, low noise and high bandwidth BHDs are needed to measure quadrature information in CV protocols, such as Gaussian-modulated CV quantum key distribution (QKD) [60], measurement-based quantum computing [61, 62], sub-shot noise quantum sensing [63]. Together, PNRD and BHDs form a complete detector set for universal fault-tolerant quantum computing [64, 65] as well as hybrid DV and CV protocols such as deterministic quantum teleportation [66].

The ideal BHD combines near-unity quantum efficiency, low optical loss, low electronic noise, > 1 GHz bandwidth, high common-mode rejection, and stable phase locking for real-time operation at telecom wavelengths.Although high quantum efficiencies ~ 99% [67] have been demonstrated with traditional BHDs using discrete photodiodes and bulk optics, they face challenges in scalability and phase-stability, particularly for large-scale systems [68] and field-deployable quantum networks. Recent progress in integrated quantum-limited BHDs addresses these limitations by leveraging integrated photonic platforms [69, 70], such as silicon photonics [71] and lithium niobate on insulator (LNOI) [72], for monolithic integration of the beamsplitter, phase shifter, and photodiodes on a chip (see Fig. 2.7). By integrating all on components on chip in a compact-form factor, photonic integrated circuits (PICs) can achieve high phase stability and scalability with high bandwidth electronic readout. In particular, silicon photonics enables large scale integration at telecom wavelengths [73, 74], with systems demonstrated with several thousands of components on chip [75], as well as interfacing with silicon electronics, such as low-noise transimpedance amplifiers (TIAs) and electronic integrated circuits (EICs), for readout and post-processing [76].

The use of integrated BHDs is increasingly motivated by the demands of large-scale quantum networks, where long-distance coherent communication over deployed telecom infrastructure requires detectors with low noise, high stability, and high bandwidths to enable high-speed quadrature measurements and phase tracking in the presence of channel dispersion and loss [79]. On-chip BHDs with co-integrated transimpedance amplifiers enable the highest achievable bandwidths by minimizing

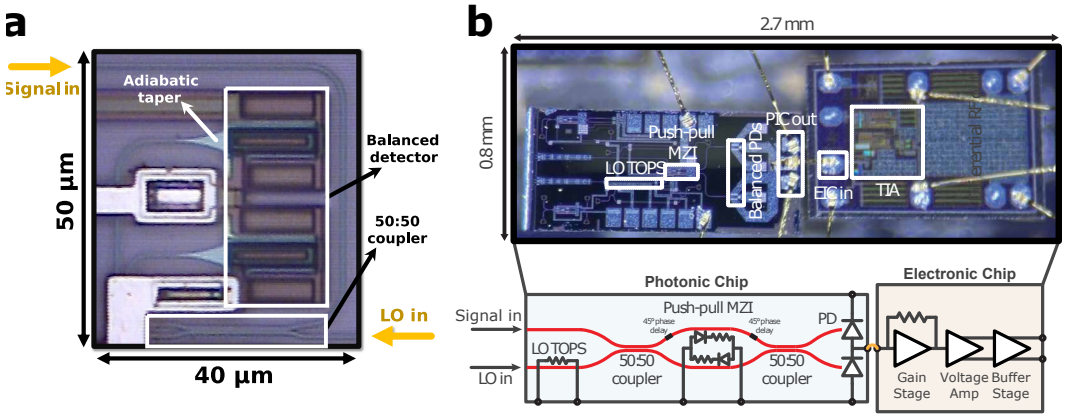

Figure 2.7: On-chip balanced homodyne detectors. a) Packaged die photo of an on-chip balanced homodyne detector from Gurses et al. (2023) [77]. b) Packaged die photo of photonic-electronic system for balanced homodyne detection from Gurses et al. (2024) [78]. The photonic chip contains a quantum-limited coherent receiver and wirebonded to the electronic chip with a transimpedance amplifier for readout.

parasitic capacitance and inductance, reducing interconnect lengths, and allowing co-design of the photodiode and amplifier circuitry. In contrast to bulk or discrete-component BHDs, where bandwidth is typically limited to the kHz-MHz range [80] due to long wirebonds, PCB traces, and large photodiode capacitance, integrated implementations eliminate these bottlenecks, preserve the amplifier's gain-bandwidth product, and enable multi-GHz operation [81]. Integration also allows precise impedance control, reduces signal degradation, and improves thermal and mechanical stability, making it essential for high-speed quantum optics applications requiring GHz-scale shot-noise-limited detection. For example, in CV-QKD and quantum random number generation (QRNG), high bandwidths directly translate to increased secure key rates and entropy generation, respectively. In quantum networks, integrated BHDs will be essential to meet the rate and distance requirements for metropolitan and backbone-level quantum repeaters, trusted-node links, and distributed quantum sensing architectures.

2.4 Heralded single-photon sources

Heralding of single photons is a common approach to produce spectrally tunable and indistinguishable photons with high purity and bandwidths. A bulk optical nonlinearity is used to probabilistically emit photon pairs via a $\chi^{(2)}$ or $\chi^{(3)}$ process, where an individual photon (in a signal mode) is "heralded" by the detection of the other photon (in an idler mode). Typically, a threshold detector is used to

discriminate between the presence of vacuum and at least one photon in the idler mode, which heralds the presence of photons in the signal mode. Heralding rates of $\sim 10^4 - 10^5$ pairs/s [82], system efficiencies of $20 - 30\%$ [82, 83], and $g^2(0) \sim 0.02 - 0.05$ [84, 18] have been demonstrated using bulk single pass SPDC sources and avalanche photodiode detectors. Spatial and spectral mode engineering can be employed to optimize the efficiency and purity, with demonstrations of up to 60% system efficiency using waveguides [84] and cavity-enhanced collection efficiency [85] as well as > 0.90 spectral factorability via pulse engineering [84] and narrowband filtering [85]. However, the emission of multiphoton pairs that contaminate the heralding restrict single-photon generation to low probability (e.g., $\mu \sim 10^{-3}$ in practice). The probability of n emitted photon pairs follows the thermal distribution, $P(n) = \mu^n/(1+\mu)^{n+1}$. Therefore, there is a trade-off in the single-photon heralding rate $\sim \mu$ and single-photon fidelity due non-negligible multiphoton pair production probability $P(n > 1)$ for increased μ [86].

Improving HSPS with PNR SNSPD

To overcome this challenge, a photon-number-resolving (PNR) detector can be used to filter out multiphoton pair events by discriminating the presence of vacuum, one photon, or multiple photons. By excluding multiphoton events at the idler mode, PNR detectors enable the heralding of single photons with high fidelities. Due to their combination of high detection efficiency, low dark counts, fast recovery time, and low jitter, PNR SNSPDs are desirable for heralding single photons at high rates. In Chapter 3, I report the first demonstration of heralding single photons with a PNR SNSPD. Using an efficient and low noise photon-number-resolving superconducting nanowire detector we herald, in real time, a single photon at telecommunication wavelength. We perform a second-order photon correlation $g^2(0)$ measurement of the signal mode conditioned on the measured photon number of the idler mode for various pump powers and demonstrate an improvement of a heralded single-photon source. We develop an analytical model using a phase-space formalism that encompasses all multiphoton effects and relevant imperfections, such as loss and multiple Schmidt modes. We perform a maximum-likelihood fit to test the agreement of the model to the data and extract the best-fit mean photon number μ of the pair source for each pump power. A maximum reduction of 0.118 ± 0.012 in the photon $g^2(0)$ correlation function at $\mu = 0.327 \pm 0.007$ is obtained, indicating a strong suppression of multiphoton emissions. For a fixed $g^2(0) = 7 \times 10^{-3}$, we increase the single pair generation probability by 25%. Our experiment, built using

fiber-coupled and off-the-shelf components, delineates a path to engineering ideal sources of single photons.

2.5 Entanglement distribution

High-fidelity entanglement distribution is an essential functionality of quantum networks. Entanglement is a key resource for a range of quantum communication protocols, including entanglement-based QKD, Bell tests and quantum teleportation. By splitting photon pairs produced by SPDC, entangled photons can be distributed to distant nodes over long distances in optical fiber or free space. However, experimental imperfections such as multiphoton noise and loss degrade the state fidelity of entangled photons over long distances. To evaluate the fidelity of distributed entanglement, the entanglement visibility is a commonly used metric. The experimental setup for the characterization of entanglement visibility with time-bin entangled photon pairs is illustrated in Fig. 2.8. Interferometers are used perform projective measurements on time-qubits. By measuring counts in the first and third bins at the output of interferometer, project on computational (Pauli Z) basis states E and L, respectively. By measuring counts in the middle bins, project onto phase basis state of the form $(|e\rangle + e^{i\varphi}|l\rangle)/\sqrt{2}$, where φ is set tuning the the interferometric phase. Projections onto the Pauli X basis states $(|e\rangle \pm |l\rangle)/\sqrt{2}$ and Pauli Y basis states $(|e\rangle \pm i|l\rangle)/\sqrt{2}$ by setting $\varphi = \pm\pi/2$ and $\varphi = 0, \pi$, respectively.

At Alice and Bob, counts measured in individual bins correspond to projections onto the mixed state

$$\rho^{A(B)} = \mathrm{Tr}_{B(A)}[\rho], \tag{2.33}$$

which is obtained by tracing out Bob's (B) and Alice's (A) subsystem, respectively, from the overall state $\rho \approx |\Phi^+\rangle\langle\Phi^+|$. This yields

$$\rho^{A(B)} = \frac{1}{2}(|e\rangle\langle e| + |l\rangle\langle l|) = \frac{1}{2}\mathbb{I}_2. \tag{2.34}$$

Therefore, counts measured in individual bins at Alice and Bob do not vary with φ, reflecting that each qubit individually carries no information—only their joint correlations are pure and maximally entangled. The phase-dependent quantum correlations are exhibited in the coincidence counts between the middle bins at Alice and Bob[1],

$$C_{AB}(\varphi) \propto \mathrm{Tr}[\rho\,|\varphi\rangle\langle\varphi|_A \otimes |\varphi\rangle\langle\varphi|_B] = \frac{1}{2}\cos^2\varphi, \tag{2.35}$$

[1]The coincidence counts between the first and third bins at Alice and Bob are constant (since $\mathrm{Tr}[\rho\,|e\rangle\langle e|_A \otimes |e\rangle\langle e|_B] = 1/2$ and $\mathrm{Tr}[\rho\,|l\rangle\langle l|_A \otimes |l\rangle\langle l|_B] = 1/2$).

where $|\varphi\rangle = (|e\rangle + e^{i\varphi}|l\rangle)/\sqrt{2}$. The entanglement visibility is defined as

$$V_{\text{ent}} = \frac{C_{AB}^{\max} - C_{AB}^{\min}}{C_{AB}^{\max} + C_{AB}^{\min}}. \tag{2.36}$$

The entanglement visibility V_{ent} quantifies the contrast of phase-dependent quantum correlations and ranges from 0 (no coherence) to 1 (perfect entanglement). Assuming the shared bipartite state can be modeled as a Werner state [87], the entanglement visibility directly relates to the fidelity with respect to the target Bell state as $F = \frac{1}{4}(1 + 3V_{\text{ent}})$. In this model, separable states satisfy the classical bound $V_{\text{ent}} \leq 1/3$, while any visibility above this threshold certifies the presence of quantum entanglement. However, not all entangled states exhibit nonlocal correlations strong enough to violate a Bell inequality. Bell non-locality is only observed when $V_{\text{ent}} > 1/\sqrt{2}$, which corresponds to violation of the CHSH inequality [88]. For applications in device-independent quantum key distribution (DI-QKD), even higher visibility is required to ensure robustness against noise and detector inefficiencies, with typical experimental thresholds around $V_{\text{ent}} \gtrsim 0.78$ [89]. These visibility bounds thus provide operational criteria for certifying entanglement and nonclassical correlations directly from interference fringe measurements.

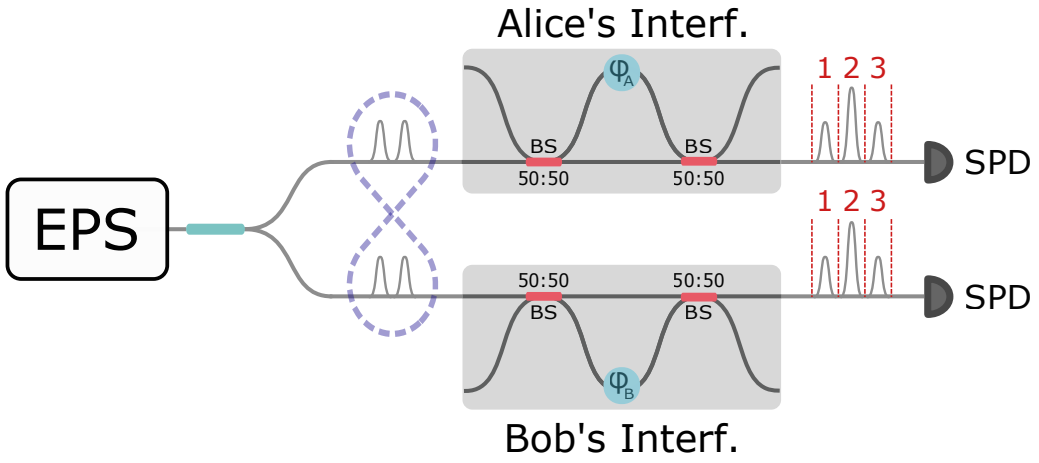

Figure 2.8: Experimental setup for measuring the entanglement visibility of time-bin qubits.

High-rate multiplexed entanglement source

Quantum networks require high-rate sources of entanglement that can maintain high entanglement visibilities over long distances. High entanglement generation rates are essential for overcoming photon losses in long-distance fiber or free-space links,

maintaining synchronization across the network, and providing high throughput for quantum communication protocols. In Chapter 5, I report a high-rate multiplexed entanglement source based on time-bin qubits for advanced quantum networks. We demonstrate a 4.09 GHz repetition rate source of photon pairs entangled across early and late time bins separated by 80 ps. Simultaneous high rates and high visibilities are achieved through frequency multiplexing the spontaneous parametric down-conversion output into 8 time-bin entangled channel pairs. We demonstrate entanglement visibilities as high as 99.4%, total entanglement rates up to 3.55×10^6 coincidences/s, and predict a straightforward path towards achieving up to an order of magnitude improvement in rates without compromising visibility. Finally, we resolve the density matrices of the entangled states for each multiplexed channel and express distillable entanglement rates in ebit/s, thereby quantifying the tradeoff between visibility and coincidence rates that contributes to useful entanglement distribution. This source is a fundamental building block for high-rate entanglement-based QKD systems or advanced quantum networks.

2.6 On-chip squeezed light detection

On-chip BHDs have been demonstrated with shot noise clearance exceeding 14 dB, bandwidths above 2.5 GHz, and total detection losses below 3.5 dB for Gaussian-modulated CV-QKD [90, 91, 92, 93] and quantum random number generation [94, 95, 96]. However, most demonstrations have been limited to the measurement of coherent or vacuum states, which have less stringent performance criteria compared to genuinely non-classical states. In particular, the detection of squeezed states, which are central to sub-shot-noise-limited sensing and continuous-variable cluster state generation for measurement-based quantum computing, is highly sensitive to both optical loss and effective loss from electronic noise [97, 98]. Moreover, there is a trade-off between shot noise clearance and bandwidth: increasing the transimpedance gain improves SNC by reducing input-referred noise, but narrows the bandwidth due to larger RC time constants. Conversely, widening the bandwidth by lowering gain increases electronic noise, thereby degrading sensitivity to quantum correlations.

To address these challenge, we develop integrated BHDs for the detection of non-classical light. First, we measure squeezed light with the on-chip BHD depicted in Fig. 2.7a and an off-chip TIA to measure squeezed light and demonstrate phase locking of squeezing on-chip [77]. Then, we design a photonic-electronic integrated circuit, which we refer to as a quantum-limited coherent receiver (QRX), for on-

chip detection of squeezed light with an on-chip TIA for readout [78]. The QRX is depicted in Fig. 2.7b. The QRX is optimized across various performance metrics: detection loss, common-mode rejection ratio (CMRR), shot-noise clearance (SNC), and bandwidth [77, 78].The CMRR quantifies the ability of the detector to suppress common-mode classical noise, particularly from the local oscillator, due to imbalance in the directional coupler of photodiode configuration. The SNC quantifies the ratio of quantum shot noise to electronic noise, where the LO knee power (P_{knee}) is the minimum LO power required for the shot noise to exceed the electronic noise floor. The detection bandwidth is quantified by the 3dB bandwidth (BW_{3dB}) and shot noise-limited bandwidth (BW_{shot}), which are the frequencies at which the optoelectronic gain drops by 3 dB from its low-frequency value and at which the quantum signal becomes equal to the electronic noise, respectively. The characterizations for the on-chip BHD (Gurses et al. (2023) and the QRX (Gurses et al. (2024)) are summarized in Table 2.1.

Reference	**Loss**	**CMRR**	**SNC**	P_{knee}	BW_{3dB}	BW_{shot}	**PIC/EIC**
Porto et al. (2018) [99]	—	—	17 dB	199 μW	7 MHz	—	Y*/N
Tasker et al. (2021) [100]	3.3 dB	61 dB	14 dB	200 μW	1.7 GHz	9 GHz	Y/Y
Gurses et al. (2023) [77]	5.4 dB	20.4 dB	26 dB	34.6 μW	3 MHz	24.3 MHz	Y/N
Gurses et al. (2024) [78]	2.7 dB	92.3 dB	14.5 dB	315 μW	2.57 GHz	3.50 GHz	Y/Y

Table 2.1: Comparison of quantum-limited BHDs on chip with demonstrated non-classical light detection. *Photodetectors not integrated.

On-chip squeezed light detection with phase-locking

With the integrated coherent receiver chip, we measured squeezed light and demonstrated an easy-to-deploy phase-locking approach to lock onto the squeezed quadrature with the setup shown in Fig. 2.9a. Squeezed vacuum states were generated with a periodically-poled lithium niobate (PPLN) waveguide and fiber-coupled to the chip. Noise floor oscillations in the output with 4 Hz LO phase modulation were measured with an electrical spectrum analyzer (ESA). A 100-second trace was recorded for both squeezed vacuum states (red) and vacuum states (black). A 1-second section of this data is shown in Fig. 2.9b. Over 100 seconds, noise floors 0.226 ± 0.096 dB below and 0.408 ± 0.146 dB above shot noise level (SNL) were observed.

Phase locking in quantum coherent receivers is necessary for maintaining sub-shot-noise-limited sensitivities with squeezed light and enabling phase-determinate

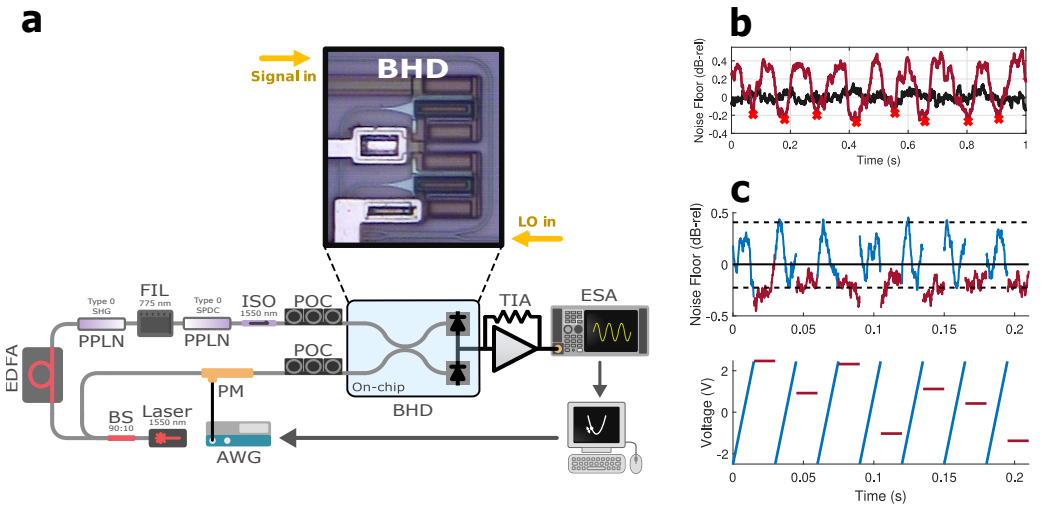

Figure 2.9: On-chip detection of squeezed light with optical phase locking. a) Setup with the silicon photonic receiver for squeezed light measurements. b) Oscillations between quadratures of the squeezed vacuum. Red crosses signify the squeezed quadrature. c) Demonstration of phase locking to the squeezed quadrature showing the noise floor (top) and modulator voltage (bottom)

quantum state tomography. A software-based phase-locking process can be useful for easily deploying coherent quantum links without the need for additional hardware in a quantum coherent transceiver system. Therefore, a phase-locking algorithm was employed to phase-lock the squeezed vacuum detected on-chip to its squeezed quadrature. The algorithm utilizes the phase modulator to do a π phase sweep and finds the phase voltage setting for the squeezed quadrature. The voltage setting is then applied to set the phase to the squeezed quadrature. This procedure is repeated at 67 Hz, as shown in Fig. 2.9c. This closed-loop phase locking approach enables sustained operation at sensitivities below the shot noise floor.

High bandwidth on-chip squeezed light detection

The QRX was used to measure squeezed vacuum to demonstrate sub-shot-noise level operation up to 3.5 GHz with integrated electronic TIA. The experimental setup is shown in Fig. 2.10b. Squeezed vacuum states were generated with a PPLN waveguide and fiber-coupled to the photonic chip with a V-groove array. Noise floor oscillations in the output with 1 Hz LO phase modulation were measured with a spectrum analyzer at different sideband frequencies up to the shot-noise-limited bandwidth Fig. 2.10c. Thirty-second traces were recorded for both squeezed vacuum states (red) and vacuum states (black) at each frequency. A ten-second

section of the data measured at 1.17 GHz is shown in Fig. 2.10d. After data collection, a peak search algorithm was used to acquire the noise level for squeezed and anti-squeezed quadratures normalized to the shot noise level (SNL) at each frequency. A maximum squeezed noise of 0.156 ± 0.039 dB below the SNL and a maximum anti-squeezed noise of 0.507 ± 0.052 above the SNL were observed, see Fig. 2.10e.

While we were limited by the source and tabletop component losses in the squeezed light measurements, on-chip loss sets the bound on how much squeezing can be observed with the QRX. The on-chip system loss comprises the optical losses and the optoelectronic loss determined by the shot noise clearance and PD quantum efficiency (QE). The QRX has a total optical loss of 2.7 dB with 1.3 dB from edge couplers, 1.4 dB from PD QE, and a negligible amount of loss from the TOPS, MZI, and routing. As shown in Fig. 2.10c, the shot noise clearance is also greater than 10 dB up to 2.24 GHz. Therefore, the system loss is at most 3 dB over the bandwidth of the receiver, enabling sensitivities of 3 dB below the SNL.

The packaged photonic-electronic QRX enables a path toward the deployment of quantum-limited coherent receivers in optical communication and sensing networks. Due to its compact size, high CMRR, highest reported 3-dB bandwidth and lowest reported system loss in the literature, it introduces the prospect of leveraging non-classical states of light to enhance the information capacity and sensitivity of optical links. With the demonstration of high shot-noise-limited bandwidth and detection of squeezed vacuum showcasing an enhancement in the SNL, this work highlights the potential of leveraging non-classical light and deploying quantum coherent receivers in classical optical networks in addition to preparing an infrastructure suitable for quantum communications.

Multiplexed BHD array on-chip for squeezed light detection

Beyond single component demonstrations, the next major milestone for CV quantum technologies is to develop large-scale quantum photonic systems on-chip, enabling massively parallelized operations with precise control in a compact form factor. While bulk optical experiments have demonstrated foundational protocols, they do not scale to the system sizes required for advanced and practical implementations of quantum technologies, such as computational quantum advantage or fault-tolerant error correction. Silicon photonics offers a CMOS-compatible platform that allows wafer-scale fabrication of stable, programmable optical circuits incorporating

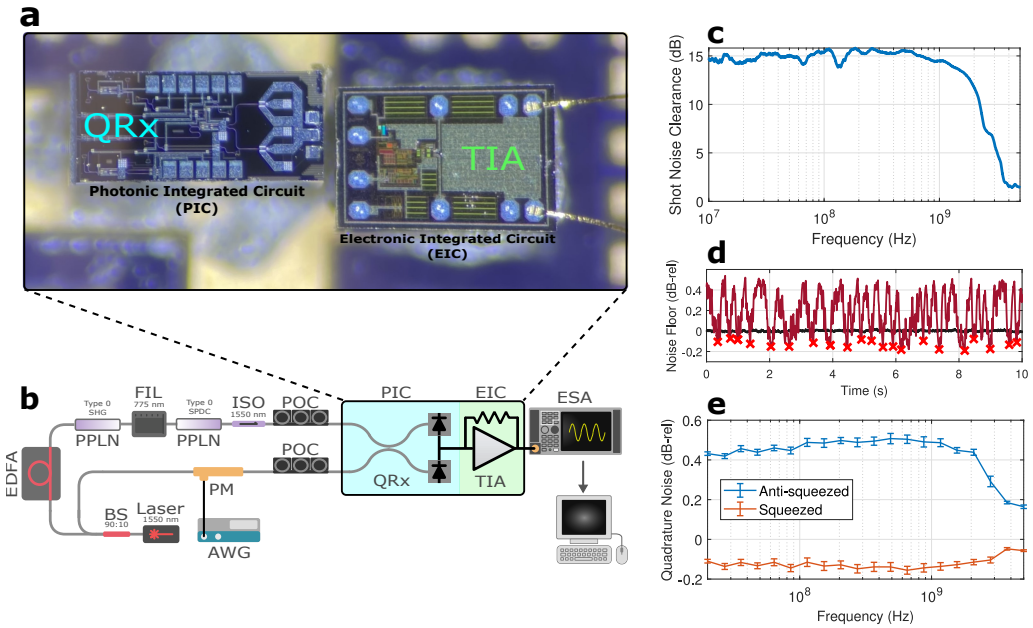

Figure 2.10: On-chip detection of squeezed light with a photonic-electronic integrated circuit. a) Die photo of photonic integrated circuit (PIC) for the quantum-limited coherent receiver (QRX) with high bandwidth photodiodes and electronic integrated circuit (EIC) for readout with a transimpedance amplifier (TIA). b) Setup with the integrated photonic-electronic coherent receiver for squeezed light measurements. c) Shot noise clearance response of the QRX with maximum LO photocurrent. d) Oscillations between quadratures of the squeezed vacuum measured at 1.17 GHz. Red crosses signify the squeezed quadrature. e) Quadrature noise normalized to the shot noise level of vacuum for squeezed and anti-squeezed quadratures.

sources, circuits, and detectors on a single chip. Advanced CV quantum technologies will require quadrature measurements across many spatial or temporal modes, critical for applications in distributed quantum sensing, measurement-based quantum computing, and broadband quantum communication. Multiplexed BHD array architectures have been proposed to boost rates in quantum random number generation (QRNG) and continuous-variable quantum key distribution (CV-QKD), enable entanglement-enhanced distributed quantum sensing, and perform mode-selective measurements in continuous-variable optical homodyne tomography. However, all demonstrations of multiplexed BHD systems to date have relied on bulk optics.

In Chapter 6, I report the first array of quantum-limited BHDs capable of detecting squeezed light on a silicon photonic chip. Scaling from a single QRX to a large-scale system introduces several design challenges, including minimizing electrical

parasitics to avoid RF oscillations, ensuring signal integrity across all channels, and suppressing electronic and optical crosstalk between densely packed channels. Using the QRX design in Fig. 2.7b as a blueprint, we spatially multiplex 32 QRXs on a silicon photonic chip. The outputs of the QRXs are wire-bonded to an interposer on a compact PCB containing an array of 32 discrete TIAs. We mitigate these challenges with a careful co-design between the photonic chip layout and electronic readout circuit. As described in the next section, the QRX array is incorporated into a larger system on the same chip, which is designed to demonstrate the basic functionalities required for chip-based wireless quantum technologies.

2.7 Quantum phased arrays

The expansion from wired to wireless links is an exciting prospect for integrated quantum technologies. For classical technologies, the advent of phased arrays enabled directional and adaptive wireless links by manipulating electromagnetic waves over free space. In a point-to-point wireless communication link, a transmitter encodes a signal in a beam of electromagnetic radiation that is sent to a receiver. The spot size of the beam spreads with distance due to diffraction, resulting in geometric loss from the overlap of the diverging spot size and the receiver aperture area. Diffraction-induced geometric loss can result in severe signal loss that ultimately limits the range and rate of communication [101, 102, 103, 104]. In classical wireless communications and sensing, beam divergence is controlled by wavefront engineering with transmitter or receiver phased arrays. A phased array is a coherent array of antenna elements that can transmit or receive electromagnetic fields. By controlling the amplitude and phase on each element, the wavefront of the electromagnetic field can be engineered over free space. Wavefront engineering allows for active manipulation of an electromagnetic field in a dynamic real-time fashion [105, 106]. Beamforming, or angular focusing, of an electromagnetic field is performed by coherently combining elements in a phased array such that the signal field constructively interferes at a selected angle [107].

Here I extend wavefront engineering to quantum fields with a concept referred to as "quantum phased arrays." A quantum phased array (QPA) is a quantum-coherent array of antenna elements, each with phase and amplitude control, that can emit or receive quantum fields. I show how beamforming with a QPA can be used to establish reconfigurable wireless quantum links for free-space quantum communications. More broadly, I demonstrate how to synthesize quantum states in the far-field with a QPA and illustrate how free-space protocols can be constructed

based on quantum state engineering with multiple QPAs.

Theory

A quantum field with annihilation operator $\hat{a}_{\text{in}}$ is input to a QPA transmitter. The field is distributed to N channels with associated spatial mode functions,

$$\hat{a}_{\text{in}} = \int \hat{a}_{\text{in}}(\rho) d\rho \tag{2.37}$$

$$\hat{a}_{\text{in}}(\rho), = \sum_{j=1}^{N} \hat{a}_j \mathcal{E}_j(\rho), \tag{2.38}$$

where $\hat{a}_j$ is the annhiliation operator for the jth channel mode. In each channel, a gain and phase shift is applied, followed by a radiation by an antenna. The antennas have an associated set of mode functions $\{\mathcal{E}_j(\rho)\}$, where $j = 1, ..., N$ and the aperture coordinates are grouped into ρ. The channel modes are related to the aperture spatial modes by,

$$\hat{a}_j = \int \mathcal{E}_j(\rho) \hat{a}_{\text{in}}(\rho) d\rho, \tag{2.39}$$

where $\hat{a}_{\text{in}}(\rho)$ is the creation operator for the field distributed to location ρ.

The field at the output of the aperture is,

$$\hat{a}_{\text{out}} = \int \hat{a}_{\text{out}}(\rho) d\rho, \tag{2.40}$$

$$\hat{a}_{\text{out}}(\rho) = \sum_{j} g_j e^{i\phi_j} \hat{a}_j \mathcal{E}_j(\rho), \tag{2.41}$$

where g_j is the gain and ϕ_j is the phase applied to each channel mode $\hat{a}_j$.

In the small pixel and large N limit, the pixel mode functions approach,

$$\mathcal{E}_j(\rho) \approx \delta^d(\rho - \rho_j), \tag{2.42}$$

where $\delta^d(\rho)$ is the d dimensional Delta function with d denoting the coordinate dimensions, ρ_j represents the coordinates of the center of the jth pixel. In this limit, $\hat{a}_j \approx \hat{a}_{\text{in}}(\rho_j)\Delta\rho_j$ where $\Delta\rho_j$ is the surface area of the jth pixel, and the output field becomes,

$$\hat{a}_{\text{out}}(\rho) = \sum_{j} g_j e^{i\phi_j} \hat{a}_{\text{in}}(\rho_j) \delta^d(\rho - \rho_j) \Delta\rho_j, \tag{2.43}$$

$$\approx \int g(\rho_j) e^{i\phi(\rho_j)} \hat{a}_{\text{in}}(\rho_j) \delta^d(\rho - \rho_j) d\rho_j, \tag{2.44}$$

$$= c(\rho) \hat{a}_{\text{in}}(\rho), \tag{2.45}$$

where the sum in Eq. 2.43 becomes a Riemann sum over the antenna coordinates and the applied gains $\{g_j\}$ and phases $\{\phi_j\}$ approach continuous gain $g(\rho_j)$ and phase $\phi(\rho_j)$ profiles, respectively. The gain and phase profiles give rise to a reconfigurable array mode function, $c(\rho) = g(\rho)e^{i\phi(\rho)}$, that can be used to engineer quantum states at the focal plane of the QPA.

In the far field limit, the field at the aperture plane can be approximated in terms of the field at focal plane by the Kirchhoff-Fresnel diffraction formula (see Methods in Chapter 6),

$$\hat{a}_{\text{out}} = \int c(\rho)\hat{a}_{\text{in}}(\rho)d\rho \approx \int c(f)\hat{a}_{\text{in}}(f)df, \tag{2.46}$$

where $f = \sin\theta/\lambda$ is the focal plane coordinate and the focal plane mode profile is,

$$c(f) \propto \int e^{i2\pi\rho f} c(\rho)d\rho. \tag{2.47}$$

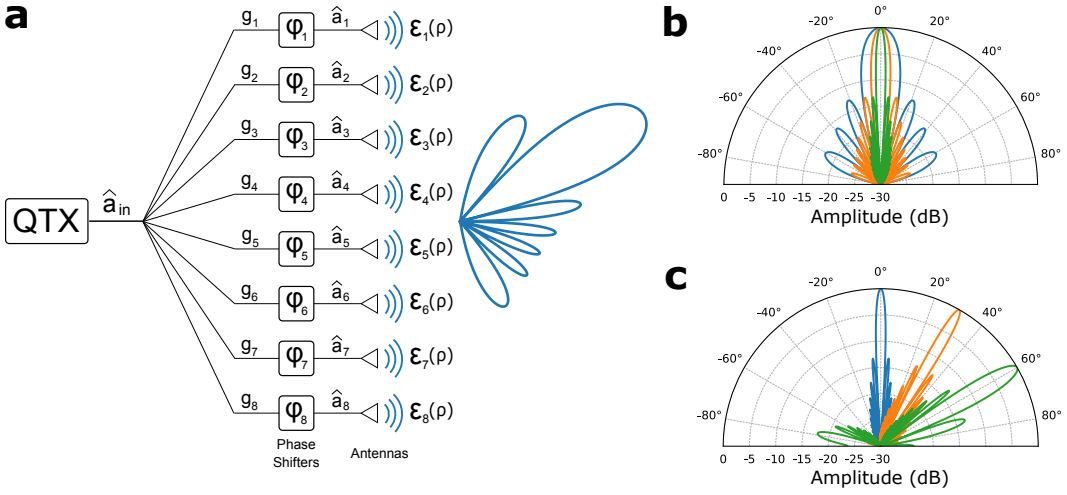

Figure 2.11: Quantum phased array transmitter. a) Conceptual diagram of a quantum phased array transmitter. The QTX is a source of a quantum states of an electromagnetic field $\hat{a}_{\text{in}}$, which is distributed across eight antenna elements. An amplitude g_n and phase shift φ_n is applied to each element, and the field from each antenna with a mode function $\mathcal{E}_n(\rho)$ is radiated to free-space, where $n \in [1, 8]$. b) Array factor for a uniform linear array of eight (blue), sixteen (orange), and 32 (green) elements, beamformed at broadside. c) Array factor for a uniform linear array of 32 elements beamformed at broadside (blue), 30° (orange), and 60° (green).

Array factor: Consider an N-element linear array with uniform amplitude and spacing,

$$\hat{a}_{\text{out}}(\rho) = \sum_{j=1}^{N} e^{i\phi_j} \hat{a}_j \mathcal{E}_j(\rho). \tag{2.48}$$

In the small pixel limit,

$$\hat{a}_{\text{out}} \approx \sum_{j} e^{i\phi_j} \hat{a}_{\text{in}}(\rho_j) \Delta\rho_j, \tag{2.49}$$

$$= \int \left(\sum_{j=1}^{N} e^{i\phi_j} \delta(\rho - \rho_j) \Delta\rho_j \right) \hat{a}_{\text{in}}(\rho) d\rho. \tag{2.50}$$

In terms of focal plane coordinates,

$$\hat{a}_{\text{out}} \propto \int \left(\sum_{j=1}^{N} e^{i(\phi_j + 2\pi\rho_j f)} \right) \hat{a}_{\text{in}}(f) df. \tag{2.51}$$

The coefficients in parentheses is the modal profile of beam in focal plane and corresponds to the array factor (AF) of the phased array [108],

$$\text{AF}(f, \beta) = \sum_{j=1}^{N} e^{i(\phi_j + 2\pi\rho_j f)}. \tag{2.52}$$

For an array with a progressive phase $\Delta\phi$ applied to the antennas that are uniformly spaced by a distance d, corresponding to $\phi_j = \Delta\phi(j-1)$ and $\rho_j = (j-1)d$, the array factor is [108],

$$\text{AF}(f, \beta) = e^{i[(N-1)/2]\varphi} \left[\frac{\sin\left(\frac{N}{2}\varphi\right)}{\sin\left(\frac{1}{2}\varphi\right)} \right], \tag{2.53}$$

where $\varphi = \Delta\phi + (2\pi d/\lambda)\sin\theta$. In normalized form, the array factor is,

$$\text{AF}_N(\varphi) = \frac{\sin\left(\frac{N}{2}\varphi\right)}{N \sin\left(\frac{1}{2}\varphi\right)} \approx \text{sinc}\left(\frac{N}{2}\varphi\right), \tag{2.54}$$

where the approximation is taken in small φ. The normalized array factor is plotted in Fig. 2.11b for $N = 8, 16$ and 32.

Beam steering: The maximum of AF_N occurs when $\varphi = 0$ at,

$$\theta_{\text{max}} = \arcsin\left(-\frac{\lambda\Delta\phi}{2\pi d}\right). \tag{2.55}$$

The beam maximum can be steered by varying the progressive phase $\Delta\phi$. The array factor for various beam angles θ_{max} are shown in Fig. 2.11c.

Beamwidth: The 3 dB point of the beam occurs for Eq. 2.54 when,

$$\theta_h^{\pm} = \arcsin\left[\frac{\lambda}{2\pi d}\left(-\Delta\phi \pm \frac{2.782}{N}\right)\right]. \tag{2.56}$$

The half-power beamwidth for a symmetrical pattern is $\Theta_h = 2|\theta_{\max} - \theta_h^-|$ [108]. For $d \gg \lambda$, $\Theta_h \sim \frac{\lambda}{Nd}$. The beamwidth scales inversely with the aperture width Nd. For large N, $\hat{a}_{\text{out}} \to \hat{a}_{\text{in}}(f_{\max})$ where $f_{\max} = \sin(\theta_{\max})/\lambda$.

Quantum state synthesis

For a target state in the focal plane, the coefficients for the aperture plane profile can be found in terms of the desired focal plane coefficients as,

$$c(\rho) \propto \int e^{-i2\pi\rho f} c(f) df. \tag{2.57}$$

Superposition states can be engineered by synthesizing multimode radiation patterns. For an N-element uniform linear array, a two-mode superposition state can be realized by,

$$\hat{a}_{\text{out}}(\rho) = \sum_{j=1}^{N} \frac{1}{\sqrt{2}}\left(e^{i\phi_j^A} + e^{i\delta}e^{i\phi_j^B}\right)\hat{a}_j \mathcal{E}_j(\rho), \tag{2.58}$$

where $\phi_j^A = \Delta\phi^A(j-1)$ and $\phi_j^B = \Delta\phi^B(j-1)$. The resulting array factor is the superpositon of the array factors,

$$\text{AF}_N = \frac{1}{\sqrt{2}}\left(\text{AF}_N(\varphi^A) + e^{i\delta}\text{AF}_N(\varphi^B)\right), \tag{2.59}$$

which in the large N limit approaches the superposition state,

$$\hat{a}_{\text{out}} \approx \frac{1}{\sqrt{2}}(\hat{a}_{\text{in}}(f^A) + e^{i\delta}\hat{a}_{\text{in}}(f^B)). \tag{2.60}$$

This can be extended to arbitrary superposition states in the focal plane with nonuniform amplitudes in and relative phases. By using multiple QPAs to synthesize superposition states and interfering them over free space, quantum information protocols for the generation and distribution of entanglement can be constructed for quantum sensing and communication (see Fig. 2.12). In Appendix A, I provide two illustrative examples of QPA protocols for realizing a reconfigurable beamplitter and generating N00N states.

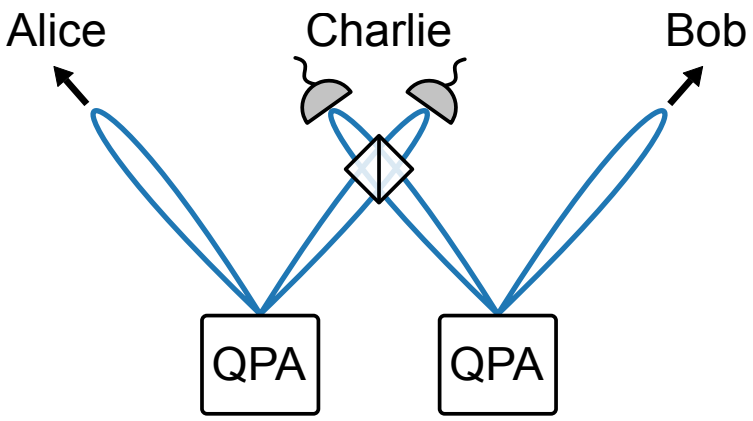

Figure 2.12: Conceptual illustration of quantum communication with multiple QPAs, where photons transmitted to Alice and Bob can be steered by reconfiguring their beams.

QPA receiver system on a chip

In Chapter 6, we used the QRX array discussed in Section 2.6 to realize a phased array system on a chip that can receive, image and manipulate non-classical light over free space. We demonstrate an integrated photonic-electronic system with more than 1000 functional components on-chip to detect squeezed light. By integrating an array of 32 sub-wavelength engineered metamaterial antennas, we demonstrate the first, to our knowledge, direct free-space-to-chip interface for reconfigurable quantum links. On the same chip, we implement the first, to our knowledge, large-scale array of quantum-limited coherent receivers that can resolve non-classical signals simultaneously across 32 channels. With coherent readout and manipulation of these signals, we demonstrate 32-pixel imaging and spatially configurable reception of squeezed light over free space. Our work advances wireless quantum technologies that could enable practical applications in quantum communications and sensing.

References

[1] Robert W. Boyd. Nonlinear Optics. 3rd. San Diego, CA, USA: Academic Press, 2008. ISBN: 978-0123694706.

[2] C.K. Hong and L. Mandel. "Theory of parametric frequency down conversion of light." In: Physical Review A 31.4 (1985), p. 2409.

[3] Bahaa E. A. Saleh and Malvin Carl Teich. Fundamentals of Photonics. 2nd. Hoboken, NJ, USA: Wiley-Interscience, 2007. ISBN: 978-0471358329.

[4] P. G. Kwiat, K. Mattle, H. Weinfurter, A. Zeilinger, A. V. Sergienko, and Y. Shih. "New High-Intensity Source of Polarization-Entangled Photon Pairs."

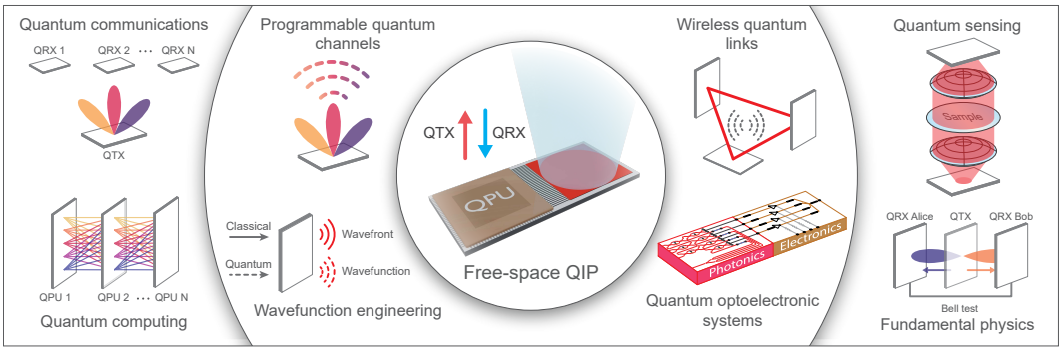

Figure 2.13: Vision for wireless quantum chip technologies with reconfigurable chip-to-free space quantum interconnects enabled by phased array interfaces and their applications in quantum communications, sensing and computing.

In: Physical Review Letters 75.24 (1995), pp. 4337–4341. DOI: 10.1103/PhysRevLett.75.4337.

[5] M. M. Fejer, G. A. Magel, D. H. Jundt, and R. L. Byer. "Quasi-phase-matched second harmonic generation: Tuning and tolerances." In: IEEE Journal of Quantum Electronics 28.11 (1992), pp. 2631–2654. DOI: 10.1109/3.161322.

[6] L. E. Myers, R. C. Eckardt, M. M. Fejer, R. L. Byer, W. R. Bosenberg, and J. W. Pierce. "Quasi-phase-matched optical parametric oscillators in bulk periodically poled LiNbO3." In: Journal of the Optical Society of America B 12.11 (1995), pp. 2102–2116. DOI: 10.1364/JOSAB.12.002102.

[7] Yanhua Shih and C. O. Alley. "New Type of Einstein-Podolsky-Rosen-Bohm Experiment Using Pairs of Light Quanta Produced by Optical Parametric Down Conversion." In: Physical Review Letters 61.26 (1988), pp. 2921–2924. DOI: 10.1103/PhysRevLett.61.2921.

[8] C. K. Hong, Z. Y. Ou, and L. Mandel. "Measurement of Subpicosecond Time Intervals between Two Photons by Interference." In: Physical Review Letters 59.18 (1987), pp. 2044–2046. DOI: 10.1103/PhysRevLett.59.2044.

[9] Wolfgang Tittel, Jürgen Brendel, Hugo Zbinden, and Nicolas Gisin. "Violation of Bell inequalities by photons more than 10 km apart." In: Physical Review Letters 81.17 (1998), p. 3563.

[10] Sébastien Tanzilli, Hugues De Riedmatten, Wolfgang Tittel, Hugo Zbinden, Pascal Baldi, Marc De Micheli, Daniel Barry Ostrowsky, and Nicolas Gisin. "Highly efficient photon-pair source using periodically poled lithium niobate waveguide." In: Electronics Letters 37.1 (2001), pp. 26–28.

[11] Jian-Wei Pan, Zeng-Bing Chen, Chao-Yang Lu, Harald Weinfurter, Anton Zeilinger, and Marek Żukowski. "Multiphoton entanglement and interferometry." In: Reviews of Modern Physics 84.2 (2012), pp. 777–838.

[12] Marco Fiorentino, Sean M Spillane, Raymond G. Beausoleil, Tony D. Roberts, Philip Battle, and Mark W. Munro. “Spontaneous parametric down-conversion in periodically poled KTP waveguides and bulk crystals.” In: Optics Express 15.12 (2007), pp. 7479–7488.

[13] Warren P. Grice and Ian A. Walmsley. “Spectral information and distinguishability in type-II down-conversion with a broadband pump.” In: Physical Review A 56.2 (1997), p. 1627.

[14] Kevin Zielnicki, Karina Garay-Palmett, Daniel Cruz-Delgado, Hector Cruz-Ramirez, Michael F. O’Boyle, Bin Fang, Virginia O. Lorenz, Alfred B U’Ren, and Paul G. Kwiat. “Joint spectral characterization of photon-pair sources.” In: Journal of Modern Optics 65.10 (2018), pp. 1141–1160.

[15] Kevin Zielnicki, Karina Garay-Palmett, Radhika Dirks, Alfred B. U’Ren, and Paul G. Kwiat. “Engineering of near-IR photon pairs to be factorable in space-time and entangled in polarization.” In: Optics Express 23.6 (2015), pp. 7894–7907.

[16] Warren P. Grice, Alfred B. U’Ren, and Ian A. Walmsley. “Eliminating frequency and space-time correlations in multiphoton states.” In: Physical Review A 64.6 (2001), p. 063815.

[17] Alfred B. U’Ren, Konrad Banaszek, and Ian A. Walmsley. “Photon engineering for quantum information processing.” In: arXiv preprint quant-ph/0305192 (2003).

[18] P. J. Mosley, J. S. Lundeen, B. J. Smith, P. Wasylczyk, A. B. U’Ren, C. Silberhorn, and I. A. Walmsley. “Heralded Generation of Ultrafast Single Photons in Pure Quantum States.” In: Physical Review Letters 100.13 (2008). Demonstrates spectral engineering for single–mode operation and reports high heralding efficiency and purity (as indicated by low $g^{(2)}(0)$)., p. 133601.

[19] Luis Edgar Vicent, Alfred B. U’Ren, Radhika Rangarajan, Clara I. Osorio, Juan P. Torres, Lijian Zhang, and Ian A. Walmsley. “Design of bright, fiber-coupled and fully factorable photon pair sources.” In: New Journal of Physics 12.9 (2010), p. 093027.

[20] D. Branning, W.P. Grice, R. Erdmann, and I. A. Walmsley. “Engineering the indistinguishability and entanglement of two photons.” In: Physical Review Letters 83.5 (1999), p. 955.

[21] Thomas Lutz, Piotr Kolenderski, and Thomas Jennewein. “Toward a downconversion source of positively spectrally correlated and decorrelated telecom photon pairs.” In: Optics letters 38.5 (2013), pp. 697–699.

[22] Yasser Jeronimo-Moreno, Saul Rodriguez-Benavides, and Alfred B. U’Ren. “Theory of cavity-enhanced spontaneous parametric downconversion.” In: Laser physics 20 (2010), pp. 1221–1233.

[23] Andrew Mueller, Samantha I. Davis, Boris Korzh, Raju Valivarthi, Andrew D. Beyer, Rahaf Youssef, Neil Sinclair, Cristián Peña, Matthew D Shaw, and Maria Spiropulu. “High-rate multiplexed entanglement source based on time-bin qubits for advanced quantum networks.” In: Optica Quantum 2.2 (2024), pp. 64–71.

[24] Jürgen Brendel, Nicolas Gisin, Wolfgang Tittel, and Hugo Zbinden. "Pulsed energy-time entangled twin-photon source for quantum communication." In: Physical Review Letters 82.12 (1999), p. 2594.

[25] A. Mair, A. Vaziri, G. Weihs, and A. Zeilinger. "Entanglement of the orbital angular momentum states of photons." In: Nature 412 (2001), pp. 313–316. DOI: 10.1038/35085529. URL: https://doi.org/10.1038/35085529.

[26] I. Marcikic, H. de Riedmatten, W. Tittel, V. Scarani, H. Zbinden, and N. Gisin. "Time-bin entangled qubits for quantum communication created by femtosecond pulses." In: Phys. Rev. A 66 (6 Dec. 2002), p. 062308. DOI: 10.1103/PhysRevA.66.062308. URL: https://link.aps.org/doi/10.1103/PhysRevA.66.062308.

[27] Samantha I. Davis, Andrew Mueller, Raju Valivarthi, Nikolai Lauk, Lautaro Narvaez, Boris Korzh, Andrew D. Beyer, Olmo Cerri, Marco Colangelo, Karl K. Berggren, et al. "Improved heralded single-photon source with a photon-number-resolving superconducting nanowire detector." In: Physical Review Applied 18.6 (2022), p. 064007.

[28] Alexander I Lvovsky. "Squeezed light." In: Photonics: Scientific Foundations, Technology and Applications 1 (2015), pp. 121–163.

[29] Hans-A. Bachor and Timothy C. Ralph. A guide to experiments in quantum optics. John Wiley & Sons, 2019.

[30] Christopher C. Gerry and Peter L. Knight. Introductory quantum optics. Cambridge University Press, 2005.

[31] Robert H. Hadfield. "Single-photon detectors for optical quantum information applications." In: Nature photonics 3.12 (2009), pp. 696–705.

[32] Adriana E. Lita, Dileep V. Reddy, Varun B. Verma, Richard P. Mirin, and Sae Woo Nam. "Development of superconducting single-photon and photon-number resolving detectors for quantum applications." In: Journal of Lightwave Technology 40.23 (2022), pp. 7578–7597.

[33] A. J. Miller, S. W. Nam, J. M. Martinis, and A. V. Sergienko. "Demonstration of a low-noise near-infrared photon counter with multiphoton discrimination." In: Applied Physics Letters 83 (2003), pp. 791–793.

[34] A. E. Lita, A. J. Miller, and S. W. Nam. "Counting near-infrared single photons with 95% efficiency." In: Optics Express 16 (2008), pp. 3032–3040.

[35] Brice Calkins, Paolo L. Mennea, Adriana E. Lita, Benjamin J. Metcalf, W. Steven Kolthammer, Antia Lamas-Linares, Justin B. Spring, Peter C. Humphreys, Richard P. Mirin, James C. Gates, et al. "High quantum-efficiency photon-number-resolving detector for photonic on-chip information processing." In: Optics Express 21.19 (2013), pp. 22657–22670.

[36] Georg Harder, Tim J. Bartley, Adriana E. Lita, Sae Woo Nam, Thomas Gerrits, and Christine Silberhorn. "Single-mode parametric-down-conversion states with 50 photons as a source for mesoscopic quantum optics." In: Physical Review Letters 116.14 (2016), p. 143601.

[37] Miller Eaton, Amr Hossameldin, Richard J. Birrittella, Paul M. Alsing, Christopher C. Gerry, Hai Dong, Chris Cuevas, and Olivier Pfister. "Resolution of 100 photons and quantum generation of unbiased random numbers." In: Nature Photonics 17.1 (2023), pp. 106–111.

[38] W. Guo, X. Liu, Y. Wang, Q. Wei, L.F. Wei, J. Hubmayr, J. Fowler, J. Ullom, L. Vale, M.R. Vissers, et al. "Counting near infrared photons with microwave kinetic inductance detectors." In: Applied Physics Letters 110.21 (2017).

[39] P. K. Day, H. G. LeDuc, B. A. Mazin, A. Vayonakis, and J. Zmuidzinas. "A broadband superconducting detector suitable for use in large arrays." In: Nature 425 (2003), pp. 817–821.

[40] Dileep V. Reddy, Robert R. Nerem, Sae Woo Nam, Richard P. Mirin, and Varun B. Verma. "Superconducting nanowire single-photon detectors with 98% system detection efficiency at 1550 nm." In: Optica 7.12 (2020), p. 1649. ISSN: 2334-2536.

[41] Andrew S. Mueller, Boris Korzh, Marcus Runyan, Emma E. Wollman, Andrew D. Beyer, Jason P. Allmaras, Angel E. Velasco, Ioana Craiciu, Bruce Bumble, Ryan M. Briggs, et al. "Free-space coupled superconducting nanowire single-photon detector with low dark counts." In: Optica 8.12 (2021), pp. 1586–1587.

[42] Giovanni V. Resta, Lorenzo Stasi, Matthieu Perrenoud, Sylvain El-Khoury, Tiff Brydges, Rob Thew, Hugo Zbinden, and Félix Bussières. "Gigahertz detection rates and dynamic photon-number resolution with superconducting nanowire arrays." In: Nano Letters 23.13 (2023), pp. 6018–6026.

[43] Boris Korzh, Qing-Yuan Zhao, Jason P. Allmaras, Simone Frasca, Travis M. Autry, Eric A Bersin, Andrew D. Beyer, Ryan M. Briggs, Bruce Bumble, Marco Colangelo, et al. "Demonstration of sub-3 ps temporal resolution with a superconducting nanowire single-photon detector." In: Nature Photonics 14.4 (2020), pp. 250–255.

[44] Andrew J. Kerman, Eric A. Dauler, William E. Keicher, Joel K.W. Yang, Karl K. Berggren, G. Gol'Tsman, and B. Voronov. "Kinetic-inductance-limited reset time of superconducting nanowire photon counters." In: Applied Physics Letters 88.11 (2006).

[45] Di Zhu, Marco Colangelo, Changchen Chen, Boris A. Korzh, Franco N.C. Wong, Matthew D. Shaw, and Karl K. Berggren. "Resolving photon numbers using a superconducting nanowire with impedance-matching taper." In: Nano Letters 20.5 (2020), pp. 3858–3863.

[46] Timon Schapeler, Niklas Lamberty, Thomas Hummel, Fabian Schlue, Michael Stefszky, Benjamin Brecht, Christine Silberhorn, and Tim J. Bartley. "Electrical trace analysis of superconducting nanowire photon-number-resolving detectors." In: Physical Review Applied 22.1 (2024), p. 014024.

[47] Marco Colangelo, Boris Korzh, Jason P. Allmaras, Andrew D. Beyer, Andrew S. Mueller, Ryan M. Briggs, Bruce Bumble, Marcus Runyan, Martin J. Stevens, Adam N. McCaughan, et al. "Impedance-matched differential superconducting nanowire detectors." In: Physical Review Applied 19.4 (2023), p. 044093.

[48] Mamoru Endo, Tatsuki Sonoyama, Mikihisa Matsuyama, Fumiya Okamoto, Shigehito Miki, Masahiro Yabuno, Fumihiro China, Hirotaka Terai, and Akira Furusawa. "Quantum detector tomography of a superconducting nanostrip photon-number-resolving detector." In: Optics Express 29.8 (2021), pp. 11728–11738.

[49] Clinton Cahall, Kathryn L. Nicolich, Nurul T. Islam, Gregory P. Lafyatis, Aaron J. Miller, Daniel J. Gauthier, and Jungsang Kim. "Multi-photon detection using a conventional superconducting nanowire single-photon detector." In: Optica 4.12 (2017), pp. 1534–1535.

[50] Aleksander Divochiy, Francesco Marsili, David Bitauld, Alessandro Gaggero, Roberto Leoni, Francesco Mattioli, Alexander Korneev, Vitaliy Seleznev, Nataliya Kaurova, Olga Minaeva, et al. "Superconducting nanowire photon-number-resolving detector at telecommunication wavelengths." In: Nature Photonics 2.5 (2008), pp. 302–306.

[51] Eric A. Dauler, Andrew J. Kerman, Bryan S. Robinson, Joel K.W. Yang, Boris Voronov, Gregory Goltsman, Scott A. Hamilton, and Karl K. Berggren. "Photon-number-resolution with sub-30-ps timing using multi-element superconducting nanowire single photon detectors." In: Journal of Modern Optics 56.2-3 (2009), pp. 364–373.

[52] Risheng Cheng, Heyu Yin, Jianshe Liu, Tiefu Li, Han Cai, Zheng Xu, and Wei Chen. "Photon-number-resolving detector based on superconducting serial nanowires." In: IEEE Transactions on Applied Superconductivity 23.1 (2012), pp. 2200309–2200309.

[53] Chandra M. Natarajan, Lijian Zhang, Hendrik Coldenstrodt-Ronge, Gaia Donati, Sander N. Dorenbos, Val Zwiller, Ian A. Walmsley, and Robert H. Hadfield. "Quantum detector tomography of a time-multiplexed superconducting nanowire single-photon detector at telecom wavelengths." In: Optics Express 21.1 (2013), pp. 893–902.

[54] Mattias Jönsson, Marcin Swillo, Samuel Gyger, Val Zwiller, and Gunnar Björk. "Temporal array with superconducting nanowire single-photon detectors for photon-number resolution." In: Physical Review A 102.5 (2020), p. 052616.

[55] Ioana Craiciu, Boris Korzh, Andrew D. Beyer, Andrew Mueller, Jason P. Allmaras, Lautaro Narváez, Maria Spiropulu, Bruce Bumble, Thomas Lehner, Emma E. Wollman, et al. "High-speed detection of 1550 nm single photons with superconducting nanowire detectors." In: Optica 10.2 (2023), pp. 183–190.

[56] Lorenzo Stasi, Gaëtan Gras, Riad Berrazouane, Matthieu Perrenoud, Hugo Zbinden, and Félix Bussières. "Fast high-efficiency photon-number-resolving parallel superconducting nanowire single-photon detector." In: Physical Review Applied 19.6 (2023), p. 064041.

[57] Lorenzo Stasi, Towsif Taher, Giovanni V. Resta, Hugo Zbinden, Rob Thew, and Felix Bussieres. “Enhanced detection rate and high photon-number efficiencies with a scalable parallel SNSPD.” In: ACS Photonics 12.1 (2024), pp. 320–329.

[58] Francesco Mattioli, Zili Zhou, Alessandro Gaggero, Rosalinda Gaudio, Roberto Leoni, and Andrea Fiore. “Photon-counting and analog operation of a 24-pixel photon number resolving detector based on superconducting nanowires.” In: Optics Express 24.8 (2016), pp. 9067–9076.

[59] Risheng Cheng, Yiyu Zhou, Sihao Wang, Mohan Shen, Towsif Taher, and Hong X. Tang. “A 100-pixel photon-number-resolving detector unveiling photon statistics.” In: Nature Photonics 17.1 (2023), pp. 112–119.

[60] Frédéric Grosshans, Gilles Van Assche, Jérôme Wenger, Rosa Brouri, Nicolas J. Cerf, and Philippe Grangier. “Quantum key distribution using gaussian-modulated coherent states.” In: Nature 421.6920 (2003), pp. 238–241.

[61] Robert Raussendorf and Hans J. Briegel. “A one-way quantum computer.” In: Physical Review Letters 86.22 (2001), p. 5188.

[62] Robert Raussendorf, Daniel E. Browne, and Hans J. Briegel. “Measurement-based quantum computation on cluster states.” In: Physical review A 68.2 (2003), p. 022312.

[63] D. Ganapathy, W. Jia, M. Nakano, V. Xu, N. Aritomi, T. Cullen, N. Kijbunchoo, S.E. Dwyer, A. Mullavey, L. McCuller, et al. “Broadband quantum enhancement of the LIGO detectors with frequency-dependent squeezing.” In: Physical Review X 13.4 (2023), p. 041021.

[64] Nicolas C. Menicucci, Peter Van Loock, Mile Gu, Christian Weedbrook, Timothy C. Ralph, and Michael A. Nielsen. “Universal quantum computation with continuous-variable cluster states.” In: Physical Review Letters 97.11 (2006), p. 110501.

[65] Daniel Gottesman, Alexei Kitaev, and John Preskill. “Encoding a qubit in an oscillator.” In: Physical Review A 64.1 (2001), p. 012310.

[66] Shuntaro Takeda, Takahiro Mizuta, Maria Fuwa, Peter Van Loock, and Akira Furusawa. “Deterministic quantum teleportation of photonic quantum bits by a hybrid technique.” In: Nature 500.7462 (2013), pp. 315–318.

[67] Axel Schönbeck, Fabian Thies, and Roman Schnabel. “13 dB squeezed vacuum states at 1550 nm from 12 mW external pump power at 775 nm.” In: Optics Letters 43.1 (2017), pp. 110–113.

[68] Han-Sen Zhong, Hui Wang, Yu-Hao Deng, Ming-Cheng Chen, Li-Chao Peng, Yi-Han Luo, Jian Qin, Dian Wu, Xing Ding, Yi Hu, et al. “Quantum computational advantage using photons.” In: Science 370.6523 (2020), pp. 1460–1463.

[69] Galan Moody, Volker J. Sorger, Daniel J. Blumenthal, Paul W. Juodawlkis, William Loh, Cheryl Sorace-Agaskar, Alex E. Jones, Krishna C. Balram, Jonathan C. F. Matthews, Anthony Laing, et al. “2022 Roadmap on integrated quantum photonics.” In: Journal of Physics: Photonics 4.1 (2022), p. 012501.

[70] Jianwei Wang, Fabio Sciarrino, Anthony Laing, and Mark G. Thompson. “Integrated photonic quantum technologies.” In: Nature Photonics 14.5 (2020), pp. 273–284.

[71] Graham T. Reed. “Silicon photonics: the state of the art.” In: (2008).

[72] Di Zhu, Linbo Shao, Mengjie Yu, Rebecca Cheng, Boris Desiatov, C. J. Xin, Yaowen Hu, Jeffrey Holzgrafe, Soumya Ghosh, Amirhassan Shams-Ansari, et al. “Integrated photonics on thin-film lithium niobate.” In: Advances in Optics and Photonics 13.2 (2021), pp. 242–352.

[73] Lukas Chrostowski and Michael Hochberg. Silicon photonics design: from devices to systems. Cambridge University Press, 2015.

[74] H. Aghaee Rad, T. Ainsworth, R. N. Alexander, B. Altieri, M. F. Askarani, R. Baby, L. Banchi, B. Q. Baragiola, J.E. Bourassa, R. S. Chadwick, et al. “Scaling and networking a modular photonic quantum computer.” In: Nature (2025), pp. 1–8.

[75] Jie Sun, Erman Timurdogan, Ami Yaacobi, Zhan Su, Ehsan Shah Hosseini, David B. Cole, and Michael R. Watts. “Large-scale silicon photonic circuits for optical phased arrays.” In: IEEE Journal of Selected Topics in Quantum Electronics 20.4 (2013), pp. 264–278.

[76] Christopher Rogers, Alexander Y. Piggott, David J. Thomson, et al. “A universal 3D imaging sensor on a silicon photonics platform.” In: Nature 590.7845 (Feb. 2021), pp. 256–261.

[77] Volkan Gurses, Samantha I. Davis, Esme Knabe, Raju Valivarthi, Maria Spiropulu, and Ali Hajimiri. “A compact silicon photonic quantum coherent receiver with deterministic phase control.” In: CLEO: Applications and Technology. Optica Publishing Group. 2023, AM4N–4.

[78] Volkan Gurses, Debjit Sarkar, Samantha Davis, and Ali Hajimiri. “An integrated photonic-electronic quantum coherent receiver for sub-shot-noise-limited optical links.” In: Optical Fiber Communication Conference. Optica Publishing Group. 2024, Tu2C–1.

[79] Mirko Pittaluga, Yuen San Lo, Adam Brzosko, Robert I. Woodward, Davide Scalcon, Matthew S. Winnel, Thomas Roger, James F. Dynes, Kim A. Owen, Sergio Juárez, et al. “Long-distance coherent quantum communications in deployed telecom networks.” In: Nature 640.8060 (2025), pp. 911–917.

[80] Alexander I Lvovsky and Michael G Raymer. “Continuous-variable optical quantum-state tomography.” In: Reviews of Modern Physics 81.1 (2009), p. 299.

[81] Behzad Razavi. Design of Integrated Circuits for Optical Communications. 2nd ed. Wiley, 2012.

[82] Alfred B. U’Ren, Christine Silberhorn, Konrad Banaszek, and Ian A. Walmsley. “Efficient conditional preparation of high-fidelity single photon states for fiber-optic quantum networks.” In: Physical Review Letters 93.9 (2004), p. 093601.

[83] Sylvain Fasel, Olivier Alibart, Sebastien Tanzilli, Pascal Baldi, Alexios Beveratos, Nicolas Gisin, and Hugo Zbinden. “High-quality asynchronous heralded single-photon source at telecom wavelength.” In: New Journal of Physics 6.1 (2004), p. 163.

[84] Andreas Eckstein, Andreas Christ, Peter J. Mosley, and Christine Silberhorn. “Highly efficient single-pass source of pulsed single-mode twin beams of light.” In: Physical Review Letters 106.1 (2011), p. 013603.

[85] Amideddin Mataji-Kojouri and Marco Liscidini. “Narrow-band photon pair generation through cavity-enhanced spontaneous parametric down-conversion.” In: Physical Review A 108.5 (2023), p. 053714.

[86] Andreas Christ and Christine Silberhorn. “Limits on the deterministic creation of pure single-photon states using parametric down-conversion.” In: Physical Review A 85.2 (2012), p. 023829.

[87] Reinhard F. Werner. “Quantum states with Einstein-Podolsky-Rosen correlations admitting a hidden-variable model.” In: Physical Review A 40.8 (1989), p. 4277.

[88] John F. Clauser, Michael A. Horne, Abner Shimony, and Richard A. Holt. “Proposed experiment to test local hidden-variable theories.” In: Physical Review Letters 23.15 (1969), p. 880.

[89] Antonio Acín, Nicolas Brunner, Nicolas Gisin, Serge Massar, Stefano Pironio, and Valerio Scarani. “Device-independent security of quantum cryptography against collective attacks.” In: Physical Review Letters 98.23 (2007), p. 230501.

[90] Joel F. Tasker, Jonathan Frazer, Giacomo Ferranti, and Jonathan C. F. Matthews. “A Bi-CMOS electronic photonic integrated circuit quantum light detector.” In: Science Advances 10.20 (2024), eadk6890.

[91] Yoann Piétri, Luis Trigo Vidarte, Matteo Schiavon, Laurent Vivien, Philippe Grangier, Amine Rhouni, and Eleni Diamanti. “Experimental demonstration of Continuous-Variable Quantum Key Distribution with a silicon photonics integrated receiver.” In: Optica Quantum 2.6 (2024), pp. 428–437.

[92] Cédric Bruynsteen, Michael Vanhoecke, Johan Bauwelinck, and Xin Yin. “Integrated balanced homodyne photonic–electronic detector for beyond 20-GHz shot-noise-limited measurements.” In: Optica 8.9 (Sept. 2021), pp. 1146–1152.

[93] G. Zhang, J. Y. Haw, H. Cai, et al. “An integrated silicon photonic chip platform for continuous-variable quantum key distribution.” In: Nature Photonics 13.12 (Dec. 2019), pp. 839–842.

[94] Yongqiang Du, Xin Hua, Zhengeng Zhao, Xiaoran Sun, Zhenrong Zhang, Xi Xiao, and Kejin Wei. “Source-independent quantum random number generators with integrated silicon photonics.” In: Communications Physics 8.1 (2025), p. 9.

[95] Cédric Bruynsteen, Tobias Gehring, Cosmo Lupo, Johan Bauwelinck, and Xin Yin. “100-Gbit/s integrated quantum random number generator based on vacuum fluctuations.” In: PRX quantum 4.1 (2023), p. 010330.

[96] Tommaso Bertapelle, Marco Avesani, Alberto Santamato, Alberto Montanaro, Marco Chiesa, Davide Rotta, Massimo Artiglia, Vito Sorianello, Francesco Testa, Gabriele De Angelis, et al. "High-speed source-device-independent quantum random number generator on a chip." In: Optica Quantum 3.1 (2025), pp. 111–118.

[97] A. I. Lvovsky and M. G. Raymer. "Continuous-variable optical quantum-state tomography." In: Rev. Mod. Phys. 81 (1 Mar. 2009), pp. 299–332.

[98] Jürgen Appel, Dallas Hoffman, Eden Figueroa, and A. I. Lvovsky. "Electronic noise in optical homodyne tomography." In: Physical Review A 75.3 (2007), p. 035802.

[99] Carmen Porto, Davide Rusca, Simone Cialdi, Andrea Crespi, Roberto Osellame, Dario Tamascelli, Stefano Olivares, and Matteo G.A. Paris. "Detection of squeezed light with glass-integrated technology embedded into a homodyne detector setup." In: Journal of the Optical Society of America B 35.7 (2018), pp. 1596–1602.

[100] Joel F. Tasker, Jonathan Frazer, Giacomo Ferranti, Euan J. Allen, Léandre F. Brunel, Sébastien Tanzilli, Virginia D'Auria, and Jonathan C. F. Matthews. "Silicon photonics interfaced with integrated electronics for 9 GHz measurement of squeezed light." In: Nature Photonics 15.1 (Jan. 2021), pp. 11–15.

[101] Stefano Pirandola. "Limits and security of free-space quantum communications." In: Physical Review Research 3.1 (2021), p. 013279.

[102] Andrej Kržič, Sakshi Sharma, Christopher Spiess, Uday Chandrashekara, Sebastian Töpfer, Gregor Sauer, Luis Javier González-Martín del Campo, Teresa Kopf, Stefan Petscharnig, Thomas Grafenauer, et al. "Towards metropolitan free-space quantum networks." In: npj Quantum Information 9.1 (2023), p. 95.

[103] Sheng-Kai Liao, Wen-Qi Cai, Wei-Yue Liu, Liang Zhang, Yang Li, Ji-Gang Ren, Juan Yin, Qi Shen, Yuan Cao, Zheng-Ping Li, et al. "Satellite-to-ground quantum key distribution." In: Nature 549.7670 (2017), pp. 43–47.

[104] Ji-Gang Ren, Ping Xu, Hai-Lin Yong, Liang Zhang, Sheng-Kai Liao, Juan Yin, Wei-Yue Liu, Wen-Qi Cai, Meng Yang, Li Li, et al. "Ground-to-satellite quantum teleportation." In: Nature 549.7670 (2017), pp. 70–73.

[105] Robert C. Hansen. Phased array antennas. John Wiley & Sons, 2009.

[106] Aobo Li, Shreya Singh, and Dan Sievenpiper. "Metasurfaces and their applications." In: Nanophotonics 7.6 (2018), pp. 989–1011.

[107] Barry D. Van Veen and Kevin M. Buckley. "Beamforming: A versatile approach to spatial filtering." In: IEEE ASSP Magazine 5.2 (1988), pp. 4–24.

[108] Constantine A. Balanis. Antenna theory: analysis and design. John wiley & sons, 2016.

Chapter 3

IMPROVING A HERALDED SINGLE-PHOTON SOURCE WITH A PHOTON-NUMBER-RESOLVING SUPERCONDUCTING NANOWIRE DETECTOR

This chapter includes the work published as:

[1] Samantha I. Davis, Andrew Mueller, Raju Valivarthi, Nikolai Lauk, Lautaro Narváez, Boris Korzh, Andrew D. Beyer, Olmo Cerri, Marco Colangelo, Karl K. Berggren, et al. "Improved heralded single-photon source with a photon-number-resolving superconducting nanowire detector." In: Physical Review Applied 18.6 (2022), p. 064007.

3.1 Introduction

A challenge in quantum optical science and technology is the realization of an ideal, i.e., deterministic, high-fidelity, tunable, and high-rate, source of indistinguishable single-photons [1, 2]. One intuitive approach to develop a single-photon source requires coupling an individual quantum emitter to light using a cavity. Significant progress in this regard [3] has been achieved using, e.g., quantum dots [4, 5, 6], crystal defects [7], or trapped ions [8] and atoms [9], albeit mired with challenges, including fabrication complexity [10, 11] or differing emitter spectra [12, 13, 14]. Instead, the strong light-matter coupling offered by solid-state bulk nonlinearities can be used to probabilistically emit photon pairs via laser-driven $\chi^{(2)}$ and $\chi^{(3)}$ processes [15], such as spontaneous parametric down-conversion (SPDC) and four-wave mixing (SFWM), respectively. Thermal statistics of the emission restrict a single photon pair to be emitted with low probability (e.g., 10^{-3} in practice [16]). An individual photon (in a signal mode) can be heralded by the detection of the other photon (in an idler mode) [1]. Typically this is performed using a threshold detector that discriminates zero from one or more photons. Heralding of photons from optical nonlinearities is scalable, and has enabled tunable and indistinguishable photons with high fidelities and bandwidths [17, 1, 18]. However, there is a non-zero probability to produce multiple pairs. To overcome this obstacle, a photon-number-resolving (PNR) detector at the idler mode can be used to exclude multi-photon events. Notable demonstrations of PNR detection have used, e.g., transition edge sensors and pseudo-PNR detectors constructed from time-multiplexed or arrays of

threshold detectors [19, 20, 21]. Optimized heralded single-photon sources require scalable, efficient, and low-noise PNR detectors with high timing resolution, that is, low jitter. Here we detect the idler mode from an SPDC process *in real time* using a PNR niobium nitride (NbN) superconducting nanowire single-photon detector (SNSPD) [22]. The detector is optimized across several performance metrics [23]. Specifically, the detection efficiency, which includes coupling loss in the cryostat, is > 0.7, the dark count rate is 10 Hz, and the jitter is < 14 ps.

To quantify the improvement of our heralded single-photon source, we perform a second-order correlation function $g^2(0)$ measurement [24] of the signal mode conditioned on the measured photon number of the idler mode using the number-resolving detector. This measurement is performed as a function of mean photon-pair number μ of the source.

We operate the detector in two configurations: (i) as a PNR SNSPD, discriminating zero-, one- and multi-photon events, and (ii) as a threshold SNSPD, discriminating zero-photon events from all other events. A $g^2(0)$ of zero is expected when a single photon pair is detected. Accounting for loss and multi-photon events, a reduction in $g^2(0)$ is expected when the detector is operated in configuration (i) versus (ii) for a fixed μ.

Since the measurements extend to large μ, we develop an analytical model for the detection rates, coincidence rates, and $g^2(0)$ using a phase-space formalism that encompasses full multi-photon contributions and all relevant imperfections, such as loss and multiple Schmidt modes [25, 26, 27]. We model the PNR detector in phase space as a $2N$-port beamsplitter followed by threshold detection at each output, which allows us to employ Gaussian characteristic function techniques. To evaluate the single-photon discrimination capability of the detector, we define the single-photon discrimination efficiency η^1_{PNR} metric, ranging from zero, for a threshold detector, to one for an ideal PNR detector. We obtain $\eta^1_{PNR} = 0.46$ corresponding to a pseudo-PNR detector comprised of no more than 18 threshold detectors, each with efficiency $\eta_d = 0.71$. We perform a simultaneous maximum likelihood fit of the model to the measured values of $g^2(0)$ and extract μ for each pump power. We measure a maximum reduction of $g^2(0)$ from 0.430 ± 0.009 to 0.312 ± 0.008 when using configuration (ii) versus (i) at $\mu = 0.327 \pm 0.007$, thereby improving the fidelity of the single-photon source. For a fixed $g^2(0) = 7 \times 10^{-3}$ [28], we increase the probability to generate a single pair by 25%, from 4×10^{-3} to 5×10^{-3}.

3.2 Experimental methods

The experimental setup is shown in Fig. 3.1. Light pulses of ~ 600 ps duration are created by injecting 1540 nm wavelength light from a continuous-wave laser into an intensity modulator (IM). The modulator is driven by an arbitrary waveform generator (AWG) at a rate $R = 1$ MHz, which is the clock rate of the experiment. The pulses are amplified by an erbium doped fiber amplifier and then directed to a second harmonic generation module with a gain-adjusted amplification stage (SHG), which amplifies the pulses then up-converts them to 770 nm wavelength. The pulses are then directed to a fiber-coupled type-0 periodically poled lithium niobate (PPLN) waveguide, which produces photon pairs centered at 1540 nm wavelength via SPDC. A coarse wavelength division multiplexer (CWDM) splits the photon pairs into the signal and idler modes, centered at 1530 nm and 1550 nm, respectively, each with a 13 nm bandwidth. Light in the signal path is split by a 50:50 beamsplitter (BS) into two paths, labelled as signal 1 and 2. Filters with a total of 60 dB extinction on the idler path and 120 dB extinction on the signal path are used to suppress the unconverted 770 nm pump light. The photons from the signal and idler paths are detected using conventional and PNR SNSPDs, respectively.

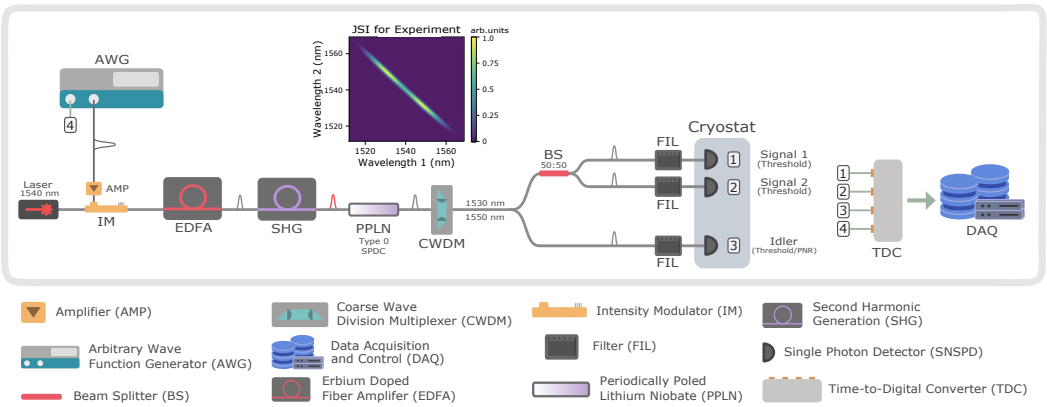

Figure 3.1: Experimental setup. AWG - Tektronix AWG7002A, BS - Thorlabs 1550nm fiber optic 50:50 beamsplitter, CWDM - FS one-channel coarse wave division multiplexing/optical add/drop multiplexer, EDFA - Pritel erbium-doped fiber amplifer, Laser - General Photonics TLS-101, PPLN - Covesion ruggedized waveguide, SHG - Pritel optical fiber amplifier/second harmonic generator. The inset shows the estimated joint spectral intensity (JSI) for the experiment including the detector and CWDM response.

Detectors

The detectors are held at 0.8 K in a Gifford-McMahon cryostat with a ^{4}He sorption stage. To measure the signal modes, we use two single-pixel tungsten silicide (WSi) SNSPDs, which have timing jitters of $\sim$ 50 ps, detection efficiencies of $\sim$ 0.8, and dark count rates below 5 Hz [16]. To measure the idler mode, we use a PNR SNSPD with a timing jitter of $<$ 14 ps, detection efficiency of $\eta_d = 0.71$ and dark counts $<$ 10 Hz. The detector efficiency was determined in an independent measurement similar to that performed in Ref. [29]. The detector has an active area of 22×15 μm^2, formed by a meander of 100 nm-wide and 5 nm-thick NbN nanowires with a 500 nm pitch. The detector employs a differential architecture to cancel the contribution of the signal propagation delays to the timing jitter [22]. An impedance-matching taper enables photon-number resolution, increases the signal-to-noise ratio, and minimizes reflections as well as distortion [22, 30]. The number of incident photons is encoded into the amplitude of the output pulse [22, 31]. A single incident photon that is absorbed by the nanowire induces a single time-dependent resistive hotspot, which results in a radio-frequency pulse [23]. Multiple incident photons absorbed by the nanowire at the same time induce multiple time-dependent resistive hotspots. This increases the total resistance of the nanowire, producing a radio-frequency pulse with an amplitude and slew rate that depends on the number of hotspots. In our experiments, rather than measuring the pulse amplitude variation [31, 22], we measure its slew rate variation [32]. This only requires a constant-threshold time tagger, i.e., time-to-digital converter, and enables real-time readout. With a fixed voltage threshold, the variation in slew rate results in a variation of the time of the detection event, i.e., time tag. Earlier (later) time-tags, plotted in a histogram in the left (right) bin of Fig. 3.2, correspond to multi-photon (single-photon) pulses with higher (lower) slew rate.

Data acquisition and analysis

The readout pulses from the detectors and the clock signal from the AWG are sent to a time tagger that is interfaced with custom-made graphical user interface (GUI) for real-time analysis and multi-photon event discrimination. The GUI is depicted in Fig. 3.3. The recorded detection events in a time bin, that is, the time-tags arriving in a temporal interval defined by the red and yellow markers, are collected over a set acquisition time interval. A range of potential arrival times of photons in the signal paths are shown in the top two channels of the GUI, and the single and multi-photon events at the idler PNR detector are shown in the bottom channel of the GUI. The

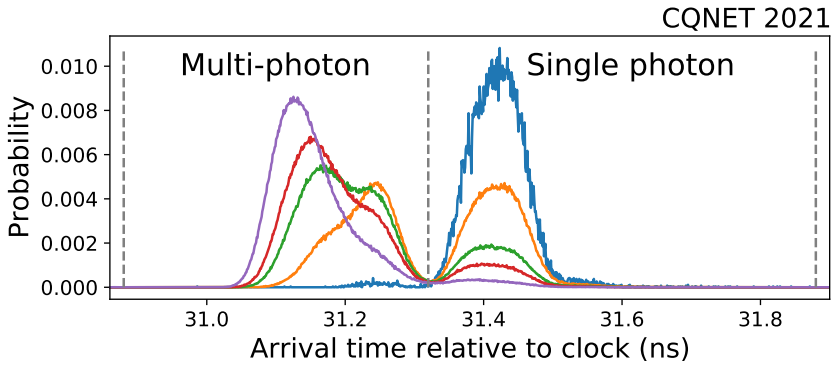

Figure 3.2: Probability distribution of the arrival times of detection events by the PNR SNSPD for $\mu \approx 8 \times 10^{-3}$ (blue), $\mu \approx 3$ (orange), $\mu \approx 9$ (green), $\mu \approx 11$ (red), and $\mu \approx 16$ (purple). The dashed lines define the time bins corresponding to single- (right) and multi-photon (left) events. The total number of events in the single- and multi-photon bins are used when operating the SNSPD as a threshold detector, while the number of events in the single-photon bin are used when operating the SNSPD as a PNR detector.

GUI is used to collect single detection events, two-fold coincidence events, and three-fold coincidence events conditioned on the single- and multi-photon detection events at the idler detector. In other words, the GUI allows collecting all events for analyzing heralding of photons in the signal path conditioned on threshold and PNR detection of photons in the idler path.

Characterization

We characterize the setup in two ways: by (1) theoretical calculation and measurement of the joint spectral properties of the photon pair source and (2) by measuring the signal 1, signal 2, and idler path efficiencies from detection rates with low μ, as described below.

Joint spectral intensity

The two photon component of the quantum state describing SPDC at the output of the PPLN waveguide is

$$|\Psi\rangle = A \int_0^\infty \int_0^\infty f(\omega_1, \omega_2) \hat{a}^\dagger(\omega_1) \hat{a}^\dagger(\omega_2) d\omega_1 d\omega_2 \, |0\rangle \,,$$

where A is a constant prefactor that depends on the effective nonlinearity and interaction length, $\hat{a}(\omega_1)$ and $\hat{a}(\omega_2)$ are the signal and idler modes with frequencies

Figure 3.3: Custom-made Graphical User Interface (GUI) allows time-resolved detection of photons and real-time filtering of multi-photon events. The idler mode depicts a bimodal distribution of time tags relative to the clock for an acquisition time of 1 s. The left bin corresponds to the multi-photon events and the right bin corresponds to the single-photon events.

ω_1 and ω_2, respectively. The joint spectral amplitude (JSA) is

$$f(\omega_1, \omega_2) = \psi_{ph}(\omega_1, \omega_2) \cdot \psi_p(\omega_1, \omega_2),$$

comprised of the phase-matching and pump envelope amplitudes $\psi_{ph}(\omega_1, \omega_2)$ and $\psi_p(\omega_1, \omega_2)$, respectively. The joint spectral intensity (JSI) is $|f(\omega_1, \omega_2)|^2$. We model the phase-matching envelope intensity as

$$|\psi_{ph}(\omega_1, \omega_2)|^2 = \mathrm{sinc}^2\left(\frac{\Delta k L}{2}\right),$$

where $L = 1$ cm is the length of the waveguide and Δk is the phase-mismatch. The calculated phase-matching envelope intensity is depicted in Fig. 3.4a. The phase mismatch for co-linear quasi-phase-matching is

$$\Delta k = 2\pi\left(\frac{n(\lambda_p)}{\lambda_p} - \frac{n(\lambda_1)}{\lambda_1} - \frac{n(\lambda_2)}{\lambda_2} - \Gamma\right),$$

where $n_{p(1)(2)}$ is the pump (signal) (idler) index of refraction, $\lambda_{p(1)(2)} = \frac{2\pi c}{\omega_{p(1)(2)}}$ is the pump (signal) (idler) wavelength, m is an integer, Λ is the poling period of

the crystal, and $\Gamma = m/\Lambda = 400\ \mathrm{mm}^{-1}$ [33]. The index of refraction for light of wavelength λ in our PPLN waveguide is approximately

$$n(\lambda) = \sqrt{1 + \frac{2.6734\lambda^2}{\lambda^2 - 0.01764} + \frac{1.2290\lambda^2}{\lambda^2 - 0.05914} + \frac{12.614\lambda^2}{\lambda^2 - 474.60}},$$

where $n(1540\ \mathrm{nm}) = 2.21$ and $n(770\ \mathrm{nm}) = 2.26$ [34]. We model the pump envelope intensity as

$$|\psi_p(\omega_1, \omega_2)|^2 = \exp\left(-\frac{(\omega_p - \omega_1 - \omega_2)^2}{\sigma_p^2}\right),$$

where $\omega_p = \frac{2\pi c}{770\ \mathrm{nm}}$ and $\sigma_p \sim \frac{2\pi}{100\ \mathrm{ps}} = 60\ \mathrm{GHz}$, as estimated from independent measurements, which is subject to energy conservation $\omega_p = \omega_1 + \omega_2$. Fig. 3.4b shows the calculated pump envelope intensity.

To characterize the photon pair source, its JSI is determined by performing coincidence measurements of the signal and idler modes after they pass tunable filters with 0.22 nm bandwidths (setup not shown in Fig. 3.1). The measured JSI accounts for the detector response:

$$|f_m(\omega_1, \omega_2)|^2 = |\psi_{ph}(\omega_1, \omega_2)|^2 \cdot |\psi_p(\omega_1, \omega_2)|^2 \cdot |\psi_d(\omega_1, \omega_2)|^2, \tag{3.1}$$

where the third factor is the detector efficiency distribution

$$|\psi_d(\omega_1, \omega_2)|^2 = \exp\left(-\frac{(\lambda_1 - \lambda_d)^2 + (\lambda_2 - \lambda_d)^2}{\sigma_d^2}\right),$$

which we model as a Gaussian centered at the optimal detection wavelength of $\lambda_d = 1550$ nm with a spread of $\sigma_d = 53$ nm found from independently performed detector reflectivity measurements. See Fig. 3.4c for the calculated detector response. The measured JSI including detector response is shown in Fig. 3.4d using circular markers, with brighter color proportional to the rate of coincidence detection events. The contour depicts the theoretical prediction from Eq. 3.1.

The most relevant JSI is that used for the main experiment in configurations (i) with the PNR detector and (ii) with the threshold detector depicted in Fig. 3.1. This JSI includes the detector response as well as the response of the CWDM. The two output modes of the CWDM are centered at 1550 nm, the idler, and 1530 nm, the signal, with $\sigma_{\mathrm{CWDM}} = 13$ nm bandwidths. Thus, the JSI for the main experiment is modeled as

$$|f_{exp}(\omega_1, \omega_2)|^2 = |f_m(\omega_1, \omega_2)|^2 \cdot |\psi_f(\omega_1, \omega_2)|^2, \tag{3.2}$$

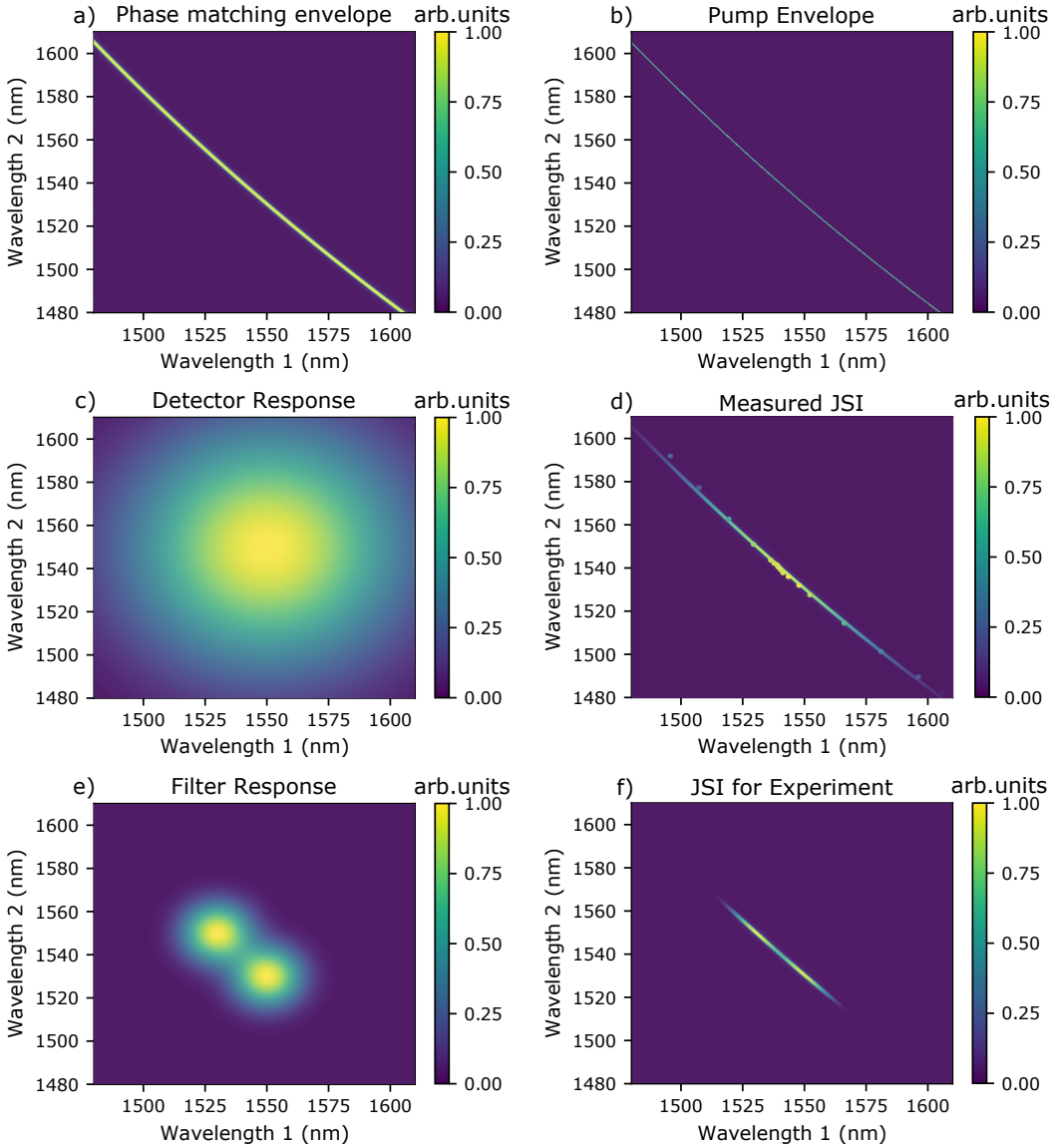

Figure 3.4: Measured and theoretically calculated joint spectral information used to characterize the photon pair source. a) Phase-matching envelope, b) pump spectral envelope, c) detector response, d) measured (circles) and calculated (contour) JSI, e) filter response of CWDM, and f) JSI for the main experiment, also shown in Fig. 3.1.

with the filter response being

$$|\psi_f(\omega_1,\omega_2)|^2 = \exp\left(-\frac{(\lambda_1-\lambda_{\mathrm{f},1})^2+(\lambda_2-\lambda_{\mathrm{f},2})^2}{\sigma_f^2}\right) + \exp\left(-\frac{(\lambda_1-\lambda_{\mathrm{f},2})^2+(\lambda_2-\lambda_{\mathrm{f},1})^2}{\sigma_f^2}\right),$$

where $\lambda_{f,1} = 1550$ nm and $\lambda_{f,2} = 1530$ nm. The theoretical response of the CWDM is shown in Fig. 3.4e whereas Fig. 3.4f depicts the JSI for the main experiment as calculated from Eq. 3.2.

We perform a Schmidt decomposition of the JSI shown in Fig. 3.4f by calculating the singular value decomposition of Eq. 3.2 [35]. This is relevant for modeling our $g^2(0)$ results, as discussed in Sec. 3.3, and for determining the fidelity of a heralded single photon, see Sec. 3.5. The obtained eigenvalues λ_s from the decomposition, normalized by their sum over index s, are shown in Fig. 3.5, corresponding to a Schmidt number of $K = 1/\sum_s \lambda_s^2 \approx 772$.

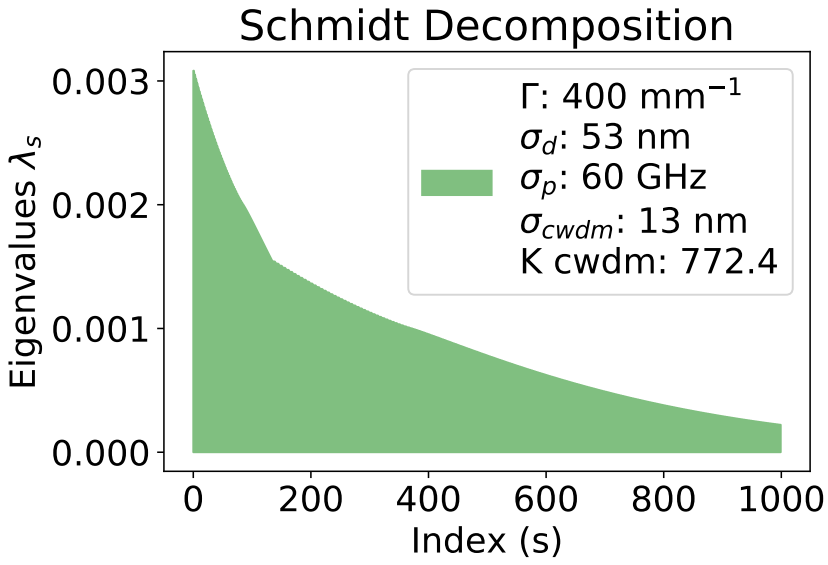

Figure 3.5: Eigenvalue spectrum $\sum_s \lambda_s = 1$ obtained from a Schmidt decomposition of the JSI used in the main experiment.

Finally, we determine the sensitivity of the Schmidt decomposition to any potential uncertainty in its key underlying parameters. We independently vary σ_p, σ_{CWDM}, Γ and σ_d, see Eq. 3.2, and re-calculate Schmidt decomposition, with results shown in Fig. 3.6 and its caption. We find that, unsurprisingly, the variations of the pump σ_p and filter σ_{CWDM} bandwidths have a significant impact on the Schmidt decomposition [36]. Indeed a single spectral mode can be approximated if $\sigma_p \gg \sigma_{\mathrm{CWDM}}$ [37]. Consequently, the variations of σ_p and σ_{CWDM} have the largest impact on our theoretical model introduced in Sec. 3.3, and are hence propagated in the fit of the model to the data, see Sec. 3.4.

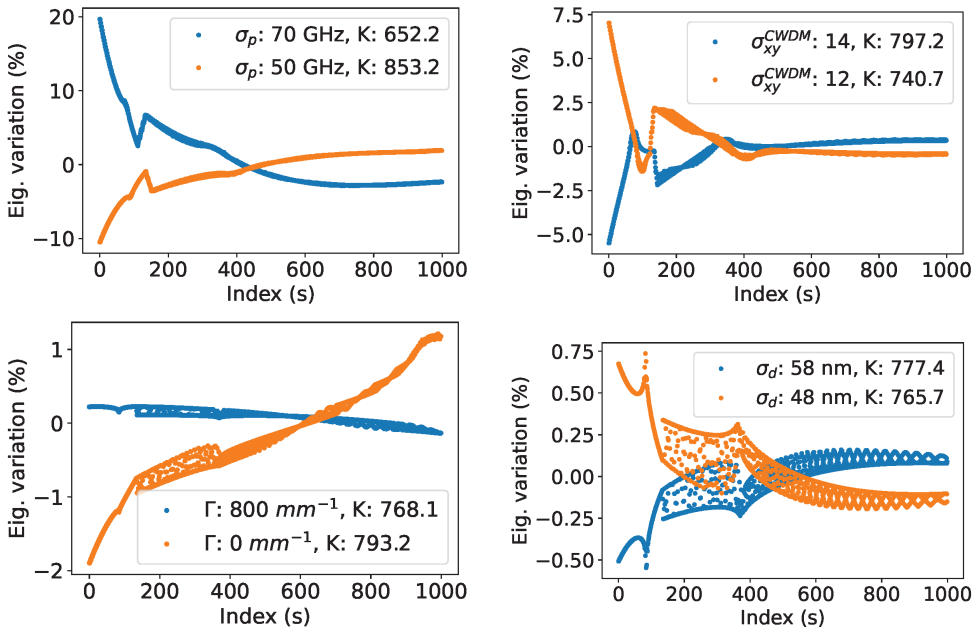

Figure 3.6: Sensitivity of the Schmidt eigenvalue decomposition of the JSI for the main experiment is probed by varying key parameters of Eq. 3.2. Central values and variations for each relevant parameter are as follows: $\sigma_p = 60 \pm 10$ GHz, $\sigma_{\text{CWDM}} = 13 \pm 1$ nm, $\Gamma = 400 \pm 400$ mm^{-1} and $\sigma_d = 53 \pm 5$ nm, with maximum and minimum variations shown. These variations are beyond typical experimental uncertainties and are taken as a worst-case scenario. The variation of each eigenvalue is normalized to the size of the first eigenvalue λ_0.

Path efficiencies

We determine the efficiencies of the signal and idler paths, that is, from PPLN to detection as shown in Fig. 3.1, by calculating the ratio of coincidence to single-photon detection rates using our photon pair source [38]. The output of our photon-pair source can be approximated as

$$|\psi\rangle_{\text{TMSV}} \approx \sqrt{1-\mu}\,|0_i 0_s\rangle + \sqrt{\mu}\,|1_i 1_s\rangle\,,$$

if $\mu \ll 1$, neglecting loss. In this limit, the probability of generating one pair of photons is given by μ, and can be determined by measuring the coincidence-to-accidental ratio [39]. Correspondingly, the relevant detection rates in our main

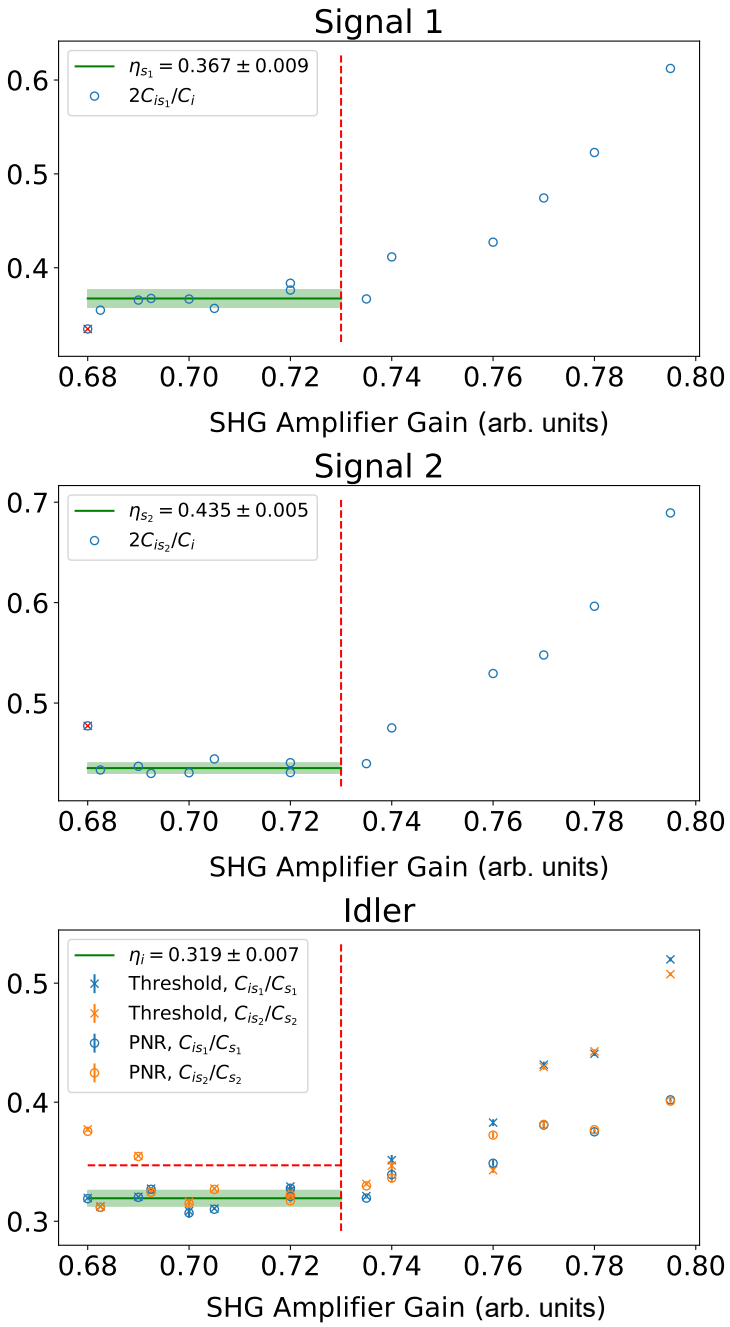

Figure 3.7: Ratios of single and two-fold coincidence detection rates for the signal and idler paths for varied gain of the amplifier in SHG module. The signal 1, signal 2, and idler path efficiencies, are estimated as shown in the insets using the data on the left (and below) of the red dashed lines, which corresponds to $\mu \ll 1$. Idler efficiencies are measured in configurations with the PNR and threshold detector. The mean and standard deviation of the fitted efficiencies are indicated by green lines, with numerical values in the insets.

experiment can be approximated to lowest order in μ:

$$C_i \approx R\eta_i\mu, \tag{3.3}$$

$$C_{s_j} \approx \frac{1}{2}R\eta_{s_j}\mu, \tag{3.4}$$

$$C_{is_j} \approx \frac{1}{2}R\eta_i\eta_{s_j}\mu, \tag{3.5}$$

$$C_{s_1s_2} \approx \frac{1}{2}R\eta_{s_1}\eta_{s_2}\mu^2, \tag{3.6}$$

$$C_{is_1s_2} \approx R\eta_{s_1}\eta_{s_2}\eta_i\mu^2, \tag{3.7}$$

where C_i is the detection rate of the idler photons, whereas C_{s_j} and C_{is_j} are the detection rates of signal j and idler-signal j two-fold coincidence events, $j = 1, 2$. The two-fold coincidence detection rates for photons in the signal 1 and 2 paths is $C_{s_1s_2}$ and $C_{is_1s_2}$ is the rate of three-fold coincidence detection events for photons in the idler and the two signal paths. The transmission efficiencies of the idler and two signal paths are η_i and η_{s_j}, respectively, and include detector the efficiencies.

To estimate the path efficiencies, we calculate the ratios of two-fold coincidences to single detection rates the signal 1, signal 2, and idler paths, plotting them in Fig. 3.7 for varied μ. The amplification in the SHG module is adjusted as a proxy for μ and a linear fit to the data (green line) is used to obtain the average efficiencies and associated uncertainties at $\mu \ll 1$, bounded by the red vertical dashed lines. The mean efficiencies and associated uncertainties (standard deviations) for the signal 1 and 2 paths are $\eta_{s_1} = 2C_{is_1}/C_i = 0.367 \pm 0.009$ and $\eta_{s_2} = 2C_{is_2}/C_i = 0.435 \pm 0.005$, respectively. The idler path efficiency $\eta_i = C_{is_1}/C_{s_1} = 0.319 \pm 0.007$ is estimated from both the PNR and threshold detector configurations. The mean and uncertainty of each path efficiency is used to constrain the fit shown in Fig. 3.9 of Sec. 3.4.

3.3 Theoretical model

Photon pair sources from bulk optical nonlinearities are typically operated at $\mu \ll 1$ to suppress multi-photon events. The $g^2(0)$ measurement performed in our work extends to large μ, where multi-photon contributions are non-negligible and become significantly suppressed in the (i) PNR detection configuration compared to that using (ii) threshold detection. To incorporate full multi-photon effects without approximation, we use methods from the phase space formulation of quantum optics to derive an expression for $g^2(0)$ as a function of μ. We take into account all major imperfections, including coupling and detector inefficiencies. We note that our model can be extended to include dark counts, which are negligible for our

experiment.

Characteristic function-based approach

The second order correlation function of photons in the signal 1 and 2 paths conditioned on the detection of photons in the idler path for both detector configurations (i) and (ii) is

$$g^2(0) = \frac{C_{is_1s_2}C_i}{C_{is_1}C_{is_2}},$$

where $C_{is_1s_2}$ is the rate of three-fold coincidence detection events of photons in the idler and signal 1 and 2 paths, C_i is the rate of idler detection events, and C_{is_j} is the two-fold coincidence detection rate of idler and signal j events, where $j = 1, 2$. Since we are interested in large μ, we cannot utilize Eqs. 3.3-3.7. Hence, to find an expression for $g^2(0)$, we derive analytical expressions for the single path detection rates, two-fold coincidence rates, and three-fold coincidence rates using a characteristic function-based approach [25].

A characteristic function for an $N-$mode bosonic system is defined as

$$\chi(\xi) = \mathrm{Tr}\left\{\hat{\rho}\exp(-i(\hat{x}_1, \hat{p}_1, \hat{x}_2, \hat{p}_2, \ldots \hat{x}_N, \hat{p}_N)\cdot\xi)\right\}, \tag{3.8}$$

where $\hat{\rho}$ is the density matrix describing the state of the system, $\hat{x}_i$ and $\hat{p}_i$ are the conjugate quadrature operators for mode i, and $\xi \in \mathbb{R}^{2N}$. The quadrature operators can be expressed in term of the bosonic creation and annihilation operators as

$$\hat{x}_i = \frac{1}{\sqrt{2}}\left(\hat{a}_i^\dagger + \hat{a}_i\right), \qquad \hat{p}_i = \frac{i}{\sqrt{2}}\left(\hat{a}_i^\dagger - \hat{a}_i\right).$$

Eq. 3.8 defines a unique mapping from the space of all possible quantum states to a space of functions over $\mathbb{R}^{2N}$, i.e., a quantum system is completely characterized by its characteristic function $\chi(\xi)$ [40].

An important subclass of quantum states is defined by the states whose characteristic function is given by a multivariate Gaussian function:

$$\chi(\xi) = \exp\left(-\xi^T\gamma\xi - id^T\xi\right),$$

i.e., they are completely characterized by the displacement vector d and covariance matrix γ, corresponding to the first and second moments. Representatives of this subclass include vacuum, coherent, and thermal states as well as single- and two-mode squeezed states.

Relevant for our experiment is the non-degenerate output of an SPDC process, which can be described as a two-mode squeezed vacuum state whose covariance matrix is given by

$$\gamma_{\mathrm{SPDC}}(\mu) = \begin{pmatrix} \mathbf{A} & \mathbf{B} \\ \mathbf{B} & \mathbf{A} \end{pmatrix},$$
$$\mathbf{A} = \begin{pmatrix} 1+2\mu & 0 \\ 0 & 1+2\mu \end{pmatrix},$$
$$\mathbf{B} = \begin{pmatrix} 2\sqrt{\mu(\mu+1)} & 0 \\ 0 & -2\sqrt{\mu(\mu+1)} \end{pmatrix},$$

in block matrix form, where μ is the mean photon pair number. This description is only valid for an SPDC source where only one signal and one idler mode are present. If the source allows for multiple signal and idler modes, like in the broadband source we use in our experiment, then the initial state must be modified to include all relevant Schmidt modes, determined through the singular value decomposition of the JSI [35], as calculated in Sec. 3.2. In this case, the initial state is a product state of the two-mode squeezed vacuum states in the corresponding Schmidt modes. The covariance matrix of the system is then given by a direct sum of the covariance matrices of the respective modes

$$\gamma = \gamma_{\mathrm{SPDC}}(\lambda_1\mu) \oplus \gamma_{\mathrm{SPDC}}(\lambda_2\mu) \oplus \ldots,$$

for an SPDC source that supports N modes with Schmidt coefficients $\lambda_1, \lambda_2, \cdots \lambda_N$, where the sum runs over all relevant modes, $\lambda_1 \geq \lambda_2 \geq \ldots \lambda_N$, and $\sum_{s=1}^{N} \lambda_s = 1$, as before.

Since linear optics preserves the Gaussian nature of states [40], i.e., it maps Gaussian states onto Gaussian states, linear optical operations can be described by a symplectic transformation S of the displacement vector and covariance matrix:

$$d' = S^T d, \qquad \gamma' = S^T \gamma S.$$

For example, the transformation between the input modes $\hat{a}$, $\hat{b}$ and the output modes $\hat{a}'$, $\hat{b}'$ of a beamsplitter with transmittivity t is given by

$$\hat{a}' = t\hat{a} + i\sqrt{1-t^2}\hat{b},$$
$$\hat{b}' = t\hat{b} + i\sqrt{1-t^2}\hat{a}.$$

We can now find the symplectic transformation S of the beamsplitter that transforms the quadrature operators:

$$\begin{pmatrix} \mathbf{x}_{a'} \\ \mathbf{x}_{b'} \end{pmatrix} = S^T \begin{pmatrix} \mathbf{x}_a \\ \mathbf{x}_b \end{pmatrix} = \begin{pmatrix} \mathbf{T} & \mathbf{R} \\ \mathbf{R} & \mathbf{T} \end{pmatrix} \begin{pmatrix} \mathbf{x}_a \\ \mathbf{x}_b \end{pmatrix},$$
$$\mathbf{x}_i = (\hat{x}_i, \hat{p}_i)^T,$$
$$\mathbf{T} = \begin{pmatrix} t & 0 \\ 0 & t \end{pmatrix}, \quad \mathbf{R} = \begin{pmatrix} 0 & -\sqrt{1-t^2} \\ \sqrt{1-t^2} & 0 \end{pmatrix},$$

in block matrix form, where $(\mathbf{x}_i, \mathbf{x}_j)^T = (\hat{x}_i, \hat{p}_i, \hat{x}_j, \hat{p}_j)^T$. The beamsplitter transformation is particularly important because it is used to model path efficiency η_{path}, which is reduced from unity by propagation and coupling loss as well as detector inefficiency. This is accomplished by combining the mode of interest and vacuum on a beamsplitter of transmittivity η_{ch} and tracing out the reflected mode.

Given that our setup consists of linear optics, and that loss is modeled as a linear optic transformation, we are able to derive a symplectic transformation S_{system}, with which we calculate the characteristic function of the system up to detection

$$\gamma_{\text{out}} = S_{\text{system}}^T \gamma_{\text{in}} S_{\text{system}}.$$

From the covariance matrix of the final Gaussian state, we can calculate several relevant experimental values such as detection probabilities or rates, which can be used to predict key figures of merit such as fringe visibilities or state fidelities of qubits [16].

Concerning the photon detection step, consider a measurement operator $\hat{\Pi}$. The probability of detecting the measurement outcome for a given state $\hat{\rho}$ is

$$Tr[\hat{\rho}\hat{\Pi}] = \left(\frac{1}{2\pi}\right)^N \int dx^{2N} \chi_\rho(x) \chi_\Pi(-x), \tag{3.9}$$

where $\chi_\Pi(-x)$ is the characteristic function of the measurement operator and is defined in the same way as Eq. 3.8 but with $\hat{\Pi}$ instead of $\hat{\rho}$. For threshold detectors, which destructively discriminate between non-zero and zero photons, that is, a detection event and non-event, their measurement operators are

$$\hat{\Pi}_{\text{no-event}} = |0\rangle \langle 0|,$$
$$\hat{\Pi}_{\text{event}} = \hat{I} - |0\rangle \langle 0|,$$

i.e., we can model the threshold detectors by projections onto the vacuum state. Since the vacuum state is a Gaussian state, the integrand in Eq. 3.9 is a multi-variant Gaussian function yielding

$$Tr[\hat{\rho}\hat{\Pi}_{\text{no-event}}] = \frac{2}{\sqrt{\det(\gamma_{\text{red}} + I)}} e^{-d_{\text{red}}^T(\gamma_{\text{red}}+I_{\text{red}})^{-1}d_{\text{red}}}, \tag{3.10}$$

where γ_{red} is the reduced covariance matrix and d_{red} is the reduced displacement vector obtained from γ and d by tracing out all modes but those measured.

Photon-number-resolving detector

Since the measurement operators describing PNR detectors are not Gaussian operators [41], we cannot evaluate Eq. 3.10 to find the probability of detecting one or more photons for the PNR detector. Instead, we model the PNR detector as an effective $2N$-port beamsplitter with threshold detectors at each output port [21, 42, 26, 27]. We implement the $2N$-port beamsplitter as a network of beamsplitters forming a so-called "binary tree" architecture, which has N input and output ports, as depicted in Fig. 3.8 for the case $N = 8$.

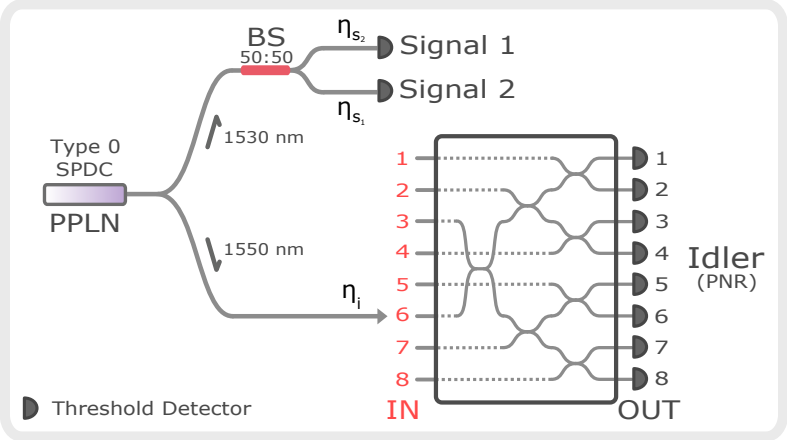

Figure 3.8: Schematic of the setup used for theoretical modeling. The PNR detector is modeled as a $2N$-port beamsplitter in a binary tree architecture with threshold detectors at the outputs. Only 8 ports are shown in the figure for simplicity. The SPDC source and paths depict a simplified representation of that shown in Fig. 3.1. The efficiencies, including all coupling and detection loss, of the signal 1, signal 2, and idler paths, are η_{s_1}, η_{s_2}, and η_i, respectively.

To model a PNR detector, photons are injected to an input of the "top-most" beamsplitter of the tree, e.g. input 6 in Fig. 3.8. The detection of photons with the

PNR SNSPD is modeled as detection events from any combination of threshold detectors at the output ports of the tree. For an input Fock state $|n\rangle$, the probability that multiple photons arrive to the same output port is negligible when $N \gg n$, corresponding to ideal photon number discrimination. In this case, the number of detection events equals the number of input photons. For $N \sim n$, the probability of multiple photons arriving to the same output port is non-negligible, corresponding to non-ideal photon number discrimination. In this case, the number of detection events does not equal the number of input photons. Therefore, the depth of the tree $k = \log_2(N)$, is a figure of merit for photon number discrimination.

With our beamsplitter tree and threshold detector model, we are able to employ Gaussian characteristic function techniques to find photon detection probabilities, which we later employ to calculate coincidence detection probabilities, and hence detection rates. We append $N-1$ vacuum modes to the state at idler mode and find the symplectic matrix that transforms the characteristic function of the input state to the tree to that of the output state. The symplectic matrix S_{k} of a beamsplitter tree with depth k can be constructed using the recursive symmetry of the binary tree architecture

$$S_k = (S_{k-1} \oplus S_{k-1}) S_{k,t},$$

where $S_{k,t}$ is the symplectic matrix corresponding to the top-most beamsplitter for a tree with depth k. The covariance matrix γ_N and displacement vector d_N of the N-mode input state to the tree then transform as

$$d'_N = S_k^T d_N, \qquad \gamma'_N = S_k^T \gamma_N S_k,$$

which is followed by threshold detection at each of the N outputs.

The probability of detecting non-zero photons at m of the modes, i.e., having a m-fold coincidence event, for an N-mode Gaussian state with covariance matrix γ_N is

$$\sum_{\{m\}} Tr[\hat{\rho}^{\gamma_N}(\hat{\Pi}_{\text{event}}^{\otimes m} \otimes \hat{\Pi}_{\text{no-event}}^{\otimes (N-m)})] \\ = \sum_{\{m\}} Tr[\hat{\rho}^{\gamma_N}((\hat{I} - |0\rangle\langle 0|)^{\otimes m} \otimes |0\rangle\langle 0|^{\otimes (N-m)})],$$

where $\sum_{\{m\}}$ indicates a sum over the all possible choices of m output modes. This results in a linear combination of $\binom{N}{m}$ terms of the form

$$Tr[\hat{\rho}^{\gamma_N}(\hat{I}^{\otimes j} \otimes |0\rangle\langle 0|^{\otimes (N-j)})] = Tr[\hat{\rho}_{\text{red}}^{\gamma_N} |0\rangle\langle 0|^{\otimes (N-j)}], \tag{3.11}$$

where $\hat{\rho}_{\text{red}}^{\gamma_N}$ is the reduced density matrix of the system obtained by taking a partial trace over $N-j$ modes with $0 \leq j \leq N$. One useful property of Gaussian states is that the covariance matrix of the reduced state after a partial trace is simply the sub-matrix corresponding to the remaining system. It can be shown that for an N-mode system with covariance matrix γ_N and displacement vector d_N, the probability of measuring zero photons across the N modes is

$$\begin{aligned} Tr[\hat{\rho}\hat{\Pi}_{\text{no-event}}^{\otimes N}] &= Tr[\hat{\rho}\,|0\rangle\langle 0|^{\otimes N}] \\ &= \frac{2^N}{\sqrt{\det(\gamma_N + I_N)}} e^{-d_N^T(\gamma_N+I_N)^{-1}d_N}. \end{aligned}$$

Eq. 3.11 then simplifies to

$$Tr[\hat{\rho}_{\text{red}}^{\gamma_N}\,|0\rangle\langle 0|^{\otimes(N-j)}] = \frac{2^{N-j}}{\sqrt{\det(\gamma_{N-j} + I_{N-j})}} e^{-d_{N-j}^T(\gamma_{N-j}+I_{N-j})^{-1}d_{N-j}},$$

where I_m is the m by m identity matrix, γ_{N-j} is the sub-matrix of γ_N and d_{N-j} is the sub-vector of d_N corresponding to the remaining subsystem of $N-j$ modes. By knowing γ_N and d_N of the full N-mode system, we can find the m-fold coincidence event probability for arbitrary m, where $0 \leq m \leq N$.

For our experiment, we are interested in the single-photon detection probability P_1^N of the PNR detector. We model this as the probability that a single output mode of the beamsplitter tree contains a photonic excitation:

$$\begin{aligned} P_1^N &= NTr[\hat{\rho}^{\gamma'_N}(\hat{\Pi}_{\text{event}} \otimes \hat{\Pi}_{\text{no-event}}^{\otimes(N-1)})] \\ &= \frac{N2^{N-1}}{\sqrt{\det(\gamma'_{N-1} + I_{N-1})}} e^{-{d'_{N-1}}^T(\gamma'_{N-1}+I_{N-1})^{-1}d'_{N-1}} \\ &\quad - \frac{N2^N}{\sqrt{\det(\gamma'_N + I_N)}} e^{-{d'_N}^T(\gamma'_N+I_N)^{-1}d'_N}. \end{aligned} \tag{3.12}$$

We can also use the $2N$-port beamsplitter model to describe the photon number discrimination capability of the detector, as discussed in the following sections.

Photon-number detection

When a single-photon is sent to an input of the $2N$-port beamsplitter, the action of the beamsplitter corresponding to unitary U_N splits the photon into an equal superposition of the N output modes. An arbitrary Fock state $|n\rangle$ directed to a single input port transforms as

$$U_N\,|n\rangle = \frac{1}{(\sqrt{N})^n} \sum_{j_1+\cdots+j_N=n} \sqrt{\frac{n!}{j_1!\cdots j_N!}}\,|j_1\rangle\cdots|j_N\rangle\,.$$

Thus, the joint probability of finding j_1 photons at output 1, j_2 photons at output 2, ..., and j_N photons at output N is

$$P_n(j_1, \cdots, j_N) = \frac{1}{N^n} \frac{n!}{j_1! \cdots j_N!}, \qquad \text{where} \quad \sum_{i=1}^{N} j_i = n.$$

The probability that n photons at a single input port trigger an m-fold coincidence event, i.e., a detection at each of the m output ports, is

$$P^N_{m,n} = \frac{n!}{N^n} \sum_{j_1+\cdots+j_N=n}^{(m)} \frac{1}{j_1! \cdots j_N!} = \frac{m!}{N^n} \binom{N}{m} S_2(n, m), \tag{3.13}$$

where $1 \leq m \leq n$, the notation (m) refers to the condition that m of $\{j_i\}$ are non-zero, and $S_2(n, m)$ is the Stirling number of the second kind. The Stirling number corresponds to the number of ways of partitioning a set of n elements into m non-empty sets [43].

As $N \to \infty$, the $2N$-port model approaches a PNR detector with perfect discrimination efficiency, such that the single-photon detection probability equals the single-photon probability of a general input state,

$$\lim_{N\to\infty} P^N_1 = \langle 1 | \rho^{\gamma'_N} | 1 \rangle .$$

For example, from Eq. 3.12, we can find the probability of a detection event at one output of a tree with depth k for an input thermal state with mean photon number μ as

$$P^k_1 = \frac{2^k \mu}{(1+\mu)\left(2^k + \left(2^k - 1\right)\mu\right)}.$$

Similarly, for a coherent state with mean photon number $|\alpha|^2$ as

$$P(1)_k = 2^k e^{-|\alpha|^2} \left(e^{|\alpha|^2/2^k} - 1 \right).$$

By taking the limit $k \to \infty$, we recover the single photon probabilities for a thermal state and coherent state, respectively, as

$$\lim_{k\to\infty} \frac{2^k \mu}{(1+\mu)\left(2^k + \left(2^k - 1\right)\mu\right)} = \frac{\mu}{(1+\mu)^2},$$
$$\lim_{k\to\infty} 2^k e^{-|\alpha|^2} \left(e^{|\alpha|^2/2^k} - 1 \right) = e^{-|\alpha|^2} |\alpha|^2.$$

POVM elements and counting statistics

The values of $P^N_{m,n}$, from Eq. 3.13, correspond to the matrix elements of a conditional probability matrix $\mathbf{C}$, following the definition used in Ref. [27]. The rows correspond to the positive-operator value measure (POVM) elements of the measurement outcomes and the columns correspond to the Fock projection operators. The matrix for a threshold detector, in other words, a tree with $k = 0$ is

$$\begin{array}{c} \\ \hat{\Pi}_{\text{no-event}} \\ \hat{\Pi}_{\text{event}} \end{array} \begin{array}{c} \begin{array}{cccccccc} |0\rangle\langle 0| & |1\rangle\langle 1| & |2\rangle\langle 2| & |3\rangle\langle 3| & |4\rangle\langle 4| & |5\rangle\langle 5| & |6\rangle\langle 6| & \cdots \end{array} \\ \begin{pmatrix} 1 & 0 & 0 & 0 & 0 & 0 & 0 & \cdots \\ 0 & 1 & 1 & 1 & 1 & 1 & 1 & \cdots \end{pmatrix} \end{array},$$

with measurement outcomes (rows) and projections (columns) indicated. The matrix for an ideal PNR detector is the identity matrix,

$$\begin{array}{c} \\ \hat{\Pi}_0 \\ \hat{\Pi}_1 \\ \hat{\Pi}_2 \\ \hat{\Pi}_3 \\ \hat{\Pi}_4 \\ \hat{\Pi}_5 \\ \hat{\Pi}_6 \\ \vdots \end{array} \begin{array}{c} \begin{array}{cccccccc} |0\rangle\langle 0| & |1\rangle\langle 1| & |2\rangle\langle 2| & |3\rangle\langle 3| & |4\rangle\langle 4| & |5\rangle\langle 5| & |6\rangle\langle 6| & \cdots \end{array} \\ \begin{pmatrix} 1 & 0 & 0 & 0 & 0 & 0 & 0 & \cdots \\ 0 & 1 & 0 & 0 & 0 & 0 & 0 & \cdots \\ 0 & 0 & 1 & 0 & 0 & 0 & 0 & \cdots \\ 0 & 0 & 0 & 1 & 0 & 0 & 0 & \cdots \\ 0 & 0 & 0 & 0 & 1 & 0 & 0 & \cdots \\ 0 & 0 & 0 & 0 & 0 & 1 & 0 & \cdots \\ 0 & 0 & 0 & 0 & 0 & 0 & 1 & \cdots \\ \vdots & \vdots & \vdots & \vdots & \vdots & \vdots & \vdots & \ddots \end{pmatrix} \end{array}.$$

For a detector with efficiency η_d, i.e., modeled as path loss of transmittivity η_d before an ideal detector, the probability that n photons trigger an m-fold coincidence detection event is

$$\begin{aligned} P^N_{m,n}(\eta_d) &= \sum_{j=0}^{n} P^N_{m,j} \binom{n}{j} {\eta_d}^j (1-\eta_d)^{n-j} \\ &= \sum_{j=0}^{n} C_{m,j} L_{j,n} \\ &= (\mathbf{C} \cdot \mathbf{L})_{m,n}\,, \end{aligned}$$

where $\mathbf{L}$ is the loss matrix with matrix elements,

$$L_{j,n} = \binom{n}{j} {\eta_d}^j (1-\eta_d)^{n-j}.$$

The matrix corresponding to $\mathbf{C}\cdot\mathbf{L}$ for a tree with $k = 3$ and $\eta_d = 0.71$ is,

$$
\begin{array}{c}
 \\
\hat{\Pi}_0 \\
\hat{\Pi}_1 \\
\hat{\Pi}_2 \\
\hat{\Pi}_3 \\
\hat{\Pi}_4 \\
\hat{\Pi}_5 \\
\hat{\Pi}_6 \\
\vdots
\end{array}
\begin{array}{c}
\begin{array}{ccccccccc}
|0\rangle\langle 0| & |1\rangle\langle 1| & |2\rangle\langle 2| & |3\rangle\langle 3| & |4\rangle\langle 4| & |5\rangle\langle 5| & |6\rangle\langle 6| & \cdots
\end{array} \\
\left(\begin{array}{ccccccccc}
1 & 0.29 & 0.084 & 0.024 & 0.007 & 0.002 & 0.001 & \cdots \\
0 & 0.71 & 0.475 & 0.240 & 0.108 & 0.046 & 0.019 & \cdots \\
0 & 0 & 0.441 & 0.501 & 0.383 & 0.246 & 0.144 & \cdots \\
0 & 0 & 0 & 0.235 & 0.398 & 0.425 & 0.368 & \cdots \\
0 & 0 & 0 & 0 & 0.104 & 0.244 & 0.346 & \cdots \\
0 & 0 & 0 & 0 & 0 & 0.037 & 0.114 & \cdots \\
0 & 0 & 0 & 0 & 0 & 0 & 0.010 & \cdots \\
\vdots & \vdots & \vdots & \vdots & \vdots & \vdots & \vdots & \ddots
\end{array}\right)
\end{array}.
$$

As we will show in detail in Sec. 3.4, this matrix corresponds to our experimental PNR configuration.

The counting statistics $p(n)$ can be related to the input photon number distribution $\varrho(n)$ by

$$p_m = \sum_n \sum_{j=0}^{n} C_{m,j} L_{j,n} \varrho_n,$$

where $p_m = p(m)$ and $\varrho_n = \varrho(n)$, following the notation of Eq. 9 from Ref. [27]. In matrix notation this is $\vec{p} = \mathbf{C}\cdot\mathbf{L}\vec{\varrho}$. The transpose of the matrix $(\mathbf{C}\cdot\mathbf{L})^T$ is matrix $\mathbf{B}$ from Ref. [26], which relates probabilities and density matrices as $\vec{p} = \mathbf{B}\hat{\rho}$.

Photon-number discrimination efficiency

A key figure of merit of our detector PNR configuration is its ability to discriminate single-photon events from others. To quantify this, we define the "$m-$photon discrimination efficiency" and use it to calculate the "single-photon discrimination efficiency" as follows.

A POVM element corresponding to the m-photon outcome for a non-ideal PNR detector can be described by

$$\hat{\Pi}_m = \sum_{n=0}^{\infty} c_n^m \left|n\right\rangle\left\langle n\right|, \tag{3.14}$$

where c_n^m are the matrix elements corresponding to the representation of the operator in the photon number basis, and are each equal to the probability of registering m

photons given n incident photons. The m-photon outcome for an ideal PNR detector is

$$\hat{\Pi}_m^{ideal} = |m\rangle\langle m| . \tag{3.15}$$

Note that for a threshold detector, the m-photon outcome for $m > 0$ is the "event" outcome $\hat{\Pi}_{\text{event}} = \sum_{n=1}^{\infty} |n\rangle\langle n|$, and $m = 0$ outcome corresponds to "no-event" $\hat{\Pi}_{\text{no-event}} = |0\rangle\langle 0|$. We define the m-photon discrimination efficiency as

$$\eta_{PNR}^m = 1 - \frac{1}{2}\,\text{Tr}\left[\sqrt{\left(\frac{\hat{\Pi}_m}{\text{Tr}[\hat{\Pi}_m]} - \frac{\hat{\Pi}_m^{\text{ideal}}}{\text{Tr}[\hat{\Pi}_m^{\text{ideal}}]}\right)^2}\right], \tag{3.16}$$

where the second term is the trace distance between elements $\hat{\Pi}_m$ and $\hat{\Pi}_m^{ideal}$, normalized by their trace, corresponding to the m-photon measurement outcome of the PNR detector. Using Eqs. 3.14 and 3.15, we simplify Eq. 3.16 to

$$\eta_{PNR}^m = \frac{c_m^m}{\sum_{n=0}^{\infty} c_n^m} = \frac{P(m|m)}{\sum_{n=0}^{\infty} P(m|n)}, \tag{3.17}$$

where $c_n^m = P(m|n)$ is the probability that the detector registers m photons given that n photons were incident on the detector. Relevant to our experiment is the single-photon discrimination efficiency ($m = 1$). As defined in Eq. 3.17, η_{PNR}^1 is zero for a threshold detector and unity for an ideal PNR detector.

Analytical expressions of detection probabilities

For a 2N-port beamsplitter realized as a finite-depth binary tree, we derive the following expressions for detection probabilities of the signal and idler paths, as well as two-fold and three-fold coincidence event probabilities as a function of the efficiencies and tree depth k, where $N = 2^k$. The equations reduce to the threshold detection case for $k = 0$.

We use $\hat{\Pi}_{\text{no-event},m}$ and $\hat{\Pi}_{\text{event},m}$ to denote the measurement operators for a threshold detector at the mth tree output:

$$\hat{\Pi}_{\text{no-event},m} = |0\rangle\langle 0|_m ,$$
$$\hat{\Pi}_{\text{event},m} = \hat{I}_m - |0\rangle\langle 0|_m .$$

For the PNR detector, we use $\hat{\Pi}_{\text{event},m} \otimes \hat{\Pi}_{\text{no-event}}^{\otimes N-1}$ to denote an "event" measurement outcome for a detector at the mth output and "no-event" measurement outcomes for the detectors at the remaining $N - 1$ outputs of the tree.

Detection probabilities for signal and idler detectors

The probabilities P_{s_1} and P_{s_2} of a detection event for the signal 1 and 2 detectors, respectively, are

$$P_{s_1} = \mathrm{Tr}\left[\rho\left(\hat{\Pi}_{s_1,\mathrm{event}} \otimes \hat{I}_{s_2} \otimes \hat{I}^{\otimes N}\right)\right],$$
$$P_{s_2} = \mathrm{Tr}\left[\rho\left(\hat{I}_{s_1} \otimes \hat{\Pi}_{s_2,\mathrm{event}} \otimes \hat{I}^{\otimes N}\right)\right],$$

and evaluate to

$$P_{s_j} = 1 - \prod_s \frac{2}{2 + \eta_{s_j}\lambda_s\mu},$$

where $j = 1, 2$ and λ_s are the Schmidt coefficients obtained from the singular value decomposition of the JSI as discussed in Sec. 3.2. The products in the expressions run over all Schmidt coefficients. The mean number of pairs μ as well as path efficiencies η_i and η_{s_j}, where $j = 1, 2$, as depicted in Fig. 3.8 and used here and in the following, are as defined earlier.

The probability P_i of a detection event for the idler detector is then

$$P_i = N\mathrm{Tr}\left[\rho\left(I_{s_1} \otimes I_{s_2} \otimes \hat{\Pi}_{\mathrm{event},m} \otimes \hat{\Pi}^{\otimes N-1}_{\mathrm{no\text{-}event}}\right)\right],$$

and evaluates to

$$P_i = 2^k\left(\prod_s \frac{2^k}{2^k + (2^k - 1)\lambda_s\mu\eta_i} - \prod_s \frac{1}{1 + \lambda_s\mu\eta_i}\right). \tag{3.18}$$

Two-fold coincidence detection probabilities

The probabilities of a two-fold coincidence detection event at the idler and one of the signal detectors, P_{is_1} and P_{is_2}, are

$$P_{is_1} = N\mathrm{Tr}\left[\rho\left(\hat{\Pi}_{\mathrm{event},s_1} \otimes I_{s_2} \otimes \hat{\Pi}_{\mathrm{event},m} \otimes \hat{\Pi}^{\otimes N-1}_{\mathrm{no\text{-}event}}\right)\right],$$
$$P_{is_2} = N\mathrm{Tr}\left[\rho\left(I_{s_1} \otimes \hat{\Pi}_{\mathrm{event},s_2} \otimes \hat{\Pi}_{\mathrm{event},m} \otimes \hat{\Pi}^{\otimes N-1}_{\mathrm{no\text{-}event}}\right)\right],$$

and evaluate to

$$\begin{aligned} P_{is_j} = 2^k\Bigg(&\prod_s \frac{2^k}{2^k + (2^k - 1)\lambda_s\mu\eta_i} \\ &- \prod_s \frac{2^{k+1}}{\lambda_s\mu\eta_{s_j}(2^k - (2^k - 1)\eta_i) + 2(2^k + (2^k - 1)\lambda_s\mu\eta_i)} \\ &- \prod_s \frac{1}{1 + \lambda_s\mu\eta_i} + \prod_s \frac{2}{2 + 2\lambda_s\mu\eta_i + \eta_{s_j}\lambda_s\mu(1 - \eta_i)}\Bigg), \end{aligned} \tag{3.19}$$

where $j = 1, 2$.

The probability of a two-fold coincidence detection event at the signal 1 and 2 detectors is

$$P_{s_1 s_2} = \mathrm{Tr}\left[\rho\left(\hat{\Pi}_{\mathrm{event},s_1} \otimes \hat{\Pi}_{\mathrm{event},s_2} \otimes \hat{I}_m^{\otimes N}\right)\right],$$

and evaluates to

$$P_{s_1 s_2} = 1 - \prod_s \frac{2}{2 + \eta_{s_1}\lambda_s\mu} - \prod_s \frac{2}{2 + \eta_{s_2}\lambda_s\mu} + \prod_s \frac{2}{2 + (\eta_{s_1} + \eta_{s_2})\lambda_s\mu}.$$

Three-fold coincidence detection probabilities

The probability of a three-fold coincidence detection event at the idler, signal 1, and signal 2 detectors, $P_{i,s_1,s_2}(\mu, \eta_{s_1}, \eta_{s_2}, \eta_i, k)$, is

$$P_{i,s_1,s_2} = N\mathrm{Tr}\left[\rho\left(\hat{\Pi}_{\mathrm{event},s_1} \otimes \hat{\Pi}_{\mathrm{event},s_1} \otimes \hat{\Pi}_{\mathrm{event},m} \otimes \hat{\Pi}_{\text{no-event}}^{\otimes N-1}\right)\right],$$

and evaluates to

$$\begin{aligned}
P_{i,s_1,s_2} = 2^k\Bigg(&\prod_s \frac{2^k}{2^k + (2^k - 1)\lambda_s\mu\eta_i} \\
&- \prod_s \frac{2^{k+1}}{\lambda_s\mu\eta_{s_1}(2^k - (2^k - 1)\eta_i) + 2(2^k + (2^k - 1)\lambda_s\mu\eta_i)} \\
&- \prod_s \frac{2^{k+1}}{\lambda_s\mu\eta_{s_2}(2^k - (2^k - 1)\eta_i) + 2(2^k + (2^k - 1)\lambda_s\mu\eta_i)} \\
&+ \prod_s \frac{2^{k+1}}{\lambda_s\mu(\eta_{s_1} + \eta_{s_2})(2^k - (2^k - 1)\eta_i) + 2(2^k + (2^k - 1)\lambda_s\mu\eta_i)} \\
&- \prod_s \frac{1}{1 + \lambda_s\mu\eta_i} + \prod_s \frac{2}{2 + 2\lambda_s\mu\eta_i + \eta_{s_1}\lambda_s\mu(1 - \eta_i)} \\
&+ \prod_s \frac{2}{2 + 2\lambda_s\mu\eta_i + \eta_{s_2}\lambda_s\mu(1 - \eta_i)} \\
&- \prod_s \frac{2}{2 + 2\mu\lambda_s\eta_i + (\eta_{s_1} + \eta_{s_2})\mu\lambda_s(1 - \eta_i)}\Bigg).
\end{aligned} \tag{3.20}$$

Second-order correlation function $g^{(2)}(0)$

Finally, we readily derive the analytical expression for $g^{(2)}(0)$ by substituting Eqs. 3.18, 3.19, and 3.20 and into

$$g^{(2)}(0) = \frac{P_{i,s_1,s_2}P_i}{P_{i,s_1}P_{i,s_2}} = \frac{C_{i,s_1,s_2}C_i}{C_{i,s_1}C_{i,s_2}}, \tag{3.21}$$

where the respective probabilities P can be used to calculate detection rates C using $C = RP$.

3.4 Results

We vary the gain of the amplifier in the SHG module and measure single detector, i.e., signal 1 and 2 and idler, events as well as two- and three-fold coincidence detection events for (i) the PNR configuration and (ii) the threshold configuration for the idler detector. We then perform a maximum-likelihood fit of our theoretical model for $g^2(0)$, i.e., Eq. 3.21, to the measured $g^2(0)$ for configurations (i) with PNR and (ii) with threshold detection. The likelihood is optimized using the MINUIT [44] implementation in *iminuit* [45]. The experimental $g^2(0)$ data and curve corresponding to the best-fitted model are shown in Fig. 3.9.

Maximum-likelihood fit

The theoretical model for $g^2(0)$ includes several parameters, as introduced in Secs. 3.2 and 3.3. Our fit extracts the following key experimental values: mean photon-pair number μ, tree depth k, path efficiencies η_i, η_{s_1} and η_{s_2}, as well as the filter and pump bandwidths, σ_{CWDM} and σ_p, which strongly influence the eigenvalue spectrum of JSI. The best-fit values and uncertainties of the mean photon number for each amplifier setting is shown in Fig. 3.9. We also calculate the pull for $g^2(0)$, which is the distance of the best fit value from the Gaussian constraint measured in values of the constraint width. The best-fit, uncertainties and pull of the other values are shown in Tab. 3.1. We find the best-fit path efficiencies and the filter bandwidth are identical, within uncertainty, to that evaluated by independent measurements in Sec. 3.2. The predicted pump bandwidth (88 GHz) is larger than that measured in Sec. 3.2 (60 GHz) likely because it was inferred by measurements at telecommunication wavelength.

In the fit, the path efficiencies are free parameters, while the mean and uncertainties thereof, measured in Sec. 3.2, are used to place Gaussian constraints on the fit. Each measured $g^2(0)$ is ascribed an independent value of μ, and given the path efficiencies, is determined by fitting the single detector and two-fold coincidence detection probabilities, i.e., those shown in Fig. 3.10, collected during the measurements. The mean and statistical uncertainties of these detection rates is used to place a Gaussian constraint on the value of μ for each data point. The eigenvalue spectrum of the JSI is computed by varying $\sigma_{\mathrm{CWDM}} = 13 \pm 1$ nm and $\sigma_p = 60 \pm 10$ GHz as discussed in Sec. 3.2, and a linear approximation is used to allow the fit for a continuous variation. Additional fit details are discussed in the captions of Fig. 3.9 and Tab. 3.1.

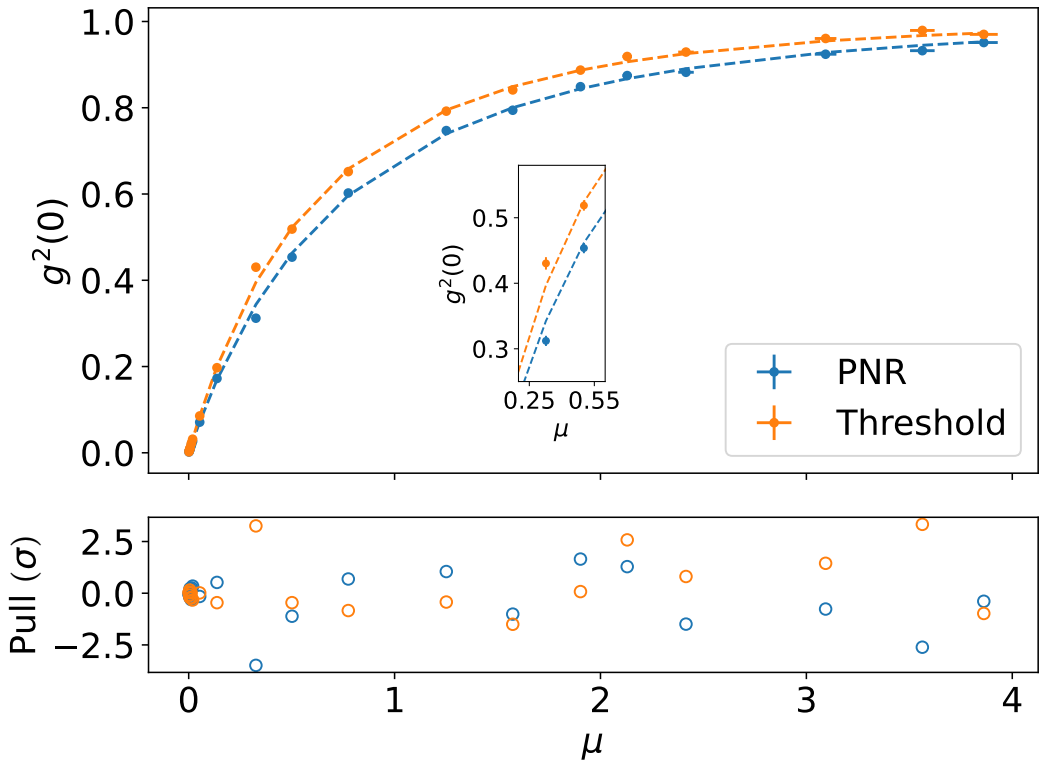

Figure 3.9: Measured correlation function $g^2(0)$ as a function of mean photon-pair number μ. The experimental data using threshold (orange) and PNR (blue) idler detector configurations are represented by the circular markers whereas the respective fitted models are shown by dashed lines. Uncertainties of $g^2(0)$, referred to as $\sigma_{g^2(0)}$, are derived from the statistical uncertainties of the coincidence detection events whereas the uncertainties of μ, that is, σ_μ, are extracted from the fit to the model. The inset depicts the region where the largest reduction in $g^2(0)$ is measured. The pull between the measured $g^2(0)$ and the model, computed as $[\sigma^2_{g^2(0)} + |\partial_\mu g^2(0)|^2 \, \sigma^2_\mu]^{1/2}$ and plotted in units of standard deviations, is shown at the bottom of the canvas.

Single-photon discrimination efficiency

With $k = 3.45^{+0.71}_{-0.50}$ extracted from the fit, the single-photon discrimination efficiency of our PNR detector is comparable to that of a pseudo-PNR detector comprised of approximately 11^{+7}_{-3} threshold detectors, each with efficiency $\eta_d = 0.71$. Therefore, following the model developed in Sec. 3.3, the experimental POVM is

$$\begin{aligned}\hat{\Pi}_1^{exp} \approx\ & 0.710\,|1\rangle\langle 1| + 0.458\,|2\rangle\langle 2| + 0.222\,|3\rangle\langle 3| \\ & + 0.096\,|4\rangle\langle 4| + 0.039\,|5\rangle\langle 5| + 0.015\,|6\rangle\langle 6|\,,\end{aligned} \tag{3.22}$$

Parameter	Best fit	Pull (σ)
η_i	0.319 ± 0.026	-0.1 (3.9)
η_{s_1}	0.370 ± 0.024	0.3 (2.5)
η_{s_2}	0.436 ± 0.017	0.2 (3.3)
σ_{CWDM} (nm)	11.97 ± 0.95	-1.0 (0.9)
σ_p (GHz)	87.7 ± 14.0	2.8 (1.4)
k	$3.45^{+0.71}_{-0.50}$	-

Table 3.1: Maximum-likelihood best-fit results for key experimental parameters. Uncertainties are computed by inverting the Hessian, except for k, where a likelihood scan has been performed. There is no value of pull for k as it is extracted from a fit without a constraint.

corresponding, according to the arguments in Sec. 3.3, to a single-photon discrimination efficiency of $\eta^1_{PNR} \approx 0.46$, limited mainly by η_d.

Improvement with a PNR SNSPD

The reduction of $g^2(0)$ shown in Fig. 3.9 demonstrates a suppression of multi-photon events. A maximum reduction of 0.118 ± 0.012 at $\mu = 0.327 \pm 0.007$ is observed; it is more clearly indicated in the inset of Fig. 3.9.

The data and fit for $\mu \ll 1$ is presented in Fig. 3.11. Configurations (ii) and (i) are denoted by orange and blue colors, respectively, with the data indicated by large dots and the fit by solid curves. To give context, orange and blue dotted lines indicate the μ corresponding to a $g^2(0)$ of 7×10^{-3} (gray dashed line) measured in Ref. [28], Specifically, we observe a 25% improvement in μ, from 4×10^{-3} (orange dotted line) with configuration (ii), to 5×10^{-3} (blue dotted line) with configuration (i).

To estimate the performance of our experiment with future improvements, we calculate $g^2(0)$ using the properties of our PNR detector ($k = 3.45$, green curve) and those of a PNR detector with a higher tree depth ($k = 10$, red curve). We also assume higher path efficiencies of $\eta_{s_1} = \eta_{s_2} = \eta_i = 0.87$, which are the product of the coupling (0.91) and detector (0.96) efficiencies from Refs. [46] and [47], respectively, and are among the best-achieved to date. With these upgrades, for a $g^2(0)$ of 7×10^{-3} (gray dashed line), we predict an improved $\mu = 20.5 \times 10^{-3}$ (green curve) and $\mu = 26.7 \times 10^{-3}$ (red curve) using our PNR SNSPD and a nearly ideal PNR detector, respectively.

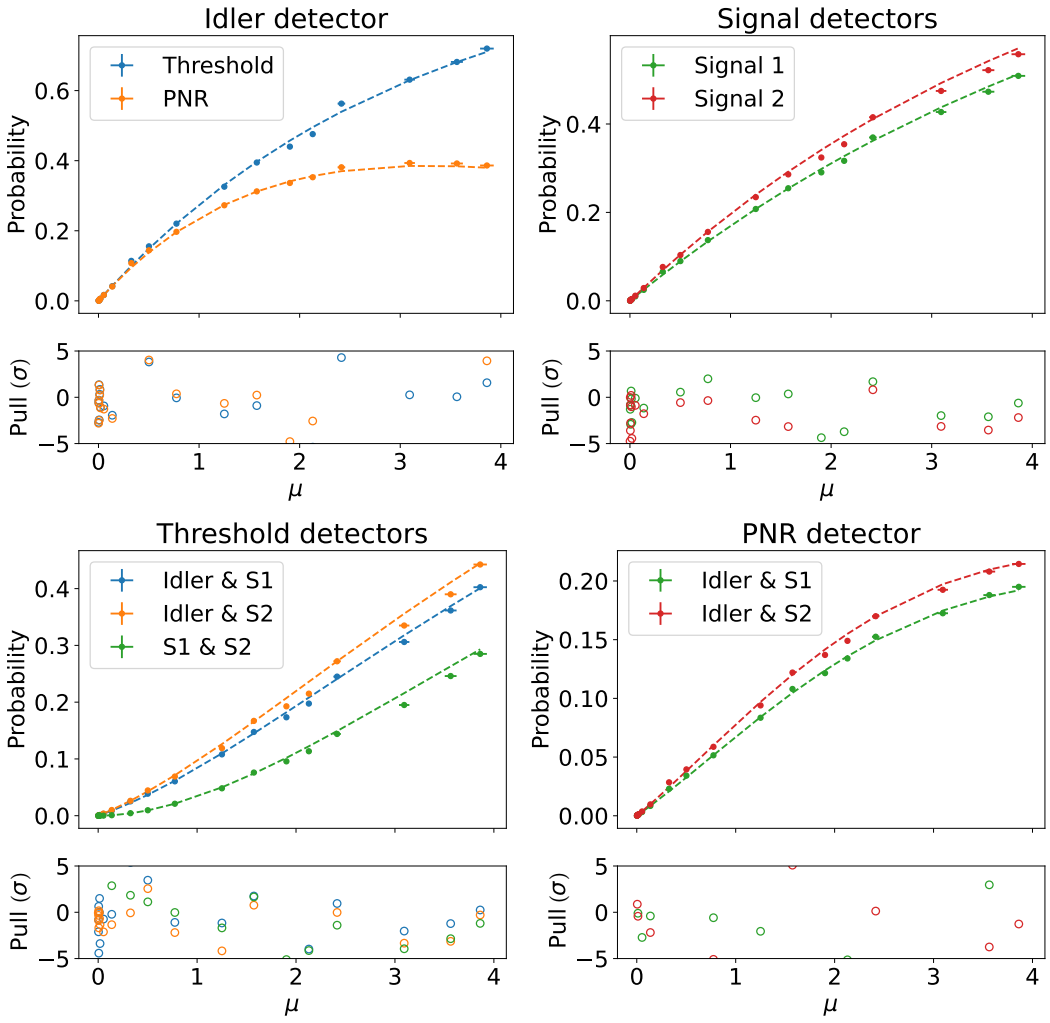

Figure 3.10: Idler detection probabilities (top left), signal 1 and signal 2 detection probabilities (top right), signal detector two-fold coincidence probabilities and signal detectors with idler in threshold configuration (bottom left), two-fold signal and idler in PNR configuration two-fold coincidence probabilities. The prediction from the theoretical model is shown for the best fit parameters in Tab. 3.1.

3.5 Discussion

By measuring the idler mode of a spontaneous parametric down-conversion source using a photon-number-resolving nanowire detector, we reduce the $g^2(0)$ of the signal mode or, on the other hand, increase the probability to generate a photon. The results and key performance metrics of our experiment are supported by a detailed analytical model which captures multi-photon effects, imperfections, and multiple spectral modes. Using a setup consisting of fiber-coupled and off-the-shelf

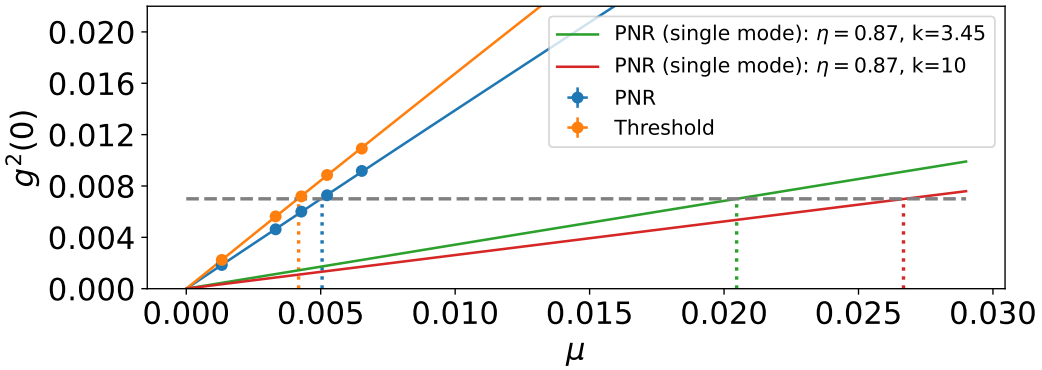

Figure 3.11: Correlation function $g^2(0)$ as a function of mean photon number $\mu \ll 1$ for our experiment and improved heralded single-photon sources. The experimental data (large dots) are represented with their uncertainties. The models for the threshold configuration (orange curve) and PNR configuration (blue curve) of our detector are compared with the green and red curves, which correspond to model predictions using improved sources, as discussed in the main text, with key parameters (tree depth k, path efficiencies $\eta \equiv \eta_{s_1} = \eta_{s_2} = \eta_i$) shown in the inset. The grey dashed line corresponds to a $g^2(0)$ measured in Ref. [28].

devices, we generate photons that can be used in quantum information applications, in particular quantum communications [48, 49].

To realize an ideal single-photon source [1], a number of improvements to our experiment must be implemented [36]. First, the Schmidt number of our SPDC source must be decreased from its current value of $K \approx 772$ to $K = 1$. This can be accomplished by either narrower spectral filtering of the pairs or increasing the pump pulse bandwidth [50], the use of cavity-enhanced SPDC [51], or by engineering the phase matching function of the nonlinear crystal [52, 53]. A near-unity Schmidt number renders the photons suitable for interference with other independently generated photons in a quantum circuit or network.

Next, the system efficiency should be increased to near unity. Coupling between fibers and devices can be improved with enhanced modal engineering [54] or using anti-reflection-coated free-space components [55]. Alternatively, components could be integrated onto the same chip, for instance using Si- or SiN-on-insulator with SFWM sources [56, 17], or using thin-film lithium niobate [57]. Furthermore, multiplexing strategies must be employed to increase the probability of generating a single pair beyond the theoretical maximum of 25% per mode. Such multiplexing, using, for instance, spatial [58, 59], temporal [60, 46], or frequency modes [61, 62],

could also be employed to circumvent loss in the signal mode [63]. This requires on-demand feed-forward mode mapping using switches [64], quantum memories [65], or frequency shifters [66], respectively. Feed-forward requires the real-time readout that our PNR SNSPD allows. Note that feed-forward also allows for temporal filtering of the signal mode, a method that yields a significant reduction in $g^2(0)$ [67, 68, 69]. We also point out that our improvement in $g^2(0)$ significantly reduces the number of spatially multiplexed sources ($\sim 1/\mu$ for $\mu \ll 1$) that are required to render our heralded photon source to be quasi-deterministic. For instance, for $g^2(0) = 7 \times 10^{-3}$, in which we observe a 25% improvement in μ from 4×10^{-3} to 5×10^{-3}, see Fig. 3.11, corresponds to a reduction of the number of multiplexed spatial modes from 250 to 200. Further, with an improved detector efficiency of 0.87 [46, 47], only $\sim$ 49 multiplexed modes will be required to quasi-deterministically generate a heralded single photon.

Multiplexing with feed-forward also allows a multi-mode source to be rendered as single mode, i.e., it effectively decreases its Schmidt number to unity [62]. Our broadband SPDC source is naturally suited for frequency multiplexing, as indicated by the strong frequency correlations in our JSI [70]. This suggests our measured $\mu = 5 \times 10^{-3}$ for $g^2(0) = 7 \times 10^{-3}$ exceeds state-of-the-art SPDC sources using threshold detection, as well as quantum dots [28], accounting for such frequency multiplexing.

Additional gains can be offered by improvements to the PNR SNSPD. A higher detector efficiency, i.e., ideally increasing η_d to one, would increase the single-photon discrimination efficiency and improve the fidelity of the heralded single photon. This may be achieved through improvements to the optical stack around the nanowire by replacing the gold mirror with a distributed Bragg reflector mirror [71]. Also, the detector reset time of nearly 100 ns restricts the maximum repetition rate of the source to be $\sim$ 10 MHz. An SNSPD with a reduced reset time based on a lower kinetic inductance nanowire material, or integrated with an active quenching circuit [72], would allow for high single-photon generation rates. A multiplexing method based on multiple PNR SNSPDs would also support a high repetition rate in addition to a substantial increase in detection efficiency [73].

Beyond single-photon sources, extensions of our setup allow efficient generation of qubits or qudits, as well as entanglement swapping using PNR SNSPDs [49]. Further uses encompass preparation of heralded photon-number states [74] and non-Gaussian continuous-variable states [75], vital resources to realize fault-tolerant

photonic quantum computers [76]. Lastly, and of note, by using PNRs to improve teleportation rates [16], novel applications can benefit including microwave to optical transduction [77]. During the preparation of our manuscript we became aware of relevant results achieved independently of this work [78].

References

[1] Matthew D. Eisaman, Jingyun Fan, Alan Migdall, and Sergey V. Polyakov. "Invited review article: Single-photon sources and detectors." In: Review of Scientific Instruments 82.7 (2011), p. 071101.

[2] Jeremy L. O'Brien, Akira Furusawa, and Jelena Vučković. "Photonic quantum technologies." In: Nature Photonics 3.12 (2009), pp. 687–695.

[3] Igor Aharonovich, Dirk Englund, and Milos Toth. "Solid-state single-photon emitters." In: Nature Photonics 10.10 (2016), pp. 631–641.

[4] Peter Michler, Alper Kiraz, Christoph Becher, W. V. Schoenfeld, P. M. Petroff, Lidong Zhang, Ella Hu, and A. Imamoglu. "A quantum dot single-photon turnstile device." In: Science 290.5500 (2000), pp. 2282–2285.

[5] Andrew J. Shields. "Semiconductor quantum light sources." In: Nature Photonics 1.4 (Apr. 2007), pp. 215–223. ISSN: 1749-4893. DOI: 10.1038/nphoton.2007.46. URL: https://doi.org/10.1038/nphoton.2007.46.

[6] Pascale Senellart, Glenn Solomon, and Andrew White. "High-performance semiconductor quantum-dot single-photon sources." In: Nature Nanotechnology 12.11 (2017), pp. 1026–1039.

[7] Thomas M. Babinec, Birgit J. M. Hausmann, Mughees Khan, Yinan Zhang, Jeronimo R. Maze, Philip R. Hemmer, and Marko Lončar. "A diamond nanowire single-photon source." In: Nature nanotechnology 5.3 (2010), pp. 195–199.

[8] H. G. Barros, A. Stute, T. E. Northup, C. Russo, P. O. Schmidt, and R. Blatt. "Deterministic single-photon source from a single ion." In: New Journal of Physics 11.10 (2009), p. 103004.

[9] Martin Mücke, Joerg Bochmann, Carolin Hahn, Andreas Neuzner, Christian Nölleke, Andreas Reiserer, Gerhard Rempe, and Stephan Ritter. "Generation of single photons from an atom-cavity system." In: Physical Review A 87.6 (2013), p. 063805.

[10] Carlo Bradac, Weibo Gao, Jacopo Forneris, Matthew E. Trusheim, and Igor Aharonovich. "Quantum nanophotonics with group IV defects in diamond." In: Nature Communications 10.1 (Dec. 2019), p. 5625. ISSN: 2041-1723. DOI: 10.1038/s41467-019-13332-w. URL: https://doi.org/10.1038/s41467-019-13332-w.

[11] Stefan Bogdanović, Madelaine S. Z. Liddy, Suzanne B. van Dam, Lisanne C. Coenen, Thomas Fink, Marko Lončar, and Ronald Hanson. "Robust nanofabrication of an integrated platform for spin control in a tunable microcavity." In: APL Photonics 2.12 (2017), p. 126101.

[12] Daniel Huber, Marcus Reindl, Yongheng Huo, Huiying Huang, Johannes S. Wildmann, Oliver G. Schmidt, Armando Rastelli, and Rinaldo Trotta. "Highly indistinguishable and strongly entangled photons from symmetric GaAs quantum dots." In: Nature Communications 8.1 (May 2017), p. 15506. ISSN: 2041-1723. DOI: 10.1038/ncomms15506. URL: https://doi.org/10.1038/ncomms15506.

[13] Alp Sipahigil, Kay D. Jahnke, Lachlan J. Rogers, Tokuyuki Teraji, Junichi Isoya, Alexander S. Zibrov, Fedor Jelezko, and Mikhail D. Lukin. "Indistinguishable photons from separated silicon-vacancy centers in diamond." In: Physical Review Letters 113.11 (2014), p. 113602.

[14] Hannes Bernien, Lilian Childress, Lucio Robledo, Matthew Markham, Daniel Twitchen, and Ronald Hanson. "Two-photon quantum interference from separate nitrogen vacancy centers in diamond." In: Physical Review Letters 108.4 (2012), p. 043604.

[15] Robert W. Boyd. Nonlinear optics. Academic Press, 2020.

[16] Raju Valivarthi, Samantha I Davis, Cristián Peña, Si Xie, Nikolai Lauk, Lautaro Narváez, Jason P Allmaras, Andrew D Beyer, Yewon Gim, Meraj Hussein, et al. "Teleportation systems toward a quantum internet." In: PRX Quantum 1.2 (2020), p. 020317.

[17] Jianwei Wang, Fabio Sciarrino, Anthony Laing, and Mark G. Thompson. "Integrated photonic quantum technologies." In: Nature Photonics 14.5 (2020), pp. 273–284.

[18] Justin B. Spring, Paolo L. Mennea, Benjamin J. Metcalf, Peter C. Humphreys, James C Gates, Helen L. Rogers, Christoph Söller, Brian J. Smith, W. Steven Kolthammer, Peter G. R. Smith, et al. "Chip-based array of near-identical, pure, heralded single-photon sources." In: Optica 4.1 (2017), pp. 90–96.

[19] Adriana E. Lita, Aaron J. Miller, and Sae Woo Nam. "Counting near-infrared single-photons with 95% efficiency." In: Optics Express 16.5 (2008), pp. 3032–3040.

[20] Leaf A. Jiang, Eric A. Dauler, and Joshua T. Chang. "Photon-number-resolving detector with 10 bits of resolution." In: Physical Review A 75.6 (2007), p. 062325.

[21] M. J. Fitch, B. C. Jacobs, T. B. Pittman, and J. D. Franson. "Photon-number resolution using time-multiplexed single-photon detectors." In: Physical Review A 68.4 (2003), p. 043814.

[22] Marco Colangelo, Boris Korzh, Jason P. Allmaras, Andrew D. Beyer, Andrew S. Mueller, Ryan M Briggs, Bruce Bumble, Marcus Runyan, Martin J. Stevens, Adam N. McCaughan, et al. "Impedance-matched differential superconducting nanowire detectors." In: preprint arXiv:2108.07962 (2021).

[23] Chandra M. Natarajan, Michael G. Tanner, and Robert H. Hadfield. "Superconducting nanowire single-photon detectors: physics and applications." In: Superconductor Science and Technology 25.6 (2012), p. 063001.

[24] Roy J. Glauber. "The quantum theory of optical coherence." In: Physical Review 130.6 (1963), p. 2529.

[25] Masahiro Takeoka, Rui-Bo Jin, and Masahide Sasaki. “Full analysis of multi-photon pair effects in spontaneous parametric down conversion based photonic quantum information processing.” In: New Journal of Physics 17.4 (2015), p. 043030.

[26] Alvaro Feito, J. S. Lundeen, Hendrik Coldenstrodt-Ronge, Jens Eisert, Martin B. Plenio, and Ian A. Walmsley. “Measuring measurement: theory and practice.” In: New Journal of Physics 11.9 (2009), p. 093038.

[27] Daryl Achilles, Christine Silberhorn, Cezary Sliwa, Konrad Banaszek, Ian A. Walmsley, Michael J. Fitch, Bryan C. Jacobs, Todd B. Pittman, and James D Franson. “Photon-number-resolving detection using time-multiplexing.” In: Journal of Modern Optics 51.9-10 (2004), pp. 1499–1515.

[28] F. Kaneda and P. G. Kwiat. “High-efficiency single-photon generation via large-scale active time multiplexing.” In: Science Advances 5.10 (2019), eaaw8586.

[29] F. Marsili, V. B. Verma, J. A. Stern, et al. “Detecting single infrared photons with 93% system efficiency.” In: Nature Photonics 7.3 (Mar. 2013), pp. 210–214. ISSN: 1749-4893. DOI: 10.1038/nphoton.2013.13. URL: https://doi.org/10.1038/nphoton.2013.13.

[30] Di Zhu, Marco Colangelo, Boris A. Korzh, Qing-Yuan Zhao, Simone Frasca, Andrew E Dane, Angel E. Velasco, Andrew D. Beyer, Jason P. Allmaras, Edward Ramirez, et al. “Superconducting nanowire single-photon detector with integrated impedance-matching taper.” In: Applied Physics Letters 114.4 (2019), p. 042601.

[31] Di Zhu, Marco Colangelo, Changchen Chen, Boris A. Korzh, Franco N.C. Wong, Matthew D. Shaw, and Karl K. Berggren. “Resolving photon numbers using a superconducting nanowire with impedance-matching taper.” In: Nano Letters 20.5 (2020), pp. 3858–3863. ISSN: 15306992.

[32] Clinton Cahall, Kathryn L. Nicolich, Nurul T. Islam, Gregory P. Lafyatis, Aaron J. Miller, Daniel J. Gauthier, and Jungsang Kim. “Multi-photon detection using a conventional superconducting nanowire single-photon detector.” In: Optica 4.12 (Dec. 2017), pp. 1534–1535.

[33] Fabian Laudenbach, Hannes Hübel, Michael Hentschel, Philip Walther, and Andreas Poppe. “Modelling parametric down-conversion yielding spectrally pure photon pairs.” In: Optics Express 24.3 (2016), pp. 2712–2727.

[34] David E. Zelmon, David L. Small, and Dieter Jundt. “Infrared corrected Sellmeier coefficients for congruently grown lithium niobate and 5 mol.% magnesium oxide–doped lithium niobate.” In: Journal of the Optical Society of America (JOSA) B 14.12 (1997), pp. 3319–3322.

[35] Kevin Zielnicki, Karina Garay-Palmett, Daniel Cruz-Delgado, Hector Cruz-Ramirez, Michael F. O’Boyle, Bin Fang, Virginia O. Lorenz, Alfred B U’Ren, and Paul G. Kwiat. “Joint spectral characterization of photon-pair sources.” In: Journal of Modern Optics 65.10 (2018), pp. 1141–1160.

[36] Andreas Christ and Christine Silberhorn. “Limits on the deterministic creation of pure single-photon states using parametric down-conversion.” In: Physical Review A 85.2 (2012), p. 023829.

[37] Marek Zukowski, Anton Zeilinger, and Harald Weinfurter. "Entangling Photons Radiated by Independent Pulsed Sources a." In: Annals of the New York academy of Sciences 755.1 (1995), pp. 91–102.

[38] D. N. Klyshko. "Use of two-photon light for absolute calibration of photoelectric detectors." In: Soviet Journal of Quantum Electronics 10.9 (1980), p. 1112.

[39] Felix Bussieres, Joshua A. Slater, Nicolas Godbout, and Wolfgang Tittel. "Fast and simple characterization of a photon pair source." In: Optics Express 16.21 (2008), pp. 17060–17069.

[40] Christian Weedbrook, Stefano Pirandola, Raúl García-Patrón, Nicolas J. Cerf, Timothy C. Ralph, Jeffrey H. Shapiro, and Seth Lloyd. "Gaussian quantum information." In: Reviews of Modern Physics 84.2 (2012), p. 621.

[41] Ulf Leonhardt. Measuring the quantum state of light. Vol. 22. Cambridge university press, 1997.

[42] H. Paul, P. Törmä, T. Kiss, and I. Jex. "Photon chopping: new way to measure the quantum state of light." In: Physical Review Letters 76.14 (1996), p. 2464.

[43] Eric W. Weisstein. Stirling Number of the Second Kind. From MathWorld–A Wolfram Web Resource. https://mathworld.wolfram.com/StirlingNumberoftheSecondKind.html.

[44] F. James and M. Roos. "Minuit: A System for Function Minimization and Analysis of the Parameter Errors and Correlations." In: Comput. Phys. Commun. 10 (1975), pp. 343–367. DOI: 10.1016/0010-4655(75)90039-9.

[45] Hans Dembinski and Piti Ongmongkolkul et al. scikit-hep/iminuit. Dec. 2020. DOI: 10.5281/zenodo.3949207. URL: https://doi.org/10.5281/zenodo.3949207.

[46] Fumihiro Kaneda, Karina Garay-Palmett, Alfred B. U'Ren, and Paul G. Kwiat. "Heralded single-photon source utilizing highly nondegenerate, spectrally factorable spontaneous parametric downconversion." In: Optics Express 24.10 (2016), pp. 10733–10747.

[47] Mohsen K. Akhlaghi, Ellen Schelew, and Jeff F. Young. "Waveguide integrated superconducting single-photon detectors implemented as near-perfect absorbers of coherent radiation." In: Nature Communications 6.1 (Sept. 2015), p. 8233. ISSN: 2041-1723. DOI: 10.1038/ncomms9233. URL: https://doi.org/10.1038/ncomms9233.

[48] C. Bennett and G. Brassard. "Quantum cryptography: public key distribution and coin tossing int." In: Conf. on Computers, Systems and Signal Processing. Vol. 175. 1984.

[49] Hari Krovi, Saikat Guha, Zachary Dutton, Joshua A Slater, Christoph Simon, and Wolfgang Tittel. "Practical quantum repeaters with parametric down-conversion sources." In: Applied Physics B 122.3 (2016), p. 52.

[50] J. G. Rarity. "Interference of Single Photons from Separate Sources a." In: Annals of the New York academy of Sciences 755.1 (1995), pp. 624–631.

[51] T. J. Herzog, J. G. Rarity, H. Weinfurter, and A. Zeilinger. “Frustrated two-photon creation via interference.” In: Physical Review Letters 72.5 (1994), p. 629.

[52] P. J. Mosley, J. S. Lundeen, B. J. Smith, P. Wasylczyk, A. B. U’Ren, C. Silberhorn, and I. A. Walmsley. “Heralded Generation of Ultrafast Single Photons in Pure Quantum States.” In: Physical Review Letters 100.13 (2008). Demonstrates spectral engineering for single–mode operation and reports high heralding efficiency and purity (as indicated by low $g^{(2)}(0)$)., p. 133601.

[53] C. J. Xin, Jatadhari Mishra, Changchen Chen, Di Zhu, Amirhassan Shams-Ansari, Carsten Langrock, Neil Sinclair, Franco N. C. Wong, M. M. Fejer, and Marko Lončar. “Spectrally separable photon-pair generation in dispersion engineered thin-film lithium niobate.” In: Optics Letters 47.11 (June 2022), pp. 2830–2833. DOI: 10.1364/OL.456873. URL: http://opg.optica.org/ol/abstract.cfm?URI=ol-47-11-2830.

[54] Brian S. Kawasaki, Kenneth O. Hill, and R. G. Lamont. “Biconical-taper single-mode fiber coupler.” In: Optics Letters 6.7 (1981), pp. 327–328.

[55] Lynden K Shalm, Evan Meyer-Scott, Bradley G Christensen, Peter Bierhorst, Michael A Wayne, Martin J Stevens, Thomas Gerrits, Scott Glancy, Deny R Hamel, Michael S Allman, et al. “Strong loophole-free test of local realism.” In: Physical Review Letters 115.25 (2015), p. 250402.

[56] Joshua W. Silverstone, Damien Bonneau, Kazuya Ohira, Nob Suzuki, Haruhiko Yoshida, Norio Iizuka, Mizunori Ezaki, Chandra M. Natarajan, Michael G. Tanner, Robert H. Hadfield, et al. “On-chip quantum interference between silicon photon-pair sources.” In: Nature Photonics 8.2 (2014), pp. 104–108.

[57] Di Zhu, Linbo Shao, Mengjie Yu, Rebecca Cheng, Boris Desiatov, C. J. Xin, Yaowen Hu, Jeffrey Holzgrafe, Soumya Ghosh, Amirhassan Shams-Ansari, et al. “Integrated photonics on thin-film lithium niobate.” In: Advances in Optics and Photonics 13.2 (2021), pp. 242–352.

[58] M. J. Collins, C. Xiong, I. H. Rey, et al. “Integrated spatial multiplexing of heralded single-photon sources.” In: Nature Communications 4.1 (Oct. 2013), p. 2582. ISSN: 2041-1723. DOI: 10.1038/ncomms3582. URL: https://doi.org/10.1038/ncomms3582.

[59] Gabriel J. Mendoza, Raffaele Santagati, Jack Munns, Elizabeth Hemsley, Mateusz Piekarek, Enrique Martín-López, Graham D. Marshall, Damien Bonneau, Mark G. Thompson, and Jeremy L. O’Brien. “Active temporal and spatial multiplexing of photons.” In: Optica 3.2 (2016), pp. 127–132.

[60] C. Xiong, X. Zhang, Z. Liu, et al. “Active temporal multiplexing of indistinguishable heralded single photons.” In: Nature Communications 7.1 (Mar. 2016), p. 10853. ISSN: 2041-1723. DOI: 10.1038/ncomms10853. URL: https://doi.org/10.1038/ncomms10853.

[61] Chaitali Joshi, Alessandro Farsi, Stéphane Clemmen, Sven Ramelow, and Alexander L. Gaeta. “Frequency multiplexing for quasi-deterministic heralded single-photon sources.” In: Nature Communications 9.1 (Feb. 2018), p. 847. ISSN: 2041-

1723. DOI: 10.1038/s41467-018-03254-4. URL: https://doi.org/10.1038/s41467-018-03254-4.

[62] M. Grimau Puigibert, G. H. Aguilar, Q. Zhou, F Marsili, M. D. Shaw, V. B. Verma, S. W. Nam, D. Oblak, and W. Tittel. "Heralded single photons based on spectral multiplexing and feed-forward control." In: Physical Review Letters 119.8 (2017), p. 083601.

[63] Neil Sinclair, Erhan Saglamyurek, Hassan Mallahzadeh, et al. "Spectral Multiplexing for Scalable Quantum Photonics using an Atomic Frequency Comb Quantum Memory and Feed-Forward Control." In: Physical Review Letters 113 (5 July 2014), p. 053603. DOI: 10.1103/PhysRevLett.113.053603. URL: https://link.aps.org/doi/10.1103/PhysRevLett.113.053603.

[64] Peipeng Xu, Jiajiu Zheng, Jonathan K Doylend, and Arka Majumdar. "Low-loss and broadband nonvolatile phase-change directional coupler switches." In: ACS Photonics 6.2 (2019), pp. 553–557.

[65] Alexander I. Lvovsky, Barry C. Sanders, and Wolfgang Tittel. "Optical quantum memory." In: Nature Photonics 3.12 (2009), p. 706.

[66] Yaowen Hu, Mengjie Yu, Di Zhu, Neil Sinclair, Amirhassan Shams-Ansari, Linbo Shao, Jeffrey Holzgrafe, Eric Puma, Mian Zhang, and Marko Lončar. "On-chip electro-optic frequency shifters and beam splitters." In: Nature 599.7886 (2021), pp. 587–593.

[67] Giorgio Brida, Ivo Pietro Degiovanni, M Genovese, Fabrizio Piacentini, Paolo Traina, Adriano Della Frera, Alberto Tosi, Andrea Bahgat Shehata, Carmelo Scarcella, Angelo Gulinatti, et al. "An extremely low-noise heralded single-photon source: A breakthrough for quantum technologies." In: Applied Physics Letters 101.22 (2012), p. 221112.

[68] Stephan Krapick, Harald Herrmann, Viktor Quiring, Benjamin Brecht, Hubertus Suche, and Christine Silberhorn. "An efficient integrated two-color source for heralded single photons." In: New Journal of Physics 15.3 (2013), p. 033010.

[69] Marcello Massaro, Evan Meyer-Scott, Nicola Montaut, Harald Herrmann, and Christine Silberhorn. "Improving SPDC single-photon sources via extended heralding and feed-forward control." In: New Journal of Physics 21.5 (2019), p. 053038.

[70] T. Hiemstra, T. F. Parker, P. Humphreys, J. Tiedau, M. Beck, M. Karpiński, B. J. Smith, A. Eckstein, W. S. Kolthammer, and I. A. Walmsley. "Pure single photons from scalable frequency multiplexing." In: Physical Review Applied 14.1 (2020), p. 014052.

[71] Dileep V. Reddy, Robert R. Nerem, Sae Woo Nam, Richard P. Mirin, and Varun B. Verma. "Superconducting nanowire single-photon detectors with 98% system detection efficiency at 1550 nm." In: Optica 7.12 (2020), p. 1649. ISSN: 2334-2536.

[72] Prasana Ravindran, Risheng Cheng, Hong Tang, and Joseph C. Bardin. "Active quenching of superconducting nanowire single photon detectors." In: Optics Express 28.3 (2020), pp. 4099–4114.

[73] Ferenc Bodog, Matyas Mechler, Matyas Koniorczyk, and Peter Adam. “Optimization of multiplexed single-photon sources operated with photon-number-resolving detectors.” In: Physical Review A 102.1 (2020), p. 013513.

[74] Merlin Cooper, Laura J Wright, Christoph Söller, and Brian J. Smith. “Experimental generation of multi-photon Fock states.” In: Optics Express 21.5 (2013), pp. 5309–5317.

[75] Daiqin Su, Casey R. Myers, and Krishna Kumar Sabapathy. “Conversion of Gaussian states to non-Gaussian states using photon-number-resolving detectors.” In: Physical Review A 100.5 (2019), p. 052301.

[76] J. Eli Bourassa, Rafael N. Alexander, Michael Vasmer, Ashlesha Patil, Ilan Tzitrin, Takaya Matsuura, Daiqin Su, Ben Q. Baragiola, Saikat Guha, Guillaume Dauphinais, et al. “Blueprint for a scalable photonic fault-tolerant quantum computer.” In: Quantum 5 (2021), p. 392.

[77] Changchun Zhong, Zhixin Wang, Changling Zou, et al. “Proposal for Heralded Generation and Detection of Entangled Microwave–Optical-Photon Pairs.” In: Physical Review Letters 124 (1 Jan. 2020), p. 010511. DOI: 10.1103/PhysRevLett.124.010511. URL: https://link.aps.org/doi/10.1103/PhysRevLett.124.010511.

[78] S. Sempere-Llagostera, G. S. Thekkadath, R. B. Patel, W. S. Kolthammer, and I. A. Walmsley. “Reducing g(2)(0) of a parametric down-conversion source via photon-number resolution with superconducting nanowire detectors.” In: Opt. Express 30.2 (Jan. 2022), pp. 3138–3147. DOI: 10.1364/OE.450172. URL: http://opg.optica.org/oe/abstract.cfm?URI=oe-30-2-3138.

Chapter 4

PHOTON-NUMBER-RESOLVING SUPERCONDUCTING NANOWIRE ARRAY DETECTORS

This chapter includes the work in preparation for publication:

[1] Samantha I. Davis, Prathwiraj Umesh, Ioana Craiciu, Raju Valivarthi, Boris Korzh, Matthew Shaw, and Maria Spiropulu. "Photon number resolution with superconducting nanowire arrays." In: Manuscript in preparation. (2025).

4.1 Introduction

Photon-number-resolving detectors (PNRDs) are indispensable for a wide range of quantum technologies, including linear-optical quantum computing, quantum key distribution and quantum metrology. Transition-edge sensors (TESs), microwave kinetic-inductance detectors (MKIDs), and superconducting nanowire single-photon detectors (SNSPDs) already deliver high efficiencies and sub-nanosecond timing, yet their intrinsic photon number resolution eventually saturates as incident photon flux increases, limiting dynamic range [1, 2, 3]. Pseudo-PNR schemes based on temporal, spatial or spectral multiplexing circumvent this ceiling by distributing photons over many modes and reading them out with threshold detectors [4, 5]. Parallel advances in nanofabrication now enable dense on-chip integration of hundreds of SNSPD pixels and sophisticated fan-out architectures [6, 7, 8]. There are therefore two types of PNR detection: (1) intrinsic PNR where a single detector is sensitive to the energy difference between one, two, or more photons being absorbed in a short time window, (2) pseudo-PNR, where incoming photons are distributed over multiple spatial or temporal modes before being detected. The two types can be combined, for example by an array of intrinsic-PNRDs, or combining one intrinsic-PNRD with temporal multiplexing. Merging the advances in multiplexing with single-pixel photon number resolution charts a practical route toward the ideal, high-dynamic-range PNRD.

The quantitative behaviour of a PNRD is fully specified by its positive-operator-valued measure (POVM). Closed-form solutions for POVM elements are known for the case of uniform splitting probabilities across an array of click detectors [9], relevant to spatially and temporally mulitplexed pseudo-PNRDs [4, 5]. Uniform-splitting

assumptions, however, break down in large-scale array detectors [10, 11] where spatial-mode weights are inherently non-uniform and pixel-to-pixel efficiencies vary because of optical coupling and fabrication tolerances. A general treatment requires a multinomial expansion over all detector outcomes whose term count grows exponentially with array size, rendering brute-force evaluation intractable for state-of-the-art devices. No analytic solution has yet been reported for this non-uniform regime. More broadly, a model for the POVM elements of detector arrays with arbitrary POVMs is needed to support the development of scalable architectures composed of photon-number-resolving detectors.

Here we close this gap by developing a generalized theoretical framework for POVM modeling of realistic PNR detector arrays. First we present a model for an array of detectors with arbitrary POVMs and splitting topologies. We find a closed-form solution for case of click detectors and non-uniform splitting probabilities, and present an iterative method for efficiently constructing the POVM of an array detector from known detector POVMs and splitting probabilities. Next, we validate the model by experimentally reconstructing the POVMs of two detector configurations: (1) a pseudo-PNR array of threshold detectors with heterogeneous splitting probabilities–an architecture exemplified by recent developments in SNSPD detector arrays [10, 11], and (2) an array of six intrinsic-PNRDs. We perform experimental detector tomography of (1) the PEACOQ detector from Ref. [10] and (2) a spatially-mutliplexed array of six PNR SNSPDs to demonstrate configurations 1 and 2, respectively. These two experimental demonstrations showcase our modeling framework as a practical toolset for designing and optimizing next-generation PNR arrays, which will advance the broader quest for detectors that approach the ideal photon-number-resolving limit.

4.2 Generalized POVM model for array detectors

In quantum optics, the measurement statistics of a single-photon detector are fully characterized by a set of positive operator value measure (POVM) elements $\{\hat{\pi}_n\}$, where each $\hat{\pi}_m$ is a positive semi-definite operator associated with the outcome m. For an input state ρ, the probability of observing outcome m is given by,

$$p_m = \mathrm{Tr}[\rho\hat{\pi}_m]. \tag{4.1}$$

The POVM elements can be expanded in a complete basis over any Hilbert space. Relevant to photon-number-resolving detection, under the assumption that the detector is insensitive to the phase of the input light, the POVM elements can be

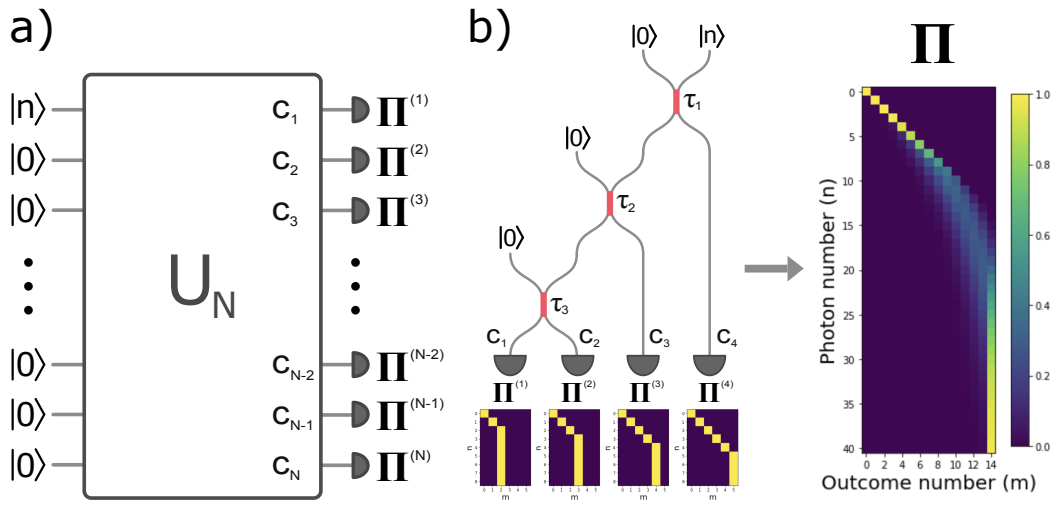

Figure 4.1: Setup for theoretical modeling. a) An n-photon number state, $|n\rangle$, is injected into the first input port of a $2N$-port beamsplitter, described by the unitary operator U_N. The n photons are distributed across a set of N detectors, where c_k is the splitting amplitude for the kth output port and $\mathbf{\Pi}^{(k)}$ is the conditional probability matrix of the kth detector. b) Conceptual illustration of POVM construction from an array of detectors with different photon number resolving capabilities. $\mathbf{\Pi}^{(n)}$ is the conditional probability matrix for the nth detector $\mathbf{\Pi}$ is the conditional probability matrix for the overall array of multiplexed detectors.

expressed in the photon number basis as,

$$\hat{\pi}_m = \sum_{n=0}^{\infty} P(m|n)\,|n\rangle\langle n| = \sum_{n=0}^{\infty} \mathbf{\Pi}_{m,n}\,|n\rangle\langle n|\,, \tag{4.2}$$

where $P(m|n)$ is the conditional probability that the detector outputs outcome m given n input photons and $|n\rangle$ is the photon number state of n photons. In this notation, the POVM of a detector can be completely summarized by the conditional probability matrix $\hat{\Pi}$, with matrix elements $\mathbf{\Pi}_{m,n} = P(m|n)$. For an ideal photon-number-resolving detector, the POVM elements are $\{\hat{\pi}_n = |n\rangle\langle n|\}$ and the conditional probability matrix is the identity matrix, $\mathbf{\Pi}_{mn} = \delta_{mn}$. In practice, the photon number resolution of a realistic detector saturates, with photon resolution demonstrated up to 15 photons at 1550 nm with single TES detector [12], resulting in a truncated number of measurement outcomes. In turn, this limits the dynamic range of a detector up to the photon number saturation.

Multiplexing is a common approach to overcoming photon number saturation, whereby n photons are distributed over a set of spatial [9], temporal [4, 5], or

spectral modes such that a smaller number of photons are incident to the detector at each mode. The splitting operation can be modeled using linear optics as a $2N$-port beamsplitter with an associated unitary operator U_N, where N is the number of input and output modes (see Fig. 4.1a). A photon number state $|n\rangle$ inserted into one of the input modes, with all others in the vacuum state. The photons are distributed to a set of N detectors, one at each output mode, where c_k represents the probability of a single photon arriving to output mode $k \in \{1, ..., N\}$ ("splitting probability"). Each detector has a set of POVM elements $\{\hat{\pi}_n^{(k)}\}$, where the POVM elements of the detector at output mode k are described by the conditional probability matrix $\mathbf{\Pi}^{(k)}$. The measurement outcomes of the multiplexed detector are found by summing the measurement outcomes of each detector. Let $\mathbf{\Pi}$ denote the conditional probability matrix of the multiplexed detector. The matrix element $\mathbf{\Pi}_{mn}$ corresponding to the mth measurement outcome given n input photons is,

$$\mathbf{\Pi}_{mn} = \sum_{\{\sum_k m_k = m\}} \sum_{\{\sum_k j_k = n\}} \frac{n!}{j_1! \cdots j_N!} c_1^{j_1} \cdots c_N^{j_N} \mathbf{\Pi}^{(1)}_{m_1 j_1} \cdots \mathbf{\Pi}^{(N)}_{m_N j_N}, \tag{4.3}$$

where the right hand side calculated as a multinomial expansion over the splitting probabilities $(c_1, ..., c_N)$, and individual detector matrices $(\mathbf{\Pi}^1, ..., \mathbf{\Pi}^N)$. In Eq. 4.3, the inner sum accounts for all possible ways n photons can be distributed over the N detectors, denoted as $\{\sum_k j_k = n\}$, where j_k is the number of photons incident to the kth detector. The outer sum accounts for each set of coincident photon number outcomes that sums to the measurement outcome m, denoted as $\{\sum_k m_k = m\}$, where m_k is the measured photon number by the kth detector.

Click detector arrays

For the case of click detection at each output, in which each detector can resolve either zero or at least one photon, the conditional probability matrix of the kth detector is given by,

$$\mathbf{\Pi}^{(k)} = \begin{pmatrix} 1 & 0 & \cdots & 0 \\ 0 & 1 & \cdots & 1 \end{pmatrix}, \tag{4.4}$$

where the first row corresponds to the detection of the vacuum state and the second row corresponds to the detection of at least one photon, interpreted as the measurement outcome of zero photons ($m_k = 0$) and one photon ($m_k = 1$), respectively.

In this case, Eq. 4.3 simplifies to [3],

$$\mathbf{\Pi}_{mn} = \sum_{\{\sum_k j_k = n\}}^{(m)} \frac{n!}{j_1! \cdots j_N!} c_1^{j_1} \cdots c_N^{j_N}, \tag{4.5}$$

where (m) denotes the condition that exactly m of $(j_1, ..., j_N)$ are nonzero. The number of terms in the sum of Eq. 4.5 scales polynomially in m and exponentially in n, which becomes computationally intractable for large n. To compute $\mathbf{\Pi}_{nm}$, a closed-form solution is desirable.

We obtain a closed-form expression by finding a recursion equation satisfied by the matrix elements in Eq. 4.5. Let $P(n, \vec{c}^{(m)})$ be the probability that n photons arrive to a subset of m wires, where $\vec{c}^{(m)}$ is the vector of probabilities for those m wires; there are $\binom{N}{m}$ such vectors, each of size m. We can rewrite $\mathbf{\Pi}_{m,n}$ as

$$\mathbf{\Pi}_{m,n} = \sum_{\vec{c}^{(m)}} P(n, \vec{c}^{(m)}) \tag{4.6}$$

where the sum is over all possible $\vec{c}^{(m)}$, i.e. over all possible subsets of m wires.

For a given subset of m wires, $P(n, \vec{c}^{(m)})$ obeys the recursion relation,

$$P(n, \vec{c}^{(m)}) = P(n-1, \vec{c}^{(m)}) \left(\sum_{k=1}^{m} \vec{c}_k^{(m)} \right) + \sum_{k=1}^{m} P(n-1, \vec{c}^{(m-1)}[k]) \vec{c}_k^{(m)} \tag{4.7}$$

where $\vec{c}_k^{(m)}$ is the kth element of $\vec{c}_k^{(m)}$ and $\vec{c}^{(m-1)}[k]$ is the subvector of $\vec{c}^{(m)}$ that excludes the element $\vec{c}_k^{(m)}$. The right hand side (RHS) accounts for the two cases of the nth photon arriving to the m wires: (1) the first term is the probability that the nth photon goes to one of the m wires given that $n-1$ photons already arrived to the m wires; (2) the second term is the probability the nth photon arrives to the kth wire given that $n-1$ photons already arrived to the other $m-1$ wires, summed over all $k = 1$ to $k = m$ wires.

The solution to the recursion relation yields (see Methods),

$$\mathbf{\Pi}_{m,n} = \binom{N}{m} \sum_{i=0}^{m} (-1)^i \frac{\binom{m}{i}}{\binom{N}{m-i}} \sum_{\vec{c}^{(m-i)}} \left(\sum_{k=1}^{m-i} \vec{c}_k^{(m-i)} \right)^n \tag{4.8}$$

where $\vec{c}^{(m-i)}$ is the vector of probabilities formed by removing a subset of i elements from $\vec{c}^{(m)}$; there are $\binom{N}{m-i}$ such vectors. The second sum in Eq. 4.8 is over all possible choices of $\vec{c}^{(m-i)}$. With Eq. 4.8, the number of terms is independent of n, providing an exponential improvement for large n in the computation of $\mathbf{\Pi}_{m,n}$ over the brute force computation using Eq. 4.5.

Without assumptions in the splitting probabilities, Eq. 4.8 is the most general closed-form solution for calculating the POVM elements of multiplexed threshold detector arrays. The scaling in N and m can be further improved leveraging symmetries in

$\vec{c}$. In the case of uniform splitting probabilities ($c_j = 1/N$ for $j = 1, ..., N$), Eq. 4.8 simplifies to the commonly used expression [9],

$$\mathbf{\Pi}_{mn} = \frac{m!}{N^n}\binom{N}{m} S(n, m), \quad N \geq n \geq m, \tag{4.9}$$

where $S(n, m) = \frac{1}{m!}\sum_{i=0}^{m}(-1)^i\binom{m}{i}(m-i)^n$ is the Stirling number of the second kind, that is, the number of ways of partitioning a set of n elements into exactly m non-empty subsets.

Detector arrays with arbitrary POVMs: iterative construction

Next, we consider the general case of Eq. 4.3 for an array of detectors with arbitrary POVMs. For the simplest case of two detectors with splitting probabilities $\vec{c} = (c_1, c_2)$, which corresponds to a 2-port beamsplitter with transmittance τ where $c_1 = |\tau|^2$ and $c_2 = 1 - |\tau|^2$, the conditional probability matrix is,

$$\mathbf{\Pi}_{mn} = \sum_{i=0}^{m}\sum_{j=0}^{n}\binom{n}{j}(c_1)^j(c_2)^{n-j}\mathbf{\Pi}^{(1)}_{i,j}\mathbf{\Pi}^{(2)}_{m-i,n-j}, \tag{4.10}$$

where $\mathbf{\Pi}^{(k)}$ and $\mathbf{\Pi}^{(2)}$ are the conditional probability matrices of detectors 1 and 2, respectively.

The $\mathbf{\Pi}$ matrix of an array of N detectors can be iteratively constructed by pairing subsets of detectors using Eq. 4.10. The N splitting probabilities $\vec{c} = (c_1, c_2, ...c_n)$ can be mapped to a $2N$-port beamsplitter comprised of $N - 1$ beamsplitters with transmittances $\vec{\tau} = (\tau_1, \tau_2, ...\tau_{N-1})$ (see Methods). The iterative construction is illustrated in Fig. 4.1b for an array of four detectors. The heat maps for the conditional probability matrices $\mathbf{\Pi}^{(k)}$ where $k = 1, \cdots, 4$ of the four detectors, which have ideal photon number resolution up to 2, 3, 4 and 5 photons for detectors 1, 2, 3, and 4, respectively. The heat map for the conditional probability matrix $\mathbf{\Pi}$ of the four-detector array is shown on the right for uniform splitting probabilities $\vec{c} = (1/4, 1/4, 1/4, 1/4)$, corresponding to $\vec{\tau} = (1/2, 1/\sqrt{3}, 1/\sqrt{2})$, demonstrating the improvement in photon number resolution with spatial multiplexing.

With this iterative method, given predetermined $\mathbf{\Pi}$ matrices of the detectors in the array, the number of terms to compute is linear in n and m. By leveraging the recursive structure of arrays, this approach is significantly more efficient than brute-force computation with Eq. 4.3 (see Methods).

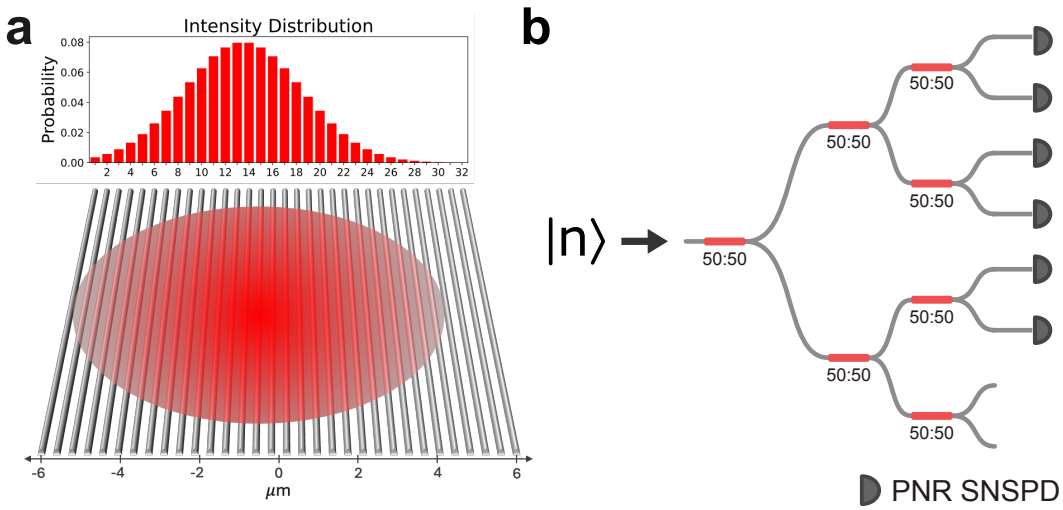

Figure 4.2: Array detector configurations for experimental detector tomography. a) Illustration of PEACOQ detector with the experimental Gaussian spatial mode of 1550 nm light coupled to 32 parallel nanowires. b) Illustration of splitting configuration for the spatially multiplexed array of six PNR SNSPDs.

4.3 Experimental detector tomography

We compare the models against experimentally reconstructed POVMs of two detector array configurations: (1) nonuniform spatial distribution across an array of 32 detectors, each without intrinsic PNR capability, and (2) uniform splitting distribution across array of six detectors, each with intrinsic PNR capability. For configuration 1, we use the PEACOQ detector, which is an array of 32 superconducting nanowires coupled to a single-mode SMF-28 telecommunications wavelength optical fiber [10]. The gaussian mode of the optical fiber is distributed across the linear array of nanowires (Fig. 4.2a), which enables pseudo-PNR through multiplexing, as well as faster photon counting than is possible with a single nanowire. For configuration 2, we use an array of six PNR SNSPDs, where input photons distributed uniformly across a optical fiber beamsplitter network (Fig. 4.2b).

To reconstruct the POVMs of the two detector configurations, we perform experimental detector tomography using the approach in Ref. [13]. For each configuration, counting statistics are acquired for various mean photon numbers of input coherent light pulses. The measured counting statistics can be related to the conditional probability matrix by expressing Eq. 4.1 as,

$$\mathbf{P} = \mathbf{F\Pi}, \tag{4.11}$$

where $\mathbf{P}$ is a $D \times N$ matrix containing the measured probabilities for N detector

outcomes over D probe states, $\mathbf{F}$ is $D \times M$ matrix that contains the photon number distributions of the D input states, each truncated at a maximum Hilbert space dimension M, and $\mathbf{\Pi}$ is the $M \times N$ conditional probability matrix of the detector, corresponding to the POVM elements in Eq. 4.2 with the sum truncated at $M - 1$. Each row of $\mathbf{P}$ corresponds to a histogram of the measurement outcome frequency for each mean photon number. For coherent states, each row of $\mathbf{F}$ is the computed Poisson distribution for each mean photon number. From known $\mathbf{P}$ and $\mathbf{F}$, $\mathbf{\Pi}$ is determined from matrix inversion with a CVXPY-based python module [13] using the code from [14].

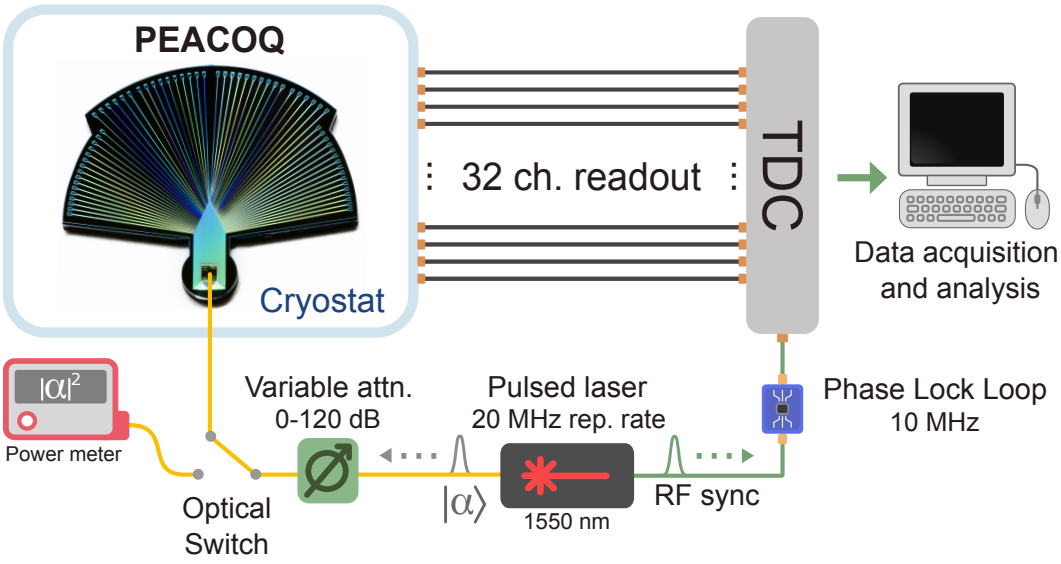

Figure 4.3: Experimental setup for tomography of the PEACOQ detector (pictured).

PEACOQ Detector

The experimental setup for tomography of the PEACOQ detector is shown in Fig. 4.3. The PEACOQ was measured in 0.9 K cryostat, in a modified version of Setup A as described in Ref. [10]. Figure 4.3 shows a schematic of the experimental setup. The ceramic ferrule of the optical fiber coupler was in direct contact with the detector chip. Each of the 32 channels is individually biased and read out. Three stages of amplifications, two of which were inside the cryostat at 40 K were used to amplify the pulses corresponding to photon detections. The pulses were then converted to time stamps using a custom 128-channel time-to-digital converter (TDC). The source of optical coherent states was a 1550 nm pulsed laser with a repetition rate of 20 MHz. Pulses from the laser passed through a variable attenuator, a polarization controller, and a switch before entering the cryostat. The switch sent

light to either the PEACOQ or a power meter, which was used to measure the mean photon number. The sync signal of the pulsed laser was converted to a 10 MHz signal using a phase-locked loop then sent to the TDC for synchronization.

Counting statistics are acquired at twelve attenuation settings corresponding to mean photon numbers ranging from $\mu = 0.4$ to 82. For each mean photon number, the time tags from each detector are accumulated over a duration of $\leq$ 1s, depending on the count rate. The time tags are binned to obtain the number of coincident clicks out the 32 detectors per pulse. The counting probabilities are constructed from the histogram of the number of the binned time tags, which is normalized to one and forms a row of the $\mathbf{P}$ matrix. Each row of the $\mathbf{F}$ matrix calculated from the Poisson distribution,

$$p_n(\mu) = \frac{\mu^n}{n} e^{-n}, \tag{4.12}$$

where n is truncated at $n = 124$ to fully capture the statistics for all probe states. The reconstructed $\mathbf{\Pi}$ is depicted in Fig. 4.4a up to $m = 25$ and $n = 50$.

We model the $\mathbf{\Pi}$ matrix using the iterative method, where each detector is assumed to be click detector with $\mathbf{\Pi}^{(k)}$ described by Eq. 4.4 for $k = 1$ to 32. The splitting probabilities $(c_1, ..., c_N)$ are obtained from the normalized intensity distribution depicted in Fig. 4.2a. To account for the detection efficiency of $\eta = 0.78$, a Bernoulli transformation is applied to the total $\mathbf{\Pi}$ matrix,

$$\mathbf{\Pi}^{(\eta)}_{mn} = \sum_{j=0}^{n} \mathbf{\Pi}_{mj} \binom{n}{j} \eta^j \, (1-\eta)^{n-j} \, . \tag{4.13}$$

The theoretical $\mathbf{\Pi}$ is depicted in Fig. 4.4b. The columns of the reconstructed and theoretical $\mathbf{\Pi}$ matrices are plotted in Fig. 4.4c and d, respectively. Despite discrepancies likely introduced by smoothing artifacts in the matrix inversion, both the reconstructed and modeled $\mathbf{\Pi}$ matrices reproduce the experimental counting probabilities (Fig. 4.4e). The predicted counting probabilities, calculated as $\mathbf{P} = \mathbf{F} \cdot \mathbf{\Pi}$ for the reconstructed and theoretical $\mathbf{\Pi}$ matrices are plotted in Figs. 4.4f and g, respectively. The solid curves are calculated from the Poisson distribution for each mean photon number, corresponding to counting probabilities measured with an ideal PNRD.

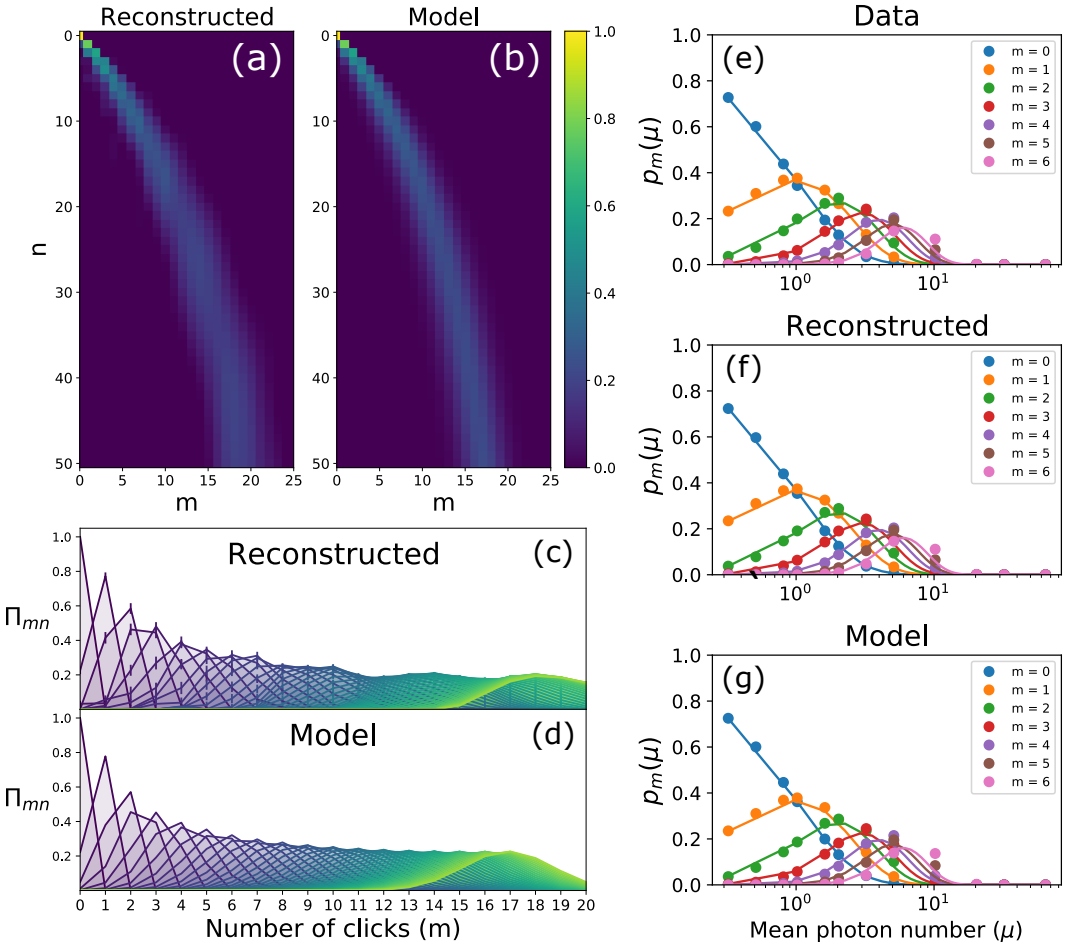

Figure 4.4: Heatmaps of a) reconstructed and b) theoretical $\mathbf{\Pi}$ matrices for the PEACOQ detector. The c) reconstructed and d) theoretical matrix elements $\mathbf{\Pi}_{\mathrm{m,n}}$ are plotted as a function of the measurement outcome $m = 0, \cdots, 32$ for $n = 0, \cdots, 50$. Each curve corresponds to a column of $\mathbf{\Pi}$. (e) Measured count probabilities $p_m(m)$ as a function of the mean photon number μ, for the first seven measurement outcomes $m = 0$ to 7. Reconstructed (f) and modeled (g) count probabilities as function of μ, calculated from the corresponding $\mathbf{\Pi}$ matrices. In (e)-(g), the detection efficiency is absorbed into the mean photon numbers.

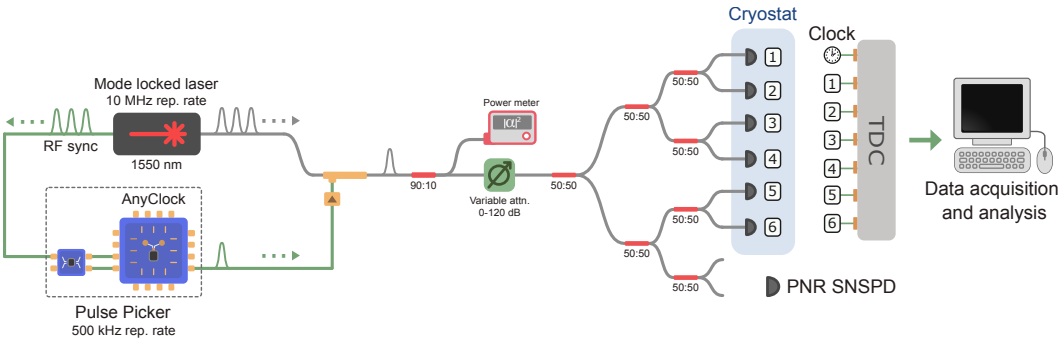

Figure 4.5: Experimental setup for detector tomography of spatially multiplexed PNR SNSPDs with uniform splitting distribution.

Spatially multiplexed PNR SNSPDs

The experimental setup for reconstruction of the POVM for an array of six PNR SNSPDs is shown in Fig. 4.5. We employ a mode-locked laser (Calmar) operating at a wavelength of 1550 nm with a repetition rate of 10 MHz. The emitted optical pulses have a temporal width of less than 2 ps and are directed to a high-extinction-ratio intensity modulator (extinction ratio > 40 dB). Simultaneously, the RF synchronization output from the laser is routed to a pulse picker module based on the Anyclock system (Skyworks, Si5344), which generates a 500 kHz RF signal. This output is passed through a digital delay generator (Stanford Research Systems, DG648) for precise temporal alignment with the optical pulse train. The delayed RF signal is amplified and used to drive the intensity modulator, selecting one out of every twenty optical pulses and reducing the repetition rate to 500 kHz. This downsampling avoids detector saturation and suppresses time-walk distortions in the SNSPD outputs at high count rates [15]. The modulator is carefully tuned to maximize extinction and minimize leakage from unpicked pulses. The modulated optical pulse train is passed through a 90:10 fiber splitter. The 90% output is used for optical power monitoring and serves as a clock reference for the time tagger. The remaining 10% is attenuated using variable optical attenuators (Yokogawa) and distributed to six superconducting nanowire single-photon detectors (SNSPDs) via a cascade of fiber beam splitters. Polarization controllers are placed before each detector to ensure optimal polarization alignment and coupling efficiency. The detectors, based on niobium nitride (NbN) nanowires, are housed in a Photonspot cryostat operating below 0.8 K. Detection signals are recorded using a Swabian Instruments Time Tagger X operated in standard mode for high-resolution time-correlated single-photon counting.

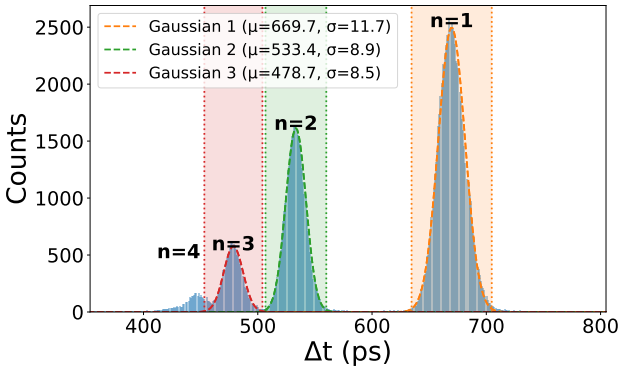

Figure 4.6: Histogram of time-tags accumulated over 10s for a mean photon number of ≈ 7 relative to the clock for the detector in channel 6. The windows for labeling time-tags with photon number are shown.

To reconstruct the POVMs of the individual detectors and the multiplexed detector array, time-tags are accumulated for a range of mean photon numbers of the input coherent light pulses. When multiple photons are incident on a single nanowire, multiple resistive hotspots are generated, which vary the amplitude and slew rate of the resulting RF output pulse. With a constant-threshold time-tagger, variations in slew rate translate into shifts in the registered time-tags [16]. This effect produces temporally distinguishable time-tag distributions for different numbers of incident photons. The histogram of time-tags accumulated over ten seconds is shown in Fig. 4.6 for one of the detectors, which can resolve up to four photons. The time-tags are assigned a photon number depending on the arrival time. To extract the range of arrival times associated with each photon number outcome, a Gaussian fit is performed on the first three time tag distributions, corresponding to $m = 1, 2$ and 3 photons. The arrival time windows for $m = 1, 2$ and 3 are extracted from $\pm 3\sigma$ from the mean of each distribution, depicted as the shaded regions in Fig. 4.6. Arrival times less than the -3σ of the $m = 3$ distribution are assigned $m = 4$. This procedure is performed for each detector in the array, with the windows for each detector held fixed across all measurements. For the multiplexed array of six detectors, each coincident event is assigned a total photon number equal to the sum of the individual photon numbers assigned to the time-tags registered by each detector.

The reconstructed $\mathbf{\Pi}^{(k)}$ for each detector ($k = 1, \cdots, 6$) are plotted in Fig. 4.7a-f. To isolate the PNR capability from the effects of optical loss, the detection efficiency is absorbed into the mean photon number for each detector. The reconstructed

and modeled $\mathbf{\Pi}$ for the detector array are plotted in Fig. 4.7g and h, respectively. For the model, we construct $\mathbf{\Pi}$ with the iterative procedure of Sec. 4.2 using the reconstructed $\mathbf{\Pi}^{(k)}$ of six detectors, assuming uniform splitting probabilities. The matrix elements for the reconstructed and modeled $\mathbf{\Pi}$ are compared for $n = 0, \cdots, 20$ in Figs. 4.7i-j. The counting probabilities from the reconstructed (Fig. 4.7l) and modeled (Fig. 4.7m) $\mathbf{\Pi}$ matrices reproduce the measured counting probabilities (Fig. 4.7k) for all mean photon numbers. The solid curves are calculated from Poisson statistics, corresponding to that measured with an ideal PNRD.

4.4 Discussion

We have developed a generalized theoretical framework for modeling POVMs of array detectors. We presented a model for $\mathbf{\Pi}$ (Eq. 4.3) that accommodates detectors with arbitrary POVM elements and arbitrary splitting probabilities across the array. We analyzed the computational complexity of computing $\mathbf{\Pi}_{mn}$ in various cases. For the case of click detectors, we found a closed-form solution for $\mathbf{\Pi}_{mn}$ that provides an exponential speedup over the multinomial representation. We then find an efficient construction of $\mathbf{\Pi}$ for a given set of detector POVMs and splitting probabilities. We take an iterative approach where individual POVMs are fused in pairs, taking advantage of the recursive structure of arrays. This allows us to model the POVMs of (1) the PEACOQ detector and (2) a spatially multiplexed array of PNR SNSPDs, corresponding to the cases of (1) 32 click detectors with Gaussian splitting probabilities and (2) six PNRDs with distinct POVMs and uniform splitting probabilities, respectively. We validate the models by perform experimental detector tomography of the PEACOQ detector and the multiplexed array of PNR SNSPDs, which demonstrate near ideal PNRD response for mean photon numbers up to $\mu \sim 10$ (see Methods). This work supports the development of PNRD arrays towards the goal of practical and near-ideal photon number discrimination for diverse photon counting applications.

4.5 Methods

Derivation of closed-form solution

Here we generalize the derivation for the 2N-port beamsplitter model of Paul et al. [9] to find a closed-form expression for $\mathbf{\Pi}^{m,n}$ for non-uniform distribution of photons across the output ports, with probabilities $\vec{c} = (c_1, c_2, ..., c_N)$. The $2N$-port beamsplitter has corresponding unitary U_N, which can be decomposed into 2×2 beamsplitters [17] for a given set of splitting probabilities. The $2N$-port beamsplitter

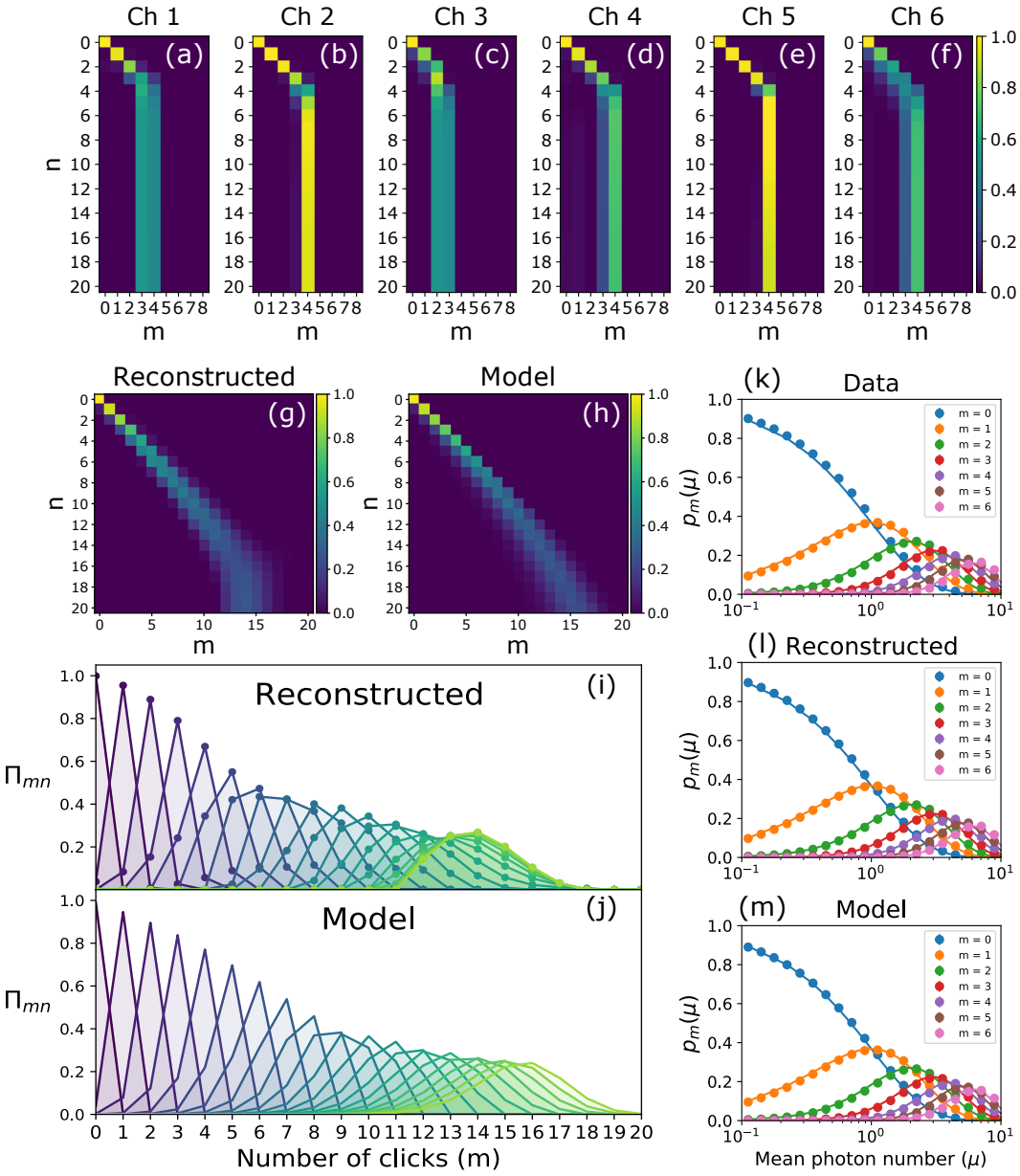

Figure 4.7: Heatmaps of reconstructed and theoretical $\mathbf{\Pi}$ matrices for the spatially multiplexed PNR SNSPDs configuration. (a)-(f) Heatmaps of reconstructed $\mathbf{\Pi}$ matrices for the Ch 1-6 detectors. Heatmaps of (g) reconstructed and (h) model $\mathbf{\Pi}$ matrices for the multiplexed array of Ch 1-6 detectors. Matrix elements for (i) reconstructed and (j) model $\mathbf{\Pi}$ matrices for the multiplexed array of Ch 1-6 detectors, where the curves ($n = 0 \cdots 20$) correspond to each column of $\mathbf{\Pi}$. (k) Measured count probabilities $p_m(m)$ as a function of the mean photon number μ, for the first seven measurement outcomes $m = 0$ to 7. Reconstructed (l) and modeled (m) count probabilities as function of μ, calculated from the corresponding $\mathbf{\Pi}$ matrices.

has the effect of sending a single photon at the first port into a superposition over the N output ports (see Fig. 4.1a),

$$\hat{a}_1^\dagger \xrightarrow{U_N} \sum_{i=1}^{N} \lambda_i \hat{b}_i^\dagger, \tag{4.14}$$

where λ_i is the amplitude for port i, $|\lambda_i|^2 = c_i$ is the probability that the photon is measured at port i, and $\sum_{i=1}^{N} c_i = 1$. Consider n photons incident to the first input port of the $2N$-port beamsplitter,

$$|n\rangle_1 |0\rangle_2 \cdots |0\rangle_N = \frac{1}{\sqrt{n!}} (\hat{a}_1^\dagger)^n |0\rangle \xrightarrow{U_N} \frac{1}{\sqrt{n!}} \left(\sum_{i=1}^{N} \lambda_i \hat{b}_i^\dagger \right)^n |0\rangle . \tag{4.15}$$

Applying the multinomial theorem, the RHS can be expanded as,

$$\left(\sum_{i=1}^{N} \lambda_i \hat{b}_i^\dagger \right)^n |0\rangle = \sum_{\sum j_i = n} \sqrt{\frac{n!}{j_1! \cdots j_N!}} (\lambda_1)^{j_1} \cdots (\lambda_N)^{j_N} |j_1\rangle \cdots |j_N\rangle , \tag{4.16}$$

where the sum is over all possible ways n photons can be distributed over the N wires.

Therefore, the probability of distributing n photons into j_1 photons at wire 1, j_2 photons at wire 2, ..., j_N photons at wire N is,

$$P_n(j_1, \cdots, j_N) = \frac{n!}{j_1! \dots j_N!} c_1^{j_1} \dots c_N^{j_N}, \tag{4.17}$$

where the probability of “on" outcomes on m wires is the sum of $P_n(j_1, \cdots, j_N)$ over m nonzero j's is,

$$\mathbf{\Pi}_{m,n} = \sum_{\sum j_i = n}^{(m)} P_n(j_1, \cdots, j_N) = \sum_{\sum j_i = n}^{(m)} \frac{n!}{j_1! j_2! \dots j_N!} c_1^{j_1} \dots c_N^{j_N}. \tag{4.18}$$

For the recursion relation in Eq. 4.7, the solution can be expressed in the more familiar form,

$$P(n, \mathbf{p}^{(m)}) = \sum_{i=0}^{m} (-1)^i \sum_{\mathbf{p}^{(m,i)}} \left(\sum_k p_k^{(m)} - \sum_k p_k^{(m,i)} \right)^n , \tag{4.19}$$

where $\mathbf{p}^{(m,i)}$ is the vector formed by taking a subset of i elements in $\mathbf{p}^{(m)}$; there are $\binom{m}{i}$ such vectors. The second sum in Eq. 4.19 is over all possible choices of $\mathbf{p}^{(m,i)}$.

In this form, it is clear that for $\mathbf{\Pi}_{m,n} = \sum_{\vec{c}^{(m)}} P(n, \vec{c}^{(m)})$ for the case of uniform splitting probabilities with $\vec{c}_k^{(m-i)} = 1/N$, Eq. 4.19 simplifies to expression from Ref. [9],

$$\mathbf{\Pi}_{mn} = \frac{1}{N^n}\binom{N}{m}\sum_{i=0}^{m}(-1)^i\binom{m}{i}(m-i)^n. \tag{4.20}$$

Plugging Eq. 4.19 into Eq. 4.6,

$$\mathbf{\Pi}_{mn} = \sum_{\mathbf{p}^{(m)}} P(n, \mathbf{p}^{(m)}) = \sum_{\mathbf{p}^{(m)}}\sum_{i=0}^{m}(-1)^i \sum_{\mathbf{p}^{(m,i)}}\left(\sum_k p_k^{(m)} - \sum_k p_k^{(m,i)}\right)^n \tag{4.21}$$

$$= \sum_{i=0}^{m}(-1)^i \sum_{\mathbf{p}^{(m)}}\sum_{\mathbf{p}^{(m,m-i)}}\left(\sum_k p_k^{(m,m-i)}\right)^n. \tag{4.22}$$

We can further simplify the solution. Two of the sums can be combined due to redundancy,

$$\sum_{\mathbf{p}^{(m)}}\sum_{\mathbf{p}^{(m,m-i)}}\left(\sum_k p_k^{(m,m-i)}\right)^n = \frac{\binom{N}{m}\binom{m}{i}}{\binom{N}{m-i}}\sum_{\mathbf{p}^{(m-i)}}\left(\sum_k p_k^{(m-i)}\right)^n. \tag{4.23}$$

yielding the expression in Eq. 4.8,

$$\mathbf{\Pi}_{mn} = \binom{N}{m}\sum_{i=0}^{m}(-1)^i\frac{\binom{m}{i}}{\binom{N}{m-i}}\sum_{\mathbf{p}^{(m-i)}}\left(\sum_k p_k^{(m-i)}\right)^n.$$

Iterative construction of the POVM elements

For an array of N detectors, each with a set of POVM elements, which are described the matrix $\mathbf{\Pi}^{(j)}$ for the jth detector, the splitting probabilities $(c_1, \cdots, c_N)$ can be mapped to transmittances of a $2N$-port beamsplitter (see Fig. 4.8) as,

$$\hat{a}_{\text{in}} \xrightarrow{U_N} \tau_1\hat{a}_1 + r_1\tau_2\hat{a}_2 + ... + (r_1\cdots r_{N-1}\tau_{N-1})\hat{a}_{N-1} + (r_1\cdots r_{N-1})\hat{a}_N, \tag{4.24}$$

where $|r_n|^2 = 1 - |\tau_n|^2$ for $n \in [1, N-1]$. The splitting probabilities are related to the transmittances as,

$$c_n = \begin{cases} |r_1|^2\cdots|r_{N-1}|^2, & \text{for } n = 1, \\ |\tau_n|^2(|r_1|^2\cdots|r_{n-1}|^2), & \text{for } 1 < n < N, \\ |\tau_1|^2, & \text{for } n = N, \end{cases} \tag{4.25}$$

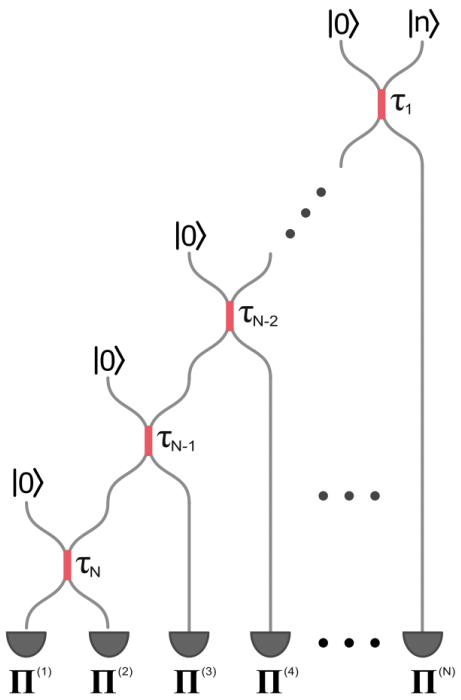

Figure 4.8: Setup for the iterative construction of the POVM elements for an array of N detectors.

satisfying $\sum_{j=1}^{N} c_j = 1$. Therefore, given a set of a splitting probabilities $\vec{c} = (c_1, ..., c_N)$, the transmittances (neglecting phase) can be computed recursively as,

$$|\tau_1|^2 = c_N, \qquad |\tau_n|^2 = \frac{c_{N-(n-1)}}{(1-|\tau_1|^2)\cdots(1-|\tau_{n-1}|^2)} \quad \text{for } 1 < n < N. \tag{4.26}$$

After computing the transmittances, the conditional probability matrix elements can be computed recursively using Eq. 4.10 as,

$$\mathbf{\Pi}^{(1,2)}_{m,n} = \sum_{i=0}^{m}\sum_{j=0}^{n}\binom{n}{j}(|\tau_N|^2)^j(1-|\tau_N|^2)^{n-j}\mathbf{\Pi}^{(1)}_{i,j}\mathbf{\Pi}^{(2)}_{m-i,n-j}, \tag{4.27}$$

$$\mathbf{\Pi}^{(1,2,3)}_{m,n} = \sum_{i=0}^{m}\sum_{j=0}^{n}\binom{n}{j}(|\tau_{N-1}|^2)^j(1-|\tau_{N-1}|^2)^{n-j}\mathbf{\Pi}^{(1,2)}_{i,j}\mathbf{\Pi}^{(3)}_{m-i,n-j}, \tag{4.28}$$

$$\vdots \tag{4.29}$$

$$\mathbf{\Pi}^{(1,\cdots,N)}_{m,n} = \sum_{i=0}^{m}\sum_{j=0}^{n}\binom{n}{j}(|\tau_1|^2)^j(1-|\tau_1|^2)^{n-j}\mathbf{\Pi}^{(1,\cdots,N-1)}_{i,j}\mathbf{\Pi}^{(N)}_{m-i,n-j}, \tag{4.30}$$

where $\mathbf{\Pi}^{(1,\cdots,k)}$ is the conditional probability matrix for an array comprised of detector 1 through k, where $k \in 1, \cdots, N$, and $\mathbf{\Pi} = \mathbf{\Pi}^{(1,\cdots,N)}$ is the conditional probability matrix of the entire array of N detectors.

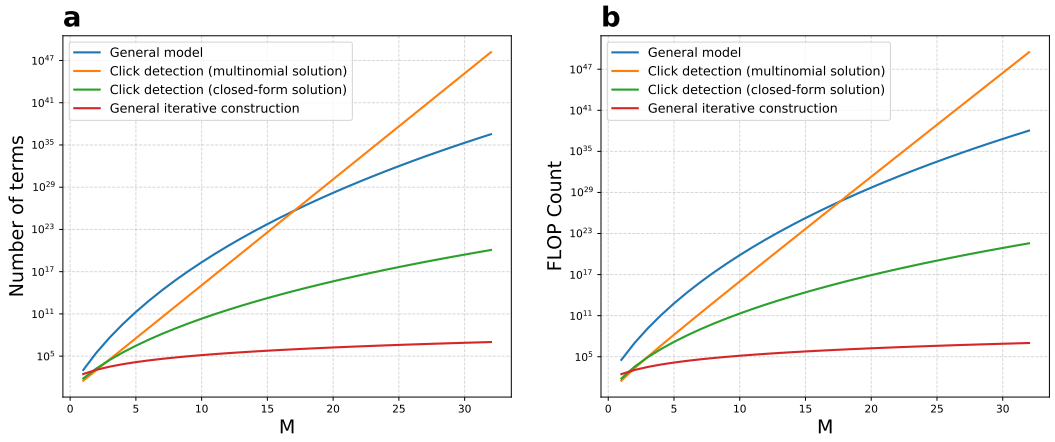

Figure 4.9: Computational complexity as a function of conditional probability matrix ($\mathbf{\Pi}$) size. a) Number of terms to calculate and b) estimated number of FLOP counts for the general model (Eq. 4.3), the multinomial solution for the click detection model (Eq. 4.5), the closed-form solution for the click detection model (Eq. 4.8), and the generalized iterative construction for computing a conditional probability matrix $\mathbf{\Pi}$ of dimensions $M \times M$.

Computational complexity

The number of terms in each expression directly affects the computational complexity of evaluating $\mathbf{\Pi}$, since each term corresponds to a unique combination of photon distributions and detector responses that must be explicitly computed. In the computation of $\mathbf{\Pi}_{mn}$, each term incurs a number of floating-point operations (FLOPs), such as exponentiations, multiplications, and factorial evaluations, where the total FLOP count is a proxy for runtime. The total FLOP count is a widely used metric for estimating algorithmic efficiency, particularly in numerical linear algebra and scientific computing, where it serves as a hardware-agnostic measure of computational cost [18]. The number of terms and estimated FLOP count for Eq. 4.3, Eq. 4.5, Eq. 4.8, and the iterative method are summarized in Table 4.1. For each equation, the number of terms and estimated FLOP counts for computing a $\mathbf{\Pi}$ matrix of size $M \times M$ are plotted in Fig. 4.9 as a function of M for an array size of $N = 32$. The general model Eq. 4.3 and multinomial expression Eq. 4.5 quickly become intractable even for models values of $M \geq 10$. The closed-form solution in Eq. 4.8 provides a improvement for the click detection case with roughly polynomial scaling in M, but still becomes intractable for modest values of M. The iterative method is the most efficient, with scaling $O(M^2)$.

Method	Term count	FLOPs per term	Total FLOPs
General model (Eq. 4.3)	$\binom{m+N-1}{N-1}\binom{n+N-1}{N-1}$	$O(N)$	$O\left(N\binom{m+N-1}{N-1}\binom{n+N-1}{N-1}\right)$
Multinomial solution (Eq. 4.5)	$\binom{N}{m}\, S(n,m)\, m!$	$O(m)$	$O\left(m\binom{N}{m}S(n,m)m!\right)$
Closed-form solution (Eq. 4.8)	$\sum_{i=0}^{m}\binom{m}{i}\binom{N}{m-i}$	$O(m)$	$O\left(m\sum_{i=0}^{m}\binom{m}{i}\binom{N}{m-i}\right)$
Iterative construction	$N(m+1)(n+1)$	$O(1)$	$O(N(m+1)(n+1))$

Table 4.1: Computational complexity of computing the matrix elements $\mathbf{\Pi}_{mn}$ for the different approaches and configurations. FLOPs per term estimate the number of operations per term including binomial coefficients and multiplications.

Count fidelity

We evaluate the performance of the detector arrays for the given probe states with the count fidelity,

$$F = \left(\sum_n \sqrt{p_n q_n}\right)^2, \tag{4.31}$$

which quantifies how near the measured count distribution ($\{p_n\}$) match the true photon number distribution ($\{q_n\}$) of the probe states. The fidelities for the PEACOQ detector and the PNR SNSPD array detector are plotted in Fig. 4.10 as a function of mean photon number. Both detectors exhibit $\geq 90\%$ count fidelities for coherent states with up to $\mu \sim 10$.

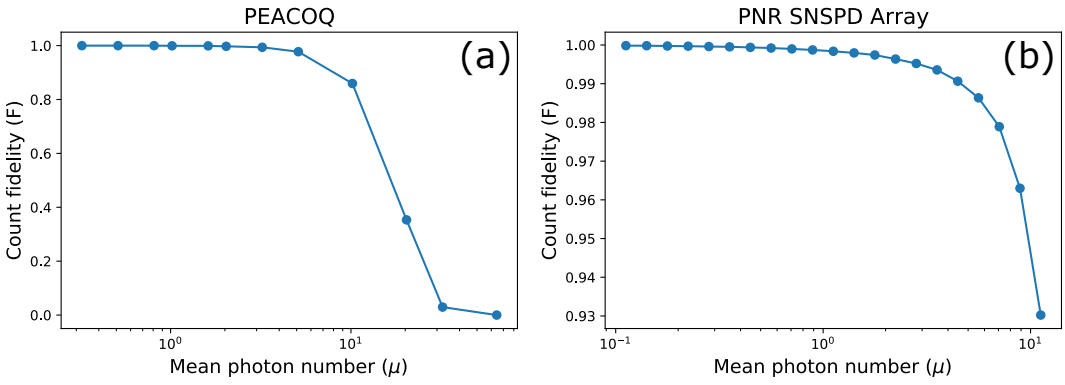

Figure 4.10: Count fidelities for a) the PEACOQ detector and b) the array of six PNR SNSPDs.

References

[1] Aleksander Divochiy, Francesco Marsili, David Bitauld, Alessandro Gaggero, Roberto Leoni, Francesco Mattioli, Alexander Korneev, Vitaliy Seleznev, Nataliya Kaurova, Olga Minaeva, et al. "Superconducting nanowire photon-number-resolving detector at telecommunication wavelengths." In: Nature Photonics 2.5 (2008), pp. 302–306.

[2] F. Marsili, D. Bitauld, A. Gaggero, S. Jahanmirinejad, R. Leoni, F. Mattioli, and A. Fiore. "Physics and application of photon number resolving detectors based on superconducting parallel nanowires." In: New Journal of Physics 11.4 (2009), p. 045022.

[3] Di Zhu, Qing-Yuan Zhao, Hyeongrak Choi, Tsung-Ju Lu, Andrew E. Dane, Dirk Englund, and Karl K. Berggren. "A scalable multi-photon coincidence detector based on superconducting nanowires." In: Nature Nanotechnology 13.7 (2018), pp. 596–601.

[4] M. J. Fitch, B. C. Jacobs, T. B. Pittman, and J. D. Franson. "Photon-number resolution using time-multiplexed single-photon detectors." In: Physical Review A 68 (2003), p. 043814. DOI: 10.1103/PhysRevA.68.043814.

[5] Daryl Achilles, Christine Silberhorn, Cezary Sliwa, Konrad Banaszek, Ian A. Walmsley, Michael J. Fitch, Bryan C. Jacobs, Todd B. Pittman, and James D Franson. "Photon-number-resolving detection using time-multiplexing." In: Journal of Modern Optics 51.9-10 (2004), pp. 1499–1515.

[6] Fadri Grünenfelder, Alberto Boaron, Giovanni V Resta, Matthieu Perrenoud, Davide Rusca, Claudio Barreiro, Raphaël Houlmann, Rebecka Sax, Lorenzo Stasi, Sylvain El-Khoury, et al. "Fast single-photon detectors and real-time key distillation enable high secret-key-rate quantum key distribution systems." In: Nature Photonics 17.5 (2023), pp. 422–426.

[7] Rajveer Nehra, Chun-Hung Chang, Qianhuan Yu, Andreas Beling, and Olivier Pfister. "Photon-number-resolving segmented detectors based on single-photon avalanche-photodiodes." In: Optics Express 28.3 (2020), pp. 3660–3675.

[8] Timon Schapeler, Jan Philipp Höpker, and Tim J Bartley. "Quantum detector tomography of a 2× 2 multi-pixel array of superconducting nanowire single photon detectors." In: Optics Express 28.22 (2020), pp. 33035–33043.

[9] H. Paul, P. Törmä, T. Kiss, and I. Jex. "Photon chopping: new way to measure the quantum state of light." In: Physical Review Letters 76.14 (1996), p. 2464.

[10] Ioana Craiciu, Boris Korzh, Andrew D. Beyer, Andrew Mueller, Jason P. Allmaras, Lautaro Narváez, Maria Spiropulu, Bruce Bumble, Thomas Lehner, Emma E. Wollman, et al. "High-speed detection of 1550 nm single photons with superconducting nanowire detectors." In: Optica 10.2 (2023), pp. 183–190.

[11] Lorenzo Stasi, Gaëtan Gras, Riad Berrazouane, Matthieu Perrenoud, Hugo Zbinden, and Félix Bussières. "Fast high-efficiency photon-number-resolving parallel superconducting nanowire single-photon detector." In: Physical Review Applied 19.6 (2023), p. 064041.

[12] Adriana E. Lita, Aaron J. Miller, and Sae Woo Nam. “Counting near-infrared single-photons with 95% efficiency.” In: Optics Express 16.5 (2008), pp. 3032–3040.

[13] Timon Schapeler, Jan Philipp Höpker, and Tim J. Bartley. “Quantum detector tomography of a 2× 2 multi-pixel array of superconducting nanowire single photon detectors.” In: Optics Express 28.22 (2020), pp. 33035–33043.

[14] Timon Schapeler. Detector Tomography Python Code. https://physik.uni-paderborn.de/en/mesoscopic-quantum-optics/resources/downloads. 2020.

[15] Andrew Mueller, Emma E. Wollman, Boris Korzh, Andrew D. Beyer, Lautaro Narvaez, Ryan Rogalin, Maria Spiropulu, and Matthew D. Shaw. “Time-walk and jitter correction in SNSPDs at high count rates.” In: Applied Physics Letters 122.4 (Jan. 2023), p. 044001. DOI: 10.1063/5.0129147.

[16] Samantha I. Davis, Andrew Mueller, Raju Valivarthi, Nikolai Lauk, Lautaro Narvaez, Boris Korzh, Andrew D. Beyer, Olmo Cerri, Marco Colangelo, Karl K. Berggren, et al. “Improved heralded single-photon source with a photon-number-resolving superconducting nanowire detector.” In: Physical Review Applied 18.6 (2022), p. 064007.

[17] Michael Reck, Anton Zeilinger, Herbert J. Bernstein, and Philip Bertani. “Experimental realization of any discrete unitary operator.” In: Phys. Rev. Lett. 73 (1 July 1994), pp. 58–61.

[18] Gene H. Golub and Charles F. Van Loan. Matrix Computations. 4th. Johns Hopkins University Press, 2013.

Chapter 5

HIGH-RATE MULTIPLEXED ENTANGLEMENT SOURCE BASED ON TIME-BIN QUBITS FOR ADVANCED QUANTUM NETWORKS

This chapter includes the work published as:

[1] Andrew Mueller, Samantha I. Davis, Boris Korzh, Raju Valivarthi, Andrew D. Beyer, Rahaf Youssef, Neil Sinclair, Cristián Peña, Matthew D Shaw, and Maria Spiropulu. "High-rate multiplexed entanglement source based on time-bin qubits for advanced quantum networks." In: Optica Quantum 2.2 (2024), pp. 64–71.

5.1 Introduction

Quantum computing represents an upcoming threat to public-key cryptography [1, 2]. Quantum Key Distribution (QKD) is a method for overcoming this threat by sharing secret cryptographic keys between parties in a manner that is sufficiently secure against potential eavesdroppers and the decryption capabilities of quantum computers. Point-to-point QKD networks are a precursor to more advanced quantum networks which enable the transfer of quantum states for multiple applications including distributed quantum computing, sensing, or secure communication. We characterize any quantum network as 'advanced' if it enables protocols and capabilities that go beyond point-to-point QKD [3]. These include teleportation [4, 5], entanglement swapping [6], memory-assisted networks [7], and others. Entangled photons are a fundamental resource for such demonstrations, and entanglement distribution is therefore a key component of premier quantum network initiatives including the European Quantum Communication Infrastructure (EuroQCI) project, the Illinois Express Quantum Network (IEQNET), the Chinese Quantum Experiments at Space Scale (QUESS) initiative, the United Kingdom UKQNTel network, and the Washington DC-QNet Research Consortium. Future quantum networks should enable high-fidelity and high-rate transfer of individual quantum states across multiple quantum nodes, mediated by distribution of entangled photons, quantum memories, and entanglement swapping measurements.

High-rate entanglement distribution enables high-rate entanglement-based QKD, as well as more general operations that characterize advanced quantum networks.

Entanglement distribution and entanglement-based QKD have been demonstrated with impressive performance across a number of metrics. These include 40 kbps data rates in a QKD system deployed over 50 km of fiber [8] as well as multiple polarization entangled sources that leverage spectral multiplexing. These polarization sources include a demonstration of 181 kebits/s across 150 ITU channel pairs and a high-throughput source potentially capable of gigabit rates with many added channels and detectors [9, 10]. Multiple works have highlighted the need to leverage high total brightness, spectral brightness, collection efficiency, and visibility from pair-generating non-linear crystals to realize practical high-rate entanglement distribution [10, 11, 12, 13, 14, 15, 16].

A time-bin entangled photon source has certain advantages over a polarization-based system [17]. Time-bin entanglement can be measured with no moving hardware and does not require precise polarization tracking to maximize visibility [18, 19]. Also, with suitable equipment, robust time-bin modulation is possible over free space links with turbulence [20]. Therefore, the possibility of simplified fiber-to-free-space interconnects and larger quantum networks based on a shared time-bin protocol motivates development of improved time-bin sources. Furthermore, time-bin encoding is suited for single-polarization light-matter interfaces [21].

We direct 4.09 GHz mode locked laser light into a nonlinear crystal via 80-ps delay-line interferometers (12.5 GHz free-spectral range) to realize a high-rate entanglement source. The ability to resolve time-bin qubits into 80 ps wide bins is enabled by newly developed low-jitter differential superconducting nanowire single-photon detectors (SNSPDs) [22]. Wavelength multiplexing is used to realize multiple high visibility channel pairings which together sum to a high coincidence rate. Each of the pairings can be considered an independent carrier of photonic entanglement [23, 24] and therefore the system as a whole is applicable to flex-grid architectures through the use of wavelength selective switching [25, 26]. However, we focus on maximizing the rate between two receiving stations, Alice and Bob (Fig. 5.1a). Each station is equipped with a DWDM that separates the frequency multiplexed channel into multiple fibers for detection. The SNSPDs are used with a real-time pulse pileup and time-walk correction technique [27] to keep jitter low even at high count rates.

We quantify per-channel brightness and visibility as a function of pump power, as well as collection efficiencies, coincidence rates across 8 channel pairs. We show that the 8-channel system achieves visibilities that average to 99.3% at low mean

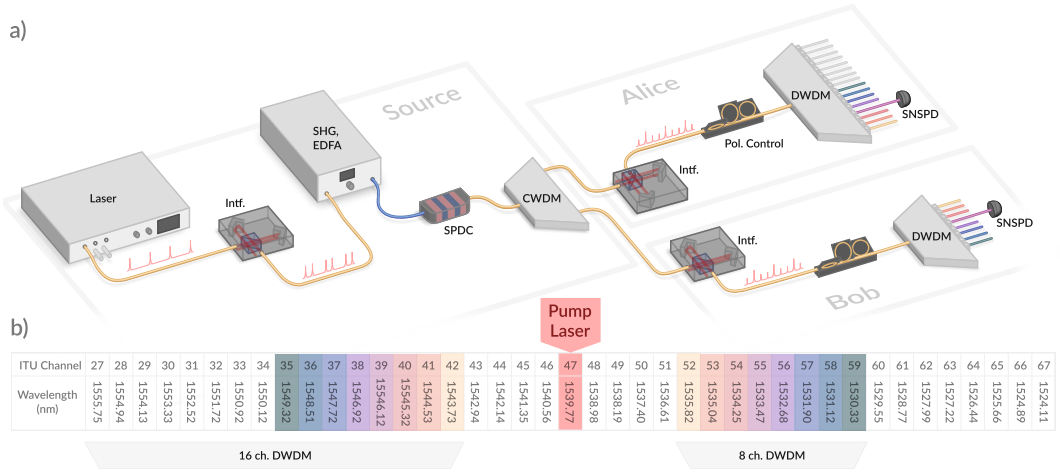

Figure 5.1: Experimental setup. a) Pulses from a 1539.47 nm mode locked laser (Pritel UOC) are split into two by an 80-ps delay-line interferometer before up-conversion and amplification in a second harmonic generation + erbium doped fiber amplifier (SHG + EDFA) module (Pritel). A short PM fiber from the SHG module connects to a nonlinear crystal generating photon pairs by spontaneous parametric down-conversion (SPDC). The coarse wavelength division multiplexing (CWDM) module separates the photon pair spectrum into eight 13 nm-wide bands around 1530 and 1550 nm, for the signal and idler photon, respectively. The signal and idler are directed to the Bob and Alice stations, respectively. The readout interferometers introduce the same time delay as the source interferometer. Polarization controllers are used to maximize the coincidence rates. 100 GHz spacing dense wavelength division multiplexer (DWDM) modules are used to direct each frequency channel into a distinct fiber. Two superconducting nanowire single photon detectors (SNSPDs) are used to measure a specific frequency multiplexed channel pair. Measurements for different multiplexed channels are performed in succession to resolve full system performance. b) ITU channels used in the experiment. Pairs of channels highlighted with the same color obey the phase and pump-energy matching condition for SPDC. To assess the full 16 channels (27-42) of Alice's DWDM multiplexer, Bob's 8-channel DWDM is replaced with a narrowband filter with tunable resonance frequency (not shown in figure).

photon number $\mu_L = 5.6{\times}10^5 \pm 9{\times}10^6$. At a higher power ($\mu_H = 5.0{\times}10^3 \pm 3{\times}10^4$), we demonstrate a total coincidence rate of 3.55 MHz with visibilities that average to 96.6%. Through quantum state tomography we bound the distillable entanglement rate of the system to between 69% and 91% of the μ_H coincidence rate (2.46 - 3.25 Mebits/s).

Quantifying a source's spectral mode purity is important for gauging its utility in advanced quantum networks that rely on interferometric measurements like two-photon interference which enables Bell-state measurements (BSM) [5]. With Schmidt decomposition we quantify the modal purity of single DWDM channel pairs and derive the inverse Schmidt number which serves as an estimate for two-photon interference visibility between two such sources. Ultimately, we demonstrate that an entanglement generation source of this design makes for a robust and powerful building block for future high-rate quantum networks.

5.2 System

Figure 5.1 shows the experimental setup. Pulses from the 4.09 GHz mode-locked laser, with a center wavelength at 1539.47 nm, are sent through an 80 ps delay-line interferometer (Optoplex DPSK Phase Demodulator). All interferometers used are the same type; they have insertion loss of 1.37 $\pm$ 0.29 dB, are polarization independent, and have extinction ratios greater than 18 dB. The source interferometer produces two pulses each clock cycle used to encode early/late basis states ($|e\rangle, |l\rangle$), which are subsequently up-converted by a second harmonic generation (SHG) module (Pritel) and down-converted into entangled photon pairs by a type-0 spontaneous parametric down conversion (SPDC) crystal (Covesion) [17]. The SPDC module uses a 1 cm long waveguide-coupled MgO-doped lithium niobate crystal with an 18.3 µ polling period. The up-converted pulses at 769 nm have a FWHM bandwidth of 243 GHz (0.48 nm), which along with the phase matching condition of the SPDC waveguide, defines a wide joint spectral intensity (JSI) function [28].

The photon pairs are separated by a coarse wavelength division multiplexer (CWDM) which serves to split the SPDC spectrum into two wide-bandwidth halves. For a system using more than 16 DWDM channels at Alice and Bob, the CWDM would be replaced with a splitter that efficiently sends the full SPDC spectrum shorter than 1540 nm to Bob, and the spectrum longer than 1540 nm to Alice. A dichroic splitter with a sharp transition at 1540 nm would also enable the use of DWDM channels 43-46 and 48-51. The pairs are of the form $|\psi\rangle = \frac{1}{\sqrt{2}}\left(|e\rangle_s|e\rangle_i + e^{i\phi}|l\rangle_s|l\rangle_i\right)$.

Entangled idler and signal photons are sent to the receiving stations labeled Alice and Bob, respectively. One readout interferometer at each station projects all spectral bands into a composite time-phase basis. From here, dense wavelength division multiplexers (DWDM) divide up the energy-time entangled photon pairs into spectral channels.

The DWDM outputs are sent to differential niobium nitride (NbN) single pixel SNSPDs [22] with 22 × 15 μm active areas formed by meanders of 100-nm-wide and 5-nm-thick niobium nitride (NbN) nanowires on a 500 nm pitch. These measure the arrival time of photons with respect to a clock signal derived from the mode locked laser. Use of the high system repetition rate and compact 80 ps delay interferometers is only possible due to the high timing resolution of these detectors. Low jitter performance is achieved by incorporating impedance matching tapers for efficient RF coupling, resulting in higher slew rate pulses, and by enabling RF pulse readout from both ends of the nanowire. The dual-ended readout allows for the cancellation of jitter caused by the variable location of photon arrival along the meander when the differential signals are recombined with a balun. SNSPDs of this type reach system jitters down to 13.0 ps FWHM, and 47.6 ps FW(1/100)M [22]. We use two SNSPDs for this demonstration with efficiencies at 1550 nm of 66% and 74%. They exhibit 3 dB maximum count rates of 15.1 and 16.0 MHz. A full 8-channel implementation of this system would require 16 detectors operating in parallel at both Alice and Bob. To read out both outputs of both interferometers, 4 detectors per channel are required, resulting in 32 detectors total.

In the following, rigorous tests of entanglement are primarily done with the 8 ITU 100 GHz channel pairings: Ch. 35-42 at Alice and Ch. 52-59 at Bob. However, the source brightness measurements were conducted on a partially realized 16-channel configuration which makes use of all 16 channels available on Alice's DWDM.

Signals from the SNSPDs are directed to a free-running time tagger (Swabian) and processed with custom software. The resulting histograms, referenced from a shared clock (Fig 5.2a), depict three peaks, which are caused by the sequential delays of the source and readout interferometers. Some intensity imbalance between long and short paths is present in these interferometers, which explains the asymmetry between early and late peaks in Fig. 5.2a. Such imbalances are present in both the source and readout interferometers to varying degrees. The interferometer used for the source exhibits an early/late intensity balance ratio of 1.13. Alice and Bob's interferometers exhibit early/late imbalances of 1.24 and 1.15, respectively. These

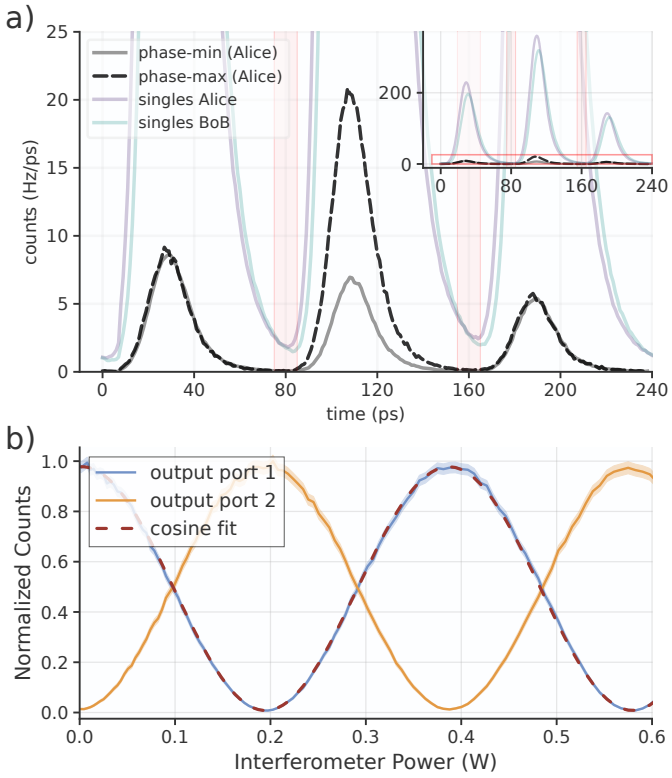

Figure 5.2: Entanglement visibility characterization. a) Histogram of photon arrival events with respect to the 4.09 GHz clock. Dashed black and grey lines show the response functions for coincidence events. Events within 10 ps guard regions centered at 80 and 160 ps (shaded red) are discarded for analysis of coincidences between individual bins. This is done to maximize visibility in the presence of some minor overlap of the pulses. The coincidence histograms include pairings from any combination of early, middle, and late time bins. Therefore, the height of the center peak in the phase-min state is not near zero, as non-phase-varying terms contribute. b) Coincidence rate interference fringes for the center time bin in isolation. Based on the good agreement between the fringe data and a cosine fit, we make subsequent tomographic measurements assuming that phase is linear with the electrical power applied to the interferometer phase shifter.

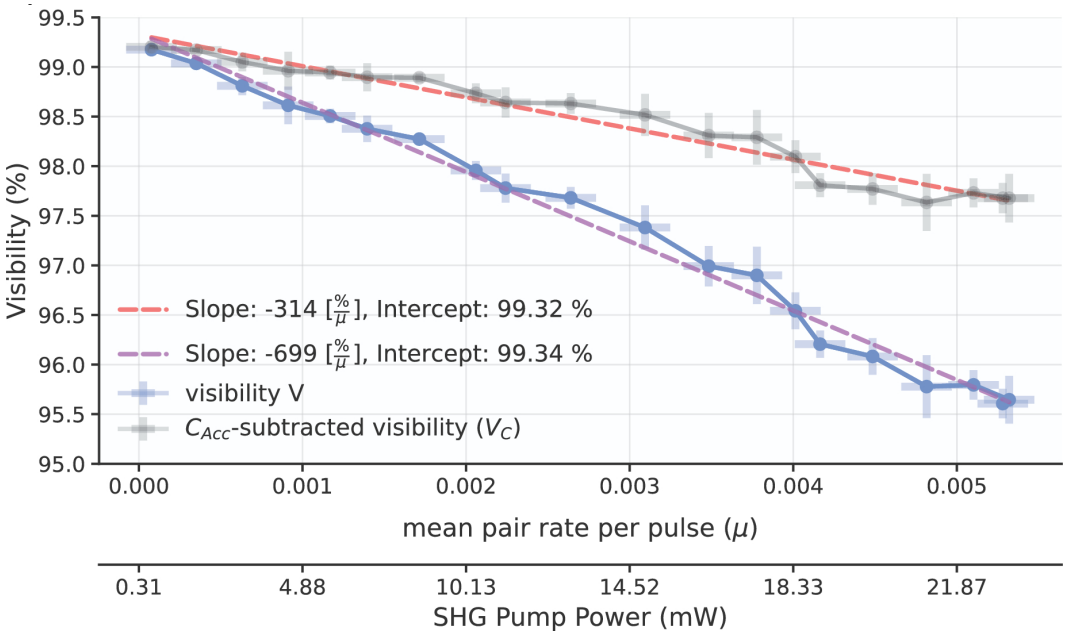

Figure 5.3: Entanglement visibility versus mean pair rate per pulse (μ) and SHG pump power. Error bars are calculated by taking multiple measurements of the center bin coincidence rate over some integration time. These measurements span small ranges of interferometer phase, as the extremum-finding algorithm jitters the interferometer voltage. V_C (grey data, red line) is a construction that models how visibility would be affected if accidental coincidences from mutually incompatible spectral modes could be mitigated in future systems.

induce imperfect overlap of certain time-bin modes of differing amplitudes. This mismatch lowers interference visibilities, see Section 5.4.

5.3 Results

The coincidence rate across Alice and Bob's middle bins varies sinusoidally with respect to the combined phase relationship of the source and readout interferometers [29, 17] (see Fig. 5.2b). In Fig. 5.2a the coincidences shown are for any combination of early, middle, or late bins. For tomography and visibility measurements, coincidence detections across specific bin pairings are considered.

Due to the small size (3×3 cm) and temperature insensitivity of the interferometers, minimal temporal phase drift is observed. Without active temperature control or phase feedback, we observe minimized coincidence rates of the center time bin stay within 6% of their original values after 50 minutes. Nevertheless, software is used to lock the voltage-controlled phase at a minimum or maximum with a

simple hill-climbing algorithm. This varies the phase by small amounts over several minutes to search for or maintain an extremum. This is simpler to implement than the techniques needed to stabilize interferometers of longer path length difference, including the use of precise temperature control [5] or co-propagating stabilization lasers [30].

Channels 35 and 59 are chosen for an analysis of entanglement visibility and rates versus pump power. Visibility with respect to pump power or mean entangled pair rate is shown in Fig. 5.3a. We define the entanglement visibility as $V = 100\% * (C_{max} - C_{min})/(C_{max} + C_{min})$ where C_{min} and C_{max} are the minimum and maximum coincidence rates in the middle bin for varied phase. As this coincidence rate depends on the total phase across the source and readout interferometers, only Bob's interferometer is actively controlled to scan the full state space.

The raw visibility versus μ is shown in blue in Fig. 5.3a. Relative to similar measurements [31], this drops quickly with increasing μ, and one reason is the presence of accidental coincidences across mutually incompatible spectral modes. The presence of these unwanted coincidences is a consequence of the narrowband filtering regime, and depends on factors included the singles rates S_A and S_B, and the geometric compensation factor δ. We model this type of accidental coincidence rate C_{Acc} versus μ, and subtract it off from coincidence measurements to produce the grey data in Fig. 5.3a. This simulated visibility's more gradual drop with increasing μ highlights the detrimental effect of our high single-to-coincidence rates S_A/C_{AB}, S_B/C_{AB}. As detailed in the Discussion section below, this motivates special source engineering techniques for future systems.

5.4 Impact of experimental imperfections

The experiment employs three Michelson interferometers with a path-length delay of 80 ps: one at the source to generate the early and late time-bins, and one prior to each detector to control the measurement basis. To determine the effect of interferometric imperfections on the entanglement visibility, we model the interferometers as equivalent Mach-Zehnder interferometers as shown in Fig. 5.4. Imperfections in the interferometer are captured by the transmittance t of the beamsplitter and internal path (mirror) efficiencies $|\alpha|^2$ and $|\beta|^2$. An ideal Michelson interferometer has $t = 1/\sqrt{2}$ and $|\alpha|^2 = |\beta|^2 = 1$.

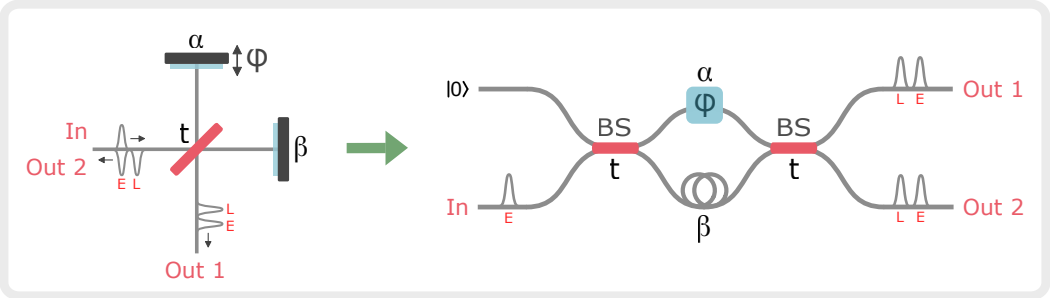

Figure 5.4: Model for Michelson interferometers employed in the experiment. The interferometer contains a beamsplitter with transmittance t and two mirrors with efficiencies α and β.

Source interferometer imperfections

In the experiment, pulses of coherent light from a mode-locked laser (MLL) are injected into the input of the source interferometer. A field $\hat{E}$ at the input of the source interferometer transforms as

$$\hat{E}_{\text{in}} \rightarrow rt\alpha e^{i\varphi}\hat{E}_{E,1} + r^2\alpha e^{i\varphi}\hat{E}_{E,2} + rt\beta\hat{E}_{L,1} + t^2\beta\hat{E}_{L,2} \tag{5.1}$$

$$+ ir\sqrt{1-|\alpha|^2}\hat{E}_{\text{vac}_1} + it\sqrt{1-|\beta|^2}\hat{E}_{\text{vac}_2} \tag{5.2}$$

where the early and late temporal modes are denoted by subscripts "E" and "L", the input and output modes are denoted by subscripts "in", "1" and "2", and $r = i\sqrt{1-|t|^2}$. Due to imperfect path efficiencies, part of the light leaks into the vacuum field mode $\hat{E}_{\text{vac}}$, which corresponds to the last term in Eq. 5.2. It follows that the power of the early and late output pulses in terms of the power of the input pulse are

$$P_{E,1} = |r|^2|t|^2|\alpha|^2P_{in}, \qquad P_{E,2} = |r|^4|\alpha|^2P_{in} \tag{5.3}$$

$$P_{L,1} = |r|^2|t|^2|\beta|^2P_{in}, \qquad P_{L,2} = |t|^4|\beta|^2P_{in}.$$

To generate the entangled photon pairs, one of the output ports of the source interferometer is up-converted by second harmonic generation (SHG) then down-converted via spontaneous parametric down conversion (SPDC), resulting in two-mode squeezed vacuum states (TMSVs) in early and late temporal modes with mean photon numbers μ_E and μ_L, respectively. The ratio of μ_E to μ_L depends on which output port of the source interferometer is used. Note that the definition of μ used in the main text is per source laser period or per experiment cycle (4.09 GHz). Therefore μ from the main text is equal to $\mu_E + \mu_L$. The output power of SHG

(P_{SHG}) as a function of the SHG pump power (P_p) is [32],

$$P_{SHG} = P_p \tanh^2 \sqrt{\eta_{SHG} P_p} \approx \eta_{SHG} P_p^2, \tag{5.4}$$

where η_{SHG} is the conversion efficiency of the SHG crystal. After SPDC, the squeezing parameter (ξ) of the TMSVs in terms of the SPDC pump power (P_{SHG}) is $\xi = \lambda\sqrt{P_{SHG}} \approx \lambda\sqrt{\eta_{SHG}} P_p$, where λ is proportional to the SPDC crystal length and nonlinear interaction strength [33]. The mean photon number in terms of the squeezing parameter is $\mu = \sinh^2 \xi \approx \xi^2$. Therefore, the mean photon numbers of the TMSVs as a function of the output pulses of the source interferometer are,

$$\mu_E \approx \lambda^2 \eta_{SHG} P_{E,i} \qquad\qquad \mu_L \approx \lambda^2 \eta_{SHG} P_{L,i}^2, \tag{5.5}$$

where $i = 1(2)$ corresponds to output port 1(2) of the source interferometer.

If output port 1 is used,

$$\mu_E/\mu_L \approx P_{E,1}^2/P_{L,1}^2 = |\alpha|^4/|\beta|^4,$$

whereas if output port 2 is used,

$$\mu_E/\mu_L \approx P_{E,2}^2/P_{L,2}^2 = |r|^8|\alpha|^4/|t|^8|\beta|^4.$$

When output port 1 of the source interferometer is used, if the internal path efficiencies of the source interferometer are different, there is an imbalance in the early and late mean photon numbers. When output port 2 is used, the effect of the imbalance in the internal path efficiencies on the ratio of early and late mean photon numbers can be compensated by imperfect transmittance: $\mu_E/\mu_L = 1$ when $|t|^2/|r|^2 = |\alpha|/|\beta|$.

Measurement interferometer imperfections

Imperfections in the measurement interferometers limit the entanglement visibility of the experiment. As described in the previous section, early and late TMSVs are generated by pumping the SPDC with early and late pulses. Each half of each TMSV is sent to a measurement interferometer (see Fig. 5.5). Let $|\xi\rangle$ denote the TMSV state,

$$|\xi\rangle = \sum_{n=0}^{\infty} (-1)^n \sqrt{\frac{\mu^n}{(1+\mu)^{n+1}}}\, |n_A, n_B\rangle\,, \tag{5.6}$$

where $|n_A, n_B\rangle$ denotes the state with n_A photons at the input of interferometer A and n_B photons at the input port of interferometer B. We model the input state to the

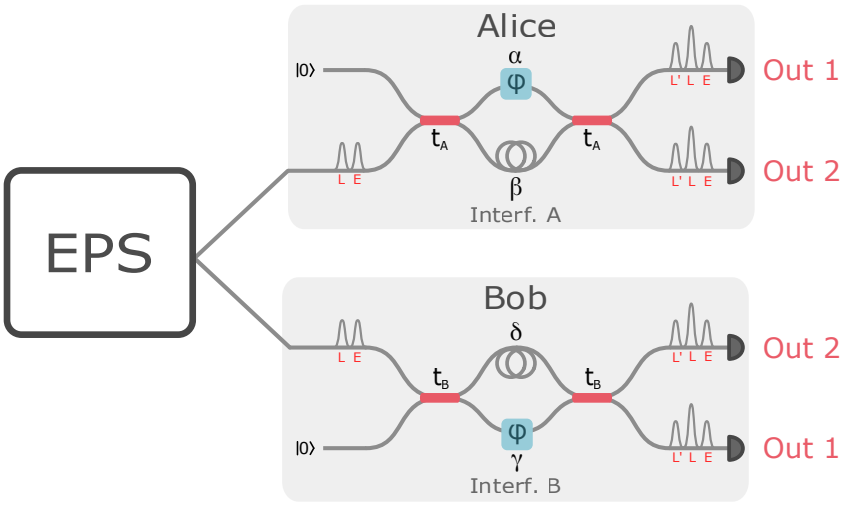

Figure 5.5: Setup for theoretical model of entanglement visibility experiment.

measurement interferometers as a product state of TMSV in early and late temporal modes, to lowest order in μ_E and μ_L:

$$\begin{aligned} |\Psi_{in}\rangle &= |\xi\rangle_E \otimes |\xi\rangle_L \\ &\approx \sqrt{1-(\mu_E+\mu_L)}\,|0,0\rangle_E\,|0,0\rangle_L \\ &\quad - \sqrt{\mu_E}\,|1,1\rangle_E\,|0,0\rangle_L - \sqrt{\mu_L}\,|0,0\rangle_E\,|1,1\rangle_L\,. \end{aligned} \tag{5.7}$$

We can express Eq. 5.7 in terms of the creation operators $\hat{a}^\dagger$ and $\hat{b}^\dagger$ of the field modes at the inputs of interferometers A and B, respectively:

$$|\Psi_{in}\rangle = \left(\sqrt{1-(\mu_E+\mu_L)} - \sqrt{\mu_E}\hat{a}_E^\dagger\hat{b}_E^\dagger - \sqrt{\mu_L}\hat{a}_L^\dagger\hat{b}_L^\dagger\right)|0,0\rangle_E\,|0,0\rangle_L\,. \tag{5.8}$$

Since the measurement interferometers are also Michelson interferometers, the

transformation relations are,

$$\hat{a}_E \mapsto r_A t_A \alpha e^{i\varphi} \hat{a}_{E,1} + r_A^2 \alpha e^{i\varphi} \hat{a}_{E,2} \tag{5.9}$$
$$+ r_A t_A \beta \hat{a}_{L,1} + t_A^2 \beta \hat{a}_{L,2} + c_A \hat{a}_{\mathrm{vac}_1} + d_A \hat{a}_{\mathrm{vac}_2},$$
$$\hat{b}_E \mapsto r_B t_B \gamma e^{i\varphi} \hat{b}_{E,1} + r_B^2 \gamma e^{i\varphi} \hat{b}_{E,2} \tag{5.10}$$
$$+ r_B t_B \delta \hat{b}_{L,1} + t_B^2 \delta \hat{b}_{L,2} + c_B \hat{b}_{\mathrm{vac}_1} + d_B \hat{b}_{\mathrm{vac}_2},$$
$$\hat{a}_L \mapsto r_A t_A \alpha e^{i\varphi} \hat{a}_{L,1} + r_A^2 \alpha e^{i\varphi} \hat{a}_{L,2} \tag{5.11}$$
$$+ r_A t_A \beta \hat{a}_{L',1} + t_A^2 \beta \hat{a}_{L',2} + c_A \hat{a}_{\mathrm{vac}_1} + d_A \hat{a}_{\mathrm{vac}_2},$$
$$\hat{b}_L \mapsto r_B t_B \gamma e^{i\varphi} \hat{b}_{L,1} + r_B^2 \gamma e^{i\varphi} \hat{b}_{L,2} \tag{5.12}$$
$$+ r_B t_B \delta \hat{b}_{L',1} + t_B^2 \delta \hat{b}_{L',2} + c_B \hat{b}_{\mathrm{vac}_1} + d_B \hat{b}_{\mathrm{vac}_2},$$
$$c_A = i r_A \sqrt{1 - |\alpha|^2}, \quad d_A = i t_A \sqrt{1 - |\beta|^2},$$
$$c_B = i r_B \sqrt{1 - |\delta|^2}, \quad d_B = i t_B \sqrt{1 - |\gamma|^2},$$

where L' denotes the temporal mode obtained by sending a photon in the late (L) mode through the long arm of an interferometer, and $\hat{a}_{\mathrm{vac}_i}$, $\hat{b}_{\mathrm{vac}_i}$ correspond to vacuum modes. To find the state at the output of the interferometers, we combine Eq. 5.8 with Eq. 5.9-5.12, and consider only terms relevant to post-selection on coincidences of the middle bins (L) of different interferometer outputs, to lowest order in μ_E and μ_L,

$$\begin{aligned}
|\Psi_{\mathrm{out}}\rangle &= r_A^* t_A r_B^* t_B \left(\beta\delta\sqrt{\mu_E} + \alpha\gamma\sqrt{\mu_L} e^{-2i\varphi}\right) |0,0;0,0\rangle_E \, |1,0;1,0\rangle_L \, |0,0;0,0\rangle_{L'} \\
&+ r_A^* t_A \left(t_B^2 \beta\delta\sqrt{\mu_E} + (r_B^*)^2 \alpha\gamma\sqrt{\mu_L} e^{-2i\varphi}\right) |0,0;0,0\rangle_E \, |1,0;0,1\rangle_L \, |0,0;0,0\rangle_{L'} \\
&+ r_B^* t_B \left(t_A^2 \beta\delta\sqrt{\mu_E} + (r_A^*)^2 \alpha\gamma\sqrt{\mu_L} e^{-2i\varphi}\right) |0,0;0,0\rangle_E \, |0,1;1,0\rangle_L \, |0,0;0,0\rangle_{L'} \\
&+ \left(t_A^2 t_B^2 \beta\delta\sqrt{\mu_E} + (r_A^*)^2 (r_B^*)^2 \alpha\gamma\sqrt{\mu_L} e^{-2i\varphi}\right) |0,0;0,0\rangle_E \, |0,1;0,1\rangle_L \, |0,0;0,0\rangle_{L'} \\
&+ \cdots
\end{aligned} \tag{5.13}$$

where $\left|n_{A,1}, n_{A_2}; n_{B_1}, n_{B,2}\right\rangle$ denotes the state with $n_{A,1}$ photons at output 1 of interferometer A, $n_{A,2}$ photons at output 2 of interferometer A, $n_{B,1}$ photons at output 1 of interferometer B, and $n_{B,2}$ photons at output 2 of interferometer B. We define the following parameters to simplify notation:

$$x \equiv \frac{\mu_E}{\mu_L}, \qquad \kappa_A \equiv \frac{|\beta|^2}{|\alpha|^2}, \qquad \kappa_B \equiv \frac{|\gamma|^2}{|\delta|^2}, \tag{5.14}$$

$$\epsilon_A = \frac{|t_A|^2}{|r_A|^2}, \qquad \epsilon_B \equiv \frac{|t_B|^2}{|r_B|^2}. \tag{5.15}$$

From Eq. 5.13, it follows that the coincidence probabilities for each combination of output ports are proportional to,

$$C_{A_1,B_1}(\varphi) \propto \sqrt{\frac{\kappa_B}{\kappa_A}} + \sqrt{\frac{\kappa_A}{\kappa_B}}x + 2\sqrt{x}\cos 2\varphi, \tag{5.16}$$

$$C_{A_1,B_2}(\varphi) \propto \frac{1}{\epsilon_B}\sqrt{\frac{\kappa_B}{\kappa_A}} + \epsilon_B\sqrt{\frac{\kappa_A}{\kappa_B}}x + 2\sqrt{x}\cos 2\varphi, \tag{5.17}$$

$$C_{A_2,B_1}(\varphi) \propto \frac{1}{\epsilon_A}\sqrt{\frac{\kappa_B}{\kappa_A}} + \epsilon_A\sqrt{\frac{\kappa_A}{\kappa_B}}x + 2\sqrt{x}\cos 2\varphi, \tag{5.18}$$

$$C_{A_2,B_2}(\varphi) \propto \frac{1}{\epsilon_A\epsilon_B}\sqrt{\frac{\kappa_B}{\kappa_A}} + \epsilon_A\epsilon_B\sqrt{\frac{\kappa_A}{\kappa_B}}x + 2\sqrt{x}\cos 2\varphi, \tag{5.19}$$

where the phase factors in the reflectivities r_A, r_B are absorbed into the definition of φ. Therefore, the entanglement visibilities, $V = \frac{\max(C(\varphi))-\min(C(\varphi))}{\max(C(\varphi))+\min(C(\varphi))}$, for each combination of output ports are:

$$V_{A_1,B_1} = \frac{2\sqrt{x}}{\sqrt{\frac{\kappa_B}{\kappa_A}} + \sqrt{\frac{\kappa_A}{\kappa_B}}x}, \tag{5.20}$$

$$V_{A_1,B_2} = \frac{2\sqrt{x}}{\frac{1}{\epsilon_B}\sqrt{\frac{\kappa_B}{\kappa_A}} + \epsilon_B\sqrt{\frac{\kappa_A}{\kappa_B}}x}, \tag{5.21}$$

$$V_{A_2,B_1} = \frac{2\sqrt{x}}{\frac{1}{\epsilon_A}\sqrt{\frac{\kappa_B}{\kappa_A}} + \epsilon_A\sqrt{\frac{\kappa_A}{\kappa_B}}x}, \tag{5.22}$$

$$V_{A_2,B_2} = \frac{2\sqrt{x}}{\frac{1}{\epsilon_A\epsilon_B}\sqrt{\frac{\kappa_B}{\kappa_A}} + \epsilon_A\epsilon_B\sqrt{\frac{\kappa_A}{\kappa_B}}x}. \tag{5.23}$$

Unity visibility is achievable for each combination of output ports: $V_{A_1,B_1} = 1$ when $x = \kappa_B/\kappa_A$, $V_{A_1,B_2} = 1$ when $x = \kappa_B/(\kappa_A\epsilon_B^2)$, $V_{A_2,B_1} = 1$ when $x = \kappa_B/(\kappa_A\epsilon_A^2)$, and $V_{A_2,B_2} = 1$ when $x = \kappa_B/(\kappa_A\epsilon_A^2\epsilon_B^2)$. Therefore, the effect of imbalances in the source and measurement interferometers is to shift the optimal ratio of early to late mean photon numbers. Imbalances in the measurement interferometers can be compensated by imbalances in the source interferometer in order to obtain unity visibility. Moreover, in the single photon limit, the visibility is insensitive to the absolute path efficiencies in the experiment. The visibility depends only on the ratio of path efficiencies between the measurement interferometers (κ_A/κ_B). The entanglement visibilities for each combination of output ports as a function of

$x = \mu_E/\mu_L$ for various ratios of interferometric path efficiencies are shown in Fig. 5.6.

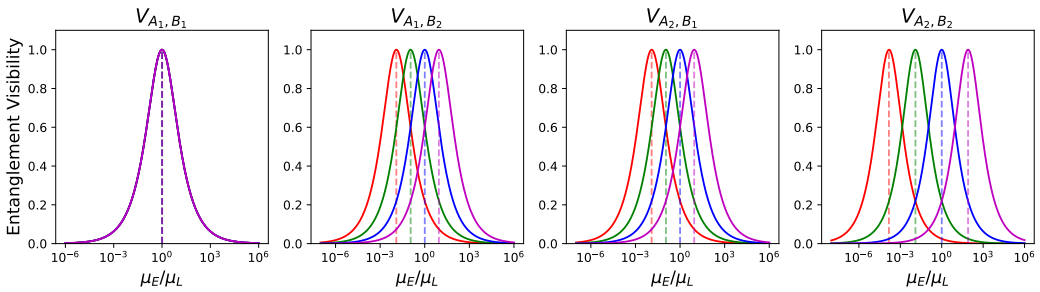

Figure 5.6: Entanglement visibility as function of μ_E/μ_L for fixed $\kappa_B/\kappa_A = 1$ and $\epsilon_A = \epsilon_B = 90/10$ (red), $75/25$ (blue), $50/50$ (green), $25/75$ (purple).

Multiphoton effects

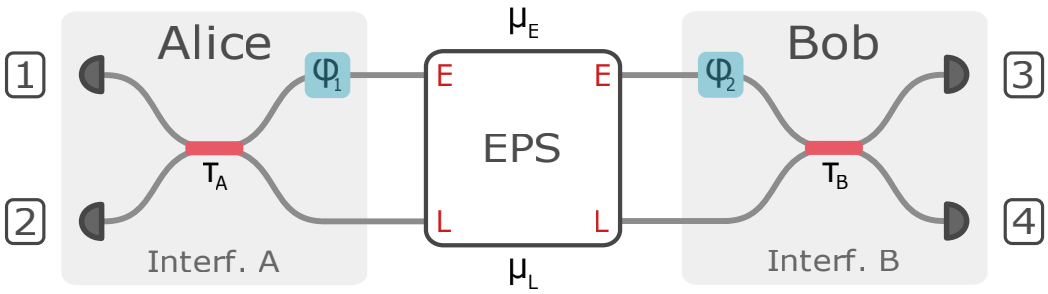

Figure 5.7: Setup for phase space modeling of entanglement visibility experiment.

Calculating the entanglement visibility to higher order photon number contributions quickly becomes intractable with the Fock space approach in the previous section. To study the effect of multiphoton events on the entanglement visibility, we model the experiment using phase space methods based on a characteristic function formalism [34, 35]. The model setup is shown in Fig 5.7. As in the Fock space approach, the input state is modeled as a product state of TMSV in early and late temporal modes, with mean photon numbers μ_E and μ_L, respectively. The measurement interferometers are modeled as beamsplitters in the temporal domain that mix the early and late input modes with transmittances τ_A and τ_B, which absorb the interferometric path efficiencies and spatial beamsplitter transmittances. Since the input state is modeled as a Gaussian state, and the measurement interferometers are modeled as Gaussian operations, we can find the symplectic transformation that maps the characteristic function of the input state to that of the state prior to detection.

Following Ref. [36], the characteristic function for an N-mode bosonic state is

$$\chi(\xi) = \mathrm{Tr}\left[\hat{\rho}\exp(-i(\hat{x}_1, \hat{p}_1, \hat{x}_2, \hat{p}_2, \cdots \hat{x}_N, \hat{p}_N)\xi)\right] \tag{5.24}$$

where $\xi \in \mathbb{R}^{2N}$, ρ is the density matrix, and $\hat{x}_i = \frac{1}{\sqrt{2}}(\hat{a}_i^\dagger + \hat{a}_i)$ and $\hat{p}_i = \frac{1}{\sqrt{2}}(\hat{a}_i^\dagger + \hat{a}_i)$ are the quadrature operators for mode i with annihilation operator $\hat{a}_i$. A Gaussian state is a state whose characteristic function that takes a Gaussian form,

$$\chi(\xi) = \exp\left(-\frac{1}{4}\xi^T\gamma\xi - id^T\xi\right), \tag{5.25}$$

which is fully characterized by the displacement vector d and covariance matrix γ, i.e., the first and second moments. For the TMSV state, the displacement vector is the null vector $d = (0, 0, 0, 0)$ and the covariance matrix is given by,

$$\gamma_{TMSV}(\mu) = \begin{pmatrix} \mathbf{A} & \mathbf{B} \\ \mathbf{B} & \mathbf{A} \end{pmatrix}, \quad \mathbf{A} = \begin{pmatrix} 1+2\mu & 0 \\ 0 & 1+2\mu \end{pmatrix}, \tag{5.26}$$

$$\mathbf{B} = \begin{pmatrix} 2\sqrt{\mu(\mu+1)} & 0 \\ 0 & -2\sqrt{\mu(\mu+1)} \end{pmatrix}, \tag{5.27}$$

where $\gamma_{TMSV}(\mu)$ is written in block matrix form. Therefore, the covariance matrix for the input state of our experiment is,

$$\gamma_{in}(\mu_E, \mu_L) = \gamma_{TMSV}(\mu_E) \oplus \gamma_{TMSV}(\mu_L). \tag{5.28}$$

The characteristic function of the input state is mapped to the characteristic function of the state prior to detection by a symplectic transformation,

$$\chi_{in}(\xi) = \exp\left(-\frac{1}{4}\xi^T\gamma_{in}\xi\right) \mapsto \chi_{out}(\xi) = \exp\left(-\frac{1}{4}\xi^T S^T\gamma_{in}S\xi\right), \tag{5.29}$$

where S is the Symplectic matrix of the interferometers. We construct S from the Symplectic matrices of the phase shifter (S_{PS}) and beamsplitter (S_{BS}) [35],

$$S_{PS}(\varphi) = \begin{pmatrix} \cos\varphi & \sin\varphi \\ -\sin\varphi & \cos\varphi \end{pmatrix}, \tag{5.30}$$

$$S_{BS}(\tau) = \begin{pmatrix} \mathbf{T} & \mathbf{R} \\ \mathbf{R} & \mathbf{T} \end{pmatrix}, \quad \mathbf{T} = \begin{pmatrix} \tau & 0 \\ 0 & \tau \end{pmatrix}, \quad \mathbf{R} = \begin{pmatrix} 0 & -\sqrt{1-\tau^2} \\ \sqrt{1-\tau^2} & 0 \end{pmatrix}. \tag{5.31}$$

From the output characteristic function χ_{out}, we obtain the coincidence probabilities using Eq. 9 of Ref. [36],

$$\mathrm{Tr}\left[\hat{\rho}_{\mathrm{out}}\hat{\Pi}\right] = \left(\frac{1}{2\pi}\right)^N \int dx^{2N}\chi_{\mathrm{out}}(x)\chi_{\Pi}(-x), \tag{5.32}$$

where $\hat{\rho}_{\text{out}}$ is the state prior to detection with characteristic function χ_{out}, and $\hat{\Pi}$ is the measurement operator corresponding to coincidences between detectors from different interferometers. The measurement operators for a threshold detector, which distinguishes between a detection event (at least one photon) and no detection event (zero photons), are,

$$\hat{\Pi}_{\text{event}} = \hat{I} - |0\rangle\langle 0|, \quad \hat{\Pi}_{\text{no event}} = |0\rangle\langle 0|, \tag{5.33}$$

where $\hat{I}$ is the 2 by 2 identity matrix. The measurement operator for coincidences between, e.g., detectors 1 and 4 are,

$$\hat{\Pi}_{1,4} = \hat{\Pi}_{\text{event},1} \otimes \hat{I}_2 \otimes \hat{I}_3 \otimes \hat{\Pi}_{\text{event},4}, \tag{5.34}$$

where the subscripts denote the output modes labeled in Fig. 5.7. We derive an analytical expression for the coincidence probability, $C(\varphi) = \text{Tr}\left[\hat{\rho}_{\text{out}}\hat{\Pi}_{1,4}\right]$, that encompasses all multiphoton contributions,

$$C(\varphi) = 1 - \frac{1}{|f(\mu_E, \mu_L, \tau_A)|} - \frac{1}{|g(\mu_E, \mu_L, \tau_B)|} + \frac{1}{|h(\mu_E, \mu_L, \tau_A, \tau_B, \varphi)|}, \tag{5.35}$$

$$f(\mu_E, \mu_L, \tau_A) = 1 + \mu_L + \tau_A(\mu_E - \mu_L), \tag{5.36}$$

$$g(\mu_E, \mu_L, \tau_B) = 1 + \mu_E + \tau_B(\mu_L - \mu_E), \tag{5.37}$$

$$\begin{aligned} h(\mu_E, \mu_L, \tau_A, \tau_B) = {} & 1 + \mu_E + \mu_L(1 + \mu_E)(1 - \tau_A) \\ & - \mu_E\tau_B(1 + \mu_L) + \tau_A\tau_B(\mu_E + \mu_L + 2\mu_E\mu_L) \\ & - 2\sqrt{\mu_E\mu_L\tau_A(1 + \mu_E)(1 + \mu_L)(1 - \tau_A)}\sqrt{\tau_B(1 - \tau_B)}\cos\varphi, \end{aligned} \tag{5.38}$$

where $\varphi = \varphi_A - \varphi_B$ is the relative phase between interferometers A and B. The different visibilities in each output port combination as a result of interferometric imbalances can be obtained by adjusting τ accordingly. To isolate the impact of multiphoton contributions to the visibility, we set $\tau_A = \tau_B = \frac{1}{\sqrt{2}}$, and obtain the following expression for the entanglement visibility, $V(\mu_E, \mu_L) = \frac{C(0) - C(\pi)}{C(0) + C(\pi)}$:

$$V(\mu_E, \mu_L) = \frac{2/\sqrt{G_-(\mu_E, \mu_L)} - 2/\sqrt{G_+(\mu_E, \mu_L)}}{1 - 4/(2 + \mu_E + \mu_L) + 2/\sqrt{G_-(\mu_E, \mu_L)} + 2/\sqrt{G_+(\mu_E, \mu_L)}}, \tag{5.39}$$

$$
\begin{aligned}
G_{\pm}(\mu_E,\mu_L) = {} & \mu_E^2(9+8\mu_L(2+\mu_L)) \\
& \pm (4+3\mu_L)\left(\pm 4 \pm 3\mu_L + 4\sqrt{\mu_E\mu_L(1+\mu_E)(1+\mu_L)}\right) \\
& + 2\mu_E\left(12 \pm 6\sqrt{\mu_E\mu_L(1+\mu_E)(1+\mu_L)}\right) \\
& + 2\mu_E\mu_L\left(19+8\mu_L \pm 4\sqrt{\mu_E\mu_L(1+\mu_E)(1+\mu_L)}\right).
\end{aligned} \tag{5.40}
$$

By expanding Eq. 5.39 to first order in μ_E and μ_L,

$$
V(\mu_E,\mu_L) = \frac{2\sqrt{\frac{\mu_E}{\mu_L}}}{1+\frac{\mu_E}{\mu_L}} - \frac{\mu_E}{\mu_L}\frac{\left(5(\frac{\mu_E}{\mu_L}+\frac{\mu_L}{\mu_E})+6\right)}{2(1+\frac{\mu_E}{\mu_L})^2}\sqrt{\mu_E\mu_L} + \cdots \tag{5.41}
$$

we see that the first term matches Eq. 5.20-5.23 for $t_A = t_B = \frac{1}{\sqrt{2}}$, $\beta/\alpha = \gamma/\delta = 1$. Moreover, for $\mu_{eq} \equiv \mu_E = \mu_L$, Eq. 5.41 reduces to $V(\mu_{eq}) = 1 - 2\mu_{eq}$. Thus, the upper bound on the visibility is set by the mean photon number, i.e., multiphoton effects. Entanglement visibilities of more than 90% are possible when $0.39 < \mu_E/\mu_L < 2.55$ and $\mu_L < 0.0.056$. The entanglement visibility $V(\mu_E,\mu_L)$ in Eq. 5.39 is plotted for various mean photon numbers in Fig. 5.8.

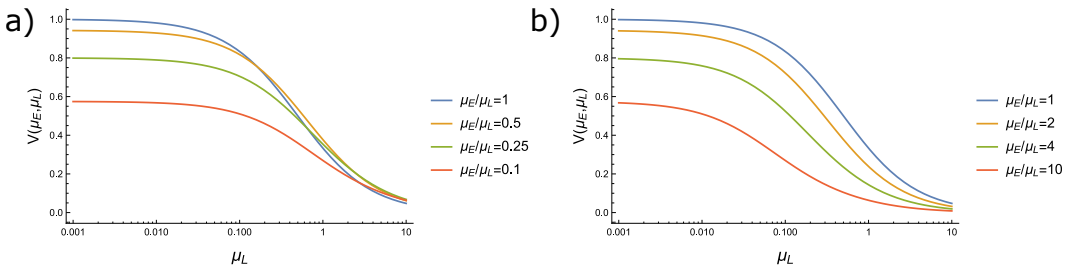

Figure 5.8: Entanglement visibility as a function of mean photon number for a) $\mu_E/\mu_L \geq 1$ and b) $\mu_E/\mu_L \leq 1$ with $\tau_A = \tau_B = 1/\sqrt{2}$.

5.5 Discussion

We have demonstrated that a time-bin entanglement source based on a mode-locked laser, spectral multiplexing and low-jitter detectors produces high entangled photon rates suitable for QKD or advanced quantum networks. The distillable entanglement rate, achievable secret key rate, and visiblilities of this source are highly competitive relative to other multiplexed entanglement distribution systems [10, 9, 31, 24, 23]. Still, there is potential to increase rates beyond those measured here with some straightforward changes to the setup. First, a higher power EDFA-amplified SHG

rate metric (μ at max)	1 Channel	8 Channels	16 Channels	60 Channels
coincidence rate, C_{AB} (0.014)	0.755	5.41	11.6	34.9
log negativity, C_N (0.010)	0.600	4.30	9.19	27.7
coherent info., C_I (0.006)	0.345	2.47	5.28	15.9
secret key rate, SKR (0.007)	0.309	2.21	4.73	14.3

Table 5.1: Per-channel predicted maximum values for the 4 rate metrics are shown in the '1 Channel' column. Depending on the metric, the maxima are achieved for different pump powers μ. The μ value that maximizes each metric is shown in parenthesis on the left.

module or tapered amplifier may be used. With this, we predict a single channel pair could sustain rates up to those specified in the first column of Table 5.1. These metrics all depend on both entanglement quality and coincidence rate C_{AB}. Due to the trade-off between C_{AB} and entanglement quality or visibility, they all reach maximum values for particular pump powers. Our measurements of 8 channel and 16 channel configurations imply the approximately multiplicative scalings in columns 2 and 3 of Table 5.1, as coincidence rates of these channels pairs are all withing 27% of each other. From measurements of the SPDC spectrum, it is also possible to extrapolate rates to a 60-channel 100 GHz DWDM configuration that includes channels spanning the L, C, and S ITU bands. This configuration could sustain 34.9 MHz total coincidence rate, and a distillable entanglement rate between 27.7 (C_N) and 15.9 Mebits/s (C_I). These rates are impressive considering they are achievable with existing SNSPDs and other technology.

The ratio of singles rates S_A, S_B to coincidence rates C_{AB} are high in this system due to the relatively wide-band JSI and narrow filters. Each DWDM channel at Alice picks up a large fraction of photons that can't be matched with pairs passing though the corresponding channel passband at Bob, a feature quantified by the δ factor. The high singles rates lead to accidental coincidences from mutually incompatible spectral modes that lower visibility and load the detectors with useless counts. However, there is potential to mitigate these extra counts by embedding the nonlinear crystal undergoing SPDC in a cavity that enhances emission at the center frequencies of multiple DWDM channels [37, 38, 39]. Also, there are other approaches to achieving such intensity islands that require dispersion engineering [40, 41]. With such periodically enhanced emission, the resulting JSI would exhibit a series of intensity islands lying along the energy-matching anti-diagonal, easily

separable with DWDMs at Alice and Bob. The photon flux for each each channel would originate primarily from these islands covered by both signal and idler DWDM passbands, resulting in a higher ratio of coincidences to singles. The probability of accidental coincidences C_{Acc} would be lower, and therefore bring the decrease of visibility with μ more in line with the modeled V_C data in Fig. 5.3. We intend for the V_C construction to represent how visibility would degrade primarily due to multi-pair effects, assuming accidental coincidences from incompatible spectral modes could be mitigated. The more gradual decrease in visibility with μ would enable substantially higher maximum rate metrics than those in Table 5.1.

This source is a fundamental building block for future space-to-ground and ground-based quantum networks. It leverages the strengths of the latest SNSPD developments–namely simultaneous high count rates, low jitter and high efficiency–and in doing so adopts interferometers and DWDM systems that are compact, stable and accessible. By elevating the system clock rate to 4.09 GHz and shrinking the time bin size to 80 ps, we have demonstrated a new state of the art in quantum communication that enables adoption of mature and extensively developed technologies from classical optical networks. Also, the spectral multiplexing methods used here are potentially compatible with those demonstrated in broadband quantum memories [42] and optical quantum computing [43].

References

[1] Peter W. Shor. "Polynomial-Time Algorithms for Prime Factorization and Discrete Logarithms on a Quantum Computer." In: SIAM Journal on Computing 26.5 (1997), pp. 1484–1509. DOI: 10.1137/S0097539795293172. eprint: https://doi.org/10.1137/S0097539795293172. URL: https://doi.org/10.1137/S0097539795293172.

[2] Michael A. Nielsen and Isaac L. Chuang. Quantum computation and quantum information. Cambridge university press, 2010.

[3] Stephanie Wehner, David Elkouss, and Ronald Hanson. "Quantum internet: A vision for the road ahead." In: Science 362.6412 (2018), eaam9288.

[4] Charles H. Bennett, Gilles Brassard, Claude Crépeau, Richard Jozsa, Asher Peres, and William K. Wootters. "Teleporting an unknown quantum state via dual classical and Einstein-Podolsky-Rosen channels." In: Phys. Rev. Lett. 70 (13 Mar. 1993), pp. 1895–1899. DOI: 10.1103/PhysRevLett.70.1895. URL: https://link.aps.org/doi/10.1103/PhysRevLett.70.1895.

[5] Raju Valivarthi, Samantha I. Davis, Cristián Peña, et al. "Teleportation Systems Toward a Quantum Internet." In: PRX Quantum 1 (2 Dec. 2020), p. 020317. DOI:

10.1103/PRXQuantum.1.020317. URL: https://link.aps.org/doi/10.1103/PRXQuantum.1.020317.

[6] Jian-Wei Pan, Dirk Bouwmeester, Harald Weinfurter, and Anton Zeilinger. "Experimental Entanglement Swapping: Entangling Photons That Never Interacted." In: Phys. Rev. Lett. 80 (18 May 1998), pp. 3891–3894. DOI: 10.1103/PhysRevLett.80.3891. URL: https://link.aps.org/doi/10.1103/PhysRevLett.80.3891.

[7] S. L. N. Hermans, M. Pompili, H. K. C. Beukers, S. Baier, J. Borregaard, and R. Hanson. "Qubit teleportation between non-neighbouring nodes in a quantum network." In: Nature 605.7911 (May 2022), pp. 663–668. ISSN: 1476-4687. DOI: 10.1038/s41586-022-04697-y. URL: https://doi.org/10.1038/s41586-022-04697-y.

[8] Yoann Pelet, Grégory Sauder, Mathis Cohen, Laurent Labonté, Olivier Alibart, Anthony Martin, and Sébastien Tanzilli. "Operational entanglement-based quantum key distribution over 50 km of real-field optical fibres." In: arXiv:2207.14707 (2022). URL: https://arxiv.org/abs/2207.14707.

[9] Muneer Alshowkan, Joseph M. Lukens, Hsuan-Hao Lu, Brian T. Kirby, Brian P. Williams, Warren P. Grice, and Nicholas A. Peters. "Broadband polarization-entangled source for C+L-band flex-grid quantum networks." In: Opt. Lett. 47.24 (Dec. 2022), pp. 6480–6483. DOI: 10.1364/OL.471363. URL: https://opg.optica.org/ol/abstract.cfm?URI=ol-47-24-6480.

[10] Sebastian Philipp Neumann, Mirela Selimovic, Martin Bohmann, and Rupert Ursin. "Experimental entanglement generation for quantum key distribution beyond 1 Gbit/s." In: Quantum 6 (Sept. 2022), p. 822. ISSN: 2521-327X. DOI: 10.22331/q-2022-09-29-822. URL: https://doi.org/10.22331/q-2022-09-29-822.

[11] Simone Atzeni, Adil S. Rab, Giacomo Corrielli, Emanuele Polino, Mauro Valeri, Paolo Mataloni, Nicolò Spagnolo, Andrea Crespi, Fabio Sciarrino, and Roberto Osellame. "Integrated sources of entangled photons at the telecom wavelength in femtosecond-laser-written circuits." In: Optica 5.3 (2018), pp. 311–314.

[12] Chang-Wei Sun, Su-Heng Wu, Jia-Chen Duan, Jian-Wei Zhou, Jun-Lei Xia, Ping Xu, Zhenda Xie, Yan-Xiao Gong, and Shi-Ning Zhu. "Compact polarization-entangled photon-pair source based on a dual-periodically-poled Ti: LiNbO 3 waveguide." In: Optics letters 44.22 (2019), pp. 5598–5601.

[13] Wen-Zhao Liu, Ming-Han Li, Sammy Ragy, Si-Ran Zhao, Bing Bai, Yang Liu, Peter J Brown, Jun Zhang, Roger Colbeck, Jingyun Fan, et al. "Device-independent randomness expansion against quantum side information." In: Nature Physics 17.4 (2021), pp. 448–451.

[14] Florian Kaiser, Lutfi Arif Ngah, Amandine Issautier, Tom Delord, Djeylan Aktas, MP De Micheli, A Kastberg, L Labonté, O Alibart, A Martin, et al. "Polarization entangled photon-pair source based on quantum nonlinear photonics and interferometry." In: Optics Communications 327 (2014), pp. 7–16.

[15] Ali Anwar, Chithrabhanu Perumangatt, Fabian Steinlechner, Thomas Jennewein, and Alexander Ling. "Entangled photon-pair sources based on three-wave mixing in bulk crystals." In: Review of Scientific Instruments 92.4 (2021).

[16] Sebastian Philipp Neumann, Thomas Scheidl, Mirela Selimovic, Matej Pivoluska, Bo Liu, Martin Bohmann, and Rupert Ursin. "Model for optimizing quantum key distribution with continuous-wave pumped entangled-photon sources." In: Physical Review A 104.2 (2021), p. 022406.

[17] I. Marcikic, H. de Riedmatten, W. Tittel, V. Scarani, H. Zbinden, and N. Gisin. "Time-bin entangled qubits for quantum communication created by femtosecond pulses." In: Phys. Rev. A 66 (6 Dec. 2002), p. 062308. DOI: 10.1103/PhysRevA.66.062308. URL: https://link.aps.org/doi/10.1103/PhysRevA.66.062308.

[18] Dong-Dong Li, Song Gao, Guo-Chun Li, et al. "Field implementation of long-distance quantum key distribution over aerial fiber with fast polarization feedback." In: Opt. Express 26.18 (Sept. 2018), pp. 22793–22800. DOI: 10.1364/OE.26.022793. URL: https://opg.optica.org/oe/abstract.cfm?URI=oe-26-18-22793.

[19] Erik Fitzke, Lucas Bialowons, Till Dolejsky, Maximilian Tippmann, Oleg Nikiforov, Thomas Walther, Felix Wissel, and Matthias Gunkel. "Scalable Network for Simultaneous Pairwise Quantum Key Distribution via Entanglement-Based Time-Bin Coding." In: PRX Quantum 3 (2 May 2022), p. 020341. DOI: 10.1103/PRXQuantum.3.020341. URL: https://link.aps.org/doi/10.1103/PRXQuantum.3.020341.

[20] Jeongwan Jin, Jean-Philippe Bourgoin, Ramy Tannous, Sascha Agne, Christopher J. Pugh, Katanya B. Kuntz, Brendon L. Higgins, and Thomas Jennewein. "Genuine time-bin-encoded quantum key distribution over a turbulent depolarizing free-space channel." In: Opt. Express 27.26 (Dec. 2019), pp. 37214–37223. DOI: 10.1364/OE.27.037214. URL: https://opg.optica.org/oe/abstract.cfm?URI=oe-27-26-37214.

[21] Christoph Simon, Mikael Afzelius, Jürgen Appel, A. Boyer de La Giroday, S. J. Dewhurst, Nicolas Gisin, C. Y. Hu, F. Jelezko, Stefan Kröll, J. H. Müller, et al. "Quantum memories: a review based on the European integrated project "qubit applications (QAP)"." In: The European Physical Journal D 58 (2010), pp. 1–22.

[22] Marco Colangelo, Boris Korzh, Jason P. Allmaras, et al. "Impedance-Matched Differential Superconducting Nanowire Detectors." In: Phys. Rev. Appl. 19 (4 Apr. 2023), p. 044093. DOI: 10.1103/PhysRevApplied.19.044093. URL: https://link.aps.org/doi/10.1103/PhysRevApplied.19.044093.

[23] Djeylan Aktas, Bruno Fedrici, Florian Kaiser, Tommaso Lunghi, Laurent Labonté, and Sébastien Tanzilli. "Entanglement distribution over 150 km in wavelength division multiplexed channels for quantum cryptography." In: Laser & Photonics Reviews 10.3 (2016), pp. 451–457. DOI: https://doi.org/10.1002/lpor.201500258. eprint: https://onlinelibrary.wiley.com/doi/pdf/10.1002/lpor.201500258. URL: https://onlinelibrary.wiley.com/doi/abs/10.1002/lpor.201500258.

[24] Sören Wengerowsky, Siddarth Koduru Joshi, Fabian Steinlechner, Hannes Hübel, and Rupert Ursin. "An entanglement-based wavelength-multiplexed quantum communication network." In: Nature 564.7735 (2018), pp. 225–228.

[25] Félicien Appas, Florent Baboux, Maria I. Amanti, Aristide Lemaítre, Fabien Boitier, Eleni Diamanti, and Sara Ducci. "Flexible entanglement-distribution network with an AlGaAs chip for secure communications." In: npj Quantum Information 7.1 (July 2021), p. 118. ISSN: 2056-6387. DOI: 10.1038/s41534-021-00454-7. URL: https://doi.org/10.1038/s41534-021-00454-7.

[26] Muneer Alshowkan, Philip G. Evans, Brian P. Williams, Nageswara S. V. Rao, Claire E. Marvinney, Yun-Yi Pai, Benjamin J. Lawrie, Nicholas A. Peters, and Joseph M. Lukens. "Advanced architectures for high-performance quantum networking." In: J. Opt. Commun. Netw. 14.6 (June 2022), pp. 493–499. DOI: 10.1364/JOCN.450201. URL: https://opg.optica.org/jocn/abstract.cfm?URI=jocn-14-6-493.

[27] Andrew Mueller, Emma E. Wollman, Boris Korzh, Andrew D. Beyer, Lautaro Narvaez, Ryan Rogalin, Maria Spiropulu, and Matthew D. Shaw. "Time-walk and jitter correction in SNSPDs at high count rates." In: Applied Physics Letters 122.4 (Jan. 2023). 044001. ISSN: 0003-6951. DOI: 10.1063/5.0129147. eprint: https://pubs.aip.org/aip/apl/article-pdf/doi/10.1063/5.0129147/16690545/044001_1_online.pdf. URL: https://doi.org/10.1063/5.0129147.

[28] Yoon-Ho Kim and Warren P. Grice. "Measurement of the spectral properties of the two-photon state generated via type II spontaneous parametric downconversion." In: Optics Letters 30.8 (2005), pp. 908–910.

[29] Takahiro Inagaki, Nobuyuki Matsuda, Osamu Tadanaga, Masaki Asobe, and Hiroki Takesue. "Entanglement distribution over 300 km of fiber." In: Opt. Express 21.20 (Oct. 2013), pp. 23241–23249. DOI: 10.1364/OE.21.023241. URL: https://opg.optica.org/oe/abstract.cfm?URI=oe-21-20-23241.

[30] P. Toliver, J. M. Dailey, A. Agarwal, and N. A. Peters. "Continuously active interferometer stabilization and control for time-bin entanglement distribution." In: Opt. Express 23.4 (Feb. 2015), pp. 4135–4143. DOI: 10.1364/OE.23.004135. URL: https://opg.optica.org/oe/abstract.cfm?URI=oe-23-4-4135.

[31] Jin-Hun Kim, Jin-Woo Chae, Youn-Chang Jeong, and Yoon-Ho Kim. "Quantum communication with time-bin entanglement over a wavelength-multiplexed fiber network." In: APL Photonics 7.1 (2022), p. 016106. DOI: 10.1063/5.0073040. eprint: https://doi.org/10.1063/5.0073040. URL: https://doi.org/10.1063/5.0073040.

[32] Krishnan R. Parameswaran, Jonathan R. Kurz, Rostislav V. Roussev, and Martin M. Fejer. "Observation of 99% pump depletion in single-pass second-harmonic generation in a periodically poled lithium niobate waveguide." In: Optics letters 27.1 (2002), pp. 43–45.

[33] Florian Kaiser, Bruno Fedrici, Alessandro Zavatta, Virginia d'Auria, and Sébastien Tanzilli. "A fully guided-wave squeezing experiment for fiber quantum networks." In: Optica 3.4 (2016), pp. 362–365.

[34] Samantha I. Davis, Andrew Mueller, Raju Valivarthi, Nikolai Lauk, Lautaro Narváez, Boris Korzh, Andrew D. Beyer, Olmo Cerri, Marco Colangelo, Karl K. Berggren, et al. "Improved heralded single-photon source with a photon-number-resolving superconducting nanowire detector." In: Physical Review Applied 18.6 (2022), p. 064007.

[35] Masahiro Takeoka, Rui-Bo Jin, and Masahide Sasaki. "Full analysis of multi-photon pair effects in spontaneous parametric down conversion based photonic quantum information processing." In: New Journal of Physics 17.4 (2015), p. 043030.

[36] Samantha I. Davis, Andrew Mueller, Raju Valivarthi, et al. "Improved Heralded Single-Photon Source with a Photon-Number-Resolving Superconducting Nanowire Detector." In: Phys. Rev. Appl. 18 (6 Dec. 2022), p. 064007. DOI: 10.1103/PhysRevApplied.18.064007. URL: https://link.aps.org/doi/10.1103/PhysRevApplied.18.064007.

[37] Enrico Pomarico, Bruno Sanguinetti, Nicolas Gisin, Robert Thew, Hugo Zbinden, Gerhard Schreiber, Abu Thomas, and Wolfgang Sohler. "Waveguide-based OPO source of entangled photon pairs." In: New Journal of Physics 11.11 (Nov. 2009), p. 113042. DOI: 10.1088/1367-2630/11/11/113042. URL: https://dx.doi.org/10.1088/1367-2630/11/11/113042.

[38] T. Brydges, A. S. Raja, A. Gelmini, et al. "Integrated photon-pair source with monolithic piezoelectric frequency tunability." In: Phys. Rev. A 107 (5 May 2023), p. 052602. DOI: 10.1103/PhysRevA.107.052602. URL: https://link.aps.org/doi/10.1103/PhysRevA.107.052602.

[39] Oliver Slattery, Lijun Ma, Kevin Zong, and Xiao Tang. "Background and review of cavity-enhanced spontaneous parametric down-conversion." In: Journal of Research of the National Institute of Standards and Technology 124 (2019), p. 1.

[40] Christopher L. Morrison, Francesco Graffitti, Peter Barrow, Alexander Pickston, Joseph Ho, and Alessandro Fedrizzi. "Frequency-bin entanglement from domain-engineered down-conversion." In: APL Photonics 7.6 (2022).

[41] CJ Xin, Jatadhari Mishra, Changchen Chen, Di Zhu, Amirhassan Shams-Ansari, Carsten Langrock, Neil Sinclair, Franco NC Wong, MM Fejer, and Marko Lončar. "Spectrally separable photon-pair generation in dispersion engineered thin-film lithium niobate." In: Optics Letters 47.11 (2022), pp. 2830–2833.

[42] Neil Sinclair, Erhan Saglamyurek, Hassan Mallahzadeh, et al. "Spectral multiplexing for scalable quantum photonics using an atomic frequency comb quantum memory and feed-forward control." en. In: Phys. Rev. Lett. 113.5 (Aug. 2014), p. 053603.

[43] Joseph M. Lukens and Pavel Lougovski. "Frequency-encoded photonic qubits for scalable quantum information processing." In: Optica 4.1 (2017), pp. 8–16.

Chapter 6

ON-CHIP PHASED ARRAY SYSTEM FOR NON-CLASSICAL LIGHT

This chapter includes the work published as:

[1] Volkan Gurses, Samantha I. Davis, Raju Valivarthi, Neil Sinclair, Maria Spiropulu, and Ali Hajimiri. "An on-chip phased array for non-classical light." In: Nature Communications 16.1 (2025), p. 6849.

[1] Volkan Gurses, Samantha I. Davis, Ali Hajimiri, and Maria Spiropulu. "Quantum Phased Arrays." Patent Application Filed: 2023-06-2023. 2023.

6.1 Introduction

The science and engineering of quantum systems have expanded in the last two decades to realize technologies that can manipulate quantum information [1, 2, 3]. Miniaturization and scaling of quantum systems with on-chip integration are crucial to accelerate their use cases toward practical applications [4, 5]. Free-space-interfaced integrated systems enable wireless technologies including free-space sensors [6, 7], imagers [8, 9], and communication transceivers [10, 11]. The expansion from wired to wireless links for classical information technologies led to numerous advancements from mobile devices [12] to the Internet-of-Things [13] and facilitated the proliferation of information technologies [14]. For a similar transformation to happen for quantum information technologies, the networking of integrated quantum systems needs to move beyond wired links [15, 16, 17, 18].

In most wireless links, phased arrays are used to enable spatiotemporally configurable signal reception or transmission with high signal gain [19, 20]. A phased array is a coherent array of antenna elements capable of transmitting or receiving electromagnetic waves. Through the interference of the electromagnetic waves transmitted or received by each element, arbitrary wavefronts can be engineered [19, 20]. The first phased arrays were implemented to control electromagnetic waves at radio frequencies [21], facilitating RADAR [7], wireless communications [11], remote sensing [22] and radio astronomy [23]. In the last decade, advancements in nanophotonics enabled large-scale phased arrays at optical frequencies [24], opening

up applications including LiDAR [25, 26], 3D imaging [8], and free-space optical communications [10].

All previous developments in reconfigurable antenna arrays have been achieved only with classical states of light. Extending phased arrays to the non-classical domain [27, 28] could enable potentially interesting use cases for quantum information technologies, such as wirelessly-interfaced quantum systems (Fig. 6.1a) and reconfigurable wireless quantum links (Fig. 6.1b). However, due to the high coupling loss and noise in conventional transceivers, there has not been a phased array system capable of interfacing with non-classical light.

In this work, we realize a phased array system-on-chip with quantum-limited performance that can receive and control non-classical light. The 32-channel silicon photonic-electronic system provides a low-loss, low-noise and scalable free-space-to-chip interface for non-classical light. Simultaneous readout of the signals across all 32 channels enables 32-pixel imaging of squeezed light transmitted over free space. Coherent manipulation of these signals allows us to establish reconfigurable free-space links for squeezed light. In Appendix D, we also report a proof-of-concept demonstration of cluster state generation with our system to illustrate the potential of large-scale, quantum-limited photonic-electronic systems-on-chip for information processing.

6.2 Quantum phased array theory

A phased array receiving non-classical light is illustrated in Fig. 6.1c. A quantized electromagnetic field is transmitted over free space to a phased array receiver with N elements. The field incident to the aperture is represented by the local bosonic operator $\hat{a}_{\text{in}}(\rho)$, where ρ represents the spatial aperture coordinates. Due to diffraction over free space, the incident field is spread out over the aperture and a portion of the field is coupled onto each antenna element. The antenna elements define a set of N pixel modes, $\{\mathcal{E}_j(\rho)\}$, each with an associated bosonic operator $\hat{a}_{\mathcal{E}_j} = \int \mathcal{E}_j^*(\rho)\hat{a}_{\text{in}}(\rho)d\rho$. The pixel modes are combined after applying a phase, ϕ_j, and amplitude weight, g_j, to each mode. The combined output field is described by,

$$\hat{a}_{\text{out}} = \sum_j g_j e^{i\phi_j}\hat{a}_{\mathcal{E}_j} = \int \mathcal{A}^*(\rho)\hat{a}_{\text{in}}(\rho)d\rho, \tag{6.1}$$

where $\mathcal{A}(\rho) = \sum_j g_j e^{-i\phi_j}\mathcal{E}_j(\rho)$. The set of applied phases, amplitude weights, and pixel modes gives rise to a reconfigurable array mode function $\mathcal{A}(\rho)$ that can be

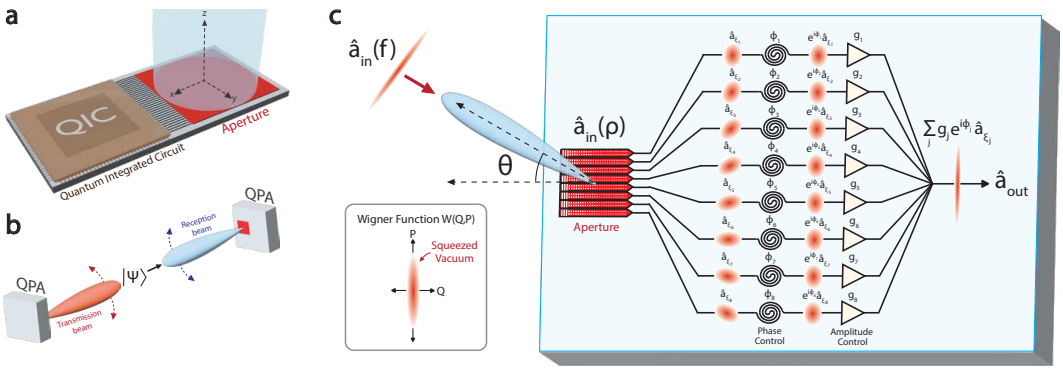

Figure 6.1: Quantum phased arrays. a) Conceptual illustration of a wirelessly-interfaced quantum integrated circuit. b) Conceptual illustration of a wireless quantum link with phased arrays. A phased array transmitter transmits a quantum state $|\Psi\rangle$ to a phased array receiver over free space. c) Conceptual illustration of beamforming on squeezed light with an eight-element phased array receiver. An input field ($\hat{a}_{\text{in}}(f)$) in a squeezed state is transmitted to a phased array receiver over free space. The field incident to the aperture ($\hat{a}_{\text{in}}(\rho)$) is spread out over the aperture with a uniform phasefront, resulting in high geometric loss per pixel mode. After applying a phase (ϕ_j) and amplitude weight (g_j) to each pixel mode ($\hat{a}_{\mathcal{E}_j}$), the pixel modes are combined to recover the original squeezed state. Squeezed states are represented by their Wigner functions in phase space, where Q and P represent the field quadratures (see inset).

used to engineer the wavefunction of the incident field (see theory in Methods) [29, 30].

The output field can be expressed in terms of the angle θ from normal incidence to the aperture,

$$\hat{a}_{\text{out}} \propto \int \text{SF}(f)\hat{a}_{\text{in}}(f)df, \tag{6.2}$$

where $f = \sin\theta/\lambda$, $\text{SF}(f) = \int \exp(-i2\pi\rho \cdot f)\mathcal{A}(\rho)d\rho$, and $\hat{a}_{\text{in}}(f)$ represents the input field in the far-field limit. In Eq. 6.2, $\text{SF}(f)$ corresponds to the space factor, or array factor for discrete antenna elements, in classical antenna theory [19, 20]. Beamforming refers to the calibration of the phase settings to form a main lobe, or beam, in the radiation pattern at a desired angle [31]. After beamforming, the beam can be steered to a different angle by applying a progressive phase shift to the elements [19, 20] (see theory in Methods).

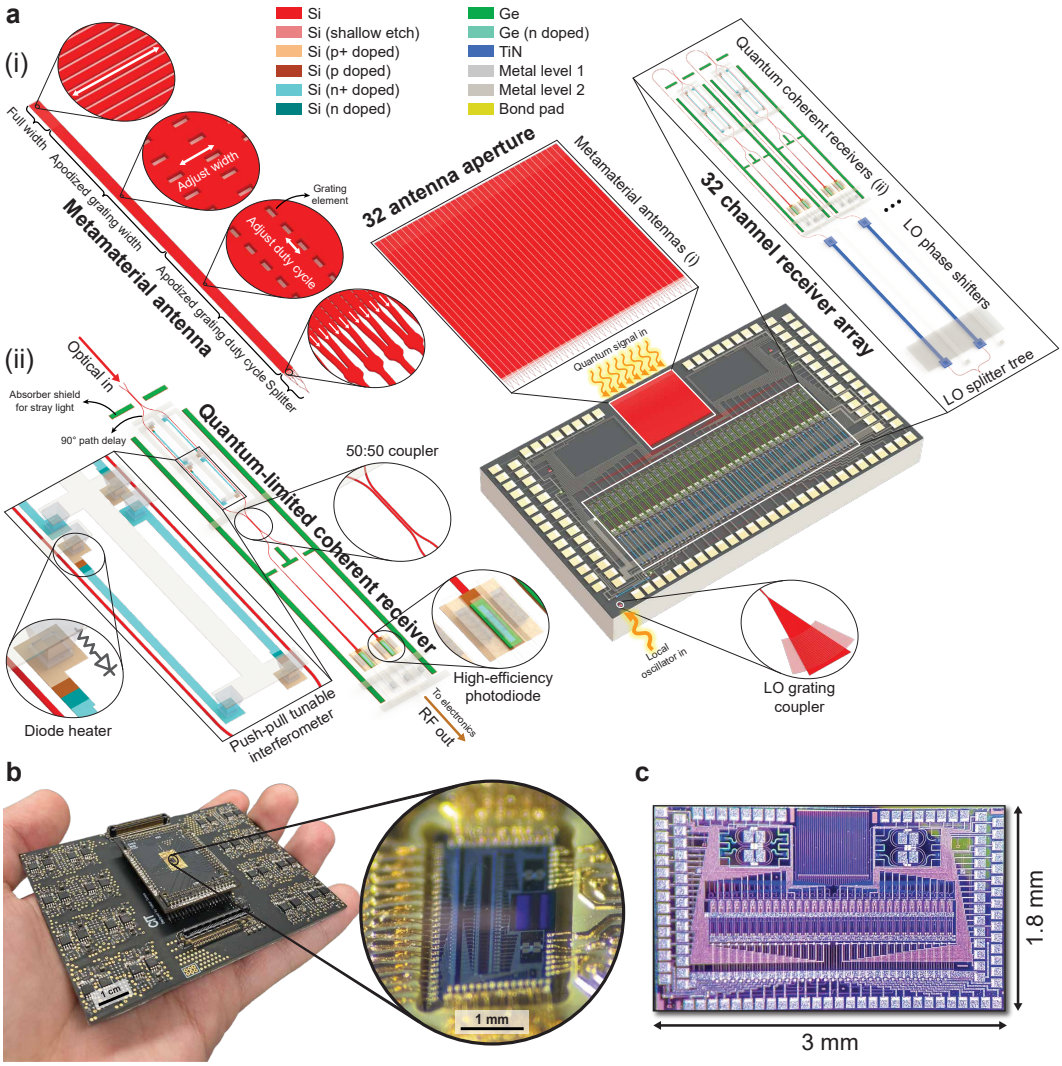

Figure 6.2: Photonic-electronic system. a) Diagram of the photonic integrated circuit (PIC) illustrating the key building blocks, including i) the metamaterial antenna (MMA) and ii) the quantum(-limited) coherent receiver (QRX). An array of 32 MMAs couple non-classical light from free space to on-chip waveguides, followed by an array of 32 QRXs that measure the light via homodyne detection. An array of 32 thermo-optic phase shifters (TOPS) applies a phase shift to the local oscillator at each QRX. b) Image of our PIC packaged with co-designed electronics, demonstrating the compact form factor of the system. The PIC is wirebonded to an interposer, which is plugged into a radio-frequency motherboard that hosts a 32-channel TIA array and the CMRR auto-correction circuit. c) Die photo of the PIC showing a footprint of 3 mm $\times$ 1.8 mm.

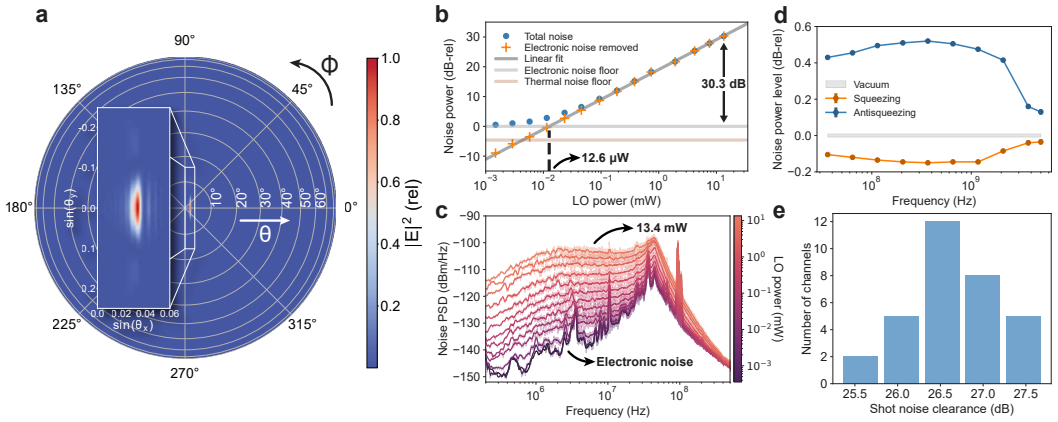

Figure 6.3: System characterization. a) Simulated far-field radiation pattern of the antenna. The radiation pattern has no grating lobes, namely scattering to higher diffraction orders, showing that the MMA is sub-wavelength engineered for diffraction-limited performance. b) Noise powers of a single-channel QRX in the 32-channel system integrated over its 3-dB bandwidth for different LO powers, characterizing the shot noise clearance and LO power knee. A linear regression fit is applied to the data above the LO power knee to obtain a near-unity gradient of 1.004±0.006, showing that the QRX noise floor is limited by the signal shot noise. c) Output noise spectra of a single QRX for different LO powers ranging from 0 to 13.4 mW, characterizing the shot-noise-limited bandwidth. d) Squeezed light detection with a single QRX using a high-speed TIA, showing squeezing and antisqueezing measured up to 5 GHz with a shot-noise-limited bandwidth of 3.70 GHz. e) Shot noise clearance distribution across all channels measured with 1.54 mW LO power at each channel.

6.3 Photonic-electronic system

We realize a proof-of-concept phased array system-on-chip that operates at the quantum-limited sensitivity and interfaces with non-classical light to demonstrate different functionalities of our concept. The system is implemented using a commercial silicon photonics process packaged with silicon electronics, as shown in Fig. 6.2. The system is designed to realize as many functions on chip as possible, with more than 1000 functional components integrated on a 3 mm × 1.8 mm footprint.

Compared to conventional phased arrays, our phased array system needs to be designed to introduce as little loss and noise as possible to minimize quantum decoherence. The most significant loss for free-space-interfaced systems is geometric loss due to the mode mismatch between an incident beam and the receiving aperture

[19, 32]. In the case of a collimated beam, the mode mismatch is caused by beam divergence. To mitigate this, the aperture needs to be large enough to be able to match the amplitude and phase profile of the incident beam. Phased arrays enable arbitrarily large apertures that can be mode matched by arraying multiple antennas and coherently combining the received signals [19, 20]. Our system demonstrates this for squeezed light by arraying 32 nanophotonic antennas. To minimize the loss, the aperture also needs to be fully filled without any gaps in the active area. We achieve this by demonstrating a metamaterial antenna (MMA) design that acts as a rectangular building block and can be sized to fill the aperture (see chip design in Methods).

An array of 32 MMAs fill an aperture with a 550×550 μm^2 footprint and more than 500,000 sub-wavelength-engineered grating elements, each of which scatter light to interface with free space. This active area is large enough for low-loss free-space coupling to the chip over meter-scale distances with off-the-shelf fiber collimators.

The simulated 3D radiation pattern for the MMA design is shown in Fig. 6.3a. The aperture can be characterized by its geometric loss given an incident beam and its insertion loss, which includes the propagation loss in the MMA and loss due to downward scattering. The MMA has a measured (simulated) insertion loss of 3.82 dB (3.78 dB). The 32-antenna aperture mode matched to a collimated beam with a beam diameter of 200 μm, which is the beam diameter used in the experiments, has a measured (simulated) geometric loss of 1.14 dB (1.35 dB). This is at least an order of magnitude lower than those of the previously reported on-chip aperture designs [33, 34], which affords interfacing free-space quantum optics with photonic integrated circuits (PICs).

The waveguides after the antennas are path-length matched and are connected to 32 quantum(-limited) coherent receivers (QRXs). Each QRX comprises a push-pull tunable Mach-Zehnder interferometer (MZI), a pair of balanced Ge photodiodes, a transimpedance amplifier (TIA), and a common-mode rejection ratio (CMRR) auto-correction circuit, whose output is fed back to the MZIs to automatically correct the imperfect CMRR of each QRX caused by the fabrication variations on the PIC (see chip design in Methods). The MZI interferes a signal field with a strong local oscillator (LO) for homodyne detection. The LO is coupled to the chip with a grating coupler and is split into 32 channels with a 1-to-32 splitter tree. The LO input to each channel hosts a thermo-optic phase shifter (TOPS) for phase tuning. Each output of the MZI is sent to a photodiode, and the currents at the outputs of

the photodiodes are subtracted and amplified by the TIA.

The performance of a QRX is quantified by its insertion loss, common-mode rejection ratio (CMRR), shot noise clearance (SNC), LO power knee (P_{knee}), 3-dB bandwidth (BW_{3dB}) and shot-noise-limited bandwidth (BW_{shot}) [35, 36, 37, 15]. We first measure a single channel of the 32-channel QRX array used in the experiments to characterize these specifications, as shown in Fig. 6.3b,c. The measured insertion loss is 1.58 dB, limited by the quantum efficiency of the photodiodes. A time-averaged CMRR over 10 seconds is measured to be 90.2 dB at 1.1 MHz. The measured SNC is 30.3 dB, P_{knee} is 12.6 μW, BW_{3dB} is 10.4 MHz and BW_{shot} is 381 MHz.

While this gives one of the highest SNCs demonstrated with an integrated coherent receiver in the literature [35, 15], the measured bandwidth is relatively low due to the intrinsic trade-off between noise floor and bandwidth in the TIA design. To show the high-speed detection capability of our PIC with on-chip photodiodes, a single channel of the PIC is packaged with a bare die TIA, and the same characterization sweeps are performed [38]. In this high-bandwidth configuration, squeezed vacuum is injected as signal, and noise power fluctuations below and above the shot noise floor are measured up to 5 GHz with a BW_{shot} of 3.70 GHz, as shown in Fig. 6.3d.

Furthermore, we characterize all 32 channels while they work simultaneously. With 1.54 mW of LO power, the SNCs across all of the channels are measured, and the SNC distribution is plotted in a histogram as seen in Fig. 6.3e. The SNC variation is low, with a median SNC of 26.6 dB, a minimum SNC of 25.3 dB, and a maximum SNC of 27.7 dB. All channels operate well into the shot noise limited regime, showing that the quantum-limited performance of the QRX is achieved at scale.

6.4 Squeezed light imaging

We first operate the system as a 32-pixel quantum-limited coherent imager. Broadband squeezed vacuum is generated off-chip using a fiber-coupled periodically poled lithium niobate (PPLN) waveguide at a central wavelength of 1550 nm, as shown in Fig. 6.4a (see squeezed light generation in Methods). The squeezed light is sent to a fiber collimator with a 200 μm beam diameter and is transmitted to the chip over free space. At the chip aperture, the squeezed light is spatially distributed across the 32 antennas with a Gaussian amplitude profile, $u_0(\rho)$. A portion of the squeezed light is coupled into each MMA, which has the associated pixel mode $\mathcal{E}_j(\rho)$ and bosonic

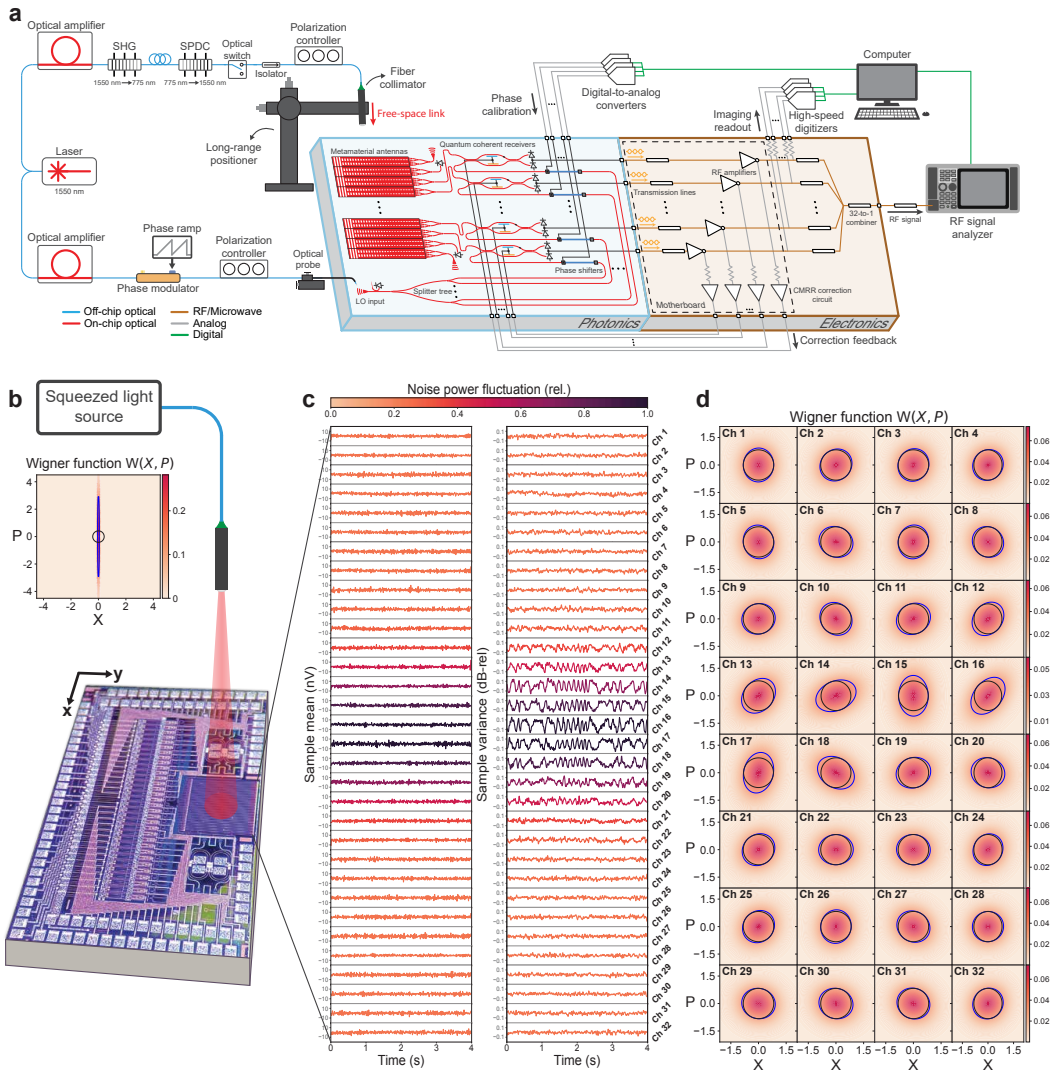

Figure 6.4: Squeezed light imaging. a) Experimental setup for the squeezed light measurements. Squeezed light is generated off-chip and transmitted over free space to the chip (blue, Photonics), which is interfaced with electronics (orange, Electronics) for processing. b) Illustration of squeezed light transmitted to the chip, showing the Wigner function of the generated squeezed vacuum state as a function of the quadrature observables (Q, P) and the experimental squeezing parameter ($r = 1.95$). c) Sample means and variances of the channel output voltages as a function of time. For each channel, the sample variances are normalized to the mean variance. d) Wigner functions of the 32 pixel modes characterized simultaneously as a function of the squeezing parameter ($r = 1.95$), phase, and geometric efficiency for each channel. The dark and light blue contours correspond to the half-maximum points of the squeezed vacuum and vacuum states, respectively.

operator $\hat{a}_{\mathcal{E}_j}$, where $j \in \{1, \cdots, 32\}$. The pixel mode is interfered with an LO in a QRX, which outputs a voltage proportional to the phase-dependent quadrature of the pixel mode,

$$\hat{Q}_j(\phi_j) = \frac{1}{2}(\hat{a}_{\mathcal{E}_j} e^{-i\phi_j} + \hat{a}^\dagger_{\mathcal{E}_j} e^{i\phi_j}), \tag{6.3}$$

where ϕ_j is the phase of the jth pixel mode relative to the LO. For an input squeezed vacuum state, the quadrature mean is $\langle \hat{Q}_j(\phi_j) \rangle = 0$, and the quadrature variance is,

$$\mathrm{Var}\left(\hat{Q}_j(\phi_j)\right) = \frac{\eta_j}{4}(e^{-2r}\cos^2\phi_j + e^{2r}\sin^2\phi_j) + \frac{1-\eta_j}{4}, \tag{6.4}$$

where r is the squeezing parameter and η_j is the effective efficiency of channel j, which includes the effects of source loss, free-space loss dominated by geometric loss, on-chip loss, and radio-frequency (RF) loss. Here, $\phi_j = 0$ and $\phi_j = \pi/2$ correspond to the squeezed and the antisqueezed quadratures, respectively.

To image the squeezed light, the output voltages are read out to a 32-channel digitizer (see data acquisition in Methods). A 0.5 Hz phase ramp is applied to the LO off-chip to acquire voltage samples over various phases, and sample means and variances are calculated over sets of 260,000 voltage samples. The time evolution of the sample means and variances for all 32 pixel modes are shown in Fig. 6.4c. Without phase locking, thermal drifts in the fiber-optic setup give rise to nonuniform phase fluctuations on top of the phase ramp, which are coherent across all channels. The corresponding Wigner functions for the source and the pixel modes are shown in Fig. 6.4b and Fig. 6.4d, respectively (see Wigner function calculation in Methods).

6.5 Reconfigurable free-space links

Next, we operate the system as a reconfigurable quantum receiver. A QRX is used to apply a phase shift and amplitude weight to the quadrature of each pixel mode by varying the phase of the LO and the amplitude of the RF output. After coherently combining the QRX outputs, the combined RF output is a voltage proportional to the quadrature of the engineered output field, $\hat{a}_{\mathrm{out}}$ in Eq. 6.1-6.2 (see implementation in Methods),

$$\hat{Q}_{\mathrm{out}} = \sum_j g_j \hat{Q}_j(\phi_j) = \frac{1}{2}(\hat{a}_{\mathrm{out}} + \hat{a}^\dagger_{\mathrm{out}}). \tag{6.5}$$

Beamforming on squeezed light with the system is illustrated in Fig. 6.5a. After calibrating the LO phases for all 32 channels, squeezed light with $r = 0.76$ (6.61 dB

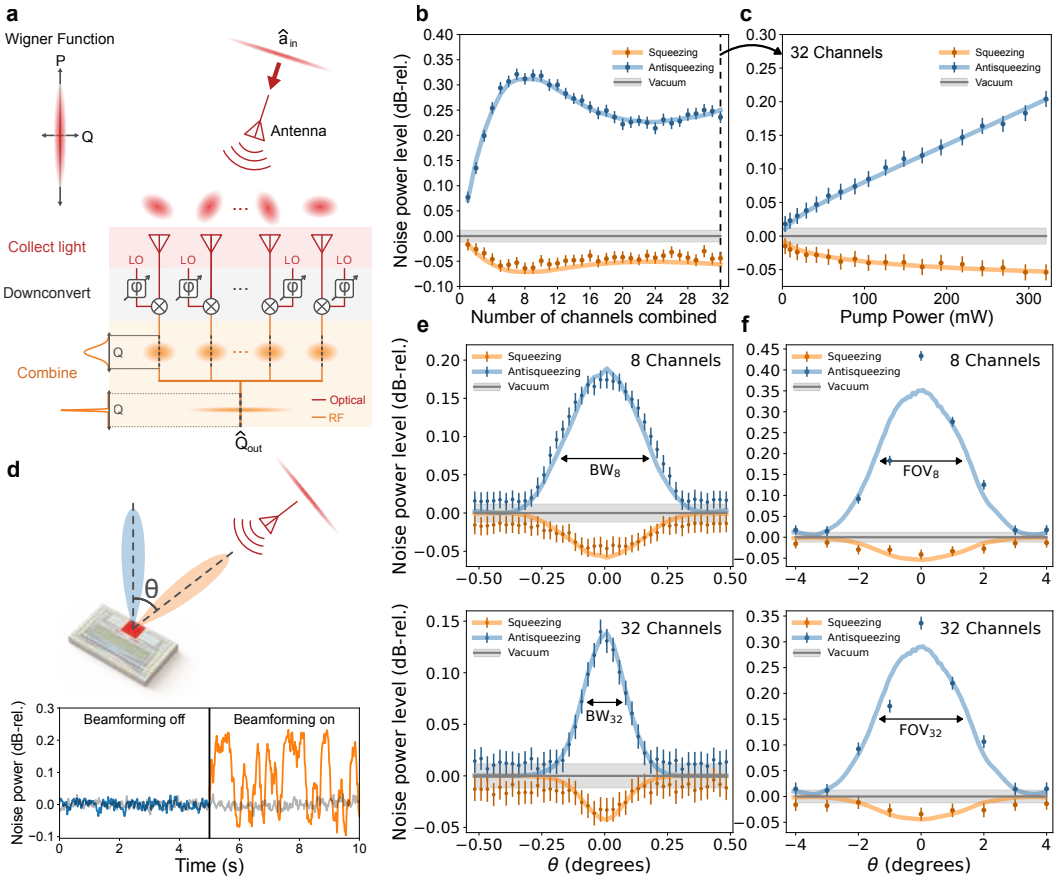

Figure 6.5: Reconfigurable free-space links. a) Conceptual illustration of beamforming on squeezed light with the chip, where $\hat{a}_{\text{in}}$ represents the input field and $\hat{Q}_{\text{out}}$ is the quadrature proportional to the combined output signal at RF. b) Squeezing and antisqueezing levels as a function of the number of combined channels relative to the vacuum level after the chip is beamformed toward the squeezed light transmitter. c) Squeezed light source characterization showing squeezing and antisqueezing levels as a function of source pump power for 32 combined channels. d) Demonstration of reconfigurable free-space links, illustrating the lack of squeezed light signal when the receiver is beamformed toward empty space (blue) and the reception of the signal when the receiver is beamformed toward the transmitter (orange). The grey trace is the vacuum signal. e) Squeezing and antisqueezing levels characterizing the beamwidth of the link for 8 and 32 combined channels. f) Squeezing and antisqueezing levels characterizing the field of view of the receiver for 8 and 32 combined channels. In b), c), e), and f), the orange and blue solid lines are fits of the data to a model obtained from the classical characterization of the corresponding measurement.

generated squeezing) is transmitted to the chip through the fiber collimator. A 1 Hz phase ramp is applied to the LO before coupling to the chip, and the outputs of the channels are coherently combined with a 32:1 RF power combiner. The combined output signal is sent to an RF signal analyzer, which measures the noise power proportional to the variance of Eq. 6.5 (see beamforming and data acquisition in Methods).

Noise powers for squeezed vacuum and vacuum states are measured for various numbers of combined channels. Disconnected channels have zero amplitude weight and connected channels have approximately uniform amplitude weights. For a given set of amplitude weights, the phase calibration step in beamforming maximizes the modal overlap of the array mode function $\mathcal{A}(\rho)$ and the squeezed input mode $u_0(\rho)$, corresponding to the geometric efficiency $\eta_g = \left|\int \mathcal{A}^*(\rho)u_0(\rho)d\rho\right|^2$. Therefore, by configuring the amplitude weights in the array mode function, the number of combined channels sets the geometric efficiency. The squeezing and antisqueezing levels relative to the shot noise level for each channel combination are shown in Fig. 6.5b. The squeezing (antisqueezing) improves from $-0.017(+0.077) \pm 0.012$ dB-rel for a single channel to $-0.064(+0.312) \pm 0.012$ dB-rel for eight combined channels, corresponding to an increase in the geometric efficiency by a factor of 4.5. For more than eight combined channels, the observed squeezing and antisqueezing decreases due to reduced modal overlap. The squeezing and antisqueezing increase again for more than 24 combined channels, most likely due to parasitic effects at RF (see channel combination and measurement characterization Methods).

After beamforming on 32 channels, we perform a source characterization to confirm that the combined RF signals correspond to the measurement of the squeezed light source. For all 32 channels combined, the squeezing and antisqueezing levels for various source pump powers (P) are shown in Fig 6.5c. The solid lines correspond to a least-squares fit of the data to a model, where the effective efficiency of the system, η, and the spontaneous parametric downconversion (SPDC) efficiency, $\mu = r/\sqrt{P}$, are taken as floating parameters. We obtain $\eta = 0.016$ and $\mu = 0.038$ $[\mathrm{mW}]^{-1/2}$, which is consistent with the independently characterized SPDC efficiency of the source (see theoretical modeling in Methods).

Establishing directional free-space links for squeezed light with our system is illustrated in Fig. 6.5d. Squeezed light is transmitted to the system over free space. First, the phased array forms a reception beam directed away from the transmitter and no light is detected (blue). The phase settings are then reconfigured by apply-

ing a linear phase mask to the LO phase shifters, which steers the reception beam toward the transmitter and forms a free-space link (orange). In the first five seconds, no squeezed light signal is observed, demonstrating successful spatial filtering. In the next five seconds, after the reception beam is electronically steered toward the transmitter, the noise power modulations of the squeezed light are observed.

The spatial selectivity, namely beamwidth, of a link is characterized in Fig. 6.5e. Phase calibration is performed for squeezed light with $r = 0.61$ (5.31 dB generated squeezing) transmitted to the chip at a normal angle of incidence. The angle of incidence (θ) of the squeezed light is swept while the chip is kept beamformed to normal incidence ($\theta = 0$). The squeezing and antisqueezing levels as a function of θ are shown in Fig. 6.5e for 8 and 32 combined channels. The beamwidths (BW_n) corresponding to 50% efficiency (3 dB loss) are 0.41±0.02 degrees and 0.20±0.02 degrees with $n = 8$ channels and $n = 32$ combined channels, respectively. The beamwidth decreases with the number of combined channels, demonstrating the expected increase in spatial selectivity as the array is scaled up [19, 20] (see measurement characterization in Methods).

The reconfigurability of the links over the field of view (FoV) of the system is demonstrated in Fig. 6.5f. At each of the nine different angles of incidence (θ), phase calibration is performed and the optimal phase settings are recorded. Squeezed light with $r = 0.91$ (7.89 dB generated squeezing) is then transmitted to the chip at each angle, and a link is programmed by applying the LO phase shifter settings that form a reception beam at the corresponding angle. The squeezing and antisqueezing levels for each angle are shown in Fig. 6.5f for 8 and 32 combined channels. The FoV for squeezed light corresponding to 50% efficiency (3 dB loss) is 2.32±0.12 degrees and 2.66±0.25 degrees with 8 channels and 32 combined channels, respectively. The FoV stays the same as the array is scaled up, matching the single antenna radiation pattern [19, 20] (see measurement characterization in Methods).

6.6 Discussion and outlook

We have demonstrated an on-chip phased array with quantum-limited performance for receiving and manipulating non-classical light in a large-scale silicon photonic-electronic system. With our system, we have demonstrated, for the first time, 32-pixel imaging of squeezed light and reconfigurable free-space-to-chip links for squeezed light. We also performed a proof-of-concept demonstration of cluster

state generation to illustrated the potential for integrated optoelectronic systems for quantum information processing. These functionalities are enabled by a fully-filled and low-loss metamaterial aperture and the first large-scale coherent receiver array capable of resolving non-classical signals, with up to 30.3 dB SNC, 90.2 dB CMRR and 3.70 GHz bandwidth.

In our work, the amount of measured squeezing was limited by ~15 dB system loss, dominated by ~8 dB off-chip source loss. Based on the improvements in component losses already demonstrated in the literature [39, 40], there is a clear path toward sub-dB (down to 0.626 dB) loss for our system.Thanks to the modular architecture of our system, the aperture can be scaled by duplicating individual channels to achieve longer-distance free-space links. Additionally, phase locking can be implemented [41], or the signal and LO can be transmitted over the same free-space channel, to remove phase fluctuations.

Together with a transmitter counterpart to our system, our approach could enable wireless quantum technologies based on phased array transceivers. Quantum-enhanced sensors could be built with phased arrays by placing a highly transmissive or reflective sample in a free-space link and imaging the sample with non-classical light [42, 43]. With the current chip, up to 18% improvement below the shot noise floor in sensitivity is possible. With 0.626 dB system loss, the sensitivity improvement could reach 87%, corresponding to 8.75 dB measured squeezing, potentially enabling practical quantum enhancement in imaging [42, 43], LiDAR [44, 45] and microscopy [46].

Wireless quantum communication networks [47] could also be built with phased array transceivers forming the nodes of a network. With our current chip, continuous-variable quantum key distribution [48] is possible with up to 3.81 Mbps secure key rate and a non-zero key rate distance of 56.3 cm. This distance could be further extended to 1.69 km and 39.2 km, limited by the atmospheric attenuation, with reticle-scale (30×30 mm^2) and wafer-scale (300×300 mm^2) apertures, respectively, putting long-distance quantum communications with chip-scale devices within reach.

6.7 Methods

Theory

Consider a quantized electromagnetic field $\hat{E}$ transmitted over free space to a phased array receiver. The field can be decomposed into positive and negative frequency

components, $\hat{E} = \hat{E}^+ + \hat{E}^-$, where $\hat{E}^+$ and $\hat{E}^-$ are Hermitian conjugates. The positive frequency component of the field at the aperture can be expressed as,

$$\hat{E}^+(\rho, t) = \sqrt{\frac{\hbar\omega}{2\epsilon_0 V}} \sum_n u_n(\rho) e^{-i\omega t} \hat{a}_{u_n}, \tag{6.6}$$

where $\rho = (x, y)$ are the transverse spatial coordinates in the aperture plane (see Fig. 6.1a), ω is the frequency, and V is the quantization volume [49, 28]. The field is expanded over a complete set of orthonormal modes $\{u_n(\rho)\}$, such as Hermite-Gaussian modes, that correspond to photon-wavefunctions in second quantization [50]. Each mode has an associated pair of bosonic operators $\hat{a}_{u_n}$ and $\hat{a}^\dagger_{u_n}$ satisfying $[\hat{a}_{u_n}, \hat{a}^\dagger_{u_m}] = \delta_{n,m}$. In Eq. 6.6, we assume a monochromatic treatment of the field. We note that the squeezed light generated in the experiments is broadband and that our analysis can be extended to multiple spectral modes.

The field incident to the aperture can be represented by the local bosonic operator, $\hat{a}_{\text{in}}(\rho) = \sum_n u_n(\rho)\hat{a}_{u_n}$. The aperture is divided into N antenna elements, which define a set of N pixel modes $\{\mathcal{E}_j(\rho)\}$ each with an associated pair of bosonic operators $\hat{a}_{\mathcal{E}_j}$ and $\hat{a}^\dagger_{\mathcal{E}_j}$. The pixel modes are combined after applying a phase shift, ϕ_j and an amplitude weight, g_j, to each pixel mode, where $\sum g_j^2 = 1$. The combined output field is described by Eq. 6.1,

$$\hat{a}_{\text{out}} = \sum_j g_j e^{i\phi_j} \hat{a}_{\mathcal{E}_j} = \int \mathcal{A}^*(\rho)\hat{a}_{\text{in}}(\rho)d\rho,$$

where $\hat{a}_{\mathcal{E}_j} = \int \mathcal{E}_j^*(\rho)\hat{a}_{\text{in}}(\rho)d\rho$ is substituted to obtain the array mode function, $\mathcal{A}(\rho)$,

$$\mathcal{A}(\rho) = \sum_j g_j e^{-i\phi_j} \mathcal{E}_j(\rho) \approx g(\rho)e^{-i\phi(\rho)}. \tag{6.7}$$

The approximation in Eq. 6.7 is taken in the small pixel limit. In this limit, the pixel modes approach $\mathcal{E}_j(\rho) \approx \delta(\rho - \rho_j)$, where ρ_j represents the coordinates at the center of the jth pixel, the set of amplitude weights and phase shifts approach continuous phase, $\phi(\rho_j)$, and amplitude, $g(\rho_j)$, distributions, and the sum becomes an integral over ρ_j. The reconfigurable array mode function can be used to engineer the state of the incident field to enable functionalities such as mode matching, beamforming and beamsteering, and more generally quantum state engineering [29, 30].

Mode matching and discrimination

Consider a quantum state transmitted over free space to a phased array receiver in mode $u_n(\rho)$, with all other modes in the vacuum state. In our experiments, we transmit a squeezed vacuum state in the Gaussian mode $u_0(\rho)$. Due to diffraction, the incident field is spread out across the aperture, with multiple vacuum modes $u_{m\neq n}(\rho)$ coupling into each antenna element. This results in a low geometric efficiency for each pixel mode, $\eta_{g,j} = \left|\int \mathcal{E}_j^*(\rho)u_n(\rho)d\rho\right|^2$. The array can mode match to $u_n(\rho)$ by configuring the array mode function, $\mathcal{A}(\rho)$, through weighted combination of the pixels such that the vacuum modes destructively interfere. The geometric efficiency of the array is described by $\eta_g = \left|\int \mathcal{A}^*(\rho)u_n(\rho)d\rho\right|^2$. Due to the orthonormality of the input basis, unity geometric efficiency can be achieved by setting $\mathcal{A}(\rho) = u_n(\rho)$, resulting in $\hat{a}_{\text{out}} = \hat{a}_n$. For multimode fields, the signal in a particular mode can be uniquely selected by setting $\mathcal{A}(\rho)$ to the desired mode function. In general, the reconfigurability of $\mathcal{A}(\rho)$ enables mode matching to quantum states in arbitrary modal profiles, such as multimode quantum states, to achieve unity geometric efficiency.

Beamforming and beamsteering

The field at the aperture can be expressed in terms of the input field in the far-field limit, $\hat{a}_{\text{in}}(f)$, using the generalized Huygen's principle [51], which can be approximated as,

$$\hat{a}_{\text{in}}(\rho) \propto \int e^{-i2\pi\rho f}\hat{a}_{\text{in}}(f)df, \tag{6.8}$$

where $f = \sin\theta/\lambda$ is in terms of the angle from normal incidence (θ) and the wavelength (λ). We assume a one dimensional linear array of antennas. The output field of the phased array in terms of the input field is given by Eq. 6.2,

$$\hat{a}_{\text{out}} \propto \int \text{SF}(f)\hat{a}_{\text{in}}(f)df,$$

where $\text{SF}(f) = \int e^{-i2\pi\rho f}\mathcal{A}^*(\rho)d\rho$ corresponds to the space factor of the array [19, 20]. In antenna theory, the total far-field radiation pattern is formed by pattern multiplication of the space factor and the element factor [19]. For our system, the element factor corresponds to the radiation pattern of a single antenna.

For a discrete linear array with spacing d and a progressive phase shift $\Delta\phi$ applied to the antenna elements, the radiation pattern features a primary lobe, or a beam,

at $\theta_{\max} = \arcsin\left[-(\lambda/2\pi d)\Delta\phi\right]$ [19]. The phased array transmitter is the reciprocal counterpart to a phased array receiver, and for a phased array receiver (transmitter), the beam corresponds to the range of reception (transmission) angles over which the pixel modes constructively interfere for a given set of phases and amplitude weights applied to the pixels. Beamforming refers to the optimization of the phase and amplitude settings of a phased array receiver (transmitter) in order to form a reception (transmission) beam at a given angle. In the receiver case, beamforming is equivalent to maximizing the geometric efficiency of the array, η_g. By varying the progressive phase to shift $\theta_{\max}$, the reception or transmission beam can be steered toward a different location [19, 20].

Implementation

Quantum phased arrays could be implemented in various platforms for discrete-variable or continuous-variable quantum information. In integrated photonics, phase control in Eq. 6.2 can be implemented with phase shifters using, for instance, the thermo-optic effect. Amplitude control in weighted combination can be implemented with meshes of interferometers [52] or homodyne detection [53]. In the case of homodyne detection, the amplitude weights are applied by tuning the amplitude of the LOs or the gains of the electronic amplifiers. Each coherent receiver outputs an RF field that generates a voltage or current proportional to the phase-dependent quadrature of its pixel mode defined in Eq. 6.3. Leveraging the coherence of the receiver outputs across the array, the output signals are combined at RF, yielding a combined signal proportional to the quadrature $\hat{Q}_{\text{out}} = (\hat{a}_{\text{out}} + \hat{a}^{\dagger}_{\text{out}})/2$ of an effective output field [49], $\hat{a}_{\text{out}}$, described by Eq. 6.1. For our system, since phase control is performed with the thermo-optic phase shifters on the LO side and amplitude control is performed with electronic gains, the reconfigurability of the system adds no loss to the received non-classical light. In our implementation, configuring $\mathcal{A}(\rho)$ is equivalent to shaping the spatial-mode profile of the LO throughout the array. Therefore, our system acts as a reconfigurable, coherent spatial filter, in addition to spectral filtering enabled by the choice of the LO spectral mode for each pixel.

Chip fabrication and design

Chip fabrication

The PIC was fabricated with Advanced Micro Foundry using a 193 nm silicon-on-insulator (SOI) process. The process has two metal layers (2000 nm thick and 750 nm thick) for electronic routing, a titanium nitride heater layer, a 220 nm thick silicon layer, a 400 nm thick silicon nitride layer, germanium epitaxy, and various implantations for active devices. A process design kit (PDK) from the foundry was provided. The PIC was laid out using KLayout and Cadence Virtoso and was simulated using Lumerical for design verification.

Chip design

To interface with non-classical light, the aperture requires an antenna design that can be sized to fill the aperture without any gaps. This requires a design methodology that can increase the active area of the antenna arbitrarily in both lateral and longitudinal dimensions. Increasing the active area requires minimizing the scattering strength per unit area while abiding by the design rules to be foundry compatible with the silicon photonics process.

To increase longitudinal area, grating elements are placed around the antenna waveguide with apodized scattering strength. To increase lateral area, sixteen of these waveguide grating antennas are connected and parallelized. The 0.82 μm wide waveguides keep a single mode confined throughout the length of the antenna so that the phasefront of the coupled light across the cross-section of the antenna is flat. At one end of the antenna active area, a mode converter comprising a taper couples the light from 0.82 μm waveguides to 0.5 μm waveguides. A Y-junction-based 16-to-1 combiner tree combines all the outputs from a single antenna into a single mode propagating in the 0.5 μm wide waveguide that is used to route the signal on the PIC.

Three grating regions with apodized coupling strengths are designed, as seen in Fig. 6.2. The physical footprint of the antenna is 597×16.7 μm^2. Across the length of the antenna, the splitter tree region is from 0 μm to 47 μm, the apodized grating duty cycle region is from 47 μm to 347 μm, the apodized grating width region is from 347 μm to 547 μm, and the full width region is from 547 μm to 597 μm. The aperture of the chip comprises 32 of these antennas with 17.5 μm pitch to ensure sufficiently low optical crosstalk between the antennas. Two antennas are added on each side of the aperture, resulting in 36 total antennas. On each side,

one antenna is connected to a standard grating coupler and the other is connected to a photodiode to aid free-space alignment with an optical measurement and an electronic measurement, respectively. By measuring the power at these antennas, the PIC aperture can be aligned more easily to the incident beam. Furthermore, these extra antennas ensure that the edge antennas of the aperture have the same response as the middle antennas.

The QRX design comprises a tunable Mach-Zehnder interferometer (MZI) made out of two 50:50 directional couplers and two diode phase shifters. Each phase shifter is 100 μm long, comprising a resistive heater made out of doped silicon with 1 kΩ resistance and a diode in series with 1 V forward voltage. Doped Si is placed 0.9 μm away from the waveguides to minimize loss from free carriers. The MZI is configured in a push-pull configuration to extend the tuning range of the coupling coefficients and is designed to provide sufficient tuning with ±5 V drivers. One branch of the MZI includes an optical delay with 90° phase shift to set the nominal coupling of the MZI to 50:50. Fabrication imperfections such as changes in the gap of the coupling region and surface roughness on the waveguides shift the ideal 50:50 coupling randomly across different channels. The tunability of the MZIs allows for the correction of these imperfections to set 50:50 coupling. The MZIs are also designed to be symmetric to ensure a high extinction ratio.

After the MZI, the waveguides are adiabatically tapered to connect to a balanced Ge photodiode pair with >20 GHz bandwidth at 3 V reverse bias, >70% quantum efficiency, and <100 nA dark current. The QRX is surrounded by a Ge shield to absorb stray light propagating in the chip substrate and prevent it from coupling to the photodiodes. Each QRX output is connected to a separate on-chip pad to be interfaced with a transimpedance amplifier and subsequent electronics for RF processing.

The LO is coupled to the chip with a standard grating coupler and is sent to each QRX through a 1-to-32 splitter tree. Each Y-junction in the splitter tree has 0.28 dB loss, and the grating coupler has 3.30 dB loss. Before the splitter tree, a directional coupler on the LO waveguide couples 1% of the LO power to a monitor photodiode for LO power monitoring. After the splitter tree, a TOPS is included in each branch to tune the LO phase of each channel for phase calibration. Each TOPS for phase tuning is 315 μm long, comprising a resistive heater made out of titanium nitride above the waveguide with 630 Ω resistance.

Chip losses

Expected on-chip losses consist of 3.78 dB from simulated antenna insertion loss, 0.321 dB from waveguide propagation loss, and 1.52 dB from photodiode quantum efficiency. This results in a total expected on-chip loss of 5.62 dB. The on-chip losses are verified experimentally by sending 200 μm collimated beam to the chip aperture after setting all QRXs to the unbalanced (100:0) configuration and summing all QRX currents. For 0.452 mW input power, the output current is 0.0615 μA, resulting in an insertion loss of 8.66 dB. In this measurement, in addition to on-chip losses, there is also the geometric loss due to the mode mismatch between the aperture and the collimated beam as well as the insertion loss of the collimator. For a 200 μm collimated beam, the geometric loss is 1.14 dB, the insertion loss of the collimator is 0.8 dB, and the insertion loss of the connectors is expected to be <1 dB. De-embedding these losses from the measurement, the on-chip losses are measured to be 5.72 dB, which agrees well with the 5.62 dB expected loss. Other losses for all of the measurement setups are outlined in Section C.4 of Appendix C.

Squeezed light generation

To generate squeezed light, continuous wave light from a fiber-coupled 1550 nm laser is split into a signal path and an LO path. The light in each path is amplified by an erbium-doped fiber amplifier. After amplification in the signal path, the 1550 nm coherent light is upconverted to 775 nm by a PPLN waveguide via second harmonic generation (SHG). The upconverted light is used as a continuous-wave pump for Type 0 spontaneous parametric downconversion (SPDC) with another PPLN waveguide, which generates broadband light in a squeezed vacuum state at a central wavelength of 1550 nm. The characterization of the PPLN waveguide used for SPDC in each experiment is in Section C.2 of Appendix C. The squeezed light is sent to a fiber-optic collimator, which transmits the light over free space with a uniform phase front to the chip aperture. After amplification in the LO path, the 1550 nm coherent light is sent to a bulk lithium niobate electro-optic modulator for phase control. The phase-modulated LO is sent to a cleaved fiber, which is coupled to the LO input of the chip. Polarization controllers before the collimator and on the LO fiber are used to optimize the coupling efficiency to the chip.

System electronics

The PIC is packaged with an interposer board for fanning the 104 electronic input/output (IO) to/from the chip. The interposer board is designed with a laser-

milled cavity in the middle to place the PIC surrounded by pads with blind vias for high-density routing. The chip and the interposer are assembled so that the on-chip pads are level and parallel with the on-board pads to shorten the bond wire length. The traces from the interposer pads to the TIA inputs on the motherboard are minimized and spaced apart sufficiently to minimize electronic crosstalk with 50 Ω coplanar waveguide (CPW) transmission lines. The TIA circuit on the motherboard utilizes a FET-input operational amplifier (op-amp) with resistive feedback. The op-amp IC (LTC6269-10) has a 4 GHz gain-bandwidth product and is used with a 50 kΩ feedback resistor. The capacitance of the feedback trace is used to ensure sufficient phase margin while keeping the closed-loop gain greater than 10 since the op-amp is decompensated. A 50 Ω resistor is placed in series with the output of the TIA for impedance matching and to dampen any oscillations from capacitive loading at the output. The TIA outputs are routed with 50 Ω CPW transmission lines to a high-speed, high-density connector to route the signals to data acquisition.

The DC voltage across the TIA feedback resistor is used as the error signal for the CMRR correction and drives an integrator circuit with a chopper-stabilized op-amp IC (OPA2187) for low voltage offset, flicker noise, and offset drift. The integrator's unity-gain bandwidth is set close to DC (23 Hz) to dampen any oscillations in the CMRR auto-correction feedback. The integrator's output is fed back to the MZI on the PIC to correct the CMRR continuously. The polarity of the integrator is designed to match the polarity of the push-pull MZI so that the correction circuit always maximizes the CMRR, whether the error signal is a negative or a positive DC signal. The correction is limited by the dark current of each QRX and the offset voltage at the input of each integrator, but offset correction can be applied to each integrator to further maximize the CMRR. A high-speed coaxial cable assembly is used to connect to the motherboard. The cable coming out of the motherboard first connects to a power board, which powers the active electronics on the motherboard. This board also routes the output from two photodiodes, which are connected to the two edge antennas of the aperture, and the output from the monitor photodiode, which is connected to the LO coupler, to current meters for continuous monitoring of the signal and LO alignment on the chip. Another cable then connects the remaining IO to a splitter board that splits the 32 QRX outputs for simultaneous imaging and RF data acquisition. The remaining control lines for tuning the on-chip TOPS are connected to 32 digital-to-analog converters (DACs) for independent phase tuning of each QRX.

Data acquisition

The 32 QRX outputs after the splitter is connected to boards that host SMA connectors to interface with data acquisition equipment. One board, used for parallelized 32-channel readout, connects to 32 channels of digitizers with 100 MHz bandwidth, 100 MSa/s adjustable sampling rate, and 14-bit resolution. The digitizers are used in high-impedance mode to read out the voltage of each QRX output for squeezed light imaging and during RF measurements. For squeezed light imaging in Fig. 6.4c, the digitizers are configured to have a sampling rate of 20 MSa/s. The other board, used for RF single channel readout, connects to a 32-to-1 RF power combiner assembly with an operating frequency range of 0.1-200 MHz. The output from the power combiner is connected to the RF signal analyzer (ESA). For squeezed light measurements in Fig. 6.5b,c,e, and f, the ESA is configured to be used in the zero-span mode at a center frequency of 5.5 MHz, with a resolution bandwidth of 2 MHz and a video bandwidth of 5 Hz. Center frequency and resolution bandwidth are selected to maximize the shot noise clearance after a parameter sweep.

Beamforming

Phase calibration

For each angle of incidence, we calibrate the settings for the 32 LO TOPS such that the quadratures for all pixel modes are aligned to the same phase. Precise phase calibration is crucial to prevent additional loss due to vacuum noise leaking into the combined output. Phase calibration is performed with a 1550 nm coherent state transmitted by the collimator, and a 5 MHz phase ramp is applied to the LO before coupling to the chip. The 5 MHz downconverted RF signal after channel combination is used as feedback to the computer to tune the on-chip TOPS iteratively. Various signal processing schemes and algorithms have been developed for beamforming in classical phased arrays, such as random search, gradient search, direct matrix inversion, and recursive algorithms [54]. We employ a modified gradient search algorithm by sweeping phase settings of on-chip TOPS with an orthogonal mask set.

Channel combination

For the beamforming measurements in Fig. 6.5, the array mode function for N channels connected to the power combiner is,

$$\mathcal{A}_N(\rho) \approx \sum_{j \in S_N} \frac{1}{\sqrt{N}} e^{-i\phi_j} \mathcal{E}_j(\rho), \tag{6.9}$$

where j is summed over the set of connected channels (S_N). For beamforming, the phase calibration algorithm optimizes the phases, $\{\phi_j\}$, such that all channels are in phase. Starting with only channel 16 connected to the power combiner, the number of connected channels (N) is increased by adding channels to the power combiner symmetrically about the center of the array (i.e., one channel ($N = 1$): $S_1 = \{16\}$; two channels ($N = 2$): $S_2 = \{16, 17\}$; three channels ($N = 4$): $S_3 = \{15, 16, 17\}$; etc.). Fig. 6.5b shows the noise power levels as a function of the number of connected channels, $N = 1, \cdots, 32$. In practice, imperfections or parasitic effects such as impedance mismatch or crosstalk affect the array mode function in Eq. 6.9, which could result in different amplitude weights for different combinations of channels. To fully account for these effects, the mode matching is classically characterized by measuring the signal-to-noise ratio (SNR) of coherent light (see Section C.3 in the Appendix C), which is proportional to the array geometric efficiency, $\eta_g \approx |\int \mathcal{A}_N(\rho)\hat{a}_{\text{in}}(\rho)d\rho|^2$, for each channel combination.

Squeezing level estimation

The squeezing and antisqueezing levels relative to the shot noise level are estimated from a statistical analysis of the quadrature sample variances or noise powers. For the squeezed light experiments in Fig. 6.4 (6.3,6.5), quadrature sample variances (noise powers) are acquired for squeezed vacuum and vacuum states over an approximately uniform distribution of phases, and histograms are constructed for the acquired data. The squeezing and antisqueezing levels are estimated from the inflection points of the probability density functions (PDFs) of quadrature variances, which are obtained from the Gaussian kernel density estimates (KDEs) of the histograms. The squeezing and antisqueezing level estimates correspond to the locations of the peak slopes at the left (right) edges of the PDF, respectively. In particular, the quadrature variances for the squeezing and antisqueezing levels are identified from the peaks in the derivative of the KDEs, which provide a well-defined measure of the edges of the quadrature variance distribution. The same estimation procedure applied to the vacuum data yields the standard deviation in the vacuum sample variance (shot

noise level). Error bars are obtained from the propagation of the vacuum standard deviation on the squeezing and antisqueezing level estimates. Further information on the estimation procedure is presented in Appendix B.

Wigner function calculation

For the calculations of the Wigner functions in Fig. 6.4b, the experimental squeezing parameter $r = 1.95$, which corresponds to 16.9 dB generated squeezing, is plugged into the Wigner function $W(Q, P, r, \phi, \eta)$ of a squeezed vacuum state, setting $\phi = 0$ and $\eta = 1$ to obtain the Wigner function at the source. The Wigner function for each pixel mode is obtained by plugging its squeezing parameter ($r = 1.95$), phase and geometric efficiency into the Wigner function. The phases are estimated from a sinusoidal fit to the quadrature sample variances of each channel over data with approximately uniform phase variation. From the squeezing parameter, the effective efficiency of each channel is estimated using,

$$\eta_j = \frac{(A_j - 1)\exp(2r)}{(\exp(2r) - 1)(A_j + \exp(2r))}, \tag{6.10}$$

where $A_j = \Delta Q^2_{j,+}/\Delta Q^2_{j,-}$ is the ratio of the antisqueezing level ($\Delta Q^2_{j,+}$) to the squeezing level ($\Delta Q^2_{j,-}$) of the jth pixel. The geometric efficiencies of the channels are calculated from the effective efficiencies of the channels divided by their total sum. The characterization of the squeezing parameter, phases, and geometric efficiencies are in Section C.3 of Appendix C.

Measurement characterization

For each non-classical measurement in the reported experiments, a classical measurement is also taken to characterize the system. The classical measurements are taken using the same photonic and electronic hardware chain as the non-classical measurements to ensure consistency. For the squeezed light imaging experiment in Fig. 6.4b,c,d, a classical multi-pixel image is taken by sending a coherent state as signal while the LO phase is ramped at 5 MHz. The 5 MHz tone from each channel is digitized by the imaging readout, and its corresponding amplitude is measured. For the experiments in Fig. 6.5b,e,f, a coherent state is sent as the signal while the LO phase is ramped at 5 MHz. The 5 MHz tone at the output of the power combiner is measured on the ESA for each measurement setting. For each channel combination in Fig. 6.5b, an SNR is calculated by taking the ratio of the signal power to the

corresponding shot noise acquired from the squeezed light measurement. Classical data and more detailed analysis are presented in Section C.3 of Appendix C.

Theoretical modeling

The theoretical models in Fig. 6.5 are constructed from classical characterizations of the effective efficiency for each experimental configuration using,

$$\Delta Q_{\pm}^2 = \eta e^{\pm 2r} + 1 - \eta, \tag{6.11}$$

where $\Delta Q_{\pm}^2$ are the squeezing (−) and antisqueezing (+) levels relative to the shot noise level, r is the squeezing parameter, and η is the effective efficiency of the system.

For Fig. 6.5b, the model is obtained from Eq. 6.11 with $\eta \propto$ SNR for each combination of channels. A least-squares fit is performed by taking the proportionality constant (η_c) to the classical SNR data as the only free parameter, with the squeezing parameter bounded in the range $r = 0.748 \pm 0.019$ (see Section C.3 of Appendix C). Using SNR data normalized to its peak value, we obtain optimal parameters of $\eta_c = 0.021$ and $r = 0.761$ (6.61 dB generated squeezing).

For Fig. 6.5c, the model is obtained from Eq. 6.11 with $r = \mu\sqrt{P}$, where P is the SPDC pump power and μ is the SPDC efficiency, and a least-squares fit is performed taking the μ and η as free parameters. The optimal parameters are reported in the main text, $\eta = 0.016$ and $\mu = 0.038$ $[\mathrm{mW}]^{-1/2}$, which matches the the SPDC efficiency of the PPLN waveguide characterized in Section C.2 and reported in Table C.2 of Appendix C.

For Fig. 6.5e, the models are obtained from Eq. 6.11 and η proportional to classical beamwidth data for 8 and 32 channels combined. For each data set, a least-squares fit is performed taking the proportionality constant ($\eta_c^{(N)}$) to the classical beamwidth data as the only free parameter, with the squeezing parameter bounded in the range $r = 0.607 \pm 0.015$ (see Section C.3 of Appendix C). Using beamwidth data normalized to their peak powers, we obtain optimal parameters of $\eta_c^{(8)} = 0.019$, $\eta_c^{(32)} = 0.014$, and $r = 0.611$ (5.31 dB generated squeezing). Using this estimated r, the 8 and 32 channel beamwidths are characterized directly from the squeezed light data by extracting the effective efficiencies using Eq. 6.10. With linear interpolation, angles corresponding to 0.5 effective efficiency are found to calculate the beamwidths.

For Fig. 6.5f, the models are obtained from Eq. 6.11 and η proportional to the classical radiation pattern of a single antenna. For each data set, a least-squares fit is performed taking the proportionality constant ($\eta_c^{(N)}$) to the classical radiation pattern as the only free parameter, with the squeezing parameter bounded in the range $r = 0.865 \pm 0.043$ (see Section C.3 in the of Appendix C). Using the radiation pattern data normalized to its peak power, we find optimal parameters of $\eta_c^{(8)} = 0.017$, $\eta_c^{(32)} = 0.015$, and $r = 0.908$ (7.89 dB generated squeezing). Using this estimated r, the 8 and 32 channel FoVs are characterized directly from the squeezed light data in the same way as beamwidth characterization using Eq. 6.10.

The squeezing parameters for the models are obtained from independent characterizations of the sources (see Section C.2 of of Appendix C). We note that for the measurements in Fig. 6.5b,c,e, phase calibration was performed once before acquisition of all the data, whereas for the FoV data in Fig. 6.5f, separate phase calibration was performed for each data point. Imperfect phase calibration contributes to RF loss due to imperfect destructive interference of vacuum terms in the pixel quadratures. Therefore, depending on the phase calibration, different angles exhibited different amounts of RF loss, specifically $\theta = -1°$, which affected the fit in 6.5f. Loss due to phase calibration can be further minimized with more sophisticated phase calibration algorithms [54]. Further details of the theoretical modeling are in Section C.3 of Appendix C.

References

[1] T. D. Ladd, F. Jelezko, R. Laflamme, Y. Nakamura, C. Monroe, and J. L. O'Brien. "Quantum computers." In: Nature 464.7285 (Mar. 2010), pp. 45–53.

[2] Stephanie Wehner, David Elkouss, and Ronald Hanson. "Quantum internet: A vision for the road ahead." In: Science 362.6412 (2018), eaam9288.

[3] Christian L Degen, Friedemann Reinhard, and Paola Cappellaro. "Quantum sensing." In: Reviews of Modern Physics 89.3 (2017), p. 035002.

[4] Emanuele Pelucchi, Giorgos Fagas, Igor Aharonovich, et al. "The potential and global outlook of integrated photonics for quantum technologies." In: Nature Reviews Physics 4.3 (Mar. 2022), pp. 194–208.

[5] Jianwei Wang, Fabio Sciarrino, Anthony Laing, and Mark G. Thompson. "Integrated photonic quantum technologies." In: Nature Photonics 14.5 (May 2020), pp. 273–284.

[6] Inki Kim, Renato Juliano Martins, Jaehyuck Jang, Trevon Badloe, Samira Khadir, Ho-Youl Jung, Hyeongdo Kim, Jongun Kim, Patrice Genevet, and Junsuk Rho. "Nanophotonics for light detection and ranging technology." In: Nature Nanotechnology 16.5 (May 2021), pp. 508–524.

[7] Alan J Fenn, Donald H Temme, William P Delaney, and William E Courtney. “The development of phased-array radar technology.” In: Lincoln laboratory journal 12.2 (2000), pp. 321–340.

[8] Christopher Rogers, Alexander Y. Piggott, David J. Thomson, et al. “A universal 3D imaging sensor on a silicon photonics platform.” In: Nature 590.7845 (Feb. 2021), pp. 256–261.

[9] Abbas El Gamal and Helmy Eltoukhy. “CMOS image sensors.” In: IEEE Circuits and Devices Magazine 21.3 (2005), pp. 6–20.

[10] Christopher Vincent Poulton, Matthew J. Byrd, Peter Russo, Erman Timurdogan, Murshed Khandaker, Diedrik Vermeulen, and Michael R. Watts. “Long-Range LiDAR and Free-Space Data Communication With High-Performance Optical Phased Arrays.” In: IEEE Journal of Selected Topics in Quantum Electronics 25.5 (2019), pp. 1–8.

[11] Cheng-Xiang Wang, Fourat Haider, Xiqi Gao, Xiao-Hu You, Yang Yang, Dongfeng Yuan, Hadi M. Aggoune, Harald Haas, Simon Fletcher, and Erol Hepsaydir. “Cellular architecture and key technologies for 5G wireless communication networks.” In: IEEE Communications Magazine 52.2 (2014), pp. 122–130.

[12] Qi Bi, G.L. Zysman, and H. Menkes. “Wireless mobile communications at the start of the 21st century.” In: IEEE Communications Magazine 39.1 (2001), pp. 110–116.

[13] Luigi Atzori, Antonio Iera, and Giacomo Morabito. “The internet of things: A survey.” In: Computer networks 54.15 (2010), pp. 2787–2805.

[14] Andrea Goldsmith. Wireless communications. Cambridge University Press, 2005.

[15] Joel F. Tasker, Jonathan Frazer, Giacomo Ferranti, Euan J. Allen, Léandre F. Brunel, Sébastien Tanzilli, Virginia D’Auria, and Jonathan C. F. Matthews. “Silicon photonics interfaced with integrated electronics for 9 GHz measurement of squeezed light.” In: Nature Photonics 15.1 (Jan. 2021), pp. 11–15.

[16] Taofiq K. Paraïso, Thomas Roger, Davide G. Marangon, Innocenzo De Marco, Mirko Sanzaro, Robert I. Woodward, James F. Dynes, Zhiliang Yuan, and Andrew J. Shields. “A photonic integrated quantum secure communication system.” In: Nature Photonics 15.11 (Nov. 2021), pp. 850–856.

[17] G. Zhang, J. Y. Haw, H. Cai, et al. “An integrated silicon photonic chip platform for continuous-variable quantum key distribution.” In: Nature Photonics 13.12 (Dec. 2019), pp. 839–842.

[18] P. Magnard, S. Storz, P. Kurpiers, et al. “Microwave Quantum Link between Superconducting Circuits Housed in Spatially Separated Cryogenic Systems.” In: Phys. Rev. Lett. 125 (26 Dec. 2020), p. 260502.

[19] Constantine A. Balanis. Antenna theory: analysis and design. John wiley & sons, 2016.

[20] Robert J Mailloux. Phased array antenna handbook. Artech house, 2017.

[21] Karl Ferdinand Braun. Nobel Lecture. Nobel Foundation. Dec. 1909.

[22] John Alan Richards et al. Remote sensing with imaging radar. Vol. 1. Springer, 2009.

[23] A. Hewish, S. J. Bell, J. D. H. Pilkington, P. F. Scott, and R. A. Collins. "Observation of a Rapidly Pulsating Radio Source." In: Nature 217.5130 (Feb. 1968), pp. 709–713.

[24] Jie Sun, Erman Timurdogan, Ami Yaacobi, Ehsan Shah Hosseini, and Michael R. Watts. "Large-scale nanophotonic phased array." In: Nature 493.7431 (Jan. 2013), pp. 195–199.

[25] Xiaosheng Zhang, Kyungmok Kwon, Johannes Henriksson, Jianheng Luo, and Ming C. Wu. "A large-scale microelectromechanical-systems-based silicon photonics LiDAR." In: Nature 603.7900 (Mar. 2022), pp. 253–258.

[26] Christopher V. Poulton, Matthew J. Byrd, Peter Russo, Benjamin Moss, Oleg Shatrovoy, Murshed Khandaker, and Michael R. Watts. "Coherent LiDAR With an 8,192-Element Optical Phased Array and Driving Laser." In: IEEE Journal of Selected Topics in Quantum Electronics 28.5: Lidars and Photonic Radars (2022), pp. 1–8.

[27] Leonard Mandel. "Non-classical states of the electromagnetic field." In: Physica scripta 1986.T12 (1986), p. 34.

[28] Leonard Mandel and Emil Wolf. Optical coherence and quantum optics. Cambridge university press, 1995.

[29] Tomás Santiago-Cruz, Sylvain D. Gennaro, Oleg Mitrofanov, Sadhvikas Addamane, John Reno, Igal Brener, and Maria V. Chekhova. "Resonant metasurfaces for generating complex quantum states." In: Science 377.6609 (2022), pp. 991–995.

[30] Kai Wang, James G. Titchener, Sergey S. Kruk, et al. "Quantum metasurface for multiphoton interference and state reconstruction." In: Science 361.6407 (2018), pp. 1104–1108.

[31] Barry D. Van Veen and Kevin M. Buckley. "Beamforming: A versatile approach to spatial filtering." In: IEEE ASSP Magazine 5.2 (1988), pp. 4–24.

[32] H.T. Friis. "A Note on a Simple Transmission Formula." In: Proceedings of the IRE 34.5 (1946), pp. 254–256.

[33] Maziyar Milanizadeh, SeyedMohammad SeyedinNavadeh, Francesco Zanetto, Vittorio Grimaldi, Christian De Vita, Charalambos Klitis, Marc Sorel, Giorgio Ferrari, David AB Miller, Andrea Melloni, et al. "Separating arbitrary free-space beams with an integrated photonic processor." In: Light: Science & Applications 11.1 (2022), p. 197.

[34] Farshid Ashtiani, Alexander J. Geers, and Firooz Aflatouni. "An on-chip photonic deep neural network for image classification." In: Nature 606.7914 (June 2022), pp. 501–506.

[35] Cédric Bruynsteen, Michael Vanhoecke, Johan Bauwelinck, and Xin Yin. "Integrated balanced homodyne photonic–electronic detector for beyond 20-GHz shot-noise-limited measurements." In: Optica 8.9 (Sept. 2021), pp. 1146–1152.

[36] B. Volkan Gurses and Ali Hajimiri. “Performance Limits of Sub-Shot-Noise-Limited Balanced Detectors.” In: Frontiers in Optics + Laser Science 2022. Optica Publishing Group, 2022, JW4A.32.

[37] Volkan Gurses, Samantha I. Davis, Esme Knabe, Raju Valivarthi, Maria Spiropulu, and Ali Hajimiri. “A compact silicon photonic quantum coherent receiver with deterministic phase control.” In: 2023 Conference on Lasers and Electro-Optics. 2023, pp. 1–2.

[38] Volkan Gurses, Debjit Sarkar, Samantha I. Davis, and Ali Hajimiri. “An integrated photonic-electronic quantum coherent receiver for sub-shot-noise-limited optical links.” In: Optical Fiber Communication Conference (OFC) 2024. Optica Publishing Group, 2024, Tu2C.1.

[39] Henning Vahlbruch, Moritz Mehmet, Karsten Danzmann, and Roman Schnabel. “Detection of 15 dB squeezed states of light and their application for the absolute calibration of photoelectric quantum efficiency.” In: Physical Review Letters 117.11 (2016), p. 110801.

[40] Daniel Benedikovic, Cosimo Zuffada, Stefan Krohn, Horst Zimmermann, and Laurent Vivien. “25 Gbps low-voltage heterostructured silicon-germanium waveguide pin photodetectors for monolithic on-chip nanophotonic architectures.” In: Photonics Research 7.4 (2019), pp. 437–444. DOI: 10.1364/PRJ.7.000437.

[41] J. Aasi, J. Abadie, B. P. Abbott, et al. “Enhanced sensitivity of the LIGO gravitational wave detector by using squeezed states of light.” In: Nature Photonics 7.8 (Aug. 2013), pp. 613–619.

[42] Paul-Antoine Moreau, Ermes Toninelli, Thomas Gregory, and Miles J. Padgett. “Imaging with quantum states of light.” In: Nature Reviews Physics 1.6 (June 2019), pp. 367–380.

[43] Jonathan P. Dowling and Kaushik P. Seshadreesan. “Quantum Optical Technologies for Metrology, Sensing, and Imaging.” In: J. Lightwave Technol. 33.12 (June 2015), pp. 2359–2370.

[44] Gregory Slepyan, Svetlana Vlasenko, Dmitri Mogilevtsev, and Amir Boag. “Quantum Radars and Lidars: Concepts, realizations, and perspectives.” In: IEEE Antennas and Propagation Magazine 64.1 (2022), pp. 16–26.

[45] Gaetana Spedalieri and Stefano Pirandola. “Optimal squeezing for quantum target detection.” In: Phys. Rev. Res. 3 (4 Dec. 2021), p. L042039.

[46] Catxere A. Casacio, Lars S. Madsen, Alex Terrasson, Muhammad Waleed, Kai Barnscheidt, Boris Hage, Michael A. Taylor, and Warwick P. Bowen. “Quantum-enhanced nonlinear microscopy.” In: Nature 594.7862 (June 2021), pp. 201–206.

[47] Yu-Ao Chen, Qiang Zhang, Teng-Yun Chen, et al. “An integrated space-to-ground quantum communication network over 4,600 kilometres.” In: Nature 589.7841 (Jan. 2021), pp. 214–219.

[48] Fabian Laudenbach, Christoph Pacher, Chi-Hang Fred Fung, Andreas Poppe, Momtchil Peev, Bernhard Schrenk, Michael Hentschel, Philip Walther, and Hannes Hübel. "Continuous-variable quantum key distribution with gaussian modulation—the theory of practical implementations." In: Advanced Quantum Technologies 1.1 (2018), p. 1800011.

[49] Claude Fabre and Nicolas Treps. "Modes and states in quantum optics." In: Reviews of Modern Physics 92.3 (2020), p. 035005.

[50] Brian J Smith and MG Raymer. "Photon wave functions, wave-packet quantization of light, and coherence theory." In: New Journal of Physics 9.11 (2007), p. 414.

[51] Walter Greiner and Joachim Reinhardt. Quantum electrodynamics. Springer Science & Business Media, 2008.

[52] Michael Reck, Anton Zeilinger, Herbert J. Bernstein, and Philip Bertani. "Experimental realization of any discrete unitary operator." In: Phys. Rev. Lett. 73 (1 July 1994), pp. 58–61.

[53] M Beck. "Quantum state tomography with array detectors." In: Physical Review Letters 84.25 (2000), p. 5748.

[54] R.A. Monzingo, R.L. Haupt, and T.W. Miller. Introduction to Adaptive Arrays. Electromagnetic Waves Series. Institution of Engineering and Technology, 2011. ISBN: 9781891121579.

Part II

Teleportation systems toward the quantum internet

Chapter 7

THE QUANTUM INTERNET

This chapter includes the work in preparation for publication:

[1] Prathwiraj Umesh, Samantha I. Davis, Jordan Smith, Sophie Hermans, Joaquin Chung, Prem Kumar, Boris Korzh, and Raju Valivarthi. "Regional quantum networks: recent progress and outlook." In: Manuscript in preparation for Optica Quantum. (2025).

The long-term vision of quantum networks is to connect globally-distributed users in a quantum internet [1, 2]. An emerging blueprint for the quantum internet consists of regional quantum networks deployed in optical fiber infrastructure interconnected by free-space and satellite links for long-distance communications [3, 4, 5]. Regional networks, spanning metropolitan and national regions, need to be able to distribute quantum resources, such as qubits and entanglement, on the order of hundreds of kilometers. An architecture for a regional quantum network is shown in Fig. 7.1, consisting of (1) a physical layer comprised of quantum nodes (Q-Nodes) with hardware primitives such as entangled photon pair sources, single photon detectors, and quantum memories (see Fig. 7.2); (2) a control and management layer that oversees routing for user connectivity, channel calibration and synchronization; (3) a service layer that translates user-requested services to physical protocols; and (4) a software layer for user interfacing.

Over the past few decades, there has been substantial progress in developing regional quantum network testbeds [6], although the majority of field trials have focused on prepare-and-measure quantum key distribution (QKD), which typically requires only the transmission and detection of single qubits. The next generation of testbeds demand functionalities such as entanglement distribution, multiphoton interference, and transduction to achieve advanced networking protocols such as measurement-device-independent (MDI) QKD [7], distributed sensing, and ultimately networked quantum computation. Because direct qubit transmission is limited by exponential loss and decoherence, long-haul communications require entanglement-based techniques, such as quantum teleportation [8] and entanglement swapping [9], that transfer quantum information without physically propagating the qubit. These operations form the basis of quantum repeaters [10, 11], which are expected to be crucial

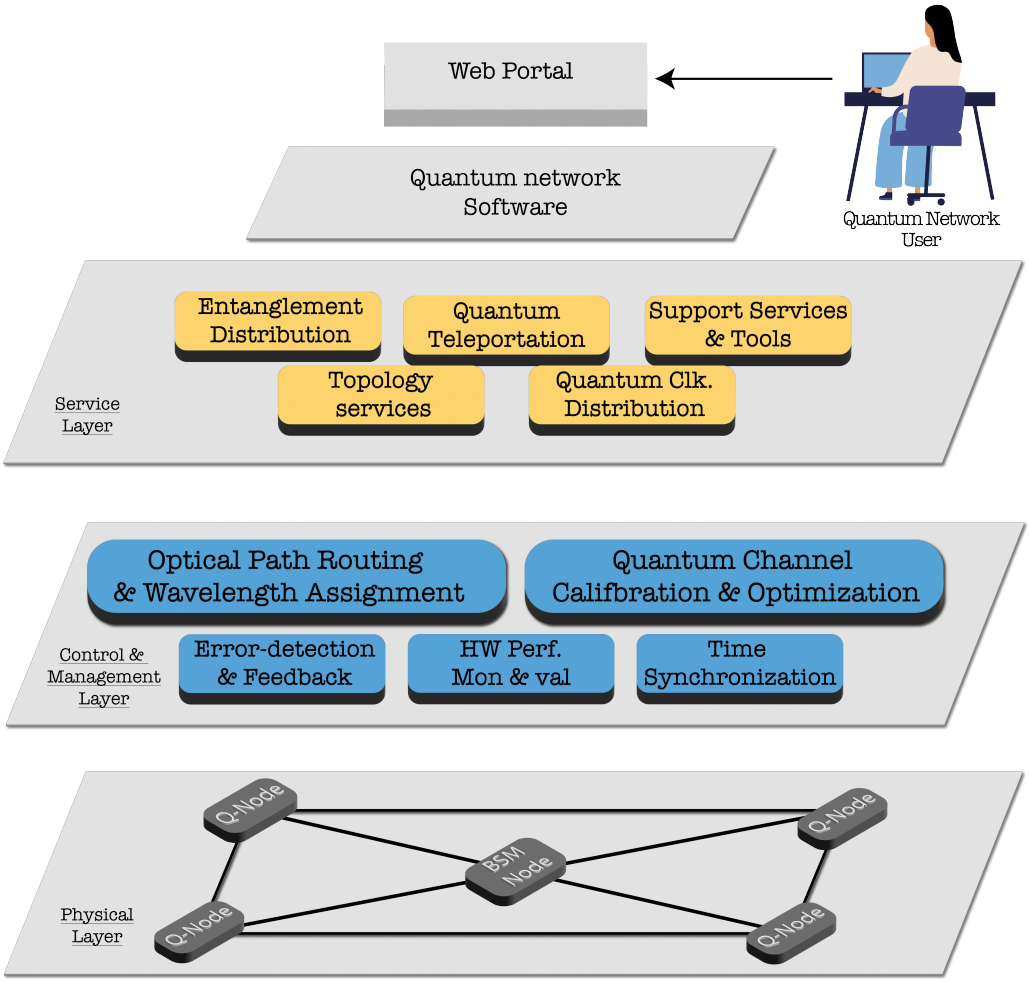

Figure 7.1: Depiction of the regional quantum network architecture. Users interface with the network through a web-based portal linked to quantum software that orchestrates interactions across multiple layers. The service layer translates user-requested services into the necessary protocol-level controls. The control and management layer oversees key operational functions such as optical path routing for user connectivity, quantum channel calibration, clock synchronization, and channel syndrome measurement. The physical layer comprises multiple quantum nodes (Q-Nodes) interconnected through a central node, enabling end-to-end quantum communication.

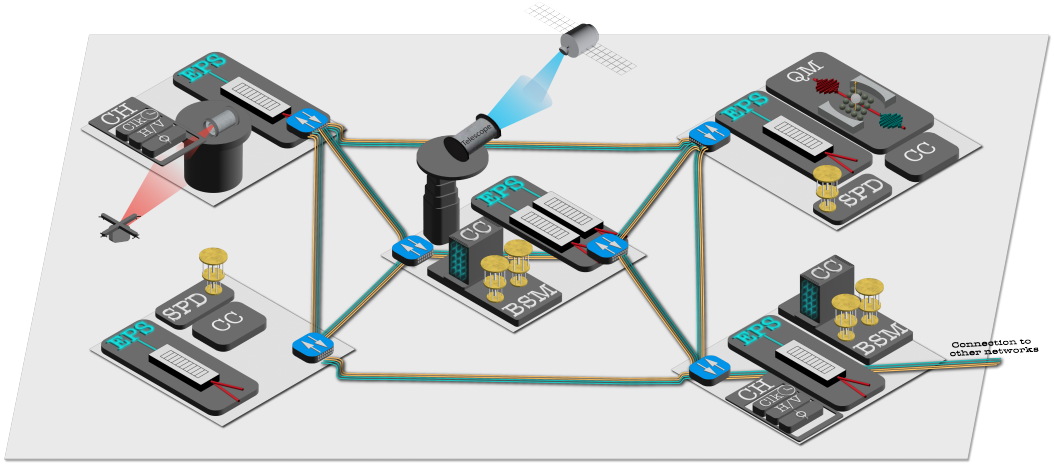

Figure 7.2: Detailed depiction of the physical layer of a regional quantum network. Quantum nodes (Q-Nodes) comprise key components of quantum networks, including the Entangled Photon Source (EPS), Single-Photon Detector (SPD), Channel Stabilizer (CH), Bell-State Measurement (BSM) module, Quantum Memory (QM), and a Classical Computer (CC). These nodes are interconnected via optical fiber and free-space links. Yellow fibers represent dark fibers dedicated solely to quantum communication, while cyan fibers denote optical fibers where quantum and classical communication coexist. Free-space communication links connect Q-Nodes to quantum satellites for long-distance quantum communication and to drones for short-range, line-of-sight quantum communication.

for fault-tolerant long-distance quantum communications in the quantum internet [12].

7.1 Regional quantum networks

Quantum network testbeds have evolved to support a wide array of protocols and applications, transitioning from early demonstrations of QKD to implementations of entanglement-based protocols such as quantum teleportation and entanglement swapping. Deployed in 2004, the DARPA quantum network [13] demonstrated the first 10-node multi-protocol QKD network between Boston and Cambridge, implementing both weak-coherent-state and entanglement-based QKD protocols over fiber and free-space links. In 2008, the SECOQC project [14] in Vienna demonstrated a city-wide QKD network integrating BB84 [15], SARG [16], and continuous variable QKD protocols. SECOQC implemented a modular, multi-layer architecture that separated the quantum, key management, and application layers,

enabling compatibility with classical telecommunication infrastructure. The Swiss Quantum Network [17] later validated the long-term stability of QKD, maintaining continuous operation over months and establishing QKD as a reliable protocol for secure communication in operational environments. In 2011, the Tokyo Quantum Network [18] demonstrated a metropolitan QKD network integrating six different systems that supported GHz-clocked links for secure TV conferencing over 45 km and showcased features such as secure mobile phone interfaces, eavesdropper detection, path rerouting, and key relay via trusted nodes.

In the past five years, quantum network testbeds have expanded to larger scales and advanced architectures. In 2020, the Bristol Quantum Network [19] demonstrated an eight-user metropolitan network in a fully-connected mesh topology with reconfigurable wave division multiplexing (WDM) over deployed fiber. In 2021, the Beijing-Shanghai [3] quantum network reported a fiber backbone spanning over 2,000 km with more than 700 QKD links in a trusted relay structure. The network interfaces with two satellites for space-to-ground quantum communication, enabling high-speed QKD with total network connectivity over 4,600 km. In parallel, the emergence of twin-field QKD (TF-QKD) [20] has drawn attention due to its ability to surpass the repeater-less PLOB bound [21] without trusted relays. In 2021, the Jinan-Qingdao QKD Network [22] reported a TF-QKD demonstration over 511 km using a 12-fiber bundle, the sending-or-not-sending protocol, and active odd-parity pairing. Recently, field trials have generated secure keys over 830 km of deployed fiber [23] and 1,002 km of ultra-low-loss fiber spool using a sending-or-not-sending protocol [24], illustrating TF-QKD's potential for ultra-long-distance secure links.

Going beyond QKD, testbeds are increasingly exploring the implementation of quantum teleportation and entanglement distribution. In 2022, the Munich Quantum Network [25] demonstrated heralded entanglement between two Rubidium (Rb) atoms (400 m apart) via a Bell state measurement node with fiber links up to 33 km. The demonstration leveraged quantum frequency conversion (QFC) to convert a photon emitted by a Rb atom at 780 nm to the telecom band (1570 nm). Two years later (2024), the Delft-Hague Quantum Network [26] reported the development of a three-node midpoint network over 25 km of deployed fiber for the demonstration of heralded entanglement of diamond nitrogen vacancy spin qubits using a single-click protocol. In the same year, the Hefei Quantum Entanglement Network [27] reported a four-node star network with Rb atomic ensemble memories and QFC to the telecom O-band (1342 nm) for the demonstration of three-qubit matter-photon

entanglement via the DLCZ protocol [28].

Literature	Description	Sources	Detectors
Joshi et al. (2020) [19]	Eight-user metropolitan network with reconfigurable DWDM over deployed fiber (10 m–16.6 km). Fully connected graph topology without trusted nodes. BBM92 protocol with polarization-entangled photon pairs distributed via in-fiber beam splitters and 100 GHz DWDM. Each user has PAM hardware and two detectors.	One MgO:PPLN Type-0 source in Sagnac loop (1550.217 nm), producing 8 frequency-multiplexed polarization-entangled pairs.	SNSPDs, SPADs
Chen et al. (2021) [22]	TF-QKD over 511 km with 12-fiber bundle, using sending-or-not-sending protocol and active odd-parity pairing. Three weak coherent sources in X basis, random Z-basis pulses, decoy-state analysis.	Continuous wave fiber lasers locked to ultra-low-expansion cavity (Alice: 1550.12460 nm).	SNSPDs
van Leent et al. (2022) [25]	Three-node network with midpoint; fiber links up to 33 km. Heralded entanglement between two Rb atoms 400 m apart, with telecom QFC. BSM for entanglement heralding.	Rb atoms emit 780 nm photons, converted to 1517 nm via PPLN QFC. Spin-photon entanglement in Zeeman substates.	SNSPDs
Stolk et al. (2024) [26]	Three-node midpoint network over 25 km deployed fiber. Heralded entanglement of diamond nitrogen vacancy (NV) spin qubits using single-click protocol.	NV center spin qubits; 637 nm photons converted to 1588 nm (L-band) via NORA/PPLN QFC.	SNSPDs
Liu et al. (2024) [27]	Four-node star network with Rb atomic ensemble memories and QFC to 1342 nm (O-band). Links of 9.6–11.5 km to central server. Three-qubit matter-photon entanglement via DLCZ protocol.	Rb atomic ensembles in ring cavities; photons converted via PPLN QFC.	SNSPDs

Table 7.1: Summary of regional quantum network testbeds, highlighting key technologies, protocols, and architectures. BSM: Bell state measurement; DWDM: dense wavelength division multiplexing; NV: nitrogen vacancy; PAM: phase amplitude modulation; PPLN: periodically poled lithium niobate; QFC: quantum frequency conversion; SNSPDs: superconducting nanowire single photon detectors; SPADs: single-photon avalanche detectors; TF-QKD: twin-field QKD.

Table 7.1 summarizes recent developments in regional quantum network testbeds. Open challenges include co-designing a scalable, multipurpose quantum network capable of supporting multipartite entanglement-based protocols, with quantum

information sent through fiber or free-space links at varying wavelengths or encodings, while ensuring that entanglement distribution operates seamlessly alongside coexisting classical control channels required for real-world deployment. To this end, I report the development of regional quantum network testbeds at Caltech and Fermi National Accelerator Laboratory (referred to as FNAL or Fermilab). The Caltech Quantum Network (CQNET) is designed to eventually interface with free-space quantum communication links at NASA Jet Propulsion Laboratory (JPL), while the Fermilab Quantum Network (FQNET) is designed to eventually interface with adjacent laboratories and universities as part of the U.S. Department of Energy's roadmap for a quantum internet prototype connecting the seventeen national laboratories [29].

7.2 Caltech and Fermilab quantum network testbeds

Our dual-site approach involves first prototyping networking systems at Caltech in parallel with detector R&D at the NASA-JPL Microdevices Laboratory, leveraging access to state-of-the-art superconducting nanowire single-photon detectors (SNSPDs). These detectors ultimately set the performance limit of quantum communication protocols, and developing systems in close coordination with detector development allows for co-design and optimization. Next, we commission these systems at Fermilab, which offers robust facilities and access to deployed fiber infrastructure interconnecting various on-campus labs, Argonne National Laboratory, and nearby research institutions such as Northwestern University and the University of Illinois, which host advanced quantum technologies including atomic memories and superconducting qubits.

Our testbeds focus on entanglement-based protocols, particularly quantum teleportation and entanglement swapping, with time-bin qubits for robust, long-distance communications over optical fiber (see Figs. 7.3 and 7.4). We first constructed teleportation systems at CQNET and FQNET using optical fiber-coupled devices at telecom-band wavelengths, achieving record teleportation fidelities of $\geq 90\%$ for time-bin qubits transmitted over 44 km of fiber (Chapter 8). To complement these experiments, we developed theoretical models based on a phase-space formalism to account for realistic imperfections, yielding analytical predictions for performance metrics including Hong–Ou–Mandel interference visibility, entanglement visibility, and teleportation fidelity, that guide system design and optimization (Chapter 9).

We then upgraded the FQNET system to support entanglement swapping, demon-

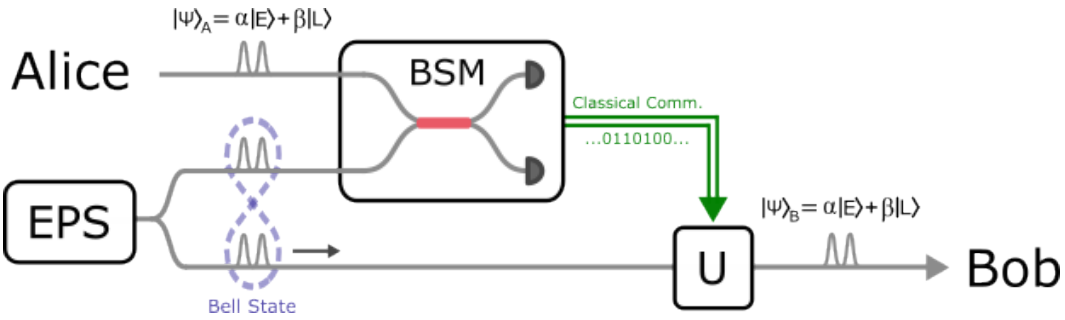

Figure 7.3: Quantum teleportation with time-bin qubits. Alice wants to send a time-bin qubit ($|\psi_A\rangle = \alpha\,|E\rangle + \beta\,|L\rangle$) to Bob. A Bell state measurement (BSM) is performed on her qubit and one member of a Bell pair produced by an entangled photon pair source (EPS). The other member of the Bell pair is sent to Bob. The outcome of the BSM is classically communicated (e.g., in a bit string) to Bob, who applies a unitary transformation (U) to his qubit conditioned on the BSM measurement outcome. As a result, Alice's original qubit is "teleported" to Bob's qubit, ($|\psi_B\rangle = \alpha\,|E\rangle + \beta\,|L\rangle$), without direct physical transmission to Bob.

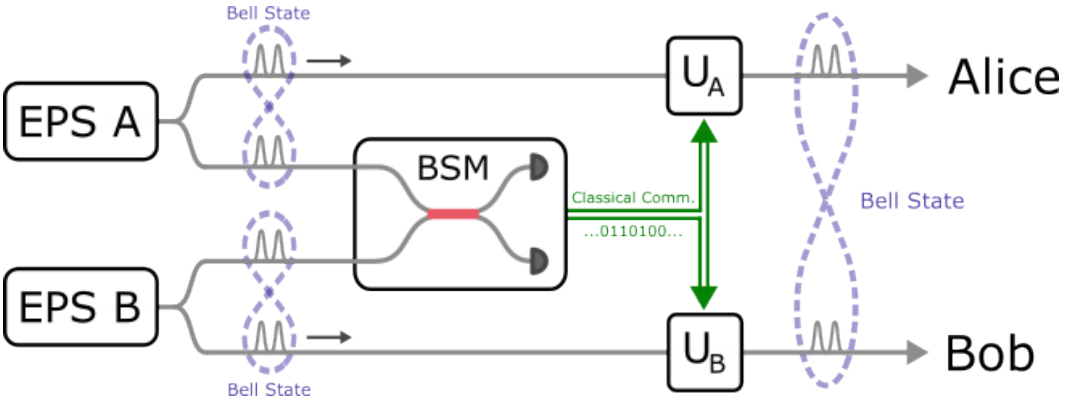

Figure 7.4: Entanglement swapping, i.e., "teleportation of entanglement," with time-bin qubits. Alice and Bob want to share a pair of entangled qubits. Alice and Bob each locally prepare a Bell pair using entangled photon pair source (EPS) A and B, respectively. One member of each pair is sent to a Bell state measurement (BSM) node. The outcome of the BSM is classically communicated to Alice and Bob. Alice and Bob each apply a unitary (U_A and U_B, respectively) to their remaining qubit conditioned on the BSM outcome. As a result, the entanglement is "swapped" between the original Bell pairs, such that the remaining qubits at Alice and Bob are entangled.

strating high-fidelity swapping of time-bin qubits with visibilities up to 92 ± 3.8%, corresponding to a Bell violation exceeding five standard deviations (Chapter 10). To support field deployment and physically separated nodes, precise synchronization of a universal clock reference is required across all network nodes. To this end, we developed a clock synchronization system capable of co-distributing entangled qubits and classical optical clock signals over the same fiber, achieving picosecond-level synchronization using SNSPDs. Following successful demonstrations at Caltech, we deployed the system over a metropolitan-scale fiber network and demonstrated entanglement distribution between nodes at Fermilab and Argonne National Laboratory with 2 ps synchronization precision (Chapter 11). This body of work provides a scalable blueprint for constructing regional quantum networks for the quantum internet.

References

[1] H. J. Kimble. "The quantum internet." In: Nature 453.7198 (June 2008), pp. 1023–1030.

[2] Stephanie Wehner, David Elkouss, and Ronald Hanson. "Quantum internet: A vision for the road ahead." In: Science 362.6412 (Oct. 2018), eaam9288. ISSN: 0036-8075. DOI: 10.1126/science.aam9288. URL: http://www.sciencemag.org/lookup/doi/10.1126/science.aam9288.

[3] Yu-Ao Chen, Qiang Zhang, Teng-Yun Chen, Wen-Qi Cai, Sheng-Kai Liao, Jun Zhang, Kai Chen, Juan Yin, Ji-Gang Ren, Zhu Chen, et al. "An integrated space-to-ground quantum communication network over 4,600 kilometres." In: Nature 589.7841 (2021), pp. 214–219.

[4] Ji-Gang Ren, Ping Xu, Hai-Lin Yong, Liang Zhang, Sheng-Kai Liao, Juan Yin, Wei-Yue Liu, Wen-Qi Cai, Meng Yang, Li Li, et al. "Ground-to-satellite quantum teleportation." In: Nature 549.7670 (2017), pp. 70–73.

[5] Juan Yin, Yuan Cao, Yu-Huai Li, Sheng-Kai Liao, Liang Zhang, Ji-Gang Ren, Wen-Qi Cai, Wei-Yue Liu, Bo Li, Hui Dai, et al. "Satellite-based entanglement distribution over 1200 kilometers." In: Science 356.6343 (2017), pp. 1140–1144.

[6] Jianqing Liu, Thinh Le, Tingxiang Ji, Ruozhou Yu, Demitry Farfurnik, Greg Byrd, and Daniel Stancil. "The road to quantum internet: Progress in quantum network testbeds and major demonstrations." In: Progress in Quantum Electronics 99 (2025), p. 100551.

[7] Hoi-Kwong Lo, Marcos Curty, and Bing Qi. "Measurement-device-independent quantum key distribution." In: Physical review letters 108.13 (2012), p. 130503.

[8] Charles H. Bennett, Gilles Brassard, Claude Crépeau, Richard Jozsa, Asher Peres, and William K. Wootters. "Teleporting an unknown quantum state via dual classical and Einstein-Podolsky-Rosen channels." In: Phys. Rev. Lett. 70 (13 Mar. 1993),

pp. 1895–1899. DOI: 10.1103/PhysRevLett.70.1895. URL: https://link.aps.org/doi/10.1103/PhysRevLett.70.1895.

[9] Jian-Wei Pan, Dirk Bouwmeester, Harald Weinfurter, and Anton Zeilinger. "Experimental Entanglement Swapping: Entangling Photons That Never Interacted." In: Phys. Rev. Lett. 80 (18 May 1998), pp. 3891–3894. DOI: 10.1103/PhysRevLett.80.3891. URL: https://link.aps.org/doi/10.1103/PhysRevLett.80.3891.

[10] H-J Briegel, Wolfgang Dür, Juan I. Cirac, and Peter Zoller. "Quantum repeaters: the role of imperfect local operations in quantum communication." In: Physical Review Letters 81.26 (1998), p. 5932.

[11] Koji Azuma, Kiyoshi Tamaki, and Hoi-Kwong Lo. "All-photonic quantum repeaters." In: Nature Communications 6 (2015), p. 6787.

[12] Koji Azuma, Sophia E. Economou, David Elkouss, Paul Hilaire, Liang Jiang, Hoi-Kwong Lo, and Ilan Tzitrin. "Quantum repeaters: From quantum networks to the quantum internet." In: Reviews of Modern Physics 95 (4 Dec. 2023), p. 045006. DOI: 10.1103/RevModPhys.95.045006. URL: https://link.aps.org/doi/10.1103/RevModPhys.95.045006.

[13] Chip Elliott, Alexander Colvin, David Pearson, Oleksiy Pikalo, John Schlafer, and Henry Yeh. "Current status of the DARPA quantum network." In: Quantum Information and computation III. Vol. 5815. SPIE. 2005, pp. 138–149.

[14] Momtchil Peev, Christoph Pacher, Romain Alléaume, Claudio Barreiro, Jan Bouda, Winfried Boxleitner, Thierry Debuisschert, Eleni Diamanti, Mehrdad Dianati, James F. Dynes, et al. "The SECOQC quantum key distribution network in Vienna." In: New journal of physics 11.7 (2009), p. 075001.

[15] Charles H. Bennett and Gilles Brassard. "Quantum cryptography: Public key distribution and coin tossing." In: Theoretical computer science 560 (2014), pp. 7–11.

[16] Valerio Scarani, Antonio Acin, Grégoire Ribordy, and Nicolas Gisin. "Quantum Cryptography Protocols Robust against Photon Number Splitting Attacks for Weak Laser Pulse Implementations." In: Physical Review Letters 92.5 (2004), p. 057901.

[17] Damien Stucki, Matthieu Legre, Francois Buntschu, B. Clausen, Nadine Felber, Nicolas Gisin, Luca Henzen, Pascal Junod, Gérald Litzistorf, Patrick Monbaron, et al. "Long-term performance of the SwissQuantum quantum key distribution network in a field environment." In: New Journal of Physics 13.12 (2011), p. 123001.

[18] Masahide Sasaki, Mikio Fujiwara, H. Ishizuka, W. Klaus, K. Wakui, M. Takeoka, S. Miki, T. Yamashita, Z. Wang, A. Tanaka, et al. "Field test of quantum key distribution in the Tokyo QKD Network." In: Optics Express 19.11 (2011), pp. 10387–10409.

[19] Siddarth Koduru Joshi, Djeylan Aktas, Sören Wengerowsky, Martin Lončarić, Sebastian Philipp Neumann, Bo Liu, Thomas Scheidl, Guillermo Currás Lorenzo, Željko Samec, Laurent Kling, et al. "A trusted node–free eight-user metropolitan quantum communication network." In: Science advances 6.36 (2020), eaba0959.

[20] M. Lucamarini, Z. L. Yuan, J. F. Dynes, and A. J. Shields. "Overcoming the rate–distance limit of quantum key distribution without quantum repeaters." en. In: Nature 557.7705 (May 2018). Publisher: Nature Publishing Group, pp. 400–403. ISSN: 1476-4687. DOI: 10.1038/s41586-018-0066-6. URL: https://www.nature.com/articles/s41586-018-0066-6 (visited on 11/21/2024).

[21] Stefano Pirandola, Riccardo Laurenza, Carlo Ottaviani, and Leonardo Banchi. "Fundamental limits of repeaterless quantum communications." In: Nature communications 8.1 (2017), p. 15043.

[22] Jiu-Peng Chen, Chi Zhang, Yang Liu, et al. "Twin-field quantum key distribution over a 511 km optical fibre linking two distant metropolitan areas." en. In: Nature Photonics 15.8 (Aug. 2021). Publisher: Nature Publishing Group, pp. 570–575. ISSN: 1749-4893. DOI: 10.1038/s41566-021-00828-5. URL: https://www.nature.com/articles/s41566-021-00828-5 (visited on 02/05/2025).

[23] Shuang Wang, Zhen-Qiang Yin, De-Yong He, et al. "Twin-field quantum key distribution over 830-km fibre." en. In: Nature Photonics 16.2 (Feb. 2022), pp. 154–161. ISSN: 1749-4893. DOI: 10.1038/s41566-021-00928-2. URL: https://www.nature.com/articles/s41566-021-00928-2 (visited on 11/21/2024).

[24] Yang Liu, Wei-Jun Zhang, Cong Jiang, Jiu-Peng Chen, Di Ma, Chi Zhang, Wen-Xin Pan, Hao Dong, Jia-Min Xiong, Cheng-Jun Zhang, et al. "1002 km twin-field quantum key distribution with finite-key analysis." In: Quantum Frontiers 2.1 (2023), p. 16.

[25] Tim van Leent, Matthias Bock, Florian Fertig, Robert Garthoff, Sebastian Eppelt, Yiru Zhou, Pooja Malik, Matthias Seubert, Tobias Bauer, Wenjamin Rosenfeld, et al. "Entangling single atoms over 33 km telecom fibre." In: Nature 607.7917 (2022), pp. 69–73.

[26] Arian J. Stolk, Kian L. van der Enden, Marie-Christine Slater, et al. "Metropolitan-scale heralded entanglement of solid-state qubits." In: Science Advances 10.44 (Oct. 2024). Publisher: American Association for the Advancement of Science, eadp6442. DOI: 10.1126/sciadv.adp6442. URL: https://www.science.org/doi/10.1126/sciadv.adp6442 (visited on 02/05/2025).

[27] Jian-Long Liu, Xi-Yu Luo, Yong Yu, et al. "Creation of memory–memory entanglement in a metropolitan quantum network." en. In: Nature 629.8012 (May 2024). Publisher: Nature Publishing Group, pp. 579–585. ISSN: 1476-4687. DOI: 10.1038/s41586-024-07308-0. URL: https://www.nature.com/articles/s41586-024-07308-0 (visited on 11/19/2024).

[28] L.-M. Duan, M. D. Lukin, J. I. Cirac, and P. Zoller. "Long-distance quantum communication with atomic ensembles and linear optics." en. In: Nature 414.6862 (Nov. 2001). Publisher: Nature Publishing Group, pp. 413–418. ISSN: 1476-4687. DOI: 10.1038/35106500. URL: https://www.nature.com/articles/35106500 (visited on 11/27/2024).

[29] Nicholas Peters, Kerstin Kleese Van Dam, Inder Monga, and Thomas Schenkel. Report of the DOE Quantum Internet Blueprint Workshop. Tech. rep. Oak Ridge National Laboratory (ORNL), Oak Ridge, TN (United States), 2020.

Chapter 8

TELEPORTATION SYSTEMS TOWARDS A QUANTUM INTERNET

This chapter includes the work published as:

[1] Raju Valivarthi, Samantha I. Davis, Cristián Peña, Si Xie, Nikolai Lauk, Lautaro Narváez, Jason P. Allmaras, Andrew D. Beyer, Yewon Gim, Meraj Hussein, et al. "Teleportation systems toward a quantum internet." In: PRX Quantum 1.2 (2020), p. 020317.

8.1 Introduction

Quantum teleportation [1], one of the most captivating predictions of quantum theory, has been widely investigated since its seminal demonstrations over 20 years ago [2, 3, 4]. This is due to its connections to fundamental physics [5, 6, 7, 8, 9, 10, 11, 12, 13, 14], and its central role in the realization of quantum information technology such as quantum computers and networks [15, 16, 17, 18, 19]. The goal of a quantum network is to distribute qubits between different locations, a key task for quantum cryptography, distributed quantum computing and sensing. A quantum network is expected to form part of a future quantum internet [20, 21, 22]: a globally distributed set of quantum processors, sensors, or users there-of that are mutually connected over a network capable of allocating quantum resources (e.g., qubits and entangled states) between locations. Many architectures for quantum networks require quantum teleportation, such as star-type networks that distribute entanglement from a central location or quantum repeaters that overcome the rate-loss trade-off of direct transmission of qubits [19, 23, 24, 25, 26].

Quantum teleportation of a qubit can be achieved by performing a Bell-state measurement (BSM) between the qubit and another that forms one member of an entangled Bell state [1, 18, 27]. The quality of the teleportation is often characterized by the fidelity $F = \langle\psi| \rho |\psi\rangle$ of the teleported state ρ with respect to the state $|\psi\rangle$ accomplished by ideal generation and teleportation [15]. This metric is becoming increasingly important as quantum networks move beyond specific applications, such as quantum key distribution, and towards the quantum internet.

Qubits encoded by the time-of-arrival of individual photons, i.e., time-bin qubits [28], are useful for networks due to their simplicity of generation, interfacing with quantum devices, as well as independence of dynamic transformations of real-world fibers. Individual telecom-band photons (around 1.5 μm wavelength) are ideal carriers of qubits in networks due to their ability to rapidly travel over long distances in deployed optical fibers [17, 29, 30, 31] or atmospheric channels [32], among other properties. Moreover, the improvement and growing availability of sources and detectors of individual telecom-band photons has accelerated progress towards workable quantum networks and associated technologies, such as quantum memories [33], transducers [34, 35], or quantum non-destructive measurement devices [36].

Teleportation of telecom-band photonic time-bin qubits has been performed inside and outside the laboratory with impressive results [37, 38, 39, 40, 41, 30, 29, 42, 31]. Despite this, there has been little work to increase F beyond $\sim 90\%$ for these qubits, in particular using practical devices that allow straightforward replication and deployment of quantum networks (e.g., using fiber-coupled and commercially available devices). Moreover, it is desirable to develop teleportation systems that are forward-compatible with emerging quantum devices for the quantum internet.

In the context of Caltech's multi-disciplinary multi-institutional collaborative public-private research program on Intelligent Quantum Networks and Technologies (INQ-NET) founded with AT&T as well as Fermi National Accelerator Laboratory (Fermilab) and Jet Propulsion Laboratory in 2017, we designed, built, commissioned and deployed two quantum teleportation systems: one at Fermilab, the Fermilab Quantum Network (FQNET), and one at Caltech's Lauritsen Laboratory for High Energy Physics, the Caltech Quantum Network (CQNET). The CQNET system serves as an R&D, prototyping, and commissioning system, while FQNET serves as an expandable system, for scaling up to long distances and is used in multiple projects funded currently by DOE's Office of High Energy Physics (HEP) and Advanced Scientific Research Computing (ASCR). Material and devices level R&D in both systems is facilitated and funded by the Office of Basic Energy Sciences. Both systems are accessible to quantum researchers for R&D purposes as well as testing and integration of various novel devices, such as for example on-chip integrated nanophotonic devices and quantum memories, needed to upgrade such systems towards a realistic quantum internet. Importantly both systems are also used for improvements of the entanglement quality and distribution with emphasis

on implementation of protocols with complex entangled states towards advanced and complex quantum communications channels. These will assist in studies of systems that implement new teleportation protocols whose gravitational duals correspond to wormholes [43], error correlation properties of wormhole teleportation, on-chip codes as well as possible implementation of protocols on quantum optics communication platforms. Hence the systems serve both fundamental quantum information science as well as quantum technologies.

Here we perform quantum teleportation of time-bin qubits at a wavelength of 1536.5 nm with an average $F \geq 90\%$. This is accomplished using a compact setup of fiber-coupled devices, including low-dark-count single photon detectors and off-the-shelf optics, allowing straight-forward reproduction for multi-node networks. To illustrate network compatibility, teleportation is performed with up to 44 km of single-mode fiber between the qubit generation and the measurement of the teleported qubit, and is facilitated using semi-autonomous control, monitoring, and synchronization systems, with results collected using scalable acquisition hardware. Our systems, which operates at a clock rate of 90 MHz, can be run remotely for several days without interruption and yield teleportation rates of a few Hz using the full length of fiber. Our qubits are also compatible with erbium-doped crystals, e.g., Er:Y_2SiO_5, that are used to develop quantum network devices like memories and transducers [44, 45, 46]. Finally, we develop an analytical model of our system, which includes experimental imperfections, predicting that the fidelity can be improved further towards unity by well-understood methods (such as improvement in photon indistinguishability). Our demonstrations provide a step towards a workable quantum network with practical and replicable nodes, such as the ambitious U.S. Department of Energy quantum research network envisioned to link the U.S. National Laboratories.

In the following we describe the components of our systems as well as characterization measurements that support our teleportation results, including the fidelity of our entangled Bell state and Hong-Ou-Mandel (HOM) interference [47] that underpins the success of the BSM. We then present our teleportation results using both quantum state tomography (QST) [48] and projection measurements based on a decoy state method [49], followed by a discussion of our model. We conclude by considering improvements towards near-unit fidelity and GHz level teleportation rates.

8.2 Setup

Our fiber-based experimental system is summarized in the diagram of Fig. 8.1. It allow us to demonstrate a quantum teleportation protocol in which a photonic qubit (provided by Alice) is interfered with one member of an entangled photon-pair (from Bob) and projected (by Charlie) onto a Bell-state whereby the state of Alice's qubit can be transferred to the remaining member of Bob's entangled photon pair. Up to 22 (11) km of single mode fiber is introduced between Alice and Charlie (Bob and Charlie), as well as up to another 11 km at Bob, depending on the experiment (see Sec. 8.3). All qubits are generated at the clock rate, with all of their measurements collected using a data acquisition (DAQ) system. Each of the Alice, Bob, Charlie subsystems are further detailed in the following subsections, with the DAQ subsystem described in Section 8.6.

Alice: single-qubit generation

To generate the time-bin qubit that Alice will teleport to Bob, light from a fiber-coupled 1536.5 nm continuous wave (CW) laser is input into a lithium niobate intensity modulator (IM). We drive the IM with one pulse, or two pulses separated by 2 ns. Each pulse is of ~65 ps full width at half maximum (FWHM) duration. The pulses are produced by an arbitrary waveform generator (AWG) and amplified by a 27 dB-gain high-bandwidth amplifier to generate optical pulses that have an extinction ratio of up to 22 dB. We note that this method of creating time-bin qubits offers us flexibility not only in terms of choosing a suitable time-bin separation, but also for synchronizing qubits originating from different nodes in a network. A 90/10 polarization-maintaining fiber beam splitter combined with a power monitor (PWM) is used to apply feedback to the DC-bias port of the IM so as to maintain a constant 22 dB extinction ratio [50]. In order to successfully execute the quantum teleportation protocol, photons from Alice and Bob must be indistinguishable in all degrees of freedom (see Sec. 8.3). Hence, the optical pulses at the output of the IM are band-pass filtered using a 2 GHz-bandwidth (FWHM) fiber Bragg grating (FBG) centered at 1536.5 nm to match the spectrum of the photons from the entangled pair-source (described in Sec. 8.2). Furthermore, the polarization of Alice's photons is determined by a manual polarization controller (POC) in conjunction with a polarizing beam splitter (PBS) at Charlie. Finally, the optical pulses from Alice are attenuated to the single photon level by a variable optical attenuator (VOA), to approximate photonic time-bin qubits of the form $|A\rangle = \gamma |e\rangle_A + \sqrt{1-\gamma^2}\,|l\rangle_A$, where the late state $|l\rangle_A$ arrives 2 ns after the early state $|e\rangle_A$, γ is real and set to be

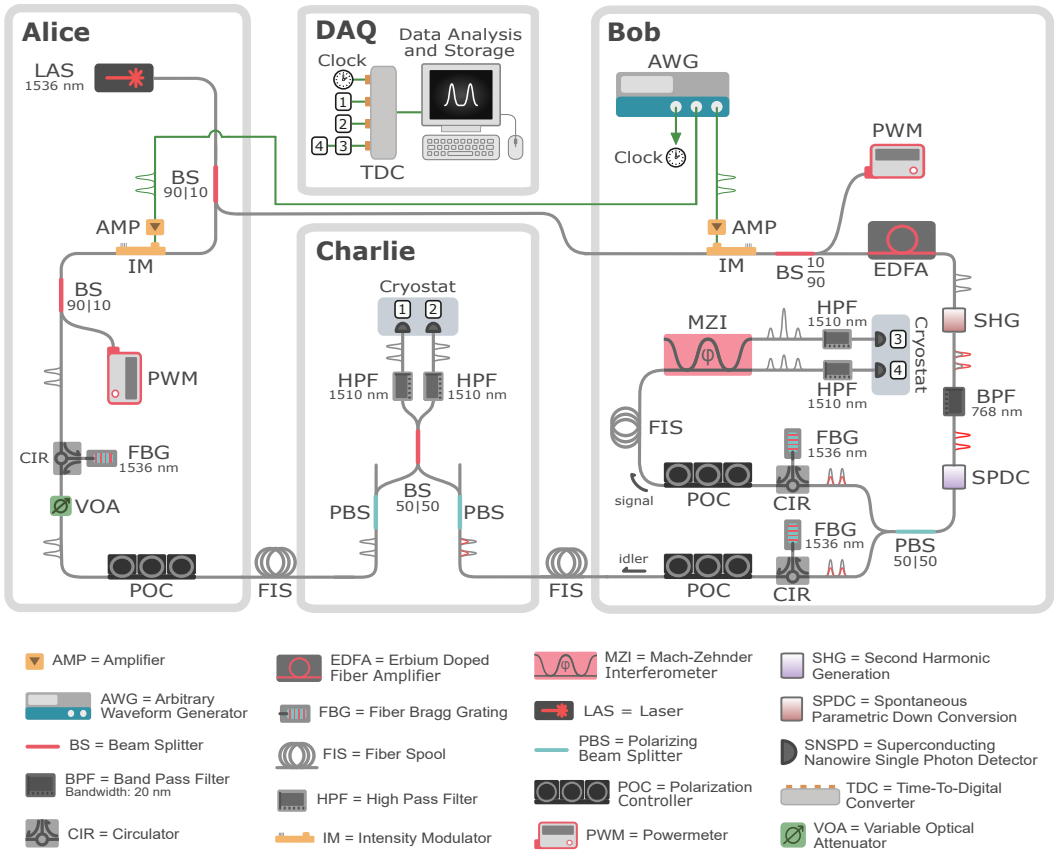

Figure 8.1: Schematic diagram of the quantum teleportation system consisting of Alice, Bob, Charlie, and the data acquisition (DAQ) subsystems. See the main text for descriptions of each subsystem. One cryostat is used to house all SNSPDs, it is drawn as two for ease of explanation. Detection signals generated by each of the SNSPDs are labelled 1-4 and collected at the TDC, with 3 and 4 being time-multiplexed. All individual components are labeled in the legend, with single-mode optical fibers (electronic cables) in grey (green), and with uni- and bi-chromatic (i.e., unfiltered) optical pulses indicated.

either 1, 0, or $1/\sqrt{2}$ to generate $|e\rangle_A$, $|l\rangle_A$, or $|+\rangle_A = (|e\rangle_A + |l\rangle_A)/\sqrt{2}$, respectively, depending on the experiment. The complex relative phase is absorbed into the definition of $|l\rangle_A$. The duration of each time bin is 800 ps.

Bob: entangled qubit generation and teleported-qubit measurement

Similar to Alice, one (two) optical pulse(s) with a FWHM of $\sim$ 65 ps is (and separated by 2 ns are) created using a 1536.5 nm CW laser in conjunction with a lithium niobate IM driven by an AWG, while the 90/10 beam splitter and PWM are used to maintain an extinction ratio of at least 20 dB. An Erbium-Doped Fiber Amplifier (EDFA) is used after the IM to boost the pulse power and thus maintain a high output rate of photon pairs.

The output of the EDFA is sent to a Type-0 periodically poled lithium niobate (PPLN) waveguide for second harmonic generation (SHG), upconverting the pulses to 768.25 nm. The residual light at 1536.5 nm is removed by a 768 nm band-pass filter with an extinction ratio $\geq$ 80 dB. These pulses undergo spontaneous parametric down-conversion (SPDC) using a Type-II PPLN waveguide coupled to a polarization-maintaining fiber (PMF), approximately producing either a photon pair $|pair\rangle_B = |ee\rangle_B$, or the time-bin entangled state $|\phi^+\rangle_B = (|ee\rangle_B + |ll\rangle_B)/\sqrt{2}$, if one or two pulses, respectively, are used to drive the IM. The ordering of the states refers to so-called signal and idler modes of the pair of which the former has parallel, and the latter orthogonal, polarization with respect to the axis of the PMF. As before, the relative phase is absorbed into the definition of $|ll\rangle_B$. Each photon is separated into different fibers using a PBS and spectrally filtered with FBGs akin to that at Alice. Note the bandwidth of the FBG is chosen as a trade-off between spectral purity and generation rate of Bob's photons [51]. The photon in the idler mode is sent to Charlie for teleportation or HOM measurements (see Sec. 8.3), or to the MZI (see below) for characterizations of the entangled state (see Sec. 8.3), with its polarization determined using a POC. The photon in the signal mode is sent to a Mach Zehnder interferometer (MZI) by way of a POC (and an additional 11 km of single-mode fiber for some measurements), and is detected by superconducting nanowire single photon detectors (SNSPDs) [52] after high-pass filtering (HPF) to reject any remaining 768.25 nm light. The MZI and detectors are used for projection measurements of the teleported state, characterization of the time-bin entangled state, or measuring HOM interference at Charlie. The time-of-arrival of the photons is recorded by the DAQ subsystem using a time-to-digital converter (TDC) referenced to the clock signal from the AWG.

All SNSPDs are installed in a compact sorption fridge cryostat [53], which operates at a temperature of 0.8 K for typically 24 h before a required 2 h downtime. Our SNSPDs are developed at the Jet Propulsion Laboratory and have detection efficiencies between 76 and 85%, with low dark count rates of 2-3 Hz. The FWHM temporal resolution of all detectors is between 60 and 90 ps while their recovery time is ∼50 ns. A detailed description of the SNSPDs and associated setup is provided in Section 8.6.

The MZI has a path length difference of 2 ns and is used to perform projection measurements of $|e\rangle_B$, $|l\rangle_B$, and $(|e\rangle_B + e^{i\varphi}|l\rangle_B)/\sqrt{2}$, by detecting photons at three distinct arrival times in one of the outputs, and varying the relative phase φ [28]. Detection at the other output yields the same measurements except with a relative phase of $\varphi + \pi$. Using a custom temperature-feedback system, we slowly vary φ for up to 15 hour time intervals to collect all measurements, which is within the cryostat hold time. Further details of the MZI setup is described in Section 8.6.

Charlie: Bell-state measurement

Charlie consists of a 50/50 polarization-maintaining fiber beam splitter (BS), with relevant photons from the Alice and Bob subsystems directed to each of its inputs via a PBSs and optical fiber. The photons are detected at each output with an SNSPD after HPFs, with their arrival times recorded using the DAQ as was done at Bob. Teleportation is facilitated by measurement of the $|\Psi^-\rangle_{AB} = (|el\rangle_{AB} - |le\rangle_{AB})/\sqrt{2}$ Bell state, which corresponds to the detection of a photon in $|e\rangle$ at one detector followed by the detection of a photon in $|l\rangle$ at the other detector after Alice and Bob's (indistinguishable) qubits arrive at the BS [54]. Projection on the $|\Psi^-\rangle_{AB}$ state corresponds to teleportation of $|A\rangle$ up to a known local unitary transformation, i.e., our system produces $-i\sigma_y|A\rangle$, with σ_y being the Pauli y-matrix.

8.3 Experimental results

Prior to performing quantum teleportation, we measure some key parameters of our system that underpin the teleportation fidelity. Specifically, we determine the fidelity of the entangled state produced by Bob by measuring the entanglement visibility V_{ent} [55], and also determine to what extent Alice and Bob's photons are indistinguishable at Charlie's BS using the HOM effect [47].

Entanglement visibility

The state $|pair\rangle_B$ (and hence the entangled state $|\phi^+\rangle_B$) described in Sec. 8.2 is idealized. In reality, the state produced by Bob is better approximated by a two-mode squeezed vacuum state $|\text{TMSV}\rangle_B = \sqrt{1-p}\sum_{n=0}^{\infty}\sqrt{p}^n\,|nn\rangle_B$ after the FBG filter and neglecting loss [56]. Here, n is the number of photons per temporal mode (or qubit), p is the emission probability of a single pair per mode (or qubit), with state ordering referring to signal and idler modes. However, $|\text{TMSV}\rangle_B$ approximates a photon pair for $p \ll 1$, with $p \approx \mu_B$ mean number of pairs per mode (or qubit), conditioned on measurement of a pair such that the $n = 0$ term is eliminated. As a compromise between the pair-creation rate $\propto p$ and the quality of entanglement, here and henceforth we set the mean photon number of our pair source to be $\mu_B = (8.0 \pm 0.4) \times 10^{-3}$ per time bin, which is feasible because of the exceptionally low dark counts of our SNSPDs. The measurement of μ_B is outlined in Section 8.6.

We generate $|\phi^+\rangle_B$ and measure V_{ent} by directing the idler photon to the second input port of the MZI, slightly modifying the setup of Fig. 8.1. The idler photon is delayed compared to the signal, allowing unambiguous measurement of each qubit. We vary φ and project each qubit of the entangled state onto phase-varied superpositions of $|e\rangle$ and $|l\rangle$ by accumulating coincidence events of photons at both the outputs of the interferometer [55].

The results shown in Fig. 8.2 are fit proportional to $1 + V_{ent}\sin(\omega T + \Phi)$, where $V_{ent} = (R_x - R_n)/(R_x + R_n)$, with $R_{x(n)}$ denoting the maximum (minimum) rate of coincidence events [55], ω and Φ are unconstrained constants, and T is the temperature of the MZI, finding $V_{ent} = 96.4 \pm 0.3\%$.

The deviation from unit visibility is mainly due to non-zero multi photon emissions [57], which is supported by an analytical model that includes experimental imperfections (see Chapter 9). Nonetheless, this visibility is far beyond the $1/3$ required for non-separability of a Werner state [58] and the locality bound of $1/\sqrt{2}$ [59, 55]. Furthermore, it predicts a fidelity $F_{ent} = (3V_{ent} + 1)/4 = 97.3 \pm .2\%$ with respect to $|\phi^+\rangle$ [58], and hence is sufficient for quantum teleportation.

HOM interference visibility

The BSM relies on quantum interference of photons from Alice and Bob. This is ensured by the BS at Charlie, precise control of the arrival time of photons with IMs, identical FBG filters, and POCs (with PBSs) to provide the required indistinguishabiliy. The degree of interference is quantified by way of the HOM interference

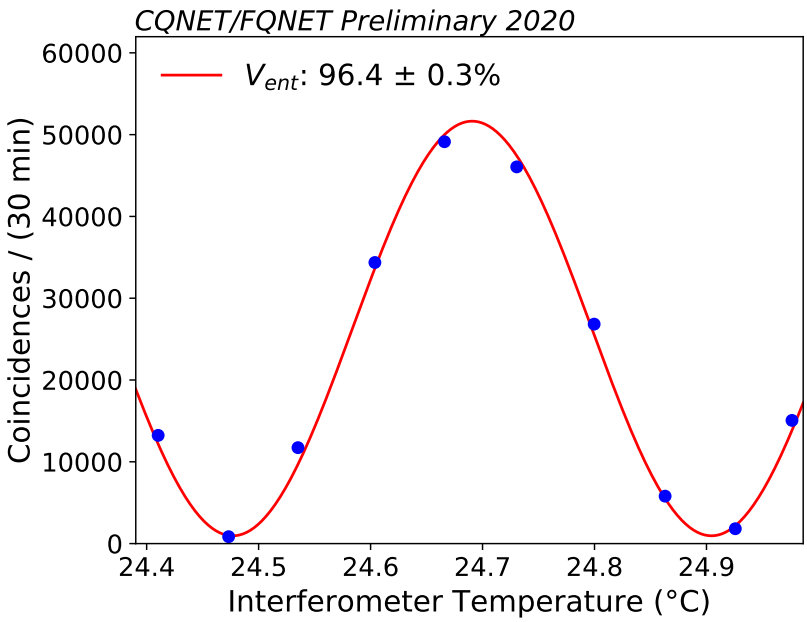

Figure 8.2: Entanglement visibility. The temperature of the interferometer is varied to reveal the expected sinusoidal variations in the rate of coincidence events. A fit reveals the entanglement visibility $V_{ent} = 96.4 \pm 0.3\%$, see main text for details. Uncertainties here and in all measurements are calculated assuming Poisson statistics.

visibility $V_{HOM} = (R_d - R_i)/R_d$, with $R_{d(i)}$ denoting the rate of coincident detections of photons after the BS when the photons are rendered as distinguishable (indistinguishable) as possible [47]. Completely indistinguishable single photons from Alice and Bob may yield $V_{HOM} = 1$. However in our system, Alice's qubit is approximated from a coherent state $|\alpha\rangle_A = e^{-|\alpha|^2/2} \sum_{n=0}^{\infty} \frac{\alpha^n}{\sqrt{n!}} |n\rangle_A$ with $\alpha \ll 1$, akin to how Bob's pair is approximated from $|\text{TMSV}\rangle_B$ (see Sec. 8.3), with $\mu_A = |\alpha|^2$ being Alice's mean photon number per mode (or qubit) [56]. Therefore, the contribution of undesired photons from Alice and Bob lowers the maximum achievable V_{HOM} below unity, with a further reduction if the interfering photons are not completely indistinguishable. The dependence of V_{HOM} with varied μ_A and μ_B, including effects of losses or distinguishable photons in our system is analytically modeled in Chapter 9, and briefly discussed in Sec. 8.4.

We measure V_{HOM} by slightly modifying the setup of Fig. 8.1: We prepare $|A\rangle = |e\rangle_A$ with $\mu_A = 2.6 \times 10^{-3}$ and Bob as $|pair\rangle_B$ and direct Alice's photon and Bob's idler to Charlie, with Bob's signal bypassing the MZI to be directly measured by an SNSPD. Alice's IM is used to introduce distinguishability by way of a relative difference in arrival time Δt_{AB} of Alice and Bob's photons at Charlie's BS. Using

Charlie's SNSPDs and the third detector at Bob, a three-fold coincidence detection rate is measured for varying Δt_{AB}, with results shown in Fig. 8.3a. Since the temporal profiles of our photons are approximately Gaussian, we fit our results to $A[1 - V_{HOM} \exp\left(-\frac{\Delta t_{AB}^2}{2\sigma^2}\right)]$, where A is the maximum coincidence rate when the photons are completely distinguishable and $\sigma = 300$ ps is the $1/e$ temporal duration of the optical pulses [47, 60], finding $V_{HOM} = 70.9 \pm 1.9\%$. The maximum V_{HOM} for this experiment is 83.5% if the photons were completely indistinguishable (see Chapter 9), with the difference ascribed to slight distinguishability between our photons as supported by the further measurements and analytical modeling in Sec. 8.4. Improvements to our system to remove this distinguishability is discussed in Sec. 8.5.

To test our system for quantum teleportation over long distances, we introduce the aforementioned 22, 11, and 11 km lengths of single-mode fiber between Alice and Charlie, Bob and Charlie, and in the path of Bob's signal photon, respectively, repeat our measurement of V_{HOM} and fit the results as before (see Fig. 8.3b). We find $V_{HOM} = 63.4 \pm 5.9\%$, which is consistent with the maximum V_{HOM} we expect when including the impact of the additional 5.92 (2.56) dB loss between Charlie and Alice (Bob) as well as the effect of photon distinguishability (analyzed in Sec. 8.4). This suggests that the additional fiber importantly does not introduce any further distinguishability (that we cannot account for), thereby supporting our system's use in quantum networking. Overall, the presence of clear HOM interference suggests our system (with or without the additional fiber) introduces relatively little imperfections that can negatively impact the BSM and hence the fidelity of quantum teleportation.

Quantum teleportation

We now perform quantum teleportation of the time-bin qubit basis states $|e\rangle$, $|l\rangle$ and $|+\rangle$, so as to measure the teleportation fidelities, F_e, F_l, an F_+, respectively, of the teleported states with respect to their ideal counterparts, up to the local unitary introduced by the BSM (see Sec. 8.2). Since measurement of $|+\rangle$ in our setup by symmetry is equivalent to any state of the form $(|e\rangle + e^{i\varphi}|l\rangle)/\sqrt{2}$ (and in particular the remaining three basis states $(|e\rangle - |l\rangle)/\sqrt{2}$ and $(|e\rangle \pm i|l\rangle)/\sqrt{2}$), we may determine the average teleportation fidelity $F_{avg} = (F_e + F_l + 4F_+)/6$ of any time-bin qubit.

First, we prepare $|e\rangle_A$ and $|l\rangle_A$ with $\mu_A = 3.53\times10^{-2}$, with Bob's idler bypassing the

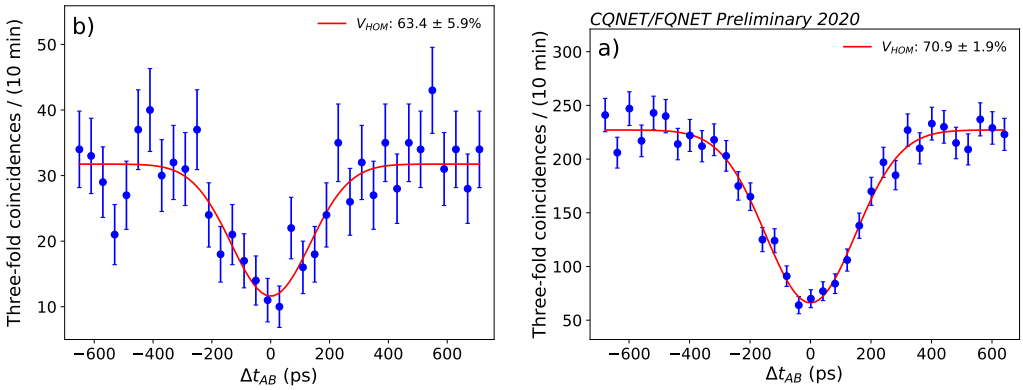

Figure 8.3: Hong-Ou-Mandel (HOM) interference. A relative difference in arrival time is introduced between photons from Alice and Bob at Charlie's BS. HOM interference produces a reduction of the three-fold coincidence detection rate of photons as measured with SNSPDs after Charlie's BS and at Bob. A fit reveals a) $V_{HOM} = 70.9 \pm 1.9\%$ and b) $V_{HOM} = 63.4 \pm 5.9\%$ when lengths of fiber are added, see main text for details.

MZI to be detected by a single SNSPD. We measure $F_e = 95 \pm 1\%$ and $F_l = 96 \pm 1\%$, conditioned on a successful measurement of $|\Psi^-\rangle_{AB}$ at Charlie, with fidelity limited by multiphoton events in Alice and Bob's qubits and dark counts of the SNSPDs (see Chapter 9). We then repeat the measurement with $\mu_A = 9.5 \times 10^{-3}$ after inserting the aforementioned 44 km length of fiber as before to emulate Alice, Charlie and parts of Bob being separated by long distances. This gives $F_e = 98 \pm 1\%$ and $F_l = 98 \pm 2\%$, with no reduction from the additional fiber loss owing to our low noise SNSPDs.

Next, we prepare $|+\rangle_A$ with $\mu_A = 9.38 \times 10^{-3}$, insert the MZI and, conditioned on the BSM, we measure $F_+ = (1 + V_+)/2 = 84.9 \pm 0.5\%$ by varying φ. Here, $V_+ = 69.7 \pm 0.9\%$ is the average visibility obtained by fits to the resultant interference measured at each output of the MZI, as shown in Fig. 8.4a. The reduction in fidelity from unity is due to multiphoton events and distinguishability, consistent with that inferred from HOM interference, as supported by further measurements and analytical modeling in Sec. 8.4.

The measurement is repeated with the additional long fiber, giving $V_+ = 58.6 \pm 5.7\%$ and $F_+ = 79.3 \pm 2.9\%$ with results and corresponding fit shown in Fig. 8.4b. The reduced fidelity is likely due to aforementioned polarization variations over the long fibers, consistent with the reduction in HOM interference visibility, and exacerbated here owing to the less than ideal visibility of the MZI over long measurement times

(see Sec. 8.6).

The results yield $F_{avg} = 89 \pm 1\%$ ($86 \pm 3\%$) without (with) the additional fiber, which is significantly above the classical bound of $2/3$, implying strong evidence of quantum teleportation [61], and limited from unity by multiphotons events, distinguishability, and polarization variations, as mentioned in Chapter 9.

To glean more information about our teleportation system beyond the fidelity, we reconstruct the density matrices of the teleported states using a maximum-likelihood QST [48] described in Section 8.6. The results of the QST with and without the additional fiber lengths are summarized in Figs. 8.8a and b, respectively. As can be seen, the diagonal elements for $|+\rangle$ are very close to the expected value indicating the preservation of probabilities for the basis states of $|e\rangle$ and $|l\rangle$ after teleportation, while the deviation of the off-diagonal elements indicate the deterioration of coherence between the basis states. The decoherence is attributed to multiphoton emissions from our entangled pair source and distinguishability, consistent with the aforementioned teleportation fidelities of $|+\rangle_A$, and further discussed in Sec. 8.4. Finally, we do also extract the teleportation fidelity from these density matrices, finding the results shown in Fig. 8.5, and $F_{avg} = 89 \pm 1\%$ ($88 \pm 3\%$) without (with) the fiber spools, which are consistent with previous measurements given the similar μ_A used for QST.

We point out that the $2/3$ classical bound may only be applied if Alice prepares her qubits using genuine single photons, i.e., $|n = 1\rangle$, rather than using $|\alpha \ll 1\rangle$ as we do in this work [62]. As a way to account for the photon statistics of Alice's qubits we turn to an analysis using decoy states.

Teleportation fidelity using decoy states

To determine the minimum teleportation fidelity of qubits prepared using single photons, we use a decoy state method [49] and follow the approach of Refs. [63, 29]. Decoy states, which are traditionally used in quantum key distribution to defend against photon-number splitting attacks, are qubits encoded into coherent states $|\alpha\rangle$ with varying mean photon number $\mu_A = |\alpha|^2$. Measuring fidelities of the teleported qubits for different μ_A, the decoy-state method allows us to calculate a lower bound F_A^d on the teleportation fidelity if Alice had encoded her qubits using $|n = 1\rangle$.

We prepare decoy states $|e\rangle_A$, $|l\rangle_A$, and $|+\rangle_A$ with varying μ_A, as listed in Table 8.1, and perform quantum teleportation both with and without the added fiber, with

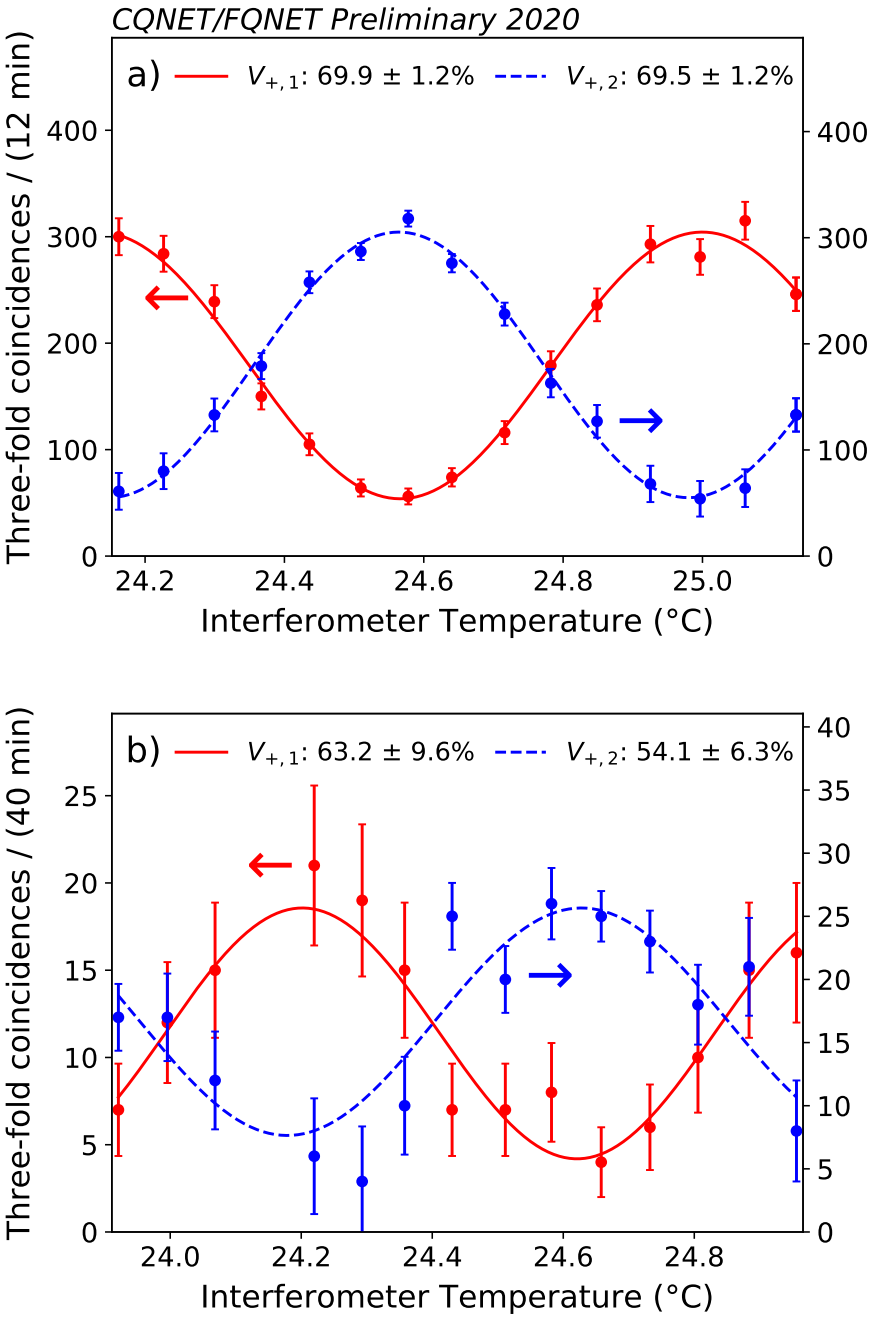

Figure 8.4: Quantum teleportation of $|+\rangle$. Teleportation is performed b) with and a) without an additional 44 km of single-mode fiber inserted into the system. The temperature of the inteferometer is varied to yield a sinusoidal variation of the three-fold coincidence rate at each output of the MZI (blue and red points). A fit of the visibilities (see Sec. 8.3) measured at each output ($V_{+,1}$, $V_{+,2}$) of the MZI gives an average visibility $V_+ = (V_{+,1} + V_{+,2})/2$ of a) 69.7 ± 0.91% without the additional fiber and b) 58.6 ± 5.7% with the additional fiber.

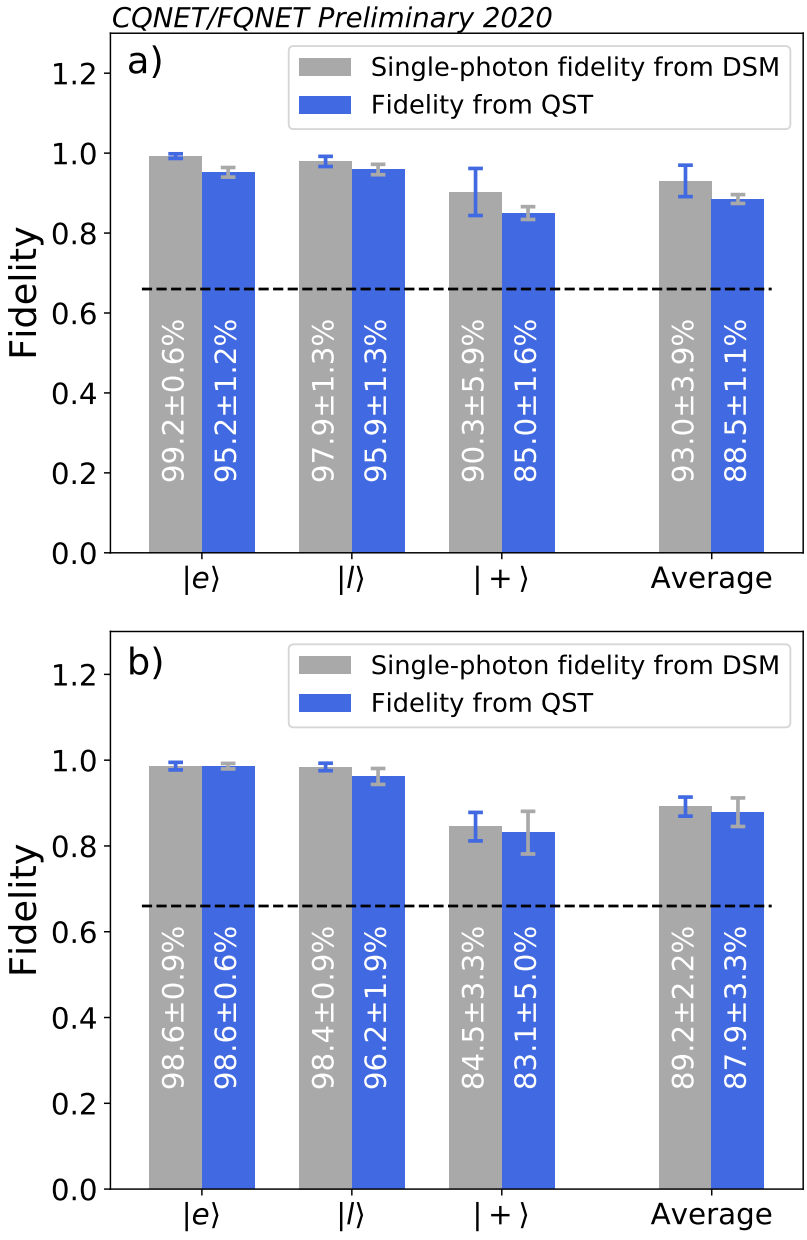

Figure 8.5: Quantum teleportation fidelities for $|e\rangle_A$, $|l\rangle_A$, and $|+\rangle_A$, including the average fidelity. The dashed line represents the classical bound. Fidelities using quantum state tomography (QST) are shown using blue bars while the minimum fidelities for qubits prepared using $|n = 1\rangle$, F_e^d, F_l^d, and F_+^d, including the associated average fidelity F_{avg}^d, respectively, using a decoy state method (DSM) is shown in grey. Panels a) and b) depicts the results without and with additional fiber, respectively. Uncertainties are calculated using Monte-Carlo simulations with Poissonian statistics.

teleportation fidelities shown in Table 8.1. From these results we calculate F_A^d as shown in Fig. 8.5, with $F_{avg}^d \geq 93 \pm 4\%$ ($F_{avg}^d \geq 89 \pm 2\%$) without (with) the added fiber, which significantly violate the classical bound and the bound of $5/6$ given by an optimal symmetric universal cloner [64, 65], clearly demonstrating the capability of our system for high-fidelity teleportation. As depicted in Fig. 8.5 these fidelities nearly match the results we obtained without decoy states within statistical uncertainty. This is due to the suitable μ_A, as well as low μ_B and SNSPD dark counts in our previous measurements (see Chapter 9).

qubit	without long fiber		with long fiber	
	μ_A ($\times 10^{-3}$)	F_A^d (%)	μ_A ($\times 10^{-3}$)	F_A^d (%)
$\|e\rangle_A$	3.53	95.2 ± 1	26.6	95.7 ± 1.5
	1.24	86.7 ± 2	9.01	98.4 ± 1.1
	0	52.8 ± 3.4	-	-
$\|l\rangle_A$	3.53	95.9 ± 1	32.9	98.6 ± 0.7
	1.24	90.5 ± 2	9.49	98.4 ± 1.6
	0	52.8 ± 3.4	-	-
$\|+\rangle_A$	9.38	84.7 ± 1.1	29.7	73.6 ± 3.0
	2.01	83.2 ± 3.6	10.6	82.21 ± 3.9
	0	52.8 ± 3.4	-	-

Table 8.1: Teleportation fidelities with (right column) and without (center column) the 44 km-length of fiber for Alice's qubit states prepared with varying μ_A. Mean photon numbers and fidelities for vacuum states with fiber are assumed to be zero and 50%, respectively.

8.4 Analytical model and simulation

As our measurements have suggested, multi-photon components in, and distinguishability between, Alice and Bob's qubits reduce the values of key metrics including HOM interference visibility and, consequently, quantum teleportation fidelity. To capture these effects in our model, we employ a Gaussian-state characteristic-function method developed in Chapter 9, which was enabled by work in Ref. [66]. This approach is well-suited to analyze our system because the quantum states, operations, and imperfections (including losses, dark counts, etc.) of the experiment can be fully described using Gaussian operators, see e.g., Ref. [67]. We now briefly outline the model of Chapter 9, and employ it to estimate the amount of indistinguishability ζ between Alice and Bob's qubits in our measurements of HOM

interference and quantum teleportation.

The distinguishability in any degree-of-freedom may be modeled by introducing a virtual beam splitter of transmittance ζ into the paths of Alice and Bob's relevant photons. As shown in Fig. 8.6, indistinguishable components of incoming photon modes are directed towards Charlie's BS where they interfere, whereas distinguishable components are mixed with vacuum at the BS and do not contribute to interference. Here $\zeta = 1$ ($\zeta = 0$) corresponds to the case when both incoming photons are perfectly indistinguishable (distinguishable). Now we may calculate the probability of a three-fold coincidence detection event P_{3f} between D_1, D_2 (Charlies' detectors), and D_3 (detects Bob's signal photon) for a given qubit state ρ_{AB} from Alice and Bob:

$$\begin{aligned} P_{3f} = \mathrm{Tr}\{\rho_{AB}(\mathbb{I} - (|0\rangle\langle 0|)^{\otimes 3}_{\hat{a}_1,\hat{a}_2,\hat{a}_3}) \\ \otimes (\mathbb{I} - (|0\rangle\langle 0|)^{\otimes 3}_{\hat{b}_1,\hat{b}_2,\hat{b}_3}) \otimes (\mathbb{I} - (|0\rangle\langle 0|)_{\hat{c}})\}, \end{aligned} \tag{8.1}$$

where the $\hat{a}$ and $\hat{b}$ operators refer to modes, which originate from Alice and Bob's virtual beam splitters and are directed to D_1 and D_2, respectively, and $\hat{c}$ corresponds to Bob's idler mode, which is directed to D_3, see Fig. 8.6. This allows the derivation

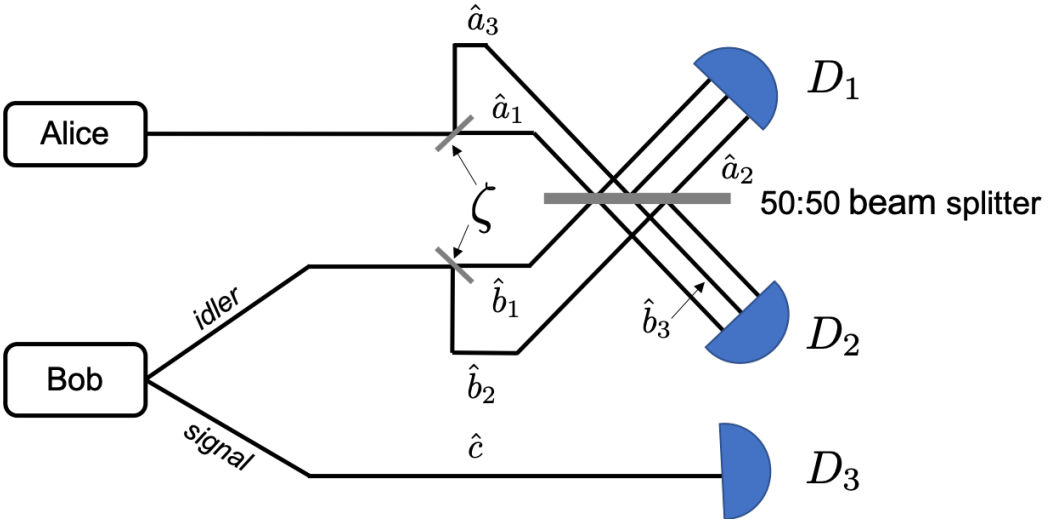

Figure 8.6: Schematic depiction of distingushability between Alice and Bob's photons at Charlie's BS. Distinguishability is modeled by means of a virtual beam splitter with a transmittance ζ. Indistinguishable photons contribute to interference at the Charlie's BS while distinguishable photons are mixed with vacuum, leading to a reduction of HOM visibility and teleportation fidelity. See main text for further details.

of an expression for the HOM interference visibility

$$V_{HOM}(\zeta) = [P_{3f}(0) - P_{3f}(\zeta)]/P_{3f}(0), \tag{8.2}$$

consistent with that introduced in Sec. 8.3. Since Alice and Bob ideally produce $\rho_{AB} = (|\alpha\rangle\langle\alpha|) \otimes (|\text{TMSV}\rangle\langle\text{TMSV}|)$, and recognizing that all operators in P_{3f} are Gaussian, we analytically derive

$$\begin{aligned} P_{3f}(\zeta) = 1 &- 2\frac{\exp\left(-\frac{\mu_A/2[1+(1-\zeta^2)\eta_i\mu_B/2]}{1+\eta_i\mu_B/2}\right)}{1+\eta_i\mu_B/2} \\ &- \frac{1}{1+\eta_s\mu_B} + \frac{\exp(-\mu_A)}{1+\eta_i\mu_B} \\ &- \frac{\exp(-\mu_A)}{1+(1-\eta_s)\eta_i\mu_B+\eta_s\mu_B} \\ &+ 2\frac{\exp\left(-\frac{\mu_A/2[1+(1-\zeta^2)(1-\eta_s)\eta_i\mu_B/2+\eta_s\mu_B]}{1+(1-\eta_s)\eta_i\mu_B/2+\eta_s\mu_B}\right)}{1+(1-\eta_s)\eta_i\mu_B/2+\eta_s\mu_B}, \end{aligned} \tag{8.3}$$

for varied ζ, where η_i and η_s are the transmission efficiencies of the signal and idler photons, including detector efficiencies. We similarly calculate the impact of distinguishability on the teleportation fidelity of $|+\rangle$:

$$F(\zeta) = P_{3f}(\zeta, \varphi_{max})/[P_{3f}(\zeta, \varphi_{max}) + P_{3f}(\zeta, \varphi_{min})], \tag{8.4}$$

where φ_{max} (φ_{min}) is the phase of the MZI added into the path of the signal photon, corresponding to maximum (minimum) three-fold detection rates.

To compare the model to our measurements, we use the experimental mean photon numbers for the photon-pair source $\eta_i = 1.2 \times 10^{-2}$ and $\eta_s = 4.5 \times 10^{-3}$ as determined by the method described in Section 8.6. We then measure the teleportation fidelity of $|+\rangle$ and HOM interference visibility (keeping the MZI in the system to ensure η_s remains unchanged) for different values μ_A. The results are plotted in Fig. 8.7. The data is then fitted to the expressions $V_{HOM}(\zeta)$ and $F(\zeta)$ derived in our model and graphed in Fig. 8.7. The fitted curves are in very good agreement with our experimental values and consistently yield a value of $\zeta = 90\%$ for both measurements types. This implies that we have only a small amount of residual distinguishability between Alice and Bob's photons. Potential effects leading to this distinguishability are discussed in Sec. 8.5.

Overall, our analytic model is consistent with our experimental data (see Chapter 9) in the regime of $\mu_A \ll 1$, which is the parameter space most often used in quantum

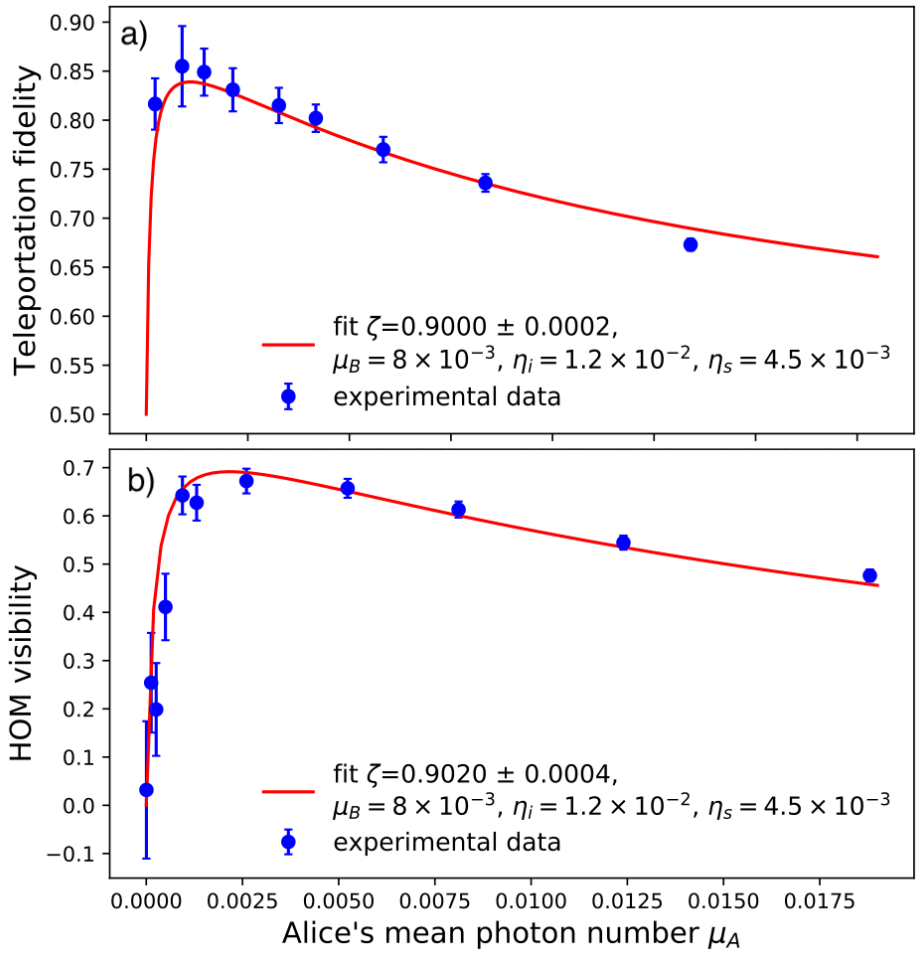

Figure 8.7: Evaluation of photon indistinguishability using an analytical model. Panel a) depicts the quantum teleportation fidelity of $|+\rangle$ while panel b) shows the HOM interference visibility, each with varied mean photon number μ_A of Alice's qubits. Fits of analytical models the data reveal $\zeta = 90\%$ indistinguishability between Alice and Bob's photons at Charlie's BS. Bob produces μ_B photon pairs on average, η_i and η_s are the probabilities for an individual idler (signal) photon to arrive at Charlie's BS and be detected at Bob's detector, respectively.

networking protocols (e.g., key distribution). Our model, thus, offers a practical way to determine any underlying distinguishability in a deployed network where a full characterization of the properties of Alice and Bob's photons may not be possible.

8.5 Discussion

We have demonstrated quantum teleportation systems for photonic time-bin qubits at a quantum channel- and device-compatible wavelength of 1536.5 nm using a fiber-

based setup comprising off-the-shelf components and state-of-the-art SNSPDs. We measure an average fidelity above 90% using QST and a decoy state analysis with up to 44 km of single mode fiber in our setup. Our results are further supported by an analytical model in conjunction with measurements of the entanglement and HOM interference visibilities.

The decoy state analysis indicates that the maximum teleportation fidelity is currently restricted by that of the teleported qubits prepared in superposition states, for which a 10% distinguishability between the qubits undergoing BSM and the contribution of multiple photon pairs play the largest role. Our model predicts that the average fidelity will increase to 95% with completely indistinguishable photons, while fidelities close to unity can be achieved with lowered mean number of photon pairs. Alternatively, we may replace our SNSPDs with efficient photon-number resolving (PNR) SNSPDs [68] to allow postselection of multiphoton events at the MZI or BSM [69]. Nonetheless, both approaches must be accompanied by increased coupling efficiencies of the pair source beyond the current $\sim$ 1% either to maintain realistic teleportation rates (above the system noise and current rate of phase drift of the MZI), or to derive any advantage from PNR capability.

As suggested by the width of our HOM interference fringe – which predicts an average photon bandwidth of $0.44/\sigma$ $\sim$1.5 GHz (see Sec. 8.3), i.e., less than the 2 GHz bandwidth of our FBGs – the indistinguishability in our system could be limited by the large difference in the bandwidth between the photons originating from the SPDC (>100 GHz) and those generated at Alice by the IM (15 GHz), leading to nonidentical filtering by the FBG. This can be improved by narrower FBGs or by using a more broadband pump at Alice (e.g., using a mode locked laser or a higher bandwidth IM, e.g., > 50 GHz, which is commercially available). Alternatively, pure photon pairs may be generated by engineered phase matching, see, e.g., Ref. [70]. Distinguishability owing to nonlinear modulation during the SHG process could also play a role [71]. The origin of distinguishability in our system, whether due to imperfect filtering or other device imperfections (e.g., PBS or BS) will be studied in future work. Coupling loss can be minimized to less than a few dB overall by improved fiber-to-chip coupling, lower-loss components of the FBGs (e.g., the required isolator), spliced fiber connections, and reduced losses within our MZI. Note that our current coupling efficiency is equivalent to $\sim$50 km of single mode fiber, suggesting that our system is well-suited for quantum networks provided loss is reduced.

While the fidelities we demonstrate are sufficient for several applications, the current ~Hz teleportation rates with the 44 km length of fiber are still low. Higher repetition rates (e.g., using high-bandwidth modulators with wide-band wavelength division multiplexed filters and low-jitter SNSPDs [72]), improvements to coupling and detector efficiencies, enhanced BSM efficiency with fast-recovery SNSPDs [73], or multiplexing in frequency [63] will all yield substantial increases in teleportation rate. Note that increased repetition rates permits a reduction in time bin separation which will allow constructing the MZI on chip, providing exceptional phase stability and hence, achievable fidelity. Importantly, the aforementioned increases in repetition rate and efficiency are afforded by improvements in SNSPD technology that are currently being pursued with our JPL, NIST and other academic partners.

Upcoming system-level improvements we plan to investigate and implement include further automation by the implementation of free-running temporal and polarization feedback schemes to render the photons indistinguishable at the BSM [29, 30]. Furthermore, several electrical components can be miniaturized, scaled, and made more cost effective (e.g., field-programmable gate arrays can replace the AWG).We note that our setup prototype will be easily extended to independent lasers at different locations, also with appropriate feedback mechanisms for spectral overlap [74, 75]. These planned improvements are compatible with the data acquisition and control systems that were built for the systems and experiments at FQNET and CQNET presented in this work.

Overall, our systems for achieving high-fidelity teleportation will serve as a blueprint for the construction of quantum network test-beds and eventually wide-spread quantum networks towards the quantum internet. In this vein, our Fermilab and Caltech Quantum Networks serve as R& D laboratories and prototypes towards real-world quantum networks. The high fidelities achieved in our experiments using practical and replicable devices are essential when expanding a quantum network to many nodes, and enable the realization of more advanced protocols, e.g., Refs. [18, 76, 77].

8.6 Methods

Detailed description of experimental components

Control systems and data acquisition Our system is built with a vision towards future replicability, with particular emphasis on systems integration. Each of the Alice, Bob and Charlie subsystems is equipped with monitoring and active feedback

stabilization systems (e.g., for IM extinction ratio), or has capability for remote control of critical network parameters (e.g., varying the qubit generation time). Each subsystem has a central classical processing unit with the following functions: oversight of automated functions and workflows within the subsystem, data acquisition and management, and handling of input and output synchronization streams. As the quantum information is encoded in the time domain the correct operation of the classical processing unit depends critically on the recorded time-of-arrival of the photons at the SNSPDs. Thus significant effort was dedicated to build a robust DAQ subsystem capable of recording and processing large volumes of time-tagged signals from the SNSPDs and recorded by our TDCs at a high rate. The DAQ is designed to enable both real-time data analysis for prompt data quality monitoring as well as post-processing data analysis that allows to achieve the best understanding of the data.

The DAQ system is built on top of the standalone Linux library of our commercial TDC. It records time tags whenever a signal is detected in any channel in coincidence with the reference 90 MHz clock. Time tags are streamed to a PC where they are processed in real-time and stored to disk for future analysis. A graphical user interface has been developed, capable of real-time visualization and monitoring of photons detected while executing teleportation. It also allows for easy control of the time-intervals used for each channel and to configure relevant coincidences between different photon detection events across all TDC channels. We expect our DAQ subsystem to serve as the foundation for future real-world time-bin quantum networking experiments (see Sec. 8.5).

Superconducting nanowire single photon detectors We employ amorphous tungsten silicide SNSPDs manufactured in the JPL Microdevices Laboratory for all measurements at the single photon level (see Sec. 8.2) [52]. The entire detection system is customized for optimum autonomous operation in a quantum network. The SNSPDs are operated at 0.8 K in a closed-cycle sorption fridge [53]. The detectors have nanowire widths between 140 to 160 nm and are biased at a current current of 8 to 9 μA. The full-width at half maximum (FWHM) timing jitter (i.e., temporal resolution) for all detectors is between 60 and 90 ps (measured using a Becker & Hickl SPC-150NXX time-tagging module). The system detection efficiencies (as measured from the fiber bulkhead of the cryostat) are between 76 and 85 %. The SNSPDs feature low dark count rates between 2 and 3 Hz, achieved by short-pass filtering of background black-body radiation through coiling of optical

fiber to a 3 cm diameter within the 40 K cryogenic environment, and an additional band-pass filter coating deposited on the detector fiber pigtails (by Andover Corporation). Biasing of the SNSPDs is facilitated by cryogenic bias-Ts with inductive shunts to prevent latching, thus enabling uninterrupted operation. The detection signals are amplified using Mini-Circuits ZX60-P103LN+ and ZFL-1000LN+ amplifiers at room temperature, achieving a total noise figure of 0.61 dB and gain of 39 dB at 1 GHz, which enables the low system jitter. Note that FWHM jitter as low as 45 ps is achievable with the system, by biasing the detectors at approximately 10 μA, at the cost of an elevated DCR on the order of 30 cps. Using commercially available components, the system is readily scalable to as many as 64 channels per cryostat, ideal for star-type quantum networks, with uninterrupted 24/7 operation. The bulkiest component of the current system is an external helium compressor, however, compact rack-mountable versions are readily available [53].

Interferometer and phase stabilization We use a commercial Kylia 04906-MINT MZI, which is constructed of free-space devices (e.g., mirrors, beam splitters) with small form-factor that fits into a hand-held box. Light is coupled into and out of the MZI using polarization maintaining fiber with loss of ~2.5 dB. The interferometer features an average visibility of 98.5% that was determined by directing $|+\rangle$ with $\mu_A = 0.07$ into one of the input ports, measuring the fringe visibility on each of the outputs using an SNSPD. The relative phase φ is controlled by a voltage-driven heater that introduces a small change in refractive index in one arm of the MZI. However, this built-in heater did not permit phase stability sufficient to measure high-fidelity teleportation, with the relative phase following the slowly-varying ambient temperature of the room. To mitigate this instability, we built another casing, thermally isolating the MZI enclosure from the laboratory environment and controlled the temperature via a closed-loop feedback control system based on a commercial thermoelectric cooler and a LTC1923 PID-controller. The temperature feedback is provided by a 10 kΩ NTC thermistor while the set-point is applied with a programmable power supply. This control system permits us to measure visbilities by slowly varying φ over up to 15 hour timescales. We remark that no additional methods of phase control were used beyond that of temperature.

Estimation of mean number of photon pairs and transmission efficiencies of signal and idler photons

Using a method described in Ref. [55], we measure the mean number of photon pairs produced by Bob μ_B as a function of laser excitation power before the PPLN waveguide used for SHG. To this end, we modify the setup of Fig. 8.1 and direct each of Bob's signal and idler photons to a SNSPD. We then measure detection events while varying the amplification of our EDFA by way of an applied current. We extract events when photon pairs which originated from the same clock cycle are measured in coincidence, and when one photon originating from a cycle is measured in coincidence with a photons originated from a preceding or following clock cycle, in other words we measure the so-called coincidence and accidental rates. The ratio of accidentals to coincidences approximates $\mu_B \ll 1$, with all results shown in Table 8.2. For all measurements we use $\mu_B = (8.0 \pm 0.4) \times 10^{-3}$ per time bin, which corresponds to an EDFA current of 600 mA.

The transmission efficiencies of the signal and idler photons, η_s and η_i, respectively, mentioned in Sec. 8.4 are determined by calculating the ratio of the independent rates of detection of the idler and signal photons, respectively, with the coincidence rate of the photons pairs (in the same clock cycle) [55]. We repeat the measurements using the setup shown in Fig. 8.1, which is that used to generate the results of Fig. 8.7 (i.e., we direct the signal and idler photons through the setup as if we are to perform teleportation). We find $\eta_s = 4.5 \times 10^{-3}$ and $\eta_i = 1.2 \times 10^{-2}$, which take into account losses between when the photons are produced to when they are detected by their respective SNSPDs.

EDFA current (mA)	Coincidences (per 10 s)	Accidentals (per 10 s)	μ_B ($\times 10^{-3}$)
400	469.2 ± 3.6	1.8 ± 0.3	3.9 ± 0.7
450	1156.3 ± 4.9	6.1 ± 0.5	5.3 ± 0.4
500	1653.9 ± 5.9	9.5 ± 0.6	5.8 ± 0.4
550	2095.8 ± 6.6	13.7 ± 0.8	6.5 ± 0.4
575	2343.2 ± 7.0	17.7 ± 0.9	7.5 ± 0.4
600	2548.7 ± 7.3	18.5 ± 0.9	8.0 ± 0.4

Table 8.2: Bob's photon pair source is characterized by the measured mean photon number per time bin μ_B, and the rate of accidental and true coincidence detections with varied EDFA current.

Quantum state tomography

We perform projection measurements on the teleported states $|e\rangle_A$, $|l\rangle_B$, and $|+\rangle_A$, in all three of the qubit bases formed by the Pauli matrices σ_x, σ_y, and σ_z, i.e., measuring photons at each of the arrival times after the MZI and varying φ. These results allow reconstructing the density matrix of each teleported state, both with and without the additional 44 km fiber, using maximum likelihood estimation [48]. Our resultant matrices clearly match the expected teleported state, with the calculated high teleportation fidelities in Sec. 8.3, up to the aforementioned effects due to multiple photons and distinguishability.

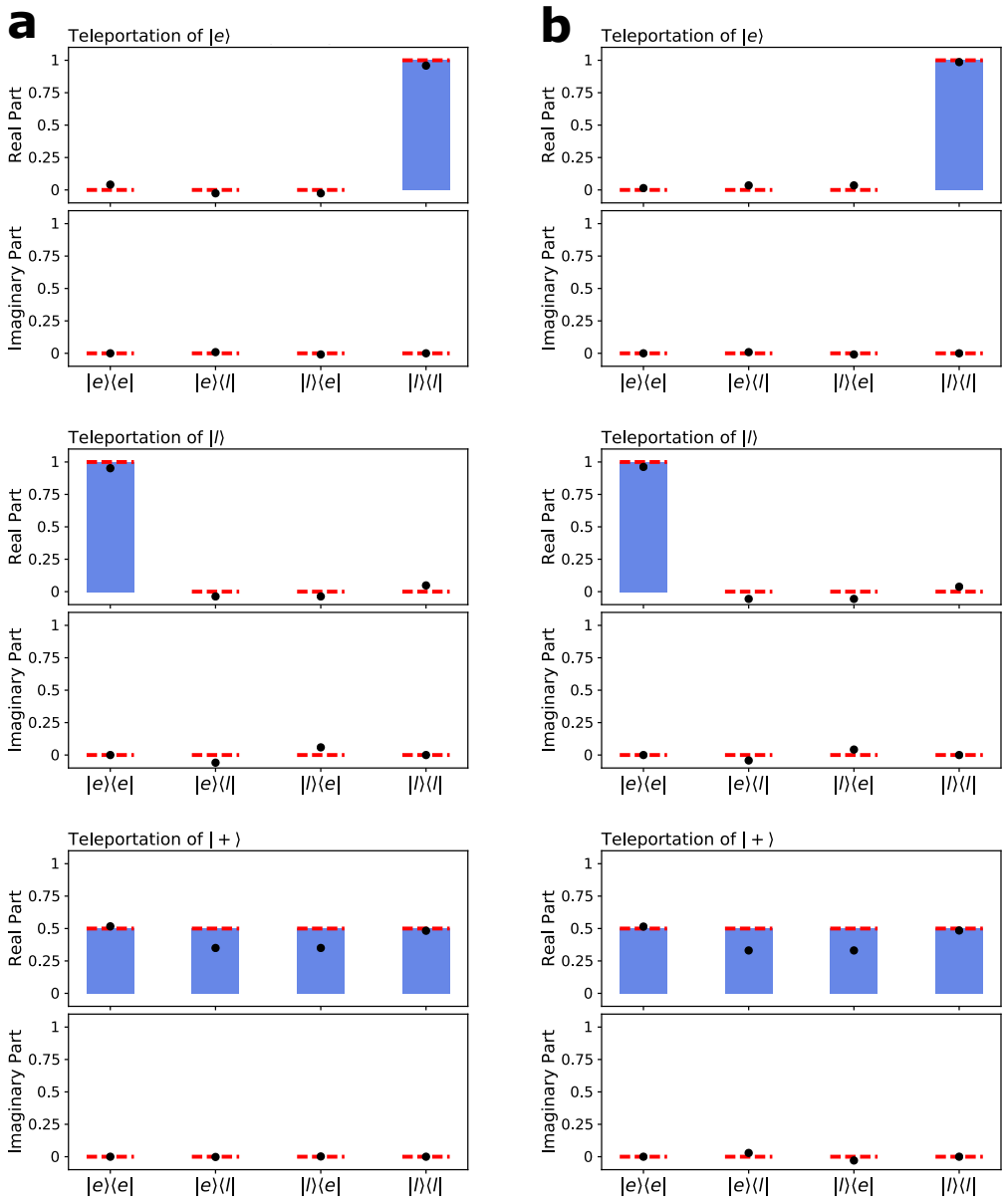

Figure 8.8: Elements of the density matrices of teleported $|e\rangle$, $|l\rangle$, and $|+\rangle$ states a) with and b) without the additional 44 km of fiber in the system. The black points are generated by our teleportation system and the blue bars with red dashed lines are the values assuming ideal teleportation.

References

[1] Charles H. Bennett, Gilles Brassard, Claude Crépeau, Richard Jozsa, Asher Peres, and William K. Wootters. "Teleporting an unknown quantum state via dual classical and Einstein-Podolsky-Rosen channels." In: Physical Review Letters 70.13 (1993), p. 1895.

[2] Dirk Bouwmeester, Jian-Wei Pan, Klaus Mattle, Manfred Eibl, Harald Weinfurter, and Anton Zeilinger. "Experimental quantum teleportation." In: Nature 390.6660 (1997), pp. 575–579.

[3] Danilo Boschi, Salvatore Branca, Francesco De Martini, Lucien Hardy, and Sandu Popescu. "Experimental realization of teleporting an unknown pure quantum state via dual classical and Einstein-Podolsky-Rosen channels." In: Physical Review Letters 80.6 (1998), p. 1121.

[4] Akira Furusawa, Jens Lykke Sørensen, Samuel L Braunstein, Christopher A Fuchs, H Jeff Kimble, and Eugene S Polzik. "Unconditional quantum teleportation." In: Science 282.5389 (1998), pp. 706–709.

[5] B. Hensen, H. Bernien, A. E. Dréau, et al. "Loophole-free Bell inequality violation using electron spins separated by 1.3 kilometres." In: Nature 526.7575 (Oct. 2015), pp. 682–686. ISSN: 1476-4687. DOI: 10.1038/nature15759. URL: https://doi.org/10.1038/nature15759.

[6] Lynden K. Shalm, Evan Meyer-Scott, Bradley G. Christensen, et al. "Strong Loophole-Free Test of Local Realism." In: Physical Review Letters 115 (25 Dec. 2015), p. 250402. DOI: 10.1103/PhysRevLett.115.250402. URL: https://link.aps.org/doi/10.1103/PhysRevLett.115.250402.

[7] Marissa Giustina, Marijn A. M. Versteegh, Sören Wengerowsky, et al. "Significant-Loophole-Free Test of Bell's Theorem with Entangled Photons." In: Physical Review Letters 115 (25 Dec. 2015), p. 250401. DOI: 10.1103/PhysRevLett.115.250401. URL: https://link.aps.org/doi/10.1103/PhysRevLett.115.250401.

[8] Wenjamin Rosenfeld, Daniel Burchardt, Robert Garthoff, Kai Redeker, Norbert Ortegel, Markus Rau, and Harald Weinfurter. "Event-Ready Bell Test Using Entangled Atoms Simultaneously Closing Detection and Locality Loopholes." In: Physical Review Letters 119 (1 July 2017), p. 010402. DOI: 10.1103/PhysRevLett.119.010402. URL: https://link.aps.org/doi/10.1103/PhysRevLett.119.010402.

[9] Ping Gao, Daniel Louis Jafferis, and Aron C Wall. "Traversable wormholes via a double trace deformation." In: Journal of High Energy Physics 2017.12 (2017), p. 151.

[10] Beni Yoshida and Norman Y Yao. "Disentangling scrambling and decoherence via quantum teleportation." In: Physical Review X 9.1 (2019), p. 011006.

[11] Kevin A. Landsman, Caroline Figgatt, Thomas Schuster, Norbert M. Linke, Beni Yoshida, Norm Y. Yao, and Christopher Monroe. "Verified quantum information scrambling." In: Nature 567.7746 (2019), pp. 61–65.

[12] Seth Lloyd, Lorenzo Maccone, Raul Garcia-Patron, et al. "Closed Timelike Curves via Postselection: Theory and Experimental Test of Consistency." In: Physical Review Letters 106 (4 Jan. 2011), p. 040403. DOI: 10.1103/PhysRevLett.106.040403. URL: https://link.aps.org/doi/10.1103/PhysRevLett.106.040403.

[13] Markus Aspelmeyer, Tobias J Kippenberg, and Florian Marquardt. "Cavity optomechanics." In: Reviews of Modern Physics 86.4 (2014), p. 1391.

[14] P-Y Hou, Y-Y Huang, X-X Yuan, X-Y Chang, Chong Zu, Li He, and L-M Duan. "Quantum teleportation from light beams to vibrational states of a macroscopic diamond." In: Nature communications 7 (2016), p. 11736.

[15] Michael A. Nielsen and Isaac L. Chuang. Quantum Computation and Quantum Information. 10th ed. USA: Cambridge University Press, 2011. ISBN: 1107002176.

[16] Thaddeus D Ladd, Fedor Jelezko, Raymond Laflamme, Yasunobu Nakamura, Christopher Monroe, and Jeremy Lloyd O'Brien. "Quantum computers." In: Nature 464.7285 (2010), pp. 45–53.

[17] Nicolas Gisin and Rob Thew. "Quantum communication." In: Nature Photonics 1.3 (2007), p. 165.

[18] Stefano Pirandola, Jens Eisert, Christian Weedbrook, Akira Furusawa, and Samuel L. Braunstein. "Advances in quantum teleportation." In: Nature Photonics 9.10 (2015), p. 641.

[19] H-J Briegel, Wolfgang Dür, Juan I. Cirac, and Peter Zoller. "Quantum repeaters: the role of imperfect local operations in quantum communication." In: Physical Review Letters 81.26 (1998), p. 5932.

[20] H Jeff Kimble. "The quantum internet." In: Nature 453.7198 (2008), pp. 1023–1030.

[21] Christoph Simon. "Towards a global quantum network." In: Nature Photonics 11.11 (2017), pp. 678–680.

[22] Stephanie Wehner, David Elkouss, and Ronald Hanson. "Quantum internet: A vision for the road ahead." In: Science 362.6412 (2018), eaam9288.

[23] Nicolas Sangouard, Christoph Simon, Hugues De Riedmatten, and Nicolas Gisin. "Quantum repeaters based on atomic ensembles and linear optics." In: Reviews of Modern Physics 83.1 (2011), pp. 33–80.

[24] Josephine Dias and Timothy C. Ralph. "Quantum repeaters using continuous-variable teleportation." In: Physical Review A 95.2 (2017), p. 022312.

[25] Marco Lucamarini, Zhiliang L. Yuan, James F. Dynes, and Andrew J. Shields. "Overcoming the rate–distance limit of quantum key distribution without quantum repeaters." In: Nature 557.7705 (2018), pp. 400–403.

[26] M. K. Bhaskar, R. Riedinger, B. Machielse, et al. “Experimental demonstration of memory-enhanced quantum communication.” In: Nature 580.7801 (Apr. 2020), pp. 60–64. ISSN: 1476-4687. DOI: 10.1038/s41586-020-2103-5. URL: https://doi.org/10.1038/s41586-020-2103-5.

[27] Xiu-Xiu Xia, Qi-Chao Sun, Qiang Zhang, and Jian-Wei Pan. “Long distance quantum teleportation.” In: Quantum Science and Technology 3.1 (2017), p. 014012.

[28] Jürgen Brendel, Nicolas Gisin, Wolfgang Tittel, and Hugo Zbinden. “Pulsed energy-time entangled twin-photon source for quantum communication.” In: Physical Review Letters 82.12 (1999), p. 2594.

[29] Raju Valivarthi, Marcelli Grimau Puigibert, Qiang Zhou, Gabriel H. Aguilar, Varun B. Verma, Francesco Marsili, Matthew D. Shaw, Sae Woo Nam, Daniel Oblak, and Wolfgang Tittel. “Quantum teleportation across a metropolitan fibre network.” In: Nature Photonics 10.10 (Oct. 2016), pp. 676–680. ISSN: 1749-4893. DOI: 10.1038/nphoton.2016.180. URL: https://doi.org/10.1038/nphoton.2016.180.

[30] Qi-Chao Sun, Ya-Li Mao, Si-Jing Chen, et al. “Quantum teleportation with independent sources and prior entanglement distribution over a network.” In: Nature Photonics 10.10 (Oct. 2016), pp. 671–675. ISSN: 1749-4893. DOI: 10.1038/nphoton.2016.179. URL: https://doi.org/10.1038/nphoton.2016.179.

[31] Hiroki Takesue and Benjamin Miquel. “Entanglement swapping using telecom-band photons generated in fibers.” In: Opt. Express 17.13 (June 2009), pp. 10748–10756.

[32] Sheng-Kai Liao, Hai-Lin Yong, Chang Liu, et al. “Long-distance free-space quantum key distribution in daylight towards inter-satellite communication.” In: Nature Photonics 11.8 (Aug. 2017), pp. 509–513. ISSN: 1749-4893. DOI: 10.1038/nphoton.2017.116. URL: https://doi.org/10.1038/nphoton.2017.116.

[33] Alexander I. Lvovsky, Barry C. Sanders, and Wolfgang Tittel. “Optical quantum memory.” In: Nature Photonics 3.12 (2009), p. 706.

[34] Nikolai Lauk, Neil Sinclair, Shabir Barzanjeh, Jacob P Covey, Mark Saffman, Maria Spiropulu, and Christoph Simon. “Perspectives on quantum transduction.” In: Quantum Science and Technology 5.2 (2020), p. 020501.

[35] Nicholas J. Lambert, Alfredo Rueda, Florian Sedlmeir, and Harald G. L. Schwefel. “Coherent conversion between microwave and optical photons—an overview of physical implementations.” In: Advanced Quantum Technologies 3.1 (2020), p. 1900077.

[36] Vladimir B. Braginsky and F. Ya Khalili. “Quantum nondemolition measurements: the route from toys to tools.” In: Reviews of Modern Physics 68.1 (1996), p. 1.

[37] Ivan Marcikic, Hugues De Riedmatten, Wolfgang Tittel, Hugo Zbinden, and Nicolas Gisin. “Long-distance teleportation of qubits at telecommunication wavelengths.” In: Nature 421.6922 (2003), pp. 509–513.

[38] Hugues De Riedmatten, Ivan Marcikic, Wolfgang Tittel, Hugo Zbinden, Daniel Collins, and Nicolas Gisin. “Long distance quantum teleportation in a quantum relay configuration.” In: Physical Review Letters 92.4 (2004), p. 047904.

[39] Hiroki Takesue, Shellee D. Dyer, Martin J. Stevens, Varun Verma, Richard P. Mirin, and Sae Woo Nam. "Quantum teleportation over 100 km of fiber using highly efficient superconducting nanowire single-photon detectors." In: Optica 2.10 (2015), pp. 832–835.

[40] Olivier Landry, Jeroen Anton Willem van Houwelingen, Alexios Beveratos, Hugo Zbinden, and Nicolas Gisin. "Quantum teleportation over the Swisscom telecommunication network." In: Journal of the Optical Society of America (JOSA) B 24.2 (2007), pp. 398–403.

[41] Matthäus Halder, Alexios Beveratos, Nicolas Gisin, Valerio Scarani, Christoph Simon, and Hugo Zbinden. "Entangling independent photons by time measurement." In: Nature physics 3.10 (2007), pp. 692–695.

[42] Félix Bussières, Christoph Clausen, Alexey Tiranov, et al. "Quantum teleportation from a telecom-wavelength photon to a solid-state quantum memory." In: Nature Photonics 8.10 (Oct. 2014), pp. 775–778. ISSN: 1749-4893. DOI: 10.1038/nphoton.2014.215. URL: https://doi.org/10.1038/nphoton.2014.215.

[43] Ping Gao and Daniel Louis Jafferis. "A traversable wormhole teleportation protocol in the SYK model." In: Journal of High Energy Physics 2021.7 (2021), pp. 1–44.

[44] Evan Miyazono, Tian Zhong, Ioana Craiciu, Jonathan M Kindem, and Andrei Faraon. "Coupling of erbium dopants to yttrium orthosilicate photonic crystal cavities for on-chip optical quantum memories." In: Applied Physics Letters 108.1 (2016), p. 011111.

[45] Björn Lauritzen, Jiří Minář, Hugues De Riedmatten, Mikael Afzelius, Nicolas Sangouard, Christoph Simon, and Nicolas Gisin. "Telecommunication-wavelength solid-state memory at the single photon level." In: Physical Review Letters 104.8 (2010), p. 080502.

[46] Sacha Welinski, Philip J. T. Woodburn, Nikolai Lauk, Rufus L. Cone, Christoph Simon, Philippe Goldner, and Charles W. Thiel. "Electron Spin Coherence in Optically Excited States of Rare-Earth Ions for Microwave to Optical Quantum Transducers." In: Physical Review Letters 122 (24 June 2019), p. 247401. DOI: 10.1103/PhysRevLett.122.247401. URL: https://link.aps.org/doi/10.1103/PhysRevLett.122.247401.

[47] C. K. Hong, Z. Y. Ou, and L. Mandel. "Measurement of subpicosecond time intervals between two photons by interference." In: Physical Review Letters 59 (18 Nov. 1987), pp. 2044–2046. DOI: 10.1103/PhysRevLett.59.2044. URL: https://link.aps.org/doi/10.1103/PhysRevLett.59.2044.

[48] Joseph B. Altepeter, Evan R. Jeffrey, and Paul G. Kwiat. "Photonic state tomography." In: Advances in Atomic, Molecular, and Optical Physics 52 (2005), pp. 105–159.

[49] Xiongfeng Ma, Bing Qi, Yi Zhao, and Hoi-Kwong Lo. "Practical decoy state for quantum key distribution." In: Physical Review A 72.1 (2005), p. 012326.

[50] George Iskander, Neil Sinclair, Cristián Peña, Si Xie, and Maria Spiropulu. "Stabilization of an electro-optic modulator for quantum communication using a low-cost microcontroller." In: Caltech Undergraduate Research Journal 20.1 (2019).

[51] J. G. Rarity. "Interference of Single Photons from Separate Sources a." In: Annals of the New York academy of Sciences 755.1 (1995), pp. 624–631.

[52] F. Marsili, V. B. Verma, J. A. Stern, et al. "Detecting single infrared photons with 93% system efficiency." In: Nature Photonics 7.3 (Mar. 2013), pp. 210–214. ISSN: 1749-4893. DOI: 10.1038/nphoton.2013.13. URL: https://doi.org/10.1038/nphoton.2013.13.

[53] Photon Spot. https://www.photonspot.com/. URL: https://www.photonspot.com/.

[54] N. Lütkenhaus, J. Calsamiglia, and K-A Suominen. "Bell measurements for teleportation." In: Physical Review A 59.5 (1999), p. 3295.

[55] Ivan Marcikic, Hugues de Riedmatten, Wolfgang Tittel, Valerio Scarani, Hugo Zbinden, and Nicolas Gisin. "Time-bin entangled qubits for quantum communication created by femtosecond pulses." In: Physical Review A 66.6 (2002), p. 062308.

[56] Leonard Mandel and Emil Wolf. Optical coherence and quantum optics. Cambridge university press, 1995.

[57] Tian Zhong and Franco NC Wong. "Nonlocal cancellation of dispersion in Franson interferometry." In: Physical Review A 88.2 (2013), p. 020103.

[58] Reinhard F. Werner. "Quantum states with Einstein-Podolsky-Rosen correlations admitting a hidden-variable model." In: Physical Review A 40.8 (1989), p. 4277.

[59] John F. Clauser, Michael A. Horne, Abner Shimony, and Richard A. Holt. "Proposed experiment to test local hidden-variable theories." In: Physical Review Letters 23.15 (1969), p. 880.

[60] Hiroki Takesue. "1.5 μ m band Hong-Ou-Mandel experiment using photon pairs generated in two independent dispersion shifted fibers." In: Applied physics letters 90.20 (2007), p. 204101.

[61] S. Massar and S. Popescu. "Optimal Extraction of Information from Finite Quantum Ensembles." In: Physical Review Letters 74 (8 Feb. 1995), pp. 1259–1263. DOI: 10.1103/PhysRevLett.74.1259. URL: https://link.aps.org/doi/10.1103/PhysRevLett.74.1259.

[62] Holger P Specht, Christian Nölleke, Andreas Reiserer, Manuel Uphoff, Eden Figueroa, Stephan Ritter, and Gerhard Rempe. "A single-atom quantum memory." In: Nature 473.7346 (2011), pp. 190–193.

[63] Neil Sinclair, Erhan Saglamyurek, Hassan Mallahzadeh, et al. "Spectral Multiplexing for Scalable Quantum Photonics using an Atomic Frequency Comb Quantum Memory and Feed-Forward Control." In: Physical Review Letters 113 (5 July 2014), p. 053603. DOI: 10.1103/PhysRevLett.113.053603. URL: https://link.aps.org/doi/10.1103/PhysRevLett.113.053603.

[64] Dagmar Bruss, Artur Ekert, and Chiara Macchiavello. "Optimal universal quantum cloning and state estimation." In: Physical Review Letters 81.12 (1998), p. 2598.

[65] Vladimir Bužek and Mark Hillery. "Quantum copying: Beyond the no-cloning theorem." In: Physical Review A 54.3 (1996), p. 1844.

[66] Masahiro Takeoka, Rui-Bo Jin, and Masahide Sasaki. "Full analysis of multi-photon pair effects in spontaneous parametric down conversion based photonic quantum information processing." In: New Journal of Physics 17.4 (Apr. 2015), p. 043030. DOI: 10.1088/1367-2630/17/4/043030. URL: http://dx.doi.org/10.1088/1367-2630/17/4/043030.

[67] Christian Weedbrook, Stefano Pirandola, Raúl García-Patrón, Nicolas J. Cerf, Timothy C. Ralph, Jeffrey H. Shapiro, and Seth Lloyd. "Gaussian quantum information." In: Rev. Mod. Phys. 84 (2 May 2012), pp. 621–669. DOI: 10.1103/RevModPhys.84.621. URL: https://link.aps.org/doi/10.1103/RevModPhys.84.621.

[68] Di Zhu, Marco Colangelo, Changchen Chen, Boris A Korzh, Franco NC Wong, Matthew D Shaw, and Karl K Berggren. "Resolving Photon Numbers Using a Superconducting Nanowire with Impedance-Matching Taper." In: Nano Letters 20.5 (2020), pp. 3858–3863.

[69] Hari Krovi, Saikat Guha, Zachary Dutton, Joshua A Slater, Christoph Simon, and Wolfgang Tittel. "Practical quantum repeaters with parametric down-conversion sources." In: Applied Physics B 122.3 (2016), p. 52.

[70] P. J. Mosley, J. S. Lundeen, B. J. Smith, P. Wasylczyk, A. B. U'Ren, C. Silberhorn, and I. A. Walmsley. "Heralded Generation of Ultrafast Single Photons in Pure Quantum States." In: Physical Review Letters 100.13 (2008). Demonstrates spectral engineering for single–mode operation and reports high heralding efficiency and purity (as indicated by low $g^{(2)}(0)$)., p. 133601.

[71] R. Maleck Rassoul, A. Ivanov, E. Freysz, A. Ducasse, and F. Hache. "Second-harmonic generation under phase-velocity and group-velocity mismatch: influence of cascading self-phase and cross-phase modulation." In: Optics Letters 22.5 (1997), pp. 268–270.

[72] Boris Korzh, Qing-Yuan Zhao, Jason P Allmaras, Simone Frasca, Travis M Autry, Eric A Bersin, Andrew D Beyer, Ryan M Briggs, Bruce Bumble, Marco Colangelo, et al. "Demonstration of sub-3 ps temporal resolution with a superconducting nanowire single-photon detector." In: Nature Photonics 14.4 (2020), pp. 250–255.

[73] R. Valivarthi, I. Lucio-Martinez, A. Rubenok, et al. In: Optics Express 22.20 (2014), pp. 24497–24506.

[74] Raju Valivarthi, Qiang Zhou, Caleb John, Francesco Marsili, Varun B Verma, Matthew D Shaw, Sae Woo Nam, Daniel Oblak, and Wolfgang Tittel. "A cost-effective measurement-device-independent quantum key distribution system for quantum networks." In: Quantum Science and Technology 2.4 (2017), 04LT01.

[75] Qi-Chao Sun, Ya-Li Mao, Yang-Fan Jiang, et al. "Entanglement swapping with independent sources over an optical-fiber network." In: Phys. Rev. A 95 (3 Mar. 2017), p. 032306. DOI: 10.1103/PhysRevA.95.032306. URL: https://link.aps.org/doi/10.1103/PhysRevA.95.032306.

[76] Samuel L Braunstein and Stefano Pirandola. "Side-channel-free quantum key distribution." In: Physical Review Letters 108.13 (2012), p. 130502.

[77] Daniel Gottesman and Isaac L. Chuang. “Demonstrating the viability of universal quantum computation using teleportation and single-qubit operations.” In: Nature 402.6760 (1999), pp. 390–393.

Chapter 9

ANALYTICAL MODELING OF REAL-WORLD PHOTONIC QUANTUM TELEPORTATION

This chapter includes the work in preparation for publication:

[1] Neil Sinclair, Samantha I. Davis, Nikolai Lauk, Chang Li, Damian R. Musk, Kelsie Taylor, Raju Valivarthi, and Maria Spiropulu. "Analytical Modeling of Real-World Photonic Quantum Teleportation." In: arXiv preprint arXiv:2503.18306. Submitted. (2025).

9.1 Introduction

Quantum teleportation [1] is a key process for distributing qubits in a quantum network [2, 3, 4]. Optical photons are used for long-distance networking due to their high velocities, carrier frequencies, and ease of encoding, manipulation, transmission, and detection [5, 6, 7, 8]. However, achieving ideal single and entangled photons for quantum networks and other quantum information tasks remains challenging [9, 10]. Photonic quantum states are often approximated using states that are easier to generate, such as those produced with room-temperature off-the-shelf equipment [11, 12]. For example, Gaussian states like weak coherent and two-mode squeezed states can substitute single and biphoton states but introduce additional photons that cause errors in quantum networks [13]. Additional errors arise from the lack of control over all degrees of freedom of a photon and device imperfections. Photon loss further hinders network deployment over distances greater than tens of kilometers [14]. Therefore, it is crucial to account for sources of loss and errors to accurately model and predict the performance of quantum networking experiments, particularly quantum teleportation. Predicting experimental performance under various operating conditions, both in the lab and in real-world applications, is also important.

We use the phase space formulation of quantum optics to analytically model post-selected discrete-variable quantum teleportation experiments with realistic imperfections such as loss, photon distinguishability, and imperfect sources of single and entangled photons. Our model is based on the time-bin qubit quantum teleportation experiment of Chapter 8, providing expressions for key figures-of-merit including Hong-Ou-Mandel (HOM) interference visibilities and teleportation fidelities as

functions of these imperfections. This experiment's use of Gaussian states allows us to model transformations and imperfections with Gaussian operations [15, 16], differing from the conventional "photon-by-photon" approach that becomes cumbersome with higher number states and experimental imperfections. We use the characteristic function formalism from the phase space representation [15] to derive closed analytical expressions for these figures-of-merit. Our models show excellent agreement with the findings in Chapter 8. Finally, we project the performance of future quantum teleportation experiments with varying degrees of imperfections and discuss our findings, their impact on future work, and the limitations of our model.

9.2 Characteristic function formalism

Phase space representation and characteristic function

Any quantum state of an n-mode bosonic system with the corresponding creation and annihilation operators $\hat{a}_k^\dagger$ and $\hat{a}_k$ that obey commutator relations

$$\left[\hat{a}_k, \hat{a}_l^\dagger\right] = \delta_{kl}, \tag{9.1}$$

can be described using the quadrature operators [12]

$$\hat{x}_l = \frac{1}{\sqrt{2}}\left(\hat{a}_l^\dagger + \hat{a}_l\right) \quad \text{and} \quad \hat{p}_l = \frac{i}{\sqrt{2}}\left(\hat{a}_l^\dagger - \hat{a}_l\right), \tag{9.2}$$

which satisfy the canonical commutator relations

$$[\hat{x}_l, \hat{p}_k] = i\delta_{kl}. \tag{9.3}$$

Using a Weyl operator $\hat{\mathcal{W}}(\vec{\xi}) = \exp\left(-i\vec{\xi}\cdot\hat{\vec{R}}\right)$ with $\hat{\vec{R}} = (\hat{x}_1, \hat{p}_1, \ldots, \hat{x}_n, \hat{p}_n)$ being a vector of quadrature operators of individual modes, we can construct an invertible mapping between functions over phase space and operators over the Hilbert space of the bosonic systems. In particular we can assign a characteristic function to any quantum state that is described by a density matrix $\hat{\rho}$ as follows

$$\chi(\vec{\xi}) = \mathrm{Tr}\left\{\hat{\rho}\hat{\mathcal{W}}(\vec{\xi})\right\}. \tag{9.4}$$

Gaussian states and unitaries

Photon number or Fock states, such as single photons or entangled two-photon states, are essential for many quantum networking schemes, including those relying on quantum teleportation. However, photon number states are highly non-classical and are difficult to produce on demand and with specific properties, such as near-unity indistinguishability. In many experiments, weak coherent states approximate

single photons, and two-mode squeezed states, produced at the output of a bulk nonlinear optical crystal, substitute photon pairs [9]. Two-mode squeezed states are also used for heralded single photon sources [17]. Besides their straightforward preparation, coherent and two-mode squeezed states have the convenient property of being Gaussian, meaning their characteristic function is given by a multivariate Gaussian function

$$\chi(\vec{\xi}) = \exp\left(-\frac{1}{4}\vec{\xi}^T\gamma\vec{\xi} - i\vec{d}^T\vec{\xi}\right), \tag{9.5}$$

where γ is the covariance matrix and $\vec{d}$ is the displacement vector. Examples of Gaussian states include single-mode vacuum $|0\rangle$ with $\gamma = \mathbb{I}$ and $\vec{d} = 0$, coherent states $|\alpha\rangle$ with $\gamma = \mathbb{I}$ and $\vec{d} = \sqrt{2}(\mathrm{Re}(\alpha), \mathrm{Im}(\alpha))^T$, as well as thermal states $\hat{\rho} = \sum_n \frac{\mu^n}{(\mu+1)^{n+1}} |n\rangle\langle n|$ with $\gamma = (1+2\mu)\mathbb{I}$ and $\vec{d} = 0$.

Gaussian representation of relevant operations in photonic quantum teleportation

A unitary operation on the Hilbert space that transforms Gaussian states into Gaussian states is called Gaussian unitary. The action of a Gaussian unitary on a Gaussian state results in simply changing the covariance matrix and displacement vectors $\gamma \to \gamma' = S\gamma S^T$ and $d \to d' = Sd$, where S the symplectic matrix corresponding to a Gaussian unitary [12, 15]. Note also that $\hat{\vec{R}}' = S\hat{\vec{R}}$. Below we consider some examples of Gaussian operations that are relevant for modeling photonic quantum teleportation.

Phase shifter operation

The first example is the addition of a constant phase ϕ to the field state. Its action in operator space is described by the following transformation: $\hat{a} \to \mathrm{e}^{i\phi}\hat{a}$, and the corresponding symplectic matrix is given by

$$S = \begin{pmatrix} \cos(\phi) & -\sin(\phi) \\ \sin(\phi) & \cos(\phi) \end{pmatrix}. \tag{9.6}$$

Beam splitter operation

Another very frequently used element in experiments are two-port beam splitters. For a beam splitter with transmittance t and reflectance r the transformation between

the input $(\hat{a}, \hat{b})$ modes and output $(\hat{c}, \hat{d})$ modes is described by

$$\begin{pmatrix} \hat{c} \\ \hat{d} \end{pmatrix} = \begin{pmatrix} t & ir \\ ir & t \end{pmatrix} \begin{pmatrix} \hat{a} \\ \hat{b} \end{pmatrix}, \tag{9.7}$$

and the corresponding symplectic transformation between the input and the output modes is

$$S = \begin{pmatrix} t & 0 & 0 & -r \\ 0 & t & r & 0 \\ 0 & -r & t & 0 \\ r & 0 & 0 & t \end{pmatrix}. \tag{9.8}$$

Channel loss

The overall channel transmission η, taking into account propagation loss, inefficient couplings and detectors, can be modeled by a mixing the mode of interest with a vacuum mode on a virtual beam splitter of transmittance $\sqrt{\eta}$ and tracing out the transmitted part of this vacuum mode. This results [15] in the following transformation of the covariance matrix and the displacement vector

$$\tilde{\gamma} = \eta\gamma + (1-\eta)\mathbb{I}, \tag{9.9}$$

$$\vec{\tilde{d}} = \sqrt{\eta}\vec{d}. \tag{9.10}$$

Measurements

Usually, the process of detection or photon counting is not a Gaussian process. However, in the case of so-called threshold or bucket-type photon detection, we can represent the measurement process as a Gaussian one. These detectors indicate either the absence of photons or the presence of at least one photon. Considering projection onto the vacuum state, we can define positive operator-valued measures for such detectors as a set of two operators

$$\hat{\Pi}_{\text{off}} = |0\rangle\langle 0| \quad \text{and} \quad \hat{\Pi}_{\text{on}} = \mathbb{I} - |0\rangle\langle 0|\,. \tag{9.11}$$

Since vacuum is a Gaussian state, the projection on vacuum is a Gaussian operation, and we obtain the probability of a detection event conditioned on a given photonic state:

$$\begin{aligned} p_{\text{on}} &= \text{Tr}\{\hat{\rho}\hat{\Pi}_{\text{on}}\} = 1 - \text{Tr}\{\hat{\rho}\,|0\rangle\langle 0|\} \\ &= 1 - \frac{1}{(2\pi)^N}\int d\vec{\xi}\,\chi_{\hat{\rho}}(\vec{\xi})\chi_{\hat{\Pi}_{\text{on}}}(-\vec{\xi}). \end{aligned} \tag{9.12}$$

where N is the number of modes and $\chi_{\hat{\Pi}_{\text{on}}}(-\vec{\xi})$ is characteristic function of the projection operator defined as in Eq. 9.4. Often we consider coincident detection events of a multi-mode state $\hat{\rho}$. The coincidence probability of m detectors recording an event is then given by

$$p_{\text{coin}} = \text{Tr}\{\hat{\rho}\hat{\Pi}_{\text{on}}^{(1)} \otimes \hat{\Pi}_{\text{on}}^{(2)} \otimes \cdots \otimes \hat{\Pi}_{\text{on}}^{(m)} \otimes \mathbb{I}^{(m+1)} \otimes \cdots \otimes \mathbb{I}^{(N)}\}, \tag{9.13}$$

which can be easily evaluated for Gaussian states using the following formula for multi-dimensional Gaussian integration

$$\int d\vec{x} e^{-\frac{1}{2}\vec{x}^T C\vec{x} - i\vec{d}^T\vec{x}} = \sqrt{\frac{(2\pi)^n}{\det(C)}} \exp\left(-\frac{1}{2}\vec{d}^T C^{-1}\vec{d}\right). \tag{9.14}$$

9.3 Analytic expressions of figures-of-merit

We now apply the phase space formalism introduced in the previous section to model quantum teleportation of a photonic time-bin qubit. We consider a post-selective projective Bell-state measurement (BSM) of the state $|\Psi^-\rangle = (|el\rangle - |le\rangle)/\sqrt{2}$, where the late state $|l\rangle$ arrives after the early state $|e\rangle$, using a 50:50 beam splitter $r = t = 1/\sqrt{2}$ [18, 19] (see Chapter 8). The time-bin qubit is in the state $\epsilon|e\rangle + \sqrt{1-\epsilon^2}|l\rangle$, with $0 \leq \epsilon \leq 1$. The entangled qubit used to facilitate teleportation takes the form $(|ee\rangle + |ll\rangle)/\sqrt{2}$. Our model incorporates the photon fields used in Chapter 8, in which the qubit to be teleported is encoded into a weak coherent state $|\alpha\rangle = e^{-|\alpha|^2/2}\sum_{n=0}^{\infty}(\alpha^n/\sqrt{n!})|n\rangle$, with mean photon number $|\alpha|^2$ when $|\alpha|^2 \ll 1$. The two-mode squeezed vacuum state $|\text{TMSV}\rangle = \sqrt{1-\mu}\sum_{n=0}^{\infty}\sqrt{\mu}^n|n\rangle|n\rangle$, neglecting loss, is used in Chapter 8 to encode the entangled state, where the kets denote the signal and the idler modes [20]. This state approximates a photon pair for $\mu \ll 1$ conditioned on measurement of a two-fold coincidence such that the $|00\rangle$ term is eliminated. The mean number of pairs per signal-idler mode pair is μ. The idler mode of the two-mode squeezed vacuum is directed to the beam splitter while the signal is encoded with the teleported state at the end of the teleportation protocol.

A high-fidelity BSM, which is necessary for faithful quantum teleportation, requires photons with indistinguishable degrees of freedom [18, 19]. One way to characterize the distinguishability of the photons prior to teleportation is to perform HOM interference between the photons used to encode the state to be teleported and the idler mode of the entangled state [21]. For HOM interference, we consider the photons to be encoded into the $|e\rangle$ bin only, neglecting all events in the $|l\rangle$ bin.

HOM interference visibility

The HOM interference visibility is defined as

$$V_{\mathrm{HOM}} = \frac{P_{\max} - P_{\min}}{P_{\max}}, \tag{9.15}$$

where $P_{\max}$ ($P_{\min}$) correspond to the probability of coincidence events between threshold detectors placed after each output of the beam splitter (cf. Fig. 9.1) when the photons are rendered maximally distinguishable (indistinguishable), e.g. by varying their relative polarization or time of arrival [17, 22]. Probabilities can be converted to detection rates by multiplying them by the clock rate of the experiment.

In practice there are some additional distinguishing properties of the photons that cannot be controlled or accessed in an experiment. We model this additional distinguishability as a finite mode mismatch ζ between the two photon fields [15] (see Chapter 8). This mode mismatch is captured by a virtual beam splitter with transmittance ζ which splits each incoming photon field into indistinguishable and distinguishable parts. Only the indistinguishable parts of both photons contribute to the interference at the actual beam splitter, whereas the distinguishable parts are combined with vacuum inputs and degrade the HOM interference visibility. The indistinguishability parameter $\zeta = 1$ corresponds to the case in which both incoming photons are completely indistinguishable, whereas $\zeta = 0$ corresponds to the case in which both photons are completely distinguishable.

The magnitude of V_{HOM} depends not only on the distinguishability of the photons but also the photon-number statistics of the fields participating in the interference [23]. It also depends on dark counts of the detector, which we neglect for our discussion, see Sec. 9.6. Nevertheless, if the statistics are known from the experimental apparatus, then V_{HOM} is an indicator of distinguishability [24]. A schematic for a HOM interference experiment is shown in Fig. 9.1.

There are two experimentally relevant cases to consider: the signal mode is ignored referred to as two-fold HOM interference, and when the signal mode is detected to herald the presence of ideally one idler photon, referred to as three-fold HOM interference. For both cases we derive the two- and three-fold coincidence probabilities respectively using the characteristic function formalism assuming a weak coherent state mixing with the idler mode of two-mode squeezed vacuum as depicted in Fig. 9.1, with details found in Appendix E.1. Measurement of two-fold HOM interference is experimentally convenient, as it allows quantification of distinguishability in much less time than three-fold HOM interference.

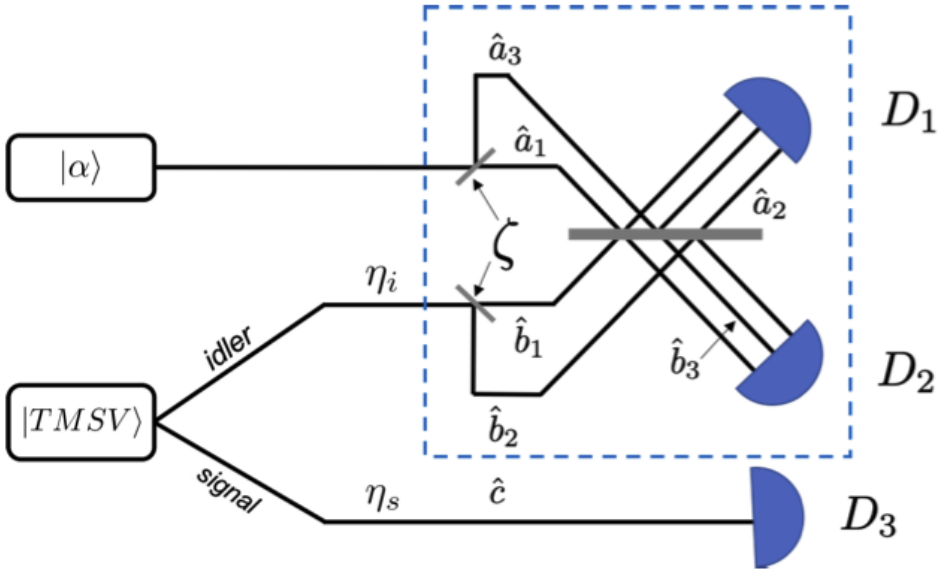

Figure 9.1: Model schematic for HOM interference within the context of a quantum teleportation experiment. The qubit to be teleported is encoded into weak coherent state $|\alpha\rangle$ whereas the entangled state is encoded into the signal and idler modes of a two-mode squeezed vacuum state $|\text{TMSV}\rangle$. Transmission efficiencies of the signal and idler modes are denoted by η_s and η_i, respectively. HOM interference is measured by correlating detection events at D_1 and D_2 after a 50:50 beamsplitter (gray line), optionally conditioned upon detection of the signal mode at D_3. Distinguishability is modeled using virtual beamsplitters of transmittance $\zeta < 1$. The $\hat{a}$, $\hat{b}$ and $\hat{c}$ operators refer to modes that originate from the virtual beam splitters and are used in the derivation shown in Appendix E.1. Blue dashed outline is discussed in the caption of Fig. 9.2.

The two- and three-fold coincidence probabilities are

$$p_{\text{2-fold}}(|\alpha|^2, \mu, \zeta, \eta_i) = 1 + \frac{\exp\left(-|\alpha|^2\right)}{1+\eta_i\mu} - 2\frac{e^{-\frac{|\alpha|^2}{2}\frac{[1+(1-\zeta^2)\eta_i\mu/2]}{1+\eta_i\mu/2}}}{1+\eta_i\mu/2}, \tag{9.16}$$

and

$$p_{3\text{-fold}}(|\alpha|^2,\mu,\zeta,\eta_s,\eta_i) = \frac{\eta_s\mu}{1+\eta_s\mu} - 2\frac{e^{-\frac{|\alpha|^2/2[1+(1-\zeta^2)\eta_i\mu/2]}{1+\eta_i\mu/2}}}{1+\eta_i\mu/2} + \frac{e^{-|\alpha|^2}(1-\eta_i)\eta_s\mu}{(1+\eta_i\mu)(1+\eta_i(1-\eta_s)\mu+\eta_s\mu)} + 2\frac{e^{-\frac{|\alpha|^2/2[1+(1-\zeta^2)(1-\eta_s)\eta_i\mu/2+\eta_s\mu]}{1+(1-\eta_s)\eta_i\mu/2+\eta_s\mu}}}{1+(1-\eta_s)\eta_i\mu/2+\eta_s\mu}, \tag{9.17}$$

respectively, where η_s and η_i are the transmission efficiencies of the signal and idler mode, respectively. The mean photon numbers and efficiencies can be independently determined experimentally, using the methods described in Chapter 8.

We now calculate the HOM interference visibility, in which $\zeta = 0$ ($\zeta \leq 1$) corresponds to $P_{\max}$ ($P_{\min}$). The corresponding two-fold and three-fold HOM visibilities are

$$\begin{aligned} V_{2\text{-HOM}}(\zeta) &= 1 - \frac{p_{2\text{-fold}}(|\alpha|^2,\mu,\zeta,\eta_i)}{p_{2\text{-fold}}(|\alpha|^2,\mu,0,\eta_i)} \\ &= -\frac{4\left(e^{|\alpha|^2/2} - \exp\left(\frac{|\alpha|^2(2+\eta_i\mu(1+\zeta^2))}{2(2+\eta_i\mu)}\right)\right)(1+\eta_i\mu)}{2+\eta_i\mu-4e^{|\alpha|^2/2}(1+\eta_i\mu)+e^{|\alpha|^2}(1+\eta_i\mu)(2+\eta_i\mu)}, \end{aligned} \tag{9.18}$$

and

$$V_{3\text{-HOM}}(\zeta) = 1 - \frac{p_{3\text{-fold}}(|\alpha|^2,\mu,\zeta,\eta_s,\eta_i)}{p_{3\text{-fold}}(|\alpha|^2,\mu,0,\eta_s,\eta_i)}, \tag{9.19}$$

respectively. We did not expand $V_{3\text{-HOM}}$ here due to its length.

As shown in Appendix E.2, the theoretical maximum visibilities for the two-fold and three-fold HOM visibilities are $\sqrt{2}-1 \approx 0.414$ and unity, respectively. The primary difference in maximum visibilities stems from the exclusion of $|00\rangle$ in $|\text{TMSV}\rangle$ by detection of the signal mode, that is, a single photon is heralded in the idler mode for $\mu \ll 1$. The two-fold visibility is limited by the combination of vacuum and multi-photon events at the inputs to the beamsplitter. Even though the twofold visibility measurement is simpler and faster, the interference fringe can be more difficult to resolve when including photon counting statistical uncertainties and potential noise. Note that the maximum two-fold HOM visibility from interference of two coherent (thermal) fields is $1/2$ ($1/3$).

Quantum teleportation fidelity

We extend the HOM interference model to that for quantum teleportation by including the $|l\rangle$ time-bin in the analysis. As depicted in Fig. 9.2, we model the $|e\rangle$ and

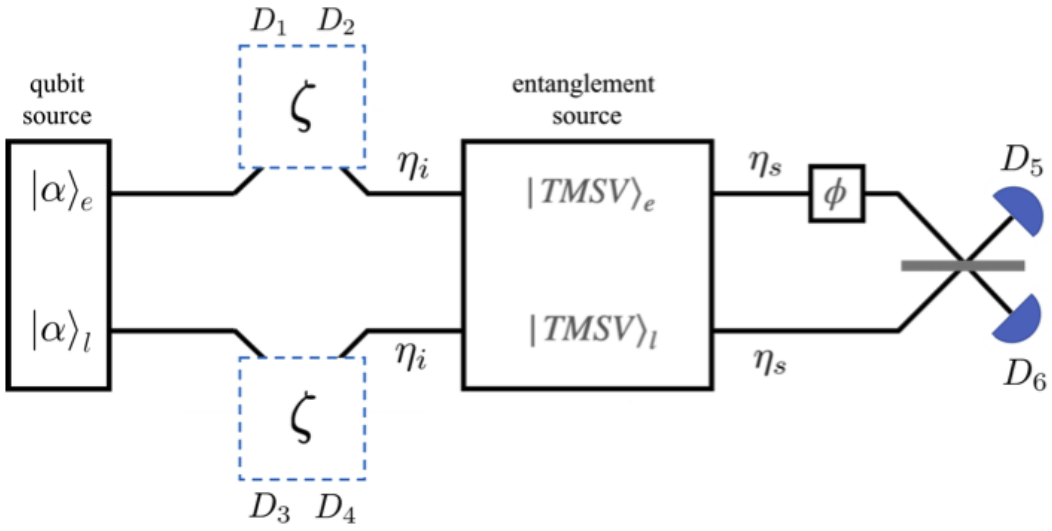

Figure 9.2: Model schematic of quantum teleportation. Each time bin, $|e\rangle$ and $|l\rangle$, is treated as a distinct spatial mode. As in HOM interference, the qubit to be teleported is encoded into $|\alpha\rangle$ whereas the entangled state is encoded into $|\text{TMSV}\rangle$, with relevant transmission efficiencies η_s and η_i. Distinguishability of photons at the BSM is modeled using virtual beamsplitters. The indistinguishability parameter ζ outlined by the blue dashed lines corresponds to the elements enclosed by the blue dashed lines in Fig. 9.1. Projection on $|\Psi^-\rangle$ is indicated by coincidence detection events at D_1 and D_4 or D_2 and D_3. Projection of the teleported qubit onto the X-basis is modeled by a phase shift ϕ, coherent mixing by a 50:50 beamsplitter (grey line), then photon detection at D_5 and D_6. Projection onto the Z-basis is modeled by removing the beamsplitter for the signal modes, that is, setting its transmittance to $t = 1$, and direct detection of the photons (not shown).

$|l\rangle$ bins as independent spatial modes, with interference for the BSM taking place at the beamsplitters ascribed for the $|e\rangle$ modes and that for the $|l\rangle$ modes.

Distinguishability is again modeled using virtual beamsplitters like the HOM interference model. Projection on $|\Psi^-\rangle$ is indicated by a specific coincidence detection event between a photon in the $|e\rangle$ and $|l\rangle$ bins. Specifically this corresponds to a photon being detected in $|e\rangle$ ($|l\rangle$) in one detector and $|l\rangle$ ($|e\rangle$) in the other [25]. Measurement of the teleported qubit in the Z-basis, that is, the $|e\rangle$ or $|l\rangle$ mode, is modeled by detection of the photon in a distinct spatial mode. Measurement in the X-basis, that is, in the state $(|e\rangle + e^{i\phi}|l\rangle)/\sqrt{2}$, is modeled by combining each spatial signal mode on a 50:50 beamsplitter after introducing a relative phase ϕ, then

detecting each photon in a distinct spatial mode. In other words, the measurement basis is rotated, as facilitated by phase-sensitive interference.

Using the characteristic function formalism, as shown in Appendix E.1, we derive the teleportation fidelity for the X-basis states using

$$F = \frac{P_{D_1D_4D_6}(\phi)}{P_{D_1D_4D_6}(\phi) + P_{D_1D_4D_5}(\phi)}, \tag{9.20}$$

where $P_{D_1D_4D_6}$ ($P_{D_1D_4D_5}$) is the coincidence detection probability for a $|\Psi^-\rangle$ projection and measurement of the teleported qubit in the intended (orthogonal) state [26]. The argument ϕ indicates that the measurement basis is oriented to the intended state of the teleported qubit such that $P_{D_1D_4D_6}$ ($P_{D_1D_4D_5}$) is maximized (minimized). Note that the detection event corresponding to $P_{D_2D_3}$ also corresponds to a projection onto $|\Psi^-\rangle$. These events are treated like those corresponding to $P_{D_1D_4}$ due to symmetry, consistent with properties of the beamsplitters and detectors used for the BSM in Chapter 8.

Considering teleportation of Z-basis states, the corresponding teleportation fidelity takes the same form as Eq. 9.20, but with different and ϕ-independent underlying expressions for $P_{D_1D_4D_6}$, and similarly $P_{D_1D_4D_5}$, because the beamsplitter used for measurement of X-basis states is removed. See Appendix E.1 for details. The maximum theoretical X- and Z-basis teleportation fidelities are one.

9.4 Fit of model with experimental results of Chapter 8

Using the expressions for two- and three-fold HOM interference visibilities and teleportation fidelity, we fit our model to data from Chapter 8 to reveal the imperfections in the experiment and validate our model. We consider only teleportation of X-basis states in this section since they sufficiently capture the behavior of Z-basis states and they are sensitive to ζ.

First, we plot the experimentally measured two- and three-fold HOM interference visibilities as well as teleportation fidelity for varied mean photon number $|\alpha|^2$ of the weak coherent state used to encode the qubit. This is shown in Fig. 9.3. We choose to probe our figures-of-merit against $|\alpha|^2$ because of the experimental ease to vary this parameter and, as discussed in Chapter 8, the use of $|\alpha|^2$ for preparing decoy states. We consider $|\alpha|^2 < 1$ since this is most relevant regime in teleportation experiments. The maximum measured two- and three-fold HOM visibilities and teleportation fidelity are 0.28 ± 0.01, 0.67 ± 0.03, and 0.86 ± 0.04, respectively, due to distinguishability and undesired multi-photon events from $|\alpha\rangle$ and in the idler

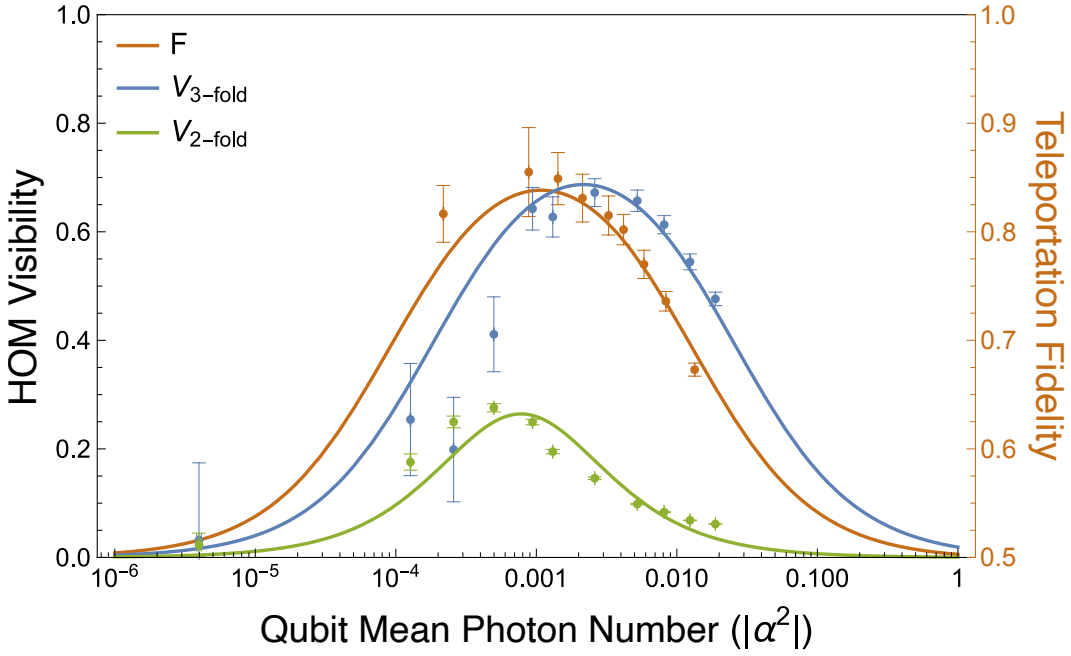

Figure 9.3: Two- and three-fold HOM interference visibilities ($V_{2\text{-fold}}$, green and $V_{3\text{-fold}}$, blue) and quantum teleportation fidelity (F, red) of X-basis states for varied qubit mean photon number $|\alpha|^2$. The model (lines) is fit to, and agrees with, the experimental data of Chapter 8 (points). The mean photon number is shown on a log scale to provide a simple representation of the model.

mode [27]. Note that the three-fold HOM interference visibility as predicted by the teleportation fidelity $2F - 1 \sim 72\%$ is consistent [28].

The teleportation fidelity and HOM visibilities decrease to 0.5 and 0, respectively, for very large or small values of $|\alpha|^2 = 0$. As $|\alpha|^2$ increases from zero, there are more events in which a single photon from $|\alpha\rangle$ and a single photon in the idler mode contribute to HOM interference and the BSM, and thus the visibility rises. Since the probability of two photons in $|\alpha\rangle$ also grows, there will be two-fold detection events that correspond to vacuum in the idler, due to idler field statistics or loss, which reduces the visibility. Therefore, the trade-off between interference events originating from single- or multi-photon states arriving at the beamsplitter leads to the visibility reaching a maximum and decreasing for higher $|\alpha|^2$. The specific value of $|\alpha|^2$ that corresponds to the maximum visibility is also conditioned on whether a two- or three-photon detection experiment is performed, as well as the values of μ, η_i, and η_s. This interpretation as well as the curve shapes and positions for two- and three-fold experiments are further discussed in Sec. 9.5 and Appendix E.2.

For the two-fold data, the maximum occurs at $|\alpha|^2 = 5.0 \times 10^{-4}$ while the three-fold visibility and teleportation fidelity are maximized around $|\alpha|^2 = 2.6 \times 10^{-3}$ and $|\alpha|^2 = 8.8 \times 10^{-4}$, respectively. The value of $|\alpha|^2$ corresponding to maximum two-fold HOM visibility is less than that for the maximum three-fold visibility because three-fold events are conditioned on detecting at least one photon in the signal mode. As a result, there are fewer vacuum events in the idler mode in the three-fold case, and thus $|\alpha|^2$ can be increased, i.e. the probability of $n = 1$ and $n = 2$ photon events can be increased, to reach maximum visibility. The three-fold HOM visibility data maximizes at a $|\alpha|^2$ that is a factor of two higher than the teleportation data because $|\alpha|^2$ is defined per qubit, which corresponds to the mean photon number in two temporal modes.

Next, we proceed to fit Eqs. 9.18, 9.19, and 9.20 to each of the relevant data sets according to the procedure discussed in Appendix E.3. We ascribe a different mode mismatch parameter, ζ_2 and ζ_3, for the two- and three-fold detection experiments, respectively. This originates from the multi-mode $|\text{TMSV}\rangle$ used in Chapter 8. Although spectral filtering of the signal and idler modes was employed in Chapter 8, detection of the signal can further filter the spectrum of the idler field due to residual non-zero frequency entanglement [29] (see Chapter 3). For the same reason, we also ascribe different idler mode efficiencies, η_{i2} and η_{i3}, for the two- and three-fold detection experiments, respectively, as heralding a photon in the signal mode effectively removes frequency modes from the idler, which manifests as additional inefficiency in the idler mode.

The three-fold HOM and teleportation data is fit together using a shared ζ_3, and with the following independently measured parameters from Chapter 8 held constant: $\eta_{i3} = 1.2 \times 10^{-2}$, $\eta_s = 4.5 \times 10^{-3}$, and $\mu = 8.0 \times 10^{-3}$. Note that these parameters were measured in Chapter 8 using coincidence detection of the filtered $|\text{TMSV}\rangle$ with $|\alpha|^2 = 0$. The two-fold HOM data is fitted separately with only $\mu = 8.0 \times 10^{-3}$ held constant. The fits reveal $\zeta_2 = 0.80 \pm 0.04$, $\eta_{i2} = (6.9 \pm 1.2) \times 10^{-2}$ and $\zeta_3 = 0.90 \pm 0.02$. The fitted curves are plotted in Fig. 9.3, and are in good agreement with the measured data. Furthermore, ζ_3 matches that fitted in Chapter 8. The fits clearly reveal that heralding removes additional frequency components to improve indistinguishability close to unity, which underpins the high teleportation fidelity observed in Chapter 8. The fits also yield $\eta_{i2} > \eta_{i3}$ as expected.

Notice the curves take on the form of a log-normal distribution, which owes to the Poission distribution of number states in $|\alpha\rangle$. When plotted on a linear scale,

as shown in Chapter 8, the long tail in the distribution for $|\alpha|^2 \gg 10^{-3}$ can be interpreted as the trade-off between interference produced by the $n = 2$ term in $|\alpha\rangle$ with vacuum in the idler, and from single photons in $|\alpha\rangle$ and the idler.

It is convenient to infer the value of $|\alpha|^2$ that will maximize V_{HOM} for a given experimental setup. Thus, in Appendix E.4 we differentiate Eqs. 9.18 and 9.19, finding $|\alpha|^2$ of 7.8×10^{-4} and 2.2×10^{-3}, for two- and three-fold HOM interference experiments, respectively, consistent with the data shown in Fig. 9.3.

9.5 Prediction of figures-of-merit under varying experimental conditions

We now employ our analytical model to further interpret the experimental imperfections in Chapter 8 and to predict the outcomes of future experiments under varying experimental imperfections: indistinguishability, transmission efficiencies, and mean photon numbers of $|\alpha\rangle$ and $|\mathrm{TMSV}\rangle$ states. For simplicity, from now on we assume a $|\mathrm{TMSV}\rangle$ such that heralding does not vary the indistinguishability or the path loss for the idler mode. We also assume the idler path efficiency to be identical for two- and three-fold detection experiments.

Indistinguishability

To determine the role of distinguishability, in Fig. 9.4 we plot two- and three-fold HOM interference visibilities as well as X-basis teleportation fidelity as a function of ζ under the experimental conditions of three-fold detection from Chapter 8: $\eta_i = \eta_{i3} = 1.2 \times 10^{-2}$, $\eta_s = 4.5 \times 10^{-3}$, and $\mu = 8.0 \times 10^{-3}$. Our model predicts

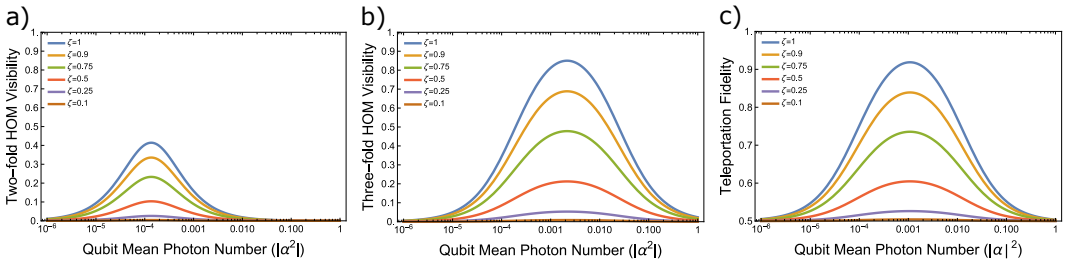

Figure 9.4: Model of a) two- and b) three-fold HOM interference visibilities as well as c) teleportation fidelity of X-basis states for varied $|\alpha|^2$ and different magnitudes of indistinguishability ζ between the interfering photons. The curves assume the transmission efficiencies and μ from the three-fold detection experiments of Chapter 8.

a simple vertical scaling of the curves. The maximum visibilities and fidelity still occur at the same $|\alpha|^2$, but with increased maxima. It is also experimentally

convenient that the optimum value of $|\alpha|^2$ is independent of distinguishability. The curves retain the log-normal behavior, supporting our interpretation that the curve shape is due to mean photon number mismatch. Note the two-fold curve has shifted to a lower central value of $|\alpha|^2$ compared to that in Fig. 9.3 due to the reduction of idler path efficiency in the model henceforth compared to that in the experimental results.

The model predicts maximum two- and three-fold HOM visibilities as well as X-basis teleportation fidelity to increase to $\sqrt{2}-1$, 0.85 and 0.92, respectively, for completely indistinguishable fields. The two-photon visibility curve reaches the theoretical maximum because idler mode inefficiency does not vary the number statistics of the idler mode, and as discussed in Appendix E.2, $|\alpha|^2 = \sqrt{2}\mu$ maximizes the visibility in the regime of low mean photon numbers we consider here. The maximum three-fold HOM visibility and teleportation fidelity does not reach unity due to multi-photon components from $|\alpha\rangle$ and non-unit transmission of the idler mode. Yet, reasonably high teleportation fidelity can be achieved even with significant path loss ($\sim 1\%$) provided μ is kept low. Note that if the 0.98 fidelity of the Z-basis states from Chapter 8 is included, the total average fidelity will reach 0.94.

Without loss of generality, we assume complete indistinguishability $\zeta = 1$ for all remaining plots in the manuscript to probe the dependence of the other experimental imperfections. Notice that the X-basis teleportation fidelity curves follow the same dependence as the three-fold HOM interference visibility curves. Thus, to avoid redundancy, we move all of the relevant teleportation curves to Appendix E.5. Note that the factor of two shift in $|\alpha|^2$ between three-fold HOM interference visibility and fidelity is retained for all curves.

Transmission efficiencies

We compare signal and idler mode transmission efficiencies of Chapter 8, i.e. those plotted in Fig. 9.3 with $\eta_i = 1.2 \times 10^{-2}$ and $\eta_s = 4.5 \times 10^{-3}$, to those of unit efficiency. We assume $\mu = 8.0 \times 10^{-3}$ as before and plot the two- and three-fold detection curves under four different configurations:

(i) $\eta_i = \eta_s = 1$,

(ii) $\eta_i = 1.2 \times 10^{-2}$ and $\eta_s = 4.5 \times 10^{-3}$ from Chapter 8,

(iii) $\eta_i = 1$ and $\eta_s = 4.5 \times 10^{-3}$,

(iv) $\eta_i = 1.2 \times 10^{-2}$ and $\eta_s = 1$.

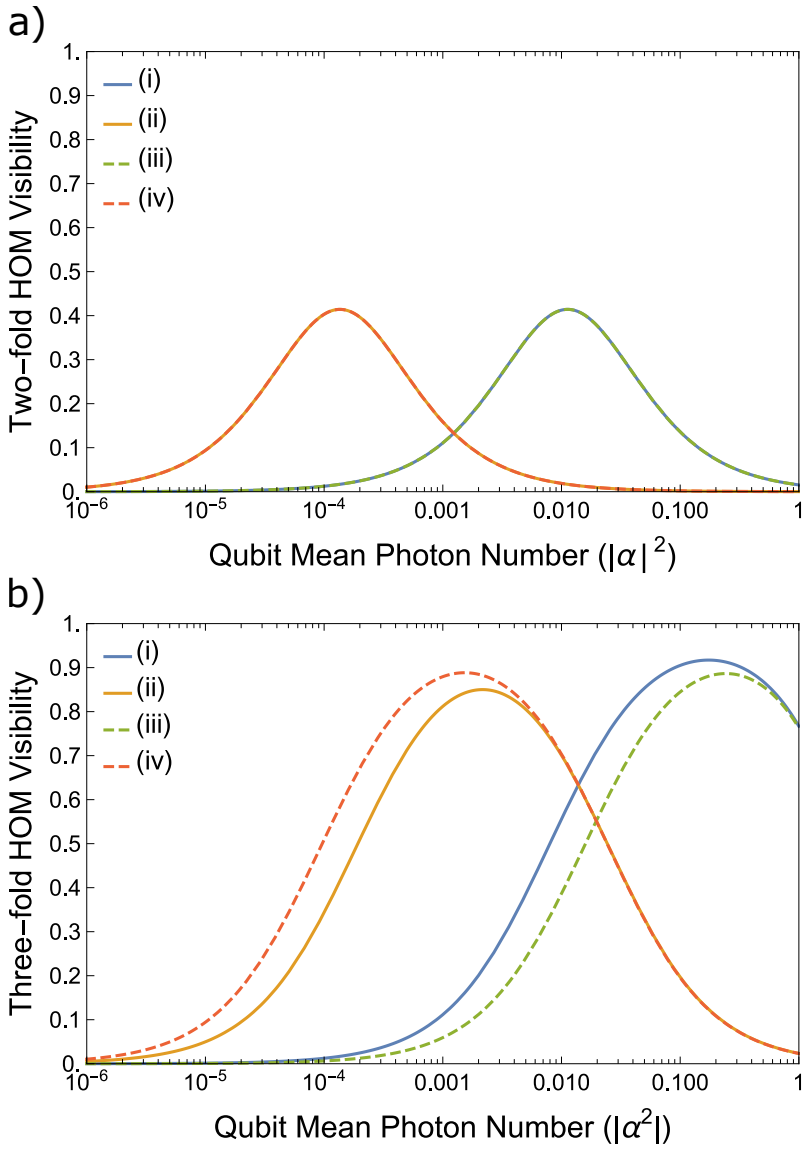

Figure 9.5: Model of a) two- and b) three-fold HOM interference visibilities for varied $|\alpha|^2$ under conditions of varied signal and idler transmission efficiencies (i-iv) in blue, orange, green, and red, respectively, as described in the main text, assuming $\mu = 8.0 \times 10^{-3}$ and complete indistinguishability $\zeta = 1$. For the two-fold HOM curves, configurations (i) and (ii) are equivalent to (iii) and (iv), respectively.

For the two-fold HOM visibility curves in Fig. 9.5, we find a reduction of idler transmission efficiency from unity (cases (i) and (iii)) to η_i (cases (ii) and (iv)) retains the curve profile, but shifts it to be centered around a value of $|\alpha|^2$ that is a factor of η_i lower. As discussed in Appendix E, the visibility is maximized when

$|\alpha|^2 = \sqrt{2}\mu$, that is, the mean photon numbers of $|\alpha|^2$ and the idler mode match to a scaling factor. Since the mean photon number of the idler scales proportional to the idler transmission efficiency, $|\alpha|^2$ must be reduced by the same factor to maximize visibility. The curve shape does not change with η_i because $\mu \ll 1$. The maximum visibility is saturated to its theoretical maximum of $\sqrt{2} - 1$ in the low mean photon number regime.

For the three-fold HOM visibility curves, the unity transmission case (i) shifts the distribution from Chapter 8 (ii) to higher $|\alpha|^2$ to better match the effective higher mean photon number in the idler mode. The maximum visibility increases for (i) because detection of a photon in the signal mode is always accompanied by a photon in the idler mode i.e. zero vacuum components in the idler mode, that is, the photon heralding efficiency [30] is unity. However, the maximum visibility is not unity, primarily due to multi-photon components from $|\alpha\rangle$ and, to some extent, the idler mode.

For case (iii), the added loss in the signal mode compared to (i) removes some single pair events in the experiment. Thus, multi-photon events from $|\text{TMSV}\rangle$ are relatively more likely to be detected by the threshold detectors. By way of heralding, this leads to a relative increase in multi-pair events from $|\text{TMSV}\rangle$, reducing the maximum visibility from (i) while effectively increasing the mean photon number in the idler mode, thereby forcing an increase in $|\alpha|^2$. The width of the curve is also reduced from the lower $|\alpha|^2$ edge, which is consistent with the increase in multi-photon events from $|\text{TMSV}\rangle$. To understand this, consider $|\alpha|^2$ being lowered from the value that maximizes the visibility. In this case, the increased multi-photon events in the idler mode reduce the visibility more strongly than the case in which non-zero vacuum is present in the idler. This narrowing becomes even more pronounced as μ is increased. The curve narrowing effect is not observed in the two-fold visibility curves because heralding, and hence the effect of signal path inefficiency, strongly changes the number distribution in the idler mode.

For case (iv), the shift of the curve to lowered $|\alpha|^2$ compared to case (ii) is similar to that when comparing case (i) to (iii). It is due to the relative decreased contribution of multi-photon detection events in the idler mode, which must be matched by $|\alpha|^2$. The maximum visibility is limited by the non-unit heralding efficiency; when a single photon is detected in the signal mode, it may not be present at the beamsplitter and multi-photon events originating from $|\alpha\rangle$ have a relatively higher probability of contributing to the visibility. This is also why maximum visibility is not as high

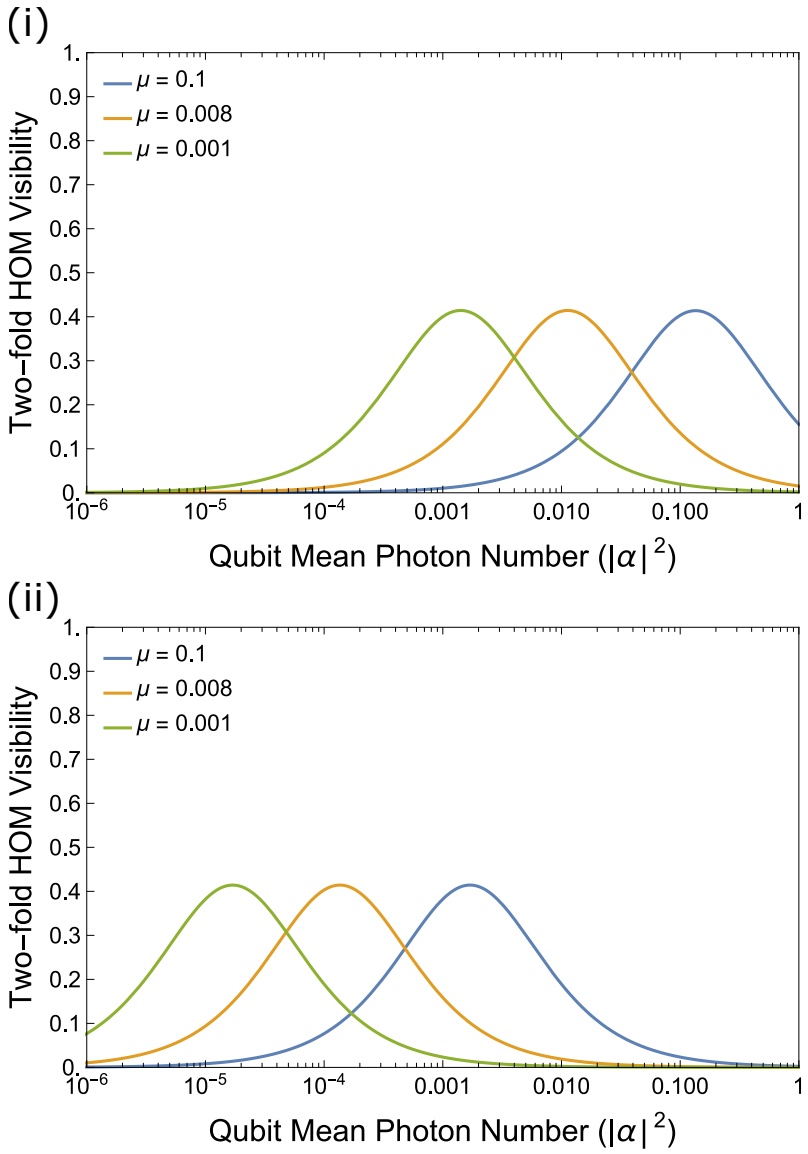

Figure 9.6: Model of two-fold HOM interference visibilities for varied $|\alpha|^2$ and $\mu < 10^{-2}$, under varied signal and idler transmission efficiencies, cases (i) and (ii), which are equivalent to (iii) and (iv), respectively, assuming complete indistinguishability $\zeta = 1$.

as case (i), but higher than the rest of the curves which have low signal efficiency and for which heralding cannot benefit as much. Akin to that observed when comparing curves (i) and (iii), the width of curve (iv) increases from the lower $|\alpha|^2$ edge relative to case (ii). This is also consistent with the presence of more heralded single photons, and fewer multi-photon events from heralding. The high $|\alpha|^2$ edge of curves in cases (ii) and (iv), and (i) and (iii), converge with increased $|\alpha|^2$ because the Poisson- distributed multi-photon components from $|\alpha\rangle$ reduce the visibility more strongly than the heralded components of $|\text{TMSV}\rangle$ in this regime.

Mean photon number of $|\text{TMSV}\rangle$

Here we compare $\mu = 10^{-1}$, $\mu = 8.0 \times 10^{-3}$ from Chapter 8, and $\mu = 10^{-3}$ under cases (i)-(iv). Two-fold HOM interference visibilities with varied $|\alpha|^2$ are plotted in Fig. 9.6 under these scenarios.

For case (i)/(iii) and (ii)/(iv) we observe the same behavior as in Fig. 9.5a. The curve profile shifts to lowered $|\alpha|^2$ to ensure the mean photon number of $|\alpha|^2$ matches that in the idler mode when either the idler transmission efficiency or, equivalently, mean photon number of $|\text{TMSV}\rangle$ is reduced. The shift in $|\alpha|^2$ matches the reduction in μ, and the overall shift of the three curves when the idler path efficiency is reduced is the same as discussed in the previous section. Furthermore, the maximum visibility can reach its theoretical maximum under these conditions, as discussed in the previous sections.

The three-fold HOM interference visibility is plotted under these scenarios (i)-(iv) in Fig. 9.7. We discuss case (i) first. To give a point of reference, the curve corresponding to $\mu = 8.0 \times 10^{-3}$ matches the case (i) curve shown in Fig. 9.5b. Interestingly, the family of curves appear to have a similar behavior to those in Fig. 9.5b, except now with μ varied instead of signal path efficiency. An increase of μ increases the number of multi-photon states that are heralded which both lowers the maximum visibility and requires a higher $|\alpha|^2$ to match, similar to that discussed for the curves in Fig. 9.5b. The width of the curve is also reduced from the lower $|\alpha|^2$ edge as μ increases, which is again consistent with the increase in multi-photon events from $|\text{TMSV}\rangle$. For high μ, as $|\alpha|^2$ is lowered from the value corresponding to maximum visibility, the curve falls more sharply than others because there are more multi-photon terms in $|\text{TMSV}\rangle$ and $|\alpha\rangle$, and a slight mismatch in mean photon numbers will lead to higher order terms contributing a larger reduction in visibility. For the case in which μ is smaller, there are fewer multi-photon terms from $|\text{TMSV}\rangle$

in the idler mode, and also $|\alpha|^2$, which leads to a broader peak on the low $|\alpha|^2$ edge. A slight mismatch of single photon probabilities is not accompanied by strong multi-photon effects in this scenario. As in Fig. 9.5b, the high $|\alpha|^2$ edge of curves converge with increased $|\alpha|^2$ because the Poisson-distributed multi-photon components from $|\alpha\rangle$ dominate in this regime relative to conditions for maximum visibility.

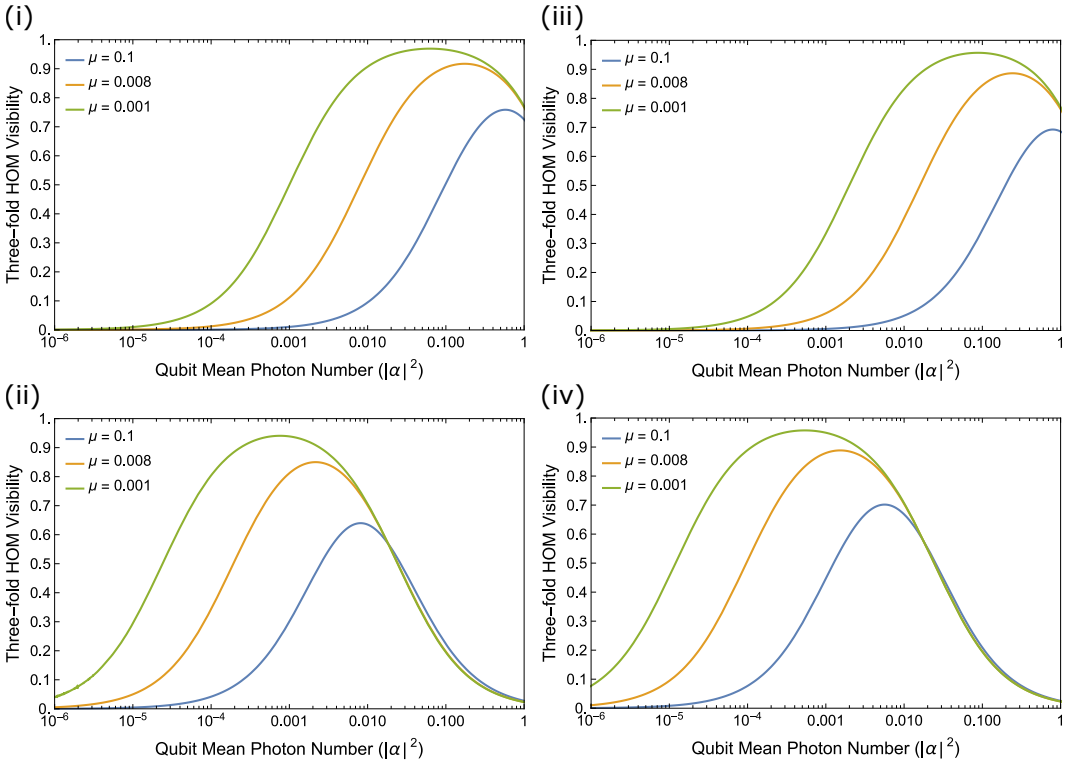

Figure 9.7: Model of three-fold HOM interference visibilities for varied $|\alpha|^2$ and $\mu < 10^{-2}$, under varied signal and idler transmission efficiencies, cases (i)-(iv), assuming complete indistinguishability $\zeta = 1$.

The curves for case (ii), which corresponds to the non-unit path efficiencies in Chapter 8, have remarkably similar shapes to case (i) with a few differences. The shift of the distributions to lowered $|\alpha|^2$ is again due to the idler path loss. The maximum visibilities are lowered because the signal loss reduces the number of single photon events in the idler path that contribute to interference, and the idler loss further decreases this number, which leads to multi-photon terms from both $|\text{TMSV}\rangle$ and $|\alpha\rangle$ contributing. This also explains why the curve widths are also reduced compared to case (i) even though the curves are centered around lower values of $|\alpha|^2$; the multi-photon terms quickly dominate when mean photon numbers are not matched. Note that the narrowing of the distribution from case (i) to case (ii)

is also slightly observed in Fig. 9.5. Observe that the $\mu = 0.1$ curve edge slightly extends over the others for high $|\alpha|^2$ because $|\text{TMSV}\rangle$ contributes more terms in the idler mode in this regime compared to the others.

The family of curves for case (iii), which corresponds to non-ideal signal path efficiency, differs from case (i) much in the same way that these cases differ in Fig. 9.5. That is, the curves take on a similar form as (i), but with lower maximum visibilities, maxima that are shifted to higher $|\alpha|^2$, and narrower curve widths compared to those in (i). The shape and offset of the curves follows reasons previously discussed, which owe to increased multi-photon events in the idler mode. For case (iv), corresponding to non-ideal idler path efficiency, differs from case (ii) again much in the same way that these cases differ in Fig. 9.5. The unit signal efficiency now increases the visibilities, shifts the curve to lower $|\alpha|^2$, and broadens the curve widths compared to those in (ii). The shape and offset again follow reasons previously discussed. The broadening is particularly pronounced for low μ, which also requires low $|\alpha|^2$, and thus very few multi-photon events contribute, and hence are less effected by idler path loss.

9.6 Discussion

Our analytical expressions for realistic photonic quantum teleportation experiments with time-bin qubits are valuable for guiding the design and optimization of future experiments. Achieving transmission efficiencies or indistinguishability beyond 99% in typical photonics experiments requires significant effort [31]. Our modeling quantifies the improvements provided by such efforts under different experimental configurations and indicates the effort needed to meet minimum acceptable standards for various applications, such as quantum communication. Additionally, our analytical expressions allow for predicting experimental outcomes using independently measured parameters, including indistinguishability, which can be estimated through mode measurements like laser linewidth or cavity resonance profiles.

By quantifying our figures-of-merit against the log of the mean photon number $|\alpha|^2$ of an input weak coherent state $|\alpha\rangle$, we find a simple log-normal distribution that aids in interpreting and utilizing our analytical expressions. The curves simplify the role of indistinguishability to a simple scaling of visibility or teleportation fidelity. The two-fold HOM interference visibility curves are the quickest to interpret and, along with their rapid measurement compared to three-fold HOM interference, are valuable for prototyping setups. For teleportation, a low mean photon number of

photon pairs μ strongly mitigates path inefficiency and relaxes the precision needed for the value of $|\alpha|^2$ that maximizes visibility. Conversely, a relatively high $\mu \sim 0.1$ significantly reduces teleportation fidelity but not below the classical bound of $2/3$ for our parameter range. Even with path efficiencies of $\sim 1\%$, the reduction is not severe, with signal path inefficiency impacting visibilities to a lesser extent. This is unsurprising given the number of successful quantum networking experiments using lossy setups or links that require extended data collection periods. However, higher mean numbers of pairs necessitate careful calibration of $|\alpha|^2$ to maximize visibility. The data in Fig. 9.3 shows that calibration of $|\alpha|^2$ in Chapter 8 was challenging for $|\alpha|^2 \ll 10^{-3}$. Nonetheless, we find good agreement between our analytical expressions and the measurement data from Chapter 8, which spans almost four decades of $|\alpha|^2$.

Although our modeling captures all relevant behavior in the experiment of Chapter 8 and can be applied to other photonic quantum teleportation experiments, future work could include more detailed modeling of the multi-mode nature of $|\text{TMSV}\rangle$. This involves incorporating the effects of pump bandwidth and frequency filtering, as done in Chapter 3. The Schmidt decomposition of $|\text{TMSV}\rangle$ approximates the number of modes, and the filter acts as a mode-selective beamsplitter [32]. This would relate differences in indistinguishability and loss in the idler path for two- and three-fold detection to specific apparatus configurations. It is also straightforward to incorporate noise or detector dark counts into the modeling. Moreover, our methods can be extended to non-Gaussian measurements, including photon number resolved detection, which can improve heralding efficiencies of single photons (see Chapter 3).

Our modeling applies to different discrete-variable encodings beyond time-bin and readily extends to more complex experiments such as entanglement swapping or GHZ-state generation. The use of Gaussian states and transformations also extends to other experiments using bosonic modes, such as atomic ensembles or other parametric interactions like electro-optics or opto-mechanics, and their relevant applications in communications, computing, and sensing. Although an analysis based on "photon counting" in the Fock basis could have been used to analyze the outcomes in Chapter 8, we believe that our presented analysis provides an intuitive picture of the underlying physics with a compact, experimentally realistic, and "universal" methodology that can be easily extended to other experimental operating regimes, such as using squeezing [33].

References

[1] Charles H. Bennett, Gilles Brassard, Claude Crépeau, Richard Jozsa, Asher Peres, and William K. Wootters. "Teleporting an unknown quantum state via dual classical and Einstein-Podolsky-Rosen channels." In: Physical Review Letters 70 (13 Mar. 1993), pp. 1895–1899. DOI: 10.1103/PhysRevLett.70.1895. URL: https://link.aps.org/doi/10.1103/PhysRevLett.70.1895.

[2] H Jeff Kimble. "The quantum internet." In: Nature 453.7198 (2008), pp. 1023–1030.

[3] Stephanie Wehner, David Elkouss, and Ronald Hanson. "Quantum internet: A vision for the road ahead." In: Science 362.6412 (Oct. 2018), eaam9288. ISSN: 0036-8075. DOI: 10.1126/science.aam9288. URL: http://www.sciencemag.org/lookup/doi/10.1126/science.aam9288.

[4] Christoph Simon. "Towards a global quantum network." In: Nature Photonics 11 (2017), pp. 678–680. ISSN: 1749-4893. DOI: 10.1038/s41566-017-0032-0. URL: https://doi.org/10.1038/s41566-017-0032-0.

[5] Nicolas Gisin and Rob Thew. "Quantum communication." In: Nature Photonics 1.3 (2007), p. 165.

[6] Raju Valivarthi, Marcelli Grimau Puigibert, Qiang Zhou, Gabriel H Aguilar, Varun B Verma, Francesco Marsili, Matthew D Shaw, Sae Woo Nam, Daniel Oblak, and Wolfgang Tittel. "Quantum teleportation across a metropolitan fibre network." In: Nature Photonics 10.10 (2016), pp. 676–680.

[7] Qi-Chao Sun, Ya-Li Mao, Si-Jing Chen, Wei Zhang, Yang-Fan Jiang, Yan-Bao Zhang, Wei-Jun Zhang, Shigehito Miki, Taro Yamashita, Hirotaka Terai, et al. "Quantum teleportation with independent sources and prior entanglement distribution over a network." In: Nature Photonics 10.10 (2016), pp. 671–675.

[8] Hiroki Takesue and Benjamin Miquel. "Entanglement swapping using telecom-band photons generated in fibers." In: Optics express 17.13 (2009), pp. 10748–10756.

[9] Matthew D Eisaman, Jingyun Fan, Alan Migdall, and Sergey V Polyakov. "Invited review article: Single-photon sources and detectors." In: Review of Scientific Instruments 82.7 (2011).

[10] Jeremy L. O'Brien, Akira Furusawa, and Jelena Vučković. "Photonic quantum technologies." In: Nature Photonics 3.12 (2009), pp. 687–695.

[11] Xiang-Bin Wang, Tohya Hiroshima, Akihisa Tomita, and Masahito Hayashi. "Quantum information with Gaussian states." In: Physics Reports 448.1-4 (2007), pp. 1–111.

[12] Christian Weedbrook, Stefano Pirandola, Raúl García-Patrón, Nicolas J Cerf, Timothy C Ralph, Jeffrey H Shapiro, and Seth Lloyd. "Gaussian quantum information." In: Reviews of Modern Physics 84.2 (2012), pp. 621–669.

[13] Andreas Christ and Christine Silberhorn. "Limits on the deterministic creation of pure single-photon states using parametric down-conversion." In: Physical Review A 85.2 (2012), p. 023829.

[14] Masahiro Takeoka, Saikat Guha, and Mark M. Wilde. "Fundamental rate-loss tradeoff for optical quantum key distribution." In: Nature Communications 5.1 (2014), p. 5235.

[15] Masahiro Takeoka, Rui-Bo Jin, and Masahide Sasaki. "Full analysis of multi-photon pair effects in spontaneous parametric down conversion based photonic quantum information processing." In: New Journal of Physics 17.4 (Apr. 2015), p. 043030. ISSN: 1367-2630. DOI: 10.1088/1367-2630/17/4/043030. URL: http://stacks.iop.org/1367-2630/17/i=4/a=043030?key=crossref.f2e700d40572762a0c854ab624e22054.

[16] Christian Weedbrook, Stefano Pirandola, Raúl García-Patrón, Nicolas J. Cerf, Timothy C. Ralph, Jeffrey H. Shapiro, and Seth Lloyd. "Gaussian quantum information." In: Rev. Mod. Phys. 84 (2 May 2012), pp. 621–669. DOI: 10.1103/RevModPhys.84.621. URL: https://link.aps.org/doi/10.1103/RevModPhys.84.621.

[17] C. K. Hong and Leonard Mandel. "Experimental realization of a localized one-photon state." In: Physical Review Letters 56.1 (1986), p. 58.

[18] Samuel L. Braunstein and Ady Mann. "Measurement of the Bell operator and quantum teleportation." In: Physical Review A 51.3 (1995), R1727.

[19] Dirk Bouwmeester, Jian-Wei Pan, Klaus Mattle, Manfred Eibl, Harald Weinfurter, and Anton Zeilinger. "Experimental quantum teleportation." In: Nature 390.6660 (1997), pp. 575–579.

[20] Leonard Mandel and Emil Wolf. Optical coherence and quantum optics. Cambridge university press, 1995.

[21] C. K. Hong, Z. Y. Ou, and L. Mandel. "Measurement of subpicosecond time intervals between two photons by interference." In: Physical Review Letters 59 (18 Nov. 1987), pp. 2044–2046. DOI: 10.1103/PhysRevLett.59.2044. URL: https://link.aps.org/doi/10.1103/PhysRevLett.59.2044.

[22] Hiroki Takesue. "1.5 μm band Hong-Ou-Mandel experiment using photon pairs generated in two independent dispersion shifted fibers." In: Applied physics letters 90.20 (2007).

[23] Christopher C. Gerry and Peter L. Knight. Introductory quantum optics. Cambridge University Press, 2005.

[24] H. Ollivier, S. E. Thomas, S. C. Wein, I. Maillette de Buy Wenniger, N. Coste, J. C. Loredo, N. Somaschi, A. Harouri, A. Lemaitre, I. Sagnes, et al. "Hong-Ou-Mandel interference with imperfect single photon sources." In: Physical Review Letters 126.6 (2021), p. 063602.

[25] R. Valivarthi, I. Lucio-Martinez, A. Rubenok, et al. In: Optics Express 22.20 (2014), pp. 24497–24506.

[26] Michael A. Nielsen and Isaac L. Chuang. Quantum computation and quantum information. Cambridge university press, 2010.

[27] Tian Zhong and Franco NC Wong. "Nonlocal cancellation of dispersion in Franson interferometry." In: Physical Review A 88.2 (2013), p. 020103.

[28] Reinhard F. Werner. “Quantum states with Einstein-Podolsky-Rosen correlations admitting a hidden-variable model.” In: Phys. Rev. A 40 (8 Oct. 1989), pp. 4277–4281. DOI: 10.1103/PhysRevA.40.4277. URL: https://link.aps.org/doi/10.1103/PhysRevA.40.4277.

[29] Yoon-Ho Kim, Rong Yu, Sergei P. Kulik, Yanhua Shih, and Marlan O. Scully. “Delayed “Choice” Quantum Eraser.” In: Physical Review Letters 84 (1 Jan. 2000), pp. 1–5. DOI: 10.1103/PhysRevLett.84.1. URL: https://link.aps.org/doi/10.1103/PhysRevLett.84.1.

[30] DN Klyshko. “Use of two-photon light for absolute calibration of photoelectric detectors.” In: Soviet Journal of Quantum Electronics 10.9 (1980), p. 1112.

[31] Koen Alexander, Andrea Bahgat, Avishai Benyamini, Dylan Black, Damien Bonneau, Stanley Burgos, Ben Burridge, Geoff Campbell, Gabriel Catalano, Alex Ceballos, et al. “A manufacturable platform for photonic quantum computing.” In: arXiv preprint arXiv:2404.17570 (2024).

[32] Kevin Zielnicki, Karina Garay-Palmett, Daniel Cruz-Delgado, Hector Cruz-Ramirez, Michael F. O’Boyle, Bin Fang, Virginia O. Lorenz, Alfred B U’Ren, and Paul G. Kwiat. “Joint spectral characterization of photon-pair sources.” In: Journal of Modern Optics 65.10 (2018), pp. 1141–1160.

[33] Volkan Gurses, Samantha I. Davis, Raju Valivarthi, Neil Sinclair, Maria Spiropulu, and Ali Hajimiri. “An on-chip phased array for non-classical light.” In: Nature Communications 16.1 (2025), p. 6849.

Chapter 10

ENTANGLEMENT SWAPPING SYSTEM TOWARD THE QUANTUM INTERNET

This chapter includes the work in preparation for publication:

[1] Samantha I. Davis, Raju Valivarthi, Andrew Cameron, Cristian Pena, Si Xie, Lautaro Narváez, Nikolai Lauk, Chang Li, Kelsie Taylor, Rahaf Youssef, et al. "Entanglement swapping systems toward a quantum internet." In: arXiv preprint arXiv:2503.18906. Submitted. (2025).

10.1 Introduction

A quantum internet, a large-scale quantum network, aims to distribute entangled qubits over long distances and between disparate quantum hardware [1, 2, 3]. For metropolitan-distance networks, qubits are encoded into photons, with fiber optics as the preferred medium for transfer [4, 5, 6, 7]. To mitigate loss, photons at telecommunication wavelengths, such as the 1550 nm C-band, are used [8, 9, 10, 11]. Since loss scales exponentially with fiber length, multiplexing, quantum repeaters, or a combination of both can ensure qubits traverse a channel. These techniques also improve the generation rate of single and entangled photons created using probabilistic processes like spontaneous parametric down conversion (SPDC) [12, 13, 14].

Entanglement swapping, where a Bell-state measurement (BSM) entangles qubits that have never interacted, is crucial for entangling remote qubits and enabling quantum repeaters [15]. Since the first demonstration of post-selective and conditional entanglement swapping of photons [16], numerous follow-up experiments have focused on quantum communications [17, 18, 19, 20]. Entanglement swapping also has applications in quantum computing [21], quantum sensing [22], and fundamental tests of quantum mechanics [23]. Various renditions of photonic entanglement swapping have been demonstrated, including using qubits encoded into different degrees of freedom [24] or derived from different sources [25].

Time-bin encoding is advantageous for quantum networks because each logical state is encoded into the same degrees of freedom except time. This avoids unintended mode-dependent transformations and phase shifts. It also allows simple interfacing

of quantum hardware, such as atomic memories or optical frequency converters, which are generally not compatible with multiple modes. Time-bin encoding provides access to high-dimensional states, i.e., qudits, that encode more information than qubits, benefiting quantum communications [26, 27] and computing [28].

Thus far, entanglement swapping of photonic time-bin qubits has yielded states with an average fidelity up to 83% [29, 17, 18]. Fidelity $F = \langle\psi|\,\rho\,|\psi\rangle$ of the swapped state ρ with respect to the state $|\psi\rangle$ [30] is an important figure of merit to optimize for in quantum networks and information applications in general. Non-classical states manifest at a fidelity greater than 50% with respect to a target Bell state. Clauser-Horne-Shimony-Holt inequality violations, which are signatures of nonlocality and benefit fundamental tests [31, 32, 33], occur for a fidelity greater than 78% [34]. The Ekert protocol for entanglement-based quantum key distribution and source-independent quantum key distribution based on swapping require a fidelity greater than 89% [35, 36]. Distributed quantum computing likely requires fidelity greater than 99.999% [30, 37, 38, 39, 40, 41]. The unavoidable presence of loss in networks further supports the pursuit of high fidelity to reduce the impact of photon counting statistics.

In this work, we demonstrate conditional entanglement swapping between two degenerate time-bin entangled photonic qubits at the telecommunication wavelength of 1536.4 nm with an average fidelity greater than 87%. This fidelity allows demonstration of source-independent quantum key distribution, a scheme that assumes qubits may be generated by an adversary, with an estimated secret key rate of approximately 0.5 bits per sifted bit. The qubits are created with modular, off-the-shelf, fiber-coupled, and electrically controlled components, facilitating setup reproduction and deployment in networks. Specifically, we generate an entangled state using SPDC in nonlinear waveguides pumped with two visible-wavelength pulses separated by 346 ps. Electro-optic modulators carve two pulses from continuous-wave laser light at 1536.4 nm, which are upconverted using another nonlinear waveguide.

Projection onto the Bell state $|\Psi^-\rangle$ and subsequent measurement of the swapped state $|\Phi^+\rangle$ (up to a known phase) with Michaelson interferometers is facilitated by superconducting nanowire single photon detectors (SNSPDs) that resolve the 346 ps bin separation. Our experiment is facilitated with semi-autonomous control, monitoring, and synchronization, with all data collected using scalable software and hardware. The system yielded swapping rates of 0.01 Hz at a clock rate of 200 MHz and was run remotely over several days. The experiment was interpreted and

guided using characteristic function-based analytical modeling based on realistic imperfections. Based on our modeling, we identify straightforward improvements, such as improved packaging and integration to reduce loss, and reduction of the bin separation to the ps-scales, which is compatible with state-of-the-art modulators [42, 43] and SNSPDs [44] (see Chapters 3, 4, 5), to improve the swapping rates to approximately Hz without compromising fidelity. Finally, our specific choice of wavelength is compatible with quantum emitters, memories, and transducers using erbium-doped crystals [45]. The demonstration extends our previous work in Chapter 8 using quantum teleportation systems toward a workable quantum internet envisioned by the U.S. Department of Energy to link the U.S. National Laboratories.

10.2 Setup

The setup for entanglement swapping is shown in Fig. 10.1. We demonstrate a swapping protocol in which a qubit of an entangled photon pair (from Alice) is interfered with a qubit of another entangled photon pair (from Bob) and then measured in the Bell state $|\Psi^-\rangle$ (at Charlie). As a result, the remaining photons at Alice and Bob are projected onto a Bell state $|\Phi^+\rangle$, which is defined with respect to a pre-determined phase offset. All qubit measurements are performed with a custom developed data acquisition (DAQ) system. The Alice, Bob, Charlie, and DAQ subsystems are detailed in the following subsections.

Alice and Bob: entangled photon pair generation

To generate the entangled photon pairs, light from a fiber-coupled continuous wave (CW) laser at a telecom wavelength of 1536.4 nm is split into two paths by a 50:50 polarization-maintaining beamsplitter (BS). In each path, the light is coupled into a lithium niobate intensity modulator (IM) driven by an arbitrary waveform generator (AWG). The AWG generates a pair of pulses separated by 346 ps at a repetition rate of 200 MHz. Each pulse has a full-width-at-half-maximum (FWHM) of approximately 65 ps. The pulses from the AWG are amplified by a 30 dB high-bandwidth amplifier and are injected into the radio-frequency (RF) input of the IM, resulting in optical pulses with an extinction ratio of at least 20 dB. A 90:10 BS at the output of the IM is used to perform feedback on the DC-bias port of the IM, which ensures a constant extinction ratio throughout the experiment. The optical pulses from the 90% ports of the BS in each path are sent to the Alice and Bob nodes.

At each node, the optical pulses are amplified with an erbium-doped fiber amplifier (EDFA) and up-converted to 768.2 nm by second harmonic generation (SHG) with

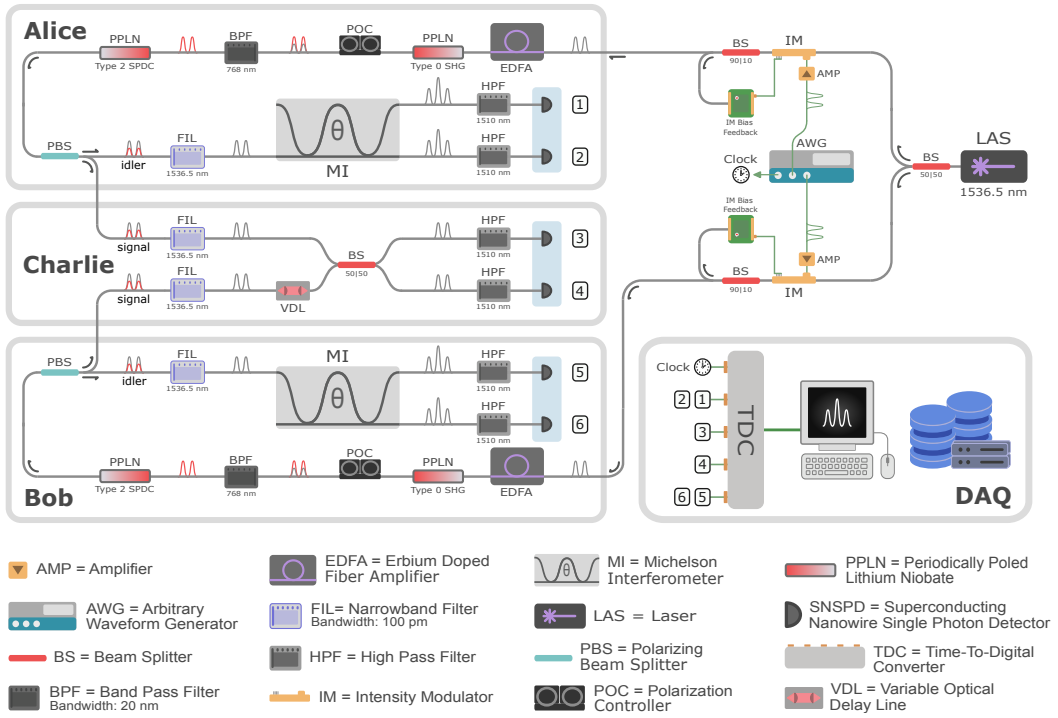

Figure 10.1: Schematic diagram of the entanglement swapping system consisting of Alice, Bob, Charlie, and the data acquisition (DAQ) subsystems. All components are labelled in the legend. Single mode fibers and electronic cables are indicated in gray and green, respectively. The detection signals generated by the SNSPDs are labeled 1-6 and sent to the TDC, with 1-2 and 5-6 time multiplexed. The clock generated by the AWG is labeled and sent to the start channel of the TDC.

a periodically poled lithium niobate (PPLN) waveguide. Residual pump light at 1536.4 nm is removed by a 768 nm bandpass filter with an extinction ratio of ≥ 80 dB. The up-converted pulse pair is used to pump a type-II SPDC with a second PPLN waveguide, which produces a pair of photons at 1536.4 nm in a Bell-state state, $|\Phi^+\rangle = (|ee\rangle + |ll\rangle)/\sqrt{2}$. The members of the entangled photon pair are produced in "signal" and "idler" modes with orthogonal polarizations $|H\rangle$ and $|V\rangle$ and are hereafter referred to as "signal" and "idler" photons, respectively. The signal and idler photons are separated with a polarizing beam splitter (PBS) and spectrally filtered with tunable narrowband optical filters. We select a bandwidth of 12.7 GHz to optimize for the trade-off in spectral purity and Bell pair generation rates. The signal photon is distributed to Charlie for the Hong-Ou-Mandel or Bell State measurements, and the idler photon is sent to an unbalanced Michelson interferometer (MI) with a delay of 346 ps between the long path and the short path.

The path difference matches the time between early and late time-bins and enables pulse overlap required for characterizing entanglement. When two time-bins enter an MI, three time-bins emerge corresponding to all combinations of short and long path trajectories of each input time-bin.

All single photon detections are performed with SNSPDs. A total of six SNSPDs, two each for Alice, Bob, and Charlie, are installed in a rack-mount cryogenic system with continuous operation at a temperature of 2.5 K. The SNSPDs have detection efficiencies of 89-93%, dark count rates of 60-135 Hz, timing resolution (jitter) of 38-59 ps, and dead times $\leq$ 30 ns. A photon detection at the SNSPD produces an RF pulse, which is sent to the DAQ subsystem described below. At the input of each detector, a high pass filter is used to remove any residual 768 nm light from the second harmonic generation process.

The MI and SNSPDs are used to project a photon onto the $|e\rangle$, $(|e\rangle + e^{i\theta}|l\rangle)/\sqrt{2}$, or $|l\rangle$ states by detection in the first, second, or third time-bins, respectively, at one of the outputs (see Fig 10.1). Detection at the other output corresponds to projections onto the same states but with $\theta + \pi$. The phase θ of a MI is set by the voltage applied to its phase shifter. For the entanglement visibility measurements, which include the characterization of entangled photon pair sources and teleportation of entanglement, the phase of Alice's MI is swept and the coincidence events of photons in the outputs of Alice's and Bob's MI are accumulated. We measure the coincidences in all four pairings of Alice and Bob's outputs to maximize the coincidence rates in the experiment.

Charlie: Bell-state measurement

At Charlie, the signal photons from Alice and Bob are interfered in a 50:50 polarization maintaining beamsplitter (BS) after spectral filtering. A variable optical delay line (VDL) at one input of the BS is used to optimize the temporal indistinguishability of the interfering photons, such that the photons arrive to the inputs of the BS at the same time. Alice and Bob's signal photons are projected onto the $|\Psi^-\rangle = (|el\rangle - |le\rangle)/\sqrt{2}$ Bell state by detection of coincidence events in the first time-bin of one BS output and the second time-bin of the other BS output. Conditioned on a successful Bell-state measurement outcome, Alice and Bob's idler photons are projected onto the $|\Psi^-\rangle$ state.

DAQ: Data acquisition and analysis

Our DAQ subsystem is an extension of the control and data acquisition systems detailed in Chapter 8. The RF pulses from the SNSPDs are sent to a time-to-digital converter (TDC) with a fixed voltage threshold, i.e., "time-tagger", to obtain a time-tag for the time-of-arrival of each pulse relative to a clock signal. The time-tagger has five input channels, one of which is used for a 10 MHz clock signal reference from the AWG. Of the remaining four channels, two are used for the outputs of Charlie's SNSPDs, one is used for the outputs of Alice's SNSPDs, and one is used for the outputs of Bob's SNSPDs. The outputs for each pair of detectors at Alice and Bob are electronically combined with a relative time delay introduced by an RF delay line to enable signals from the pair to be read out with a single time-tagger channel. The time-tagger is interfaced with a custom graphical user interface (GUI) to process the time-tags, perform the coincidence logic, store measurement outcomes in a customized database, and visualize photon statistics in real-time (see Sec. 10.6). The database forms the backbone of a centralized classical processing unit that is responsible for the monitoring of critical network parameters, remote control, active-feedback and stabilization of experimental components, acquisition and management of large volumes of time-tagged signals, and global synchronization across multiple nodes. The DAQ subsystem has been upgraded to support GHz teleportation rates, multinode entanglement distribution, and picosecond synchronization for metropolitan-scale quantum network testbeds (see Chapter 11).

10.3 Experimental results

Entanglement visibility

The entanglement swapping protocol requires high-fidelity entanglement sources, which we realize with an SPDC process using a bulk optical nonlinearity. The output state of an SPDC process can be described by the two-mode squeezed state (TMSV),

$$|\text{TMSV}\rangle = \sum_{n=0}^{\infty} (-1)^n \sqrt{\frac{\mu^n}{(1+\mu)^{n+1}}}\, |n,n\rangle\,, \tag{10.1}$$

where μ is the mean number of photon pairs, and $|n,m\rangle \equiv |n\rangle \otimes |m\rangle$ is the product state of n photons in the signal mode and m photons in the idler mode. After the narrowband filters, the output state of the pair source is described by $|\text{pair}\rangle = |\text{TMSV}\rangle_e \otimes |\text{TMSV}\rangle_l$, where $|\text{TMSV}\rangle_{e(l)}$ is a TMSV in the early (late) time-bin. For low mean photon numbers, $|\text{pair}\rangle$ approximates a Bell state conditioned on the

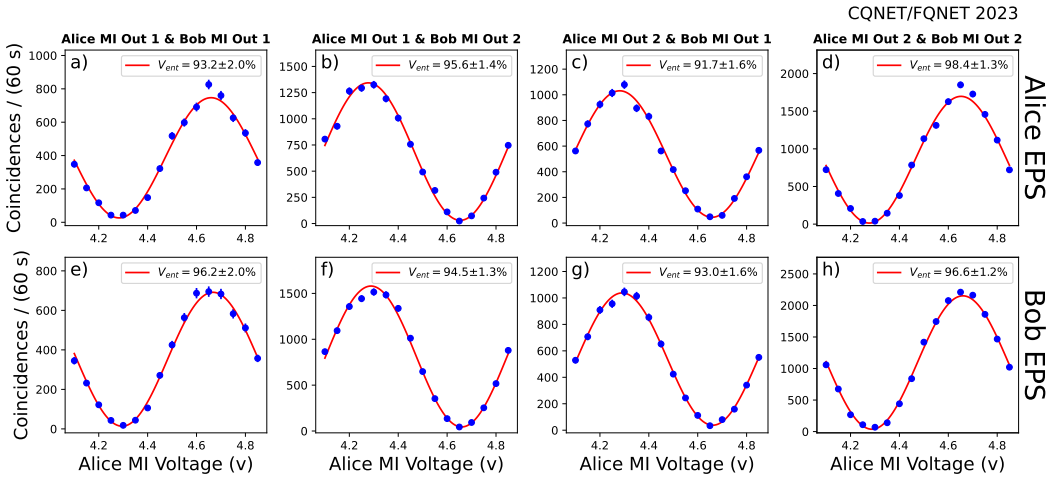

Figure 10.2: Entanglement visibility of photon pairs produced by Alice's and Bob's entangled photon pair source (EPS). The coincidence rates for each pairing of an output port of Alice's MI and Bob's MI are shown for Alice's EPS a)-d) and Bob's EPS d)-h). The entanglement visibilities are obtained from a sinusoidal fit (see main text for details), with uncertainties in all measurements calculated assuming Poisson statistics.

presence of at least one photon,

$$|\text{pair}\rangle \approx \sqrt{1-2\mu}\,|0\rangle + \sqrt{2\mu}\,\left|\Phi^+\right\rangle + O(\mu^2), \quad \mu \ll 1, \tag{10.2}$$

neglecting loss. Due to multiphoton effects arising from $O(\mu^2)$ contributions, there is a trade-off in the quality of entanglement and the pair production rate $\propto \mu$. We optimize for this trade-off by operating the sources at Alice and Bob with a mean photon number per time-bin of $\mu_A = 2.5 \times 10^{-3}$ and $\mu_B = 2.0 \times 10^{-3}$, respectively, at a repetition rate of 200 MHz.

To evaluate the entanglement sources, we measure the entanglement visibilities of the photon pairs produced by each pair source with a modification of the setup in Fig. 10.1. After the narrowband filters, the signal and idler modes of a pair source are directed to Alice's MI and Bob's MI, respectively. We vary the phase of Alice's MI and measure the coincidences of the signal and idler modes in a phase basis by accumulating coincidence events in the central time-bin of both Alice and Bob's MI. We acquire data for all four combinations of Alice and Bob MI output ports, which are used in the entanglement swapping visibility measurements. The results are shown in Fig. 10.2. The coincidence rates are fitted proportional to $1 + V_{\text{ent}} \cos(2\omega v + \phi_0)$, where the entanglement visibility is $V_{\text{ent}} = (C_{\max} - C_{\min})/(C_{\max} + C_{\min})$, with $C_{\max(\min)}$

denoting the maximimum (minimum) rate of coincidence events, ω and ϕ_0 are unconstrained constants, and v is the voltage applied to Alice's MI. We obtain average entanglement visibilities across all output port combinations of $\langle V_{\text{ent}} \rangle = 94.7 \pm 1.6\%$ for Alice's source and $\langle V_{\text{ent}} \rangle = 95.1 \pm 1.6\%$ for Bob's source. The deviations from unity are attributed to mulitphoton effects and interferometric imperfections. Imbalances in the MIs due to imperfect transmittances and internal path efficiencies can give rise to a dependence of the entanglement visibility on the combination of output ports that is used (see Chapter 5). Nevertheless, these visibilities exceed the locality bound of $1/\sqrt{2}$, and correspond to average state fidelities with respect to $|\Phi^+\rangle$ of $\langle F_{\text{ent}} \rangle = 96.0 \pm 1.2\%$ for Alice and $\langle F_{\text{ent}} \rangle = 96.3 \pm 1.2\%$ for Bob, where $F_{\text{ent}} = (3V_{\text{ent}} + 1)/4$.

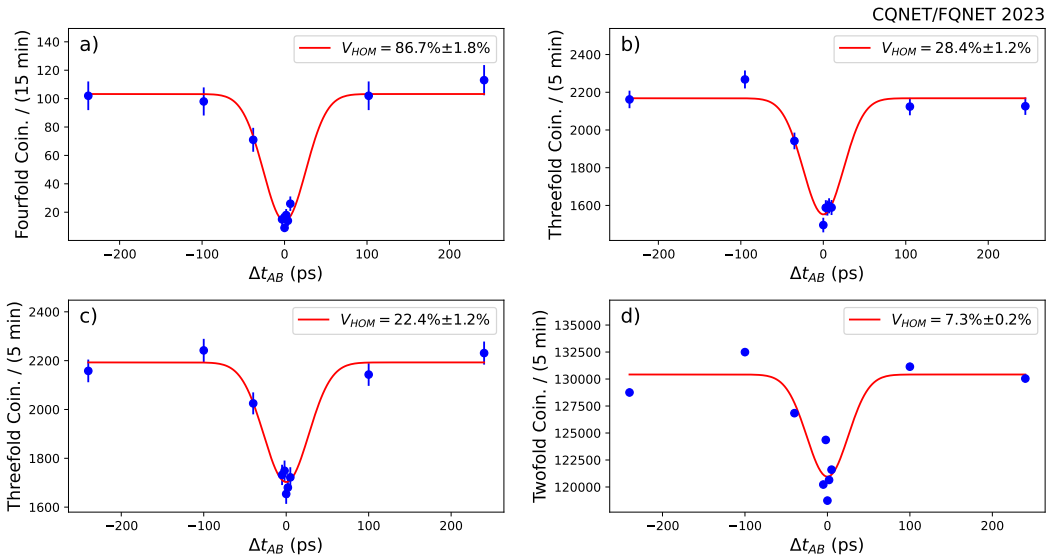

Figure 10.3: Hong-Ou-Mandel (HOM) interference. a) Fourfold coincidence rates, b) threefold coincidence rates conditioned on Bob's idler photon, c) threefold coincidence rates conditioned on Alice's idler photon, and d) twofold coincidence rates measured as a function of the relative time-delay (Δt_{AB}) between Alice and Bob's signal photons.

Hong-Ou-Mandel interference

Entanglement swapping is facilitated by a BSM at Charlie, which relies on the interference of indistinguishable photons in the standard optical implementation [46]. To evaluate the indistinguishability of the photons from Alice and Bob, we perform HOM interference at Charlie's BS. We use the same setup as Fig. 10.1 except for the removal of the MI's from Alice and Bob, such that each idler mode is

measured by a single detector. Photon pairs are prepared in the state $|\text{TMSV}\rangle_e$ by injecting a single RF pulse into each IM at a repetition rate of 200 MHz. For low mean photon numbers,

$$|\text{TMSV}\rangle_e \approx \sqrt{1-\mu}\,|0\rangle + \sqrt{\mu}\,|1,1\rangle_e + O(\mu^2), \quad \mu \ll 1, \tag{10.3}$$

neglecting loss. With mean photon numbers per time-bin of $\mu_A = 0.019$ and $\mu_B = 0.015 \ll 1$ for this measurement, each signal mode is approximately in a single photon state conditioned on the detection of its idler mode.

We interfere the signal photons and measure the coincidence events at the output of Charlie's BS. The variable delay line at Bob's input to the BS is used to sweep the relative time-delay, i.e. temporal distinguishability, of Alice and Bob's signal photons (Δt_{AB}). By heralding the signal photons with the detection of the idler photons at Alice and Bob, we measure fourfold coincidence rates for various Δt_{AB} over a range of 560 ps. The results are shown in Fig. 10.3a. Assuming Gaussian temporal profiles of the optical pulses with 1/e temporal duration of $\sigma = 25$ ps, the coincidence rates are fitted proportional to $1 - V_{\text{HOM}} \exp\left(-\Delta t_{AB}^2/2\sigma^2\right)$, where the HOM visibility is $V_{\text{HOM}} = (C_d - C_i)/C_d$, with $C_{d(i)}$ denoting the coincidence rates when the photons are made as distinguishable (indistinguishable) as possible. Single photons that are indistinguishable in all degrees of freedom (e.g., temporal, spectral, spatial) would result in a HOM visibility of 100%. We obtain a HOM visibility of $V_{\text{HOM}}^{(4)} = 86.7 \pm 1.8\%$, indicating high indistinguishability of photons from Alice and Bob. The deviation from unity visibility is expected from experimental imperfections including multiphoton contributions and distinguishability in the temporal mode profiles of the photons from Alice and Bob introduced during optical pulse generation.

To glean further information about the quantum interference at Charlie, we also measure threefold and twofold coincidence rates for various Δt_{AB}. The HOM visibility depends on the photon statistics of the interfering fields. Without heralding a signal photon by the detection of an idler photon, the state of the signal mode is described by a thermal state,

$$\rho_{\text{th}} = \text{Tr}_i\,|\text{TMSV}\rangle\langle\text{TMSV}| = \sum_{n=0} \frac{\mu^n}{(1+\mu)^{n+1}}\,|n\rangle\langle n| \tag{10.4}$$

where Tr_i denotes the partial trace over the idler mode of the TMSV. By heralding only one of the signal photons by the detection of an idler photon at Alice or Bob, we measure threefold coincidence rates corresponding to the interference of a

single photon state and thermal state. The twofold coincidence rates at the output of Charlie's BS correspond to the interference of two thermal states. We obtain HOM visibilities of $V_{\mathrm{HOM}}^{(3B)} = 28.4 \pm 1.2\%$ and $V_{\mathrm{HOM}}^{(3A)} = 22.3 \pm 1.2\%$ for the threefold coincidence rates conditioned on the idler mode at Bob (Fig. 10.3b) and Alice (Fig. 10.3c), respectively. The asymmetry in the threefold HOM visibilities is expected due to the difference in the mean photon numbers of Alice and Bob's sources and heralding path efficiencies. For the twofold coincidence rates, we obtain a HOM visibility of $V_{\mathrm{HOM}}^{(2)} = 7.3\% \pm 0.2\%$ (Fig. 10.3d).

We support our measurements with modeling as described in Section 10.4. For the twofold HOM visibility, we obtain an upper bound of 33% corresponding to the interference of ideal thermal states. We obtain an upper bound of 50% for the threefold HOM visibility corresponding to the interference of ideal single photon and thermal states with identical mean photon numbers. Threefold HOM visibilities of up to 100% could be achieved with unequal mean photon numbers (see Sec. 10.6). Relevant to the entanglement swapping configuration, we find that our fourfold HOM visibility corresponds to a photon indistinguishability of 0.92 ± 0.02 (see Sec. 10.6). The presence of clear HOM dips and estimation of high photon indistinguishability indicate that our system can perform BSMs suitable for entanglement swapping.

Entanglement swapping

After characterization of our system, we perform the entanglement swapping protocol with the setup in Fig. 10.1. We measure the entanglement visibility of idler photons at Alice and Bob conditioned on the BSM at Charlie, resulting in fourfold coincidence rates for each pairing of Alice and Bob's MI output ports. The phase of Alice's MI is varied, and for each interferometric voltage setting the fourfold coincidences are acquired for three hours.

The results are shown in Fig. 10.4. We obtain two curves by combining fourfold coincidence rates for in-phase pairings of MI outputs (see Fig. 10.2) and observe visibilities of $V_{\mathrm{swap}} = 85.0 \pm 6.5\%$ and $V_{\mathrm{swap}} = 81.2 \pm 8.9\%$, which surpass the classical bound of $1/3$ required to demonstrate entanglement [47]. The average visibility of $\langle V_{\mathrm{swap}} \rangle = 83.1 \pm 5.5\%$ corresponds to a teleported state fidelity of $\langle F_{\mathrm{swap}} \rangle = 87.3 \pm 4.1\%$ with respect to $|\Phi^+\rangle$ and a violation of the CHSH Bell inequality by 2.25 standard deviations.

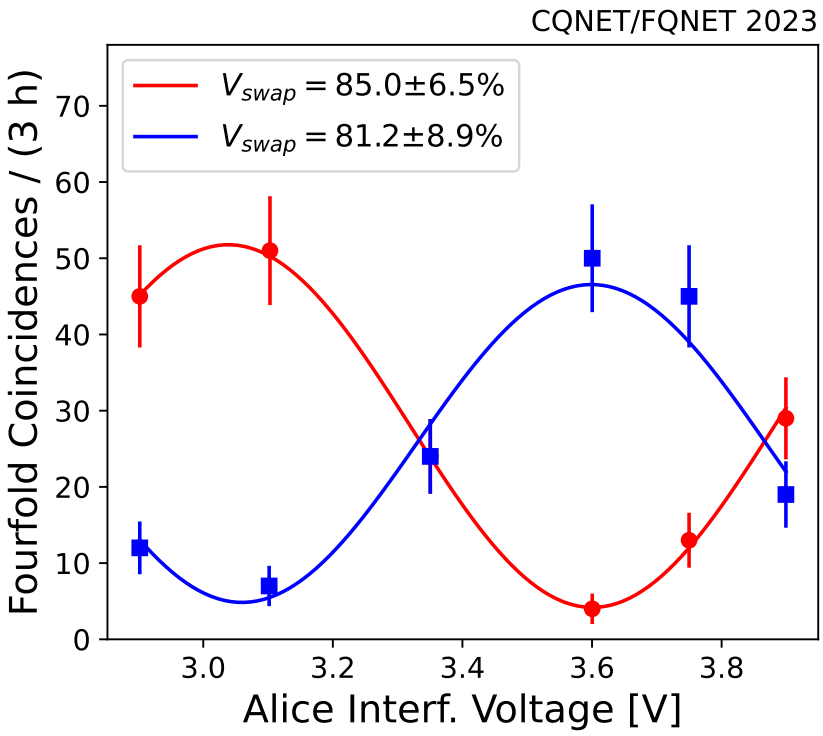

Figure 10.4: Entanglement swapping of $|\Phi^+\rangle$. The voltage of the Alice's MI is varied to yield a sinusoidal variation of the fourfold coincidence rates for each pairing of output ports of Alice's and Bob's MIs. This yields four sets of fourfold coincidence rates, with two in-phase and two out-of-phase. The in-phase sets are combined (red) and the out-of-phase sets are combined (blue) to obtain two curves. A sinusoidal fit is performed for each combined data set to extract the swapping visibilities of $V_{\text{swap}} = 85.0 \pm 6.5\%$ (red) and $V_{\text{swap}} = 81.2 \pm 8.9\%$ (blue). The average of the two visibilities is $\langle V_{\text{swap}} \rangle = 83.1 \pm 5.5\%$.

Source-independent quantum key distribution

Alice and Bob can obtain a secure key by measuring the idler photons in the time basis $\{|e\rangle, |l\rangle\}$ and phase basis $\{(|e\rangle \pm |l\rangle)/\sqrt{2}\}$ conditioned on the BSM. From the security proof of Koashi and Preskill [48], the secret key rate for quantum key distribution (QKD) [49] with a basis-independent source [36] is,

$$R \geq R_S[1 - \kappa H_2(e_t) - H_2(e_p)] \tag{10.5}$$

where R_s is the sifted key rate, κ is the error correction efficiency, e_t is the bit error rate in the time basis, e_p is the bit error rate in the phase basis, and H_2 is the binary entropy function,

$$H_2(x) = -x \log_2(x) - (1 - x) \log_2(1 - x).$$

Time basis (e_t)	Phase basis (e_p)	Secret key rate (R/R_s)
0.011 ± 0.011	0.079 ± 0.020	$0.50^{+0.18}_{-0.14}$

Table 10.1: Source-independent quantum key distribution error rates. The secret key rate (R/R_s) is calculated from the measured error rates in the time (e_t) and phase (e_p) bases for an error correction efficiency of $\kappa = 1.22$. Error bars on the rates are calculated from the propagation of Poisson statistics.

With the setup in Fig. 10.1, we measure the error rates for QKD. For the phase-basis error rate, we measure Alice and Bob's idler photons in the phase basis conditioned on the BSM and accumulate fourfold coincidences for a total of twelve hours. For the time-basis error rate, we remove the MI's to measure Alice and Bob's idler photons in the time basis and accumulate fourfold coincidences for the same period. The results are summarized in Table I. For identical time-basis and phase-basis error rates ($e_t = e_p$), an error rate of less than 11% is required for a non-zero secret key rate. In practice, the phase-basis error rate is higher than the time-basis error rate due to experimental challenges associated with the quantum interference requirements of the phase basis. We obtain $< 10\%$ error rates in both the phase and time bases. The error rate in the phase basis is consistent with the average entanglement swapping visibility of Fig. 10.4, which estimates $e_p = (1 - \langle V_{\text{swap}} \rangle)/2 = 0.085 \pm 0.028$. The secret key rate per sifted key is obtained from Eq. 10.5 with $\kappa = 1.22$. The nonzero secret key rate of $0.50^{+0.18}_{-0.14}$ bits per gate illustrates the suitability of our system for metropolitan-scale quantum key distribution.

10.4 Analytical modeling

As discussed in Sec. 10.3, experimental implementations of quantum networks introduce nonidealities, such as multiphoton effects, multiple modes, and dark counts, that can degrade the performance of quantum communication protocols in the real world.

Modeling of quantum networks that can account for all experimental imperfections will elucidate the performance criteria for quantum network components and provide valuable insight for the scale-up of quantum network testbeds towards the quantum internet [50]. Typically, SPDC-based experiments are modeled in the photon number basis, where the analytical calculations for multimode coincidence probabilities quickly become intractable without low mean photon number approximations.

In this work, we extend our phase-space-based Gaussian model for quantum tele-

portation from Chapter 9 to entanglement swapping [51]. Since the TMSV states produced by SPDC have a Gaussian characteristic function, and all subsequent experimental operations up to detection are described by linear optics, we construct the symplectic matrix that maps the characteristic function of the input state to that of the output state prior to detection [52]. By modeling each SNSPD as a threshold detector, whose POVM can be written in terms of Gaussian states, i.e., states with Gaussian characteristic functions, we derive expressions for all detection probabilities in the experiment. In this approach, all multiphoton contributions are captured by the characteristic function of the input state, and imperfections such as loss, photon distinguishability, and dark counts can be modeled with symplectic matrices. Therefore, we can efficiently compute the output state accounting for all relevant experimental imperfections and obtain exact analytical expressions for the entanglement and HOM visibilities. The derivations for HOM and entanglement swapping visibilities as a function of Alice and Bob's mean photon numbers, photon indistinguishability, path efficiencies, imperfect beamsplitter transmittances, and dark count rates are outlined in Sec. 10.6. Theoretical investigations of the HOM and entanglement swapping visibilities as a function of mean photon numbers and photon indistinguishibilities, with comparison to the data, are presented in Sec. 10.6.

We experimentally investigate the swapping visibility for asymmetric mean photon numbers of Alice and Bob's sources by fixing Bob's (Alice's) mean photon number and sweeping Alice's (Bob's) mean photon number. The swapping visibility as a function of Alice's and Bob's mean photon numbers are shown in Fig. 10.5. The mean photon number is varied by sweeping the gain of the EDFA at Alice or Bob. The EDFAs are remotely controlled by the DAQ subystem to perform automated gain sweeps, enabling long duration data collection and optimization of the system over a range of mean photon numbers. For our repetition rate of 200 MHz, the maximum accessible mean photon number was 0.05. We fit the data to the swapping model to determine the indistinguishability and obtain $\zeta^2 = 0.69 \pm 0.02$ (0.64 ± 0.02) for the sweep over Alice's (Bob's) mean photon number. The swapping visibility exceeds the classical bound up to $\mu_A = 0.28$ and $\mu_B = 0.23$ for Alice's and Bob's sweeps, respectively.

10.5 Discussion

We demonstrate entanglement swapping between entangled time-bin qubits encoded into 1536.4 nm-wavelength photon pairs with an average fidelity of 87%, which

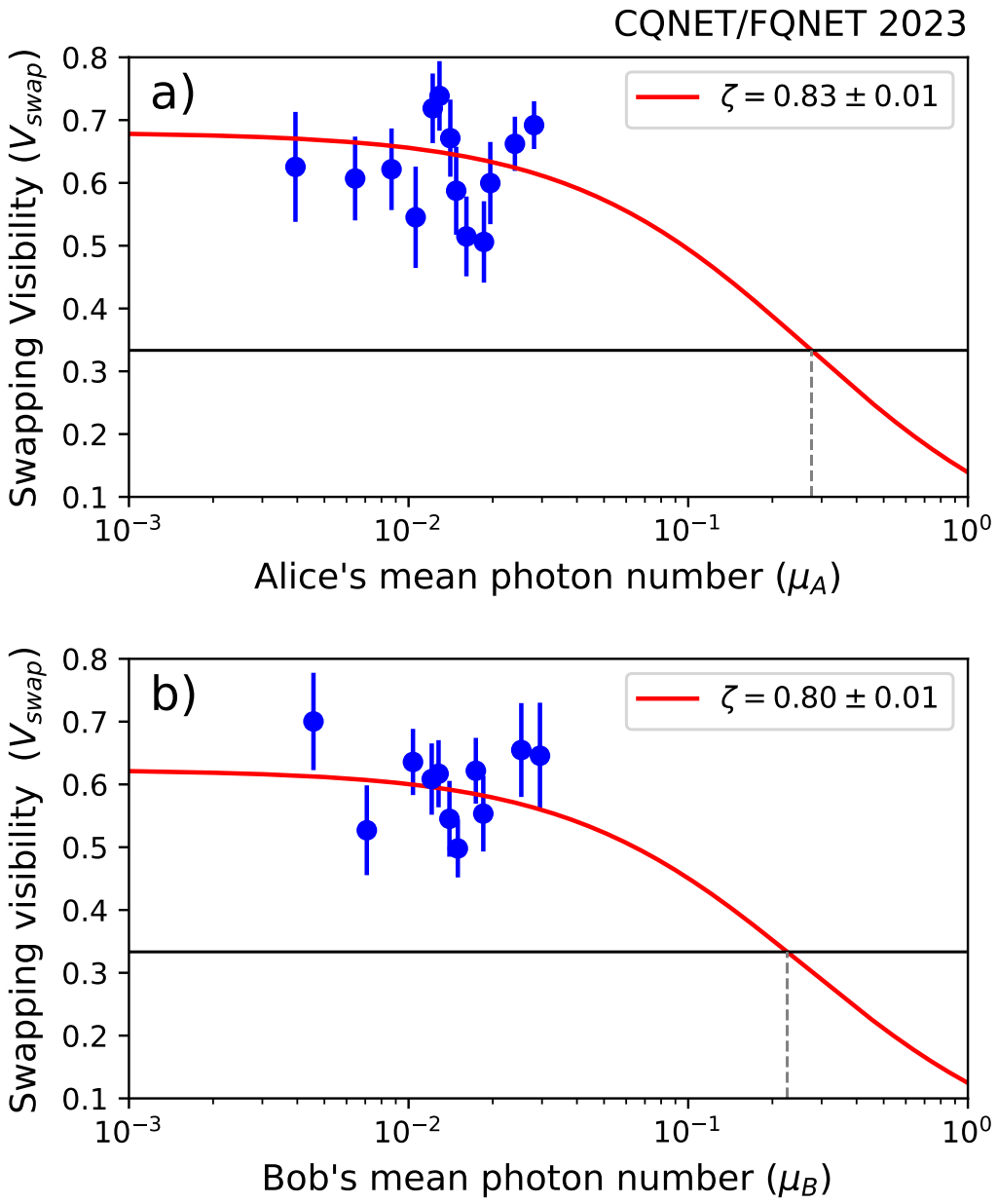

Figure 10.5: Entanglement swapping visibility as a function of a) Alice's mean photon number (μ_A) and b) Bob's mean photon number (μ_B). The data (blue) are fit to the theoretical model (red) for fixed mean photon numbers of a) $\mu_B = 4.6 \times 10^{-3}$ and b) $\mu_A = 3.9 \times 10^{-3}$, with the indistinguishability parameter ζ as a free parameter. The extracted parameters correspond to indistinguishabilities of a) $\zeta^2 = 0.69 \pm 0.02$ and b) $\zeta^2 = 0.64 \pm 0.02$. The black lines are the classical bound of $1/3$.

permits source-independent quantum key distribution with a key rate of 0.5 bits per sifted bit. Our system is interpreted using characteristic function-based analytical modeling that accounts for realistic imperfections such as loss, indistinguishability, and undesired photon-number components. The system is semi-autonomous and uses modular, fiber-coupled, off-the-shelf, and electrically interfaced components, such as modulators and SNSPD systems, that can be straightforwardly replicated for multi-node networks. Nonetheless, our current fidelities and swapping rates of 0.01 Hz are still limited.

Concerning fidelity, our modeling predicts that completely indistinguishable photons will yield a swapping fidelity of 97% (see Sec. 10.6). As suggested by the increased indistinguishability with heralding, reducing the multi-mode nature of the pairs by improved control of the photon pair spectra will also reduce ζ. Further improved indistinguishability could be achieved by broader pump bandwidths, e.g., using a mode-locked laser, narrower filtering (at the expense of rates), cavity-enhanced SPDC, or dispersion-engineered sources, in addition to improved setup stability, such as better temperature and polarization control. Even with complete indistinguishability, multi-photon events must be suppressed. Given the mean photon number is quite low at $\sim 10^{-3}$, options include replacing the SNSPDs at the BSM with photon-number-resolving (PNR) SNSPDs if allowed by the networking scheme, or using sources of near-deterministic entangled photon pairs based on single emitters, e.g., quantum dots, or multiplexed probabilistic sources, e.g., using SPDC. These approaches could lead to increased effective mean photon number and thereby improve swapping rates, but heralding of multi-photon events must be considered (see Chapters 3 and 9). Fourfold coincidence detection renders the effect of dark counts negligible.

The current coupling efficiency of $\sim 5\%$ per signal or idler channel indeed restricts swapping rates. The loss can be minimized to less than a few dB per signal or idler channel by improved device packaging, using lower-loss components, and splicing. For example, the spectral filters used in this work have a tunable passband which is accompanied by up to 10 dB loss and should be replaced with an alternative, such as a wavelength-division multiplexing (WDM) filter. Alternatively, we could integrate our system onto a chip, for instance using thin-film lithium niobate [43]. A factor of two in Bell-state measurement efficiency can be gained by projecting onto $|\Psi^+\rangle$ using faster-recovery SNSPDs [53]. The $\sim 5\%$ system coupling efficiency is equivalent to $\sim$ 70 km of single-mode fiber, which suggests our system is already

suited for deployment.

An increase in the clock rate will also benefit swapping. Without spatial multiplexing, this can be achieved by accessing the available time-frequency space. A ~100 GHz clock rate is realistic given the demonstration of SNSPDs with ps-level timing resolution and the high bandwidths of electro-optic modulators [42]. This would allow constructing the interferometer on chip, providing superior phase stability, and hence, fidelity. Another approach is to use mode-locked lasers for pumping of the SPDC. This is particularly attractive as the broadband pump will allow extending the multiplexing to the frequency domain, and the use of WDMs can access multiple distinct frequency channels, an approach that was demonstrated previously in Chapter 5. Frequency multiplexing techniques are compatible with the aforementioned sources that we suggest to increase fidelities and can be extended to repeaters with frequency shifting [13].

With some of the aforementioned improvements, we expect that our system can be deployed for metro-scale networking, demonstrations of quantum hardware interfacing, e.g., with erbium ions, or configured toward sensing protocols, e.g., long-baseline telescopes [22]. Our setup is straightforwardly extended to using independent lasers at different locations provided appropriate feedback mechanisms are employed [54]. Furthermore, our approach can be rendered more cost-effective (e.g., with field-programmable gate arrays replacing the AWG) to realize scaled quantum internet nodes.

10.6 Methods

Graphical User Interface (GUI)

We developed a Graphical User Interface (GUI) for the analysis of photon time-of-arrival statistics in quantum networks, see Fig. 10.6. The GUI contains four plots corresponding to the time-tags from each channel of the time tagger (TDC). Each plot depicts a histogram of the time-tags relative to the clock signal for a given acquisition time that is set by the user. The histograms update after each acquisition time for live visualization of photon time-of-arrival statistics. The GUI supports tunable coincidence windows for up to 10 qubits per clock cycle, enabling reconfigurable coincidence logic. Coincidences can be accumulated over selected coincidence windows for an acquisition time set by the user. All detection events are recorded to a MySQL database after each acquisition time, allowing for automated data collection, real-time monitoring, and big data storage accessible throughout the

network over long-term experimental operation.

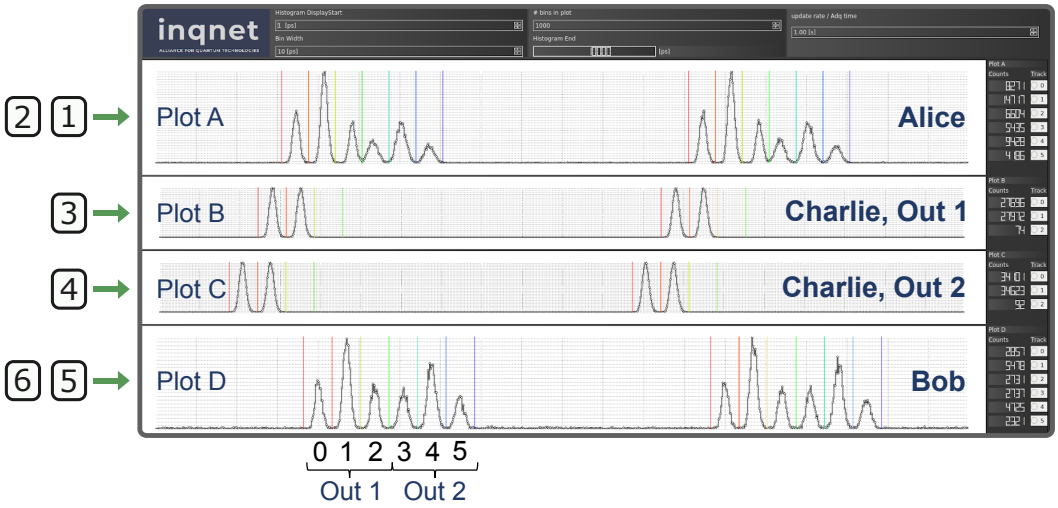

Figure 10.6: Graphical User Interface (GUI) used to perform real-time data acquisition and analysis. The top (bottom) plot corresponds to the electronically-combined outputs of the detectors at Alice (Bob) and the middle plots correspond to the outputs of each detector at Charlie. Each coincidence window is indicated by a pair of colored bars, which are user-defined and enable tunable temporal filtering.

	μ_A	μ_B	η_{Ai}	η_{As}	η_{Bs}	η_{Bi}
(a)	0.019	0.015	0.067	0.10	0.11	0.072
(b)	0.0047	0.0042	0.017	0.048	0.066	0.020
(c)	–	0.0046	0.026	0.072	0.076	0.022
(d)	0.0039	–	0.031	0.078	0.076	0.022

Table 10.2: Experimental parameters for the Hong-Ou-Mandel (HOM) and swapping configurations. $\mu_{A(B)}$ is the mean photon number of Alice's (Bob's) photon pair source, η_{Ai} is Alice's idler path efficiency, η_{As} is Alice's signal path efficiency, η_{Bs} is Bob's signal path efficiency, and η_{Bi} is Bob's idler path efficiency. (a) HOM interference measurements in Sec. 10.3, (b) entanglement swapping measurements in Sec. 10.3, and entanglement swapping measurements used to test the model in Sec. 10.4 with (c) μ_A varied while μ_B is fixed and (d) μ_B varied while μ_A fixed.

Experimental characterization

The mean photon numbers of Alice and Bob's photon pair sources and the path efficiencies of Alice and Bob's signal and idler paths for various experimental configurations are reported in Table 10.2. These parameters are substituted into the

analytical expressions for the HOM and swapping visibilities that are derived in the next section to generate the theoretical models in Sec. 10.4 and estimate the photon indistinguishabilities for the HOM and swapping experiments. The mean photon numbers are determined from the coincidence-to-accidental ratio, and the path efficiencies (see Fig. 10.1) are determined from the ratio of coincidence to single-photon detection rates [55]. The path efficiencies include the effects of component insertion loss, detection efficiency, and additional loss due to frequency entanglement and heralding (see Chapter 9). For the entanglement swapping measurements (b-d), the idler path efficiencies are obtained by summing the efficiencies calculated for each output of the interferometers.

Characteristic function approach

The models for the HOM and entanglement swapping experiments are summarized in Fig. 10.7a and b, respectively. We follow the approach proposed in Ref. [52], which has been applied to quantum teleportation in Chapters 8 and 9 and heralded single photon source experiments in Chapter 3. Using the notation of Chapter 3, the characteristic function for a Gaussian state of an N-mode bosonic system is

$$\chi(\xi) = \exp\left(-\frac{1}{4}\xi^T\gamma\xi - id^T\xi\right), \tag{10.6}$$

where $\xi \in R^{2N}$, d is the displacement vector, and γ is the covariance matrix. States that can be described by Eq. 10.6, including the vacuum, coherent, thermal, single- and two-mode squeezed states, are fully characterized by their displacement vector and covariance matrix. For a TMSV, the displacement vector is the null vector and the covariance matrix is given by

$$\gamma_{\text{TMSV}}(\mu) = \begin{bmatrix} \mathbf{A} & \mathbf{B} \\ \mathbf{B} & \mathbf{A} \end{bmatrix}, \tag{10.7}$$

$$\mathbf{A} = \begin{bmatrix} 1+2\mu & 0 \\ 0 & 1+2\mu \end{bmatrix},$$

$$\mathbf{B} = \begin{bmatrix} 2\sqrt{\mu(\mu+1)} & 0 \\ 0 & -2\sqrt{\mu(\mu+1)} \end{bmatrix},$$

in block matrix form, where μ is the mean photon number. For the HOM measurements, the input state is modeled as a tensor product of TMSV states from Alice and Bob's sources in the early (e) temporal modes,

$$|\Psi_{in}\rangle = |\text{TMSV}\rangle_{A,e}\,|\text{TMSV}\rangle_{B,e}\,,$$

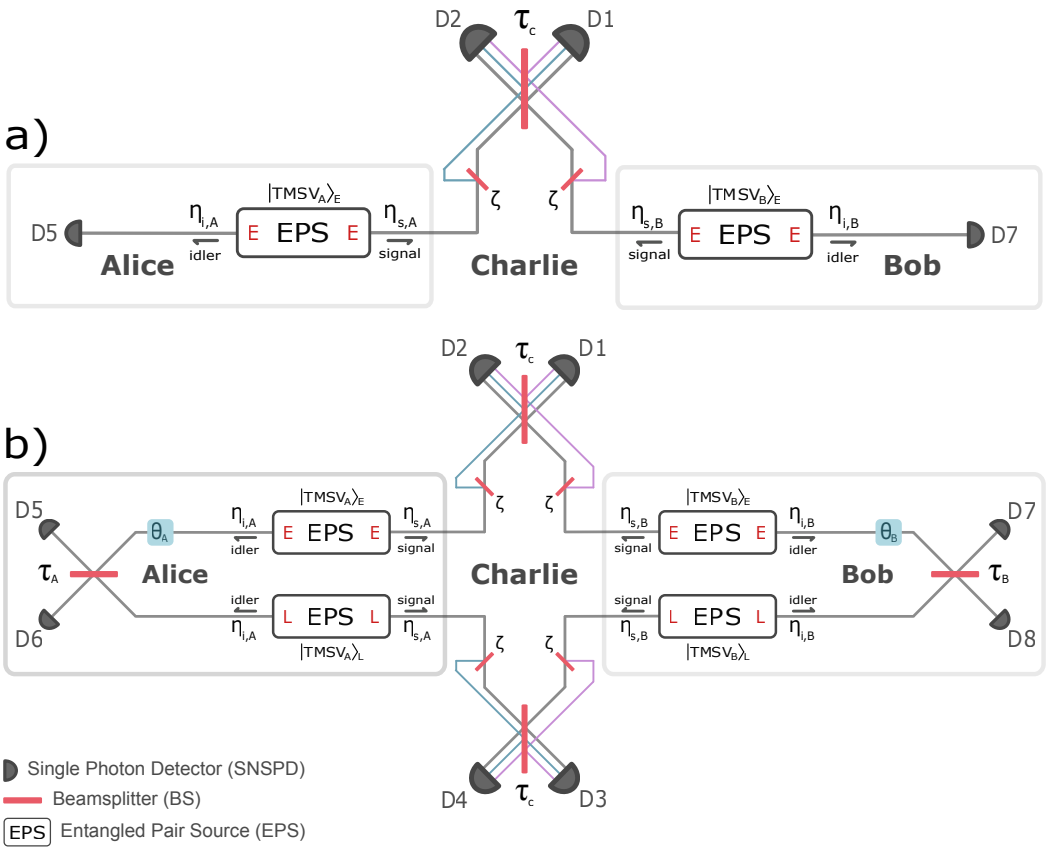

Figure 10.7: Theoretical model setups for a) Hong-Ou-Mandel interference and b) entanglement swapping. In the setups, E and L denote the early and late modes, respectively. η_{Ai} is Alice's idler path efficiency, η_{As} is Alice's signal path efficiency, η_{Bs} is Bob's signal path efficiency, and η_{Bi} is Bob's idler path efficiency. $\tau_{A(B)}$ is a transmittance accounting for imperfect interferometric visibility of Alice's (Bob's) MI, with $\tau_{A(B)} = 1/\sqrt{2}$ corresponding to ideal interferometric interference. $\theta_{A(B)}$ is the phase setting of Alice's (Bob's) MI. τ_C is the transmittance of the beamsplitter at Charlie and ζ is the photon indistinguishability parameter, where ζ^2 represents the fraction of modal overlap of the photons interfering at Charlie's beamsplitter.

which has the characteristic function,

$$\chi_{in}(\xi) = \exp\left(-\frac{1}{4}\xi^T \gamma_{in}(\mu_A, \mu_B)\xi\right), \tag{10.8}$$
$$\gamma_{in}(\mu_A, \mu_B) = \gamma_{\text{TMSV}}(\mu_{A,e}) \oplus \gamma_{\text{TMSV}}(\mu_{B,e}),$$

where $\gamma_{in}(\mu_A, \mu_B)$ is the input covariance matrix and $\mu_A = \mu_{A,e}$, $\mu_B = \mu_{B,e}$ are the mean photon numbers for Alice and Bob's pair sources, respectively. For the entanglement swapping experiment, the input is modeled as a tensor product of TMSV states from Alice and Bob's sources in the early (e) and late (l) temporal modes,

$$|\Psi_{in}\rangle = |\text{TMSV}\rangle_{A,e} |\text{TMSV}\rangle_{A,l} |\text{TMSV}\rangle_{B,e} |\text{TMSV}\rangle_{B,l},$$

which has the characteristic function of Eq. 10.8 with input covariance matrix

$$\begin{aligned}\gamma_{in}(\mu_A, \mu_B) =& \gamma_{\text{TMSV}}(\mu_{A,e}) \oplus \gamma_{\text{TMSV}}(\mu_{A,l}) \\ &\oplus \gamma_{\text{TMSV}}(\mu_{B,e}) \oplus \gamma_{\text{TMSV}}(\mu_{B,l}),\end{aligned} \tag{10.9}$$

where we take $\mu_A = \mu_{A,e} = \mu_{A,l}$ and $\mu_B = \mu_{B,e} = \mu_{B,l}$. We note that spectral impurities can be accounted for by modeling the input state with TMSV states in multiple Schmidt modes (see Chapter 3).

As mentioned in Sec. 10.4, the operations of the experiment up to detection can be modeled with linear optical transformations on the spatiotemporal input modes. Linear optics preserve the form of Gaussian characteristic functions, i.e., they map a Gaussian state onto another Gaussian state, by a symplectic transformation of the displacement vector and covariance matrix,

$$d' = S^T d \tag{10.10}$$
$$\gamma' = S^T \gamma S, \tag{10.11}$$

where S is a symplectic matrix. In the experiment, all transformations on the input state, such as Charlie's BS and the interferometers, can be constructed from beamsplitter and phase shifter transformations. The symplectic matrix S_{BS} for a

beamsplitter is,

$$S_{\mathrm{BS}}(t) = \begin{bmatrix} \mathbf{T} & \mathbf{R} \\ \mathbf{R} & \mathbf{T} \end{bmatrix}, \tag{10.12}$$

$$\mathbf{T} = \begin{bmatrix} t & 0 \\ 0 & t \end{bmatrix},$$

$$\mathbf{R} = \begin{bmatrix} 0 & -\sqrt{1-t^2} \\ \sqrt{1-t^2} & 0 \end{bmatrix},$$

and the symplectic matrix S_{P} for a phase shifter is the rotation matrix,

$$S_{\mathrm{P}}(\theta) = \begin{bmatrix} \cos\theta & -\sin\theta \\ \sin\theta & \cos\theta \end{bmatrix}. \tag{10.13}$$

Each interferometer is modeled as a phase shifter followed by a beamsplitter that interferes the early and late idler modes of an EPS. Optical loss is implemented by mixing an input mode with a virtual vacuum mode through a beamsplitter transformation with transmittance $\sqrt{\eta}$, where η is the transmission efficiency. Photon indistinguishability is also modeled with a beamsplitter transformation as detailed in Chapter 8, where the indistinguishability parameter ζ is the transmittance of a virtual beamsplitter that mediates the modal interference of input fields to Charlie's BS. The indistinguishability ζ^2 characterizes the amount of modal overlap of incoming photons, with $\zeta^2 = 1$ for photons that are indistinguishable and $\zeta^2 = 0$ for photons that are distinguishable in all degrees of freedom.

After constructing the overall symplectic matrix for the experiment S_{exp}, the coincidence probabilities are found in terms of the output covariance matrix $\gamma_{\mathrm{out}} = S_{\mathrm{exp}}^T \gamma_{\mathrm{in}} S_{\mathrm{exp}}$ for the output state $\hat{\rho}_{\mathrm{out}}$. Given the output state, the probability for a measurement outcome with a measurement operator $\hat{\Pi}$ is,

$$\mathrm{Tr}[\hat{\rho}_{\mathrm{out}}\hat{\Pi}] = \left(\frac{1}{2\pi}\right)^N \int dx^{2N} \chi_{\mathrm{out}}(x)\chi_{\Pi}(-x), \tag{10.14}$$

where $\chi_{\Pi}(x)$ is the characteristic function of the measurement operator. For a threshold detector, the measurement operators are,

$$\hat{\Pi}_{\text{no event}} = |0\rangle\langle 0|, \tag{10.15}$$

$$\hat{\Pi}_{\text{event}} = \hat{I} - \hat{\Pi}_{\text{no event}}, \tag{10.16}$$

where $\hat{I}$ is the identity matrix. Dark counts can be accounted for by taking $|0\rangle\langle 0| \rightarrow (1-\nu)|0\rangle\langle 0|$, where ν is the dark count probability of a detector. All coincidence

probabilities in the experiments can be calculated from Eqs. 10.14-10.16. For example, the fourfold coincidence probabilities for the fourfold HOM visibility (see Fig. 10.7a) are calculated as

$$P_{5217} = \mathrm{Tr}[\hat{\rho}_{\mathrm{out}}\hat{\Pi}^{(4)}_{\mathrm{HOM}}], \tag{10.17}$$

where the measurement operator $\hat{\Pi}^{(4)}_{\mathrm{HOM}}$ is,

$$\begin{aligned}\hat{\Pi}^{(4)}_{\mathrm{HOM}} &= (\hat{I}^{(2)} - |0\rangle\langle 0|_{\mathrm{D5}}) \otimes (\hat{I}^{(2)} - |0\rangle\langle 0|_{\mathrm{D2}}) \\ &\otimes (\hat{I}^{(2)} - |0\rangle\langle 0|_{\mathrm{D1}}) \otimes (\hat{I}^{(2)} - |0\rangle\langle 0|_{\mathrm{D7}}).\end{aligned} \tag{10.18}$$

Since the vacuum state has a Gaussian characteristic function, Eq. 10.14 reduces to linear combinations of Gaussian integrals that simplify using,

$$Tr[\hat{\rho}_{\mathrm{out}}\,|0\rangle\langle 0|^{\otimes N}] = \frac{2^N}{\sqrt{\det(\hat{I}^{(N)} + \gamma^{(N)}_{\mathrm{out}})}}, \tag{10.19}$$

where N is the number of modes being measured, $|0\rangle\langle 0|^{\otimes N} = |0\rangle\langle 0| \otimes \cdots \otimes |0\rangle\langle 0|$ denotes the tensor product of the vacuum operator over the N modes, $\hat{I}^{(N)}$ is the N by N identity matrix, and $\gamma^{(N)}_{\mathrm{out}}$ is the reduced output covariance matrix obtained by tracing all modes but those that are measured.

The coincidence probabilities used to compute the HOM and entanglement swapping visibilities are found from Eqs. 10.14 and 10.19 in terms of determinants of the covariance matrix of output state prior to detection. We obtain a 16 by 16 and 32 by 32 covariance matrix for the output states of the HOM and entanglement swapping models, respectively, yielding analytical expressions with a large number of terms. For simplification, we set the dark count rates, which had a negligible effect in the experiments, to zero and focus on the impact of multiphoton events and photon indistinguishability. We also set ideal transmittances of $1/\sqrt{2}$ for the beamsplitters at Charlie and inside the interferometers. The impact of imperfect beamsplitter transmittances on entanglement visibility is analyzed in Chapter 5 in this formalism.

Hong-Ou-Mandel interference model

For the HOM model, the twofold ($V^{(2)}_{\mathrm{HOM}}$), threefold ($V^{(3A)}_{\mathrm{HOM}}$, $V^{(3B)}_{\mathrm{HOM}}$), and fourfold ($V^{(4)}_{\mathrm{HOM}}$) HOM visibilities are calculated as,

$$V^{(2)}_{\mathrm{HOM}} = \frac{P_{21}(\zeta = 0) - P_{21}(\zeta = \zeta_{\max})}{P_{21}(\zeta = 0)}, \tag{10.20}$$

$$V^{(3A)}_{\mathrm{HOM}} = \frac{P_{521}(\zeta = 0) - P_{521}(\zeta = \zeta_{\max})}{P_{521}(\zeta = 0)}, \tag{10.21}$$

$$V^{(3B)}_{\mathrm{HOM}} = \frac{P_{217}(\zeta = 0) - P_{217}(\zeta = \zeta_{\max})}{P_{217}(\zeta = 0)}, \tag{10.22}$$

$$V^{(4)}_{\mathrm{HOM}} = \frac{P_{5217}(\zeta = 0) - P_{5217}(\zeta = \zeta_{\max})}{P_{5217}(\zeta = 0)}, \tag{10.23}$$

where $P_{21}(\zeta)$ is the twofold coincidence probability, $P_{521}(\zeta)$ and $P_{217}(\zeta)$ are the threefold coincidence probabilities, and $P_{5217}(\zeta)$ is the fourfold coincidence probability. In Eqs. 10.20-10.23, $\zeta = 0$ and $\zeta = \zeta_{\max}$ correspond to maximum photon distinguishability and indistinguishability, respectively. For identical mean photon numbers $\mu = \mu_A = \mu_B$ and identical path efficiencies η, the analytical expressions for the HOM visibilities are,

$$V^{(2)}_{HOM} = \frac{8\zeta^2_{\max}(1+\eta\mu)^2}{\left(6+6\eta\mu+\eta^2\mu^2\right)\left(4+4\eta\mu+\left(1-\zeta^2_{\max}\right)\eta^2\mu^2\right)}, \tag{10.24}$$

$$\begin{aligned} V^{(3A)}_{\mathrm{HOM}} = 1 - \Bigg[& \frac{1+\eta\mu+\eta^2\mu^2}{(1+\eta\mu)^2} + \frac{1}{(1+\eta\mu)\left(-1-2\eta\mu+\eta^2\mu\right)} \\ & + \frac{8}{-4-4\eta\mu+\left(-1+\zeta^2_{\max}\right)\eta^2\mu^2} \\ & + \frac{8}{2(1+\eta\mu)\left(2+\eta\mu+(-1+\eta)\eta\mu\left(-2+\left(-1+\zeta^2_{\max}\right)\eta\mu\right)\right)} \Bigg] \Bigg/ \\ & \Bigg[\frac{1+\eta\mu+\eta^2\mu^2}{(1+\eta\mu)^2} - \frac{8}{(2+\eta\mu)^2} + \frac{8}{(2+\eta\mu)\left(2+3\eta\mu-\eta^2\mu\right)} \\ & + \frac{1}{(1+\eta\mu)\left(-1-2\eta\mu+\eta^2\mu\right)} \Bigg], \end{aligned} \tag{10.25}$$

$$V^{(3B)}_{HOM} = V^{(3A)}_{HOM}, \tag{10.26}$$

$$V_{HOM}^{(4)} = 1 - \left[1 + \frac{2}{(1+\eta\mu)^2} - \frac{2}{1+\eta\mu} + \frac{-1+\eta(-3+2\eta)\mu}{(1+\eta\mu)(-1+(-2+\eta)\eta\mu)^2} + \frac{8}{-4+\eta\mu(-4+(1+\zeta_{\max}^2)\eta\mu)} + \frac{16}{4+\eta\mu(8-2\eta+(3+\zeta_{\max}^2(-1+\eta)-\eta)\eta\mu)} + \frac{8}{(2+\eta\mu(3-\zeta_{\max})+\eta^2\mu(\zeta_{\max}-1))(-2-\eta\mu(3+\zeta_{\max})+\eta^2\mu(\zeta_{\max}+1))}\right] \Bigg/ \left[\frac{1+\eta^2\mu^2}{(1+\eta\mu)^2} - \frac{8}{(2+\eta\mu)^2} - \frac{8}{(-2+(-3+\eta)\eta\mu)^2} - \frac{16}{(2+\eta\mu)(-2+(-3+\eta)\eta\mu)} + \frac{1}{(-1+(-2+\eta)\eta\mu)^2} + \frac{2}{(1+\eta\mu)(-1+(-2+\eta)\eta\mu)}\right]. \quad (10.27)$$

Entanglement swapping model

For the entanglement swapping model, the entanglement swapping visibility is calculated as,

$$V_{\text{SWAP}} = \frac{P_{1467}(\theta_A = 0, \theta_B = 0) - P_{1467}(\theta_A = \pi, \theta_B = 0)}{P_{1467}(\theta_A = 0, \theta_B = 0) + P_{1467}(\theta_A = \pi, \theta_B = 0)}, \quad (10.28)$$

where $P_{1467}(\theta_A, \theta_B)$ is the fourfold coincidence probability, corresponding to the coincidence rate of Alice and Bob conditioned on the BSM, and $\theta_{A(B)}$ is the phase setting for the interferometer at Alice (Bob). For identical mean photon numbers $\mu = \mu_A = \mu_B$, unit path efficiencies, and perfect indistinguishability $\zeta = 1$, the analytical expression for the entanglement swapping visibility is,

$$V_{\text{SWAP}} = \left[-\frac{4}{4+12\mu+13\mu^2+6\mu^3+\mu^4} + \frac{16}{16+48\mu+48\mu^2+16\mu^3}\right] \Bigg/ \left[2 + \frac{4}{(1+\mu)^2} - \frac{8}{1+\mu} - \frac{16}{2+5\mu+4\mu^2+\mu^3} + \frac{4}{4+12\mu+13\mu^2+6\mu^3+\mu^4} + \frac{32}{\sqrt{16+56\mu+73\mu^2+42\mu^3+9\mu^4}} + \frac{16}{16+48\mu+48\mu^2+16\mu^3}\right]. \quad (10.29)$$

HOM interference visibility

The HOM visibilities as a function of mean photon number ($\mu = \mu_A = \mu_B$) and photon indistinguishability (ζ^2) are shown in Fig. 10.8 and is shown in Fig. 10.9, respectively. From comparison of the experimental HOM visibilities of Fig. 10.3

with the models in Fig. 10.9, we find indistinguishabilities of $\zeta^2 = 0.22 \pm 0.01$ for the twofold HOM visibility, $\zeta^2 = 0.55 \pm 0.03$ for the threefold HOM visibility conditioned on Alice's idler photon, $\zeta^2 = 0.59 \pm 0.03$ for the threefold HOM visibility conditioned on Bob's idler photon, and $\zeta^2 = 0.92 \pm 0.02$ for the fourfold HOM visibility measurements. Notice that the indistinguishability increases with the number of coincidentally detected photons. As discussed in previous analyses of quantum teleportation (see Chapter 9), this is due to frequency entanglement of the photon pairs and spectral filtering. Filtering and detection of the idler photon reduces the number of spectral modes that are correlated with the signal, hence fourfold detection better approximates single mode behavior.

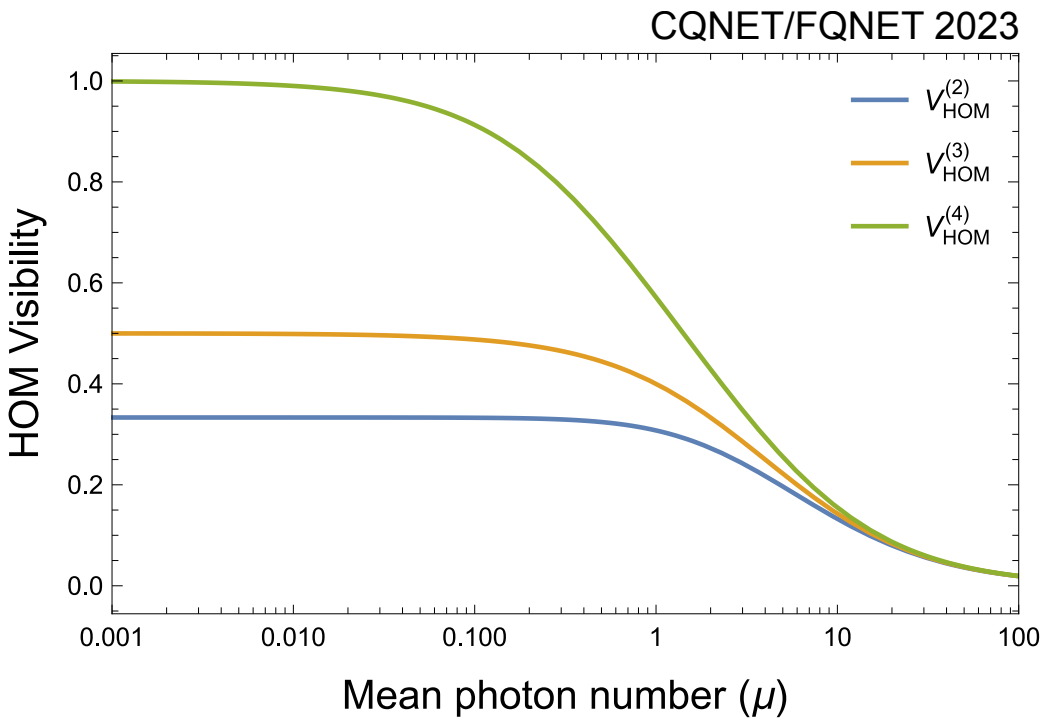

Figure 10.8: Hong-Ou-Mandel (HOM) visibilities as a function of mean photon number. The solid lines are the theoretical models for the fourfold HOM visibility (green), threefold HOM visibilities (yellow), and twofold HOM visibility (blue) with identical mean photon numbers ($\mu = \mu_A = \mu_B$), unit path efficiencies, and unity indistinguishability.

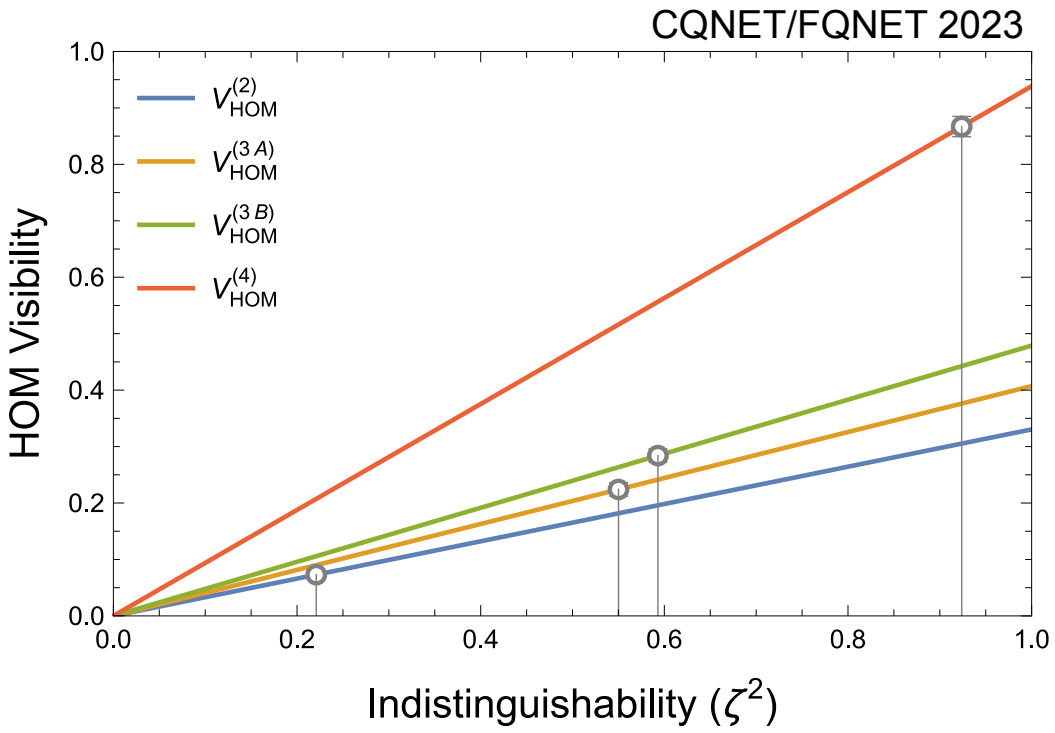

Figure 10.9: Hong-Ou-Mandel (HOM) visibilities as a function of indistinguishability. The solid lines are the models for the fourfold HOM visibility (red), threefold HOM visibility conditioned on Bob (green), threefold HOM visibility conditioned on Alice (green), and twofold HOM visibility (blue) for the experimentally characterized path efficiencies and mean photon numbers. The data are indicated with circular markers.

Taylor expansion

The HOM visibility expressions to lowest order of the multivariate Taylor expansion in μ_A, μ_B are,

$$V^{(2)}_{\mathrm{HOM}} \approx \frac{\eta_{s,B}\mu_B/\eta_{s,A}\mu_A}{1+\mu_B\eta_{s,B}/\mu_A\eta_{s,A}+(\mu_B\eta_{s,B}/\mu_A\eta_{s,A})^2}\zeta^2, \tag{10.30}$$

$$V^{(3A)}_{\mathrm{HOM}} \approx \frac{(\eta_{s,B}\mu_B/\eta_{i,A}\mu_A)}{(2-\eta_{s,A})+(\eta_{s,B}\mu_B/\eta_{i,A}\mu_A)}\zeta^2, \tag{10.31}$$

$$V^{(3B)}_{\mathrm{HOM}} \approx \frac{1}{1+(2-\eta_{s,B})(\eta_{i,B}\mu_B/\eta_{s,A}\mu_A)}\zeta^2, \tag{10.32}$$

$$V^{(4)}_{\mathrm{HOM}} \approx \zeta^2. \tag{10.33}$$

Consider the upper bounds of Eqs. 10.30-10.33 for ideal photon indistinguishability, $\zeta^2 = 1$. The maximum twofold HOM visibility is $1/3$ at $\eta_{s,B}\mu_B = \eta_{s,A}\mu_A$, as expected for the interference of two thermal states. The threefold visibility $V^{(3A)}_{\mathrm{HOM}}$

heralded on Alice approaches unity for $\eta_{s,B}\mu_B \gg \eta_{i,A}\mu_A$, and the threefold visibility $V_{\mathrm{HOM}}^{(3B)}$ heralded on Bob approaches unity for $\eta_{s,A}\mu_A \gg \eta_{i,B}\mu_B$. The maximum fourfold visibility is unity.

Optimization of HOM visibility

The complete HOM visibility expressions, without approximation, are plotted for identical $\mu = \mu_A = \mu_B$ in Fig. 10.8 and various μ_A and μ_B in Fig. 10.10 for unit photon indistinguishability and path efficiencies. The behaviors of the plots extend those produced in the previous analysis of quantum teleportation in Chapter 9.

For the case of two-fold HOM interference, the visibility is maximized for the case in which mean photon numbers of the two input thermal fields match. For low mean photon number, the maximum visibility is $1/3$, which corresponds to $\mu_A = \mu_B$, and is the global maximum. This is consistent with the linear and symmetric ridge-like topography in Fig. 10.10a. The maximum value is not unity due to $n = 2$ photon states and vacuum input into the beamsplitter for $\mu_A, \mu_B \ll 1$. For mean photon numbers approaching one and beyond, the maximum visibility is reduced and the range of mean photon numbers to maximize the visibility increases due to interference from of higher photon number terms.

Due to heralding, the three-fold HOM visibility plots in Fig. 10.10b and c have a plateau-like topography which extend the range of mean photon numbers that allow reaching maximum interference visibility. The theoretical maximum visibility is unity also due to heralding. In the case of conditional detection of photons in Alice idler mode (Fig. 10.10b), the threshold at $\mu_B \sim 1$ is due to $n = 2$ events from μ_B interfering with heralded single photons and reducing the maximum visibility. Provided $\mu_B, \mu_A \ll 1$, the visibility is maximized independent of the probability of generating a photon in Bob's signal mode because a single photon is always in Alice's signal mode and three-fold detection is performed. In the case μ_A is increased and starts to approach μ_B, the relative probability of heralding a multi-photon term in Alice's signal mode increases, which decreases the visibility, and leads to the threshold topography along the diagonal. The visibility is not maximized for $\mu_A = \mu_B$, in this case reaching up to 1/2 (see Fig. 10.8), because heralding increases the effective mean photon number of Alice's signal mode. In this case, a lower value of μ_A is required to reach maximum visibility compared to two-fold HOM interference, effectively shifting the ridge to the left in Fig. 10.10b compared to that in Fig. 10.10a. Note that the gradient is smaller at $\mu_B \sim 1$ due to the presence

of a single photon in Alice's signal mode. This renders the contributions of higher order terms to be less detrimental to the visibility than along the diagonal where effective mean photon numbers are balanced, and higher order terms contribute in both Alice and Bob's signal mode. The same arguments apply to explain the topography in Fig. 10.10c in which Bob's idler is detected. Overall, the difference in number distributions explains the symmetry breaking around the diagonal.

In the case of four-fold detection, the range of mean photon numbers that yield maximum visibility is extended further since both Alice and Bob herald single photons at the beamsplitter. Since both Alice and Bob detect their idlers, the plot in Fig. 10.10d is symmetric about the diagonal and has a topography akin to combining both three-fold plots together. The small-gradient thresholds remain because the effective number distributions that are heralded are the same as the three-fold case. In the case of high mean photon numbers, matching of the effective mean photon number is required to maximize until higher number terms dominate at beyond $\mu_A = \mu_B = 1$.

Entanglement swapping visibility

The entanglement swapping visibilities as a function of mean photon number and indistinguishability are shown in Fig. 10.11 a) and b), respectively. For the entanglement swapping measurement in Fig. 10.4, the average swapping visibility of $\langle V_{\text{swap}} \rangle = 83.1 \pm 5.5\%$ corresponds to a photon indistinguishability of $\zeta^2 = 0.86 \pm 0.06$. In Fig. 10.11c, we plot the lower bound of Eq. 10.5 per sifted key rate as a function of indistinguishability for $\kappa = 1.22$, $e_t = 0.011$, and $e_p = (1 - V_{\text{swap}})/2$, where V_{swap} is the swapping visibility model for the QKD error rate measurement reported in Table 10.1. The experimental secret key rate $R/R_s = 0.50^{+0.18}_{-0.14}$ bits per sifted bit corresponds to an indistinguishability of $\zeta^2 = 0.87^{+0.09}_{-0.10}$. For completely indistinguishable photons and the same experimental parameters as the measurement in Fig. 10.4 (see Table. 10.2b), the model predicts an swapping visibility of 96.5%, corresponding to a swapping fidelity of 97.4% and secret key rate of 0.87 bits per sifted bit.

References

[1] H Jeff Kimble. "The quantum internet." In: Nature 453.7198 (2008), pp. 1023–1030.

[2] Christoph Simon. "Towards a global quantum network." In: Nature Photonics 11.11 (2017), pp. 678–680.

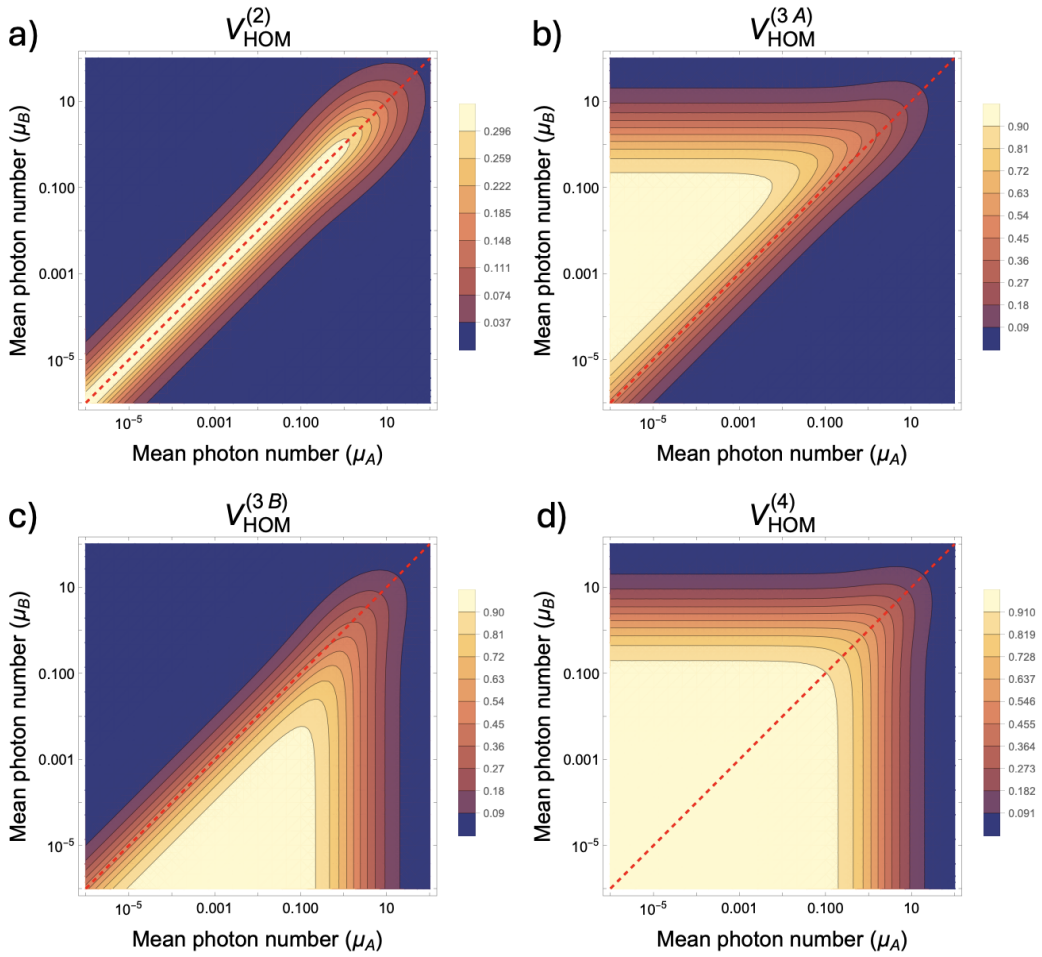

Figure 10.10: HOM interference visibilities plotted as a function of Alice and Bob's mean photon numbers for ideal path efficiencies ($\eta_i, \eta_s = 1$) and photon indistinguishability ($\zeta = 1$). The red dashed lines correspond to $\mu_A = \mu_B$, and we include in all plots to facilitate comparison to the two-fold HOM visibility plot. a) Twofold HOM interference visibility of Alice and Bob's signal modes, corresponding to the interference of two thermal states. b) Threefold HOM interference visibility of Alice and Bob's signal modes conditioned on Alice's idler mode, corresponding to the interference of a heralded single photon state and thermal state. c) Threefold HOM interference visibility of Alice and Bob's signal modes conditioned on Bob's idler mode, corresponding to the interference of a thermal state and heralded single photon state. d) Fourfold HOM interference visibility of Alice and Bob's signal modes conditioned on Alice and Bob's idler modes, corresponding to the interference of two heralded single photon states.

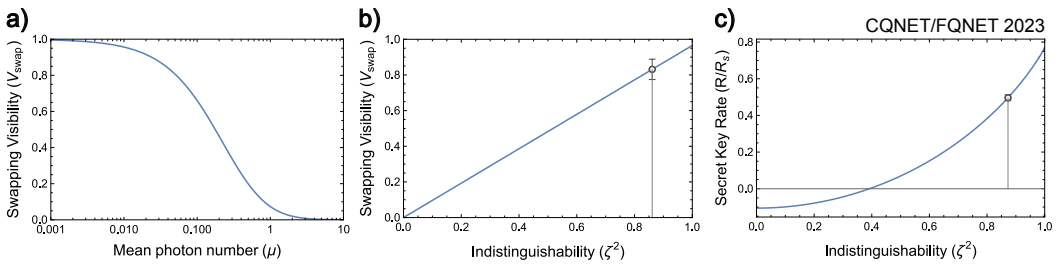

Figure 10.11: Theoretical models for teleportation of entanglement. a) Entanglement swapping visibility as a function of mean photon number for identical source mean photon numbers ($\mu = \mu_A = \mu_B$), unit path efficiencies, and unity indistinguishability. b) Entanglement swapping visibility as a function of indistinguishability for the experimentally characterized mean photon numbers and path efficiencies of the entanglement swapping measurements in Fig. 10.4. The experimental swapping visibility is indicated with the circular marker. c) Secret key rate as a function of indistinguishability for the experimentally characterized mean photon numbers and path efficiencies of the QKD measurements in Table 10.1. The experimental secret key rate is indicated with the circular marker.

[3] Stephanie Wehner, David Elkouss, and Ronald Hanson. "Quantum internet: A vision for the road ahead." In: Science 362.6412 (2018), eaam9288.

[4] Nicolas Sangouard, Christoph Simon, Hugues De Riedmatten, and Nicolas Gisin. "Quantum repeaters based on atomic ensembles and linear optics." In: Reviews of Modern Physics 83.1 (2011), pp. 33–80.

[5] Josephine Dias and Timothy C. Ralph. "Quantum repeaters using continuous-variable teleportation." In: Physical Review A 95.2 (2017), p. 022312.

[6] Marco Lucamarini, Zhiliang L. Yuan, James F. Dynes, and Andrew J. Shields. "Overcoming the rate–distance limit of quantum key distribution without quantum repeaters." In: Nature 557.7705 (2018), pp. 400–403.

[7] M. K. Bhaskar, R. Riedinger, B. Machielse, et al. "Experimental demonstration of memory-enhanced quantum communication." In: Nature 580.7801 (Apr. 2020), pp. 60–64. ISSN: 1476-4687. DOI: 10.1038/s41586-020-2103-5. URL: https://doi.org/10.1038/s41586-020-2103-5.

[8] Raju Valivarthi, Marcelli Grimau Puigibert, Qiang Zhou, Gabriel H. Aguilar, Varun B. Verma, Francesco Marsili, Matthew D. Shaw, Sae Woo Nam, Daniel Oblak, and Wolfgang Tittel. "Quantum teleportation across a metropolitan fibre network." In: Nature Photonics 10.10 (Oct. 2016), pp. 676–680. ISSN: 1749-4893. DOI: 10.1038/nphoton.2016.180. URL: https://doi.org/10.1038/nphoton.2016.180.

[9] Qi-Chao Sun, Ya-Li Mao, Si-Jing Chen, et al. "Quantum teleportation with independent sources and prior entanglement distribution over a network." In:

Nature Photonics 10.10 (Oct. 2016), pp. 671–675. ISSN: 1749-4893. DOI: 10.1038/nphoton.2016.179. URL: https://doi.org/10.1038/nphoton.2016.179.

[10] Hiroki Takesue and Benjamin Miquel. "Entanglement swapping using telecomband photons generated in fibers." In: Opt. Express 17.13 (June 2009), pp. 10748–10756.

[11] Jordan M. Thomas, Fei I. Yeh, Jim Hao Chen, Joe J. Mambretti, Scott J. Kohlert, Gregory S. Kanter, and Prem Kumar. "Quantum teleportation coexisting with classical communications in optical fiber." In: Optica 11.12 (Dec. 2024), pp. 1700–1707. DOI: 10.1364/OPTICA.540362. URL: https://opg.optica.org/optica/abstract.cfm?URI=optica-11-12-1700.

[12] A. L. Migdall, D. Branning, and S. Castelletto. "Tailoring single-photon and multiphoton probabilities of a single-photon on-demand source." In: Physical Review A 66 (5 Nov. 2002), p. 053805. DOI: 10.1103/PhysRevA.66.053805. URL: https://link.aps.org/doi/10.1103/PhysRevA.66.053805.

[13] Neil Sinclair, Erhan Saglamyurek, Hassan Mallahzadeh, et al. "Spectral Multiplexing for Scalable Quantum Photonics using an Atomic Frequency Comb Quantum Memory and Feed-Forward Control." In: Physical Review Letters 113 (5 July 2014), p. 053603. DOI: 10.1103/PhysRevLett.113.053603. URL: https://link.aps.org/doi/10.1103/PhysRevLett.113.053603.

[14] Saikat Guha, Hari Krovi, Christopher A. Fuchs, Zachary Dutton, Joshua A. Slater, Christoph Simon, and Wolfgang Tittel. "Rate-loss analysis of an efficient quantum repeater architecture." In: Physical Review A 92 (2 Aug. 2015), p. 022357. DOI: 10.1103/PhysRevA.92.022357. URL: https://link.aps.org/doi/10.1103/PhysRevA.92.022357.

[15] Koji Azuma, Sophia E. Economou, David Elkouss, Paul Hilaire, Liang Jiang, Hoi-Kwong Lo, and Ilan Tzitrin. "Quantum repeaters: From quantum networks to the quantum internet." In: Reviews of Modern Physics 95 (4 Dec. 2023), p. 045006. DOI: 10.1103/RevModPhys.95.045006. URL: https://link.aps.org/doi/10.1103/RevModPhys.95.045006.

[16] Jian-Wei Pan, Dirk Bouwmeester, Harald Weinfurter, and Anton Zeilinger. "Experimental Entanglement Swapping: Entangling Photons That Never Interacted." In: Physical Review Letters 80 (18 May 1998), pp. 3891–3894. DOI: 10.1103/PhysRevLett.80.3891. URL: https://link.aps.org/doi/10.1103/PhysRevLett.80.3891.

[17] Matthäus Halder, Alexios Beveratos, Nicolas Gisin, Valerio Scarani, Christoph Simon, and Hugo Zbinden. "Entangling independent photons by time measurement." In: Nature physics 3.10 (2007), pp. 692–695.

[18] Qi-Chao Sun, Yang-Fan Jiang, Ya-Li Mao, et al. "Entanglement swapping over 100 km optical fiber with independent entangled photon-pair sources." In: Optica 4.10 (Oct. 2017), pp. 1214–1218. DOI: 10.1364/OPTICA.4.001214. URL: https://opg.optica.org/optica/abstract.cfm?URI=optica-4-10-1214.

[19] Farid Samara, Nicolas Maring, Anthony Martin, Arslan S Raja, Tobias J Kippenberg, Hugo Zbinden, and Rob Thew. "Entanglement swapping between independent and asynchronous integrated photon-pair sources." In: Quantum Science and Technology 6.4 (Sept. 2021), p. 045024. DOI: 10.1088/2058-9565/abf599. URL: https://dx.doi.org/10.1088/2058-9565/abf599.

[20] Shengshuai Liu, Yanbo Lou, Yingxuan Chen, and Jietai Jing. "All-Optical Entanglement Swapping." In: Physical Review Letters 128 (6 Feb. 2022), p. 060503. DOI: 10.1103/PhysRevLett.128.060503. URL: https://link.aps.org/doi/10.1103/PhysRevLett.128.060503.

[21] Qin Li, Wai Hong Chan, Chunhui Wu, and Zhonghua Wen. "Triple-server blind quantum computation using entanglement swapping." In: Physical Review A 89 (4 Apr. 2014), p. 040302. DOI: 10.1103/PhysRevA.89.040302. URL: https://link.aps.org/doi/10.1103/PhysRevA.89.040302.

[22] Daniel Gottesman, Thomas Jennewein, and Sarah Croke. "Longer-Baseline Telescopes Using Quantum Repeaters." In: Physical Review Letters 109 (7 Aug. 2012), p. 070503. DOI: 10.1103/PhysRevLett.109.070503. URL: https://link.aps.org/doi/10.1103/PhysRevLett.109.070503.

[23] C. Branciard, N. Gisin, and S. Pironio. "Characterizing the Nonlocal Correlations Created via Entanglement Swapping." In: Physical Review Letters 104 (17 Apr. 2010), p. 170401. DOI: 10.1103/PhysRevLett.104.170401. URL: https://link.aps.org/doi/10.1103/PhysRevLett.104.170401.

[24] Rainer Kaltenbaek, Robert Prevedel, Markus Aspelmeyer, and Anton Zeilinger. "High-fidelity entanglement swapping with fully independent sources." In: Physical Review A 79 (4 Apr. 2009), p. 040302. DOI: 10.1103/PhysRevA.79.040302. URL: https://link.aps.org/doi/10.1103/PhysRevA.79.040302.

[25] F. Basso Basset, M. B. Rota, C. Schimpf, et al. "Entanglement Swapping with Photons Generated on Demand by a Quantum Dot." In: Physical Review Letters 123 (16 Oct. 2019), p. 160501. DOI: 10.1103/PhysRevLett.123.160501. URL: https://link.aps.org/doi/10.1103/PhysRevLett.123.160501.

[26] Nicolas J. Cerf, Mohamed Bourennane, Anders Karlsson, and Nicolas Gisin. "Security of Quantum Key Distribution Using *d*-Level Systems." In: Physical Review Letters 88 (12 Mar. 2002), p. 127902. DOI: 10.1103/PhysRevLett.88.127902. URL: https://link.aps.org/doi/10.1103/PhysRevLett.88.127902.

[27] Manuel Erhard, Robert Fickler, Mario Krenn, and Anton Zeilinger. "Twisted photons: new quantum perspectives in high dimensions." In: Light: Science & Applications 7.3 (2018), p. 17146. ISSN: 2047-7538. DOI: 10.1038/lsa.2017.146. URL: https://www.nature.com/articles/lsa2017146 (visited on 11/18/2018).

[28] Earl T. Campbell, Hussain Anwar, and Dan E. Browne. "Magic-State Distillation in All Prime Dimensions Using Quantum Reed-Muller Codes." In: Physical Review X 2 (4 Dec. 2012), p. 041021. DOI: 10.1103/PhysRevX.2.041021. URL: https://link.aps.org/doi/10.1103/PhysRevX.2.041021.

[29] H. de Riedmatten, I. Marcikic, J. A. W. van Houwelingen, W. Tittel, H. Zbinden, and N. Gisin. "Long-distance entanglement swapping with photons from separated sources." In: Physical Review A 71 (5 May 2005), p. 050302. DOI: 10.1103/PhysRevA.71.050302. URL: https://link.aps.org/doi/10.1103/PhysRevA.71.050302.

[30] Michael A. Nielsen and Isaac L. Chuang. Quantum Computation and Quantum Information. 10th ed. USA: Cambridge University Press, 2011. ISBN: 1107002176.

[31] Marek Żukowski, Anton Zeilinger, Michael A Horne, and Artur K Ekert. ""Event-ready-detectors"Bell experiment via entanglement swapping." In: Physical Review Letters 71.26 (1993), p. 4287.

[32] Asher Peres. "Delayed choice for entanglement swapping." In: Journal of Modern Optics 47.2-3 (2000), pp. 139–143. DOI: 10.1080/09500340008244032.

[33] Xiao-song Ma, Stefan Zotter, Johannes Kofler, Rupert Ursin, Thomas Jennewein, Časlav Brukner, and Anton Zeilinger. "Experimental delayed-choice entanglement swapping." In: Nature Physics 8.6 (2012), pp. 479–484.

[34] John F. Clauser, Michael A. Horne, Abner Shimony, and Richard A. Holt. "Proposed Experiment to Test Local Hidden-Variable Theories." In: Physical Review Letters 23 (15 Oct. 1969), pp. 880–884. DOI: 10.1103/PhysRevLett.23.880. URL: https://link.aps.org/doi/10.1103/PhysRevLett.23.880.

[35] Artur K Ekert. "Quantum cryptography based on Bell's theorem." In: Physical Review Letters 67.6 (1991), p. 661.

[36] Xiongfeng Ma, Chi-Hang Fred Fung, and Hoi-Kwong Lo. "Quantum key distribution with entangled photon sources." In: Physical Review A 76.1 (2007), p. 012307.

[37] Thaddeus D Ladd, Fedor Jelezko, Raymond Laflamme, Yasunobu Nakamura, Christopher Monroe, and Jeremy Lloyd O'Brien. "Quantum computers." In: Nature 464.7285 (2010), pp. 45–53.

[38] Nicolas Gisin and Rob Thew. "Quantum communication." In: Nature Photonics 1.3 (2007), p. 165.

[39] S. Pirandola, J. Eisert, C. Weedbrook, A. Furusawa, and S. L. Braunstein. "Advances in quantum teleportation." In: Nature Photonics 9.10 (Oct. 2015), pp. 641–652. ISSN: 1749-4893. DOI: 10.1038/nphoton.2015.154. URL: https://doi.org/10.1038/nphoton.2015.154.

[40] H-J Briegel, Wolfgang Dür, Juan I. Cirac, and Peter Zoller. "Quantum repeaters: the role of imperfect local operations in quantum communication." In: Physical Review Letters 81.26 (1998), p. 5932.

[41] Terry Rudolph. "Why I am optimistic about the silicon-photonic route to quantum computing." In: APL photonics 2.3 (2017).

[42] Prashanta Kharel, Christian Reimer, Kevin Luke, Lingyan He, and Mian Zhang. "Breaking voltage–bandwidth limits in integrated lithium niobate modulators using micro-structured electrodes." In: Optica 8.3 (2021), pp. 357–363.

[43] Di Zhu, Linbo Shao, Mengjie Yu, Rebecca Cheng, Boris Desiatov, C. J. Xin, Yaowen Hu, Jeffrey Holzgrafe, Soumya Ghosh, Amirhassan Shams-Ansari, et al. "Integrated photonics on thin-film lithium niobate." In: Advances in Optics and Photonics 13.2 (2021), pp. 242–352.

[44] Boris Korzh, Qing-Yuan Zhao, Jason P. Allmaras, Simone Frasca, Travis M. Autry, et al. "Demonstration of sub-3 ps temporal resolution with a superconducting nanowire single-photon detector." In: Nature Photonics 14.4 (Apr. 2020), pp. 250–255. ISSN: 1749-4893. DOI: 10.1038/s41566-020-0589-x. URL: https://www.nature.com/articles/s41566-020-0589-x (visited on 04/12/2023).

[45] Tian Zhong and Philippe Goldner. "Emerging rare-earth doped material platforms for quantum nanophotonics." In: Nanophotonics 8.11 (2019), pp. 2003–2015.

[46] Samuel L. Braunstein and Ady Mann. "Measurement of the Bell operator and quantum teleportation." In: Physical Review A 51.3 (1995), R1727.

[47] Asher Peres. "Separability criterion for density matrices." In: Physical Review Letters 77.8 (1996), p. 1413.

[48] Masato Koashi and John Preskill. "Secure quantum key distribution with an uncharacterized source." In: Physical Review Letters 90.5 (2003), p. 057902.

[49] Artur Scherer, Barry C. Sanders, and Wolfgang Tittel. "Long-distance practical quantum key distribution by entanglement swapping." In: Optics Express 19.4 (2011), pp. 3004–3018.

[50] Aeysha Khalique and Barry C. Sanders. "Practical long-distance quantum key distribution through concatenated entanglement swapping with parametric down-conversion sources." In: Journal of the Optical Society of America (JOSA) B 32.11 (2015), pp. 2382–2390.

[51] Christian Weedbrook, Stefano Pirandola, Raúl García-Patrón, Nicolas J Cerf, Timothy C Ralph, Jeffrey H Shapiro, and Seth Lloyd. "Gaussian quantum information." In: Reviews of Modern Physics 84.2 (2012), pp. 621–669.

[52] Masahiro Takeoka, Rui-Bo Jin, and Masahide Sasaki. "Full analysis of multi-photon pair effects in spontaneous parametric down conversion based photonic quantum information processing." In: New Journal of Physics 17.4 (Apr. 2015), p. 043030. DOI: 10.1088/1367-2630/17/4/043030. URL: http://dx.doi.org/10.1088/1367-2630/17/4/043030.

[53] R. Valivarthi, I. Lucio-Martinez, A. Rubenok, et al. In: Optics Express 22.20 (2014), pp. 24497–24506.

[54] Qi-Chao Sun, Ya-Li Mao, Yang-Fan Jiang, et al. "Entanglement swapping with independent sources over an optical-fiber network." In: Phys. Rev. A 95 (3 Mar. 2017), p. 032306. DOI: 10.1103/PhysRevA.95.032306. URL: https://link.aps.org/doi/10.1103/PhysRevA.95.032306.

[55] D. N. Klyshko. "Use of two-photon light for absolute calibration of photoelectric detectors." In: Soviet Journal of Quantum Electronics 10.9 (1980), p. 1112.

Chapter 11

PICOSECOND SYNCHRONIZATION SYSTEMS FOR QUANTUM NETWORKS

This chapter includes the work published as:

[1] Raju Valivarthi, Lautaro Narváez, Samantha I. Davis, Nikolai Lauk, Cristián Peña, Si Xie, Jason P. Allmaras, Andrew D. Beyer, Boris Korzh, Andrew Mueller, et al. "Picosecond synchronization system for quantum networks." In: Journal of Lightwave Technology 40.23 (2022), pp. 7668–7675.

[1] Keshav Kapoor, Si Xie, Joaquin Chung, Raju Valivarthi, Cristián Peña, Lautaro Narváez, Neil Sinclair, Jason P. Allmaras, Andrew D. Beyer, Samantha I. Davis, et al. "Picosecond synchronization system for the distribution of photon pairs through a fiber link between Fermilab and Argonne National Laboratories." In: IEEE Journal of Quantum Electronics 59.4 (2023), pp. 1–7.

11.1 Introduction

Long-distance quantum networks require distribution of qubits encoded into individual photons. For deployed networks, photons must be transmitted using low-loss, high-bandwidth, and practical channels, such as fiber optics cables. Ideally, photons must also be generated and detected at high rates, for instance using modulated lasers and high-timing resolution (low-timing jitter) nanowire detectors, respectively. The realization of such networks is at odds with environment-induced variations in the length of fiber optics cables. Since photons are identified by recording their times of generation and detection, each with respect to a local (node-based) clock, such variations can lead to misidentification of photons. To avoid this, the variations can be accounted for by adjusting the phases of each local clock based on a centrally located primary clock. This is accomplished by distributing strong optical pulses to the nodes, as conceptualized by the diagram in Fig. 11.1. These pulses can be distributed either separately in parallel fibers or jointly through the same fiber that is carrying the single-photon level quantum signal. This type of clock distribution method, which has been exploited in previous quantum networking demonstrations [1, 2, 3, 4, 5, 6], allows synchronization between all local clocks, and hence identification of photons throughout the network. Importantly, this method enables operation of the network at a high clock-rate and the possibility to perform linear-optic

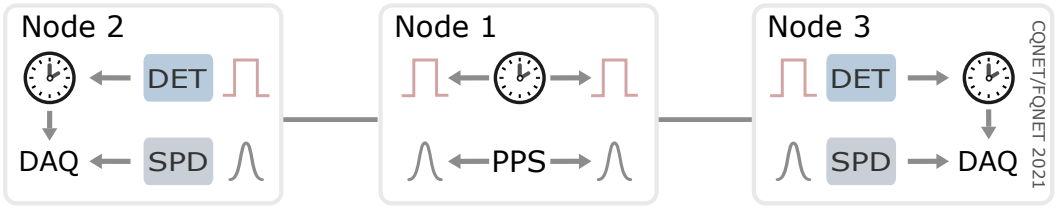

Figure 11.1: Concept of a clock distribution system for a three-node quantum network. A clock is used to generate pulses (top hats) at a central node (node 1) that are distributed to end nodes (nodes 2 and 3) by fiber channels (grey lines) where they are detected (DET) and used to lock the phase of clocks at the end nodes. Simultaneously, light (Gaussians) from a photon pair source (PPS) at the central node is directed into the same fiber towards single photon detectors (SPDs) at the end nodes. Data acqusition (DAQ) systems record the arrival times of the photons with respect to the phase of the clocks at the end nodes, thereby ensuring the clocks are synchronized with the photons.

Bell-state measurements based on two-photon interference, which requires precise synchronization of photons. Using a single fiber for both the clock synchronization and quantum signals makes better use of the limited optical fiber infrastructure that can be employed for quantum communication.

The challenge with this setting is ensuring that the strong optical pulses used for synchronization do not introduce noise that reduces the fidelity of the transmitted qubits. The leading source of noise in optical fiber channels is due to off-resonant Raman scattering of the clock pulses, which produces significantly more red-shifted than blue-shifted light [7]. Typical methods to mitigate this involve strong temporal and spectral filtering [8] or using photons that are significantly blue shifted from the clock pulses [1]. Accordingly, there is little work to investigate the role of the Raman noise when photons are red-shifted from the clock pulses and both are in the same fiber, in particular if the photons and the clock pulses are at wavelengths within the standard fiber telecommunication windows, and if such noise prohibits reaching ps-scale timing resolution of the clock distribution system.

In Section 11.2, we develop a picosecond-level clock synchronization system at Caltech and demonstrate entanglement distribution over optical fiber alongside a coexisting classical channel for optical clock distribution. We characterize the effect of noise sources, such as Raman scattering and dark counts, on the fidelity of transmitted entangled qubits over the network. In Section 11.3, we deploy the system

in a real-world fiber network with remote nodes at Fermi National Accelerator Laboratory (FNAL) and Argonne National Laboratory (ANL). We demonstrate, for the first time, picosecond-scale clock synchronization between national laboratories over metropolitan distances, achieving 2 ps synchronization of remote nodes at FNAL and ANL. This work is a crucial step for implementing advanced entanglement-based protocols, such as MDI-QKD and quantum repeaters, across metropolitan regions for the proposed quantum internet connecting DOE laboratories [9].

11.2 Picosecond synchronization system

First, we demonstrate a three-node, all-fiber, quantum network at the CQNET site (see Sec. 7.2 in Chapter 7) that is supported by a low-noise, scalable, and automated clock distribution system. This is realized by distributing photon pairs in the telecommunication C-band (1.5 μm) simultaneously with strong optical "clock" pulses in the telecommunication O-band (1.3 μm) in the same fiber. Specifically, light is distributed from a central node over two 11 km-length fibers to two end nodes. The pulses used for clock distribution are created by bias switching a laser diode whereas the pulses generating the photon pairs through spontaneous parametric down-conversion (SPDC) are carved from a continuous-wave laser by a Mach-Zehnder modulator. Our setup uses in-house, high-bandwidth, and scalable electronics to generate 3.7 V (peak-to-peak) pulses having near-Gaussian distributions with durations as low as 47 ps and sub-ps timing jitter. We quantify the effect of Raman scattering by measuring the coincidence-to-accidental ratio (CAR) of the distributed photon pairs using a free-running data acquisition and control system. We find that the clock distribution system reduces the CAR from 77 ± 14 to 42 ± 2, which is still sufficient for high-fidelity qubit distribution. Furthermore, we observe only 2 ps of timing jitter (over 1 minute of integration) between clocks at the central and end nodes, suggesting our method can be used for high-rate networks.

Experimental setup

Our three-node quantum network and corresponding synchronization system is schematized in Fig. 11.2 and, other than the custom electronics and single-photon detectors, consists of fiber-based and off-the-shelf components. The central node consists of a photon pair source (PPS) operating at the telecommunication C-band wavelength of 1536 nm and two transmitters (Tx1, Tx2) generating clock pulses at the telecommunication O-band wavelength of 1310 nm. By way of wavelength division multiplexer/demultiplexers (MUX/DEMUXs), the clock pulses and single

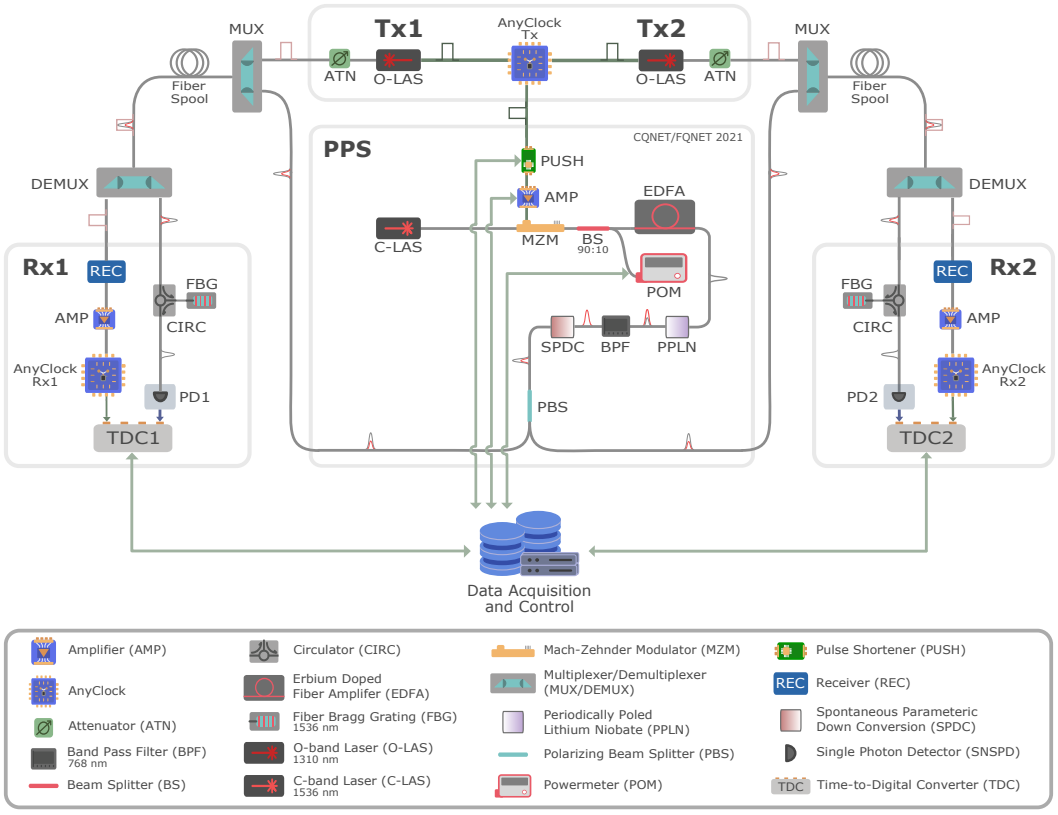

Figure 11.2: Schematic of fiber-based three-node quantum network and synchronization system at Caltech. See main text for description. Clock pulses are indicated by top hats whereas grey and red Gaussian-shaped pulses indicate light of 1536 nm and 768 nm wavelength, respectively. The loss contributions from each fiber spool is 2.26 dB and 2.8 dB, respectively, whereas each WDM and FBG adds 2 dB and 6 dB of loss, respectively.

photons are directed into fibers and distributed to end nodes via 11 km-length spools of single-mode fiber. At the end nodes, the clock pulses and photon pairs are separated using DEMUXs and subsequently detected (Rx1, Rx2). As described in detail below, we ensure the photon pair generation and detection events are synchronized by (i) generating a photon pair synchronously with a clock pulse and (ii) recording the time between the detection of the clock pulse and the individual photon at each end node.

Clock distribution is seeded by a 200 MHz voltage oscillator (AnyClockTx) at the central node. It generates 2.5 ns-duration pulses that are used to bias switch two O-band laser diodes (O-LASs), generating optical clock pulses of similar du-

ration which are subsequently attenuated to an average power of 0.25 mW. This setup is indicated by Tx1 and Tx2 in Fig. 11.2. Synchronous with the optical clock pulse generation, AnyClockTx creates a third pulse which is shortened to a duration as low as 47 ps (PUSH) and power-amplified by up to 28 dB (AMP) using customized electronics, then directed to a 20 GHz-bandwidth fiber-coupled Mach-Zehnder modulator (MZM) within the PPS setup. The pulse amplitudes approximately correspond to the π-voltage of the MZM. The PPS setup contains a C-band laser (C-LAS) emitting continuous-wave light of 1536 nm wavelength that is modulated using the MZM to create 74 ps-duration optical pulses with an extinction ratio of 28 dB at a (clock-synchronized) repetition rate of 200 MHz. After passing a 90:10 beam splitter used for monitoring (POM) the stability of the MZM, these pulses are amplified by an erbium-doped fiber amplifier (EDFA), producing pulses with average power of 100 mW, and then directed to a fiber-packaged periodically poled lithium niobate (PPLN) waveguide which up-converts the light to 768 nm wavelength. Next, residual 1536 nm light is removed using a band-pass filter (BPS) and the pulses are directed to a second PPLN waveguide configured to produce 1536 nm-wavelength photon pairs by Type-II SPDC. A fiber-based polarizing beam splitter (PBS) separates each photon from the pair into different fibers, where they are each directed to the MUXs, and combined with the optical clock pulses in the fiber spools.

At the end nodes, after passing the DEMUXs, the individual photons are filtered by fiber Bragg gratings (FBGs), by way of circulators (CIRC), to a bandwidth of 2.5 GHz and detected using cryogenically cooled superconducting nanowire single photon detectors (SNSPDs) with 50 ps timing jitter (PD1 and PD2). The electrical pulses generated by the SNSPDs are directed to time-to-digital converters (TDC1, TDC2). The optical clock pulses are received by 200 MHz-bandwidth amplified photodiodes (REC) which generate electrical pulses that are amplified (AMP) by 15 dB using scalable custom electronics. These pulses adjust the phase of 200 MHz voltage oscillators (AnyClockRx1, AnyClockRx2) at the end nodes which produce pulses that are detected by the TDCs. The TDCs then record the time difference between the electrical pulses generated by the SNSPDs and the oscillators to verify the synchronization. This time difference is logged using a scalable data acquisition and monitoring system (indicated in Fig. 11.2) that enables uninterrupted quantum networking for an extended time duration (>days).

Scalable and high-bandwidth custom electronics

Pulsed quantum networking experiments typically use either mode-locked lasers [3] or laser diodes and modulators, such as MZMs, driven by electrical pulses generated from arbitrary waveform generators [10] and off-the-shelf multi-purpose amplifiers [11] (see Chapters 8 and 10). These approaches are expensive, bulky, and not scalable to multi-node quantum networks. We address this shortcoming by in-house developing custom pulse (duration) shorteners and amplifiers, referred to as Picoshort and Picoamp modules, respectively, that shape electrical pulses from the AnyClockTx oscillator. The resulting pulses are used to drive the MZM to its π-voltage, producing high-extinction pulses (>20 dB) for the PPS. Short-duration (<100 ps) pulses allow the possibility of measuring high signal-to-noise ratios, the ability to create time-bin qubits in a single clock event (by splitting the pulse into two), and the realization of photon pairs with high spectral purity. We also use a Picoamp to increase the output voltage of the REC photodiodes for compatibility with the AnyClockRx oscillators.

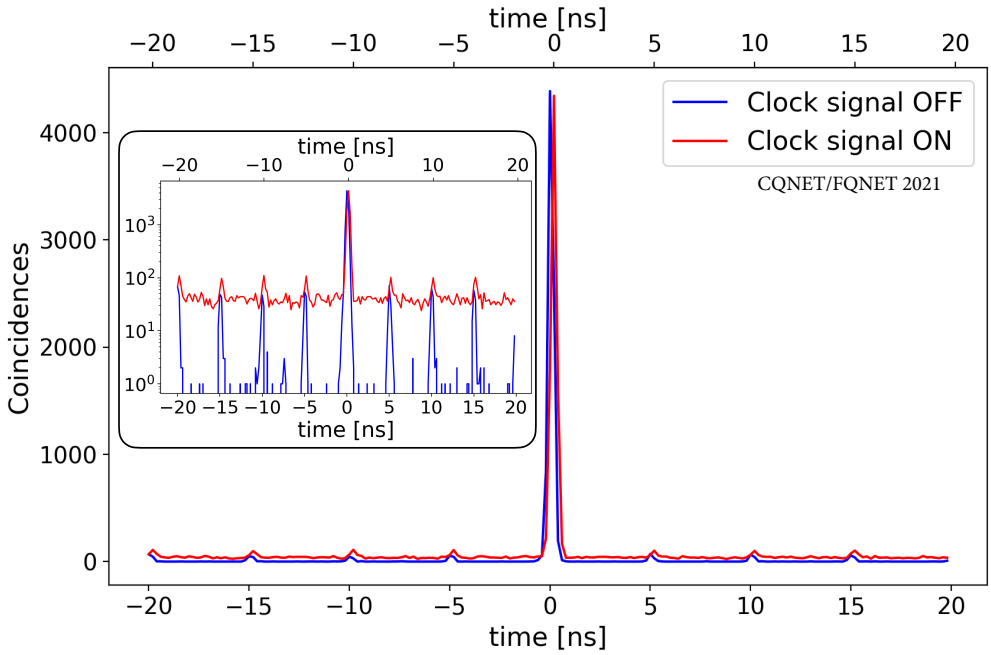

Figure 11.3: Coincidence histogram with the clock distribution enabled and disabled. The small time delay between the two histograms is due a small difference in trigger voltage threshold. Inset: Coincidence histogram with a log vertical scale reveals the Raman noise from the clock pulses.

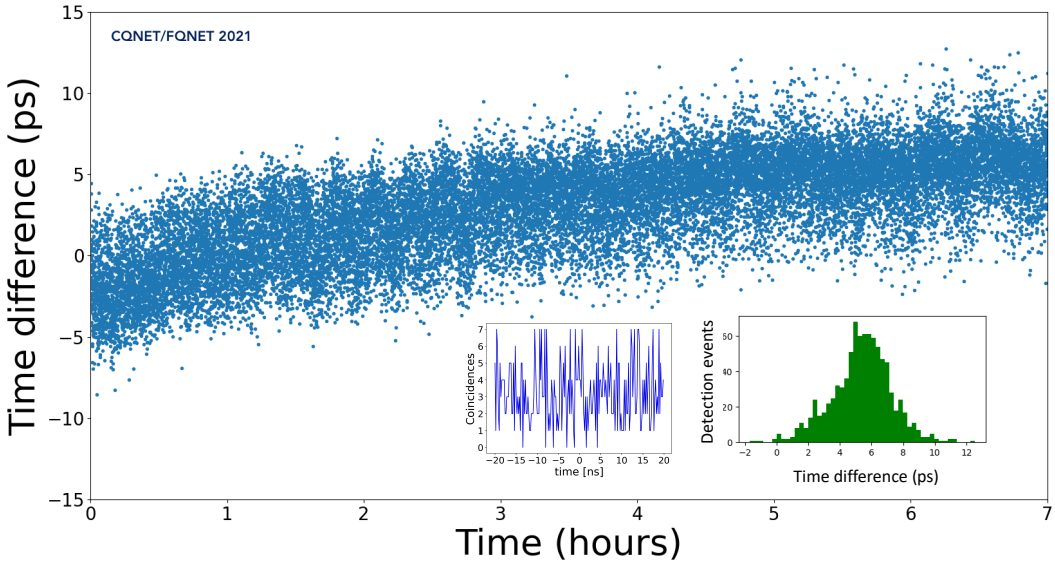

Figure 11.4: Variation of the time difference between the arrival of clock pulses at Rx1 and Rx2 over 7 h. The maximum time difference is 5 ps due to fiber length variations. Inset (left): histogram of photon pair correlations without the clock system enabled. Inset (right): histogram of the time difference over a 900 s time scale indicates a timing jitter of 2 ps.

Results

We characterize our quantum network setup by distributing photon pairs both with and without the clock distribution enabled, and measure the effect of the Raman noise from the clock pulses. The role of noise is captured by the CAR of the photon pairs, $CAR = C/A$, where, in the absence of noise, C corresponds to the coincidence detection rate of photons originating from the same event, whereas A corresponds to the coincidence detection rate of photons originating from different events. Note that in this context, the CAR is equivalent to the cross-correlation function $g^{(2)}$ [12]. Dark counts and Raman scattering can reduce CAR as a noise detection event may be recorded instead of a photon. Our method is well-suited for quantum networks as channel loss ensures accidental coincidences. Our PPS produces a pair with a probability of 1% ($\sim 1/CAR$ as measured at the output of the PPS) per pulse [13]. Channel loss, calculated by taking the ratio of the coincidence rates to the single photon detection rates [13], from PPLN waveguide to the SNSPDs are 24 dB and 26 dB, which are equivalent to ~120 km and ~130 km lengths of single-mode fiber, respectively. We measure the arrival time difference of SNSPD detection events at Rx1 and Rx2 over 5 minutes, both with and without the clock pulses, compiling all

events into histograms, see Fig. 11.3. We sum the detection events over a 200 ps interval around the peak at zero time delay to calculate coincidences (C), whereas the average number of detection events in a 200 ps interval around each of the accidental peaks is used to determine the accidentals (A). The measurements yield a CAR of 77 ± 12 without, and a CAR of 42 ± 2 with, the clock distribution enabled, respectively, which are both well above the classical limit of $CAR = 2$. To place our results into context for qubit distribution, if these photon pairs were to be time-bin entangled, e.g. using the approach demonstrated in Chapters 8 and 10, and if no other imperfections play a role, the measured reduction of CAR from the Raman noise suggests a reduction of fidelity $CAR/(CAR + 1)$ [14] from 99% to 98% or the same reduction in the entanglement visibility $(CAR - 1)/(CAR + 1)$ [15]. This visibility is well-above the $1/3$ required for non-separability of a Werner state [16] and the non-locality bound of $1/\sqrt{2}$ [17]. Thus, the noise introduced by our clock distribution system plays a minimal role in our quantum network.

Importantly, we also determine the timing jitter of our clock distribution method, which sets an upper-bound on the rate of the quantum network. To compare the arrival time of the clock pulses at Rx1 and Rx2 (after the AnyClockRx1 and AnyClockRx2 oscillators), we use an oscilloscope to measure a timing jitter of 2 ps over a timescale of 60 s, and a time difference that slowly drifts by 5 ps over 7 h owing to fiber length variations, see Fig. 11.4. Note that we use an oscilloscope because the current configuration of the TDC adds up to 7 ps timing jitter, but with a standard upgrade this can be as low as 3 ps [18]. Since the clock pulses are attenuated to ensure a minimal reduction in CAR, our measurement is limited by the noise floor of detectors only. Nevertheless, the timing jitter of our clock distribution currently sets an upper-bound on our distribution rate of $\sim$ 300 MHz, which is sufficient for quantum networks spanning a few hundred kilometers, that is, metro-scale or inter-city networks. Note that we have also measured the coincidence histogram of the photon pairs without the synchronization system enabled, finding only classically correlated noise (see inset of Fig. 11.4), further showing the necessity of our synchronization system.

11.3 Deployment in a real-world network

Next, we present a demonstration of picosecond-scale synchronization of C-band photon pairs over deployed fiber optic cables connecting three remote nodes by distributing the clock pulses in either the telecommunication standard O- or L-bands. A map of the three-node quantum network is shown in Fig. 11.5 along with

the approximate paths of the optical fiber links between the nodes. Two of the nodes are located in the Fermi National Accelerator Laboratory (FNAL) FQNET/IEQNET site (see Sec. 7.2 in Chapter 7). These include the central node at the Feynman Computing Center (FNAL-FCC) and one of the end nodes at the D0 Assembly Building (FNAL-DAB), and are stationed 2 km apart. The third node is located at the Argonne National Laboratory (ANL) IEQNET site, and is 57 km away from FNAL-FCC. Each of these nodes are connected with pairs of fibers. The central node at FNAL-FCC contains a photon pair source as well as a commercial all-optical telecom switch from Polatis and the end nodes at FNAL-DAB and ANL contain the superconducting nanowire single photon detectors (SNSPDs). The quantum-correlated photon pairs are split, and each photon in the pair is sent into one of these 2 km-2 km and 57 km-57 km fiber pairs linking the nodes, corresponding to total transmission distances of the quantum states of 4 km and 114 km, with 2 km and 57 km of shared quantum-classical coexistence with a clock signal.

Finally, we measure the noise introduced to the quantum information due to quantum-classical coexistence signals distributed between nodes in our network and find that in the FNAL-FCC to ANL link, the O- and L-band clocks reduce the coincidence-to-accidental ratios (CAR) from 51 ± 2 to 5.3 ± 0.4 and 2.6 ± 0.3, respectively. These measurements demonstrate that our research prototype network is suitable for point-to-point schemes and for two-photon interference-based teleportation protocols, representing a notable milestone towards establishing a national research quantum internet between the U.S. Department of Energy laboratories as envisioned in DOE's blueprint for the quantum internet [9].

Experimental setup

Our photon pair source is situated at FNAL-FCC. Using a commercial arbitrary waveform generator (AWG), short radio-frequency (RF) pulses with widths of 80 ps and separated by 5 ns are generated, amplified, and used as the input to a fiber-coupled Mach-Zehnder Modulator (MZM) [10, 19]. Light at 1536 nm wavelength produced by a continuous wave fiber-coupled laser is directed into the MZM to produce pulsed light. The pulsed light is directed into an erbium-doped fiber amplifier (EDFA) and then sent through a periodically poled lithium niobate (PPLN) waveguide to upconvert the 1536 nm light to 768 nm. A band-pass filter is used to remove any residual 1536 nm light. A second PPLN waveguide takes the 768 nm light as input to produce time-correlated photon pairs at the original wavelength of 1536 nm through Type-II spontaneous parametric down conversion process (SPDC). A fiber-

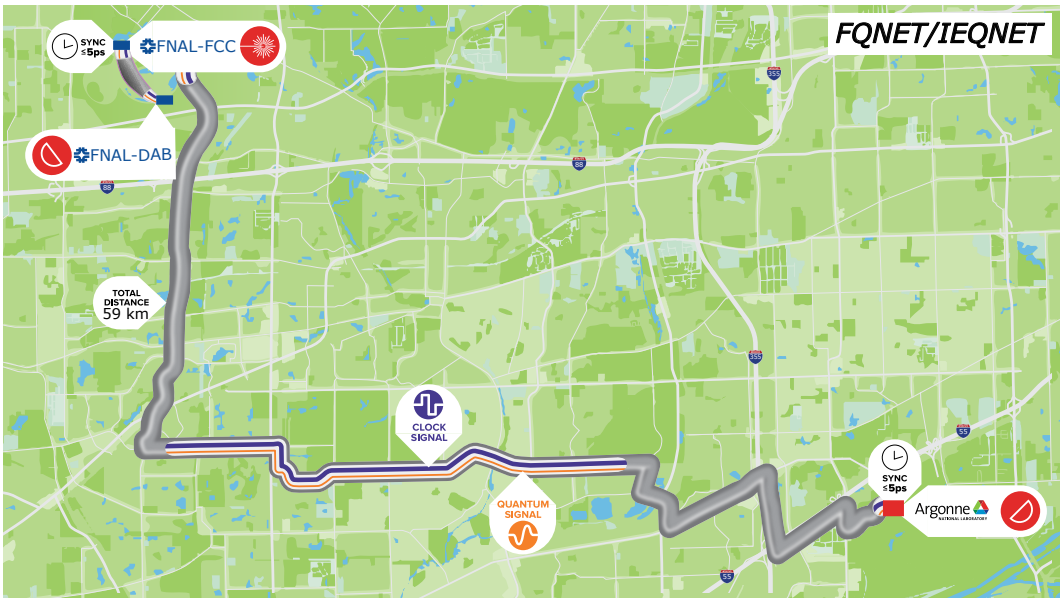

Figure 11.5: This image depicts the separation of the nodes in our real-world network. FNAL-FCC and FNAL-DAB are connected with 2 km of dark fiber and FNAL-FCC and ANL are connected with 57 km of dark fiber. We keep our master clock at FNAL-FCC, and distribute the signal to FNAL-DAB and ANL, choosing the path via an optical switch located at FNAL-FCC. The FNAL nodes are depicted by the blue rectangles and the ANL node is depicted by the red rectangle.

based polarizing beam splitter separates the photon pair into individual photons, one of which is directed to a dense wavelength division multiplexer (DWDM) and multiplexed with the clock signals described in the next subsection. The multiplexed quantum and classical channels are sent to the optical switch located at FNAL-FCC, which routes their path to FNAL-DAB or ANL. The other photon of the pair is sent directly, using a dedicated fiber, to the optical switch and routed to the same node.

At the FNAL-DAB and ANL nodes, the combined quantum and clock channels are sent through a DWDM de-multiplexer (DEMUX) to separate them. The quantum channel is filtered by two or three additional DEMUX's and then a 4 GHz bandwidth fiber Bragg grating (FBG) filter to isolate the 1536 nm quantum frequency channel to within a wavelength of 0.03 nm. These filters reduce the effects of dispersion and improves the indistinguishability of the photons. The FNAL-DAB and ANL nodes are equipped with two superconducting nanowire single photon detectors (SNSPD) to detect the incoming photons with timing jitter (resolution) of less than 50 ps. The SNSPD signals are digitized by commercial time-taggers with timing jitter below 10 ps. A schematic of our network is shown in Fig 11.6.

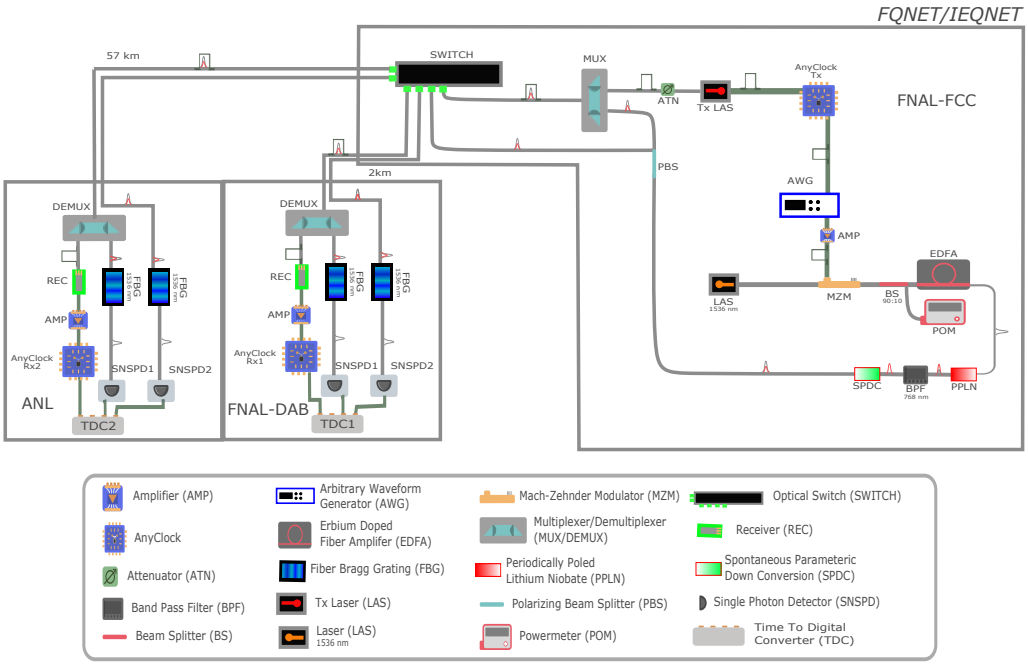

Figure 11.6: Schematic for the FQNET picosecond clock synchronization system. The square pulses represent the clock signal while the grey and red Gaussian-shaped pulses represent the quantum light and its second harmonic (768 nm), respectively. The photon pairs are produced at FNAL-FCC and routed either 2 km away to FNAL-DAB or 57 km away to ANL through software provided with the optical switch [20].

To synchronize the clocks at the FNAL-DAB and ANL nodes with the clock of the central FNAL-FCC node, we implement the system developed in Section 11.2. The transmitter (Tx) module consists of an O- (1310 nm) or L-band (1610 nm) laser diode that is bias switched via 2.5 ns-duration pulses generated by a 200 MHz voltage oscillator. This Tx is used to distribute clock signals from the central FNAL-FCC node to the FNAL-DAB and ANL nodes on the same fiber that is used to transmit the single photons. At the FNAL-DAB and ANL nodes, the receiver (Rx) consists of a 200 MHz-bandwidth photodetector that generates electrical pulses amplified by a custom-designed 15 dB amplifier.These pulses adjust the phase of 200 MHz voltage oscillator clocks at the FNAL-DAB and ANL nodes which are used as time references. The time taggers record the time difference between the electrical signal pulses generated by the SNSPDs and the reference clock signal. The time differences are logged using a scalable data acquisition and monitoring system, enabling uninterrupted quantum network operations.

Results

We characterize the three-node quantum network by measuring the Raman scattering coefficient (see Ref. [21]), timing jitter of the clock distribution system, and coincidence-to-accidental ratio (CAR) of photon pairs distributed from FNAL-FCC to FNAL-DAB and FNAL-FCC to ANL.

We evaluate the drift and timing jitter of the clock synchronization system by monitoring the time difference between the synchronized local clock and a reference signal pulse produced by the same 1536 nm laser that is used for the entangled pair source. The reference signal pulse is modulated by the MZM that is driven by an AWG synchronized with the master clock at the FNAL-FCC central node, and subsequently amplified by the EDFA. This reference signal is transmitted along a fiber parallel to the fiber used to distribute the master clock to the FNAL-DAB and ANL end nodes. At the end nodes, the reference signal is detected by a fast 20 GHz photodetector and digitized by the time tagger. The time difference between the synchronized local clock and the reference signal is collected over each second then plotted in a histogram and long term time drift is monitored through the mean difference, this drift as well as the representative time difference over a period of more than 14 hours can be seen in Figure 11.7.

We observe a drift in the mean of about 3 ps over more than 14 hours and a total jitter of 2.2 ps. This is much less than the 250 ps duration of our photons, which renders our system applicable for quantum networks including those that rely on two-photon interference (e.g., Chapters 8 and 10).

We measure the noise introduced by the clock pulses by measuring the reduction of CAR of our time-correlated photon pairs when they are measured locally at the central FNAL-FCC node compared to when they are distributed over fiber with the clock pulses. From the central FNAL-FCC node, we send to the FNAL-DAB and ANL end nodes the O- and L-band clocks multiplexed along the same fiber that is used to send one of the photons from the correlated pair carrying the quantum signal as described in the previous sections. On a separate fiber parallel to the fiber carrying the multiplexed channel, we send the second photon of the correlated pair. We send clock signals at 0.3 mW power for both the O- and L-bands to the FNAL-DAB end node, while for the ANL end node we send the O-band clock signal at 1.8 mW power and the L-band at 0.3 mW power.

In the absence of Raman scattered photons and dark counts, the CAR is equivalent to the cross-correlation $g^{(2)}(0)$ function, which quantifies the ratio of the detection

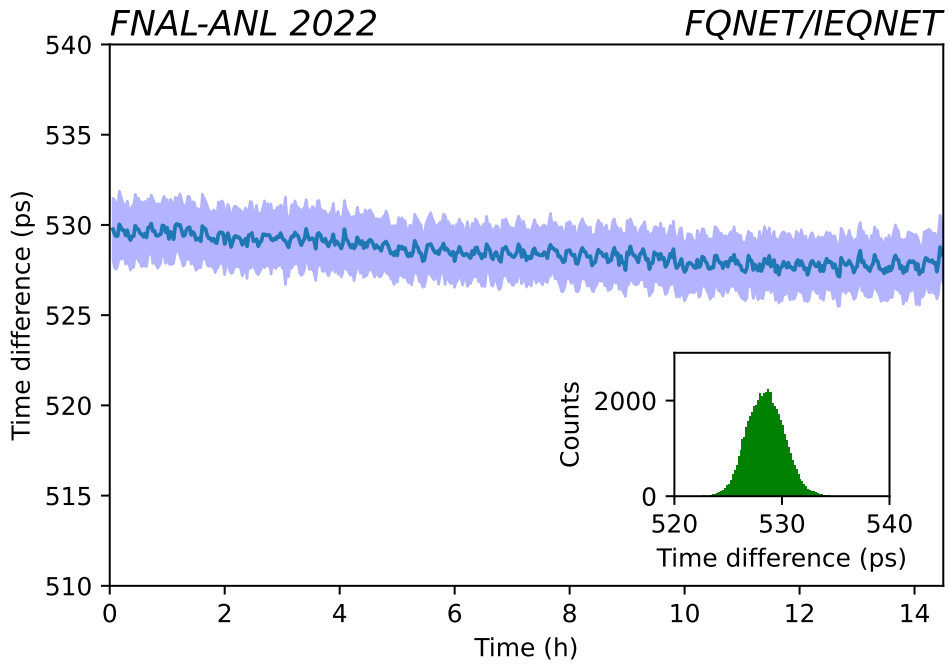

Figure 11.7: Variation of the time difference between the arrival of the reference and derived clock at ANL over 14 hours. The blue line is the average of the time difference every 100 seconds, showing the drift in the time difference of the two clocks. We observe a long term drift of about 3 ps over more than 14 hours, mainly caused by fiber length fluctuations in the link. The blue shaded region is the RMS of the time difference during each of those 100 second intervals. Inset: histogram of the time difference indicates a timing jitter of 2.2 ps.

of correlated photon pairs to non-correlated photon pairs resulting from more than one photon pair being produced at the pair source [12]. We count all photon pair detection events within a 450 ps interval around the main coincidence peak to obtain C, and take the average of the photon pair detection events within a 450 ps interval around each of the accidental peaks to determine A. The measurement is made over a period of 5 minutes for the FNAL-DAB end node. Due to higher losses from the longer distance resulting in lower coincidence rates, it takes 12 hours to make the analogous measurement for the ANL end node.

In Figure 11.8, we show the time difference distribution for the two detected photons in a background-free scenario with the photon pairs sent from the central FNAL-FCC node to the ANL end node and no synchronization clock signal being sent along the same fiber. The main coincidence peak is clearly visible at the center ($\Delta t = 0$),

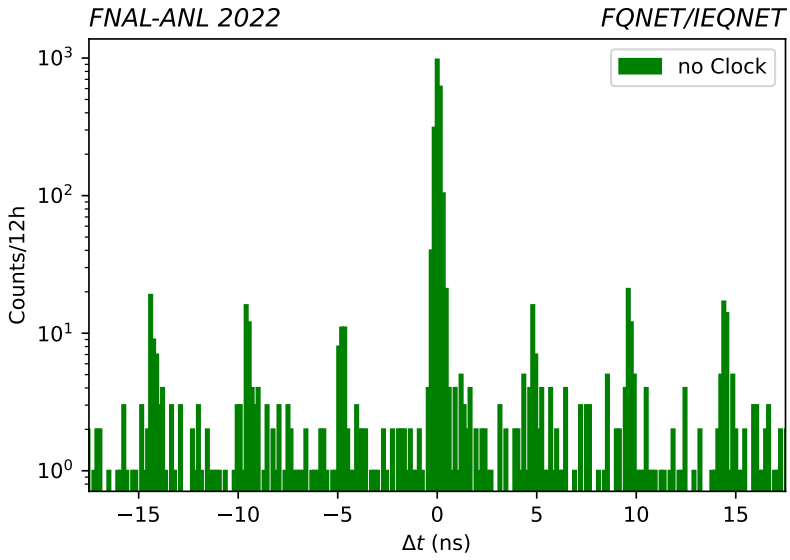

Figure 11.8: Coincidence histogram for the photon pairs sent to ANL from FNAL-FCC with the clock distribution disabled.

and the smaller peaks separated by 5 ns are the "accidental" events corresponding to a detection of one photon from one pair and another photon from preceding or subsequent pairs. We measure a CAR of 51 ± 2 in the background-free scenario.

Next, we sent the photon pairs to the FNAL-DAB and ANL end nodes with the O- and L-band clock synchronization enabled and multiplexed along the same fiber as one of the pairs. The time difference distributions of the two detected photons are shown in Figure 11.9 for the FNAL-DAB and ANL nodes. At the FNAL-DAB end node we measured a CAR of 35 ± 1 with the O-band clock, and 32 ± 1 with the L-band clock. At the ANL end node we measured a CAR of 5.3 ± 0.4 with the O-band clock, and 2.6 ± 0.3 with the L-band clock. The width of the peaks in our measurements are limited by timing jitter in our detectors and readout electronics. We see a reduction in CAR as we increase the length of the fiber, but we stay in the regime where the L-band clock introduces more noise than the O-band clock.

11.4 Discussion and outlook

We have demonstrated a clock-distribution system at the CQNET site for synchronizing remote nodes in metropolitan-scale quantum networks with picosecond-scale resolution. Despite not constituting the optimal choice of wavelength, our telecommunication O-band synchronization system introduces little noise into our telecommunication C-band quantum network. The low noise is partially due to the strong

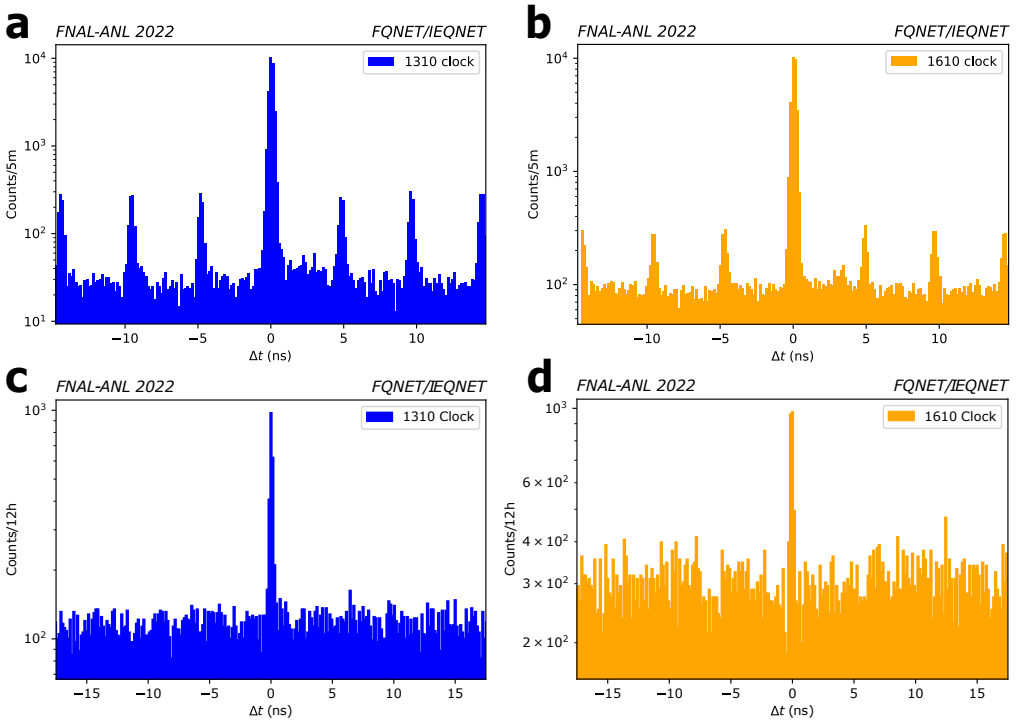

Figure 11.9: Coincidence histograms for the photon pairs sent to FNAL-DAB from FNAL-FCC with the a) 1310 nm and b) 1610 nm clock distribution enabled, and coincidence histograms for the photon pairs sent to ANL from FNAL-FCC with the c) 1310 nm and d) 1610 nm clock distribution enabled.

spectral filtering of the photons at the FBGs – a required step to ensure the photons are purified, i.e., spectral correlations are removed. This renders the photons suitable for two-photon interference, as required for implementations of advanced network protocols, e.g., based on quantum teleportation (Chapters 8 and 10). Note that the 768 nm light remaining after the SPDC step is far off-resonant from the 1536 nm photons, and is partially filtered by the long fiber spools, MUX/DEMUX filters, fiber Bragg gratings, and SNSPD devices, thus it does not contribute any measurable noise to the network. Further reduction of noise in our system can be afforded by detecting the clock pulses with more sensitive REC detectors, thus allowing a reduction of the clock pulse intensity. To this end, SNSPDs operating in the O-band could be used, and would constitute minimal system overhead given that C-band SNSPDs are already deployed. This would also result in improvements to the system clock rate as SNSPDs feature timing jitters as low as a few ps [22], which constitutes an upper-bound of a few hundred GHz to the clock rate (note that the impact of the dead time of the SNSPDs is negligible due to channel loss).

Additionally, we deployed our system over a metropolitan-scale optical fiber network at the FQNET site, demonstrating entanglement distribution with picosecond-level synchronization of remote nodes at FNAL and ANL connected with up to 57 km of optical fiber with timing resolution better than 10 ps. The obtained timing resolution enables quantum sources capable of achieving a repetition rate of the order of 10 GHz, significantly improving the detection rates reported in this study. Furthermore, the clock distribution system can be easily scaled to tens of nodes using very minimal modifications to the current design. We observe that a $CAR > 2.0$, which is above the classical limit, is maintained in all the configurations we tested including using the 57 km installed fiber link between FNAL-FCC and ANL, which has increased losses due to fiber splicing and connectors along the real world fiber connection. Comparing the idealized fiber attenuation loss coefficients in the C-band, our total losses correspond to a transmission of the quantum states over 105 km. Overall, our three-node quantum network and accompanying synchronization system sheds light on the role of noise in quantum networking and constitutes a step towards practical, as well as high-rate, classical-quantum co-existing networks.

References

[1] Akihiro Tanaka, Mikio Fujiwara, Sae Woo Nam, et al. "Ultra fast quantum key distribution over a 97 km installed telecom fiber with wavelength division multiplexing clock synchronization." In: Opt. Express 16.15 (July 2008), pp. 11354–11360. DOI: 10.1364/OE.16.011354.

[2] Yan-Lin Tang, Hua-Lei Yin, Si-Jing Chen, et al. "Field Test of Measurement-Device-Independent Quantum Key Distribution." In: IEEE Journal of Selected Topics in Quantum Electronics 21.3 (2015), pp. 116–122. DOI: 10.1109/JSTQE.2014.2361796.

[3] Raju Valivarthi, Marcelli Grimau Puigibert, Qiang Zhou, Gabriel H Aguilar, Varun B Verma, Francesco Marsili, Matthew D Shaw, Sae Woo Nam, Daniel Oblak, and Wolfgang Tittel. "Quantum teleportation across a metropolitan fibre network." In: Nature Photonics 10.10 (2016), pp. 676–680.

[4] Qi-Chao Sun, Ya-Li Mao, Si-Jing Chen, Wei Zhang, Yang-Fan Jiang, Yan-Bao Zhang, Wei-Jun Zhang, Shigehito Miki, Taro Yamashita, Hirotaka Terai, et al. "Quantum teleportation with independent sources and prior entanglement distribution over a network." In: Nature Photonics 10.10 (2016), pp. 671–675.

[5] Raju Valivarthi, Prathwiraj Umesh, Caleb John, Kimberley A Owen, Varun B Verma, Sae Woo Nam, Daniel Oblak, Qiang Zhou, and Wolfgang Tittel. "Measurement-device-independent quantum key distribution coexisting with classical communication." In: Quantum Science and Technology 4.4 (2019), p. 045002.

[6] James Williams, Martin Suchara, Tian Zhong, Hong Qiao, Rajkumar Kettimuthu, and Rikuto Fukumori. "Implementation of quantum key distribution and quantum clock synchronization via time bin encoding." In: Quantum Computing, Communication, and Simulation. Ed. by Philip R. Hemmer and Alan L. Migdall. Vol. 11699. International Society for Optics and Photonics. SPIE, 2021, pp. 16–25. DOI: 10.1117/12.2581862.

[7] Iris Choi, Robert J. Young, and Paul D. Townsend. "Quantum key distribution on a 10Gb/s WDM-PON." In: Opt. Express 18.9 (Apr. 2010), pp. 9600–9612. DOI: 10.1364/OE.18.009600.

[8] KA Patel, JF Dynes, I Choi, AW Sharpe, AR Dixon, ZL Yuan, RV Penty, and AJ Shields. "Coexistence of high-bit-rate quantum key distribution and data on optical fiber." In: Physical Review X 2.4 (2012), p. 041010.

[9] DOE's Quantum Internet Blueprint. https://www.energy.gov/sites/prod/files/2020/07/f76/QuantumWkshpRpt20FINAL_Nav_0.pdf.

[10] Tektronix. https://www.tek.com/en/products/arbitrary-waveform-generators/. Accessed: 2022-03-09.

[11] Shf. https://www.shf-communication.com/products/rf-broadband-amplifiers/. Accessed: 2022-03-09.

[12] Rodney Loudon. The quantum theory of light. Oxford, 2000.

[13] I. Marcikic, H. de Riedmatten, W. Tittel, V. Scarani, H. Zbinden, and N. Gisin. "Time-bin entangled qubits for quantum communication created by femtosecond pulses." In: Phys. Rev. A 66 (6 Dec. 2002), p. 062308. DOI: 10.1103/PhysRevA.66.062308.

[14] Hiroki Takesue and Kyo Inoue. "1.5-μm band quantum-correlated photon pair generation in dispersion-shifted fiber: suppression of noise photons by cooling fiber." In: Opt. Express 13.20 (Oct. 2005), pp. 7832–7839. DOI: 10.1364/OPEX.13.007832.

[15] Hiroki Takesue and Kyo Inoue. "Generation of 1.5$-\mu$m band time-bin entanglement using spontaneous fiber four-wave mixing and planar light-wave circuit interferometers." In: Phys. Rev. A 72 (4 Oct. 2005), p. 041804. DOI: 10.1103/PhysRevA.72.041804.

[16] Reinhard F. Werner. "Quantum states with Einstein-Podolsky-Rosen correlations admitting a hidden-variable model." In: Phys. Rev. A 40 (8 Oct. 1989), pp. 4277–4281. DOI: 10.1103/PhysRevA.40.4277. URL: https://link.aps.org/doi/10.1103/PhysRevA.40.4277.

[17] John F. Clauser, Michael A. Horne, Abner Shimony, and Richard A. Holt. "Proposed Experiment to Test Local Hidden-Variable Theories." In: Phys. Rev. Lett. 23 (15 Oct. 1969), pp. 880–884. DOI: 10.1103/PhysRevLett.23.880.

[18] Home: QuTag. https://www.qutools.com/qutag/. URL: https://www.qutools.com/qutag/.

[19] IxBlue. https://www.ixblue.com/north-america/store/dr-ve-10-mo/.

[20] Polatis. https://www.polatis.com/series_6000_multimode_switch_all-optical_switching.asp.

[21] Keshav Kapoor, Si Xie, Joaquin Chung, Raju Valivarthi, Cristián Peña, Lautaro Narváez, Neil Sinclair, Jason P. Allmaras, Andrew D. Beyer, Samantha I. Davis, et al. "Picosecond synchronization system for the distribution of photon pairs through a fiber link between Fermilab and Argonne National Laboratories." In: IEEE Journal of Quantum Electronics 59.4 (2023), pp. 1–7.

[22] Boris Korzh, Qing-Yuan Zhao, Jason P. Allmaras, et al. "Demonstration of sub-3 ps temporal resolution with a superconducting nanowire single-photon detector." In: Nature Photonics 14.4 (Apr. 2020), pp. 250–255. ISSN: 1749-4893. DOI: 10.1038/s41566-020-0589-x.

Part III

Quantum channels for fundamental physics

Chapter 12

ENTANGLEMENT AND SPACETIME

Entanglement is a fundamental feature of quantum mechanics, signifying a sharp departure from classical notions of locality and realism [1]. Its experimental verification through violations of Bell inequalities [2, 3, 4, 5] has made it central to both quantum technologies and the foundations of physics. As described in Part II of this thesis, entanglement is essential to quantum communication protocols such as teleportation (Chapter 8), entanglement swapping (Chapter 10), measurement-device-independent quantum key distribution [6] and quantum repeaters [7] that can enable secure communication, quantum-enhanced sensing, and distributed quantum processing in a quantum network. In fundamental physics, entanglement continues to play a central role in debates over the nature of reality, ever since the early days of quantum theory.

12.1 Foundations of quantum mechanics

In 1935, Einstein, Podolsky, and Rosen (EPR) raised objections to the completeness of quantum mechanics by proposing a thought experiment in which measurements are performed on a pair of entangled particles [8]. They reasoned that if a physical theory allows one to predict the outcome of a measurement on one particle by performing a measurement on its entangled partner, with out disturbing its state, then the outcome must correspond to a pre-existing "element of reality." Furthermore, because the two particles could be far apart, they assumed that no influence could travel between them faster than light. Taken together, these two assumptions—realism (that measurement outcomes reflect pre-existing properties) and locality (that no instantaneous influences exist between distant systems)—formed the basis for their argument that quantum mechanics must be supplemented by hidden variables. In the 1960s, Bell's theorem formalized this reason, stating that any theory satisfying both locality and realism must obey certain mathematical constraints, known as Bell inequalities [1]. According to quantum mechanics, maximally-entangled bipartite states, such as Bell states, violate these inequalities. In the past decade, landmark experiments demonstrated loop-hole-free violation of Bell inequalities with entangled photon pairs [9, 10], verifying the consequences of quantum mechanics and dismissing the classical assumption of "local realism."

However, Bell's theorem does not address a special case of EPR's original argument in which a measurement on one particle allows one to predict the state of the other particle with 100% certainty. Confronting this case requires moving beyond Bell's theorem and bipartite entanglement. To this end, Greenberger, Horne, and Zeilinger (GHZ) introduced a class of multipartite entangled states, known as GHZ states,

$$|\mathrm{GHZ}\rangle = \frac{|0\rangle^{\otimes N} + e^{i\phi}\,|1\rangle^{\otimes N}}{\sqrt{2}}, \tag{12.1}$$

with the minimal case of $N = 3$ qubits described by $|\mathrm{GHZ}\rangle = (|000\rangle + e^{i\phi}\,|111\rangle)/\sqrt{2}$. GHZ showed that such states allow for a contradiction with local realism at the level of deterministic predictions, providing a stronger refutation of EPR's assumptions. Experimental realizations of GHZ states can be used to prove that it is impossible to construct not only a classical, local-realistic theory of quantum mechanics in general, but also one that makes deterministic predictions of a system in the sense of EPR. In Chapter 13, I report our progress on the first experimental generation of tripartite GHZ states with time-bin qubits, which is particularly suited for implementation in a quantum network. This work not only opens a path to fundamental tests of physics, but also advanced networking protocols based on multipartite entanglement distribution, such as quantum secret sharing [11] and distributed quantum sensing [12].

12.2 Quantum nature of spacetime

Beyond the foundations of quantum mechanics, entanglement has also emerged as a key concept in understanding the quantum nature of spacetime. The interplay between quantum entanglement and the geometry of spacetime has emerged as a central theme in the quest to reconcile quantum mechanics with general relativity, particularly through the lens of the anti-de Sitter/conformal field theory (AdS/CFT) correspondence. In AdS/CFT, spacetime geometry in a $(d+1)$-dimensional gravitational theory is encoded in the entanglement structure of a d-dimensional boundary quantum field theory. This perspective leads to the idea that spacetime is not fundamental, but an emergent property arising from patterns of quantum correlations. A particularly striking manifestation of this idea is the ER=EPR conjecture, proposed by Maldacena and Susskind, which posits that entangled pairs (EPR) are dual to Einstein-Rosen bridges (ER), i.e., wormholes [13]. In this view, quantum entanglement generates geometric connectivity, with multipartite entanglement structures potentially corresponding to multiboundary wormholes or topologically complex bulk geometries [14]. These insights suggest a unifying framework where quan-

tum information is not only a tool for studying gravity but may be the microscopic substrate from which spacetime itself emerges.

A significant breakthrough in this line of thought came with the discovery that certain wormhole geometries can be rendered traversable. In the context of the AdS/CFT correspondence, wormholes can be interpreted as geometries connecting entangled black holes, such as the eternal black hole dual to the thermofield double state. However, in general relativity, such wormholes are non-traversable, meaning that no causal signal or observer can pass from one mouth to the other without encountering a singularity or violating energy conditions. This limitation arises due to the averaged null energy condition (ANEC) [15, 16], which prohibits the negative energy required to keep a wormhole throat open. In 2017, Gao, Jafferis, and Wall showed that a double-trace deformation, corresponding to a weak coupling between the two boundaries of an entangled thermofield double state, can lead to a violation of the ANEC in the bulk, thereby allowing signals to propagate through the wormhole without violating causality [17]. Remarkably, the resulting process is formally equivalent to quantum teleportation between entangled systems, with the traversable geometry offering a dual gravitational description of the underlying protocol. These results suggest that certain quantum communication protocols may admit gravitational duals, and that spacetime connectivity itself may be understood as a manifestation of quantum entanglement and information flow through an underlying quantum channel.

In 2019, Gao and Jafferis constructed a traversable wormhole teleportation protocol within the coupled Sachdev–Ye–Kitaev (SYK) model [18], where a probe inserted into one side of a thermofield double state reappears on the other after a double-trace deformation [19]. The SYK model is a many-body system of randomly interacting Majorana fermions with an emergent conformal symmetry that is holographically dual to Jackiw–Teitelboim (JT) gravity in nearly-AdS_2 spacetime [18]. In the bulk dual, the protocol corresponds to a signal traversing a dynamically opened wormhole [20]. In Chapter 14, we demonstrate an experimental realization of this protocol using a sparsified SYK model on Google's Sycamore quantum processor. This work is the first experimental simulation of traversable wormhole dynamics on a quantum processor, a step in the program of investigating quantum gravity in the lab.

References

[1] J. S. Bell. "On the Einstein Podolsky Rosen paradox." In: Physics Physique Fizika 1 (3 Nov. 1964), pp. 195–200. DOI: 10.1103/PhysicsPhysiqueFizika.1.195.

URL: https://link.aps.org/doi/10.1103/PhysicsPhysiqueFizika.1.195.

[2] John F. Clauser, Michael A. Horne, Abner Shimony, and Richard A. Holt. "Proposed experiment to test local hidden-variable theories." In: Physical Review Letters 23.15 (1969), p. 880.

[3] Stuart J. Freedman and John F. Clauser. "Experimental test of local hidden-variable theories." In: Physical review letters 28.14 (1972), p. 938.

[4] Alain Aspect, Jean Dalibard, and Gérard Roger. "Experimental test of Bell's inequalities using time-varying analyzers." In: Physical Review Letters 49.25 (1982), p. 1804.

[5] Gregor Weihs, Thomas Jennewein, Christoph Simon, Harald Weinfurter, and Anton Zeilinger. "Violation of Bell's inequality under strict Einstein locality conditions." In: Physical Review Letters 81.23 (1998), p. 5039.

[6] Hoi-Kwong Lo, Marcos Curty, and Bing Qi. "Measurement-device-independent quantum key distribution." In: Physical review letters 108.13 (2012), p. 130503.

[7] Koji Azuma, Sophia E. Economou, David Elkouss, Paul Hilaire, Liang Jiang, Hoi-Kwong Lo, and Ilan Tzitrin. "Quantum repeaters: From quantum networks to the quantum internet." In: Reviews of Modern Physics 95 (4 Dec. 2023), p. 045006. DOI: 10.1103/RevModPhys.95.045006. URL: https://link.aps.org/doi/10.1103/RevModPhys.95.045006.

[8] Albert Einstein, Boris Podolsky, and Nathan Rosen. "Can quantum-mechanical description of physical reality be considered complete?" In: Physical review 47.10 (1935), p. 777.

[9] Marissa Giustina, Marijn AM Versteegh, Sören Wengerowsky, Johannes Handsteiner, Armin Hochrainer, Kevin Phelan, Fabian Steinlechner, Johannes Kofler, Jan-Åke Larsson, Carlos Abellán, et al. "Significant-loophole-free test of Bell's theorem with entangled photons." In: Physical Review Letters 115.25 (2015), p. 250401.

[10] Lynden K. Shalm, Evan Meyer-Scott, Bradley G. Christensen, Peter Bierhorst, Michael A. Wayne, Martin J. Stevens, Thomas Gerrits, Scott Glancy, Deny R. Hamel, Michael S. Allman, et al. "Strong loophole-free test of local realism." In: Physical Review Letters 115.25 (2015), p. 250402.

[11] Xing-Ri Jin, Xin Ji, Ying-Qiao Zhang, Shou Zhang, Suc-Kyoung Hong, Kyu-Hwang Yeon, and Chung-In Um. "Three-party quantum secure direct communication based on GHZ states." In: Physics Letters A 354.1-2 (2006), pp. 67–70.

[12] Li-Zheng Liu, Yu-Zhe Zhang, Zheng-Da Li, Rui Zhang, Xu-Fei Yin, Yue-Yang Fei, Li Li, Nai-Le Liu, Feihu Xu, Yu-Ao Chen, et al. "Distributed quantum phase estimation with entangled photons." In: Nature Photonics 15.2 (2021), pp. 137–142.

[13] Juan Maldacena and Leonard Susskind. "Cool horizons for entangled black holes." In: Fortschritte der Physik 61.9 (2013), pp. 781–811.

[14] Leonard Susskind. “ER= EPR, GHZ, and the consistency of quantum measurements.” In: Fortschritte der Physik 64.1 (2016), pp. 72–83.

[15] Michael S. Morris, Kip S. Thorne, and Ulvi Yurtsever. “Wormholes, Time Machines, and the Weak Energy Condition.” In: Physical Review Letters 61.13 (1988), pp. 1446–1449. DOI: 10.1103/PhysRevLett.61.1446.

[16] David Hochberg and Matt Visser. “Null energy condition in dynamic wormholes.” In: Physical Review Letters 81.4 (1998), p. 746.

[17] Ping Gao, Daniel Louis Jafferis, and Aron C Wall. “Traversable wormholes via a double trace deformation.” In: Journal of High Energy Physics 2017.12 (2017), p. 151.

[18] Alexei Kitaev. A Simple Model Of Quantum Holography. Talks at KITP, April 7, 2015 and May 27, 2015. Available at http://online.kitp.ucsb.edu/online/entangled15/kitaev/ and http://online.kitp.ucsb.edu/online/entangled15/kitaev2/.

[19] Ping Gao and Daniel Louis Jafferis. “A traversable wormhole teleportation protocol in the SYK model.” In: Journal of High Energy Physics 2021.7 (2021), pp. 1–44.

[20] Juan Maldacena, Douglas Stanford, and Zhenbin Yang. “Diving into traversable wormholes.” In: Fortschritte der Physik 65.5 (2017), p. 1700034.

Chapter 13

GHZ STATES WITH TIME-BIN QUBITS

This chapter includes the work published as:

[1] Samantha I. Davis, Chang Li, Rahaf Youssef, Neil Sinclair, Raju Valivarthi, and Maria Spiropulu. "Generation of Time-bin GHZ States." In: Optica Quantum 2.0 Conference and Exhibition. Optica Publishing Group, 2023, QTh4A.7. DOI: 10.1364/QUANTUM.2023.QTh4A.7. URL: https://opg.optica.org/abstract.cfm?URI=QUANTUM-2023-QTh4A.7.

13.1 Introduction

Quantum entanglement, one of the unique features of quantum mechanics, is a key ingredient for several quantum information processing fields including quantum communication, quantum computing, and quantum metrology. Maximally entangled bipartite states have not only been used for the above mentioned fields but were also crucial for fundamental tests of physics such as loophole-free tests of Bell inequalities [1, 2]. Analogous tripartite maximally entangled states have been proposed, known as Greenberger-Horne-Zeilinger (GHZ) states [3], which are shown to reject local realism theories without the need to acquire statistics on the measurements, and have known applications in distributed quantum computing [4] and multiparty quantum communication [5], such as superdense coding, quantum secret sharing, and quantum Byzantine agreements. Previous experimental proposals have been mostly limited to the polarization degree of freedom [6], until a recent experimental realization with energy-time entanglement [7]. Here we report our progress toward the first experimental demonstration of GHZ states with time-bin qubits[1], which are particularly well-suited for practical implementations in quantum networks for long-distance quantum communication and tests of nonlocality. Moreover, we develop a theoretical model to support the experimental results.

13.2 Entangling time-bin qubits with a switch

As described in Part I of this thesis, Bell pairs of time-bin qubits can be generated with high-fidelity using nonlinear optical processes such as SPDC. To generate

[1] At the time this work was conducted, we became aware of concurrent work published independently [8].

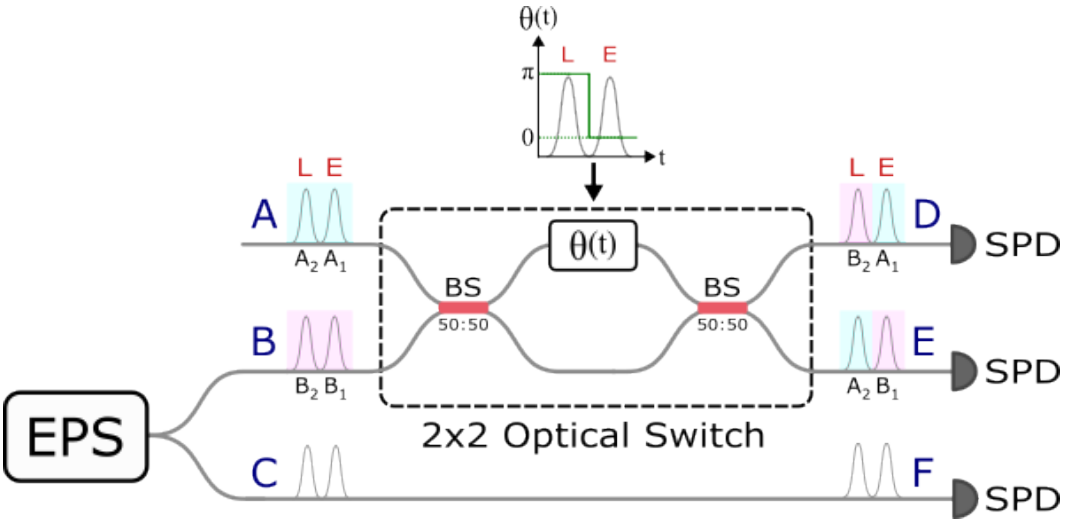

Figure 13.1: Setup for generating GHZ states with time-bin qubits. One member of a Bell pair produced by a entangled pair source (EPS) is interfered with another time-bin qubit using a 2x2 optical switch. A GHZ state is post-selected using single-photon detectors (SPDs) after the switch.

higher-order entangled states, we use the scheme proposed in Ref. [9] for entangling time-bin qubits. We generate a GHZ states by interfering one member of Bell pair with a third qubit in a 2-by-2 optical switch comprised of a balanced Mach-Zehnder interferometer (MZI) with a time-varying phase shift. The setup for the protocol is illustrated in Fig. 13.1.

Consider three qubits initialized in the state,

$$|\Psi\rangle = |\psi\rangle_A \otimes |\phi\rangle_{BC}\,, \tag{13.1}$$

$$|\psi\rangle_A = \frac{1}{\sqrt{2}}(|t_1\rangle_A + e^{i\phi_A}\,|t_2\rangle_A), \tag{13.2}$$

$$|\phi\rangle_{BC} = \frac{1}{\sqrt{2}}(|t_1\rangle_B\,|t_1\rangle_C + e^{i\phi_{BC}}\,|t_2\rangle_B\,|t_2\rangle_C), \tag{13.3}$$

where t_1 and t_2 denote the early and late time bins, respectively, and the subscripts on the states denote the spatial modes. Qubits at spatial modes A and B are inserted into the input ports the switch. The transformations of $|t_k\rangle_A$ and $|t_k\rangle_B$ through the switch are described by,

$$\begin{aligned} |t_k\rangle_A &\rightarrow \cos\left(\frac{\theta\,(t_k)}{2}\right)|t_k\rangle_D - \sin\left(\frac{\theta\,(t_k)}{2}\right)|t_k\rangle_E\,, \\ |t_k\rangle_B &\rightarrow \sin\left(\frac{\theta\,(t_k)}{2}\right)|t_k\rangle_D + \cos\left(\frac{\theta\,(t_k)}{2}\right)|t_k\rangle_E\,, \end{aligned} \tag{13.4}$$

where $k = 1, 2$ and $\theta(t_k)$ is the phase difference between the two arms of the MZI at time t_k. By setting $\theta(t_1) = 0$ and $\theta(t_2) = \pi$, the spatial modes of the input photons are unchanged in the early time bin and exchanged in the late time bin. The state of the system after the switch is,

$$|\psi\rangle_A \otimes |\phi\rangle_{\mathrm{BC}} \rightarrow \frac{1}{2}(|t_1\rangle_D |t_1\rangle_E |t_1\rangle_F + e^{i\phi_{BC}} |t_1\rangle_D |t_2\rangle_D |t_2\rangle_F \tag{13.5}$$

$$- e^{i\phi_A} |t_2\rangle_E |t_1\rangle_E |t_1\rangle_F - e^{i(\phi_A+\phi_{BC})} |t_2\rangle_D |t_2\rangle_E |t_2\rangle_F). \tag{13.6}$$

By measuring the three-fold coincidences at distinct spatial modes (D, E, F), we can post-select the time-bin GHZ state,

$$|\Psi_{GHZ}\rangle = \frac{1}{\sqrt{2}}(|t_1\rangle_D |t_1\rangle_E |t_1\rangle_F + e^{i\phi} |t_2\rangle_D |t_2\rangle_E |t_2\rangle_F). \tag{13.7}$$

13.3 Experiment

The experimental setup for generating time-bin GHZ states is shown in Fig. 13.2a. Time-bin qubits separated by 346 ps are created by injecting 1536 nm wavelength light from a continuous-wave laser into an intensity modulator (IM). The light is split into two paths by a 50:50 beamsplitter. In one path, the pulses are sent to a second harmonic generation (SHG) module containing an erbium doped fiber amplifer (EDFA) and PPLN waveguide, which up-converts the pulses to 768 nm. These pulses are used as a pump for type-II SPDC to create entangled photon pairs at 1536 nm. In the second path, the third qubit is prepared by attenuating the laser pulses. One member of the entangled state is interfered with the third qubit in a optical switch with a 20 GHz phase modulation bandwidth. Given two indistinguishable photons incident to the switch, the joint state of the three photons is described by a GHZ state after post-selection of the photons exiting the two output ports of the switch. The final output state is analyzed via measurements of the three photons (qubits) with superconducting nanowire single-photon detectors (SNSPDs) using a custom graphical user interface (see Fig. 13.2b).

13.4 Theory

We develop a theoretical model using the characteristic function-based formalism detailed in Chapter 9. The early and late time bins are modeled as independent modes, and the switch is modeled as a Mach-Zehnder interferometer with $\theta_E = 0$ for the early mode and $\theta_L = \pi$ for the late mode. Since the two-mode squeezed vacuum state and coherent state have Gaussian characteristic functions, and all subsequent operations up to detection are Gaussian, we construct the Symplectic matrix that

a)

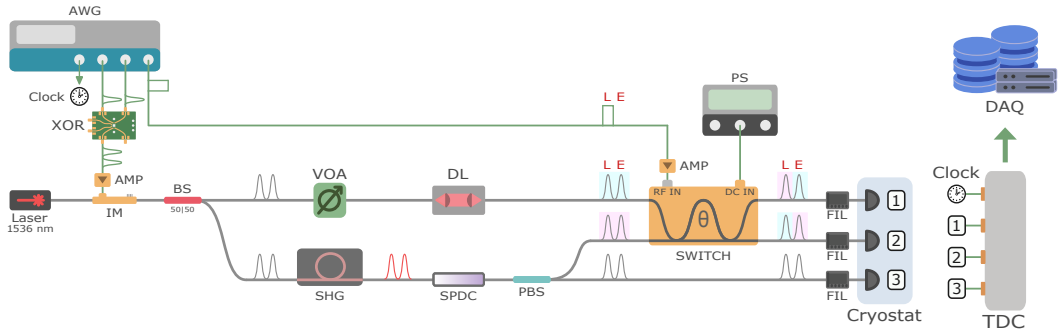

b)

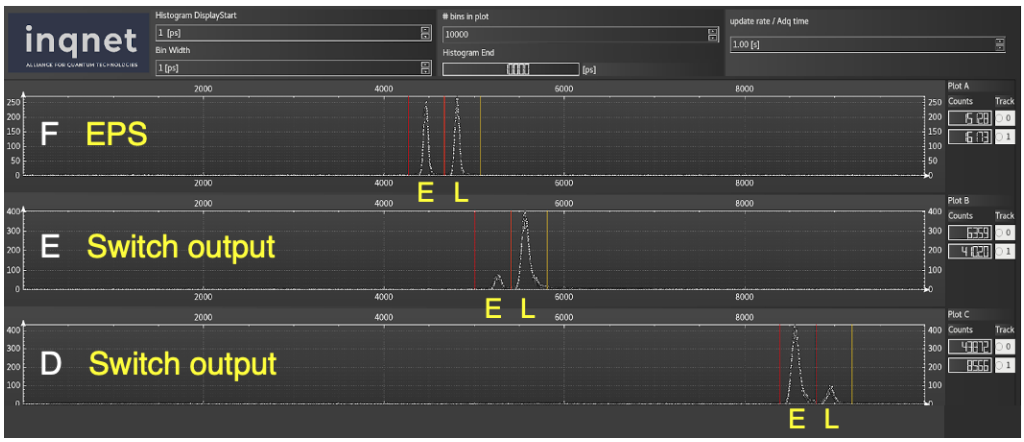

Figure 13.2: Experimental generation of time-bin GHZ states. a) Experimental setup. AWG, Tektronix AWG7002A; BS, Thorlabs 1550-nm fiber optic 50:50 beam splitter; DL, fiber optic delay line, EDFA, Pritel erbium-doped fiber amplifier; FIL, bandpass filter; Laser, MOGlabs Tunable Cateye Laser; PBS, Thorlabs 1550-nm fiber optic polarizing beam splitter; PPLN, HC Photonics waveguide; PS, power supply, SHG, Pritel optical fiber amplifier and second-harmonic generator; SNSPD, superconducting nanowire single-photon detector; TDC, quTAG time-to-digital converter; VOA, EXFO variable optical attenuator. b) Screenshot of custom Graphical User Interface (GUI) used for data acquisition and analysis. In the switch output channels, the larger peak corresponds to the weak coherent state and the smaller peak corresponds to one member of the TMSV state from SPDC. The discrepancy in peak heights is due to the different photon statistics and mean photon numbers of the coherent and TMSV states.

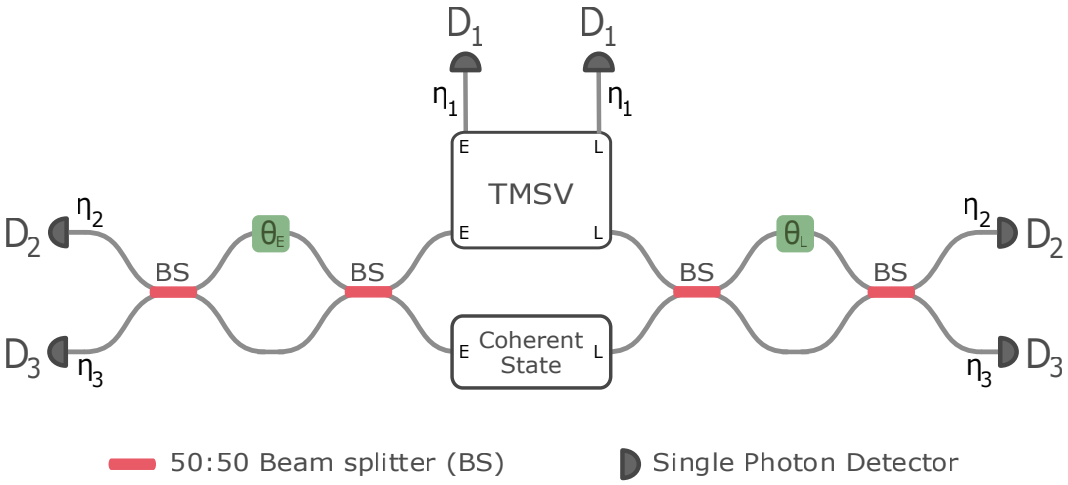

Figure 13.3: Setup for theoretical modeling. The top and bottom boxes represent a two-mode squeezed vacuum state (TMSV) and coherent state, respectively, in the product state of early and late temporal modes. Early and late temporal modes are represented as different spatial modes in the setup. The switch is modeled as an MZI acting on the early (late) modes of the coherent state and one half TMSV with phase shift $\theta_{E(L)}$. Measurement loss is modeled as mixing with a virtual vacuum mode with a beamsplitter (not depicted) with transmittances η_1, η_2, and η_3 for detectors D_1, D_2, and D_3, respectively.

maps the characteristic function of input state to that of the output state. The output characteristic function is found by substituting the displacement vector $\vec{d}$ and covariance matrix γ with $\vec{d} \rightarrow S^T \vec{d}$ and $\gamma \rightarrow S^T \gamma S$. From the output displacement vector and covariance matrix, the density matrix states produced in the experiment can be calculated as a function of relevant experimental parameters, such as the mean photon number of the coherent state μ_C, the mean photon number of the TMSV state (μ_s), measurement loss, and the extinction ratio of the switch. The extinction ratio of the switch is measured by setting the phase to $\theta = 0$ or π, sending strong coherent light into one input of the switch, and calculating the ratio of the powers measured from the output ports (P_D/P_E). Ideally, light is measured only in one output port or the other (P_D or $P_E = 0$). We measure extinction ratios of $|10 \log_{10}(P_D/P_E)| \sim 18$ dB. Switch extinction ratios are modeled as $P_D/P_E = \cot^2(\theta_{E(L)}/2)$, where the phases $\theta_E \sim 0$ and $\theta_L \sim \pi$ are set to match the experimental extinction ratios.

From the output covariance matrix γ' and displacement vector $\vec{d}'$, we obtain a model for the density matrix of the experimental output state as a function of the mean photon numbers, losses and extinction ratio. The Fock basis density matrix

elements for an ℓ-mode Gaussian state ρ are in terms of its covariance matrix γ and displacement vector $\vec{d}$ are,

$$\langle \vec{m}| \rho |\vec{n}\rangle = T \times \text{lhaf}(\text{vid}(\mathbf{A}, \vec{\beta})), \tag{13.8}$$

$$T = \frac{\exp\left(-\frac{1}{2}\vec{d}^T\gamma^{-1}\vec{d}\right)}{\sqrt{\det(\gamma)\prod_{s=1}^{\ell} n_s! m_s!}}, \tag{13.9}$$

$$\mathbf{A} = \boldsymbol{X}\left(\mathbf{I}_{2\ell} - \gamma^{-1}\right), \quad \mathbf{X} = \begin{bmatrix} 0 & \mathbf{I}_\ell \\ \mathbf{I}_\ell & 0 \end{bmatrix}, \quad \vec{\beta}^T = \vec{d}^T\gamma^{-1}, \tag{13.10}$$

where $|\vec{n}\rangle = |n_1\rangle \cdots |n_\ell\rangle$ is the ℓ-mode photon number state of n_1 photons in the first mode, n_2 photons in the second mode, etc., $\text{lhaf}(\cdots)$ is the loop Hafnian, and $\text{vid}(\mathbf{A}, \vec{\beta}) = \mathbf{A} - \text{diag}(\text{diag}(\mathbf{A})) + \text{diag}(\vec{\beta})$ [10].

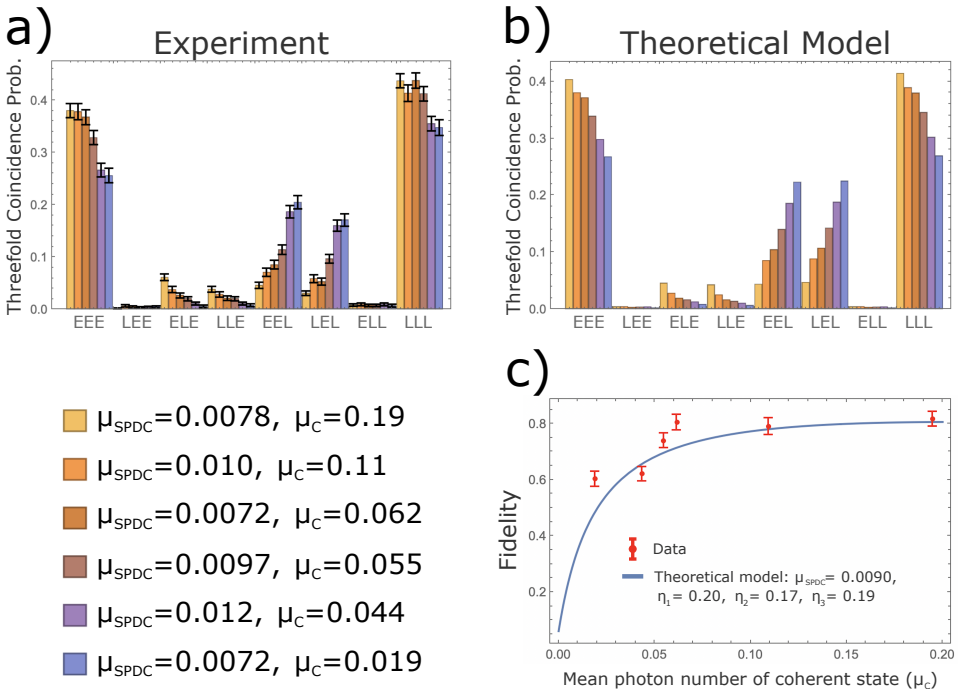

Figure 13.4: Characterization of time-bin GHZ states in the Z-basis. a) Threefold coincidence probabilities for varied mean photon number of the coherent state. The probabilities are found from dividing the coincidence rates in Hz by the repetition rate of the experiment (100 MHz). b) Theoretical model for the data in a). c) Z-basis fidelity for varied mean photon number of the coherent state. The error bars in a) and c) are calculated from Poisson statistics.

13.5 Results

With the measurement configuration in Fig. 13.2, we are able to perform projective measurements in the Z basis described by the measurement operators,

$$\hat{\Pi}_{i,j,k} = |t_i\rangle\langle t_i| \otimes |t_j\rangle\langle t_j| \otimes |t_k\rangle\langle t_k|, \tag{13.11}$$

where $i, j, k \in [1, 2]$. We measure the threefold coincidence rates,

$$C_{i,j,k} \propto \mathrm{Tr}[\hat{\rho}_{\mathrm{exp}}\hat{\Pi}_{i,j,k}],$$

for varied mean photon number of the coherent light (μ_C). The experimental and theoretical coincidence probabilities for each of the eight possible outcomes are shown in Fig. 13.4a and b, respectively. The coincidence probabilities are obtained by dividing the coincidence rates by the 100 MHz repetition rate of the experiment. The theoretical coincidence probabilities are calculated from the model using,

$$\mathrm{Tr}[\hat{\rho}\hat{\Pi}] = \left(\frac{1}{2\pi}\right)^N \int dx^{2N} \chi_\rho(x)\chi_\Pi(-x), \tag{13.12}$$

where N is the number of modes, $\chi(x)$ is the characteristic function of the output state and $\chi_\Pi(-x)$ is the characteristic function of the measurement operator of the detectors [11]. We define a "Z-basis fidelity" for the GHZ state as,

$$F_Z = \frac{P(t_1, t_1, t_1) + P(t_2, t_2, t_2)}{\sum_{i,j,k} P(t_i, t_j, t_k)}. \tag{13.13}$$

The Z-basis fidelity is plotted as function of the μ_C in Fig. 13.4c for the data in Fig 13.4a. The blue curve is the model using the average μ_{SPDC} of 0.009. The fidelity increases with μ_C for fixed μ_{SPDC} due to the mismatch in photon statistics for the coherent state and TMSV. We observe a maximum $F_Z = 82.0 \pm 4.1\%$ for $\mu_C = 0.19$.

In order to fully reconstruct the experimental states, a complete tomographic set of measurements need to be performed. This requires using interferometers before detection to project onto the X and Y bases. To estimate the overall state fidelity produced by our setup, we calculate the density matrix for $\mu_C = 0.19$ using Eq. 13.8. The density matrix elements are plotted in Fig. 13.5 for the ideal GHZ state, ρ_{GHZ}, and the model, ρ_{est}. The state fidelity is calculated as,

$$F(\rho_{\mathrm{est}}, \rho_{\mathrm{GHZ}}) = \left(\mathrm{Tr}\sqrt{\sqrt{\rho_{\mathrm{est}}}\rho_{\mathrm{GHZ}}\sqrt{\rho_{\mathrm{est}}}}\right)^2. \tag{13.14}$$

The model estimates a state fidelity of 80.6% for $\mu_C = 0.19$, $\mu_{\mathrm{TMSV}} = 0.009$, $\eta_1 = 0.2$, $\eta_2 = 0.17$, $\eta_3 = 0.19$, and an extinction ratio of 18 dB corresponding to $\theta_E = 0.25$, and $\theta_L = 0.25 + \pi$. By decreasing μ_{SPDC} to ~ 0.001, our model predicts $> 90\%$ fidelity can be achieved.

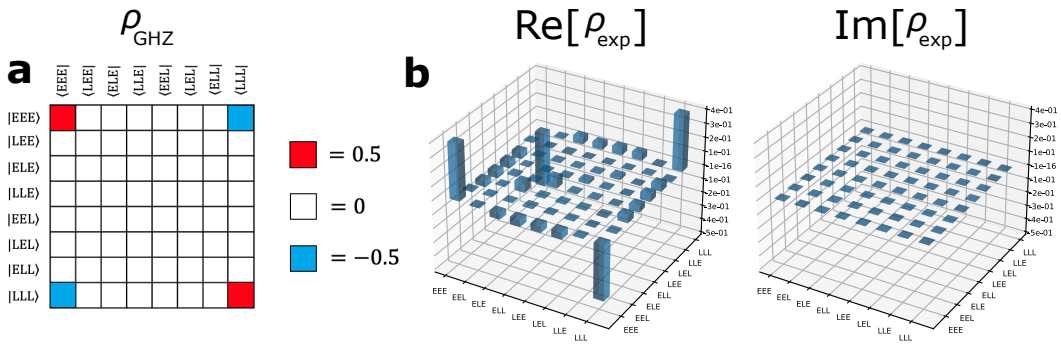

Figure 13.5: Density matrix model. a) Density matrix (ρ_{GHZ}) elements for an ideal GHZ state. b) Real and imaginary components of the density matrix model (ρ_{est}) for $\mu_C = 0.19$, $\mu_{\text{TMSV}} = 0.009$, $\eta_1 = 0.2$, $\eta_2 = 0.17$, $\eta_3 = 0.19$, and an extinction ratio of 18 dB corresponding to $\theta_E = 0.25$, and $\theta_L = 0.25 + \pi$.

References

[1] Marissa Giustina, Marijn AM Versteegh, Sören Wengerowsky, Johannes Handsteiner, Armin Hochrainer, Kevin Phelan, Fabian Steinlechner, Johannes Kofler, Jan-Åke Larsson, Carlos Abellán, et al. "Significant-loophole-free test of Bell's theorem with entangled photons." In: Physical Review Letters 115.25 (2015), p. 250401.

[2] Lynden K. Shalm, Evan Meyer-Scott, Bradley G. Christensen, Peter Bierhorst, Michael A. Wayne, Martin J. Stevens, Thomas Gerrits, Scott Glancy, Deny R. Hamel, Michael S. Allman, et al. "Strong loophole-free test of local realism." In: Physical Review Letters 115.25 (2015), p. 250402.

[3] Daniel M. Greenberger, Michael A. Horne, and Anton Zeilinger. "Going beyond Bell's theorem." In: Bell's theorem, quantum theory and conceptions of the universe. Springer, 1989, pp. 69–72.

[4] Ellie D'Hondt and Prakash Panangaden. "The computational power of the W and GHZ states." In: arXiv preprint quant-ph/0412177 (2004).

[5] Xing-Ri Jin, Xin Ji, Ying-Qiao Zhang, Shou Zhang, Suc-Kyoung Hong, Kyu-Hwang Yeon, and Chung-In Um. "Three-party quantum secure direct communication based on GHZ states." In: Physics Letters A 354.1-2 (2006), pp. 67–70.

[6] Anton Zeilinger, Michael A. Horne, Harald Weinfurter, and Marek Żukowski. "Three-particle entanglements from two entangled pairs." In: Physical Review Letters 78.16 (1997), p. 3031.

[7] Sascha Agne, Thomas Kauten, Jeongwan Jin, Evan Meyer-Scott, Jeff Z. Salvail, Deny R. Hamel, Kevin J. Resch, Gregor Weihs, and Thomas Jennewein. "Observation of Genuine Three-Photon Interference." In: Phys. Rev. Lett. 118 (15 Apr. 2017), p. 153602. DOI: 10.1103/PhysRevLett.118.153602. URL: https://link.aps.org/doi/10.1103/PhysRevLett.118.153602.

[8] Hsin-Pin Lo, Takuya Ikuta, Koji Azuma, Toshimori Honjo, William J Munro, and Hiroki Takesue. "Generation of a time–bin Greenberger–Horne–Zeilinger state with an optical switch." In: Quantum Science and Technology 8.3 (Apr. 2023), p. 035003. DOI: 10.1088/2058-9565/acc7c2. URL: https://dx.doi.org/10.1088/2058-9565/acc7c2.

[9] Hiroki Takesue. "Entangling time-bin qubits with a switch." In: Physical Review A 89.6 (2014), p. 062328.

[10] Nicolás Quesada, Luke G. Helt, Josh Izaac, Juan Miguel Arrazola, Reihaneh Shahrokhshahi, Casey R. Myers, and Krishna K. Sabapathy. "Simulating realistic non-Gaussian state preparation." In: Physical Review A 100.2 (2019), p. 022341.

[11] Masahiro Takeoka, Rui-Bo Jin, and Masahide Sasaki. "Full analysis of multi-photon pair effects in spontaneous parametric down conversion based photonic quantum information processing." In: New Journal of Physics 17.4 (2015), p. 043030.

Chapter 14

TELEPORTATION THROUGH THE WORMHOLE

This chapter includes the work published as:

[1] Daniel Jafferis, Alexander Zlokapa, Joseph D. Lykken, David K. Kolchmeyer, Samantha I. Davis, Nikolai Lauk, Hartmut Neven, and Maria Spiropulu. "Traversable wormhole dynamics on a quantum processor." In: Nature 612.7938 (2022), pp. 51–55.

14.1 Introduction

Traversable wormholes [1, 2] provide a mechanism to probe the conjectured ER=EPR relation between entanglement and spacetime geometry [3, 4] via the holographic correspondence of quantum many-body systems and gravitational physics [5]. In this construction, a pair of black holes in a thermofield double state have their interiors connected via an Einstein-Rosen bridge. Classically, the null energy condition prevents such wormholes from being traversable [6, 7, 8, 9]. The basic mechanism found in Ref. [1] is that the gravitational backreaction to quantum effects induced by couplings between the exterior regions of the pair of black holes can render the wormhole traversable [10]. It was demonstrated by Refs. [1, 2] that sending quantum information through such a wormhole is the gravitational description of quantum teleportation in the dual many-body system: the physical picture behind this teleportation is that the qubit traverses the emergent wormhole.

Considering gravity with nearly AdS_2 boundary conditions [11], the thermofield double (TFD) state corresponds to an AdS-Schwarzschild wormhole [12]. Two quantum systems — denoted L and R for the two black holes — are entangled in the TFD state at temperature $1/\beta$. In the gravitational picture, a qubit is injected into L at time $-t_0$ and arrives at R at t_1 due to a coupling interaction at $t = 0$. This coupling induces a negative null energy in the bulk that shifts the qubit away from the singularity (Fig. 14.1a), consistent with a quantum computation that recovers the infalling qubit under unitary black hole dynamics [13]. Interpreted in terms of recovering information from unitary black hole evaporation [13], the negative energy shockwave produces a quantum computation that causes the scrambled infalling qubit to reappear in the auxiliary entangled system, i.e., emerging at R after a

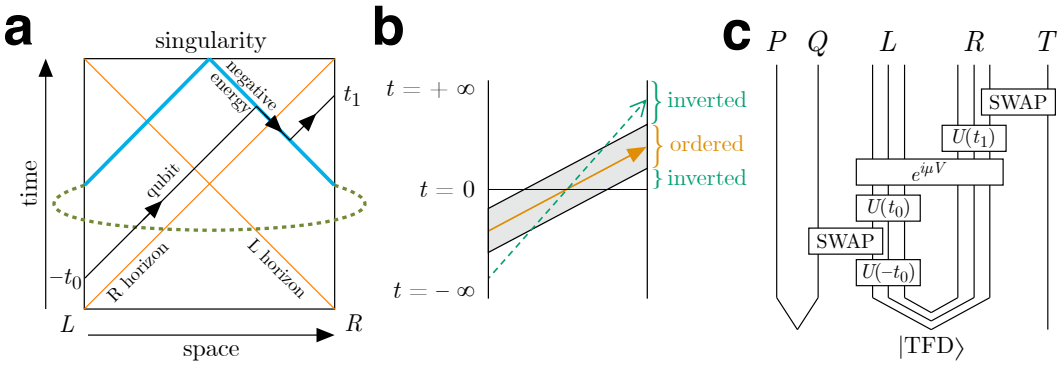

Figure 14.1: Traversable wormhole in spacetime and in the holographic dual. a) Diagram of a traversable wormhole in anti-de Sitter space. A qubit injected at $t = -t_0$ enters through the left side of the wormhole; at $t = 0$ a coupling (dashed line) is applied between the two sides of the wormhole, causing a negative energy shockwave (blue); the qubit experiences a time advance upon contact with the shockwave, causing it to emerge from the right side at $t = t_1$. b) Illustration of time-ordering (wormhole) and time-inversion (scrambling) of teleportation signals. The smooth semiclassical geometry of a traversable wormhole produces a regime of teleportation that obeys causality; non-gravitational teleportation causes the signals to arrive in reverse order. c) The traversable wormhole expressed as a quantum circuit, equivalent to the gravitational picture in the semiclassical limit of an infinite number of qubits. The unitary $\hat{U}(t)$ denotes time evolution $e^{-i(\hat{H}_L+\hat{H}_R)t}$ under the left and right SYK models. The thermofield double state ($|\mathrm{TFD}\rangle$) initializes the wormhole at $t = 0$. The time evolution and Majorana fermion SWAP gates achieve qubit injection and arrival readout at the appropriate times. When $\mu < 0$, the coupling $e^{i\mu\hat{V}}$ generates a negative energy shockwave, allowing traversability; when $\mu > 0$, the coupling generates a positive energy shockwave and the qubit falls into the singularity.

time of order the scrambling time. If the sign of the interaction is reversed, the qubit irretrievably falls into the singularity. Wormhole teleportation corresponds to on-shell propagation through the bulk from the left to the right boundary. The time-ordering of the transmitted quantum information is then preserved through the wormhole (Fig. 14.1b), unlike teleportation by random unitary dynamics [14, 15, 16, 17, 18].

In the semiclassical limit of an infinite number of qubits, it is known that the SYK model [19, 20] may be used to experimentally realize traversable wormhole dynamics [21]. In this work, we study the dynamics of traversable wormholes via many-body simulation of an SYK-like system of N fermions [19, 20], where traversable wormhole protocol is equivalent to a quantum teleportation protocol in the large-N semiclassical limit (Fig. 14.1c).

14.2 Traversable wormhole teleportation protocol

To implement the quantum teleportation protocol, we initialize the thermofield double state $|\text{TFD}\rangle = \frac{1}{\sqrt{Z}} \sum_n e^{-\beta E_n/2} |n\rangle_L \otimes |n\rangle_R$, where $|n\rangle_{L,R}$ are the energy eigenstates of the left and right SYK systems. Explicitly, given left and right Hamiltonians $\hat{H}_L$ and $\hat{H}_R$ with N Majorana fermions $\hat{\psi}$ on each side, the SYK model with q couplings is given by

$$\hat{H}_{L,R} = \sum_{1 \le j_1 < \cdots < j_q \le N} J_{j_1 \ldots j_q} \hat{\psi}^{j_1}_{L,R} \ldots \hat{\psi}^{j_q}_{L,R}, \tag{14.1}$$

where the couplings are chosen from a Gaussian distribution with mean zero and variance $J^2(q-1)!/N^{q-1}$. To swap in a qubit at $t = -t_0$, the system is time-evolved by $e^{-i\hat{H}t}$ for $\hat{H} \equiv \hat{H}_L + \hat{H}_R$. At $t = 0$, the interaction $e^{i\mu\hat{V}}$ is applied across both the left and right subsystems with coupling operator $\hat{V} = \frac{1}{qN} \sum_j \hat{\psi}^j_L \hat{\psi}^j_R$. The sign of μ must be negative to produce a negative energy shockwave that allows the qubit to travel through the wormhole. We measure the mutual information I_{PT} given by

$$I_{PT}(t) = S_P(t) + S_T(t) - S_{PT}(t), \tag{14.2}$$

where S is a measure of entropy. If a quantum system were to teleport via scrambling rather than traversing a wormhole, the mutual information would be symmetric in μ. Perfect teleportation is achieved when I_{PT} is maximal. No information is transmitted when I_{PT} is zero.

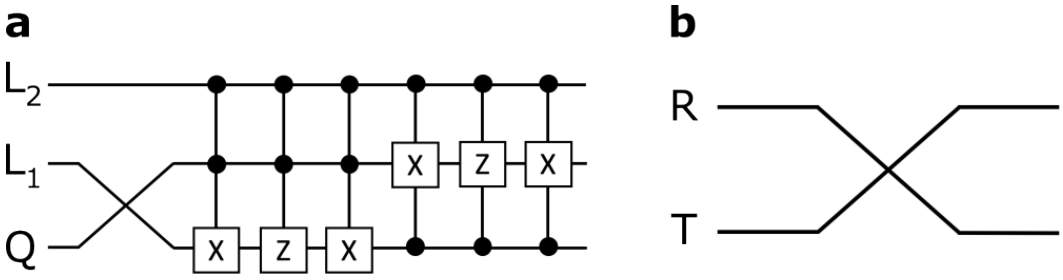

Figure 14.2: Majorana SWAP gates. a) $ZX + iZY$ Majorana SWAP gate decomposition for inserting a qubit (Q) into the wormhole. L_1, L_2 are qubits in the left subsystem. b) $X + iY$ Majorana SWAP gate for extracting the qubit from the wormhole, which coincidences with the regular SWAP gate. R is a qubit in the right subsystem and T is the register.

14.3 Experimental implementation

To implement the wormhole protocol experimentally, the protocol needs to be decomposed into a quantum circuit that can be realized on near-term quantum hardware. We consider a system of $2N$ Majorana fermions, with N Majorana fermions on each of the left and right subsystems, corresponding to a total of N qubits. Each Majorana fermion in the Hamiltonian is encoded in a digital quantum processor via the standard Jordan-Wigner transformation to Pauli strings. Specifically, Majorana fermions are transformed to the form $\frac{1}{\sqrt{2}}Z^{\otimes k}X$ or $\frac{1}{\sqrt{2}}Z^{\otimes k}Y$ for $k \in [1, N]$. The choice of the mapping between each $\hat{\psi}^i_{L,R}$ and each Pauli string is optimized to minimize the required number of two-qubit gates to perform the wormhole teleportation protocol. We choose the Jordan-Wigner transformation as follows, where Z^i indicates $Z \otimes \cdots \otimes Z$,

$$\begin{aligned}
\hat{\psi}^1_L &= \tfrac{1}{\sqrt{2}}ZX, \quad \hat{\psi}^1_R = \tfrac{1}{\sqrt{2}}X, \\
\hat{\psi}^2_L &= \tfrac{1}{\sqrt{2}}ZY, \quad \hat{\psi}^2_R = \tfrac{1}{\sqrt{2}}Y, \\
\hat{\psi}^3_L &= \tfrac{1}{\sqrt{2}}Z^5X, \quad \hat{\psi}^3_R = \tfrac{1}{\sqrt{2}}Z^5Y, \\
\hat{\psi}^4_L &= \tfrac{1}{\sqrt{2}}Z^2X, \quad \hat{\psi}^4_R = \tfrac{1}{\sqrt{2}}Z^2Y, \\
\hat{\psi}^5_L &= \tfrac{1}{\sqrt{2}}Z^4X, \quad \hat{\psi}^5_R = \tfrac{1}{\sqrt{2}}Z^4Y, \\
\hat{\psi}^6_L &= \tfrac{1}{\sqrt{2}}Z^3X, \quad \hat{\psi}^6_R = \tfrac{1}{\sqrt{2}}Z^3Y, \\
\hat{\psi}^7_L &= \tfrac{1}{\sqrt{2}}Z^6X, \quad \hat{\psi}^7_R = \tfrac{1}{\sqrt{2}}Z^6Y.
\end{aligned} \tag{14.3}$$

The particular choice of $\hat{\psi}^1_R = \frac{1}{\sqrt{2}}X$, $\hat{\psi}^2_R = \frac{1}{\sqrt{2}}Y$, $\hat{\psi}^1_L = \frac{1}{\sqrt{2}}ZX$, $\hat{\psi}^2_L = \frac{1}{\sqrt{2}}ZY$ ensures that the decomposition of Majorana SWAP gates into two-qubit gates is efficient.

To swap a qubit into or out of the wormhole, we pair up Majorana fermions on a single qubit into a Dirac fermion $\hat{\chi} = \frac{1}{2}(Z^{\otimes k}X + iZ^{\otimes k}Y)$. The appropriate SWAP operator is given by,

$$\text{SWAP} = \begin{bmatrix} \hat{\chi}\hat{\chi}^\dagger & \hat{\chi}^\dagger \\ \hat{\chi} & \hat{\chi}^\dagger\hat{\chi} \end{bmatrix}. \tag{14.4}$$

To reduce the number of two-qubit gates, we restrict our attention to Jordan-Wigner transforms that only swap into or out of $X + iY$ and $ZX + iZY$. Explicitly, the SWAP operators for extracting a qubit from and inserting a qubit into the system, respectively, are given by,

$$\text{SWAP}_{X+iY} = \begin{bmatrix} 1 & 0 & 0 & 0 \\ 0 & 0 & 1 & 0 \\ 0 & 1 & 0 & 0 \\ 0 & 0 & 0 & 1 \end{bmatrix}, \tag{14.5}$$

$$\text{SWAP}_{ZX+iZY} = \begin{bmatrix} 1 & 0 & 0 & 0 & 0 & 0 & 0 & 0 \\ 0 & 0 & 1 & 0 & 0 & 0 & 0 & 0 \\ 0 & 1 & 0 & 0 & 0 & 0 & 0 & 0 \\ 0 & 0 & 0 & 1 & 0 & 0 & 0 & 0 \\ 0 & 0 & 0 & 0 & 1 & 0 & 0 & 0 \\ 0 & 0 & 0 & 0 & 0 & 0 & -1 & 0 \\ 0 & 0 & 0 & 0 & 0 & -1 & 0 & 0 \\ 0 & 0 & 0 & 0 & 0 & 0 & 0 & 1 \end{bmatrix}. \tag{14.6}$$

The gate decomposition of the swap operators is shown in Fig. 14.2. Since the $X+iY$ Majorana SWAP coincides with the standard SWAP given by Eq. 14.5, the final SWAP in the protocol from R to T (Fig. 14.1c) is replaced by direct measurement of the rightmost qubit of R to further reduce gate count. The $ZX + iZY$ SWAP operator for the initial SWAP of the protocol is decomposed into gates using the prescription in Ref. [22], which recursively decomposes an arbitrary unitary matrix into a product of fully-controlled quantum gates.

We proceed to the decomposition of the time evolution operator, $\hat{U}(t) = e^{-i(\hat{H}_L+\hat{H}_R)t}$, for the SYK model. We choose $q = 4$ and perform numerical simulations to identify sufficiently small N that could be experimentally implemented while preserving features of the gravitational physics. Our numerical simulation shows that $N = 10$ is sufficient to produce such traversable wormhole behavior (Fig. 14.3). When $\mu < 0$, mutual information is expected to peak around the scrambling time in the limit of

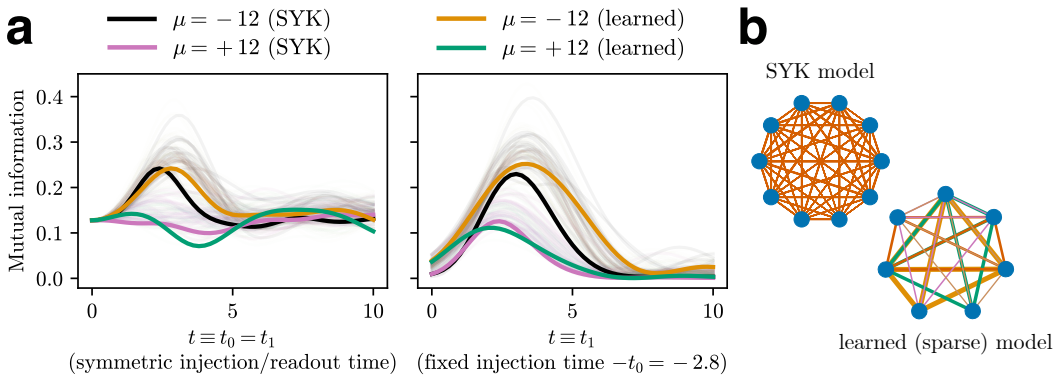

Figure 14.3: Learning a traversable wormhole Hamiltonian from the SYK model. a) Mutual information of multiple $N = 10$ SYK models (black and purple, $\beta = 4$) and corresponding learned Hamiltonians (orange and green) showing asymmetry in coupling with $\mu < 0$ (wormhole teleportation) and $\mu > 0$ (scrambling teleportation). Thick lines show a specific instantiation of an SYK model and its corresponding learned sparsification with 5 nonzero coefficients (Eq. 14.7); light lines indicate a population of SYK models and learned sparsifications with 5 to 10 nonzero coefficients, demonstrating the reliability of the learning procedure. The learned Hamiltonian is trained only on the mutual information $I_{PT}(t)$ for $t \equiv t_0 = t_1$ (left), and its behavior is consistent with the a wormhole after a qubit is injected at fixed $-t_0$ (right). b) Sparsification of the original SYK model with 210 nonzero coefficients (top) to the learned Hamiltonian with 5 nonzero coefficients (bottom, Eq. 14.7). Groups of four Majorana fermions (blue dots) are coupled with coefficients. Line thickness indicates coefficient magnitude, and color distinguishes individual coefficients (bottom only).

large N. The peaking behavior of $I_{PT}(t)$ may be observed in two ways: either by setting the injection and readout times to be symmetric ($t \equiv t_0 = t_1$), or by fixing the time of injection (fixed t_0) and measuring different readout times ($t \equiv t_1$). In the semiclassical gravity description, a pole in the causal left-right propagator corresponds to timelike geodesics connecting the left and right systems — i.e., a traversable wormhole in the bulk geometry [2]. Hence, we expect the teleportation signal to be maximized when $t_0 \approx t_1 \approx t_*$ for scrambling time t_*. We measure the corresponding peak signature in $I_{PT}(t)$ for both $t \equiv t_0 = t_1$ and $t \equiv t_1$ (fixed t_0). This result is reinforced by a theoretical analysis of chord diagrams in the double-scaled limit [23] and comparison to prior numerical results [24, 25, 26] (see Supplementary Information of Ref. [27]).

Nevertheless, the circuit depth $\sim O(N^4)$ to experimentally implement an $N = 10$ SYK system remains prohibitive on current hardware. We turn to sparsification of the SYK system and produce evidence of gravitational physics in the sparsified system. Sparsification of the SYK system (i.e., setting many $J_{j_1 \ldots j_4}$ to zero) is shown to preserve gravitational physics even when the number of terms in the Hamiltonian is randomly reduced from $O(N^4)$ to kN with k of order unity [28, 29, 30]. Here, we apply techniques from machine learning to optimize the sparsification procedure. The result reduces an $N = 10$ SYK model with 210 terms to an $N = 7$ model with 5 terms, yielding a 9-qubit circuit for the wormhole teleportation protocol. While larger Hamiltonians may provide a stronger teleportation signal, additional gates at current hardware fidelity further attenuate the signal (see Supplementary Information of Ref. [27]); hence, we restrict our attention to the smallest sparsified model with gravitational properties and do not enter the beyond-classical regime.

We construct an analogue of training a neural network. Due to unitarity and differentiability of the quantum circuit, backpropagation across the wormhole teleportation protocol allows gradient descent to optimize the $J_{j_1 \ldots j_4}$ coefficients with regularization, interpreting the Hamiltonian coefficients as neural network weights. The dataset consists of $I_{PT}(t)$ with $t \equiv t_0 = t_1$ for a standard wormhole constructed by the SYK model with Gaussian-distributed coefficients. The loss function is chosen to be the total mean squared error of $I_{PT}(t)$ for both positive and negative values of a fixed interaction coupling μ, where μ is chosen to maximize the mutual information. Training with weight regularization and truncation sparsifies the Hamiltonian while preserving mutual information dynamics.

Applying the learning process, we produce a large population of sparse Hamiltonians exhibiting the appropriate interaction sign dependence (Fig. 14.3a). We select the Hamiltonian,

$$\begin{aligned} \hat{H}_{L,R} = &- 0.36\hat{\psi}^1\hat{\psi}^2\hat{\psi}^4\hat{\psi}^5 + 0.19\hat{\psi}^1\hat{\psi}^3\hat{\psi}^4\hat{\psi}^7 \\ &- 0.71\hat{\psi}^1\hat{\psi}^3\hat{\psi}^5\hat{\psi}^6 + 0.22\hat{\psi}^2\hat{\psi}^3\hat{\psi}^4\hat{\psi}^6 \\ &+ 0.49\hat{\psi}^2\hat{\psi}^3\hat{\psi}^5\hat{\psi}^7, \end{aligned} \tag{14.7}$$

which requires 7 of the original $N = 10$ SYK model fermions, where $\hat{\psi}^j$ denotes the Majorana fermions of either the left or the right systems. Investigation of the sparse learned Hamiltonian in Eq. 14.7 and its description of gravitational physics are in Appendix F. We find that the Hamiltonian is consistent with gravitational dynamics of the dense SYK Hamiltonian beyond its training data and satisfies necessary

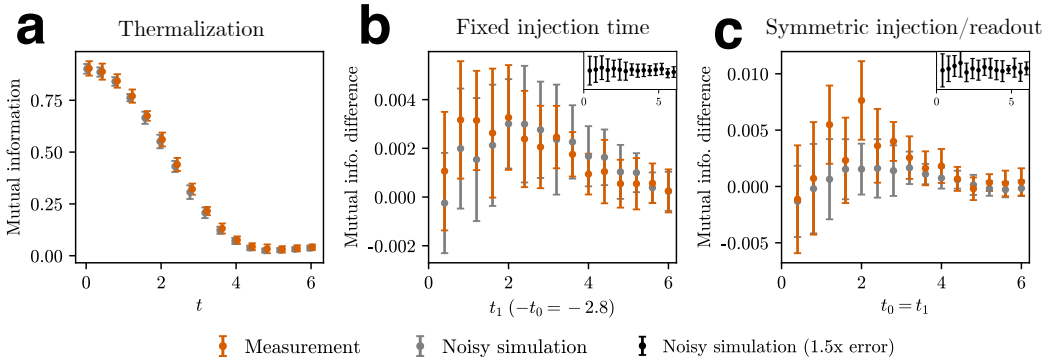

Figure 14.4: Observation of traversable wormhole dynamics. a) Thermalization protocol (109 CZ gates), measuring the mutual information between a qubit injected into a sparse SYK model at time $-t$ and at t. Error bars show three standard deviations over 20 runs. b) Traversable wormhole with fixed injection time (164 CZ gates), showing the difference in mutual information between $\mu = -12$ and $\mu = +12$. Error bars show one standard deviation over 28 runs. c) Traversable wormhole with symmetric injection and readout time (164 CZ gates), showing the difference in mutual information between $\mu = -12$ and $\mu = +12$. Error bars show one standard deviation over 20 runs. Insets show noisy simulations with gate errors increased by a factor of 1.5, plotted with y-axis mutual information range $[-3 \times 10^{-3}, 3 \times 10^{-3}]$; the peak is not visible. The measurements in b) and c) agree with noisy simulation and reproduce the sign asymmetry of the mutual information consistent with through-the-wormhole teleportation. The scrambling-unscrambling dynamics of wormhole teleportation cause the mutual information to be significantly attenuated by noise. In noisy simulations, each gate is subjected to depolarization error determined by calibration data (median CZ error: 0.3%). Each run consists of 90,000 measurements.

criteria of general holographic systems: perfect size winding, Shapiro time delay, and causally time-ordered teleportation [31, 32, 18].

We initialize the protocol of Fig. 14.1c by preparing the TFD state using a hardware-efficient variational quantum eigensolver [33] as the ground state of the Hamiltonian $\hat{H}_{\text{TFD}} = \hat{H}_L + \hat{H}_R + i\nu\hat{V}$ where $\hat{V}$ is the usual coupling operator. The ground state of $\hat{H}_{\text{TFD}}$ is approximately the thermofield double state with inverse temperature $O(1/\nu)$ [34, 35]. Time evolution and the interaction $e^{i\mu\hat{V}}$ are applied with a single Trotter step. This is sufficient to achieve a close approximation for the relevant range of t, i.e., the number of gates remains constant for all times.

14.4 Traversable wormhole dynamics on a quantum processor

Here, we proceed with a quantum experiment. Namely, we realize the entangled system on the Google Sycamore superconducting qubit array [36] with a 9-qubit circuit of 164 controlled-Z gates and 295 single-qubit gates. A noisy simulation assuming all gate errors are depolarizing noise agrees with the experimental measurement of the quantum system as shown in Fig. 14.4. A simpler protocol measuring thermalization with 109 CZ gates (Fig. 14.4a) demonstrates the high fidelity of the experiment; additional experiments with $\mu = 0$ confirm that coherent errors are dominated by the true teleportation signal (see Supplementary Information of Ref. [27]). Measuring the traversable wormhole protocol (Fig. 14.4b, c), we observe increased teleportation when the interaction introduces a negative energy shockwave rather than a positive one. The asymmetric signature is consistent with the physical interpretation that the qubit underwent teleportation through the wormhole. The scrambling-unscrambling dynamics of wormhole teleportation is sensitive to errors: at gate error rates larger than our experiment by a factor of 1.5, the asymmetric wormhole peak-like signal cannot be resolved (see Fig. 14.4 insets).

We find that the protocol is efficiently scalable to larger system sizes. To satisfy limitations of current quantum hardware, we adopted techniques from machine learning to construct a small-N sparse Hamiltonian that preserves gravitational physics. For systems with $N = O(50)$ fermions, random sparsification is as effective as optimal sparsification up to an order unity constant [28, 29, 30]. This removes the need for classical simulation without introducing significant overhead, successfully extending to the beyond-classical regime.

This work is the first successful attempt to investigate traversable wormhole dynamics in an experimental setting. Looking forward, we anticipate that near-term quantum computers that extend beyond the capabilities of classical simulation will coincide with system sizes that provide novel gravitational insight. At too large N, semiclassical gravity describes system dynamics; at too small N, relevant features may not be resolvable. In the regime of $N = O(100)$ fermions, measurement of inelastic effects in the bulk may provide quantitative insights into aspects of quantum gravity that are poorly understood from a theoretical perspective, such as string production and finite-N corrections to scattering. We conclude that the demonstrated approach of on-chip quantum experimentation of gravity promises future insights into the holographic correspondence.

References

[1] Ping Gao, Daniel Louis Jafferis, and Aron C Wall. "Traversable wormholes via a double trace deformation." In: Journal of High Energy Physics 2017.12 (2017), p. 151.

[2] Juan Maldacena, Douglas Stanford, and Zhenbin Yang. "Diving into traversable wormholes." In: Fortschritte der Physik 65.5 (2017), p. 1700034.

[3] J. Maldacena and L. Susskind. "Cool horizons for entangled black holes." In: Fortschritte der Physik 61.9 (2013), pp. 781–811. DOI: https://doi.org/10.1002/prop.201300020.

[4] Leonard Susskind. Dear Qubitzers, GR=QM. 2017. arXiv: 1708.03040 [hep-th].

[5] Juan Maldacena. "The large-N limit of superconformal field theories and supergravity." In: International journal of theoretical physics 38.4 (1999), pp. 1113–1133.

[6] David Hochberg and Matt Visser. "The Null energy condition in dynamic wormholes." In: Physical Review Letters 81 (1998), pp. 746–749. DOI: 10.1103/PhysRevLett.81.746. arXiv: gr-qc/9802048.

[7] M. S. Morris, K. S. Thorne, and U. Yurtsever. "Wormholes, Time Machines, and the Weak Energy Condition." In: Physical Review Letters 61 (1988), pp. 1446–1449. DOI: 10.1103/PhysRevLett.61.1446.

[8] Matt Visser, Sayan Kar, and Naresh Dadhich. "Traversable wormholes with arbitrarily small energy condition violations." In: Physical Review Letters 90 (2003), p. 201102. DOI: 10.1103/PhysRevLett.90.201102. arXiv: gr-qc/0301003.

[9] M. Visser. Lorentzian Wormholes: From Einstein to Hawking. Computational and Mathematical Physics. American Inst. of Physics, 1995. ISBN: 9781563963940.

[10] Noah Graham and Ken D. Olum. "Achronal averaged null energy condition." In: Physical Review D 76 (2007), p. 064001. DOI: 10.1103/PhysRevD.76.064001. arXiv: 0705.3193 [gr-qc].

[11] Juan Maldacena, Douglas Stanford, and Zhenbin Yang. "Conformal symmetry and its breaking in two dimensional Nearly Anti-de-Sitter space." In: PTEP 2016.12 (2016), p. 12C104. DOI: 10.1093/ptep/ptw124. arXiv: 1606.01857 [hep-th].

[12] Juan Maldacena. "Eternal black holes in anti-de Sitter." In: Journal of High Energy Physics 2003.04 (Apr. 2003), pp. 021–021. DOI: 10.1088/1126-6708/2003/04/021. URL: https://doi.org/10.1088/1126-6708/2003/04/021.

[13] Patrick Hayden and John Preskill. "Black holes as mirrors: quantum information in random subsystems." In: Journal of high energy physics 2007.09 (2007), p. 120.

[14] Leonard Susskind and Ying Zhao. "Teleportation through the wormhole." In: Physical Review D 98 (4 Aug. 2018), p. 046016. DOI: 10.1103/PhysRevD.98.046016. URL: https://link.aps.org/doi/10.1103/PhysRevD.98.046016.

[15] Ping Gao and Hong Liu. "Regenesis and quantum traversable wormholes." In: JHEP 10 (2019), p. 048. DOI: 10.1007/JHEP10(2019)048. arXiv: 1810.01444 [hep-th].

[16] Beni Yoshida and Norman Y. Yao. "Disentangling Scrambling and Decoherence via Quantum Teleportation." In: Physical Review X 9 (1 Jan. 2019), p. 011006. DOI: 10.1103/PhysRevX.9.011006. URL: https://link.aps.org/doi/10.1103/PhysRevX.9.011006.

[17] Kevin A. Landsman, Caroline Figgatt, Thomas Schuster, Norbert M. Linke, Beni Yoshida, Norm Y. Yao, and Christopher Monroe. "Verified quantum information scrambling." In: Nature 567.7746 (2019), pp. 61–65.

[18] Thomas Schuster, Bryce Kobrin, Ping Gao, Iris Cong, Emil T Khabiboulline, Norbert M Linke, Mikhail D Lukin, Christopher Monroe, Beni Yoshida, and Norman Y Yao. "Many-body quantum teleportation via operator spreading in the traversable wormhole protocol." In: Physical Review X 12.3 (2022), p. 031013.

[19] Subir Sachdev and Jinwu Ye. "Gapless spin-fluid ground state in a random quantum Heisenberg magnet." In: Physical Review Letters 70 (21 May 1993), pp. 3339–3342. DOI: 10.1103/PhysRevLett.70.3339. URL: https://link.aps.org/doi/10.1103/PhysRevLett.70.3339.

[20] Alexei Kitaev. "A simple model of quantum holography." In: KITP strings seminar and Entanglement. Vol. 12. 2015, p. 26.

[21] Ping Gao and Daniel Louis Jafferis. "A traversable wormhole teleportation protocol in the SYK model." In: Journal of High Energy Physics 2021.7 (2021), pp. 1–44.

[22] Chi-Kwong Li and Diane Pelejo. Decomposition of quantum gates. 2013. arXiv: 1311.3599 [quant-ph].

[23] Micha Berkooz, Mikhail Isachenkov, Vladimir Narovlansky, and Genis Torrents. "Towards a full solution of the large N double-scaled SYK model." In: JHEP 03 (2019), p. 079. DOI: 10.1007/JHEP03(2019)079. arXiv: 1811.02584 [hep-th].

[24] Jordan S. Cotler, Guy Gur-Ari, Masanori Hanada, Joseph Polchinski, Phil Saad, Stephen H. Shenker, Douglas Stanford, Alexandre Streicher, and Masaki Tezuka. "Black holes and random matrices." In: Journal of High Energy Physics 2017.5 (May 2017), p. 118. ISSN: 1029-8479. DOI: 10.1007/JHEP05(2017)118. URL: https://doi.org/10.1007/JHEP05(2017)118.

[25] Antonio M. García-García and Jacobus J. M. Verbaarschot. "Spectral and thermodynamic properties of the Sachdev-Ye-Kitaev model." In: Physical Review D 94 (12 2016), p. 126010. DOI: 10.1103/PhysRevD.94.126010. URL: https://link.aps.org/doi/10.1103/PhysRevD.94.126010.

[26] Antonio M. García-García and Jacobus J. M. Verbaarschot. "Analytical spectral density of the Sachdev-Ye-Kitaev model at finite N." In: Physical Review D 96 (6 Sept. 2017), p. 066012. DOI: 10.1103/PhysRevD.96.066012. URL: https://link.aps.org/doi/10.1103/PhysRevD.96.066012.

[27] Daniel Jafferis, Alexander Zlokapa, Joseph D. Lykken, David K. Kolchmeyer, Samantha I. Davis, Nikolai Lauk, Hartmut Neven, and Maria Spiropulu. "Traversable wormhole dynamics on a quantum processor." In: Nature 612.7938 (2022), pp. 51–55.

[28] Shenglong Xu, Leonard Susskind, Yuan Su, and Brian Swingle. A Sparse Model of Quantum Holography. 2020. arXiv: 2008.02303 [cond-mat.str-el].

[29] Antonio M. Garcia-Garcia, Yiyang Jia, Dario Rosa, and Jacobus J. M. Verbaarschot. "Sparse Sachdev-Ye-Kitaev model, quantum chaos, and gravity duals." In: Physical Review D 103 (10 2021), p. 106002. DOI: 10.1103/PhysRevD.103.106002. URL: https://link.aps.org/doi/10.1103/PhysRevD.103.106002.

[30] Elena Caceres, Anderson Misobuchi, and Rafael Pimentel. "Sparse SYK and traversable wormholes." In: JHEP 11 (2021), p. 015. DOI: 10.1007/JHEP11(2021)015. arXiv: 2108.08808 [hep-th].

[31] Adam R. Brown, Hrant Gharibyan, Stefan Leichenauer, Henry W. Lin, Sepehr Nezami, Grant Salton, Leonard Susskind, Brian Swingle, and Michael Walter. Quantum Gravity in the Lab: Teleportation by Size and Traversable Wormholes. 2021. arXiv: 1911.06314 [quant-ph].

[32] Sepehr Nezami, Henry W. Lin, Adam R. Brown, Hrant Gharibyan, Stefan Leichenauer, Grant Salton, Leonard Susskind, Brian Swingle, and Michael Walter. Quantum Gravity in the Lab: Teleportation by Size and Traversable Wormholes, Part II. 2021. arXiv: 2102.01064 [quant-ph].

[33] Abhinav Kandala, Antonio Mezzacapo, Kristan Temme, Maika Takita, Markus Brink, Jerry M Chow, and Jay M Gambetta. "Hardware-efficient variational quantum eigensolver for small molecules and quantum magnets." In: Nature 549.7671 (2017), pp. 242–246.

[34] Juan Maldacena and Xiao-Liang Qi. Eternal traversable wormhole. 2018. arXiv: 1804.00491 [hep-th].

[35] William Cottrell, Ben Freivogel, Diego M Hofman, and Sagar F Lokhande. "How to build the thermofield double state." In: Journal of High Energy Physics 2019.2 (2019), p. 58.

[36] Frank Arute, Kunal Arya, Ryan Babbush, et al. "Quantum supremacy using a programmable superconducting processor." In: Nature 574.7779 (Oct. 2019), pp. 505–510. ISSN: 1476-4687. DOI: 10.1038/s41586-019-1666-5. URL: https://doi.org/10.1038/s41586-019-1666-5.

Chapter 15

OUTLOOK

This chapter includes the work in preparation for publication:

[1] Samantha I. Davis, Joseph Lykken, Damian Musk, Neil Sinclair, and Maria Spiropulu. "Wormhole regenesis and Bell violations." In: Manuscript in preparation. (2025).

15.1 Future directions

Metropolitan quantum networks

For metropolitan-scale deployment of our quantum networking systems described in Part II, increasing entanglement distribution rates and minimizing noise will be crucial to maintain high fidelities and mitigate losses over extended fiber links. To this end, the entangled photon pair sources at CQNET and FQNET will be upgraded to the high-rate source described in Chapter 5, enabling long-distance quantum teleportation and entanglement swapping with GHz repetition rates. Additionally, the single-photon detectors can be upgraded with the low-jitter superconducting nanowire detectors from Chapters 3-5 to reduce multiphoton noise, which was identified our theoretical models in Chapter 9 as one of the main limitations for increasing the teleportation fidelities. Another experimental limitation was the phase stability of the interferometers used to implement projective measurements for X-basis teleportation and entanglement swapping. Incorporating low-jitter detectors enables the use of shorter time-bin separations, allowing time-bin qubits to be generated and measured using the compact, commercially available interferometers described in Chapter 5. These shorter interferometers offer improved mechanical and thermal stability, which translates into greater phase stability across measurement intervals. Furthermore, reducing the time-bin separation will enable higher repetition rates and lower mean photon numbers per pulse, which in turn improves the fidelity of both teleportation and swapping protocols by reducing multiphoton contributions and dark count error rates. By integrating the teleportation systems (Chapters 8 and 10) with the picosecond clock synchronization system described in Chapter 11, these upgrades will enable teleportation and entanglement swapping across multiple remote nodes in the Los Angeles and Chicago metropolitan regions.

Multipartite entanglement distribution

While many quantum network testbeds have demonstrated entanglement and quantum key distribution, few have reached the regime of multipartite entanglement protocols, particularly in a deployed metropolitan setting. The entanglement swapping system at FQNET can be upgraded to generate multipartite entanglement by replacing the beamsplitter used for the Bell state measurement with the two-by-two optical switch described in Chapter 13. By programming this switch and using the GUI from Chapter 10 for real-time post-selection and analysis, the system can dynamically toggle between configurations for entanglement swapping and multipartite entanglement generation. Using the time-bin entanglement approach described in Chapter 13, four-photon GHZ states can be generated by producing Bell pairs from Alice and Bob's sources and interfering one photon from each pair at the switch. Other multipartite entangled states, such as cluster states, can be generated by adjusting the phase settings on the switch. While cluster states are not maximally entangled, they have been shown to exhibit greater robustness to loss and noise compared to traditional maximally entangled states such as Bell or GHZ states [1]. Combined with the aforementioned upgrades for metropolitan teleportation and swapping, these upgrades will enable the first demonstrations of four-photon GHZ states using time-bin qubits and long-distance multiphoton entanglement distribution, allowing for advanced multi-party quantum communication protocols across the Chicago metropolitan region (see Fig. 15.1).

Distributed quantum sensing

Moreover, long-baseline quantum networks distributing multipartite entanglement could enable precision measurements for fundamental physics, including astronomical interferometry, gravitational wave detection, and atomic clock networks for dark matter searches [2]. With the aforementioned upgrades to FQNET, GHZ or cluster states can be distributed across multiple nodes at Fermilab for correlated measurements with precision sensors to achieve Heisenberg-limited sensitivities. Such entangled states are particularly powerful when all nodes are subject to a nearly uniform field, as expected in scenarios involving ultralight dark matter or spacetime fluctuations, enabling common-mode noise suppression and enhanced detection capability. This system can be integrated with quantum sensors under development at Fermilab, such as the atom interferometers of the MAGIS experiment [3] and the dark matter haloscopes of the BREAD experiment [4], to search for transient variations in fundamental constants and gravitational wave signatures,

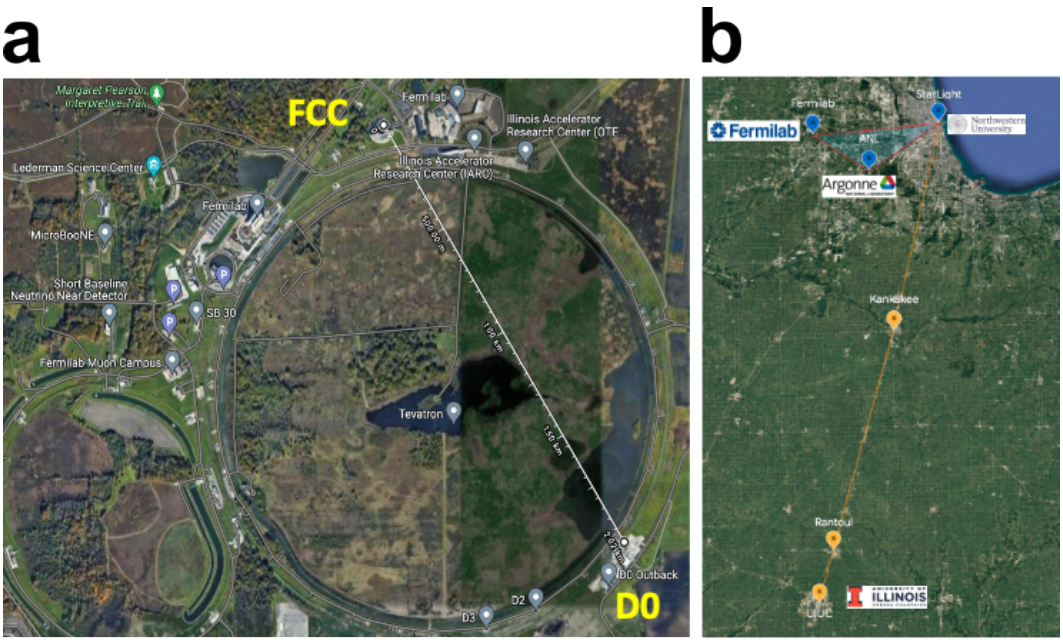

Figure 15.1: Future quantum networking between labs on the a) Fermi National Accelerator Laboratory (Fermilab) campus and b) in the Chicago metropolitan region with upgrades to the entanglement swapping system from Chapter 10.

which could reveal new physics beyond the Standard Model.

Scaling up the wormhole

In the large-N and low-temperature limit, the traversable wormhole protocol in the SYK model can approach near-unity teleportation fidelities [5]. To access higher-fidelity regimes and probe dynamics beyond the reach of classical simulation, it is necessary to scale up the system size while maintaining low circuit error rates. This requires the design of protocols tailored for larger, more complex instances that can be embedded in next-generation quantum processors. The primary technical challenge remains the high circuit depth, which introduces noise that degrades teleportation fidelity. To address this, the noise model in Chapter 14 can be used to guide circuit design, enabling simulation-driven refinements that minimize noise impact. Other directions include extending the original wormhole protocol to alternative models, such as bosonic versions of SYK, which may support larger system embeddings or implementation on different quantum platforms. For example, our recent development of a long-range wormhole teleportation protocol [6] based on a bosonic SYK model could be adapted to photonic implementations, for instance using squeezing, photon-number-resolving detectors, and programmable photonic

circuits. This could open avenues to distributed simulation over quantum networks (see Fig. 15.2) and tests of ER=EPR, as described in the next section.

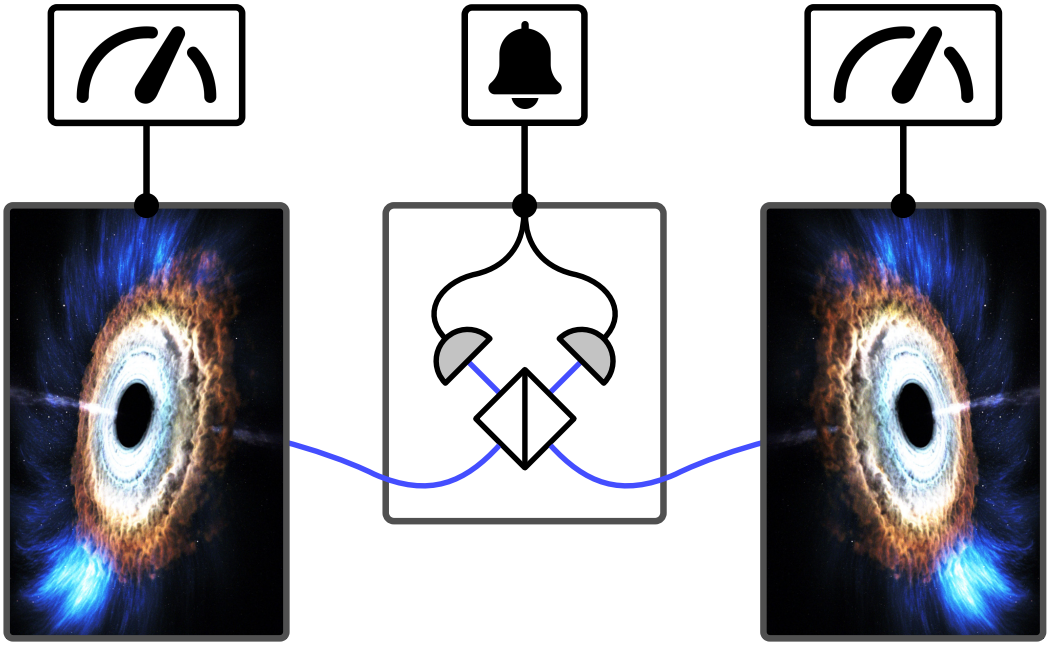

Figure 15.2: Conceptual diagram of distributed quantum simulation of wormholes in a quantum network. Image credits to NASA's Conceptual Image Lab and FlatIcon.com.

Bell tests for quantum gravity

The quest for a theory of quantum gravity remains one of the most profound and unresolved challenges in fundamental physics. In quantum mechanics, Bell inequality violations characterize nonlocal quantum correlations and provide a powerful diagnostic tool for distinguishing classical from quantum theories. One can envision developing Bell tests that probe the quantum or classical nature of gravity itself. The AdS/CFT correspondence offers a compelling setting to explore this concept, due to its tractable models and the connection between wormholes and entanglement in the context of the ER=EPR conjecture.

In the traversable wormhole setup, the gravitational dual of quantum teleportation is understood as a real-time, dynamical process in which a qubit appears to pass through the ER=EPR wormhole connecting the two entangled boundary CFTs, L and R. The wormhole becomes traversable through a specific interaction between the two boundaries, allowing this passage to occur. A striking aspect of this process is that the qubit seems to sent via the entanglement itself, rather than being transmitted directly

by the inter-boundary coupling. This differs from the standard quantum teleportation protocol, where a classical channel is used to complete the transmission. In the traversable wormhole case, it is crucial the channel between L and R is a quantum one. In the standard picture of quantum teleportation, Alice performs a measurement that projects the system onto an eigenstate, which immediately imprints Alice's qubit into Bob's system and supports transmission via classical communication. In contrast, for the traversable wormhole setup, the qubit is not projected out of the system but instead undergoes continuous, unitary dynamics, making it possible to interpret the process as the qubit traversing the bulk [7].

In Section 15.2, I propose a Bell inequality tailored for traversable wormholes that probes the non-classicality of the quantum channel activated through the Einstein–Rosen bridge. Specifically, I formulate a CHSH-type Bell inequality for correlated signals emerging at the left and right boundaries of the traversable wormhole channel, where the measurement settings correspond to spacetime translations and the expectation values map onto out-of-time-order correlators (OTOCs).

15.2 A Bell inequality for traversable wormholes

In the canonical Bell test, often formulated via the Clauser-Horne-Shimony-Holt (CHSH), [8], two distant observers (Alice and Bob) perform measurements of dichotomic variables on spatially separated subsystems (A and B) and evaluate the correlator $E(a,b) = \langle \hat{J}_A(a)\hat{J}_B(b)\rangle$, where $\hat{J}(a)$ represents a dichotomic observable[1] (e.g., spin) with a labeling the measurement apparatus setting (e.g., polarizer angle). Under the assumptions of realism and locality, the CHSH inequality,

$$S = E(a,b) + E(a,b') + E(a',b) - E(a',b') \leq 2, \tag{15.1}$$

must be satisfied. Quantum entanglement, however, can violate this bound, with a maximum quantum value of $S = 2\sqrt{2}$ for maximally entangled subsystems. Measurement settings are varied independently and the resulting correlations are compared against classical bounds. This class of inequality assumes realism—the idea that outcomes reflect pre-existing properties—and locality—the prohibition of faster-than-light influence between space-like separated events.

A more general class of Bell tests, referred to as bipartite temporal Bell tests, was first envisioned by Bell himself [9]. These tests involve both spatial and temporal separation, where a pair of entangled systems are measured at different locations and

[1] A dichotomic observable ($\hat{J}$) is an operator with two eigenvalues, i.e., measurement outcomes, and satisfies $\hat{J}^2 = \hat{\mathbb{I}}$.

at different times. For example, Alice may measure subsystem L at times t_a and t'_a, while Bob measures subsystem R at t_b and t'_b, with the two measurement sequences causally disconnected. This type of Bell test is particularly well-suited for probing the quantum channel that is opened in the traversable wormhole configuration, where the two subsystems are causally disconnected on opposite ends of the wormhole, and a qubit appears at different times on the left and right boundaries. The presence of a qubit, or more generally, a "signal" corresponding to the source of an operator $\hat{J}$, is characterized by expectation values on the left and right boundaries.

Regenesis

The traversable wormhole mechanism can be understood in the holographic description as a "regenesis" phenomenon universal to quantum chaotic many-body systems [10]. We consider the setup of Ref. [10], where two identical subsystems L and R with Hamiltonians $\hat{H}_L$ and $\hat{H}_R$, which have the same set of eigenvalues E_n and energy eigenstates $|n\rangle_L$ and $|n\rangle_R$, are prepared in a thermofield double state (TFD) at time $t = 0$,

$$\left|\Psi_\beta\right\rangle = \frac{1}{Z_\beta}\sum_n e^{-\frac{\beta E_n}{2}}\left|\bar{n}\right\rangle_L\left|n\right\rangle_R, \qquad Z_\beta = \sum_n e^{-\beta E_n}, \tag{15.2}$$

where $|\bar{n}\rangle$ is the time reversal of the energy eigenstate $|n\rangle$. The TFD has the property,

$$\left(\hat{H}^L - \hat{H}^R\right)\left|\Psi_\beta\right\rangle = 0, \quad \rightarrow \quad e^{-i\hat{H}^L t}\left|\Psi_\beta\right\rangle = e^{-i\hat{H}^R t}\left|\Psi_\beta\right\rangle; \tag{15.3}$$

if one of the subsystems is traced out, the remaining subsystem is described by the thermal state at inverse temperature β. A source φ^L is turned on in the left subsystem for a few-body operator $\hat{J}^L$ at some time $t = -t_s < 0$. Operating the Heisenberg picture, $\hat{J}^L(t) = \hat{U}(t)^\dagger \hat{J}^L \hat{U}(t)$, where $\hat{U}(t) = e^{-i(\hat{H}_L+\hat{H}_R)t}$ is the time evolution operator. In the left subsystem, there is a response $\langle \hat{J}^L(t)\rangle \equiv \left\langle\Psi_\beta\right|\hat{J}^L(t)\left|\Psi_\beta\right\rangle$ induced by the source, which quickly dissipates after the source is turned off, and in the right subsystem there is no response $\left\langle\Psi_\beta\right|\hat{J}^R(t)\left|\Psi_\beta\right\rangle = 0$, since $[\hat{J}^L, \hat{J}^R] = 0$.

Next, we consider coupling the subsystems at time $t = 0$. The total Hamiltonian is,

$$\hat{H}_\mu = \hat{H} - \mu\hat{V}\delta(t = 0), \tag{15.4}$$

where $\hat{H} = \hat{H}_L + \hat{H}_R$, μ is the coupling, and $\hat{V}$ is an operator acting on both subsystems,

$$\hat{V} = \frac{1}{k}\sum_{j=1}^{k}\hat{O}_j^L(0)\hat{O}_j^R(0), \tag{15.5}$$

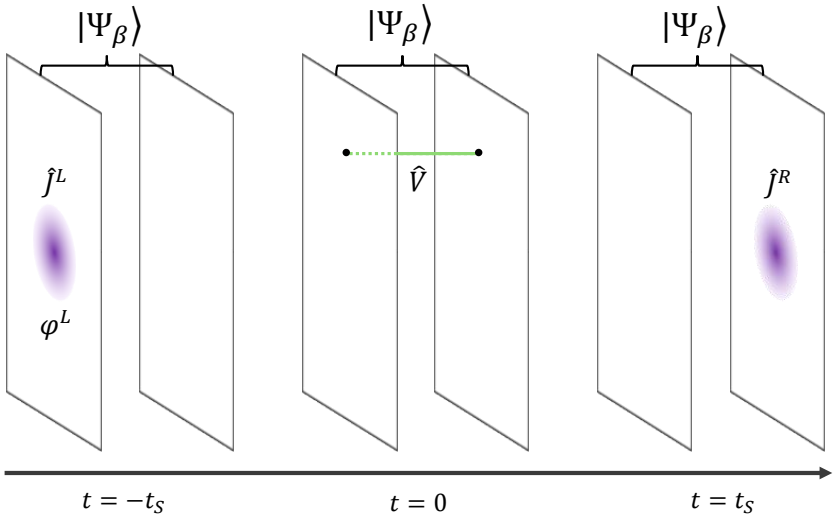

Figure 15.3: Signal regenesis in a many-body quantum-chaotic system. Two subsystems (L and L) are prepared in a thermofield double state $|\Psi_\beta\rangle$ at $t = 0$. A source φ^L is turned on in the left subsystem for a few-body operator $\hat{J}^L$ at some time $t = -t_s < 0$. In the left subsystem, there is a response induced by the source, which dissipates after the source is turned off. At $t = 0$, a coupling is introduced, where $\hat{V}$ is an operator acting on both subsystems. At a later time $t = t_s$, a signal will reappear on the right subsystem if $t_s \sim t_*$ is on the order of the scrambling time (t_*) of the system.

where j denotes different operator species and $\hat{O}(x)$ is some few-body operator. The result is that a signal will reappear in the right system at times on the order of the scrambling time, t_*, if $t_s > t_*$, see Fig. 15.3.

Bipartite temporal Bell inequality

In the regenesis setup, we consider operators $\hat{J}^L(t_L)$ and $\hat{J}^R(t_R)$ acting at fixed spatial coordinates $\vec{x}_L = 0$ and $\vec{x}_R = 0$ and times t_L and t_R on the L and R subsystems, respectively. Working in the Heisenberg picture,

$$\hat{J}^L(t_L) = \hat{U}^\dagger(t_L)\hat{J}^L\hat{U}(t_L), \qquad \hat{J}^R(t_R) = \hat{U}^\dagger(t_R)\hat{J}^R\hat{U}(t_R), \tag{15.6}$$

where $\hat{J}^L$ and $\hat{J}^R$ are the same operators but acting on the L and R subystem, respectively, and $\hat{U}(t) = e^{-i\hat{H}_\mu t}$ is the time evolution operator in terms of the total Hamiltonian $\hat{H}_\mu$ in Eq. 15.4,

$$\hat{U}(t) = \begin{cases} e^{-i\hat{H}t} & t < 0 \\ e^{-i\hat{H}t}e^{i\mu\hat{V}} & t > 0. \end{cases} \tag{15.7}$$

Although $\hat{J}^L$ and $\hat{J}^R$ commute, $\hat{J}^L(t_L)$ and $\hat{J}^R(t_R)$ need not commute; therefore, $\hat{J}^L(t_L)\hat{J}^R(t_R)$ is not generally Hermitian and its expectation value can yield imaginary values. Instead, expectation values must be defined in terms of projective measurements of a dichotomic observable. For the dichotomic observable $\hat{J}(t)$ with ± 1 measurement outcomes, the projection operator onto the $+1$ and -1 eigenspaces are given by,

$$\hat{P}_+ = \frac{1}{2}(1 + \hat{J}(t)), \qquad \hat{P}_- = \frac{1}{2}(1 - \hat{J}(t)). \tag{15.8}$$

From the Born rule, the joint probability for Alice to measure outcome $l = \pm 1$ on the L subsystem and Bob to measure outcome $r = \pm 1$ on the R subsystem is,

$$P(l, r) = \left\langle \Psi_\beta \right| \hat{P}_l^L \hat{P}_r^R \hat{P}_l^L \left| \Psi_\beta \right\rangle . \tag{15.9}$$

The expectation value for the joint projective measurement is,

$$E(t_L, t_R) = \sum_{l,r} lrP(l, r) = \frac{1}{2} \left\langle \Psi_\beta \right| \{\hat{J}^L(t_L), \hat{J}^R(t_R)\} \left| \Psi_\beta \right\rangle , \tag{15.10}$$

where $\{\hat{J}^L(t_L), \hat{J}^R(t_R)\}$ is the anticommutator of $\hat{J}^L(t_L)$ and $\hat{J}^R(t_R)$. Thus, the expectation values can be computed in terms of the out-of-time correlators of the many-body system.

Plugging into the CHSH inequality under the assumptions of realism and locality,

$$\begin{aligned} S = &\frac{1}{2} \left\langle \Psi_\beta \right| \{\hat{J}^L(t_L), \hat{J}^R(t_R)\} \left| \Psi_\beta \right\rangle + \frac{1}{2} \left\langle \Psi_\beta \right| \{\hat{J}^L(t_L), \hat{J}^R(t'_R)\} \left| \Psi_\beta \right\rangle \\ &+ \frac{1}{2} \left\langle \Psi_\beta \right| \{\hat{J}^L(t'_L), \hat{J}^R(t_R)\} \left| \Psi_\beta \right\rangle - \frac{1}{2} \left\langle \Psi_\beta \right| \{\hat{J}^L(t'_L), \hat{J}^R(t'_R)\} \left| \Psi_\beta \right\rangle \leq 2. \end{aligned} \tag{15.11}$$

For the traversable wormhole setup in the SYK model, the Majorana operators $\hat{\psi}_L, \hat{\psi}_R$ are dichotomic operators with expectation values $\pm 1/\sqrt{2}$ (see Chapter 14). Choosing a Majorana from each subystem, we construct the dichotomic operators $\hat{J}_L = \sqrt{2}\hat{\psi}_L$ and $\hat{J}_R = \sqrt{2}\hat{\psi}_R$ with eigenvalues ± 1. For the Bell test, the relevant times for probing the traversable wormhole dynamics are $-t_L \sim -t_*$ and $t_R \sim t_*$. The expectation value becomes,

$$E(-t_L, t_R) = \left\langle \Psi_\beta \right| \{\hat{\psi}_L(-t_L), \hat{\psi}_R(t_R)\} \left| \Psi_\beta \right\rangle = -\mathcal{K}(-t_L, t_R), \tag{15.12}$$

where $\mathcal{K}(-t_L, t_R)$ is the OTOC investigated in Ref. [5]. Since $\mathcal{K}(-t_L, t_R) = 0$ for $\mu = 0$, $S = 0$, so the non-traversable wormhole configuration does not violate the Bell inequality in Eq. 15.11. For nonzero μ, S can violate Eq. 15.11, where Sapproaches $2\sqrt{2}$ when $\mathcal{K} \approx 1$, corresponding to maximal teleportation fidelity [5].

Discussion

In the Bell test I described above, projective measurements of dichotomic observables are performed on the CFTs to test the nonclassicality of the traversable wormhole channel. I anticipate that such Bell tests could be used to operationally verify the existence and make statements about the local-realistic nature of the wormhole. It would be interesting to identify the corresponding hidden-variable theory that is violated for high teleportation fidelities and understand the implications of Bell violations in the gravitational picture.

References

[1] Xiao-Qi Zhou, Chao-Yang Lu, Wei-Bo Gao, Jin Zhang, Zeng-Bing Chen, Tao Yang, and Jian-Wei Pan. "Greenberger-Horne-Zeilinger-type violation of local realism by mixed states." In: Physical Review A 78.1 (2008), p. 012112.

[2] Andrei Derevianko, Eden Figueroa, Inder Monga, Andrei Nomerotski, Nicholas Peters, Raphael Pooser, Nageswara Rao, Anze Slosar, Panagiotis Spentzouris, Maria Spiropulu, et al. Quantum Networks for High Energy Physics (HEP). Tech. rep. Oak Ridge National Laboratory (ORNL), Oak Ridge, TN (United States), 2022.

[3] Mahiro Abe, Philip Adamson, Marcel Borcean, Daniela Bortoletto, Kieran Bridges, Samuel P Carman, Swapan Chattopadhyay, Jonathon Coleman, Noah M Curfman, Kenneth DeRose, et al. "Matter-wave atomic gradiometer interferometric sensor (MAGIS-100)." In: Quantum Science and Technology 6.4 (2021), p. 044003.

[4] Stefan Knirck, Gabe Hoshino, Mohamed H. Awida, Gustavo I. Cancelo, Martin Di Federico, Benjamin Knepper, Alex Lapuente, Mira Littmann, David W. Miller, Donald V. Mitchell, et al. "First results from a broadband search for dark photon dark matter in the 44 to 52 μ eV range with a coaxial dish antenna." In: Physical Review Letters 132.13 (2024), p. 131004.

[5] Ping Gao and Daniel Louis Jafferis. "A traversable wormhole teleportation protocol in the SYK model." In: Journal of High Energy Physics 2021.7 (2021), pp. 1–44.

[6] Joseph D. Lykken, Daniel Jafferis, Alexander Zlokapa, David K. Kolchmeyer, Samantha I. Davis, Hartmut Neven, and Maria Spiropulu. "Long-range wormhole teleportation." In: arXiv preprint arXiv:2405.07876 (2024).

[7] Ping Gao, Daniel Louis Jafferis, and Aron C Wall. "Traversable wormholes via a double trace deformation." In: Journal of High Energy Physics 2017.12 (2017), p. 151.

[8] John F. Clauser, Michael A. Horne, Abner Shimony, and Richard A. Holt. "Proposed Experiment to Test Local Hidden-Variable Theories." In: Phys. Rev. Lett. 23 (15 Oct. 1969), pp. 880–884. DOI: 10.1103/PhysRevLett.23.880.

[9] John S. Bell. "EPR correlations and EPW distributions." In: Ann. NY Acad. Sci 480.1 (1986), pp. 263–266.

[10] Ping Gao and Hong Liu. “Regenesis and quantum traversable wormholes.” In: Journal of High Energy Physics 2019.10 (2019), pp. 1–60.

Part IV

Appendices

Appendix A

QUANTUM PHASED ARRAY PROTOCOLS

Here I describe two illustrative examples of quantum state synthesis with QPAs.

A.1 Reconfigurable beamsplitter

With two QPAs engineered to have the input and output relations of a beamsplitter unitary, a reconfigurable beamsplitter can realized for applications requiring quantum interference. The QPAs are configured to have array factors,

$$\mathrm{AF}_N^{\pm} = \frac{1}{\sqrt{2}}\left(\mathrm{AF}_N(\varphi^A) + e^{i(\delta\pm\pi)}\mathrm{AF}_N(\varphi^B)\right), \tag{A.1}$$

one with (+) and the other with (−). The fields interfere in free space to realize quantum interference with the beamsplitter unitary. A hallmark quantum interference effect is Hong-Ou-Mandel effect [1]. The Hong-Ou-Mandel effect arises from the interference of indistinguishable single photons incident to a beamsplitter.

$$\begin{aligned} |1\rangle_{\mathrm{in}_1}|1\rangle_{\mathrm{in}_2} &= \hat{a}^\dagger_{\mathrm{in}_1}\hat{a}^\dagger_{\mathrm{in}_2}|0\rangle_{\mathrm{in}_1}|0\rangle_{\mathrm{in}_2} \\ &\rightarrow \frac{1}{2}(\hat{a}^\dagger_{\mathrm{out}_1} + i\hat{a}^\dagger_{\mathrm{out}_2})(i\hat{a}^\dagger_{\mathrm{out}_1} + \hat{a}^\dagger_{\mathrm{out}_2})|0\rangle_{\mathrm{out}_1}|0\rangle_{\mathrm{out}_2} \\ &= \frac{i}{\sqrt{2}}\left(|2\rangle_{\mathrm{out}_1}|0\rangle_{\mathrm{out}_2} + |0\rangle_{\mathrm{out}_1}|2\rangle_{\mathrm{out}_2}\right). \end{aligned} \tag{A.2}$$

A.2 N00N state generation

HOM interference can be generalized to create N00N states for any $N = 2^k$. N00N states are path entangled states of the form $(|N\rangle|0\rangle + |0\rangle|N\rangle)/\sqrt{2}$ that enable quantum-enhanced phase measurements at the Heisenberg limit, with applications in quantum metrology, imaging, and lithography [2, 3, 4]. The creation operator representation of a N00N state can be factorized as,

$$\frac{1}{\sqrt{2}}(\hat{a}_1^\dagger)^N + e^{i\theta}(\hat{a}_2^\dagger)^N = \frac{1}{2}\prod_{\pm}(\hat{a}_1^\dagger)^{N/2} + e^{i\left(\frac{\theta}{2}+\pi\pm\frac{\pi}{2}\right)}(\hat{a}_2^\dagger)^{N/2}. \tag{A.3}$$

The goal is to factorize the N00N creation operator representation into products of N single creation operator superpositions,

$$\frac{1}{\sqrt{2}}\left((\hat{a}_1^\dagger)^N + e^{i\theta}(\hat{a}_2^\dagger)^N\right) = \frac{1}{2^{N/2}}\prod_{\varphi}(\hat{a}_1^\dagger + e^{i\varphi}\hat{a}_2^\dagger). \tag{A.4}$$

We can determine what the set of φ are from recursively applying Eq. A.3. For $N = 2^k$, we find:

$$\varphi = \frac{\theta}{2^k} + \sum_{j=1}^{k} \frac{\pi}{2^{k-j}} \pm \frac{\pi}{2} \pm \frac{\pi}{4} \pm ... \pm \frac{\pi}{2^k} \tag{A.5}$$

$$= \left(\frac{\theta}{2^k} + 2\pi - \frac{\pi}{2^{k-1}} \right) \pm \frac{\pi}{2} \pm \frac{\pi}{4} \pm ... \pm \frac{\pi}{2^k}. \tag{A.6}$$

Let Φ be the set of φ. Note that the k terms with $\pm$ mean that there are a total of 2^k φ's (i.e. $|\Phi| = 2^k$) as expected. Therefore, a N00N state can be created using a multimode interferometer with N inputs and 2 outputs, where the each input sends a single photon into $\frac{1}{\sqrt{2}}(a^\dagger_{\text{out}_1} + e^{i\phi}\hat{a}^\dagger_{\text{out}_2})$ for each $\phi \in \Phi$.

This protocol can be flexibly performed this protocol[1] using N QPA's, where each QPA sends a single photon into $\frac{1}{\sqrt{2}}(\hat{a}^\dagger_{\theta_1} + e^{i\phi}\hat{a}^\dagger_{\theta_2})$, and then align the θ_1, θ_2's of all the QPA's on the detector plane.

References

[1] C. K. Hong, Z. Y. Ou, and L. Mandel. "Measurement of Subpicosecond Time Intervals between Two Photons by Interference." In: Physical Review Letters 59.18 (1987), pp. 2044–2046. DOI: 10.1103/PhysRevLett.59.2044.

[2] Jonathan P. Dowling. "Quantum optical metrology – the lowdown on high-N00N states." In: Contemporary Physics 49.2 (2008), pp. 125–143. DOI: 10.1080/00107510802091298.

[3] V. Giovannetti, S. Lloyd, and L. Maccone. "Quantum-Enhanced Measurements: Beating the Standard Quantum Limit." In: Science 306.5700 (2004), pp. 1330–1336. DOI: 10.1126/science.1104149.

[4] M. W. Mitchell, J. S. Lundeen, and A. M. Steinberg. "Super-resolving phase measurements with a multiphoton entangled state." In: Nature 429 (2004), pp. 161–164. DOI: 10.1038/nature02493.

[5] Pieter Kok, Hwang Lee, and Jonathan P. Dowling. "Creation of large-photon-number path entanglement conditioned on photodetection." In: Phys. Rev. A 65 (5 Apr. 2002), p. 052104. DOI: 10.1103/PhysRevA.65.052104. URL: https://link.aps.org/doi/10.1103/PhysRevA.65.052104.

[1] This protocol was independently derived by Ref. [5]. Here I considered the even case of $N = 2^k$.

Appendix B

STATISTICAL ANALYSIS OF SQUEEZING

Here I describe the analytical methods we used to estimate the amount of squeezing measured with the on-chip balanced homodyne detectors in Chapters 2 and 6. First, I summarize common techniques for the measurement and analysis of squeezed light. I then motivate a statistical approach to the analysis of squeezed light. I introduce a statistical estimator for squeezing and antisqueezing levels that is robust to noise. I validate this estimator by developing a theoretical model, conducting experimental tests with a fiber-optic setup, and performing numerical simulations over the range of efficiency and squeezing parameters used in the on-chip squeezing experiments.

B.1 Background

Balanced homodyne detection is a standard measurement technique for the characterization of squeezed light [1]. A typical setup for the measurement of squeezed light is shown in Fig. B.1, where the signal at the output of balanced homodyne detector is proportional to the quadrature of the input optical field. There are two common approaches to the analysis of squeezing with balanced homodyne detection [1]. In the time-domain approach, output current or voltage statistics are accumulated over time with a time-resolving device, such as an oscilloscope, and quadrature statistics of the optical field are calculated in post-processing. In the frequency-domain approach, the output noise power spectrum is measured with an electronic spectrum analyzer, providing a direct measurement of a signal proportional to the quadrature variance of the optical field.

Squeezing can be characterized in the time-domain approach by acquiring quadrature samples for known phases over many rotations and performing quantum state tomography [2]. With optical homodyne tomography [3], the Wigner function of the squeezed state can be estimated by applying a reconstruction algorithm such as an inverse Radon transformation, maximum-entropy reconstruction, or maximum-likelihood estimation to time-domain data [4]. The squeezing and antisqueezing levels can be estimated by comparing the reconstructed Wigner function of the squeezed state to that of the vacuum state. In particular, the squeezing parameter and efficiency can be found from a fit to the Wigner function of the squeezed state [5]. However, these approaches are computationally intensive and depend on assump-

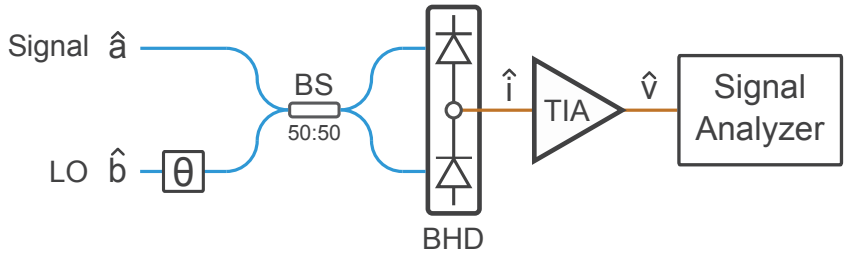

Figure B.1: Measurement of squeezed light with balanced homodyne detection. Squeezed light (signal) is interfered with strong local oscillator (LO) in a coherent state by a 50:50 beamsplitter (BS). A phase shifter on the LO controls the relative phase (θ) of the signal and LO. The mixed fields are detected with a balanced homodyne detector (BHD). The output current is amplified by a transimpedance amplifier (TIA), and the output voltage is sent to a signal analyzer, such as an oscilloscope or electronic spectrum analyzer.

tions in the reconstruction algorithm. While detection efficiency can be corrected for by means of an inverse Bernoulli transform [6], performance of such algorithms suffer for high detection loss. Moreover, numerical artifacts such as ripples in the reconstructed Wigner functions can obscure the squeezing level estimation [7].

With data measured in the time or spectral domain, squeezing and antisqueezing levels can be estimated from the minima and maxima of the normalized quadrature variances relative to the shot noise level. By fixing the relative phase between the LO and signal, sample quadrature variances in the time-domain approach or noise powers in the frequency-domain approach can be averaged over time to obtain squeezing or antisqueezing level estimates [1, 8]. Phase noise from stochastic phase fluctuations introduced in the measurement setup or imperfect phase-locking can result in averaging over various quadrature phases over the measurement time, which degrades the accuracy of squeezing estimation [9]. Alternatively, by modulating the phase of the LO, peak search methods may be applied to extract the squeezing levels [10, 5]. However, peak-searching methods are known to introduce statistical bias in the presence of noise, which can can skew the estimation of squeezing and antisqueezing levels in the presence of experimental noise sources [11, 12].

Here I introduce a method for the estimation of squeezing based on the probability density function of the quadrature sample variances. In Section B.2, I review balanced homodyne detection of squeezed light. I illustrate the observation of squeezing in both approaches by performing numerical simulations of squeezing in

the time-domain approach and experimental detection of squeezing in the frequency domain approach. In Section B.3, I develop a theoretical model for the probability density function of squeezed quadrature variances over a uniform phase distribution that accounts for sampling noise. In Section B.4, I demonstrate how the inflection points of the probability distribution of quadrature sample variances can be used as estimators of squeezing and antisqueezing. This approach allows for the estimation of squeezing without phase locking, in the presence of experimental noise sources such as phase and sampling noise. I then illustrate this method with numerical simulations and experimental measurements of squeezed light. This method is suitable for estimating squeezing levels comparable to the distribution of shot noise powers, relevant in the limit of low squeezing strength and high measurement loss.

B.2 Measurement of squeezing

Balanced homodyne detection

In balanced homodyne detection, squeezed light is mixed with a strong local oscillator and sent to a balanced homodyne detector (BHD). The output signal is a current or voltage proportional to the phase-dependent quadrature, $\hat{Q}_\theta$, of the signal field,

$$\hat{v}(\theta) \propto \beta \hat{Q}_\theta, \tag{B.1}$$

where the quadrature angle, θ, is the relative phase of the LO and the signal, β is the LO amplitude, and

$$\hat{Q}_\theta = \frac{1}{\sqrt{2}}(\hat{a}e^{-i\theta} + \hat{a}^\dagger e^{i\theta}) = \hat{Q}\cos\theta + \hat{P}\sin\theta, \tag{B.2}$$

where $\hat{a}$ is the signal field and $\hat{Q}$ and $\hat{P}$ are the canonical quadrature observables satisfying $[\hat{Q}, \hat{P}] = i$ [1, 13].

The output signal is sent to a signal analyzer that measures the time or frequency response of the voltages. Each voltage corresponds to a quadrature observable Q_θ, the eigenvalue of $\hat{Q}_\theta$ with eigenstate $|Q_\theta\rangle$. For a signal field in a Gaussian state $|\psi\rangle$, such as a vacuum, thermal, or squeezed state [14, 13], the quadrature observables are normally distributed according to,

$$|\psi(Q_\theta)|^2 = \frac{1}{\sqrt{2\pi}\langle\Delta\hat{Q}_\theta^2\rangle} \exp\left(-\frac{\left(Q_\theta - \langle\hat{Q}_\theta\rangle\right)^2}{2\langle\Delta\hat{Q}_\theta^2\rangle}\right) \tag{B.3}$$

where $\psi(Q_\theta) = \langle Q_\theta|\psi\rangle$ is the wavefunction in the phase quadrature basis, $\langle\hat{Q}_\theta\rangle = \langle\psi|\hat{Q}_\theta|\psi\rangle$ is the quadrature mean and $\langle\Delta\hat{Q}_\theta^2\rangle = \langle\psi|\Delta\hat{Q}_\theta^2|\psi\rangle$ is the quadrature variance.

For a field in a vacuum state, $\langle \hat{Q}_\theta \rangle = 0$ and $\langle \Delta \hat{Q}_\theta^2 \rangle = 1/2$. For a field in a squeezed state, the quadrature variance is given by,

$$\langle \Delta \hat{Q}_\theta^2 \rangle_{\text{sq}} = \frac{1}{2}(e^{-2r} \cos^2 \theta + e^{2r} \sin^2 \theta), \tag{B.4}$$

where r is the squeezing parameter. Decoherence is modeled as a virtual beamsplitter transformation that mixes the signal field with a vacuum mode,

$$\hat{a} \mapsto \sqrt{\eta}\hat{a} + \sqrt{1-\eta}\hat{a}_{\text{vac}}, \tag{B.5}$$

where η is the transmittance of the virtual beamsplitter. In the presence of decoherence, the quadrature variance of a squeezed vacuum state becomes,

$$\langle \Delta \hat{Q}_\theta^2 \rangle_{\text{sq}} = \frac{\eta}{2}(e^{-2r} \cos^2 \theta + e^{2r} \sin^2 \theta) + \frac{1-\eta}{2}, \tag{B.6}$$

where η represents the total measurement efficiency include effects of optical loss and electronic noise [15].

The amount of squeezing can be characterized experimentally by comparing the variance of the quadratures measured with a squeezed state input to that measured with a vacuum state input,

$$\frac{\langle \Delta \hat{Q}_\theta^2 \rangle_{\text{sq}}}{\langle \Delta \hat{Q}_\theta^2 \rangle_{\text{vac}}} = \eta(e^{-2r} \cos^2 \theta + e^{2r} \sin^2 \theta) + 1 - \eta, \tag{B.7}$$

where the squeezing and antisqueezing levels relative to the shot noise level, $\eta e^{\pm 2r} + 1 - \eta$, occur at $\theta = 0$ and $\theta = \pi/2$, respectively.

Time-domain approach

Using a time-domain analyzer in the setup in Fig. B.1, squeezing can be characterized by sweeping the LO phase and accumulating voltage statistics for various phases. A numerical simulation of quadrature samples accumulated over time for a linear phase ramp applied to the LO is shown in Fig. B.2. An array of 10^5 phases is generated from 0 to 4π. For each phase, a quadrature observable is sampled from a Gaussian distribution described by Eq. B.3 to obtain a total set of 10^5 quadrature samples. The samples for a vacuum state (orange) and a squeezed vacuum state (blue) with $r = 1$ and $\eta = 0.8$ are shown in Fig. B.2a. To obtain sample mean and variances, the total sample set is divided into subsets of 1000 samples, and the mean and variance is calculated for each subset. The sample mean and variance as function of time (phase) are shown in Fig. B.2b and c, respectively.

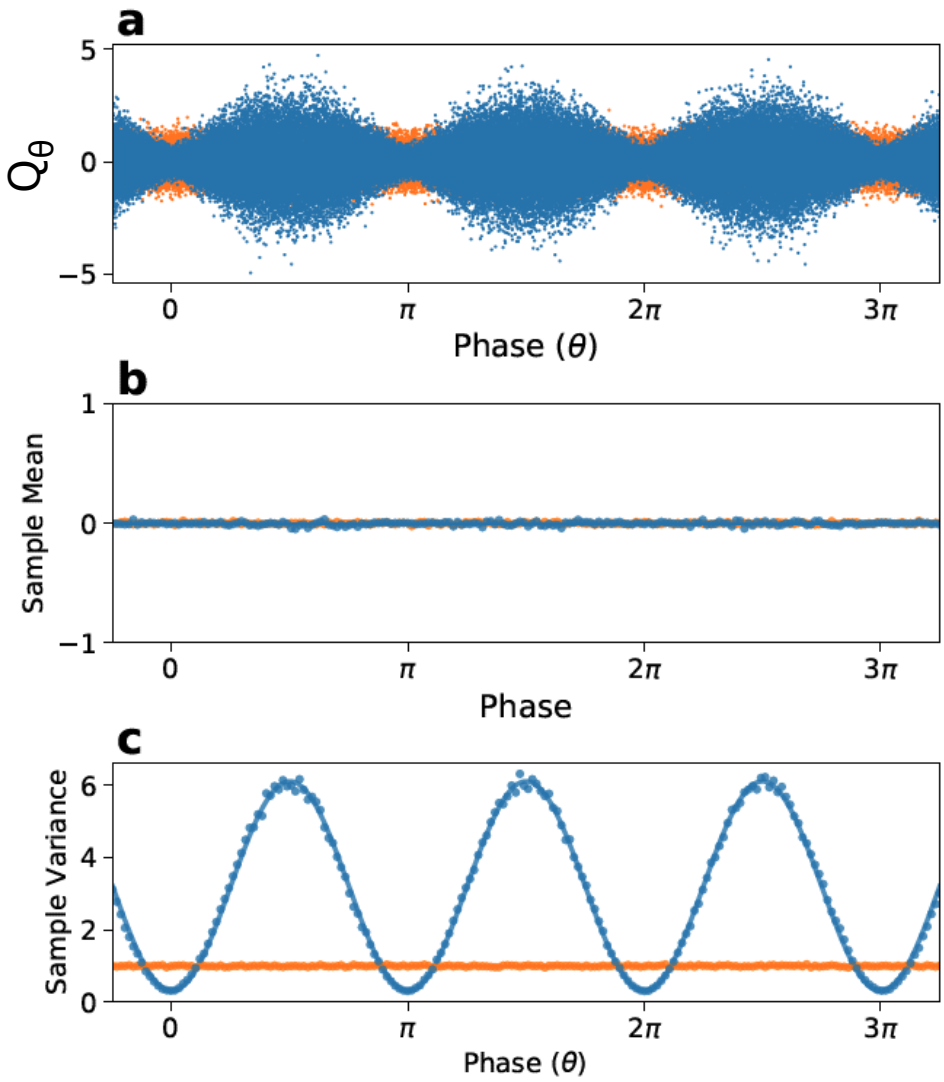

Figure B.2: Numerical simulation of quadrature statistics obtained from time-domain analyzer for a linear phase ramp applied to the LO. a) Quadrature samples as a function of time (phase) for a vacuum state (orange) and a squeezed vacuum state with $r = 1$ and $\eta = 0.8$ (blue). b) Sample means and c) normalized sample variances as a function of time. The sample variances are normalized to the mean of the vacuum sample variances. The solid lines in b) and c) are the corresponding analytic predictions for the quadrature means and variances.

Frequency domain approach

Alternatively, by using an electronic spectrum analyzer in the setup of Fig. B.1, noise power levels can be measured directly in real-time. Squeezed vacuum states of light are experimentally generated and the noise powers are measured over time using a fiber-coupled BHD. The experimental setup is shown in Fig. B.3a. Laser light at telecom wavelength of 1550 nm is split into signal path and local oscillator (LO) path. In the signal path, the light amplified by an erbium doped fiber amplifier (EDFA) and upconverted to 775 nm by second harmonic generation (SHG) by a periodically poled lithium niobate (PPLN) waveguide. The 775 nm light is used as a pump for spontaneous parametric down conversion (SPDC) by another PPLN waveguide to generate squeezed vacuum light. The pump power is controlled by tuning the gain of EDFA to vary the amount of squeezing. The squeezing parameter $r = \mu\sqrt{P}$ is related to the square root of the pump power (P) by the proportionality constant μ, which depends on the strength of the nonlinearity of the PPLN waveguide. A PPLN waveguide with $\mu = 0.038\ [\mathrm{mW}]^{-1/2}$ is used for SPDC. The squeezed light is sent through an isolator, which acts as a filter for residual 775 nm pump light and rejects backreflected light, followed by interference with the LO at a 50:50 beamsplitter for balanced homodyne detection. In the LO path, laser light is phase modulated by a lithium niobate electro-optic modulator to vary the relative phase between the signal and LO. The outputs of BS are sent to fiber-coupled balanced photodiodes, and the RF output of the BHD is sent to a RF spectrum analyzer.

Examples of noise power traces measured with the RF spectrum analyzer are shown in Fig. B.3 for various squeezing parameters and video bandwidths (VBWs). The blue traces correspond to squeezed vacuum states and the orange traces correspond to the vacuum state. Squeezed vacuum states are generated with squeezing parameters of $r = 0.35$ in Fig. B.3b,c and $r = 0.06$ in Fig. B.3d,e, corresponding to 3.04 dB and 0.52 dB generated squeezing, respectively, with a net measurement efficiency is $\eta = 0.326$. A $0-2\pi$ phase ramp at a 1 Hz modulation frequency is applied to the LO. The non-uniform phase fluctuations are due to thermal and mechanical drifts in the fiber optics, which introduce relative phase shifts between the LO and signal paths. A peak search algorithm is applied to extract minima and maxima in the squeezing data relative to the mean shot noise level. The squeezing and antisqueezing levels are obtained from the arithmetic mean of the minima and maxima, respectively (red dashed lines). The mean squeezing (antisqueezing) levels are b) -0.75 ± 0.02 (1.16 ± 0.01) dB, c) -0.78 ± 0.03 (1.20 ± 0.02) dB, d) -0.17 ± 0.01 (0.18 ± 0.01) dB, and e) -0.21 ± 0.01 (0.21 ± 0.01) dB relative to the mean shot noise level.

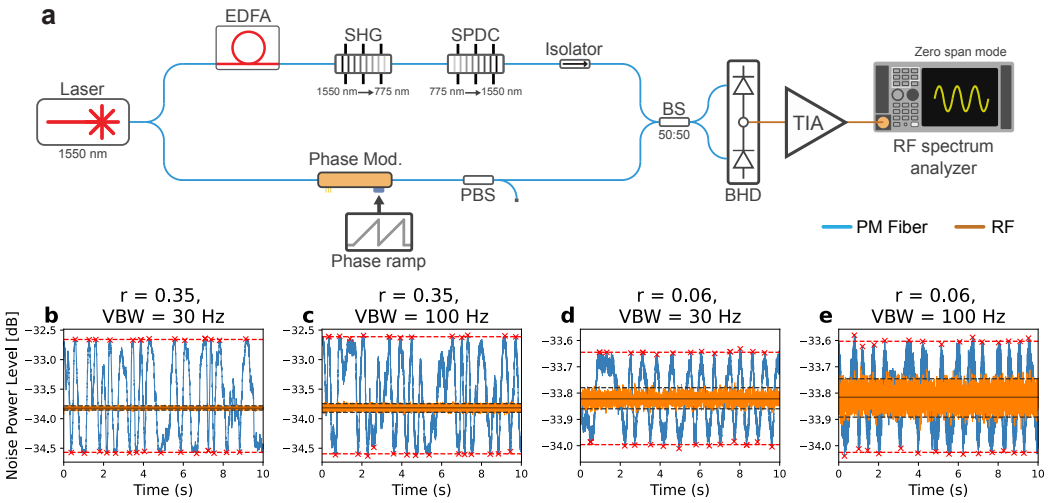

Figure B.3: Generation and measurement of squeezed light. a) Experimental setup. EDFA: erbium doped fiber amplifier, SHG: second harmonic generation, SPDC: spontaneous parametric downconversion, PBS: polarizing beamsplitter, BS: polarization maintaining beamsplitter, BHD: balanced homodyne detection, TIA: transimpedance amplifier. b-e) Experimental noise power traces of squeezed light measured with an RF spectrum analyzer. The traces are measured on zero span mode with a central frequency of 8 MHz, a resolution bandwidth (RBW) of 2 MHz, and sampling rate of 10 kHz over 10 seconds. The traces in b) and d) are measured with a video bandwidth (VBW) of 30 Hz and the traces in c) and e) are measured with a VBW of 100 Hz. The squeezing parameters are $r = 0.35$ for b) and c) and $r = 0.06$ for d) and e), with a net measurement efficiency of $\eta = 0.326$. Peaks in the squeezed light data extracted using a peak search algorithm are indicated with red markers, and the mean of the markers are indicated with dashed red lines. The same peak search algorithm is applied to the vacuum data, where the mean peak power levels are indicated by dashed black lines. The solid black lines are the mean power levels of the vacuum data.

The uncertainties on the squeezing and antisqueezing estimates are obtained from the standard deviation of minima and maxima, respectively. The same algorithm is applied to the vacuum data to obtain lower and upper bounds on the shot noise power distribution (black dashed lines). The peak search algorithm estimates upper and lower bounds of ±0.04 dB and ±0.07 dB for vacuum data taken with 30Hz and 100Hz VBW, respectively.

Shot noise power distribution

In the aforementioned methods, stable measurement of the vacuum state, that is, the shot noise level, is required for accurate estimation of squeezing. While the quadrature variance of the vacuum state is theoretically a constant (1/2), in practice, the measured variances are distributed as seen in Fig. B.3. The variance of the shot noise power distribution sets the limit on the minimum amount of squeezing that can be resolved. One possible cause for the distribution in the vacuum quadrature variances observed experimentally is optical gain instability, for example from imperfect cancellation of classical noise such as LO power fluctuations. This could be due to unbalanced detectors or imperfect LO and signal interference. Prominent in the low squeezing and high measurement loss regime, LO power fluctuations can cause significant variations in the shot noise level even for high squeezing and low measurement loss [16]. Such instabilities can be mitigated by optimizing the common mode rejection ratio (CMRR) [8], with up to 90 dB CMRR (Chapter 6) demonstrated by us in the literature.

Another cause for shot noise level uncertainty is sampling noise. Sampling noise bounds the width of the shot noise power distribution and sets the minimum amount of squeezing that can be resolved experimentally. For the time-domain approach, the quadrature sample sizes are determined by the sampling rate of the measurement. The sampling rate should be much higher than the LO phase modulations in order to obtain sufficiently high sample sizes for the calculation of the sample variances over multiple phases. In the frequency-domain approach, the sampling bandwidth is controlled with the amount of spectral and temporal filtering performed by the IF and video filters inside the spectrum analyzer [17]. Filtering can also be implemented in the time-domain approach with digital signal processing.

The effect of the shot noise power distribution on the estimation of squeezing levels is illustrated by the frequency-domain data in Fig. B.3. Since the measurements are performed with $\geq$ 30 dB CMRR, corresponding to shot noise power levels

with $\leq 0.1\%$ power fluctuations, optical gain instability is negligible relative to the sampling bandwidth. Peak searching can provide reasonable estimates for the squeezing and antisqueezing levels when the widths of the distributions are small relative to the squeezing and antisqueezing levels. However, for non-negligible widths, peak search methods overestimate the squeezing and antisqueezing levels. The overestimation in the squeezing and antisqueezing levels becomes clear for low squeezing parameters in Fig. B.3 d and e. The estimated squeezing levels depend on the width of the shot noise power distribution and are capped at the upper and lower bounds of the vacuum data, set by the sampling bandwidths.

B.3 Theoretical model

Sampling noise

To account for the effect of sampling uncertainty on the estimation of squeezing, I develop a theoretical model for the distribution of squeezed quadrature variance in the presence of sampling noise. Since the quadrature observables of Gaussian states are normally distributed, Cochran's theorem can be applied to find the probability density functions (PDFs) of the sample quadrature variance distributions for the vacuum state and squeezed state at a fixed phase. Following Cochran's theorem [18], the sample variance of n samples of a normal distribution with standard deviation σ is a random variable (S^2) that is chi-squared distributed,

$$S^2 \sim \Delta Q^2 \frac{\chi^2_{n-1}}{n-1}, \tag{B.8}$$

where χ^2_{n-1} is the chi-squared distribution with $n-1$ degrees of freedom. The sample variance distribution has mean Q^2 and approaches a normal distribution for large n.

In the frequency-domain approach, the noise powers are distributed as Eq. B.8, where the width of the distribution is set by sampling bandwidths, e.g. RBW and VBW. The powers acquired by spectrum analyzers are commonly reported in decibel (dB) scale. A statistical feature of this is that the distribution of noise powers in logarithmic scale converges faster to a normal distribution than in linear scale, and the width of the distribution is independent of the power level, see Fig. B.4e and f. This follows from Eq. B.8, as $\ln(\chi^2)$ converges to normality much faster than χ^2, and $\ln S^2 - \ln \sigma^2$ is independent of σ^2 [19].

In Fig. B.4a-d, I compare the PDFs obtained by from Eq. B.8 with a numerical simulation in the time-domain approach. With a sample size of $n = 100$, the

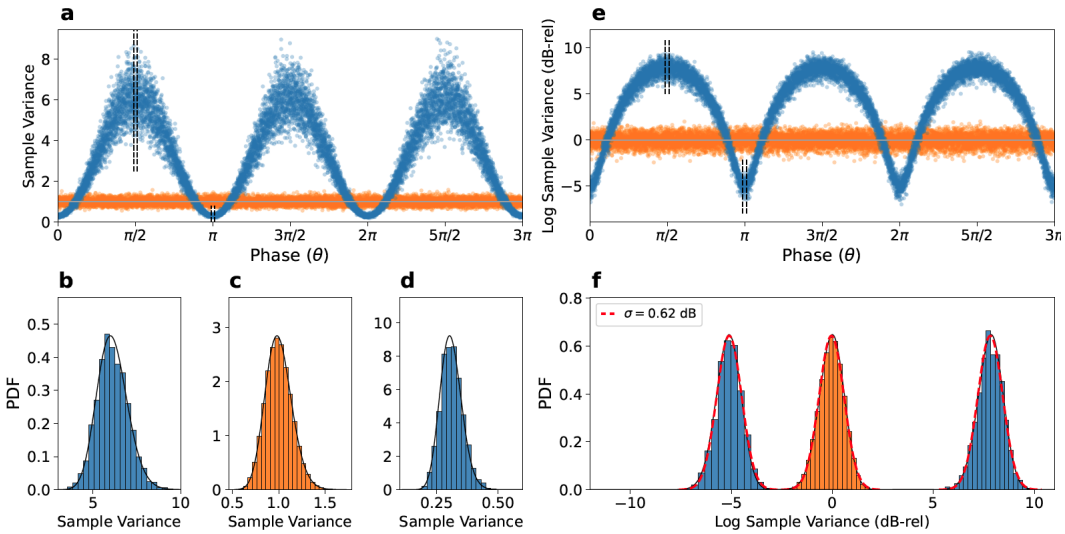

Figure B.4: Sample quadrature variance statistics in linear and logarithmic scales. a) Same simulation as in Fig. B.2 but with a $5e6$ quadrature samples of the vacuum state (orange) and squeezed vacuum state with $r = 1$ and $\eta = 0.8$ (blue) over a period. Sample variances are reported relative to the mean shot noise level. Sample variances are calculated over subsets of $n = 100$ samples. Histograms of the sample variances for b) the squeezed state at $\theta = \pi/2$, c) the vacuum state, and d) the squeezed state at $\theta = \pi$. The black lines are the corresponding theoretical predictions from obtained from Cochran's theorem in Eq. B.8. e) Simulation in a) plotted in logarithmic scale, relative to the mean shot noise level. f) Histograms of the log-scale sample variances for (left) the squeezed state at $\theta = \pi/2$, (middle) the vacuum state, and (right) the squeezed state at $\theta = \pi$. The histograms are fitted to Gaussian distributions, each with standard deviation $\sigma = 0.62$ dB. The log-scale histograms approach normality faster than the linear-scale histograms and have the same standard deviation for each phase, unlike in linear scale.

sample variances of the vacuum state are approximately normally distributed. For the squeezed state, the sample variances are approximately normally distributed for each phase, where the width scales with $Q^2 = \langle \hat{Q}_\theta^2 \rangle_{\text{sq}} / \langle \hat{Q}_\theta^2 \rangle_{\text{vac}}$.

Probability density function

Let $X \equiv S_\theta^2 / \langle \Delta \hat{Q}_\theta^2 \rangle_{\text{vac}}$ denote the quadrature sample variance, S_θ^2, normalized by the quadrature variance of the vacuum state, $\langle \Delta \hat{Q}_\theta^2 \rangle_{\text{vac}} = 1/4$. X is a random variable whose probability distribution (PDF), $f(X)$, is given by $f(X) = \delta(X - 1)$ for the

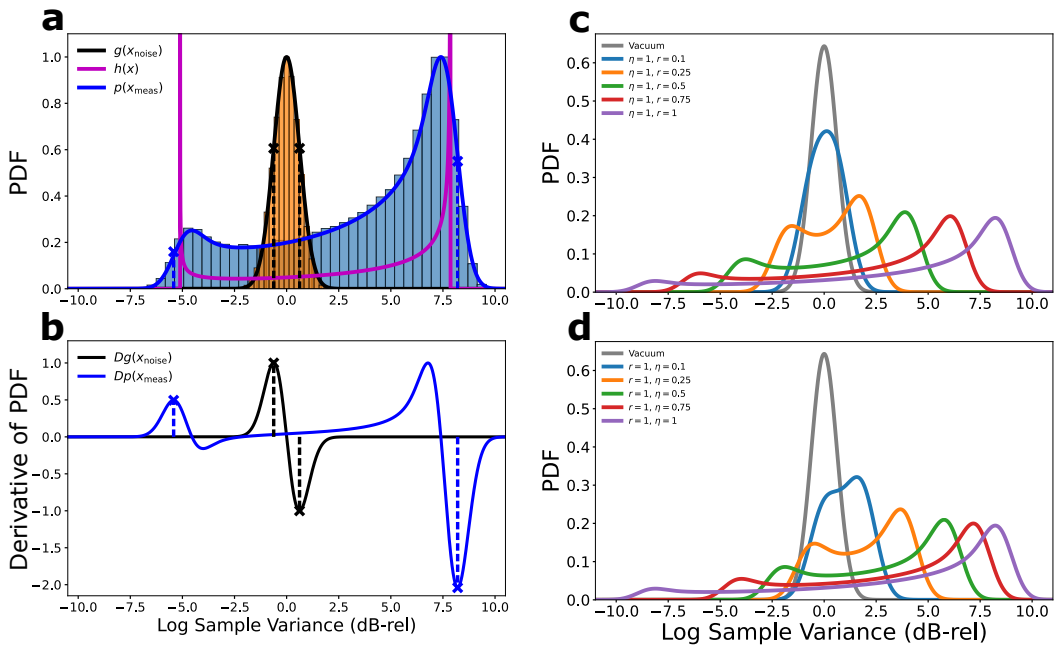

Figure B.5: Theoretical modeling for PDFs of logarithmic-scale quadrature variances sampled from a uniform phase distribution. a) PDF model for $r = 1$, $\eta = 0.8$, and a shot noise power distribution with a standard deviation of $\sigma = 0.62$ dB. The measured PDF, $p(x_{\text{meas}})$, is modeled as the convolution of the analytical squeezed vacuum PDF for uniform phase distribution, $h(x)$, with a Gaussian noise distribution, $g(x_{\text{noise}})$. The models for $g(x_{\text{noise}})$ and $p(x_{\text{meas}})$ are compared with histograms from a time-domain simulation of squeezed vacuum quadrature statistics for $r = 1$, $\eta = 0.8$, and $\sigma = 0.62$ dB. The inflection points of $g(x_{\text{noise}})$ and $p(x_{\text{meas}})$ are indicated with black and blue crosses, respectively. b) Derivatives of the PDFs for $g(x_{\text{noise}})$ and $p(x_{\text{meas}})$. The inflection points are identified from the left-most maximum and right-most minimum in the PDF derivatives, are indicated with black and blue crosses for $g(x_{\text{noise}})$ and $p(x_{\text{meas}})$, respectively. c) Measured squeezed vacuum PDF, $p(x_{\text{meas}})$, for various squeezing parameters, unit efficiency, and $\sigma = 0.62$ dB. d) Measured squeezed vacuum PDF, $p(x_{\text{meas}})$, for $r = 1$, various efficiencies, and $\sigma = 0.62$ dB.

vacuum state and

$$f(X) = \frac{1}{\pi\sqrt{(\eta \sinh 2r)^2 - (\eta \cosh 2r + 1 - \eta - X)^2}} \tag{B.9}$$

for the squeezed vacuum state. Eq. B.9 assumes that the quadratures are sampled over a uniform phase distribution.

To account for measurement noise, I model the measured quadrature sample variance as the random variable $x_{\text{meas}} = x + x_{\text{noise}}$, where $x \equiv 10\log_{10}(X)$ is the random variable for the quadrature sample variance in logarithmic scale, whose PDF is denoted by $h(x)$, and x_{noise} is the random variable that models the measurement noise, whose PDF is a Gaussian distribution with standard deviation σ,

$$g(x_{\text{noise}}) = \frac{1}{\sqrt{2\pi}\sigma} \exp\left(\frac{-x_{\text{noise}}^2}{2\sigma^2}\right). \tag{B.10}$$

Since x and x_{noise} are assumed to be mutually independent, the PDF of x_{meas}, $p(x_{\text{meas}})$, is the convolution of $h(x)$ and $g(x_{\text{noise}})$,

$$p(x_{\text{meas}}) = (h * g)(x_{\text{meas}}) = \int_{-\infty}^{\infty} h(x)g(x_{\text{meas}} - x)dx. \tag{B.11}$$

For the vacuum state, $h(x) = \delta(x)$. Therefore, the measured PDF of the vacuum state is $p(x_{\text{meas}}) = g(x_{\text{meas}})$, which corresponds to the shot noise power distribution. For the squeezed vacuum state, $h(x) = f(X(x))|X'(x)|$, where $f(X)$ is given by Eq. B.9 and $X(x) = 10^{x/10}$.

The convolved PDFs of the logarithmic sample variance for the vacuum state, $g(x_{\text{noise}})$, and squeezed vacuum state, $p(x_{\text{meas}})$, for $r = 1$ and $\eta = 0.8$ are shown in Fig. B.5a. The convolved PDFs are compared with the noiseless PDF, $h(x)$, for the squeezed vacuum state. In $h(x)$, the squeezing and antisqueezing levels are well-defined by the sharp edges of the distribution, due to the finite domain of Eq. B.9. The convolution of $h(x)$ with $g(x_{\text{noise}})$ smears out the PDF, causing the squeezing and antisqueezing levels to be poorly defined by the blurred edges. The convolved PDFs are plotted in Fig. B.5c for various squeezing parameters with unit efficiency and B.5d various efficiencies with squeezing parameter $r = 1$.

B.4 Estimation of squeezing

Estimation procedure

The left and right boundaries of the quadrature sample variance PDF are a natural choice of estimator for the squeezing and antisqueezing levels in the noiseless limit,

since the arcsine distribution of squeezed quadrature variances is sharply bounded (see Fig. B.5a). Here I use the inflection points of the quadrature sample variance PDF as estimators for the squeezing and antisqueezing levels in the presence of noise. These estimators provide a well-defined measure of the width of PDFs in the presence of unknown noise sources, motivated by the definition of the standard deviation for normal distributions. The standard deviation can be defined from the inflection points of a normal distribution, which are a standard deviation away from the mean of the distribution. Using the inflection points at the left and right boundaries extends the notion of standard deviation for non-Gaussian distributions such as $p(x_{\text{meas}})$. The estimation procedure is illustrated with $p(x_{\text{meas}})$ in Fig. B.5a, where the inflection points used as estimates for the squeezing and antisqueezing levels are indicated with blue dashed lines. The squeezing (antisqueezing) level estimates are found by identifying the location of left-most maximum (right-most minimum) in the derivative of $p(x_{\text{meas}})$ in Fig. B.5b.

Bias of estimators

Let $\hat{x}^-$ and $\hat{x}^+$ represent the estimators of the squeezing (x^-) and antisqueezing (x^+) levels, where $\hat{x}^\pm$ correspond to the inflection points of $p(x_{\text{meas}})$. For finite σ, the Gaussian blurring shifts the inflection points from x^- and x^+ by an amount that scales with σ. The biases of the estimators are $E(\hat{x}^\pm) - x^\pm = \pm c^\pm \sigma$, where c^- and c^+ are constants. For distributions that are Gaussian convolutions, $c^\pm$ are typically less than one, depending on the behavior of distribution near the inflection points [20]. In Fig. B.6a, the analytical squeezing and antisqueezing levels for squeezed states (purple) are compared with the estimates obtained from the inflection points of the logarithmic squeezed quadrature variance PDFs convolved with a Gaussian distribution with $\sigma = 0.62$ dB (blue). The bias of the estimates are less than σ. In Fig. B.6b, the bias, or the percent difference of the (anti)squeezing estimates from the analytical (anti)squeezing levels, are plotted as a function of squeezing parameter for various efficiencies. The dashed lines correspond to $\pm\sigma$ from the analytical values. For high squeezing parameters, the biases approach a constant, approximately $\pm\sigma/2$. For squeezing parameters and efficiencies corresponding to squeezing and antisqueezing levels on the order of σ, the biases reach minima of approximately $\pm\sigma/3$. For low squeezing parameters, the biases approach $\pm\sigma$. This behavior is physically meaningful as the width of $g(x_{\text{noise}})$ represents a statistical noise floor. In the large sample size limit with $\sigma \to 0$, the biases approach zero and the inflection points coincide with the true squeezing and antisqueezing levels

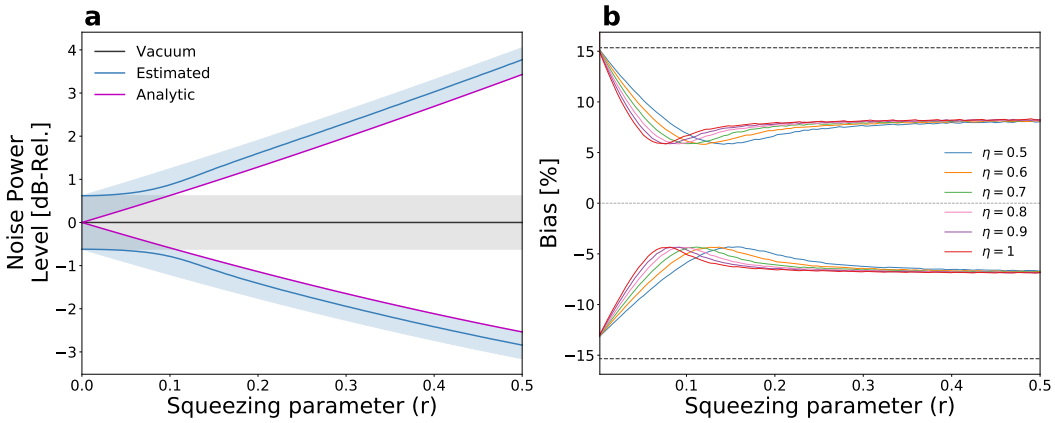

Figure B.6: Simulation of squeezing estimator bias. a) Noise power levels normalized to the mean shot noise level (black) as a function of squeezing parameter. The uncertainty in the shot noise level is depicted by the gray shaded region corresponding to $\pm\sigma$, where $\sigma = 0.62$ dB is the standard deviation of the shot noise power distribution. The squeezing (x^-) and antisqueezing (x^+) levels of a squeezed vacuum state are plotted in purple for unit measurement efficiency. The blue curves are the squeezing and antisqueezing level estimates for the observed squeezed vacuum state obtained from the inflection points of measured power distribution. The squeezing and antisqueezing estimates are within $+\sigma$ of the antisqueezing level and $-\sigma$ of the squeezing level, depicted by the blue shaded regions. b) The percent bias of the squeezing ($\hat{x}^-$) and antisqueezing ($\hat{x}^+$) estimates as a function of squeezing parameter, calculated as $100 \times (E(\hat{x}^\pm) - x^\pm)/x^\pm$.

as $p(x_{\text{meas}}) \to h(x_{\text{meas}})$.

Experimental results

The estimation procedure is applied to the experimental data from Fig. B.3b-e in Fig. B.7. The data are plotted again for reference in the first row. The histograms for the squeezed states (light blue) and vacuum states (orange) are shown in the second row. The kernal density estimates (KDEs) for the PDFs of the squeezed and vacuum states are plotted as the blue and black solid lines, respectively. The theoretical models for the squeezed state PDFs assuming a uniform phase distribution are plotted in purple. The theoretical models are calculated from Eq. B.11, where the integration is performed numerically.

To find the estimates for the squeezing and antisqueezing levels, the derivatives of the KDEs are calculated numerically. The derivatives of the KDEs of the squeezed

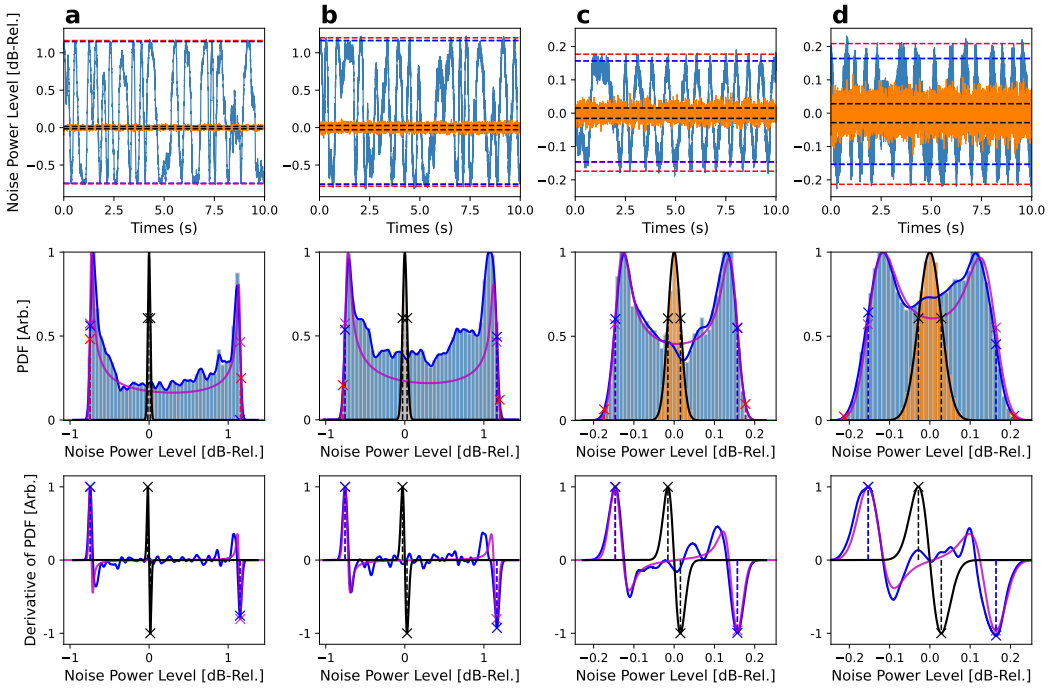

Figure B.7: Squeezing estimation with the frequency-domain measurements of squeezed light from Fig. B.3 for a) $r = 0.35$, VBW = 30 Hz, b) $r = 0.35$, VBW = 100 Hz, c) $r = 0.06$, VBW = 30 Hz, and d) $r = 0.06$, VBW = 100 Hz. First row: Noise power level traces of squeezed vacuum (light blue) and vacuum (orange) states relative to the mean shot noise level. The red dashed lines correspond to estimates of squeezing and antisqueezing levels from peak searching. The dark blue dashed lines correspond to the estimates of squeezing and antisqueezing levels from the inflection points of the noise power PDF of the squeezed vacuum data. The black dashed lines correspond to the inflection points of the shot noise power distribution. Second row: Histograms of the squeezed vacuum noise powers (light blue) and shot noise powers (orange). The Gaussian kernal density estimates (KDE) for PDFs of the squeezed vacuum and vacuum noise powers are shown in dark blue and black, respectively. The theoretical model for the squeezed vacuum PDF with the experimental squeezing parameter and system efficiency for a uniform phased distribution is shown in red. The inflection points of the squeezed vacuum KDE, vacuum KDE, and model are indicated with dark blue, black, and purple crosses, respectively. The squeezing and antisqueezing estimates from peak searching are indicated with red crosses. The histograms, KDEs, and model are rescaled to the maximum of the squeezed vacuum KDE. Third row: Derivatives of the squeezed vacuum KDE (blue), vacuum KDE (black), and theoretical model (purple), rescaled to the maximum of the vacuum KDE derivative, with the inflection points indicated with crosses.

states (blue) and vacuum states (black) are shown in the third row. The theoretical models for the squeezed state PDFs with uniform phase distribution are shown in purple. The theoretical models are calculated using the differentiation of convolution property,

$$\frac{dp(x_{\text{meas}})}{dx_{\text{meas}}} = \int_{-\infty}^{\infty} \frac{x - x_{\text{meas}}}{\sigma^2} h(x) g(x_{\text{meas}} - x) dx, \tag{B.12}$$

where the integration is performed numerically. For the squeezed state, the squeezing (antisqueezing) level is estimated as the noise power of the left-most maximum (right-most minimum). The same procedure is applied to the vacuum state KDE in order to obtain the noise floor. The procedure is also applied to the theoretical model to obtain the estimates for a uniform phase distribution.

In the first and second row, I compare the results of this procedure with those of the peak search algorithm from Fig. B.3. The squeezing and antisqueezing level estimates from the procedure and the peak search method are indicated with blue and red dashed lines, respectively. The shot noise floors are indicated with black dashed lines. The improvement over the peak search method is apparent for the low squeezing parameters, when the shot noise floor becomes significant. The peak search clearly overestimates the squeezing and antisqueezing levels, with estimates corresponding to the extrema of the noise powers as seen in the second row. Moreover, for the same squeezing parameter and effective efficiency, the peak search estimates change with the VBW setting, i.e. the standard deviation of the vacuum PDF, whereas the estimates from the procedure remain the same. This is because the peak search method relies on the tails of the PDF, and is therefore strongly influenced by the shape of the distribution. To demonstrate the robustness of this approach to experimental noise, I compare the estimates of this method to those of the theoretical model, indicated with purple dashed lines in the second row. Despite the non-uniformities in the KDEs, the estimates match closely with the theoretical model.

B.5 Discussion

I have demonstrated a method for estimating the squeezing and antisqueezing levels from the probability distribution of squeezed quadrature sample variances. The left and rightmost inflection points of the distribution are used as estimators of squeezing and antisqueezing. The squeezing parameter and system efficiency can estimated from the squeezing and antisqueezing levels from Eq. B.7. This method enables the estimation of squeezing in the the presence of high degrees of sampling

and phase noise and for low efficiencies, where the performance of characterization methods such as peak searching and optical homodyne tomography suffer. These estimators provide a well-defined measure for the left and right edges of the squeezed quadrature distribution in the presence of experimental noise sources such as phase and sampling noise, which blur the edges of the distribution. The bias of the estimators is typically within a standard deviation of the shot noise distribution and approaches zero for small shot noise distributions, in this case in the large sample size limit. This method is supported by theoretical modeling and experimental results.

References

[1] Alexander I Lvovsky. "Squeezed light." In: Photonics: Scientific Foundations, Technology and Applications 1 (2015), pp. 121–163.

[2] DT Smithey, M Beck, Michael G Raymer, and A Faridani. "Measurement of the Wigner distribution and the density matrix of a light mode using optical homodyne tomography: Application to squeezed states and the vacuum." In: Physical Review Letters 70.9 (1993), p. 1244.

[3] Alexander I Lvovsky and Michael G Raymer. "Continuous-variable optical quantum-state tomography." In: Reviews of Modern Physics 81.1 (2009), p. 299.

[4] Gerd Breitenbach, S Schiller, and J Mlynek. "Measurement of the quantum states of squeezed light." In: Nature 387.6632 (1997), pp. 471–475.

[5] Joel F. Tasker, Jonathan Frazer, Giacomo Ferranti, Euan J. Allen, Léandre F. Brunel, Sébastien Tanzilli, Virginia D'Auria, and Jonathan C. F. Matthews. "Silicon photonics interfaced with integrated electronics for 9 GHz measurement of squeezed light." In: Nature Photonics 15.1 (Jan. 2021), pp. 11–15.

[6] Alexander I Lvovsky. "Iterative maximum-likelihood reconstruction in quantum homodyne tomography." In: Journal of Optics B: Quantum and Semiclassical Optics 6.6 (2004), S556.

[7] Hauke Hansen, T Aichele, C Hettich, P Lodahl, AI Lvovsky, J Mlynek, and S Schiller. "Ultrasensitive pulsed, balanced homodyne detector: application to time-domain quantum measurements." In: Optics Letters 26.21 (2001), pp. 1714–1716.

[8] Hans-A. Bachor and Timothy C. Ralph. A guide to experiments in quantum optics. John Wiley & Sons, 2019.

[9] E Oelker, G Mansell, M Tse, J Miller, F Matichard, L Barsotti, P Fritschel, DE McClelland, M Evans, and N Mavalvala. "Ultra-low phase noise squeezed vacuum source for gravitational wave detectors." In: Optica 3.7 (2016), pp. 682–685.

[10] Florian Kaiser, Bruno Fedrici, Alessandro Zavatta, Virginia d'Auria, and Sébastien Tanzilli. "A fully guided-wave squeezing experiment for fiber quantum networks." In: Optica 3.4 (2016), pp. 362–365.

[11] Glen Cowan, Kyle Cranmer, Eilam Gross, and Ofer Vitells. “Asymptotic formulae for likelihood-based tests of new physics.” In: The European Physical Journal C 71 (2011), pp. 1–19.

[12] Louis Lyons. Statistics for nuclear and particle physicists. cambridge university press, 1989.

[13] Leonard Mandel and Emil Wolf. Optical coherence and quantum optics. Cambridge university press, 1995.

[14] Christian Weedbrook, Stefano Pirandola, Raúl García-Patrón, Nicolas J Cerf, Timothy C Ralph, Jeffrey H Shapiro, and Seth Lloyd. “Gaussian quantum information.” In: Reviews of Modern Physics 84.2 (2012), pp. 621–669.

[15] Jürgen Appel, Dallas Hoffman, Eden Figueroa, and A. I. Lvovsky. “Electronic noise in optical homodyne tomography.” In: Physical Review A 75.3 (2007), p. 035802.

[16] Rajveer Nehra, Ryoto Sekine, Luis Ledezma, Qiushi Guo, Robert M Gray, Arkadev Roy, and Alireza Marandi. “Few-cycle vacuum squeezing in nanophotonics.” In: Science 377.6612 (2022), pp. 1333–1337.

[17] Agilent Technologies. Spectrum Analysis Basics. 7th ed. Application Note 150. Originally published as Hewlett-Packard Application Note 150. Agilent Technologies. Santa Clara, CA, 2006. URL: https://www.keysight.com/zz-en/assets/7018-03115/application-notes/5965-7009.pdf.

[18] William G Cochran. “The distribution of quadratic forms in a normal system, with applications to the analysis of covariance.” In: Mathematical Proceedings of the Cambridge Philosophical Society. Vol. 30. 2. Cambridge University Press. 1934, pp. 178–191.

[19] Maurice S Bartlett and DG Kendall. “The statistical analysis of variance-heterogeneity and the logarithmic transformation.” In: Supplement to the Journal of the Royal Statistical Society 8.1 (1946), pp. 128–138.

[20] Steven M Kay. Fundamentals of statistical signal processing: estimation theory. Prentice-Hall, Inc., 1993.

Appendix C

SUPPLEMENTARY INFORMATION FOR "AN ON-PHASED ARRAY SYSTEM FOR NON-CLASSICAL LIGHT"

Our photonic integrated circuit (PIC) is one of the largest-scale PICs demonstrated in the literature with more than 1,000 functional components, as shown in Fig. C.1. Photos of the chip on top of a penny are shown in Fig. C.1a, and the packaged photonic-electronic system is shown in Fig. C.1b. Here, we provide a description of the PIC components and their characterization.

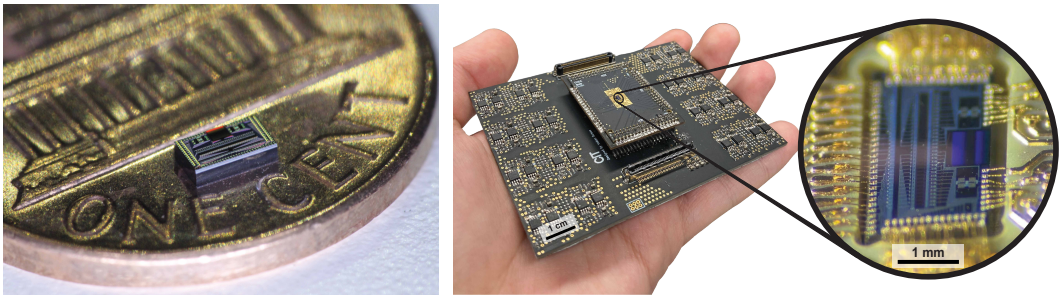

Figure C.1: Photo of the PIC on top of a penny (left). Photos of the packaged photonic-electronic system comprising the chip wirebonded to an interposer interfaced with an RF motherboard (right). The system can be packaged as a handheld device enabled by the integration and packaging of photonics and electronics.

C.1 On-chip squeezing analysis

Here we demonstrate how we extract the squeezing and antisqueezing levels for the experiments in Chapter 6 using the estimation procedure from Appendix B. We walk through the analysis of a chip data set using our estimation procedure and demonstrate how we extract the squeezing and antisqueezing levels for the experiments in Fig. 6.5 of Chapter 6. The complete analysis for the 32-channel source characterization data of Fig. 6.5c is shown in Figs. C.2-C.5 and the histograms for the remaining data of Fig. 6.5 are shown in Figs. C.6-C.9.

32-channel source characterization

For each pump power (P) of the 32-channel sweep in Fig. 6.5c, we measure noise power traces for the squeezed vacuum and vacuum states using an RF spectrum

analyzer with a 2 MHz RBW, 5 Hz VBW, and 1.25 kHz sampling rate. Each vacuum trace is taken immediately before or after a squeezed vacuum trace. For a pair of vacuum and squeezed vacuum traces, each trace is acquired over the same amount of time, typically over 5-10s. Due to random phase drifts, we acquire multiple pairs of vacuum and squeezed vacuum traces until an approximately uniform sampling of phases is achieved. To correct long-term drifts in the LO power, each pair is normalized by the mean of the vacuum trace. The normalized traces are concatenated to obtain squeezed vacuum and vacuum traces corresponding to an approximately uniform phase distribution (Fig. C.2). To perform the estimation procedure on the same number of points for all pump powers, 10^4 points are randomly sampled from each concatenated trace (Fig. C.3). The histograms are constructed for the sampled noise powers, and the PDFs are approximated by kernel density estimation (Fig. C.4). The squeezing and antisqueezed level estimates are obtained from the peaks in the derivative of the KDEs (Fig. C.5). The KDEs and their derivatives are compared with a theoretical model for a uniform phase distribution. The theoretical models are calculated from Eq. B.11 with $\sigma = 0.012$ dB, $\eta = 0.0157$, and $r = \mu\sqrt{P}$, where $\mu = 0.038\ [\mathrm{mW}]^{-1/2}$ (see Sec. C.2). The experimental estimates (blue), theoretical estimates (purple), and the noise floor (black) are indicated with dashed lines in Fig. C.3, Fig. C.4, and Fig. C.5. The experimental and theoretical estimates are in near agreement despite the phase noise in the measurements. We note that some discrepancies in the theoretical and experimental estimates are expected because the model fit was performed on the experimental estimates with only one free parameter across the entire data set rather than an individual fit to each histogram.

Beamforming

For each channel combination in Fig. 6.5b, we measure noise power traces for the squeezed vacuum and vacuum states using an RF spectrum analyzer with a 2 MHz RBW, 5 Hz VBW, and 1.25 kHz sampling rate. For each trace, 10^4 noise powers are sampled at random. The histograms and KDEs of the noise power samples for all channel combinations are shown in Fig. C.6.

Beamwidth

For each channel combination in Fig. 6.5e, we measure noise power traces for the squeezed vacuum and vacuum states using an RF spectrum analyzer with a 2 MHz RBW, 5 Hz VBW, and 625 Hz sampling rate. For each trace, 10^4 noise powers are sampled at random. The histograms and KDEs of the noise power samples for all

channel combinations are shown in Fig. C.7 for 8 channels combined and Fig. C.8 for 32 channels combined.

Field of view

For each channel combination in 6.5f, we measure noise power traces for the squeezed vacuum and vacuum states using an RF spectrum analyzer with a 2 MHz RBW, 5 Hz VBW, and 1 kHz sampling rate. For each trace, 10^4 noise powers are sampled at random. The histograms and KDEs of the noise power samples for all channel combinations are shown in Fig. C.9a for 8 channels combined and Fig. C.9b for 32 channels combined.

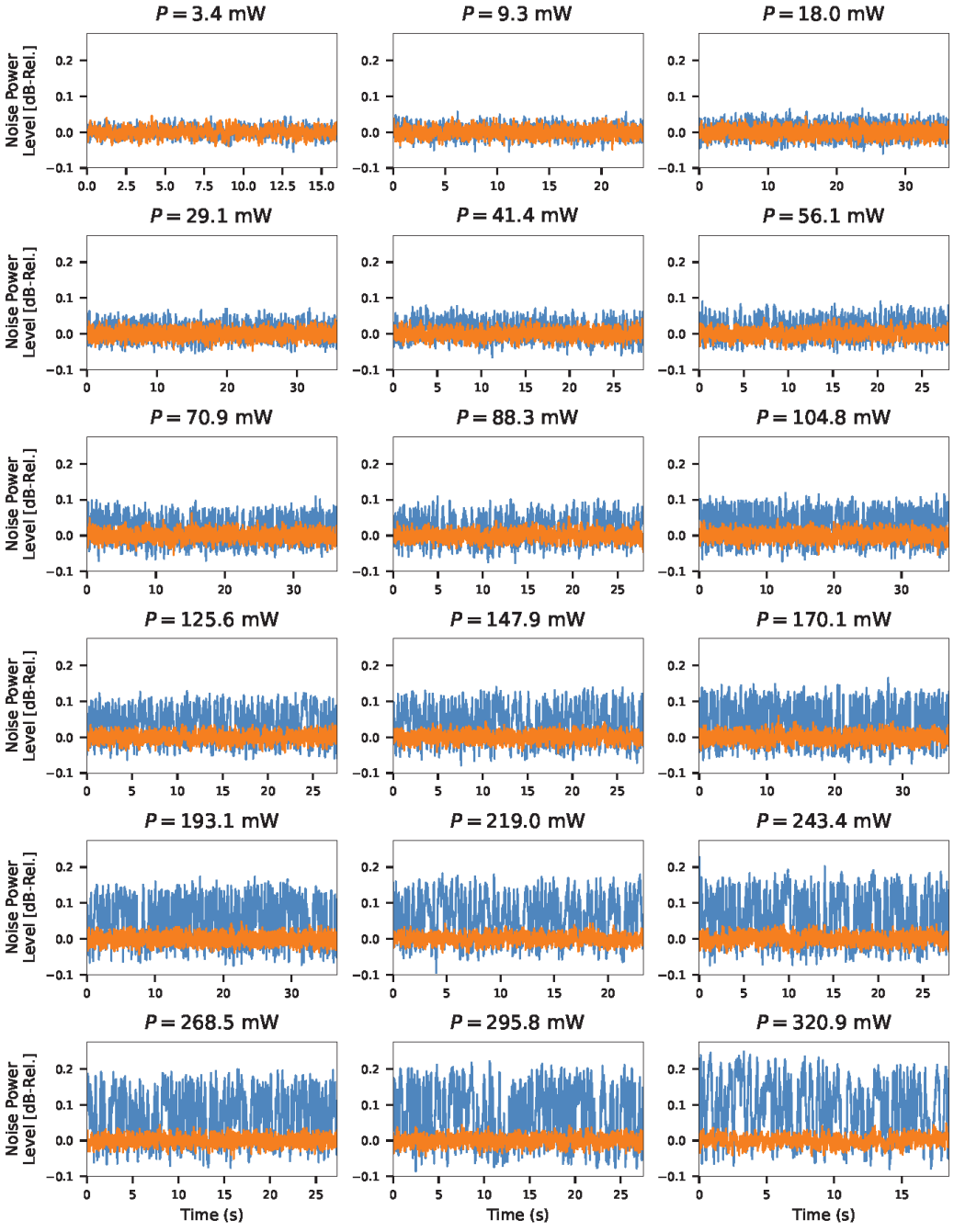

Figure C.2: Data analysis for the 32-channel source characterization in Fig. 6.5c: noise power traces for the squeezed vacuum (blue) and vacuum (orange) states.

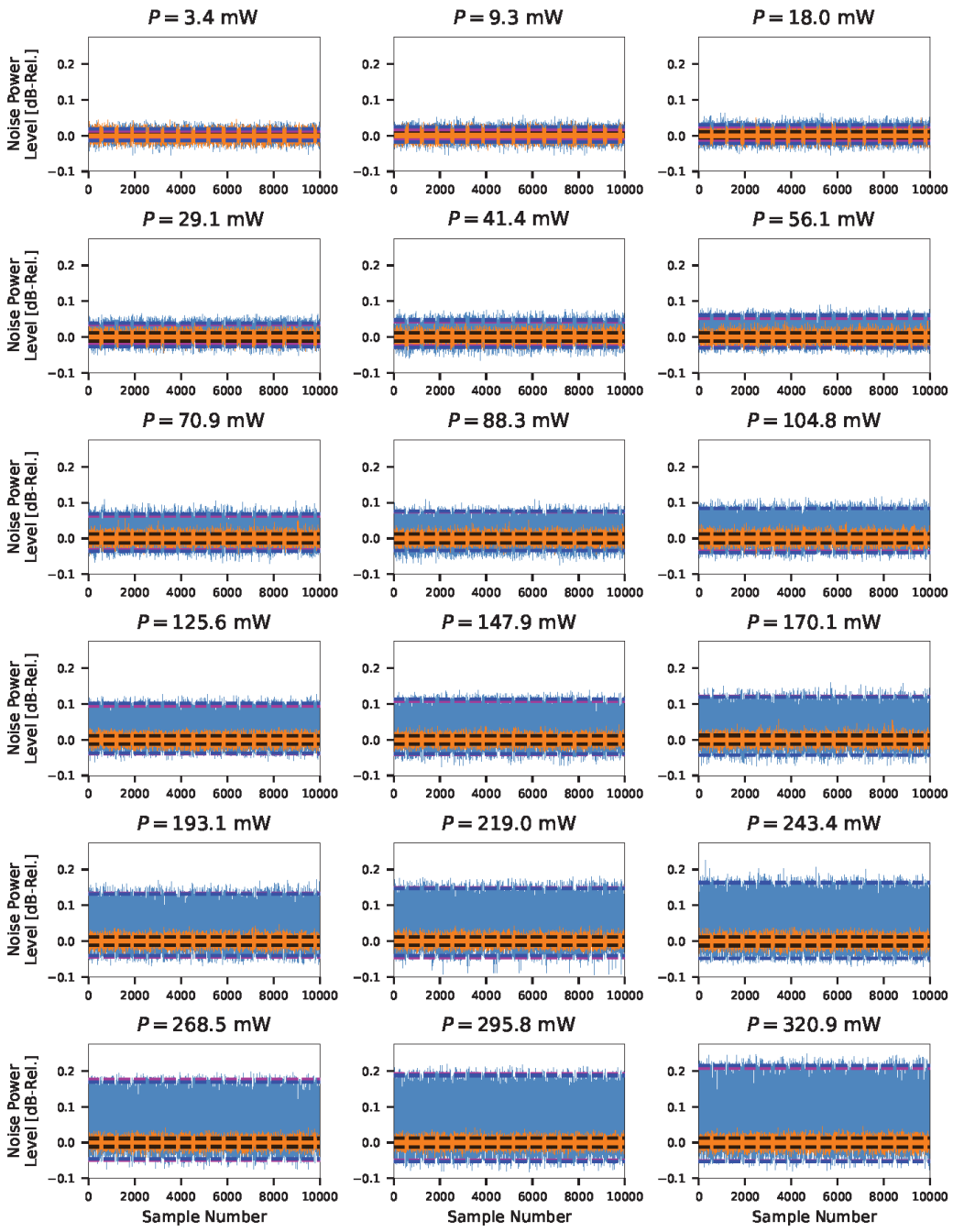

Figure C.3: Data analysis for the 32-channel source characterization in Fig. 6.5c: noise power samples for the squeezed vacuum (blue) and vacuum (orange) states are collected for various pump powers. The squeezing and antisqueezing level estimates are indicated with dashed blue lines, the theoretical model estimates are indicated with dashed purple lines, and the the shot noise floor is indicated with dashed black lines.

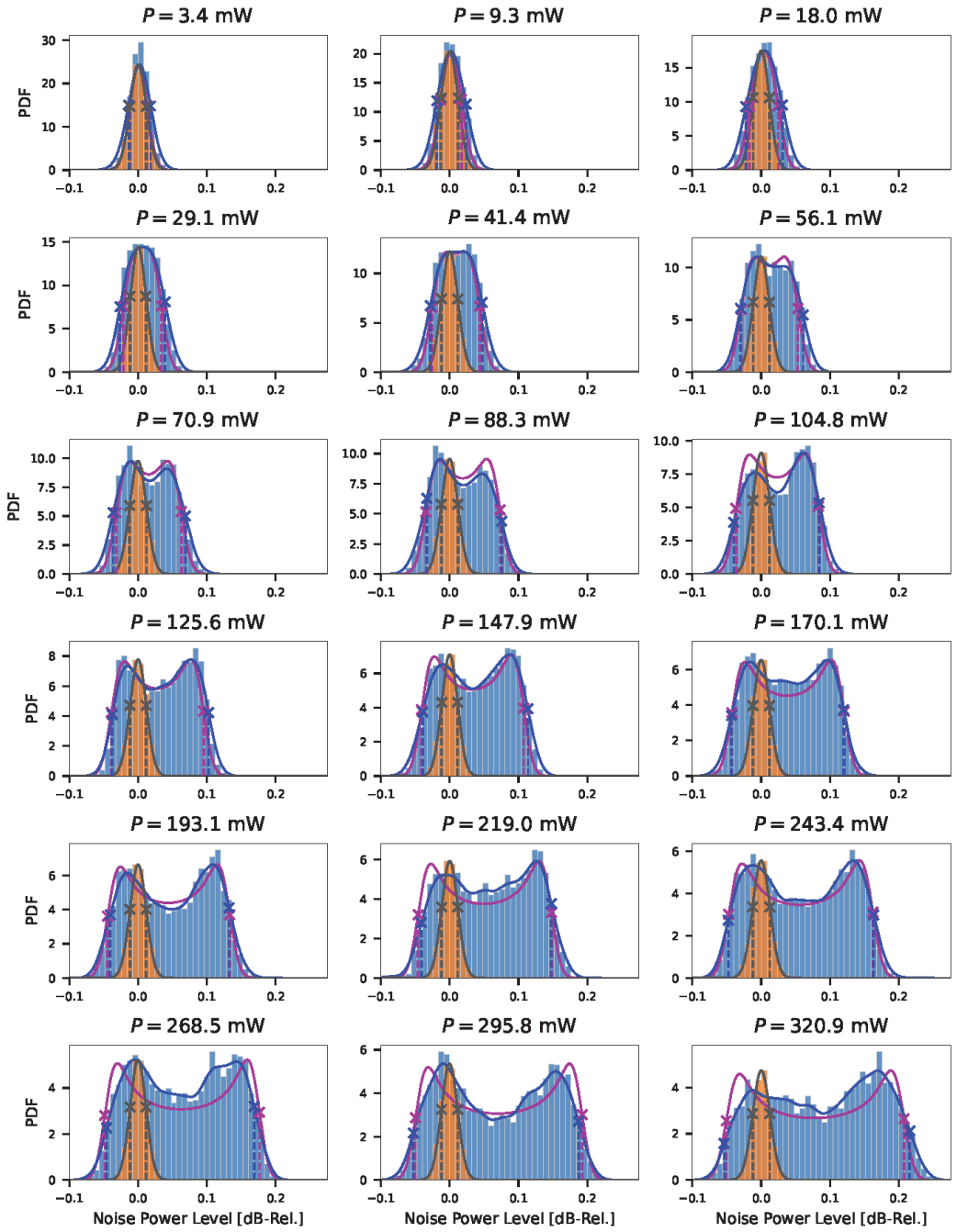

Figure C.4: Data analysis for the 32-channel source characterization in Fig. 6.5c: histograms of the sampled noise powers in Fig. C.3 for the squeezed vacuum (blue) and vacuum (orange) states. The KDE for the squeezed vacuum histogram is plotted in blue, the theoretical model of the PDF for the squeezed vacuum histogram is plotted in purple, and a Gaussian fit to the vacuum histogram is plotted in black. The locations of the maximum slopes for the squeezed state KDE, vacuum state Gaussian, and theoretical model are indicated with crosses and dashed lines, obtained from Fig. C.5.

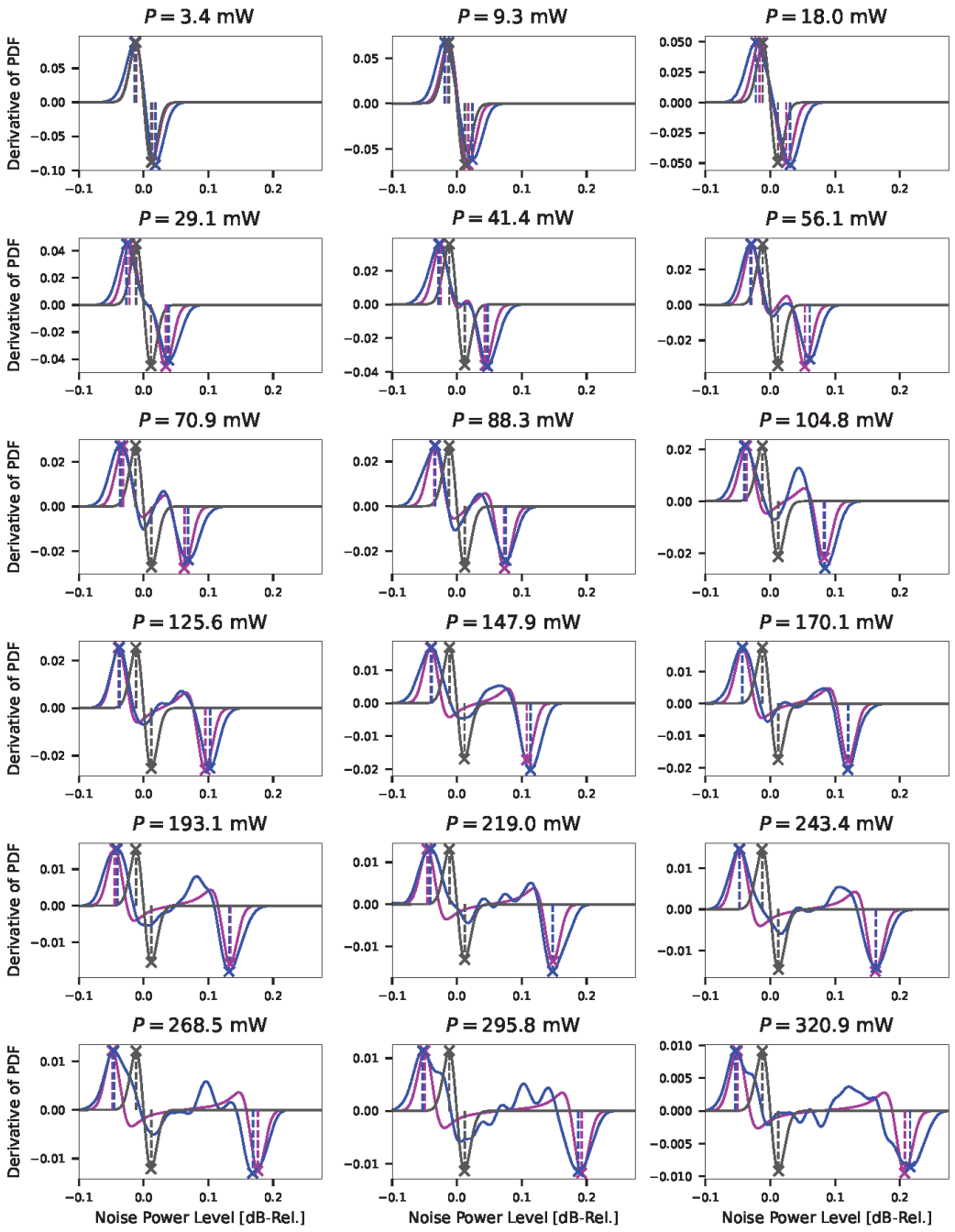

Figure C.5: Data analysis for the 32-channel source characterization in Fig. 6.5c: for each pump power in Fig. C.4, the derivative of the KDE for the squeezed vacuum histogram is plotted in blue, the derivative of the squeezed vacuum histogram is plotted in purple, and the derivative of the Gaussian fit to the vacuum histogram is plotted in black. The locations of the maxima and minima used to estimate the squeezing and antisqueezing levels are indicated with crosses and dashed lines.

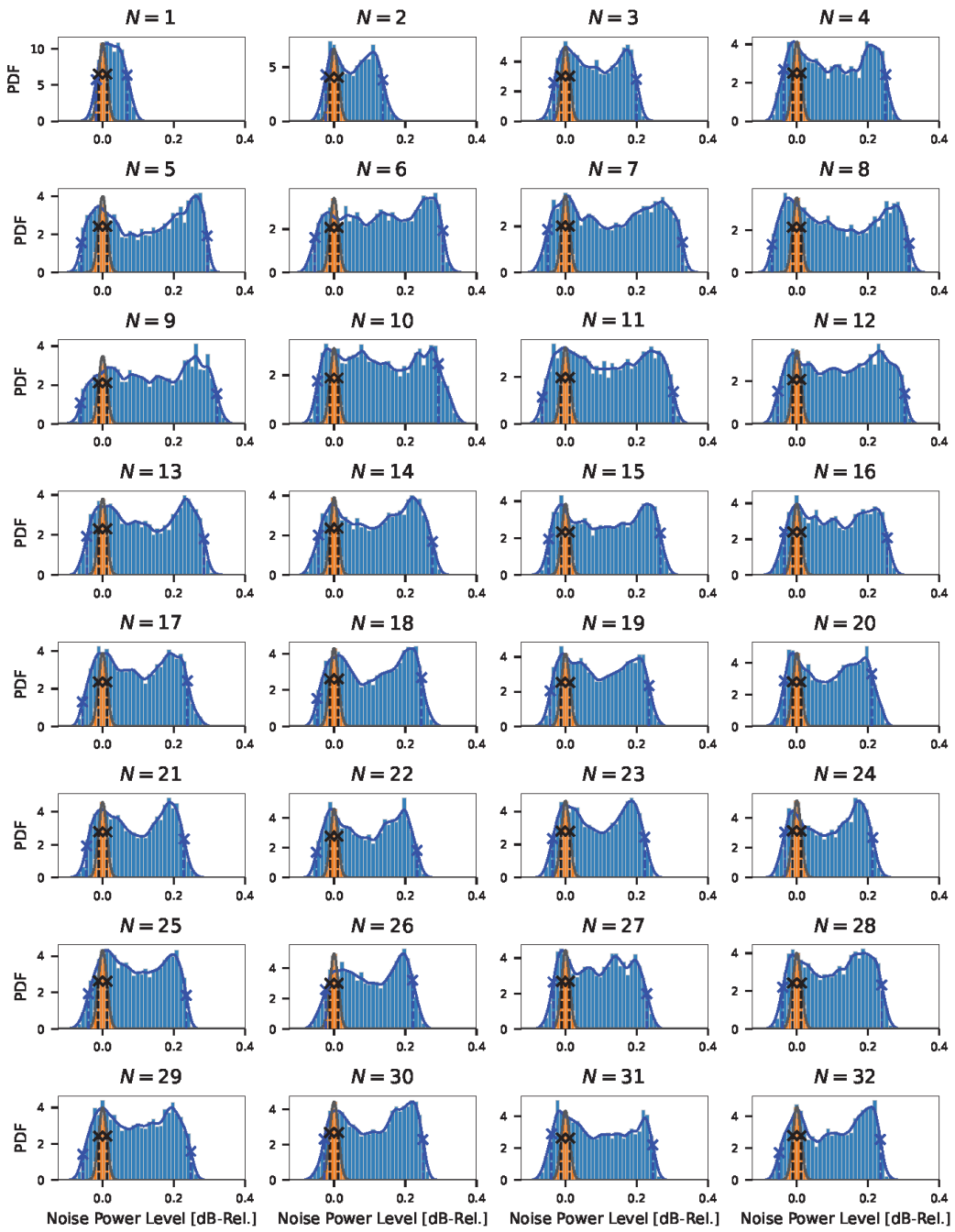

Figure C.6: Data analysis for beamforming in Fig. 6.5b: histograms of the sampled noise powers for the squeezed vacuum (blue) and vacuum (orange) states. The KDE for the squeezed vacuum histogram is plotted in blue and a Gaussian fit to the vacuum histogram is plotted in black. The locations of the peak slopes for the squeezed state KDE (blue) and vacuum state Gaussian (black) are indicated with crosses and dashed lines, which yield the squeezing/antisqueezing level estimates and the noise floor.

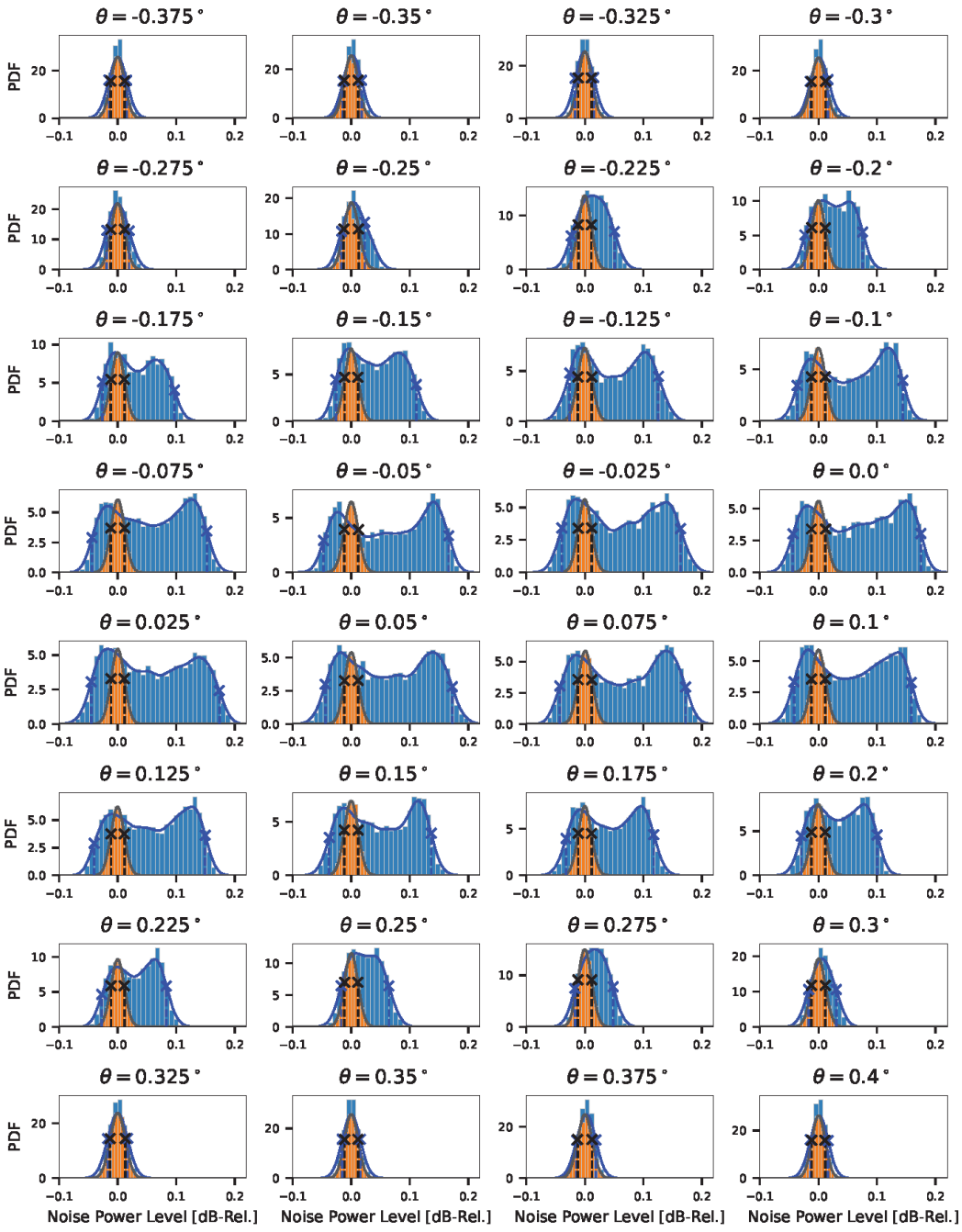

Figure C.7: Data analysis for the beamwidth characterization in Fig. 6.5e for 8 channels combined: histograms of the sampled noise powers for the squeezed vacuum (blue) and vacuum (orange) states are collected for various angles of incidence for a fixed beamforming angle (0°). The KDE for the squeezed vacuum histogram is plotted in blue and a Gaussian fit to the vacuum histogram is plotted in black. The locations of the peak slopes for the squeezed state KDE (blue) and vacuum state Gaussian (black) are indicated with crosses and dashed lines, which yield the squeezing/antisqueezing level estimates and the noise floor.

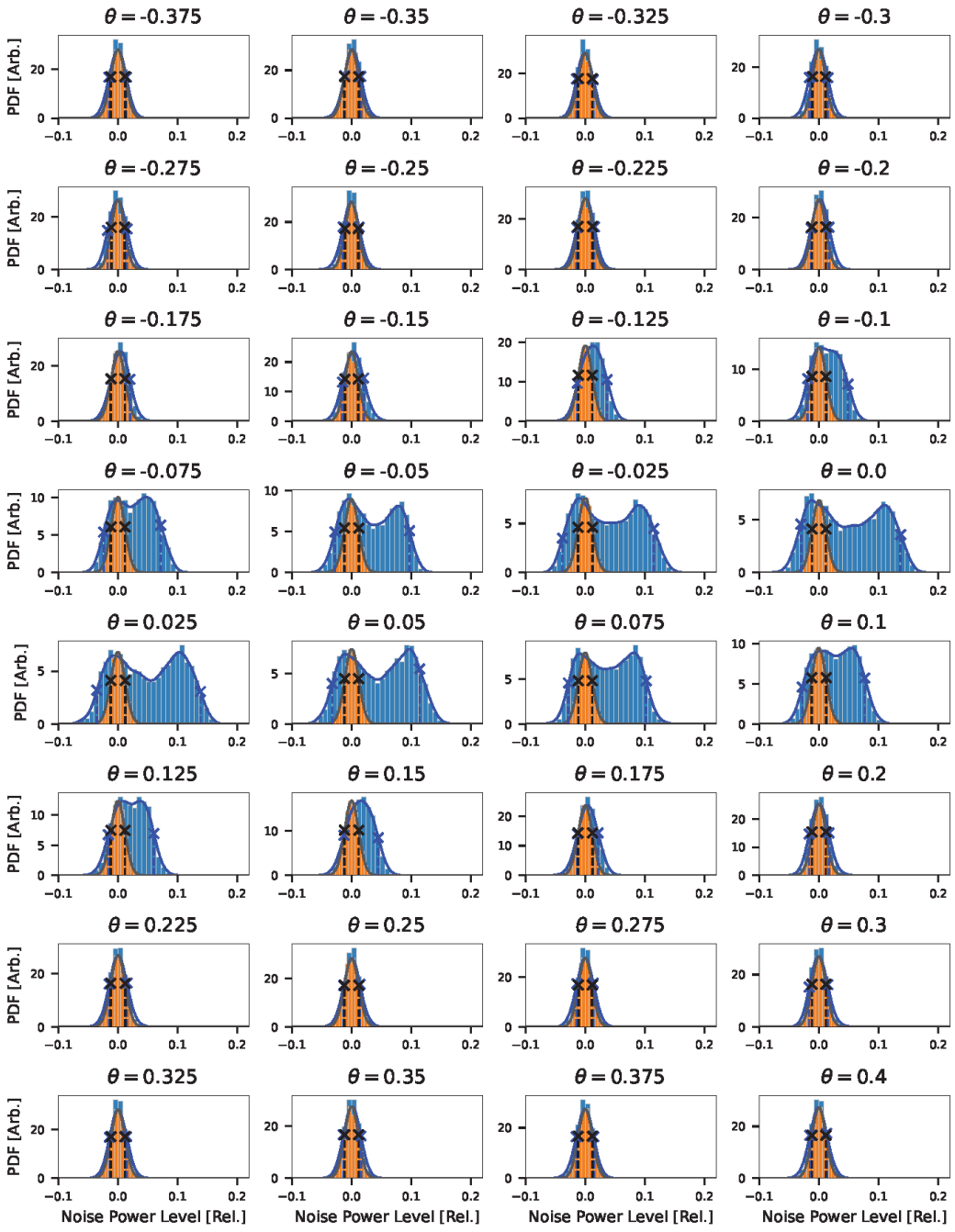

Figure C.8: Data analysis for the beamwidth characterization in Fig. 6.5e for 32 channels combined: histograms of the sampled noise powers for the squeezed vacuum (blue) and vacuum (orange) states are collected for various angles of incidence for a fixed beamforming angle (0°). The KDE for the squeezed vacuum histogram is plotted in blue and a Gaussian fit to the vacuum histogram is plotted in black. The locations of the peak slopes for the squeezed state KDE (blue) and vacuum state Gaussian (black) are indicated with crosses and dashed lines, which yield the squeezing/antisqueezing level estimates and the noise floor.

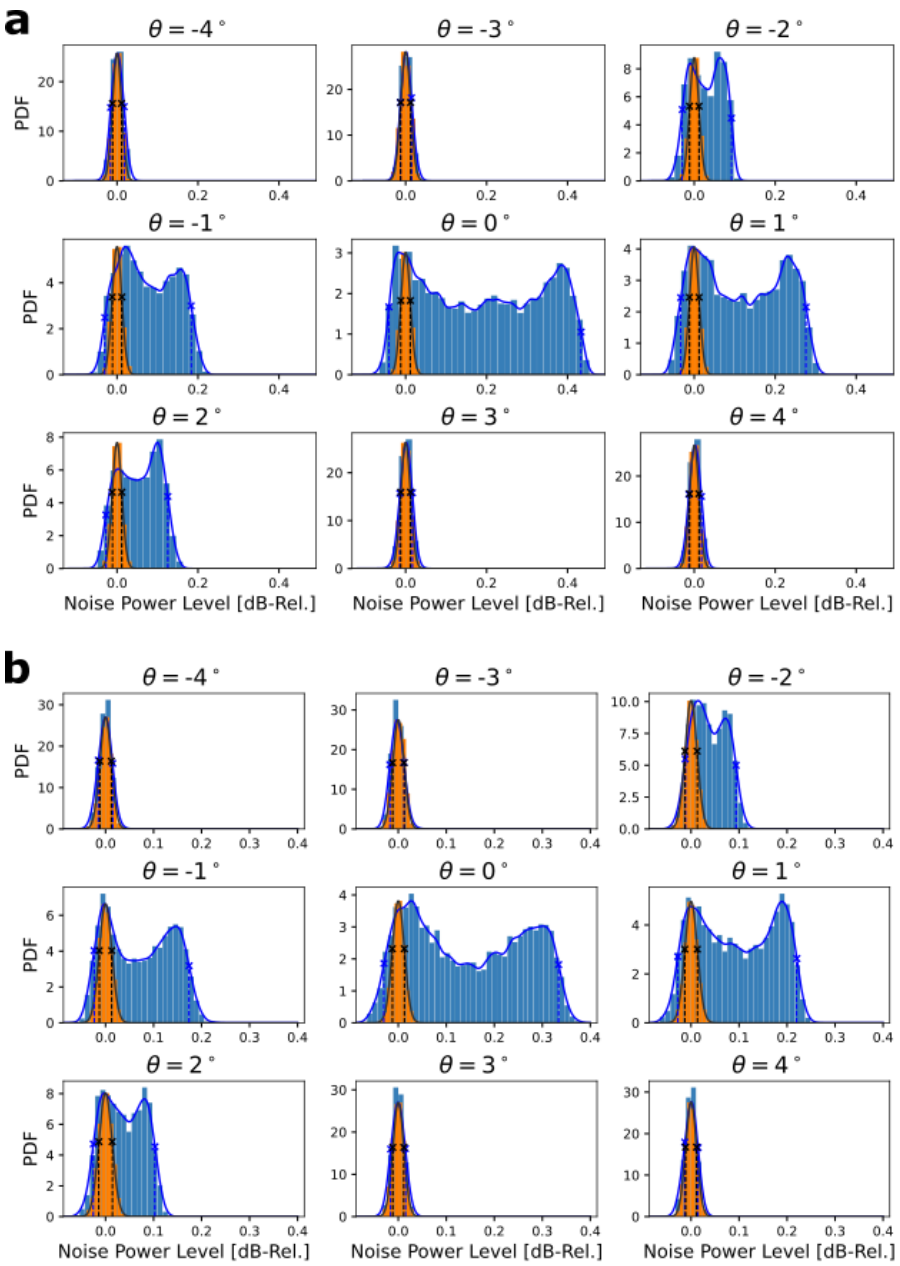

Figure C.9: Data analysis for the field-of-view characterization in Fig. 6.5f for a) 8 channels combined and b) 32 channels combined. Histograms of the sampled noise powers for the squeezed vacuum (blue) and vacuum (orange) states are collected for various angles of incidence, with beamforming performed at each angle. The KDE for the squeezed vacuum histogram is plotted in blue and a Gaussian fit to the vacuum histogram is plotted in black. The locations of the peak slopes for the squeezed state KDE (blue) and vacuum state Gaussian (black) are indicated with crosses and dashed lines, which yield the squeezing/antisqueezing level estimates and the noise floor.

C.2 Squeezed light source characterization

The squeezed light sources are characterized with a modified version of the transmitter setup from Chapter 6 as shown in Fig. C.10a. Continuous wave light from a fiber-coupled 1550 nm laser (OEWaves) is split into a signal path and a local oscillator (LO) path. The light in the signal path is sent to an erbium-doped fiber amplifier (PriTel EDFA) with a tunable gain. The amplified light is upconverted to 775 nm by second harmonic generation (SHG) with a periodically poled lithium niobate (PPLN) waveguide. The upconverted light is sent to another PPLN waveguide for Type 0 spontaneous parametric downconversion (SPDC) to generate squeezed light centered at 1550 nm. The squeezed light is sent to an isolator (Thorlabs), which rejects back-reflected light and serves as a filter for any residual 775 nm pump light. After the isolator, an optical switch is used to switch between the vacuum and squeezed vacuum state measurements. The squeezed light is sent to a polarization-maintaining 50:50 beamsplitter (BS) for interference with the LO.

In the LO path, the 1550 nm laser light is sent to an electro-optic phase modulator (EOSpace) to apply a phase ramp to the LO. The phase ramp is generated by sending a modulated signal from a function generator to the RF input of the modulator. After the modulator, a polarizing beamsplitter (PBS) removes light polarized along the fast axis to ensure interference in a single polarization mode at the beamsplitter. The outputs of the beamsplitter are sent to a fiber-coupled balanced homodyne detector (BHD). The BHD (Thorlabs PDB425C) has a 75 MHz bandwidth, 35 dB CMRR, and 1 A/W responsivity. The RF output of the BHD is sent to an RF spectrum analyzer (Keysight N9030b) operated in zero-span mode to measure the noise power levels in real time.

A total of four PPLN waveguides were used for SPDC in the experiments of the main text. The four experimental configurations are summarized in Table C.1. For each configuration, a pump power sweep was performed to characterize the SPDC waveguide and the effective efficiency of the setup [1]. For SPDC, the waveguide-coupled 775 nm pump power (P) can be related to the squeezing parameter (r) by $r \approx \mu\sqrt{P}$ [2], where μ is the SPDC efficiency [3]. The amount of squeezing can be characterized experimentally by comparing the variance of the quadratures measured with a squeezed state input to that measured with a vacuum state input in homodyne detection,

$$\frac{\langle \Delta\hat{Q}(\phi)^2 \rangle_{\mathrm{sq}}}{\langle \Delta\hat{Q}(\phi)^2 \rangle_{\mathrm{vac}}} = \eta(e^{-2r}\cos^2\phi + e^{2r}\sin^2\phi) + 1 - \eta. \tag{C.1}$$

From Eq. C.1, the squeezing (ΔQ_-^2) and antisqueezing (ΔQ_+^2) levels relative to the shot noise level in terms of the pump power are,

$$\Delta Q_\pm^2 = \eta \exp\left(\pm 2\mu\sqrt{P}\right) + 1 - \eta, \tag{C.2}$$

where η is the effective efficiency, including the effects of source loss, fiber-optic loss, detector loss, and shot noise clearance. For each pump power, the noise levels for the squeezing vacuum and vacuum states were measured over multiple LO phases. The pump power was varied by tuning the gain of the EDFA. To characterize the SPDC waveguide in configuration 1, an EDFA with up to 27 dBm output power was used, and to characterize the SPDC waveguides in configurations 2-4, an EDFA with up to 37 dBm output power was used. A phase ramp was applied to the LO to ensure that noise power levels were accumulated over multiple periods. The squeezing and antisqueezing levels for all configurations were estimated from the noise power distribution using the procedure described in Appendix B.

The characterizations for the four sources are shown in Fig. C.10b-e. The squeezing and antisqueezing estimates are plotted as a function of the waveguide-coupled power, which is calculated from,

$$P = \eta_{in} P_{\mathrm{SHG}}, \tag{C.3}$$

where η_{in} is the 775 nm input coupling efficiency and P_{SHG} is the power measured at the output of the SHG. The red curves are the theoretical model for the squeezing and antisqueezing levels from Eq. C.2. The best-fit parameters η and μ are obtained from a simultaneous least squares fit to the squeezing and antisqueezing levels. The errorbars are calculated from the Jacobian, and the residuals are evaluated at the optimal parameters. The key specifications for the four SPDC waveguides are summarized in Table C.2. The fitted effective efficiencies η of Fig. C.10b-e include the waveguide output coupling efficiencies η_{out} reported in Table C.2 as well as all other system losses (see Sec. C.4).

C.3 Measurement characterization

Squeezed light imaging

Data acquisition and analysis To image the squeezed light incident on the chip, we collect quadrature statistics of each antenna field mode over various phases by applying a 2π phase ramp on the LO at 0.5 Hz. The RF outputs from each QRX

Config.	SHG waveguide	SPDC waveguide	Experiments
1	Covesion H-spec.	HCP SC18068	Fig. 6.4c
2	HCP SC23399	Covesion H-spec.	Fig. 6.5b,c
3	HCP SC23399	HCP SC19075	Fig. 6.5f
4	HCP SC23399	Covesion M-spec.	Fig. 6.5e

Table C.1: Waveguide configurations used in experiments of Chapter 6. Configuration 1 was used for squeezed light imaging (Fig. 6.4c). Configuration 2 was used for beamforming channel sweep (Fig. 6.5b) and 32-channel pump power sweep (Fig. 6.5c). Configuration 3 was used for the field-of-view data (Fig. 6.5f). Configuration 4 was used for the beamwidth data (Fig. 6.5e).

SPDC waveguide	η_{in}	η_{out}	L (cm)	μ [mW$^{-1/2}$]
HCP SC18068	0.4	0.4	3	0.119
Covesion H-spec.	0.7	0.8	4	0.038
HCP SC19075	0.4	0.4	3	0.070
Covesion M-spec.	0.7	0.8	4	0.031

Table C.2: PPLN waveguides used as sources of squeezed light. η_{in} is the 775 nm input coupling efficiency, η_{out} is the 1550 nm output coupling efficiency, and μ is the SPDC efficiency obtained from a least-squares fit to the pump power sweep data in Fig. C.10.

are digitized and stored at a sampling rate of 20 MSa/s over 4 seconds. A digital bandpass filter with a 2 MHz bandwidth is applied to the digital data. The data is then passed through a moving mean and variance filter with a bin size of 260,000 and is downsampled by a factor of 16,000 to obtain the sample means and variances.

Squeezing parameter estimation The squeezing parameter was estimated with the source characterization setup of Fig. C.10 in Configuration 1. Five-second traces of the squeezed vacuum and vacuum noise power levels immediately before transmission to the chip are shown in Fig. C.11a. The corresponding histograms, kernel density estimates (KDEs), and derivatives of the KDEs are in C.11b-c. The estimates for the squeezed state are indicated with the blue crosses. From the squeezing estimate of -0.695 ∓ 0.029 dB and antisqueezing estimate of 9.158 ± 0.029 dB, we obtain $r = 1.945^{-0.006}_{+0.015}$ and $\eta = 0.151^{+0.003}_{-0.006}$.

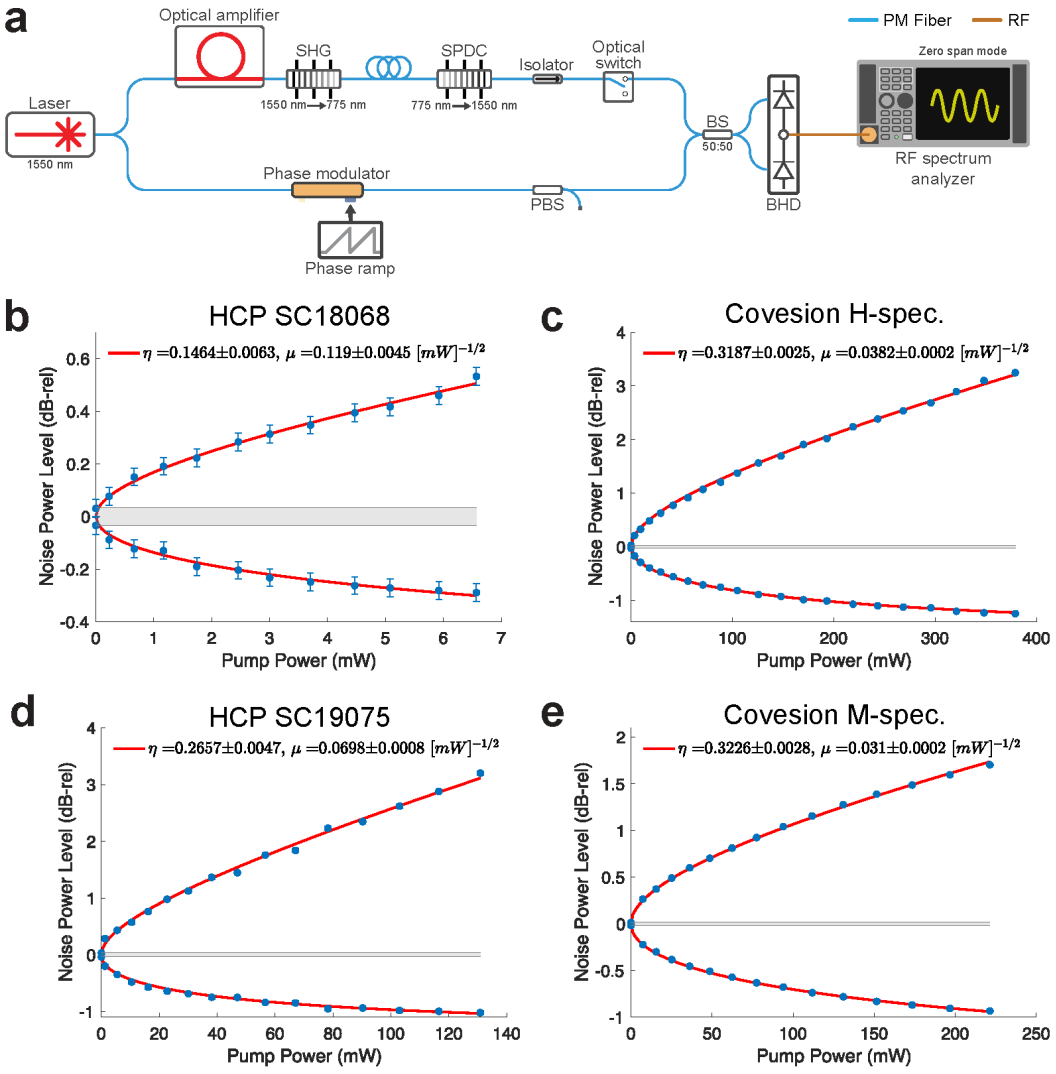

Figure C.10: Squeezed light source characterization. a) Experimental setup for source characterization. b) Configuration 1. Each noise power trace was measured over 10s with a sampling rate of 10 kHz, center frequency of 6 MHz, 1 MHz RBW, and 20 Hz VBW. c) Configuration 2. Each noise power trace was measured over 10s at 1 Hz phase modulation with a sampling rate of 5 kHz, 40 MHz CF, 8 MHz RBW, and 100 Hz VBW. d) Configuration 3. Each noise power trace was measured over 5s at 1 Hz phase modulation with a sampling rate of 20 kHz, 4 MHz CF, 20 MHz RBW, and 10 Hz VBW. e) Configuration 4. Each noise power trace was measured over 10s at 1 Hz phase modulation with a sampling rate of 10 kHz, 20 MHz CF, 8 MHz RBW, and 30 Hz VBW.

These numbers are within the error bars of the prediction from the source characterization of the SPDC waveguide (HCP SC18068). From the least-squares fit to

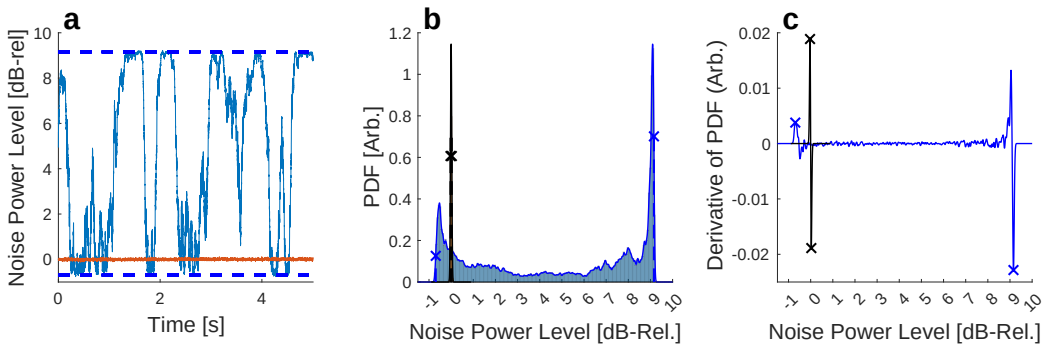

Figure C.11: Characterization of squeezing for squeezed light imaging. a) A five-second snippet of noise power levels for squeezed vacuum (blue) and vacuum (orange) measured at the source immediately before imaging. The noise powers were measured with a sampling rate of 20 kHz, center frequency of 6 MHz, 8 MHz RBW, and 100 Hz VBW. b) Histograms for the squeezed vacuum (light blue) and vacuum (orange) for the noise powers accumulated in a). The kernel density estimates (KDEs) for the squeezed vacuum (blue) and vacuum (black) histograms are plotted as solid lines. c) Derivative of KDEs for squeezed vacuum (blue) and vacuum (black).

the data in Fig. C.10a, $\eta = 0.146$ and $\mu = 0.119$ $[\mathrm{mW}]^{-1/2}$. For the waveguide-coupled pump power of $P = 315.6 \pm 47.3$ mW, the estimated squeezing parameter is $r = 2.114 \pm 0.159$.

Phase estimation The phases for the Wigner functions of the 32 antenna modes are found by performing a sinusoidal fit to a portion of the data with an approximately uniform phase ramp. The data and fits are shown in Fig. C.12.

Channel effective efficiency estimation The channel effective efficiencies are calculated from

$$\eta = \frac{(A-1)\exp(2r)}{(\exp(2r)-1)(A+\exp(2r))}, \tag{C.4}$$

where $A = \Delta Q_+^2/\Delta Q_-^2$ is the ratio of the antisqueezing (ΔQ_+^2) to squeezing (ΔQ_-^2) levels and $r = 1.945$. The ratio of antisqueezing to squeezing is obtained from the amplitudes of the sinusoidal fits in Fig. C.12. The channel effective efficiencies are plotted in Fig. C.13. For the Wigner functions, the geometric efficiency ($\eta_j^{(g)}$) for channel j is calculated as $\eta_j^{(g)} = \eta_j/\sum_j \eta_j$, where $\sum_j \eta_j = 0.017$. A Gaussian fit to the data yields a standard deviation of $\sigma = 48.8 \pm 2.5$ μm. This corresponds to

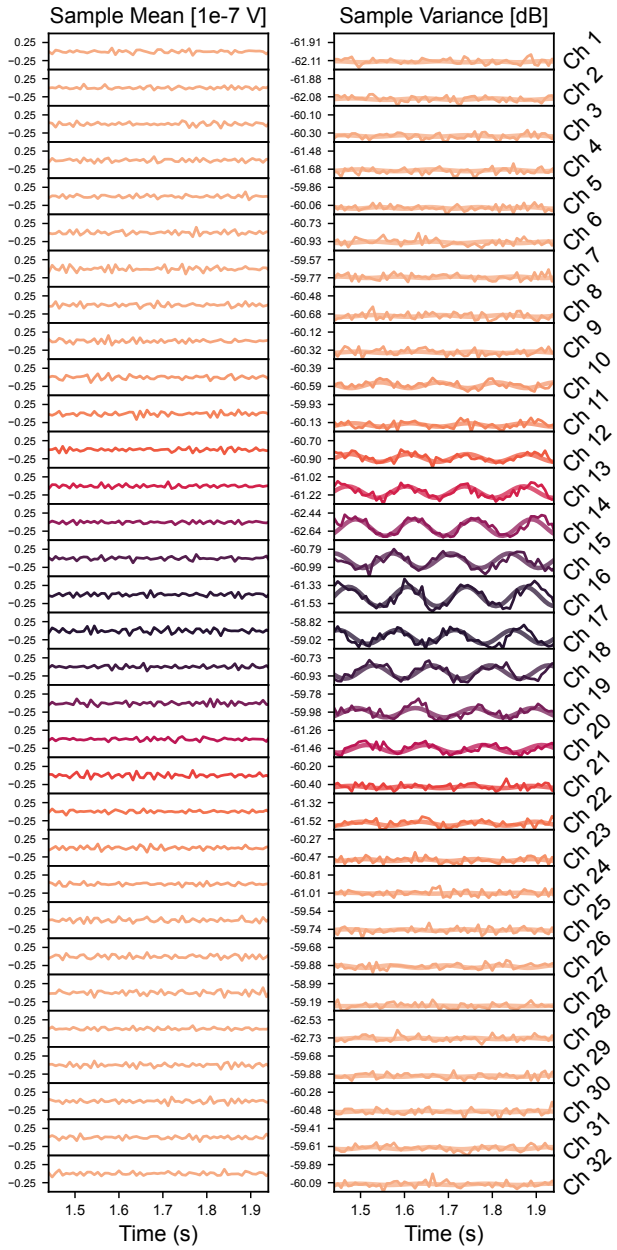

Figure C.12: Quadrature sample means and variances over time for all 32 channels. The sample means are approximately zero, while sinusoidal variations are observed in the sample variances. The fits to the variances are plotted as transparent solid lines.

a Gaussian beam diameter of $4\sigma = 195.2 \pm 10$ μm, consistent with the collimator beam diameter of 200 μm.

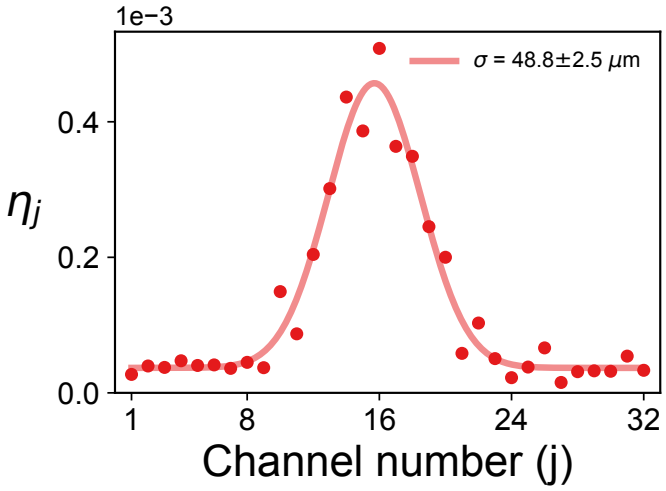

Figure C.13: Channel effective efficiencies versus channel number. The solid line is a Gaussian fit to the data.

Classical imaging

Replacing the transmitted squeezed vacuum state with a coherent state allows us to operate the chip in a classical mode, compatible with previously demonstrated classical imaging schemes [4]. This enables hybrid quantum-classical operation of the chip and comparisons of squeezed light measurements with classical measurements. In the case of imaging, we send a 1550 nm coherent state to the aperture through the collimator and apply 5 MHz phase modulation to the LO. The classical SNR is the same as effective efficiency (η), characterizing the decoherence of the quantum state in the receiver chain. Therefore, we approximate the classical SNR of this 5 MHz downconverted signal as a classical comparison to the squeezed light data. 32-channel RF outputs are digitized by a 32-channel digitizer with a sampling rate of 100 MSa/s. 10 ms of data are collected for each channel simultaneously using the same electronic readout as the squeezed light imaging measurement. By recording the outputs with and without sending light to the aperture, signal, and noise traces are collected for all 32 channels, as seen in Fig. C.14a. The raw traces are filtered with a digital bandpass filter with a center frequency of 5 MHz and a bandwidth of 100 kHz. We take the Hilbert transform of the filtered signal data to extract the analytical signal and the amplitude for each signal trace is determined, as seen in Fig. C.14b. Similarly, variances of the filtered noise data are measured and plotted

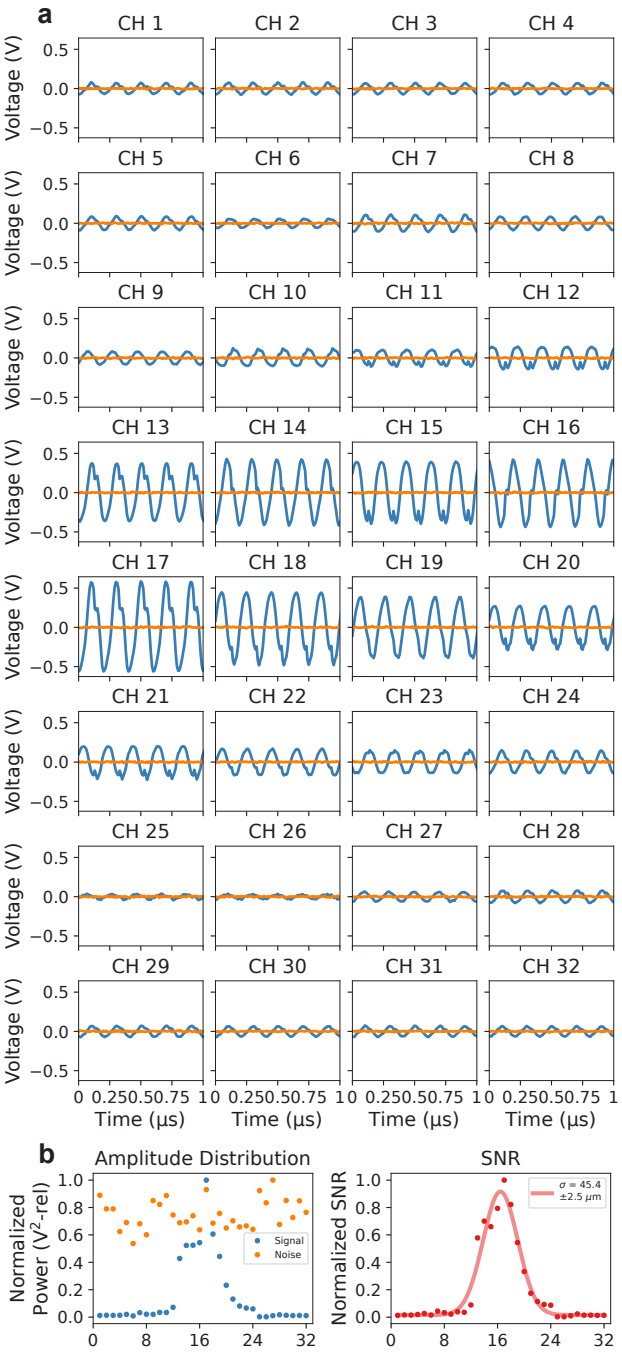

Figure C.14: Classical imaging characterization with coherent light. a) An example of signal (blue) and noise (orange) time-domain traces recorded for 32 channels. b) Extracted signal and noise powers across 32 channels in the frequency range of the downconverted tone and the corresponding SNR.

in Fig. C.14b. The ratio between these amplitudes gives the SNR, which is plotted in Fig. C.14c. A Gaussian fit is applied to the SNR data, which extracts a standard

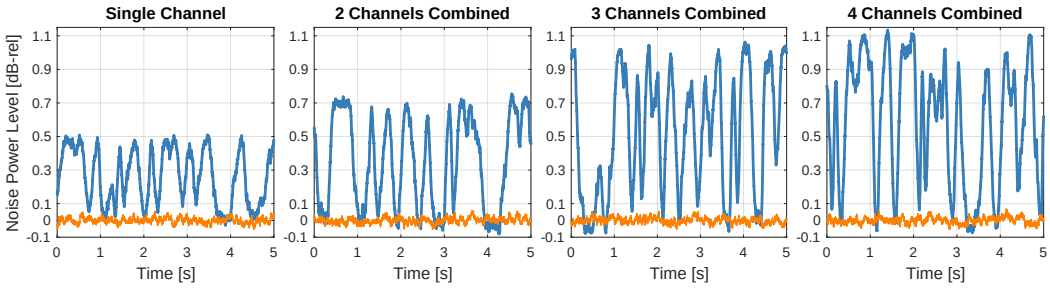

Figure C.15: Beamforming on-chip with the HCP SC18068 waveguide used for SPDC.

deviation of $\sigma = 45.4 \pm 2.5$ μm.

Beamforming and pump power sweep

The beamforming (Fig. 6.5b) and 32-channel source characterization (Fig. 6.5c) data of the main text were performed with the source in Configuration 2, using the Covesion H-spec waveguide for SPDC. The beamforming sweep was performed at a waveguide-coupled pump power of $P = 383.3 \pm 19.2$ mW. From the Covesion H-spec characterization in Sec. C.2, this corresponds to a squeezing parameter of $r = 0.748 \pm 0.019$.

Before performing the full 32-channel sweep, we first performed beamforming up to four channels using the HCP SC18068 waveguide for SPDC. A pump power of 226.8 ± 22.7 mW was coupled onto the waveguide, corresponding to a squeezing parameter of $r = 1.792 \pm 0.090$. The data are shown in Fig. C.15.

Classical channel sweep

The classical SNR data to extract the estimated efficiencies for the channel sweep (Fig. 6.5b) of the main text is done by using the same electronic readout with the ESA. We send a 1550 nm coherent state to the aperture through the collimator and apply 5 MHz phase modulation to the LO. We measure the downconverted 5 MHz signal in the ESA for each channel combination ($[1, 2, 4, \cdots, 30, 32]$ channels) as seen in Fig. C.16a (left). The video bandwidth for the signal measurements is 1 Hz, and the resolution bandwidth is 100 Hz. We also measure the noise powers for each channel combination using the ESA in zero-span mode at a center frequency of 5 MHz, with a resolution bandwidth of 2 MHz and a video bandwidth of 5 Hz as seen in Fig. C.16a (right). After collecting these traces, we measure the signal and noise amplitudes as seen in Fig. C.16b (left). For the signal amplitudes, we measure the

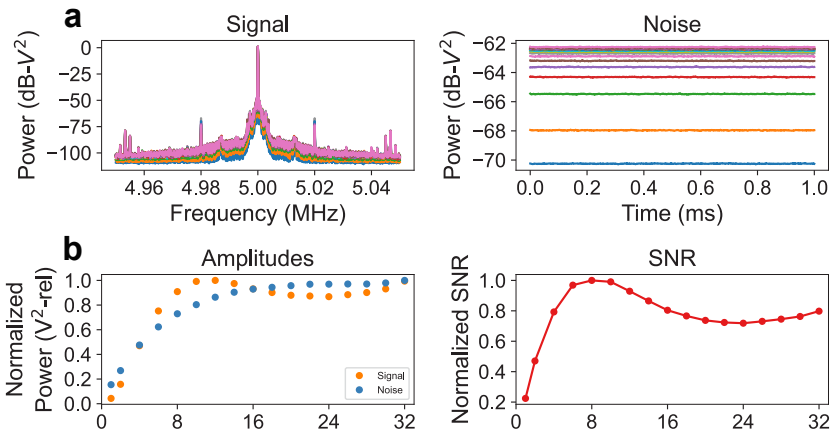

Figure C.16: Classical channel sweep characterization with coherent light. a) Signal (left) and noise (right) data recorded in the frequency domain for $[1, 2, 4, \cdots, 30, 32]$ channel combinations for the measurement in Fig. 6.5b. b) Extracted signal and noise powers (left) in the frequency range of the downconverted tone and the corresponding SNR (right).

total power in the frequency range between 4.95 MHz to 5.05 MHz in the collected data. For the noise amplitudes, we measure the mean power in the noise floor. We then extract the normalized SNR by taking the ratio of these amplitudes and normalizing the values as seen in Fig. C.16b (right). The resulting values are used to plot the expected squeezing and antisqueezing using Eq. C.1 with the squeezing parameter extracted from source characterization. For the proportionality constant, we apply a least-squares fit with η as the floating parameter with the squeezing parameter bounded as $r = 0.748 \pm 0.019$ to fit the resulting plot to the data, yielding a proportionality constant of $\eta_c = 0.021$.

Beamwidth

The beamwidth measurement (Fig. 6.5e) of the main text was performed with the source in Configuration 4, using the Covesion M-spec waveguide for SPDC. The beamwidth data were taken at a waveguide-coupled pump power of $P = 383.6 \pm 19.7$ mW. From the Covesion M-spec characterization in Sec. C.2, this corresponds to a squeezing parameter of $r = 0.607 \pm 0.015$.

Classical beamwidth

The classical SNR data to extract the estimated efficiencies for the beamwidth measurements (Fig. 6.5e) of the main text is done by using the same electronic

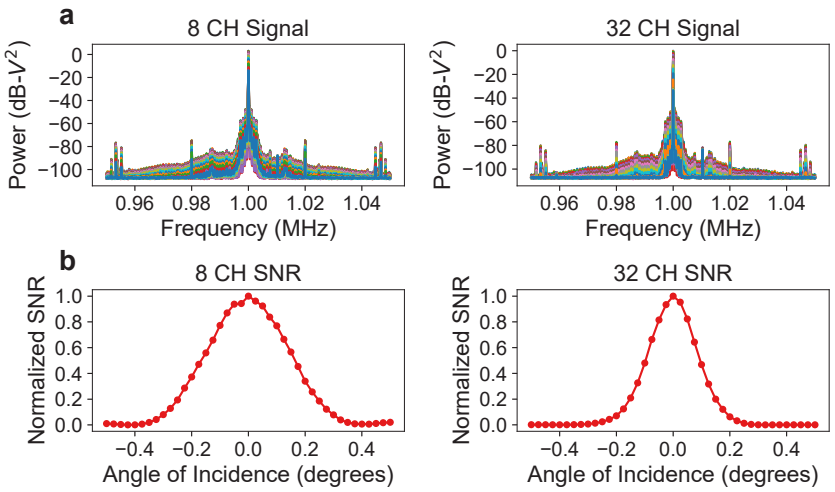

Figure C.17: Classical beamwidth characterization with coherent light. a) Signal data recorded in the frequency domain for different angles of incidence for 8 (left) and 32 (right) channels combined for the measurement in Fig. 6.5e. b) Extracted signal powers corresponding to normalized SNR in the frequency range of the downconverted tone for 8 (left) and 32 (right) channels combined.

readout with the ESA. We send a 1550 nm coherent state to the aperture through the collimator and apply 1 MHz phase modulation to the LO. We measure the downconverted 1 MHz signal in the ESA for each incidence angle for both 8 channels and 32 channels combined, as seen in Fig. C.17a. The video bandwidth for the signal measurements is 1 Hz, and the resolution bandwidth is 100 Hz. Since the electronic configuration for these measurements stays the same, the noise floor doesn't change, making signal directly proportional to SNR. Using the measured spectra in Fig. C.17a, we measure the total power in the frequency range between 0.95 MHz to 1.05 MHz to acquire the signal amplitudes proportional to SNR for both 8 channels and 32 channels combined, as seen in Fig. C.17b. The resulting values are used to plot the expected squeezing and antisqueezing using Eq. C.1 with the squeezing parameter extracted from source characterization. For the proportionality constant, we apply a least-squares fit with η as the floating parameter and the squeezing parameter bounded as $r = 0.607 \pm 0.0152$ to fit the resulting plot to the data, yielding an optimal squeezing parameter of $r = 0.611$ and proportionality constants of $\eta_c^{(8)} = 0.0191$ and $\eta_c^{(32)} = 0.0141$ for 8 and 32 channels combined, respectively.

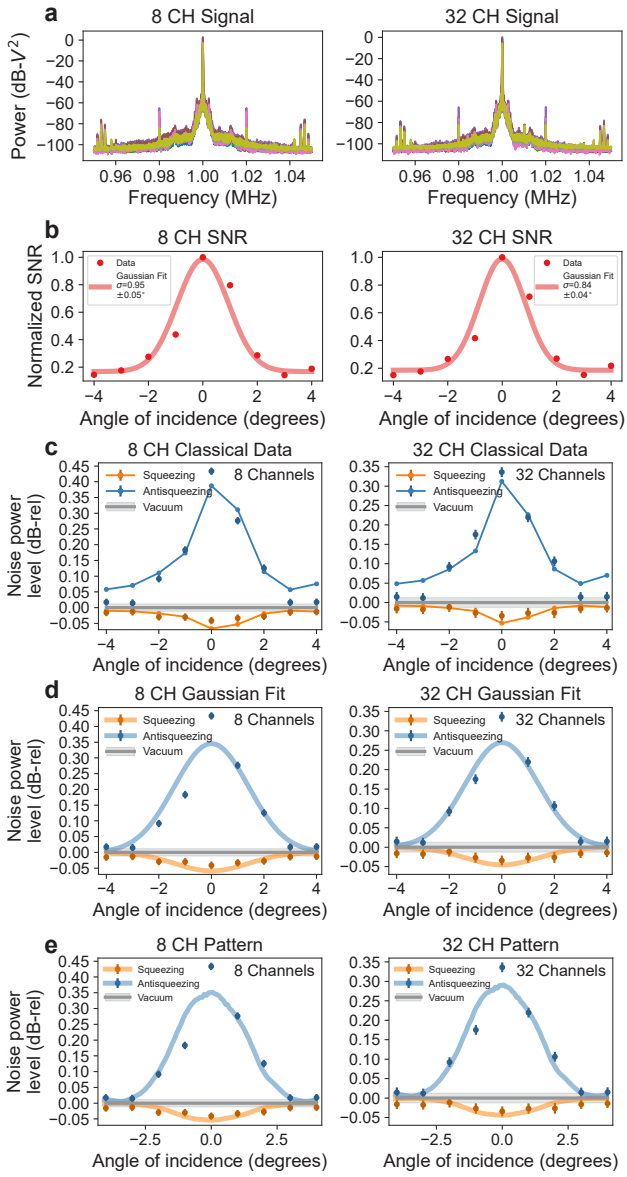

Figure C.18: Classical field-of-view characterization with coherent light. a) Signal data recorded in the frequency domain for different angles of incidence for 8 (left) and 32 (right) channels combined for the measurement in Fig. 6.5f. b) Extracted signal powers corresponding to normalized SNR in the frequency range of the downconverted tone for 8 (left) and 32 (right) channels combined. A Gaussian fit is applied to the data, yielding σ =0.95±0.05° and σ =0.84±0.04° for 8 and 32 channels combined, respectively. c) Comparison of the classical data to the squeezed light data for 8 (left) and 32 (right) channels combined. d) Comparison of the Gaussian fit of the classical data to the squeezed light data for 8 (left) and 32 (right) channels combined. e) Comparison of single antenna radiation pattern to the squeezed light data for 8 (left) and 32 (right) channels combined, repeated from Fig. 6.5f.

Field of view

The field-of-view (FoV) experiment (Fig. 6.5f) of the main text was performed with the source in Configuration 3, using the HCP SC19075 waveguide for SPDC. The FoV data were taken at a waveguide-coupled pump power of $P = 153.4 \pm 15.3$ mW. From the HCP SC19075 characterization in Sec. C.2, this corresponds to a squeezing parameter of $r = 0.865 \pm 0.043$.

Classical field of view

Multiple approaches were taken to acquire the classical comparison for the FoV measurement (Fig. 6.5f) of the main text. The single antenna radiation pattern is an accurate classical estimate of the full array pattern since the aperture is fully filled, and the electronic configuration stays the same for each angle of incidence. Therefore, the classical comparison in Fig. 6.5f uses the measured far-field single antenna radiation pattern. We normalize this pattern and set it to be proportional to SNR. The resulting values are used to plot the expected squeezing and antisqueezing using Eq. C.1 with the squeezing parameter extracted from source characterization, as shown in Fig. 6.5f and also in Fig. C.18e. For the proportionality constant, we apply a least-squares fit with η as the floating parameter and with the squeezing parameter bounded as $r = 0.865 \pm 0.043$ to fit the resulting plot to the data, yielding an optimal squeezing parameter of $r = 0.908$ and proportionality constants of $\eta_c^{(8)} = 0.0167$ and $\eta_c^{(32)} = 0.0152$ for 8 and 32 channels combined, respectively.

A beamformed classical measurement is also taken for each of the 9 angles in the FoV measurement. For classical FoV measurement, we send a 1550 nm coherent state to the aperture through the collimator and apply 1 MHz phase modulation to the LO. We measure the downconverted 1 MHz signal in the ESA for each angle of incidence for both 8 channels and 32 channels combined, as seen in Fig. C.18a. The video bandwidth for the signal measurements is 1 Hz, and the resolution bandwidth is 100 Hz. Since the electronic configuration for these measurements stays the same, the noise floor doesn't change, making signal directly proportional to SNR. Using the measured spectra in Fig. C.18a, we measure the total power in the frequency range between 0.95 MHz to 1.05 MHz to acquire the signal amplitudes proportional to SNR for both 8 channels and 32 channels combined as seen in Fig. C.18b. The resulting values are used to plot the expected squeezing and antisqueezing using Eq. C.1 with the squeezing parameter extracted from source characterization. For the proportionality constant, we apply a least-squares fit with η as the floating

parameter and with the squeezing parameter bounded as $r = 0.865 \pm 0.043$ to fit the resulting plot to the data, yielding an optimal squeezing parameter of $r = 0.908$ and a proportionality constant of $\eta_c^{(8)} = 0.0181$ and $\eta_c^{(32)} = 0.0145$ for 8 and 32 channels combined, respectively. The comparison of the classical data to the squeezed light data in Fig. 6.5f of main text is shown in Fig. C.18c. We also fit the classical data to a Gaussian function, yielding a standard deviation of 0.95±0.05 degrees and 0.84±0.04 degrees for 8 and 32 channels combined, respectively. The comparison of the Gaussian fit to the squeezed light data is shown in Fig. C.18d.

A linear interpolation is used to extract the classical FoV to directly compare with the FoV extracted from squeezed light data in the main text. With linear interpolation on the classical data, we extract an FoV of 2.5 degrees and 2.3 degrees for 8 and 32 channels combined, respectively. These classical estimates match well with the squeezed light FoV of 2.3 degrees and 2.7 degrees for 8 and 32 channels combined, respectively, in the main text. The discrepancy between classical and squeezed light data is due to the measurements being taken sequentially. Future schemes in which classical and non-classical light are multiplexed in the same link [5] would minimize this discrepancy.

C.4 Loss budget

We characterize the measurement setup losses for each experiment (see Supplementary Information of Ref. [6]) and report them here. A summary of the system losses for each measurement setup is in Table C.3.

Experiment	Source loss (dB)	Free-space loss (dB)	On-chip loss (dB)	RF loss (dB)	Total loss (dB)
Imaging	8.17	1.14	5.72	0.137	15.2
Channel sweep	6.97	2.18	5.72	0.660	15.5
Power sweep	6.97	4.85	5.72	2.16	19.7
BW (8CH)	6.97	2.18	5.72	0.306	15.2
BW (32CH)	6.97	4.85	5.72	1.43	19.0
FoV (8CH)	6.90	2.18	5.72	1.21	16.1
FoV (32CH)	6.90	4.85	5.72	2.13	19.6

Table C.3: Measurement system losses for each experiment. The table breaks down loss contributions from the source, free-space link, on-chip photonic circuit, and RF readout electronics.

References

[1] Henning Vahlbruch, Moritz Mehmet, Karsten Danzmann, and Roman Schnabel. "Detection of 15 dB squeezed states of light and their application for the absolute calibration of photoelectric quantum efficiency." In: Physical Review Letters 117.11 (2016), p. 110801.

[2] T. Hirano, K. Kotani, T. Ishibashi, S. Okude, and T. Kuwamoto. "3 dB squeezing by single-pass parametric amplification in a periodically poled KTiOPO4 crystal." In: Opt. Lett. 30.13 (July 2005), pp. 1722–1724.

[3] Florian Kaiser, Bruno Fedrici, Alessandro Zavatta, Virginia d'Auria, and Sébastien Tanzilli. "A fully guided-wave squeezing experiment for fiber quantum networks." In: Optica 3.4 (2016), pp. 362–365.

[4] Christopher Rogers, Alexander Y. Piggott, David J. Thomson, et al. "A universal 3D imaging sensor on a silicon photonics platform." In: Nature 590.7845 (Feb. 2021), pp. 256–261.

[5] R Valivarthi, P Umesh, C John, K A Owen, V B Verma, S W Nam, D Oblak, Q Zhou, and W Tittel. "Measurement-device-independent quantum key distribution coexisting with classical communication." In: Quantum Science and Technology 4.4 (July 2019), p. 045002.

[6] Volkan Gurses, Samantha I. Davis, Raju Valivarthi, Neil Sinclair, Maria Spiropulu, and Ali Hajimiri. "An on-chip phased array for non-classical light." In: Nature Communications 16.1 (2025), p. 6849.

Appendix D

ON-CHIP CLUSTER STATE GENERATION

To illustrate the potential of integrated optoelectronic systems for quantum information processing, we perform a proof-of-concept demonstration of cluster state generation in a measurement-based approach [1, 2] using the QPA system of Chapter 6. Cluster states are a class of entangled graph states that form a resource for universal measurement-based quantum computation [3]. Continuous-variable Gaussian cluster states can be generated by interfering squeezed states in linear optical networks [4, 5]. Here, we generate two-mode cluster state correlations by implementing a virtual linear optical network after optoelectronic downconversion with an RF circuit.

Cluster states of up to eight modes have been demonstrated with bulk multipixel homodyne detection systems by programming virtual optical networks in digital post-processing [1]. The virtual networks mix different spatial regions in a beam of light to match the detection basis to an entangled spatial mode basis. This method of entanglement generation allows for highly compact and versatile implementations of Gaussian quantum computation in the measurement-based model [2], which can be scaled to a higher number of modes by interfacing quantum PICs like the QPA chip with special-purpose RF or microwave ICs.

D.1 Experiment

The quantum circuit architecture used in the experiment is shown in Fig. D.1a. A squeezed state is transmitted over free space to the QPA chip, and a phase ramp at a modulation frequency of 0.5 Hz is applied to the LO before coupling it to the chip. The RF outputs of the QRXs in each half of the array are sent to a 16:1 power combiner. Beamforming is performed on all 32 channels such that the two outputs of the power combiners are in phase. To improve the geometric efficiency, the outermost 12 channels are disconnected from each 16:1 power combiner, for a total of 8 pixel modes in Fig. D.1a. The outputs of the power combiners are digitized at a sampling rate of 100 MSa/s, and an RF beamsplitter transformation is emulated on the digitized quadratures (see Methods).

With our architecture in Fig. D.1a, the overall transformation on the input field can

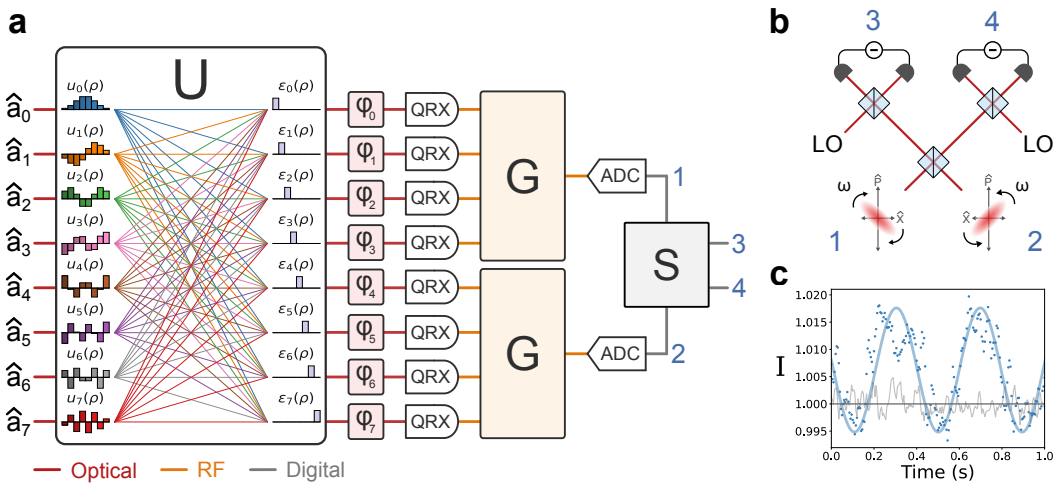

Figure D.1: Quantum optoelectronic processing. a) Optoelectronic circuit architecture for entanglement generation. The free space operation (U) corresponds to the change-of-basis matrix mapping the spatial modes of the input state to the pixel modes, where ρ represents the spatial coordinates in the aperture plane of the chip. Each colored line represents a matrix element corresponding to the overlap of an antenna and pixel mode function. A phase shifter φ_j is applied to each pixel mode, and each half of the array is combined in a 16:1 RF power combiner (G). The output voltages of the power combiners are digitized and followed by a beamsplitter transformation (S). b) Emulated optical circuit for two-mode Gaussian cluster state generation. c) The cluster state inseparability (I) measured over time for a linear phase ramp. The data for the squeezed vacuum and vacuum states are plotted in blue and gray, respectively. The solid lines are the analytical expectations with a sinusoidal fit to the squeezed data.

be summarized as,

$$\vec{a}_{\text{out}} = S(G \oplus G)DU\vec{a}_{\text{in}}, \tag{D.1}$$

where U is the free-space change-of-basis unitary mapping the input modes to pixel modes, $D = \text{diag}(e^{i\phi_1}, e^{i\phi_2}, ...)$,

$$G \oplus G = \begin{pmatrix} 1 & 1 & 1 & 1 & 0 & 0 & 0 & 0 \\ 0 & 0 & 0 & 0 & 1 & 1 & 1 & 1 \end{pmatrix} \tag{D.2}$$

is the gain matrix of the RF power combiners, and

$$S = \frac{1}{\sqrt{2}} \begin{pmatrix} 1 & i \\ i & 1 \end{pmatrix} \tag{D.3}$$

is the beamsplitter matrix. The transformation of S is performed on the digitized quadratures as an emulation of an RF directional coupler, where complex matrix elements are implemented as a $\pi/2$ phase shift. For a two-mode Gaussian cluster state generated with S, the cluster state correlations are given by,

$$\mathrm{Var}(\hat{Q}_3(\theta) - \hat{P}_4(\theta)) = \mathrm{Var}(\hat{Q}_1(\theta)), \tag{D.4}$$

$$\mathrm{Var}(\hat{Q}_4(\theta) - \hat{P}_3(\theta)) = \mathrm{Var}(\hat{Q}_2(\theta)), \tag{D.5}$$

where $\mathrm{Var}(\hat{Q}_i(\theta))$ for $i = 1, 2$ is given by,

$$\langle \Delta \hat{Q}_\theta^2 \rangle_{\mathrm{sq}} = \frac{\eta}{2}(e^{-2r}\cos^2\theta + e^{2r}\sin^2\theta) + \frac{1-\eta}{2},$$

for squeezed modes, such that the right-hand side is zero at $\theta = 0$ in the limit of large squeezing parameter and low loss. The inseparability criterion required to show cluster state entanglement is

$$I = \mathrm{Var}(\hat{P}_4 - \hat{Q}_3) + \mathrm{Var}(\hat{P}_3 - \hat{Q}_4) < 1, \tag{D.6}$$

where $\hat{Q}_i, \hat{P}_i$ are the quadrature operators for each cluster state mode denoted by $i = 3, 4$ in Fig. D.1b, and the variances are relative to those of the vacuum state.

The quadrature correlations I as a function of time are shown in Fig. D.1b. We observe the sinusoidal signature expected for a rotation of the measurement basis due to the LO phase modulation.

D.2 Cluster state inseparability

The minimum and maximum inseparability levels are estimated from the histograms of the inseparabilities with the procedure in Appendix B. The histogram and kernel density estimate of the data in D.1c is shown in Fig. D.2. The estimates for the min. and max. inseparabilities are 0.994 ± 0.002 and 1.018 ± 0.002, respectively. The sinusoidal fit in Fig. D.1c. is performed with the amplitude fixed by the minimum and maximum inseparability estimates and the angular frequency (ω) and phase (ϕ) taken as floating parameters. We obtain fit parameters of $\omega = 7.99 \pm 0.12$ and $\phi = 0.703 \pm 0.069$.

D.3 Discussion

We estimate a maximum inseparability of $I = 1.0176 \pm 0.0004$ and a minimum inseparability of $I = 0.9948 \pm 0.0004$. The resolution of the measured entanglement

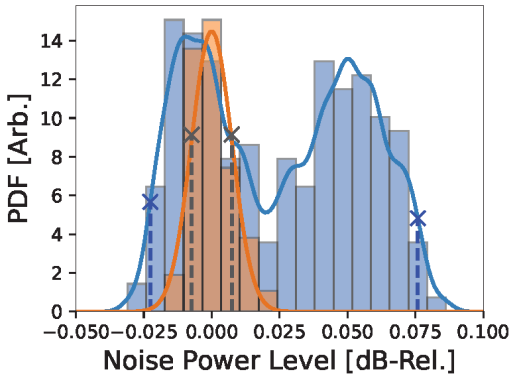

Figure D.2: Histogram of inseparability data in Fig. D.1c for squeezed vacuum (blue) and vacuum (orange) states. The solid blue and orange lines are the kernel density estimates. The min. and max. inseparability estimates are indicated with blue crosses. The vacuum standard deviations are indicated with black crosses.

is enabled by the high precision and stability offered by the chip-scale optoelectronics. We note that in our experiment, the inseparability given by Eq. D.6 has a lower bound of 0.5 since the squeezed light was generated in a single mode. This lower bound can be overcome by transmitting multiple squeezed modes to the chip, allowing for the generation of large cluster states up to 32 modes.

Our demonstration show the potential for optoelectronic systems on-chip for applications in quantum information processing. More broadly, integrating quantum photonics with electronics in the same package offers novel engineering opportunities in realizing large-scale room-temperature quantum systems. Coherent processing of downconverted quantum optical information with RF or microwave integrated circuits could enable compact and low-loss optoelectronic approaches to measurement-based quantum information processing, where certain linear operations are offloaded to electronics, as a generalization of classical microwave photonics [6].

References

[1] Seiji Armstrong, Jean-François Morizur, Jiri Janousek, Boris Hage, Nicolas Treps, Ping Koy Lam, and Hans-A Bachor. “Programmable multimode quantum networks.” In: Nature Communications 3.1 (2012), p. 1026.

[2] Giulia Ferrini, Jean-Pierre Gazeau, Thomas Coudreau, Claude Fabre, and Nicolas Treps. “Compact Gaussian quantum computation by multi-pixel homodyne detection.” In: New Journal of Physics 15.9 (2013), p. 093015.

[3] Robert Raussendorf and Hans J. Briegel. “A one-way quantum computer.” In: Physical Review Letters 86.22 (2001), p. 5188.

[4] Peter van Loock, Christian Weedbrook, and Mile Gu. “Building Gaussian cluster states by linear optics.” In: Physical Review A 76.3 (2007), p. 032321.

[5] Mitsuyoshi Yukawa, Ryuji Ukai, Peter Van Loock, and Akira Furusawa. “Experimental generation of four-mode continuous-variable cluster states.” In: Physical Review A 78.1 (2008), p. 012301.

[6] David Marpaung, Jianping Yao, and José Capmany. “Integrated microwave photonics.” In: Nature Photonics 13.2 (Feb. 2019), pp. 80–90.

Appendix E

ANALYTICAL METHODS FOR MODELING REAL-WORLD PHOTONIC QUANTUM TELEPORTATION

E.1 Analytical derivations of expressions

HOM interference visibility

We employ the characteristic function formalism described in Chapter 9 considering the setup shown in Fig. 9.2. For this derivation, we use 7×7 block matrices with 2×2 sub-matrices, with each sub-matrix representing correlations between different optical modes. The first column of the block matrix represents the coherent state mode; the third and fifth columns represent vacuum inputs at the virtual beamsplitters with transmission ζ^2 to account for the mode indistiguishability, the second and sixth columns represent the vacuum inputs at the 50:50 beamsplitter that are mixed with the distinguishable parts of the modes; and the fourth and the seventh columns represent the idler and signal modes of the TMSV state. We first describe the overall state of the system after transmission losses, given by the block covariance matrix,

$$\gamma = \begin{pmatrix} \mathbf{I_{2x2}} & 0 & 0 & 0 & 0 & 0 & 0 \\ 0 & \mathbf{I_{2x2}} & 0 & 0 & 0 & 0 & 0 \\ 0 & 0 & \mathbf{I_{2x2}} & 0 & 0 & 0 & 0 \\ 0 & 0 & 0 & (1+2\eta_i\mu)\mathbf{I_{2x2}} & 0 & 0 & 2\sqrt{\eta_i\eta_s\mu(1+\mu)}\sigma_{\mathbf{3}} \\ 0 & 0 & 0 & 0 & \mathbf{I_{2x2}} & 0 & 0 \\ 0 & 0 & 0 & 0 & 0 & \mathbf{I_{2x2}} & 0 \\ 0 & 0 & 0 & 2\sqrt{\eta_i\eta_s\mu(1+\mu)}\sigma_{\mathbf{3}} & 0 & 0 & (1+2\eta_s\mu)\mathbf{I_{2x2}} \end{pmatrix},$$

where $\sigma_{\mathbf{3}} = \begin{pmatrix} 1 & 0 \\ 0 & -1 \end{pmatrix}$. The displacement vector is $\vec{d} = \sqrt{2}\begin{pmatrix} \mathrm{Re}(\alpha) & \mathrm{Im}(\alpha) & 0 & \dots & 0 \end{pmatrix}^T$, with α already accounting for loss in the coherent state channel. From here, we

apply the mismatch matrix,

$$\begin{pmatrix} \sqrt{\zeta}\,\mathbf{I_{2x2}} & 0 & \sqrt{1-\zeta}\,\mathbf{Z} & 0 & 0 & 0 & 0 \\ 0 & \mathbf{I_{2x2}} & 0 & 0 & 0 & 0 & 0 \\ \sqrt{1-\zeta}\,\mathbf{Z} & 0 & \sqrt{\zeta}\,\mathbf{I_{2x2}} & 0 & 0 & 0 & 0 \\ 0 & 0 & 0 & \sqrt{\zeta}\,\mathbf{I_{2x2}} & \sqrt{1-\zeta}\,\mathbf{Z} & 0 & 0 \\ 0 & 0 & 0 & \sqrt{1-\zeta}\,\mathbf{Z} & \sqrt{\zeta}\,\mathbf{I_{2x2}} & 0 & 0 \\ 0 & 0 & 0 & 0 & 0 & \mathbf{I_{2x2}} & 0 \\ 0 & 0 & 0 & 0 & 0 & 0 & \mathbf{I_{2x2}} \end{pmatrix},$$

and the beam splitting matrix,

$$\frac{1}{\sqrt{2}}\begin{pmatrix} \mathbf{I_{2x2}} & 0 & 0 & \mathbf{Z} & 0 & 0 & 0 \\ 0 & \mathbf{I_{2x2}} & 0 & 0 & \mathbf{Z} & 0 & 0 \\ 0 & 0 & \mathbf{I_{2x2}} & 0 & 0 & \mathbf{Z} & 0 \\ \mathbf{Z} & 0 & 0 & \mathbf{I_{2x2}} & 0 & 0 & 0 \\ 0 & \mathbf{Z} & 0 & 0 & \mathbf{I_{2x2}} & 0 & 0 \\ 0 & 0 & \mathbf{Z} & 0 & 0 & \mathbf{I_{2x2}} & 0 \\ 0 & 0 & 0 & 0 & 0 & 0 & \sqrt{2}\,\mathbf{I_{2x2}} \end{pmatrix},$$

where $\mathbf{Z} = \begin{pmatrix} 0 & -1 \\ 1 & 0 \end{pmatrix}$. This now allows calculation of the twofold coincidence probability,

$$\begin{aligned} p_{\text{2-fold}} = \mathrm{Tr}\big\{\hat{\rho}'\big(1 &- \mathbb{I}_{b_1,b_2,b_3,c} \otimes |0\rangle\langle 0|^{\otimes 3}_{a_1,a_2,a_3} \\ &- \mathbb{I}_{a_1,a_2,a_3,c} \otimes |0\rangle\langle 0|^{\otimes 3}_{b_1,b_2,b_3} \\ &+ \mathbb{I}_c \otimes |0\rangle\langle 0|^{\otimes 6}_{a_1,a_2,a_3,b_1,b_2,b_3}\big)\big\}, \end{aligned} \tag{E.1}$$

and the threefold coincidence probability,

$$\begin{aligned} p_{\text{3-fold}} = \mathrm{Tr}\big\{\hat{\rho}'\big(1 &- \mathbb{I}_{a_1,a_2,a_3,b_1,b_2,b_3} \otimes |0\rangle\langle 0|_c \\ &- \mathbb{I}_{b_1,b_2,b_3,c} \otimes |0\rangle\langle 0|^{\otimes 3}_{a_1,a_2,a_3} \\ &- \mathbb{I}_{a_1,a_2,a_3,c} \otimes |0\rangle\langle 0|^{\otimes 3}_{b_1,b_2,b_3} \\ &+ \mathbb{I}_{b_1,b_2,b_3} \otimes |0\rangle\langle 0|^{\otimes 4}_{a_1,a_2,a_3,c} \\ &+ \mathbb{I}_{a_1,a_2,a_3} \otimes |0\rangle\langle 0|^{\otimes 4}_{b_1,b_2,b_3,c} \\ &+ \mathbb{I}_c \otimes |0\rangle\langle 0|^{\otimes 6}_{a_1,a_2,a_3,b_1,b_2,b_3} \\ &- |0\rangle\langle 0|^{\otimes 7}_{a_1,a_2,a_3,b_1,b_2,b_3,c}\big)\big\}, \end{aligned} \tag{E.2}$$

where the subscripts a_i, b_i, and c, with $i \in \{1, 2, 3\}$, represent the coherent state, idler, and signal modes respectively. Note that the subscripts of the identity matrices

indicate which modes are traced out for a given calculation. Using Eq. 9.14, we calculate

$$\mathrm{Tr}\{\hat{\rho}(\mathbb{I}_{x_1,\ldots,x_m}\otimes|0\rangle\langle 0|^{\otimes n}_{y_1,\ldots,y_n}\} = \frac{2^n}{\sqrt{\det\left(\gamma_{y_1,\ldots,y_n}+\mathbb{I}\right)}}\exp\left(-\vec{d}^{T}_{y_1,\ldots,y_n}(\gamma_{y_1,\ldots,y_n}+\mathbb{I})^{-1}\vec{d}_{y_1,\ldots,y_n}\right),$$

where x_i represents the modes traced out and y_i represents the remaining modes. We now use this expression to calculate each of the terms in Eqs. E.1 and E.2, yielding

$$\begin{aligned} p_{\text{2-fold}}(|\alpha|^2,\mu,\zeta,\eta_i) =& 1+\frac{\exp\left(-|\alpha|^2\right)}{1+\eta_i\mu} \\ &- 4\frac{\exp\left(-|\alpha|^2+\frac{|\alpha|^2(2+(1+\zeta^2)\eta_i\mu)}{4+2\eta_i\mu}\right)}{2+\eta_i\mu}, \end{aligned}$$

and

$$\begin{aligned} p_{\text{3-fold}}(|\alpha|^2,\mu,\zeta,\eta_s,\eta_i) =& \frac{\eta_s\mu}{1+\eta_s\mu}-2\frac{\mathrm{e}^{-\frac{|\alpha|^2/2[1+(1-\zeta^2)\eta_i\mu/2]}{1+\eta_i\mu/2}}}{1+\eta_i\mu/2} \\ &+\frac{\mathrm{e}^{-|\alpha|^2}(1-\eta_i)\eta_s\mu}{(1+\eta_i\mu)(1+\eta_s(1-\eta_s)\mu+\eta_s\mu)} \\ &+2\frac{\mathrm{e}^{-\frac{|\alpha|^2/2[1+(1-\zeta^2)(1-\eta_s)\eta_i\mu/2+\eta_s\mu]}{1+(1-\eta_s)\eta_i\mu/2+\eta_s\mu}}}{1+(1-\eta_s)\eta_i\mu/2+\eta_s\mu}. \end{aligned}$$

Teleportation fidelity

We now consider the setup of Fig. 9.2. Similar to the HOM visibility derivation, we use 14×14 block matrices with 2×2 sub-matrices, with each sub-matrix representing correlations between different optical modes. The first and the eight columns of the block matrices represent the early and late coherent state modes; the fourth, and eleventh columns represent the early and late idler modes; the seventh and fourteenth columns represents the early and late signal mode; and the rest represents the vacuum inputs at the virtual and the 50:50 beamsplitters. Again, the block covariance matrix, $\mathbf{I_{6x6}}\oplus\mathbf{M}$, denotes the state of the system after losses, where

$$\mathbf{M} = \mathbf{I_{11x11}}\otimes\mathbf{I_{2x2}} + 2\mu\left(\eta_s\mathbf{P_s}+\eta_i\mathbf{P_i}\right)\otimes\mathbf{I_{2x2}} + 2\sqrt{\eta_s\eta_i\,\mu(1+\mu)}\,\mathbf{A}\otimes\sigma_{\mathbf{3}},$$

$$\mathbf{P_s} = \mathrm{diag}(1,0,0,0,0,0,1,0,0,0,0), \quad \mathbf{P_i} = \mathrm{diag}(0,0,0,0,0,0,0,0,0,1,1),$$

$$\mathbf{A} = \mathbf{E}_{1,10}+\mathbf{E}_{10,1}+\mathbf{E}_{7,11}+\mathbf{E}_{11,7}, \qquad \sigma_{\mathbf{3}} = \begin{pmatrix}1 & 0\\ 0 & -1\end{pmatrix},$$

and $\mathbf{E}_{j,k}$ is an 11×11 matrix unit at (j,k) and 0 elsewhere.

The displacement vector is,

$$\vec{d} = \sqrt{2}\begin{pmatrix} \mathrm{Re}(\alpha) & \mathrm{Im}(\alpha) & 0 & 0 & 0 & 0 & 0 & 0 & 0 & 0 \\ 0 & 0 & \mathrm{Re}(\alpha) & \mathrm{Im}(\alpha) & 0 & 0 & ... & 0 & & \end{pmatrix}^T,$$

and α again already takes into account loss. The mismatch matrix,

$$\mathbf{I_{2x2}} \otimes \begin{pmatrix} \sqrt{\zeta}\,\mathbf{I_{2x2}} & 0 & \sqrt{1-\zeta}\,\mathbf{Z} & 0 & 0 & 0 \\ 0 & \mathbf{I_{2x2}} & 0 & 0 & 0 & 0 \\ \sqrt{1-\zeta}\,\mathbf{Z} & 0 & \sqrt{\zeta}\,\mathbf{I_{2x2}} & 0 & 0 & 0 \\ 0 & 0 & 0 & \sqrt{\zeta}\,\mathbf{I_{2x2}} & \sqrt{1-\zeta}\,\mathbf{Z} & 0 \\ 0 & 0 & 0 & \sqrt{1-\zeta}\,\mathbf{Z} & \sqrt{\zeta}\,\mathbf{I_{2x2}} & 0 \\ 0 & 0 & 0 & 0 & 0 & \mathbf{I_{2x2}} \end{pmatrix} \oplus \mathbf{I_{4x4}},$$

is applied, and so is the beam splitting matrix,

$$\frac{1}{\sqrt{2}}\mathbf{I_{2x2}} \otimes \begin{pmatrix} \mathbf{I_{2x2}} & 0 & 0 & \mathbf{Z} & 0 & 0 \\ 0 & \mathbf{I_{2x2}} & 0 & 0 & \mathbf{Z} & 0 \\ 0 & 0 & \mathbf{I_{2x2}} & 0 & 0 & \mathbf{Z} \\ \mathbf{Z} & 0 & 0 & \mathbf{I_{2x2}} & 0 & 0 \\ 0 & \mathbf{Z} & 0 & 0 & \mathbf{I_{2x2}} & 0 \\ 0 & 0 & \mathbf{Z} & 0 & 0 & \mathbf{I_{2x2}} \end{pmatrix} \oplus \mathbf{I_{4x4}}.$$

The above result is in the Z-basis. For the X-basis, we apply the phase shift matrix to the early signal mode,

$$\mathbf{I_{12x12}} \oplus \begin{pmatrix} \cos(\phi) & \sin(\phi) \\ -\sin(\phi) & \cos(\phi) \end{pmatrix} \oplus \mathbf{I_{14x14}},$$

and then interfere the early and late signal mode at a 50:50 beamsplitter, described by the matrix,

$$\mathbf{I_{12x12}} \oplus \begin{pmatrix} \frac{1}{\sqrt{2}}\mathbf{I_{2x2}} & 0 & 0 & 0 & 0 & 0 & 0 & \frac{1}{\sqrt{2}}\mathbf{Z} \\ 0 & \mathbf{I_{2x2}} & 0 & 0 & 0 & 0 & 0 & 0 \\ 0 & 0 & \mathbf{I_{2x2}} & 0 & 0 & 0 & 0 & 0 \\ 0 & 0 & 0 & \mathbf{I_{2x2}} & 0 & 0 & 0 & 0 \\ 0 & 0 & 0 & 0 & \mathbf{I_{2x2}} & 0 & 0 & 0 \\ 0 & 0 & 0 & 0 & 0 & \mathbf{I_{2x2}} & 0 & 0 \\ 0 & 0 & 0 & 0 & 0 & 0 & \mathbf{I_{2x2}} & 0 \\ \frac{1}{\sqrt{2}}\mathbf{Z} & 0 & 0 & 0 & 0 & 0 & 0 & \frac{1}{\sqrt{2}}\mathbf{I_{2x2}} \end{pmatrix},$$

before the detection. In both the X- and Z-basis, we calculate the relevant threefold detection probabilities as follows:

$$\begin{aligned} P_{D_1D_4D_6} = \mathrm{Tr}\{\hat{\rho}'(1 &- \mathbb{I}_{a_l,b_e,b_l,c_e,c_l} \otimes |0\rangle\langle 0|_{a_e}^{\otimes 3} - \mathbb{I}_{a_e,a_l,b_e,c_e,c_l} \otimes |0\rangle\langle 0|_{b_l}^{\otimes 3} \\ &- \mathbb{I}_{a_e,a_l,b_e,b_l,c_e} \otimes |0\rangle\langle 0|_{c_l} + \mathbb{I}_{a_l,b_e,b_l,c_e} \otimes |0\rangle\langle 0|_{a_e,c_l}^{\otimes 4} \\ &+ \mathbb{I}_{a_e,a_l,b_e,c_e} \otimes |0\rangle\langle 0|_{b_l,c_l}^{\otimes 4} + \mathbb{I}_{a_l,b_e,c_e,c_l} \otimes |0\rangle\langle 0|_{a_e,b_l}^{\otimes 6} \\ &- \mathbb{I}_{a_l,b_e,c_e} \otimes |0\rangle\langle 0|_{a_e,b_l,c_l}^{\otimes 7})\}, \end{aligned} \tag{E.3}$$

where the subscripts a, b, and c represent the coherent state, idler, and signal modes respectively, and the subscripts e and l represent the early or late bin, respectively. Again, the subscripts of the identity matrix indicate which modes are traced out for a given calculation. Similarly as before, we use Eq. 9.14 to calculate each of the terms in Eq. E.3 to yield analytical expressions of the probabilities.

E.2 Maximum theoretical HOM interference visibilities

We plot the maximum two- and three-fold interference HOM interference visibilities using Eqs. 9.18 and 9.19. Complete indistinguishability $\zeta = 1$ as well as perfect transmission $\eta_s = \eta_i = 1$ is assumed. The visibilities with varied $|\alpha|^2$ and μ are shown in Fig. E.1, finding maximum two- and three-fold visibilities of $\sqrt{2} - 1$ and unity, respectively.

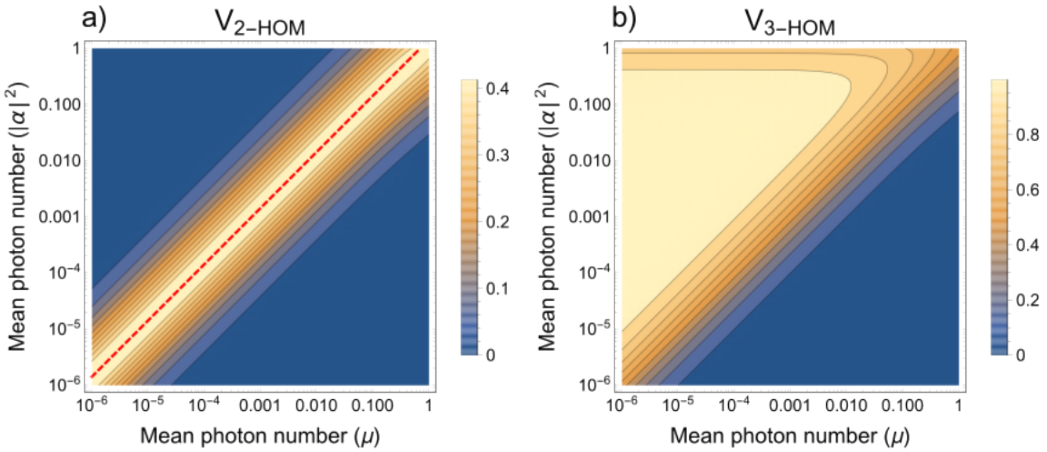

Figure E.1: Dependence of a) two-fold and b) three-fold HOM interference visibilities for varied mean photon numbers of the coherent state ($|\alpha|^2$) and TMSV (μ) assuming unity path efficiencies ($\eta_i, \eta_s = 1$) and photon indistinguishability ($\zeta = 1$). The red dashed line in a) corresponds to $|\alpha|^2 = \sqrt{2}\mu$, which maximizes the visibility for $|\alpha|^2, \mu \ll 1$.

The two-fold plot features a maximum along a symmetric diagonal for all $|\alpha|^2 \ll 1$ and $\mu \ll 1$. The maximum corresponds to the condition $|\alpha|^2/\mu = \sqrt{2}$, which is not equal to one due to the differences in number distributions. This condition effectively corresponds to matching of the mean photon numbers of the Poisson and thermal distributions, 'striking a balance" between the contributions of single photons interfering compared to $n = 2$ terms interfering with vacuum. Thus, the $\sqrt{2}$ acts to ensure that the balance is struck between the different field statistics. This is different than the case of identical field statistics, in which the maximum corresponds to an exact matching of mean photon numbers. Note the slight deviation in diagonal symmetry as $|\alpha|$ and μ approach 1; the balancing offered by $\sqrt{2}$ cannot hold because interference between single and $n = 2$ states begin to contribute to interference. Indeed the maximum visibility is not unity due to the non-zero contribution of $n = 2$ terms interfering with vacuum.

Owing to heralding, the three-fold plot has a plateau-like topography that extends the range of optimized visibility. A range of $|\alpha|^2 \ll 1$ will maximize the visibility to approach unity because the measurement is conditioned on three-fold detection and heralding will always guarantee a single photon in the idler mode when $\mu \ll 1$. Effectively, this regime renders the visibility independent of the probability of generating a photon in $|\alpha\rangle$. The threshold at $|\alpha|^2 \sim 1$ is predominantly due to $n = 2$ events from $|\alpha\rangle$ interfering with heralded single photons in the idler path, thereby reducing the maximum visibility. A steep diagonal threshold to the plateau is also present under conditions of $|\alpha|^2 \ll 1$, similar to that of the ridge in the two-fold plot. In this region, as μ is increased and approaches $|\alpha|^2$, the relative probability of heralding a multi-photon term increases, which decreases the visibility, and leads to the threshold topography along the diagonal. The condition $|\alpha|^2/\mu = \sqrt{2}$ does not maximize the visibility because heralding increases the effective mean photon number of the signal mode, and thus a lower value of μ is required to reach maximum visibility compared to two-fold HOM interference. This effect shifts the diagonal threshold to the left in Fig. E.1b.

E.3 Procedure for fitting HOM interference and teleportation fidelity datasets

We fit three data sets, two- and three-fold HOM interference visibilities as well as X-basis teleportation fidelity, using a piecewise model function based on our theory. Our code performs a nonlinear regression with Mathematica's `NonlinearModelFit` function with Differential Evolution as the fitting method. This global optimization approach is well-suited for fitting nonlinear models. As discussed in Sec. 9.4, we

utilize six physical parameters: η_s, η_{i2}, η_{i3}, μ, ζ_2, and ζ_3, as fitting parameters, subject to relevant physical constraints. Different mode mismatch and signal mode efficiency parameters, ζ_2 and ζ_3, as well as η_{i2} and η_{i3}, respectively, are ascribed to the two- and three-fold detection experiments. For the three-fold HOM and teleportation data, a shared ζ_3 is used, with independently determined parameters $\eta_{i3} = 1.2 \times 10^{-2}$, $\eta_s = 4.5 \times 10^{-3}$, and $\mu = 8.0 \times 10^{-3}$ from Ref. [1] remaining constant. The two-fold HOM data is fitted independently, retaining $\mu = 8.0 \times 10^{-3}$ as constant.

The fitting protocol is outlined as follows:

1. Use the `Map` and `Max` functions to ensure uncertainties in the data are bounded to be no less than the square root of the respective y-values.

2. Combine the three-fold HOM interference and X-basis visibility data, distinguishing them with unique markers. This is achieved using the `Join` and `Map` functions.

3. Formulate a modular fitting function, which can differentiate between X-basis visibility and three-fold HOM interference based on their respective markers. For two-fold HOM data, introduce a separate fitting function that considers the unique constraints of the two-fold detection experiment.

4. Establish the fitting framework, setting the fitting parameters such as η_{i2}, ζ_2, and ζ_3 accordingly, while holding the known parameters constant.

5. Engage in a simultaneous fitting procedure using `NonlinearModelFit`. This process will take into account the defined model function constraints, weigh the data points based on their squared uncertainties, and adopt the "DifferentialEvolution" fitting technique. The physical constraints on the fitting parameters will ensure that path efficiencies and indistinguishabilities are positive and no larger than unity.

The outcomes of the fits yield $\zeta_2 = 0.80 \pm 0.04$, $\eta_{i2} = (6.9 \pm 1.2) \times 10^{-2}$, and $\zeta_3 = 0.90 \pm 0.02$ as optimal parameter estimations.

E.4 Calculus of HOM interference visibility expressions

We differentiate the HOM visibility expressions of Eqs. 9.18 and 9.19 to determine the optimal choice of $|\alpha|^2$. The expression for the two-fold case (Eq. 9.18), when

differentiated with respect to $|\alpha|^2$ and evaluated for the relevant experimental and extracted parameters $\zeta_2 = 0.80$, $\eta_i = 6.9 \times 10^{-2}$ and $\mu = 8.0 \times 10^{-3}$, yields,

$$V'_{\text{2-HOM}}(|\alpha|^2) = \frac{-1.98781e^{|\alpha|^2/2} - 55552.9e^{0.500019|\alpha|^2} + 55554.9e^{0.500019|\alpha|^2}}{0.987811 - 1.98781e^{|\alpha|^2/2} + e^{|\alpha|^2}}. \tag{E.4}$$

The three-fold case (Eq. 9.19), given a similar treatment with $\zeta_3 = 0.90$, $\eta_i = 1.2 \times 10^{-2}$, $\eta_s = 4.5 \times 10^{-3}$ and $\mu = 8.0 \times 10^{-3}$, yields

$$\begin{aligned} V'_{\text{3-HOM}}(|\alpha|^2) = \frac{1}{\left(0.987811 - 1.98781e^{|\alpha|^2/2} + e^{|\alpha|^2}\right)^2}\Big[&-0.98179e^{|\alpha|^2/2} \\ &- 27439.2e^{0.500024|\alpha|^2} + 27440.2e^{0.500024|\alpha|^2} \\ &+ 2.22045 \times 10^{-16}e^{|\alpha|^2} + 2.63814e^{1.00002|\alpha|^2} \\ &- 2.65025e^{1.00002|\alpha|^2} + 0.993905e^{3|\alpha|^2/2} \\ &+ 27775.1e^{1.50002|\alpha|^2} - 27776.1e^{1.50002|\alpha|^2}\Big] \end{aligned} \tag{E.5}$$

Setting Eqs. E.4 and E.5 equal to zero and evaluating $|\alpha|^2$ results in 7.8×10^{-4} and 2.2×10^{-3}, respectively, which is consistent with the curves shown in Fig. 9.3.

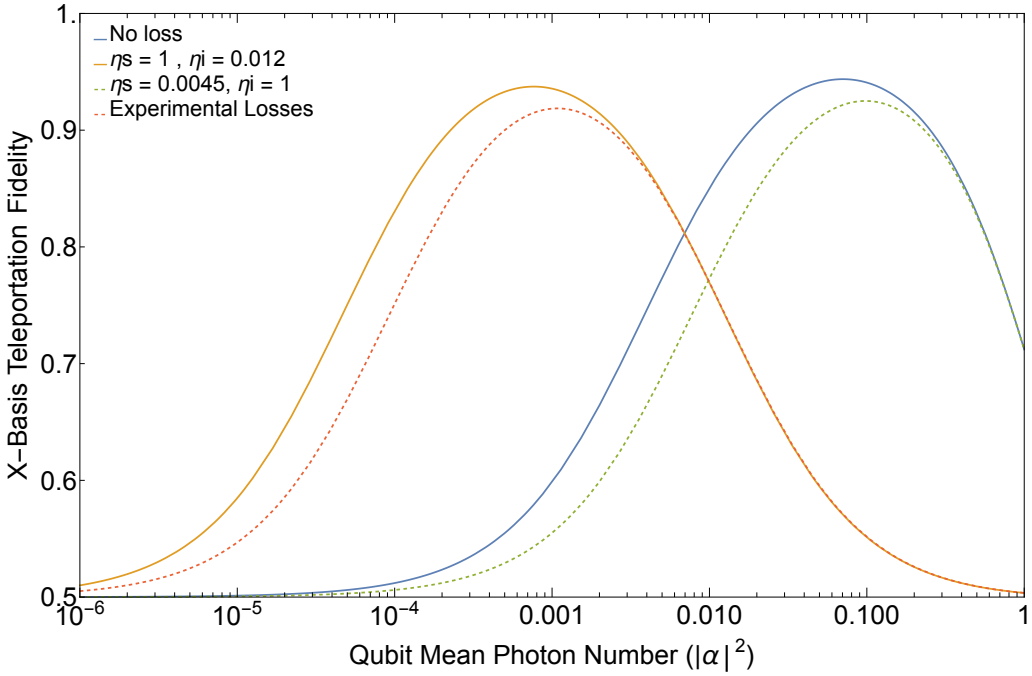

Figure E.2: Model of teleportation fidelity of X-basis states for varied $|\alpha|^2$ under conditions of varied signal and idler transmission efficiencies in blue, red, green, and orange, respectively, as described in Sec. 9.5 the main text, assuming complete indistinguishability $\zeta = 1$.

E.5 X-basis teleportation curves for varying transmission efficiencies and mean photon numbers

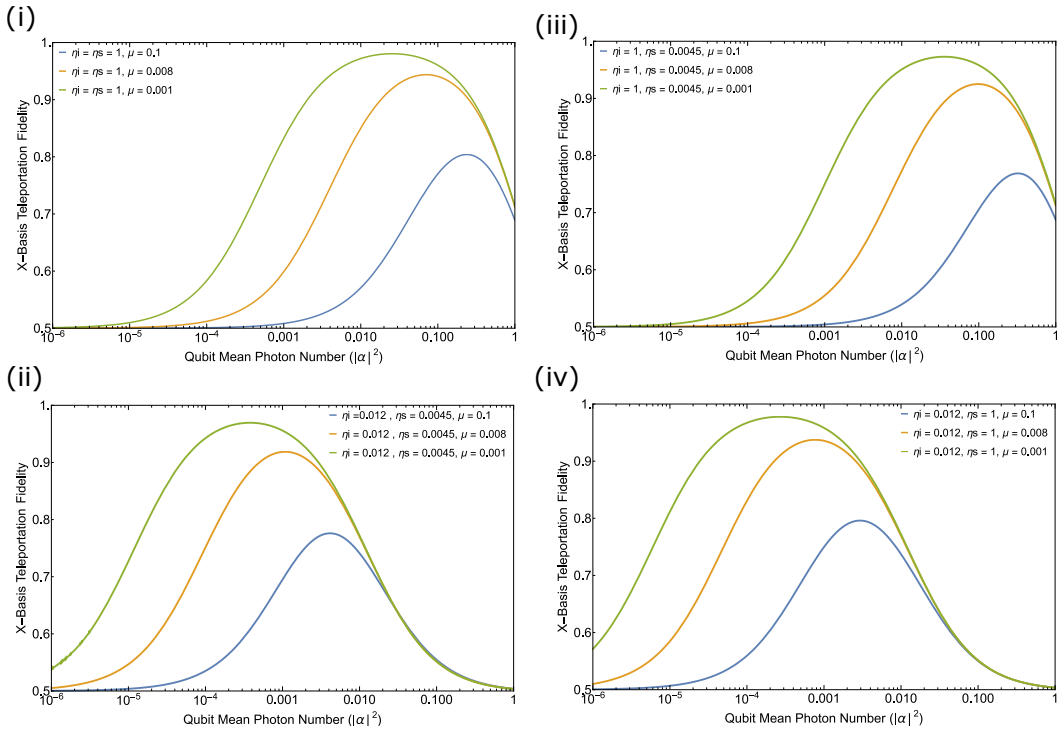

Figure E.3: Model of X-basis quantum teleportation fidelity for varied $|\alpha|^2$ and $\mu < 10^{-2}$, under varied signal and idler transmission efficiencies cases (i)-(iv), as discussed in Sec. 9.5, assuming complete indistinguishability $\zeta = 1$.

References

[1] Raju Valivarthi, Samantha I. Davis, Cristián Peña, et al. "Teleportation Systems Toward a Quantum Internet." In: PRX Quantum 1 (2 Dec. 2020), p. 020317. DOI: 10.1103/PRXQuantum.1.020317. URL: https://link.aps.org/doi/10.1103/PRXQuantum.1.020317.

Appendix F

TRAVERSABLE WORMHOLE SIGNATURES

To determine if the sparse learned Hamiltonian describes gravitational physics, we examine the Hamiltonian in Eq. 14.7,

$$\begin{aligned}\hat{H}_{L,R} = &- 0.36\hat{\psi}^1\hat{\psi}^2\hat{\psi}^4\hat{\psi}^5 + 0.19\hat{\psi}^1\hat{\psi}^3\hat{\psi}^4\hat{\psi}^7 \\ &- 0.71\hat{\psi}^1\hat{\psi}^3\hat{\psi}^5\hat{\psi}^6 + 0.22\hat{\psi}^2\hat{\psi}^3\hat{\psi}^4\hat{\psi}^6 \\ &+ 0.49\hat{\psi}^2\hat{\psi}^3\hat{\psi}^5\hat{\psi}^7,\end{aligned} \tag{F.1}$$

via two orthogonal approaches: first, we verify that it replicates relevant dynamics of the dense SYK Hamiltonian; and secondly, we evaluate if it satisfies necessary criteria of general holographic systems. These criteria are stricter than the similarity of dynamical observables: they include perfect size winding — the strongest form of size winding, which is sufficient to provide a geometric interpretation [1, 2, 3] — the causal time-ordering of teleported signals, which shows that the teleportation is not occurring due to random scrambling, and a time delay predicted by scattering in the bulk.

The learned Hamiltonian is consistent with gravitational dynamics of the dense SYK Hamiltonian beyond its training data. The mutual information $I_{PT}(t_1)$ for fixed t_0 shows behavior compatible with a qubit emerging from a traversable wormhole (Fig. 14.3a). The mutual information peak height and position strongly resemble the large-N SYK model computation in the double-scaled limit (Fig. F.1a). In the high-temperature limit, the mutual information asymmetry between couplings with $\mu < 0$ and $\mu > 0$ diminishes, corresponding to teleportation occurring via scrambling instead of through the wormhole, consistent with theoretical expectations [4]. Additionally, the learned Hamiltonian scrambles and thermalizes similarly to the original SYK model as characterized by the four-point and two-point correlators $-\langle[\hat{\psi}(0), \hat{\psi}(t)]^2\rangle$ and $\langle\hat{\psi}(0)\hat{\psi}(t)\rangle$ (Fig. F.1b). Since the scrambling time is approximately equal to the thermalization time, the gravitational interpretation suggests the boundary lies near the horizon.

Beyond comparison to the dense SYK model, we proceed to evaluate more general behavior predicted from gravity. The property of "perfect" size winding provides a necessary and sufficient "litmus test" to identify traversable wormhole behavior,

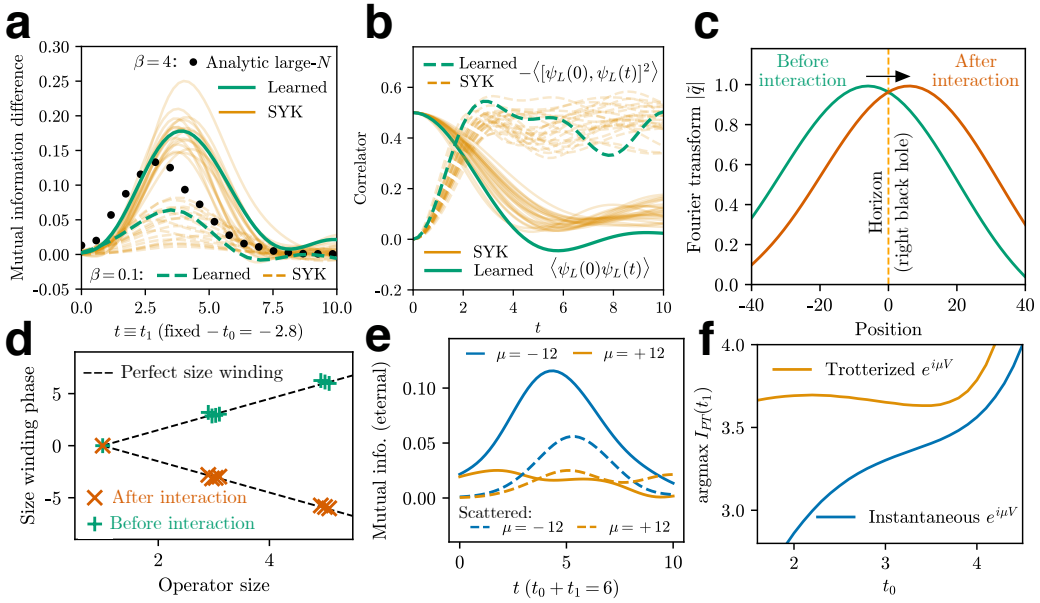

Figure F.1: Signatures of traversable wormhole dynamics for the learned sparse SYK Hamiltonian (Eq. F.1). a) Mutual information asymmetry $I_{\mu<0}(t) - I_{\mu>0}(t)$ for the learned (green) and SYK Hamiltonians (orange) at the low-temperature gravitational limit (solid) and high-temperature scrambling limit (dashed). An analytic computation in the large-N limit of the SYK model using chord diagrams (black) is shown for low temperatures, showing agreement with the peak position and height. b) Two-point function (solid) and four-point function (dashed), indicating thermalization time and scrambling time, respectively, of the SYK (orange) and learned (green) Hamiltonians. c) Bulk location of the infalling particle before and after the interaction with respect to the black hole horizon, as given by the Fourier transform $|\tilde{q}|$ of the winding size distribution. d) Perfect size winding before (green) and after (brown) the interaction; data at each operator size is horizontally staggered to make the different values visually distinct. The black dashed lines show a linear fit ($R^2 = 0.999$) with equal but opposite slopes, corresponding to the reversal of winding direction after the interaction. e) Shapiro time delay in the eternal traversable wormhole protocol caused by scattering in the bulk. The peak shifts right when an additional qubit is sent through the wormhole in the opposite direction (dashed) compared to sending a single qubit from left to right (solid). f) Causally time-ordered teleportation. The position of the mutual information peak is shown for an instantaneous at $t = 0$ (blue) and prolonged (orange) interaction over $t \in [-1.6, 1.6]$.

holding for quantum systems with a nearly AdS_2 bulk [1, 2, 3]. Perfect size winding is equivalent to a maximal Lyapunov exponent at large N, but unlike the Lyapunov exponent, size winding remains a meaningful quantity at small N. Non-gravitational systems, such as random non-local Hamiltonians, may teleport in the low-temperature limit with a weak asymmetry in μ; unlike gravitational systems, these have "imperfect" size winding. Systems that teleport in the high-temperature fully scrambled regime, such as random circuits [5] or chaotic spin chains, do not exhibit any size winding.

Given the thermal state $\rho_\beta \propto e^{-\beta \hat{H}_L}$, size winding describes the decomposition $\rho_\beta^{1/2} \hat{\psi}_L^1(t) = \sum_P c_P(t) \hat{\psi}_L^P$ over strings of $|P|$ fermions. The system exhibits perfect size winding at time t if the c_P^2 coefficients have a phase that linearly depends on $|P|$. For the Hamiltonian in Eq. F.1, an injected fermion is supported by operators of three sizes. We find that the learned Hamiltonian exemplifies perfect size winding (Fig. F.1c, d) at the time of teleportation, with the phases of the eight nonzero coefficients forming a line with $R^2 = 0.999$. This analysis shows that teleportation under the learned Hamiltonian is caused by the "teleportation by size" mechanism, not by scrambling or other non-gravitational dynamics. We visualize the resulting geometric interpretation of the learned Hamiltonian by taking the Fourier transform to obtain the bulk location of the infalling particle relative to the horizon.

The Hamiltonian is shown to adhere to the microscopic mechanism of wormhole teleportation via its perfect size winding description. To observe this at a macroscopic scale, we examine two phenomena: a Shapiro time delay and causal time-ordering of signals. For the time delay, we interrogate the learned Hamiltonian within the eternal traversable wormhole framework [6]. Besides sending a single qubit from left to right, we insert an additional qubit across the wormhole from right to left. From a gravitational perspective, this should cause the left-to-right signal to arrive later due to scattering in the bulk. We observe this in the learned Hamiltonian (Fig. F.1e). For causal time-ordering, we inspect the order in which infalling particles emerge from the wormhole. If a geometric interpretation is valid, infalling particles should arrive in a causally consistent order (Fig. 14.1b): signals must emerge in the same order they enter (time-ordered teleportation). In contrast, teleportation in the fully scrambled regime produces a time-inverted ordering of signals. Our learned Hamiltonian generates time-ordered teleportation (Fig. F.1f). The position of the mutual information peak is shown for an instantaneous at $t = 0$ (blue) and prolonged (orange) interaction over $t \in [-1.6, 1.6]$. A positive slope indicates time-inverted

teleportation and a negative slope indicates time-ordered teleportation. When the coupling is applied over a window of time, the time-ordering of signals confirms through-the-wormhole behavior. When the coupling is instantaneous, the decreased slope suggests a combination of teleportation by scrambling and by traversing the wormhole.

The above analyses demonstrate gravitational teleportation by the learned Hamiltonian via an emergent wormhole; additional analyses examining spectral characteristics, dynamics at different temperatures and interaction strengths, and further properties of size winding are provided in the Supplementary Information of Ref. [7].

References

[1] Adam R. Brown, Hrant Gharibyan, Stefan Leichenauer, Henry W. Lin, Sepehr Nezami, Grant Salton, Leonard Susskind, Brian Swingle, and Michael Walter. Quantum Gravity in the Lab: Teleportation by Size and Traversable Wormholes. 2021. arXiv: 1911.06314 [quant-ph].

[2] Sepehr Nezami, Henry W. Lin, Adam R. Brown, Hrant Gharibyan, Stefan Leichenauer, Grant Salton, Leonard Susskind, Brian Swingle, and Michael Walter. Quantum Gravity in the Lab: Teleportation by Size and Traversable Wormholes, Part II. 2021. arXiv: 2102.01064 [quant-ph].

[3] Thomas Schuster, Bryce Kobrin, Ping Gao, Iris Cong, Emil T Khabiboulline, Norbert M Linke, Mikhail D Lukin, Christopher Monroe, Beni Yoshida, and Norman Y Yao. "Many-body quantum teleportation via operator spreading in the traversable wormhole protocol." In: Physical Review X 12.3 (2022), p. 031013.

[4] Ping Gao and Daniel Louis Jafferis. "A traversable wormhole teleportation protocol in the SYK model." In: Journal of High Energy Physics 2021.7 (2021), pp. 1–44.

[5] Kevin A. Landsman, Caroline Figgatt, Thomas Schuster, Norbert M. Linke, Beni Yoshida, Norm Y. Yao, and Christopher Monroe. "Verified quantum information scrambling." In: Nature 567.7746 (2019), pp. 61–65.

[6] Juan Maldacena and Xiao-Liang Qi. Eternal traversable wormhole. 2018. arXiv: 1804.00491 [hep-th].

[7] Daniel Jafferis, Alexander Zlokapa, Joseph D. Lykken, David K. Kolchmeyer, Samantha I. Davis, Nikolai Lauk, Hartmut Neven, and Maria Spiropulu. "Traversable wormhole dynamics on a quantum processor." In: Nature 612.7938 (2022), pp. 51–55.